Cell

Best of 2014

Featuring SnapShot Collection

CellPress
www.cell.com

Patient - derived samples

Functional metabolic data on live cells in real time!

Phenotyping

Pairwise comparisons

XFp Extracellular Flux Analyzer

The new, compact XFp Analyzer is built on innovative and proven XF Technology, and is ideal for use in pairwise comparisons, phenotyping and with patient-derived samples. The XFp Analyzer delivers the Gold Standard assays that are providing scientists with the necessary functional data that is enabling a greater understanding of cell metabolism.

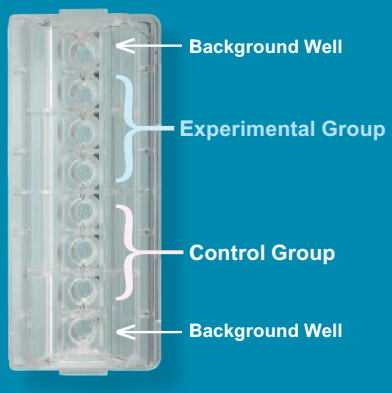

See what's possible.

Scan this QR code to view videos and see what XF Technology Analyzer can achieve. Visit www.seahorsebio.com/XFp for more information!

Seahorse Bioscience

Visit Us at the 2014 ASCB/IFCB Meeting, Booth 505

Create Your Masterpiece

Direct Antibody Conjugates for Multicolor Microscopy

For multicolor fluorescence microscopy, bright fluorescence with little background is critical for specific detection of antigens. Furthermore, directly labeled antibodies are essential for multicolor microscopy. BioLegend now introduces our line of antibodies directly conjugated to **Alexa Fluor® 594**, a bright, stable fluorophore emitting into the red range of the color spectrum, ideal for imaging applications. **Brilliant Violet 421™** is an exceptionally bright and photostable fluorescent polymer well-suited for microscopy applications. BioLegend has over 100 IHC or IF suitable clones conjugated to Brilliant Violet™, Alexa Fluor®, and DyLight®, including secondary antibodies and streptavidin.

Learn more: **biolegend.com/AF594**
biolegend.com/brilliantviolet

BioLegend®

Alexa Fluor® 594 anti-Ki-67

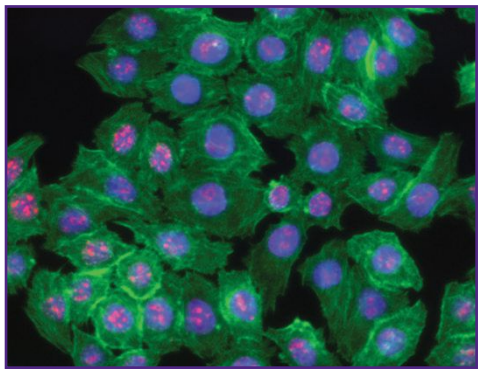

HeLa cells were fixed, permeabilized, and blocked, then intracellularly stained with Ki-67 (clone Ki-67) Alexa Fluor® 594 (*red*) and Alexa Fluor® 488 Phalloidin (*green*). Nuclei were counterstained with DAPI (*blue*). The image was captured with 40x objective.

BioLegend is ISO 9001:2008 and ISO 13485:2003 Certified

Toll-Free Tel: (US & Canada): 1.877.BIOLEGEND (246.5343)
Tel: 1.858.768.5800
biolegend.com

08-0040-07

World-Class Quality | Superior Customer Support | Outstanding Value

Living up to Life

Come see us at SfN 2014 and ASCB 2014

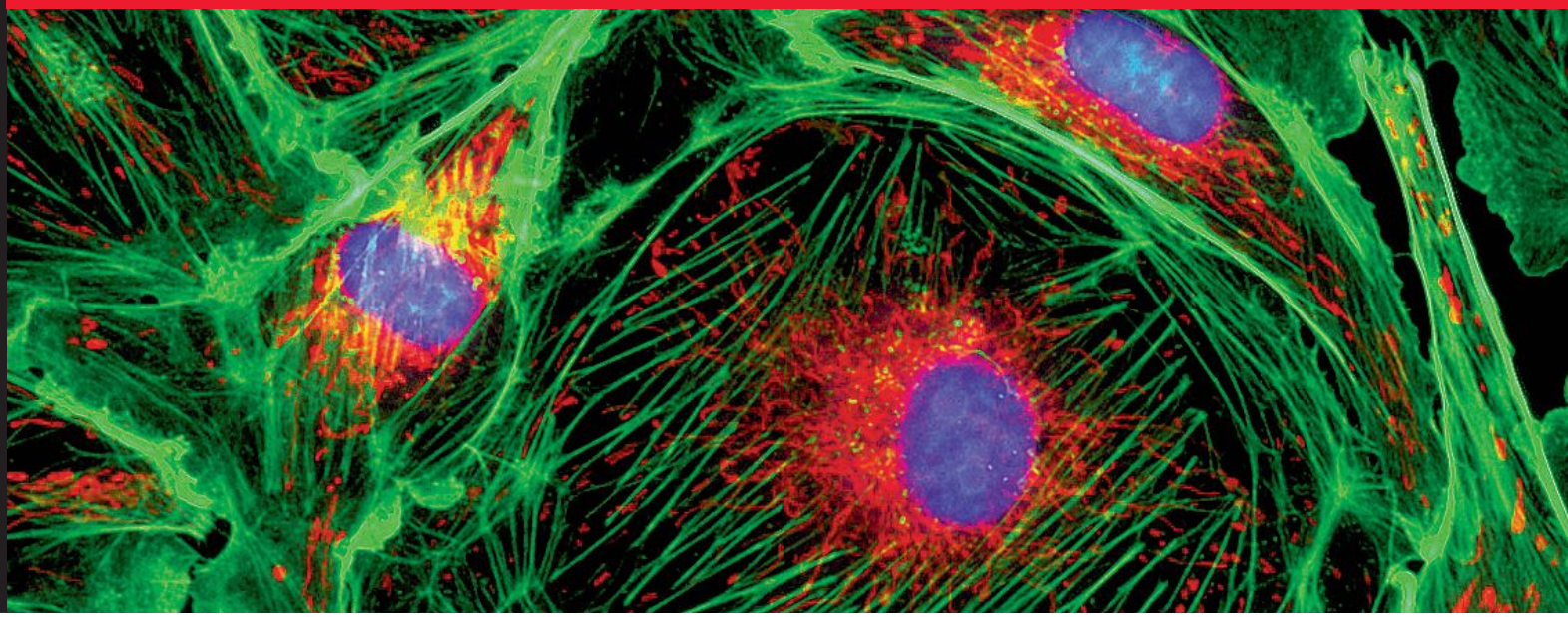

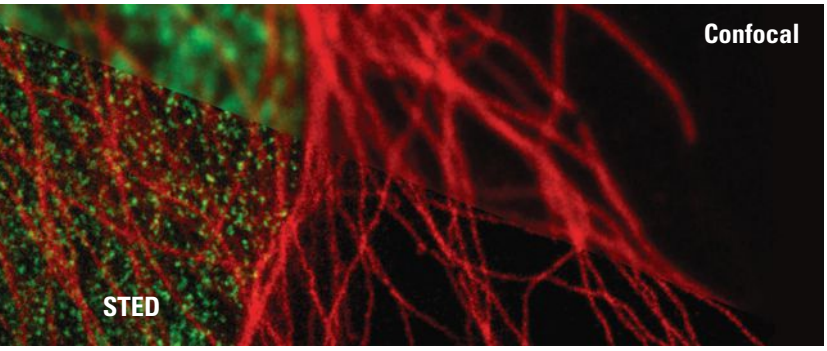

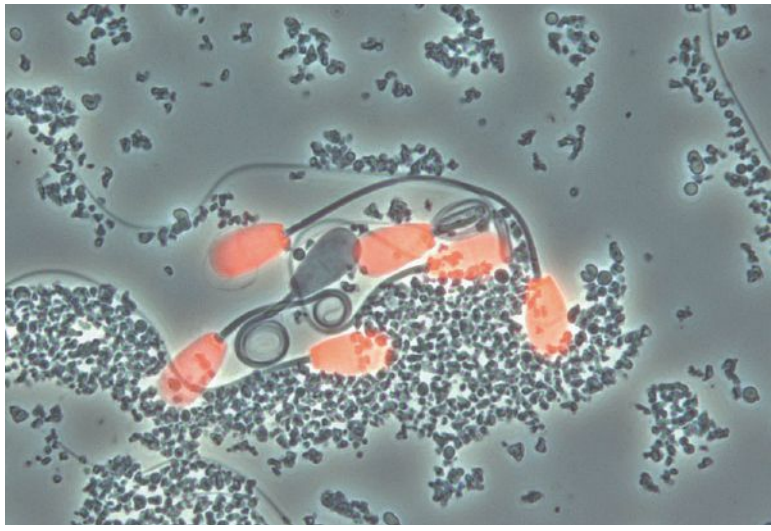

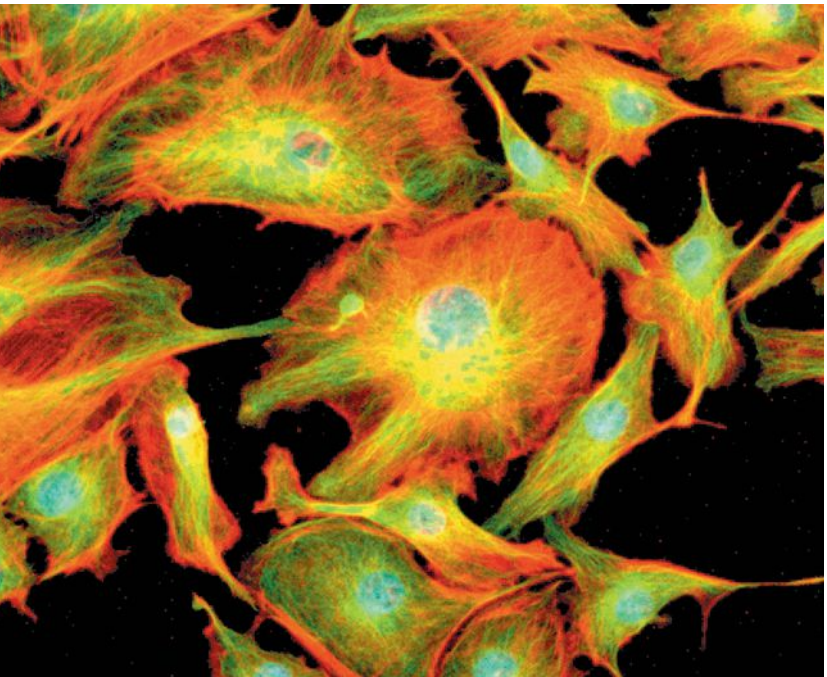

Leica
MICROSYSTEMS

Infinite Possibilities ... for Your Research

The observation of live cells requires special care and fast image acquisition.

Live cell imaging microscopes from Leica Microsystems offer innovations that allow you to take your research into new areas. From the quick check and tissue culture Leica DMi1 inverted microscope to the Leica TCS SP8 confocal platform, Leica Microsystems delivers powerful solutions for precise analysis and documentation.

- See how the NEW Leica DMi8 – facilitated by its modular design, intuitive software, and open Infinity Port concept – is the one platform to match the future of life science.
- The Leica TCS SP8 confocal simplifies the challenges of imaging living specimens without compromising the details that matter most to your research.

Leica DMi1

Leica DMi8

Leica TCS SP8

Visit us at the Society for Neuroscience Annual Meeting booth #3003

Visit us at the American Society for Cell Biology booth #801

www.leica-microsystems.com/ascb2014

Try our new Cell and Tissue Culture Microscope
FREE for a Limited Time
leica-microsystems.com/tryleica

Molecules That Count®

Gene Expression • miRNA Expression • Epigenomics • Copy Number Variation • Single Cell

www.nanostring.com

Multiplex REDEFINED

The nCounter® Analysis System offers digital detection of target molecules and high levels of multiplexing with no compromise between data quality and data quantity. Data output files include the target identifier and count number along with a comprehensive set of internal controls that enable each assay to be highly quantitative and reproducible.

- Multiplex up to 800 targets in a single tube
- Directly assay tissue, cell & blood lysates, FFPE
- No amplification*, no RT, no sample partitioning
- Fully automated with 15-min hands-on time
- Simple workflow – up to 800 targets in a single tube

www.nanostring.com/technology

nCounter® Analysis System

Direct Digital Quantification of Nucleic Acids

nanoString® TECHNOLOGIES

www.nanostring.com | info@nanostring.com | 888 358 6266

FOR RESEARCH USE ONLY. Not for use in diagnostic procedures.

*Single Cell assay requires reverse transcription and amplification prior to analysis on the nCounter System.

Foreword

2014 was a landmark year for *Cell*, as the journal celebrated its 40th anniversary. Throughout the year, we have *Cell*-ebrated the exciting biology published on the pages of *Cell*, looking back at the tremendous advancements in science since 1974. While we looked back over the past four decades, we were equally excited about the present and future, as we saw fascinating science being submitted from around the world. We'd like to invite you to join us in enjoying this *Best of Cell collection*, an inspiring look back at some of these notable stories.

We have selected the papers presented here based on a number of criteria. We began by looking at the most highly read papers, based on article downloads and html usage. Within this list, we sought papers that best represent the vision for the scope and breadth of *Cell*. We've included papers that we were exceptionally excited about when they first came in, ones that we found ourselves talking about in the hallways of the office and at the proverbial water cooler, and papers that the reviewers were extremely enthusiastic about.

Looking at the papers with the greatest numbers of downloads gives a sense for which papers caught the eye of a large swath of the scientific community. Of course, this measure is heavily slanted towards articles published in the beginning of the year, so we took efforts to "control" for that. We've also included a selection of SnapShots that we hope will pique your interest and help your research.

Cell was conceived of as and continues to be a journal representing the broad interests of the biology community. Over the years, the boundaries of this community have expanded to welcome chemists, physicists, clinicians, and a host of other researchers in the spirit of collaboration and cross-pollination of ideas. *Cell*'s scope has grown with the community, and you'll see that reflected in this collection.

Clearly, any list like this must also omit many important and valuable papers, but hopefully this collection gives you a flavor of some of the standout moments of the year.

Of course, all of this great science would not be featured in *Cell* if it were not for the support of the scientists who submit their best work for consideration, provide expertise as advisors and peer reviewers, serve on our editorial board, and read the journal and share our enthusiasm for exciting biology. *Cell* is first and foremost a journal of, by, and for scientists. Thank you all for your contributions.

We hope that you will enjoy reading this special collection, and we welcome your feedback on how we are doing at the journal (you can also access this collection online at www.cell.com/bestof, where you can see freely available digital editions of other Cell Press journals' *Best of… collections*). Please feel free to leave a comment at Cell.com on a paper that has caught your interest, or drop us a line at celleditor@cell.com or email one of the editors directly. We are always happy to hear from you.

If you haven't gotten a chance to revel in our 40 years, check out www.cell.com/40/home. Here, you can read highlights from the past four decades, walk through our history with our Cell Lines timelines, and hear our "40 under 40"—top scientists who haven't yet celebrated their 40th birthdays—talk about the direction they envision science going.

We hope that you have had a fruitful 2014, and we look forward to working with you in 2015 and beyond.

Emilie, Elena, Karen, Robert, Mirna, Cindy, Steve, João, Sri, Lara, and Jiaying

Cell

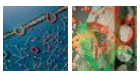

Staining the brain: a novel method for streamlined immunohistochemistry

Summary

Because the brain's function and dysfunction is determined by the spatiotemporal localization of proteins, and because there is no meaningful cell culture model of the brain, immunohistochemistry (IHC) of brain tissue remains a linchpin of neuroscience. While manual IHC provides reproducible tissue staining, it is time-consuming and laborious. Multiple hands-on steps translate into high potential for inherent process variability.

Here, we present a novel IHC format using the new SNAP i.d.® 2.0 protein detection system (Figure 1). This system streamlines the immunodetection reagent application phases of antigen detection using a controlled vacuum force that removes solutions evenly from all slides at once – in seconds. Tissue slides can be processed in about two hours using any typical IHC protocol with no detectable staining artifacts or loss in sensitivity.

We demonstrate the versatility of the system and its ability to minimize slide handling while generating consistent results. We compare sensitivity and staining patterns to those achieved using standard (manual) IHC protocols, using tissue sections from human kidney, Alzheimer's disease (AD) human brain, and mouse brain.

Figure 1. The SNAP i.d.® 2.0 system for immunohistochemistry. Flexibility of multiple slide configurations enables the processing of 1 to 24 slides at a time. The system is compatible with standard IHC slides and protocols and employs a controlled, uniform vacuum force to rapidly and thoroughly remove reagents during the blocking, washing, and antibody incubation steps. Antibodies can be collected and reused.

Consistency in the staining process

Twelve slides of formalin-fixed paraffin-embedded (FFPE) human kidney tissue sections (Figure 2) were simultaneously processed using vacuum-driven IHC and the traditional manual process, in order to detect aquaporin 1. Aquaporin 1 (stained in brown) is an integral membrane protein capable of forming water-specific channels to increase permeability. High sensitivity and lower background was observed in all the samples. We also observed consistent, sensitive staining in fresh, frozen rat kidney tissue (not shown).

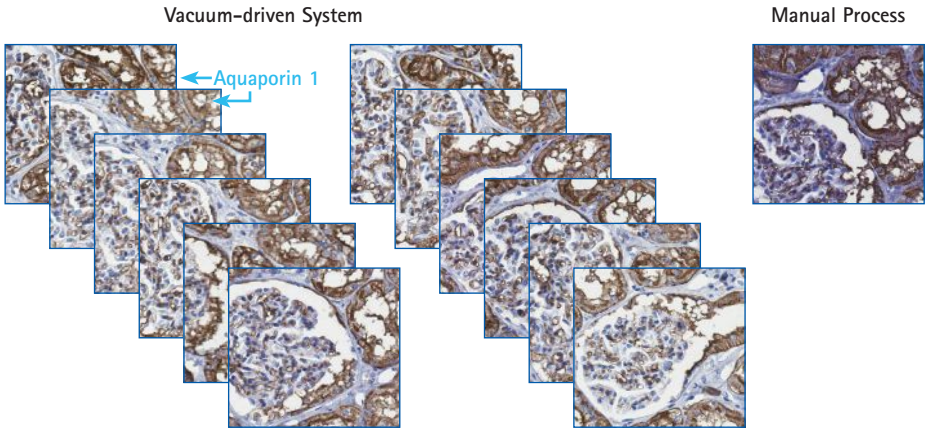

Figure 2. Consistent detection of aquaporin 1 in 20 µm sections of FFPE human kidney tissue using vacuum-driven IHC. Aquaporin 1 was detected in the proximal tubes of human kidney tissue using anti-aquaporin 1 primary antibody (EMD Millipore) at 1:2,000 dilution (60 min) and stained with HRP-DAB. Heat-induced epitope retrieval was performed for 15 min at 110 °C.

Equivalent results: vacuum-driven vs. manual staining of brain tissue

As shown in Figure 3A, samples of human brain thalamus were stained with anti-amyloid β primary antibody (EMD Millipore) using the traditional manual process and compared with staining using the SNAP i.d.® 2.0 system. Amyloid β peptide, one of the major constituents of the plaques occurring in Alzheimer's disease, was detected in the samples processed by both methods. A negative control slide (no primary antibody) was also processed using the vacuum-driven IHC system (center panel of Figure 3A) and showed no staining, indicating that positive signal was not due to nonspecific signals from the immunodetection reagents.

Human cerebral cortex and cerebellum were stained for the neuron-specific protein NeuN (Figure 3B). The distribution of NeuN is restricted to neuronal nuclei, perikarya and some proximal neuronal processes in fetal and adult brains; however, some cells, like the Purkinje, inferior olivary, and dentate nucleus, fail to show positive NeuN staining at any age.

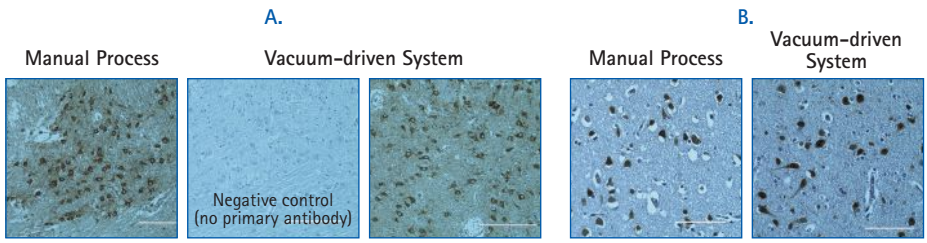

Figure 3. Comparing staining of human brain thalamus (anti-amyloid β) in Panel A and human cerebral cortex (anti-NeuN) in Panel B using manual IHC and the vacuum-driven SNAP i.d.® 2.0 system. Images were acquired at 20X magnification.

EMD MILLIPORE

Antibody recovery and reuse

Deposits of amyloid β in the brain of AD patients were detected in human cerebral cortex samples processed by the manual traditional method as well as in samples prepared using the vacuum-driven system, even after three cycles of antibody use, recovery and reuse, with a volumetric recovery higher of 90% even after the third collection (Figure 4 and Table 1).

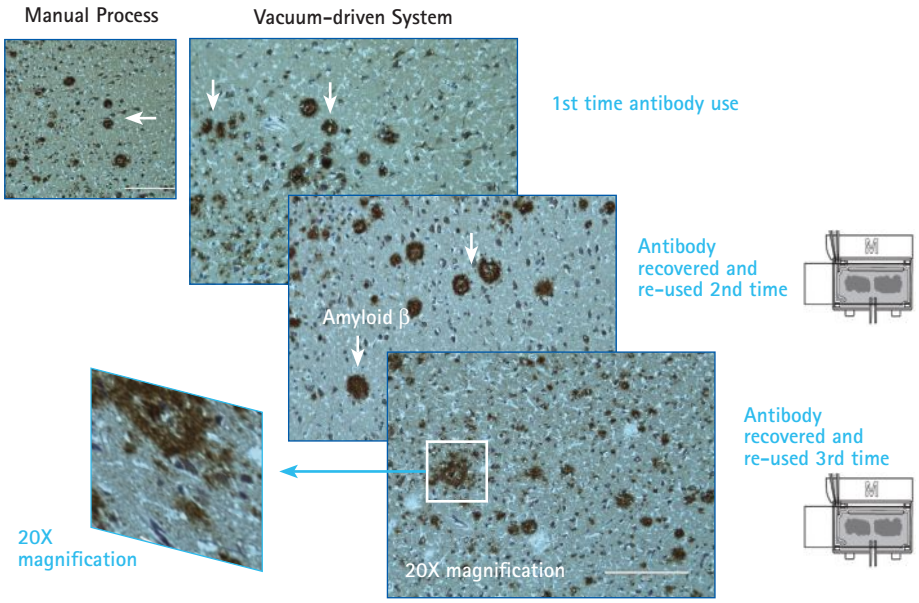

Figure 4. **Antibody could be used three times with no detectable change in sensitivity.** A total of 600 µL of mouse monoclonal anti-amyloid β (1:2,000) was used to probe three slides of FFPE human AD brain tissue slides, with a volumetric recovery higher than 90% even after the third recovery with no loss in sensitivity compared to manual methods. White arrows point to amyloid β signal and higher magnification inset shows details of plaque formation.

	Vol. recovered (µL)	% recovery of original volume
Recovery 1	590	98
Recovery 2	584	97
Recovery 3	573	96

Table 1. Anti-amyloid β antibody recovery after each round of use in the SNAP i.d.® system.

Fluorescent localization of mouse brain markers in FFPE tissue

Using the vacuum-driven SNAP i.d.® system for IHC, FFPE mouse brain was analyzed using a cocktail of two different primary antibodies [anti-mouse Glial Fibrillary Acidic Protein (GFAP, EMD Millipore), diluted 1:1,000) and anti-rabbit Sox 11 (EMD Millipore, diluted 1:500)]. Fluorescent detection was performed after the addition of goat anti-mouse DyLight® 488 and goat anti-rabbit DyLight® 549 and counterstained with DAPI (blue stained nuclei).

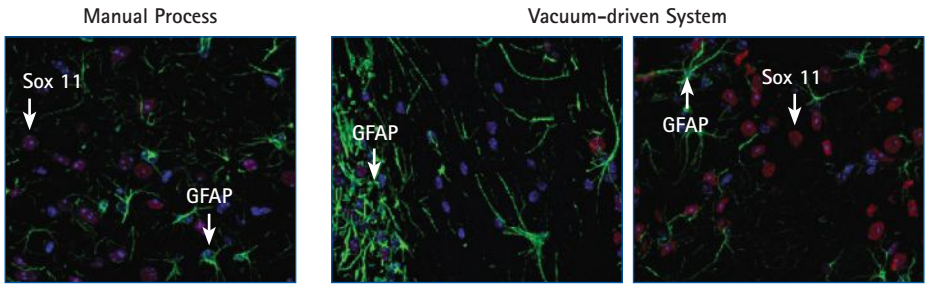

Figure 5. Fluorescent localization of markers in FFPE mouse brain tissue using manual and vacuum-driven IHC shows equivalent expression patterns.

Conclusions

The vacuum-driven SNAP i.d.® 2.0 system helps to streamline the immunohistochemistry process by reducing the slide handling and by eliminating the tedious process of using a pap pen. As this system is best suited to low and medium throughput workflows, it promises to be helpful in the antibody optimization process and/or during the process of reagent scale-up for automated systems. Different manual protocols, such as chromogenic staining and fluorescent staining, can be reproduced easily in this vacuum-driven IHC system, and it can be used for a variety of tissues, including fresh frozen (not shown) and FFPE archival samples.

Learn more about the SNAP i.d.® 2.0 system for IHC at: **www.emdmillipore.com/snap**

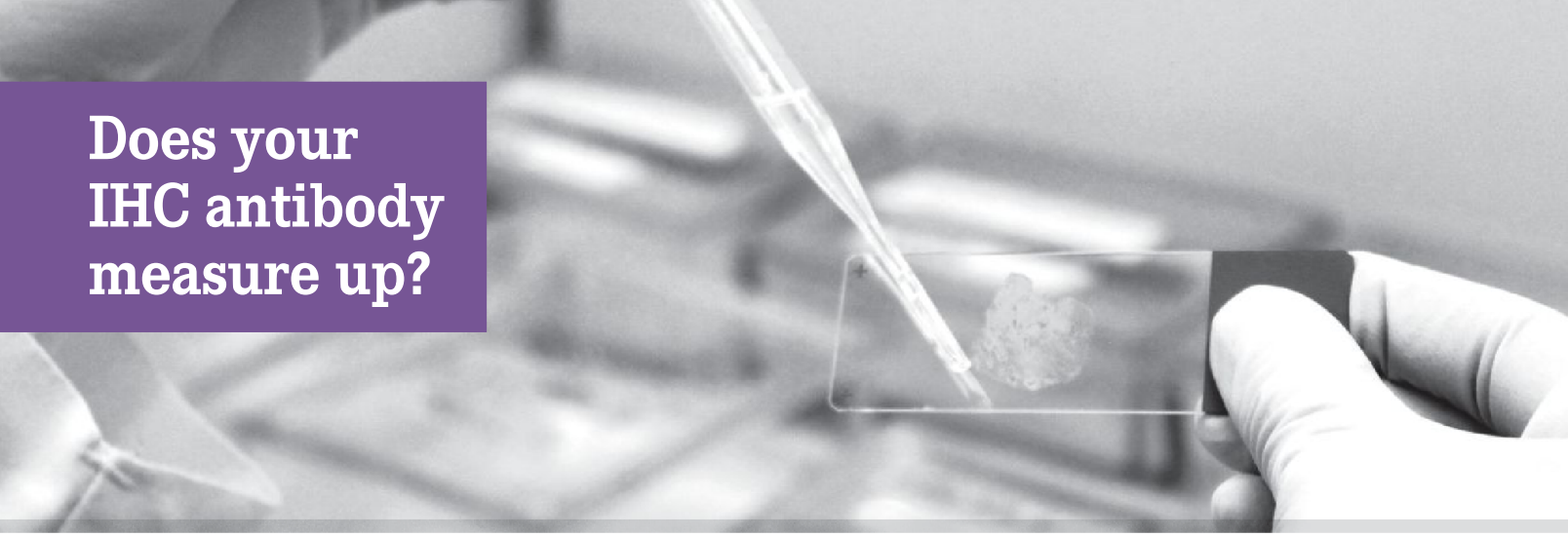

Does your IHC antibody measure up?

Rigorously Validated IHC Antibodies Against High Impact Research Targets

from Cell Signaling Technology

Paraffin-embedded human lung and ovarian carcinoma tissues using CST™ HER3/ErbB3 (D22C5) XP® Rabbit mAb #12708 or Company 2 mouse monoclonal antibody.

	CST HER3/ErbB3 (D22C5) XP® Rabbit mAb #12708	Company 2 Mouse Monoclonal Antibody
Lung Carcinoma	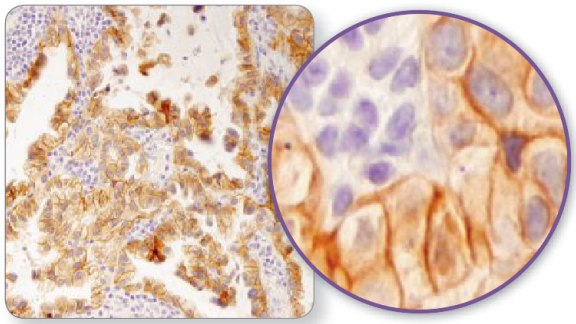 Strong, specific plasma membrane-associated HER3 staining in the epithelium	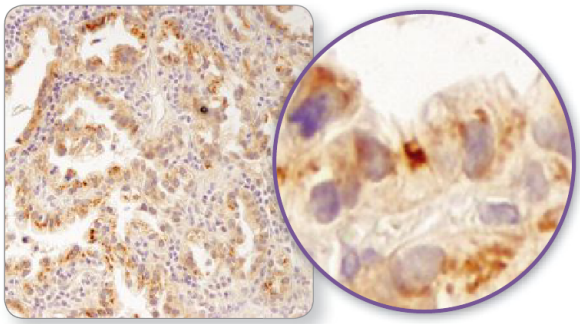 Non-specific, non-membranous staining in the epithelium
Ovarian Carcinoma	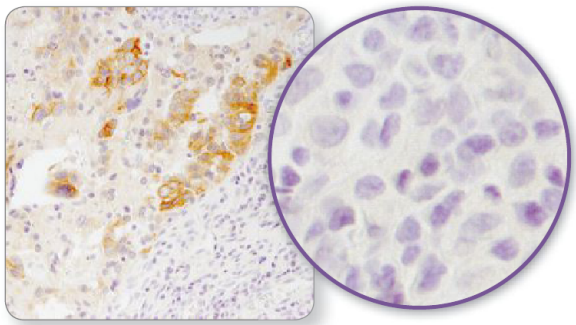 Strong, specific signal in tumor cells, and no staining seen in stromal cells	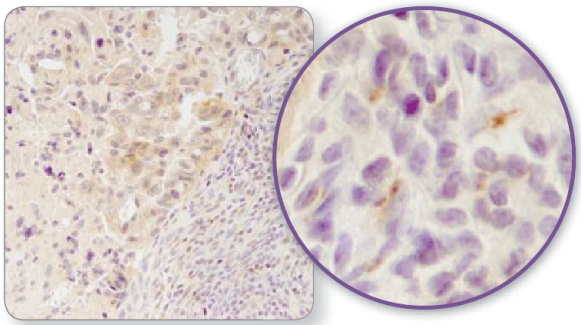 Weak signal in tumor cells, and non-specific staining in stromal cells

WB IP IHC IF F ChIP

For Research Use Only. Not For Use In Diagnostic Procedures.

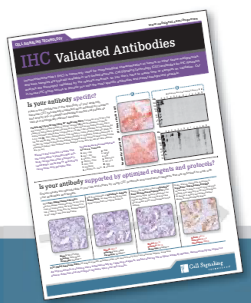

Skeptical? Go to **www.cellsignal.com/ihccell** to see more

Cell Signaling TECHNOLOGY®

14PADIHC_NONE0160ENG_00

Cell
Best of 2014

SnapShots

Reviews

Articles

(continued)

Discovery of a Class of Endogenous Mammalian Lipids with Anti-Diabetic and Anti-inflammatory Effects	*Mark M. Yore, Ismail Syed, Pedro M. Moraes-Vieira, Tejia Zhang, Mark A. Herman, Edwin A. Homan, Rajesh T. Patel, Jennifer Lee, Shili Chen, Odile D. Peroni, Abha S. Dhaneshwar, Ann Hammarstedt, Ulf Smith, Timothy E. McGraw, Alan Saghatelian, and Barbara B. Kahn*
Epigenetic Priming of Memory Updating during Reconsolidation to Attenuate Remote Fear Memories	*Johannes Gräff, Nadine F. Joseph, Meryl E. Horn, Alireza Samiei, Jia Meng, Jinsoo Seo, Damien Rei, Adam W. Bero, Trongha X. Phan, Florence Wagner, Edward Holson, Jinbin Xu, Jianjun Sun, Rachael L. Neve, Robert H. Mach, Stephen J. Haggarty, and Li-Huei Tsai*
The Bacterial Cytoplasm Has Glass-like Properties and Is Fluidized by Metabolic Activity	*Bradley R. Parry, Ivan V. Surovtsev, Matthew T. Cabeen, Corey S. O'Hern, Eric R. Dufresne, and Christine Jacobs-Wagner*
Generation of Gene-Modified Cynomolgus Monkey via Cas9/RNA-Mediated Gene Targeting in One-Cell Embryos	*Yuyu Niu, Bin Shen, Yiqiang Cui, Yongchang Chen, Jianying Wang, Lei Wang, Yu Kang, Xiaoyang Zhao, Wei Si, Wei Li, Andy Peng Xiang, Jiankui Zhou, Xuejiang Guo, Ye Bi, Chenyang Si, Bian Hu, Guoying Dong, Hong Wang, Zuomin Zhou, Tianqing Li, Tao Tan, Xiuqiong Pu, Fang Wang, Shaohui Ji, Qi Zhou, Xingxu Huang, Weizhi Ji, and Jiahao Sha*
Neural Networks of the Mouse Neocortex	*Brian Zingg, Houri Hintiryan, Lin Gou, Monica Y. Song, Maxwell Bay, Michael S. Bienkowski, Nicholas N. Foster, Seita Yamashita, Ian Bowman, Arthur W. Toga, and Hong-Wei Dong*
Tissue-Specific Signals Control Reversible Program of Localization and Functional Polarization of Macrophages	*Yasutaka Okabe and Ruslan Medzhitov*
Skin β-Endorphin Mediates Addiction to UV Light	*Gillian L. Fell, Kathleen C. Robinson, Jianren Mao, Clifford J. Woolf, and David E. Fisher*
Vulnerability of Glioblastoma Cells to Catastrophic Vacuolization and Death Induced by a Small Molecule	*Satish Srinivas Kitambi, Enrique M. Toledo, Dmitry Usoskin, Shimei Wee, Aditya Harisankar, Richard Svensson, Kristmundur Sigmundsson, Christina Kalderén, Mia Niklasson, Soumi Kundu, Sergi Aranda, Bengt Westermark, Lene Uhrbom, Michael Andäng, Peter Damberg, Sven Nelander, Ernest Arenas, Per Artursson, Julian Walfridsson, Karin Forsberg Nilsson, Lars G.J. Hammarström, and Patrik Ernfors*
Whole-Body Imaging with Single-Cell Resolution by Tissue Decolorization	*Kazuki Tainaka, Shimpei I. Kubota, Takeru Q. Suyama, Etsuo A. Susaki, Dimitri Perrin, Maki Ukai-Tadenuma, Hideki Ukai, and Hiroki R. Ueda*

CRISPRs for Everything

Engineer Something Great

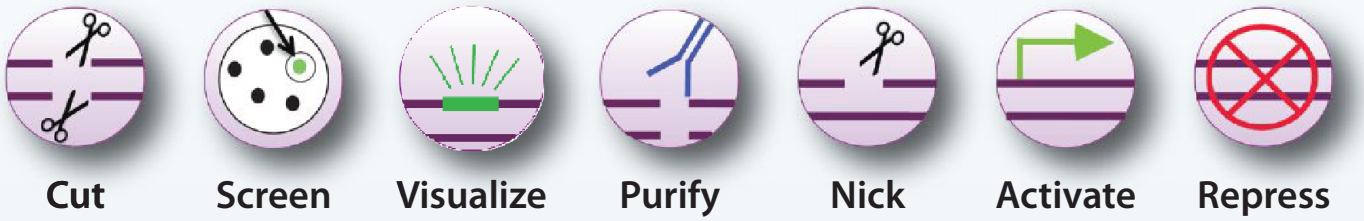

Over 500 ready to use CRISPR plasmids for gene targeting.
Addgene's plasmid collection is sure to jump-start your genome engineering research.

Start using CRISPRs for **just $65 USD.**

addgene
The nonprofit plasmid repository

www.addgene.org/CRISPR

Plasmids available for global distribution to academic labs

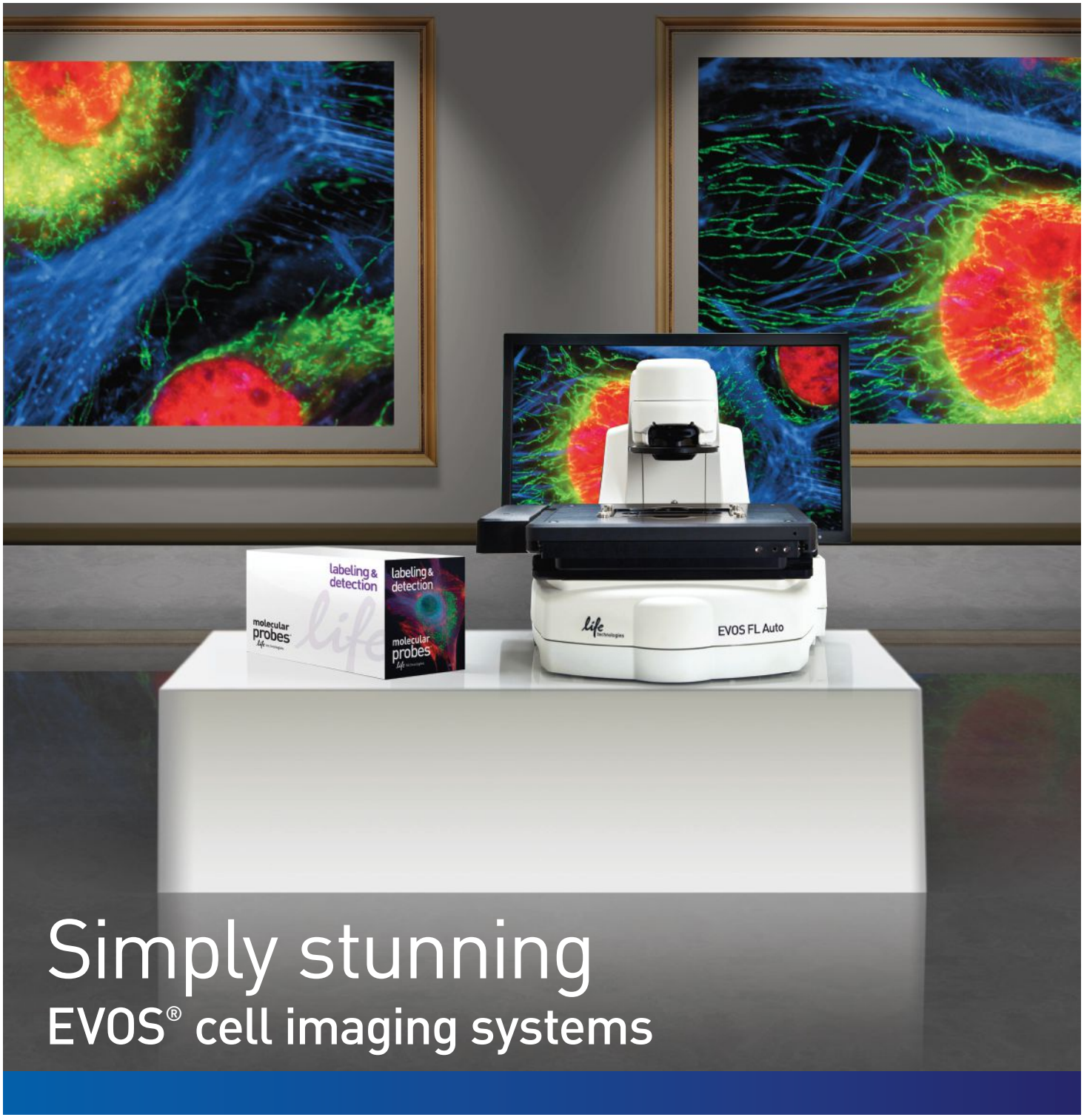

Simply stunning

EVOS® cell imaging systems

Minimize the complexities of microscopy without compromising performance

Smarter systems | Easier cell imaging | Faster results

Compare systems at **lifetechnologies.com/simplystunning**

life technologies

A Thermo Fisher Scientific Brand

eppendorf

Smooth Operator

The new Eppendorf micromanipulators TransferMan® 4r and InjectMan® 4

The new Eppendorf micromanipulators have been developed to simplify your work and increase the quality of your micromanipulation results. Based on their ergonomic design, the robust and reliable devices provide excellent performance for a wide range of applications.

> Unprecedented movement control and maximum stability
> Pre-defined functions for various applications to optimize your workflow
> Connection with new Eppendorf electronic microinjectors FemtoJet® 4i/4x and Eppendorf PiezoXpert®

www.eppendorf.com/cellmanipulation

89 NORTH®

OptoSplit

Acquire simultaneous images with one camera.

The OptoSplit II LS and OptoSplit III LS from Cairn Research enable simultaneous, multi-channel imaging by splitting the image into multiple components on the same camera. Record differences in color, polarization, ion concentrations or pH using the dual emission channel II LS and the triple emission channel III LS. Now you can perform:

- Simultaneous multicolor imaging
- Single molecule, TIRF, and Super-Resolution Microscopy
- Simultaneous FRET imaging
- Dual polarization imaging
- Calcium imaging (and other ion indicators), pH imaging
- Simultaneous phase contrast and fluorescence

This intuitive, modular system allows you to choose almost any combination of UltraFlat dichroics and ET emission filters to split the images with user-interchangeable cubes. Simple controls allow you to precisely register images pixel-by-pixel.

Eliminate temporal artifacts in your imaging data by acquiring images at the same time.

PHONE +1-802-881-0302 1-877-417-8313 **WEB** sales@89north.com 89north.com

CHROMA®

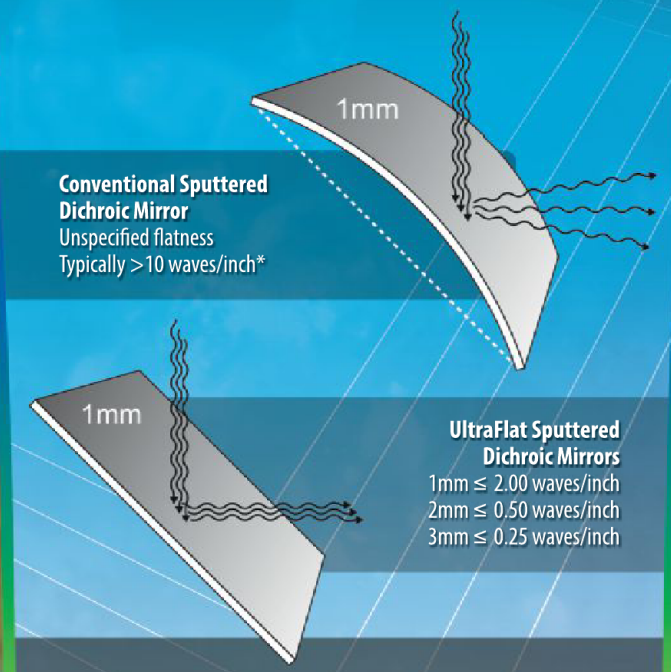

UltraFlat Dichroics

Superior surface flatness for distortion-free reflection.

Chroma's UltraFlat dichroics provide the flattest surfaces available for splitting wavelengths in critical applications, such as:

IMAGE SPLITTING ▸ Chroma's UltraFlat dichroics provide reflected images that are in focus from edge to edge, matching the transmitted images.

TIRF ▸ Eliminate spurious fluorescence signals by using dichroics with surfaces flat enough to reflect TIRF lasers without distortion, producing optimal evanescent waves. With other dichroics, some laser photons will propagate into the sample, producing unwanted fluorescence.

SIM ▸ Maintain the focus of reflected structured illumination and photoactivation micro-patterns.

STED ▸ Reflect well-defined, undistorted STED laser patterns onto your samples.

LASER BEAM COMBINING ▸ Maintain laser beam profile integrity when combining lasers.

Have confidence in the integrity of your reflected light without having to resort to dichroics >3mm thick.

PHONE +1-802-428-2500 1-800-824-7662 **WEB** sales@chroma.com chroma.com

Cell 158, August 28, 2014 ©2014 Elsevier Inc. DOI http://dx.doi.org/10.1016/j.cell.2014.08.019

SnapShot: Branching Morphogenesis

Cheng-Ming Chuong,[1,3] Ramray Bhat,[2] Randall B. Widelitz,[1] and Mina J. Bissell[2]
[1]Department of Pathology, University of Southern California, Los Angeles, CA 90033, USA, [2]Life Sciences Division, Lawrence Berkeley National Laboratory, Berkeley, CA 94720, USA, [3]Center of Wound Repair and Regeneration, Cheng Kung University, Tainan, Taiwan

Mammary gland
Branching by invasion

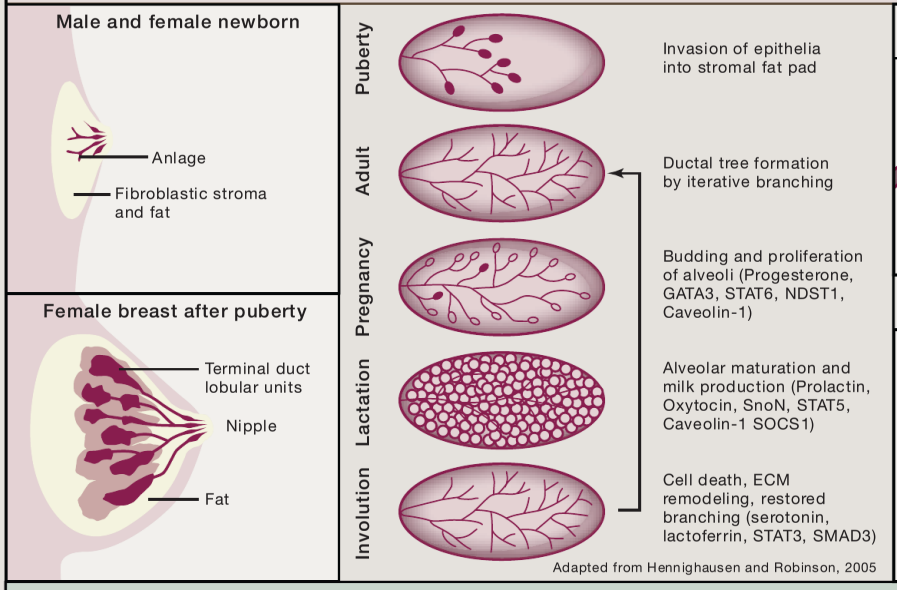

Secondary branching	Regulating factors
	Estrogen ↑ ER-α ↑ MMP3 ↑ HS2ST ↑ HGFR ↑ VDR ↓ MMP2 ↓ TIMP1 ↓ TGF-β ↓

Terminal end buds (TEBs)	Regulating factors
	MMP14 ↑ TIMP1 ↑ Nuclear actin ↑ FGFR2 ↑ MMP2 ↑ HSP90β ↑ Macrophages & eosinophils ↑ Patterned stromal collagen I ↑ TGF-β ↓ Laminin-1/BM ↓

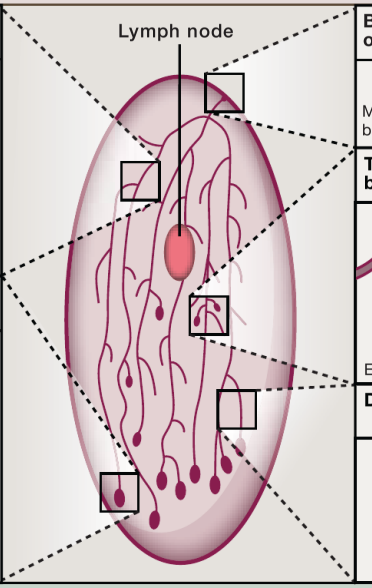

Bud outgrowth	Regulating factors
Mammary bud	PTHrP ↑ BMP4 ↑ BMPR1A ↑ FGF10 ↑

Tertiary branching	Regulating factors
End bud	Progesterone ↑ PR-B ↑ Wnt4 ↑ MMP3 ↑ HS2ST ↑ HGFR ↑ MMP2 ↓ TIMP1 ↓ TGF-β ↓

Duct	Regulating factors
	Laminin-1/BM ↑ MMP14 ↓ nuclear actin ↓ Leukocytes ↓ TGF-β ↓ Mechanical stress ↑

Feather
Branching by cell death

Barb and rachis formation by a periodic invagination
BMP, Noggin, Sprouty, FGF

Basal branch patterns form by differential cell death
NCAM, Shh, caspase

Radial, bilateral symmetric, and asymmetric branching patterns form by modulating basal branching circuit
Wnt3a gradient, Sprouty

Feather follicle opens by apoptosis to form a vane
Shh, Caspase

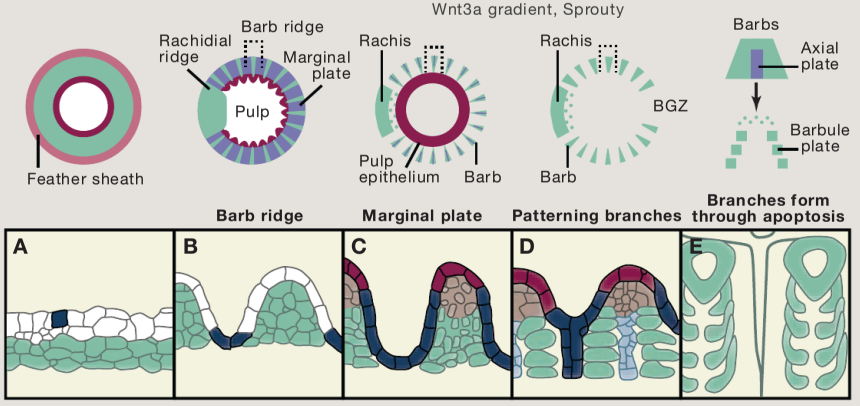

Follicle formation	Regulating factors
Stem cells Dermal papilla	β-catenin ↔ Wnt ↑ FGF ↑ BMP ↑ Shh ↑ TGFβ ↑ MMP2 ↑

Bilateral symmetry	Regulating factors
Rachis zone Barb forming zone A P	**Anterior** Wnt3a ↑ Shh ↓ BMP ↓ **Posterior** Wnt3a ↓ β-catenin ↑

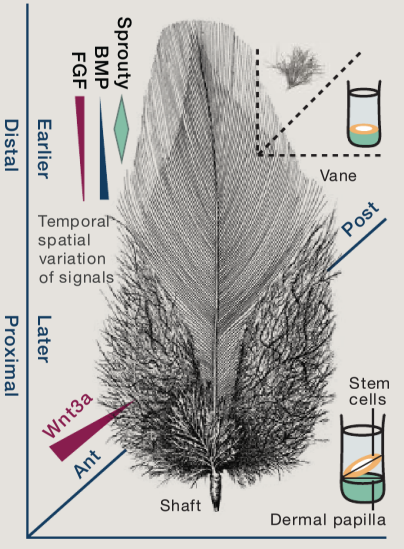

Radial symmetry	Regulating factors
Barb forming zone	FGF10 ↑ Sprouty ↑ Noggin ↑ **Marginal plate** Shh ↑ Apoptosis ↑ MMP2 ↑ **Barb plate** Ptc1 ↑ Proliferation ↑ TIMP2 ↑ Keratinization ↑

Shaft formation	Regulating factors
	Proliferation ↓ BMP2 ↑ Sprouty ↓ FGF ↓

See online version for legend and references.

We make human cells.

We can't state it more simply: We manufacture human cells from induced pluripotent stem cells. Our highly pure iCell® and MyCell® products are consistent and reproducible from lot-to-lot, enabling you to focus on the biology . . . and what drives your research.

True Human Biology. Why use an animal or immortalized cell model as a proxy when a true human model, consistent across lots, is available? If you have a phenotype of interest, we can make iPSCs and terminal cells from your donors.

Highly Characterized. Highly Predictive. Our cells have the appropriate gene and protein expression and the relevant physiological response of the target cell type, with numerous peer-reviewed publications detailing their characterization and predictivity of human response.

MORE Cells. CDI provides more cells than other providers: 96-well capacity per vial. GUARANTEED.

Any cell type.
Any genotype.
Any quantity.

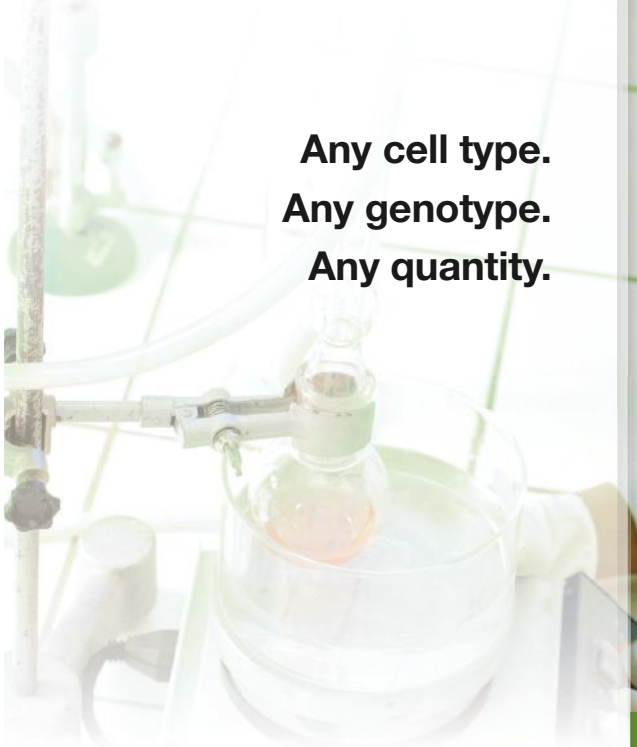

Cellular Dynamics international

You make:

safer medicines
discoveries
therapies
breakthroughs
tenure
your peers envious with a tier 1 publication

Check out the iCell community of scientists who discuss the difference iCell products have made in their research:

www.cellulardynamics.com/community

Cell 157, April 10, 2014 ©2014 Elsevier Inc. DOI http://dx.doi.org/10.1016/j.cell.2014.03.044

SnapShot: Cancer Vaccines

Karolina Palucka[1] and Jacques Banchereau[2]
[1]Ralph M. Steinman Center for Cancer Vaccines, Baylor Institute for Immunology Research, Baylor Research Institute, Dallas, TX 75204, USA
[2]The Jackson Laboratory, Farmington, CT 06030, USA

Cell

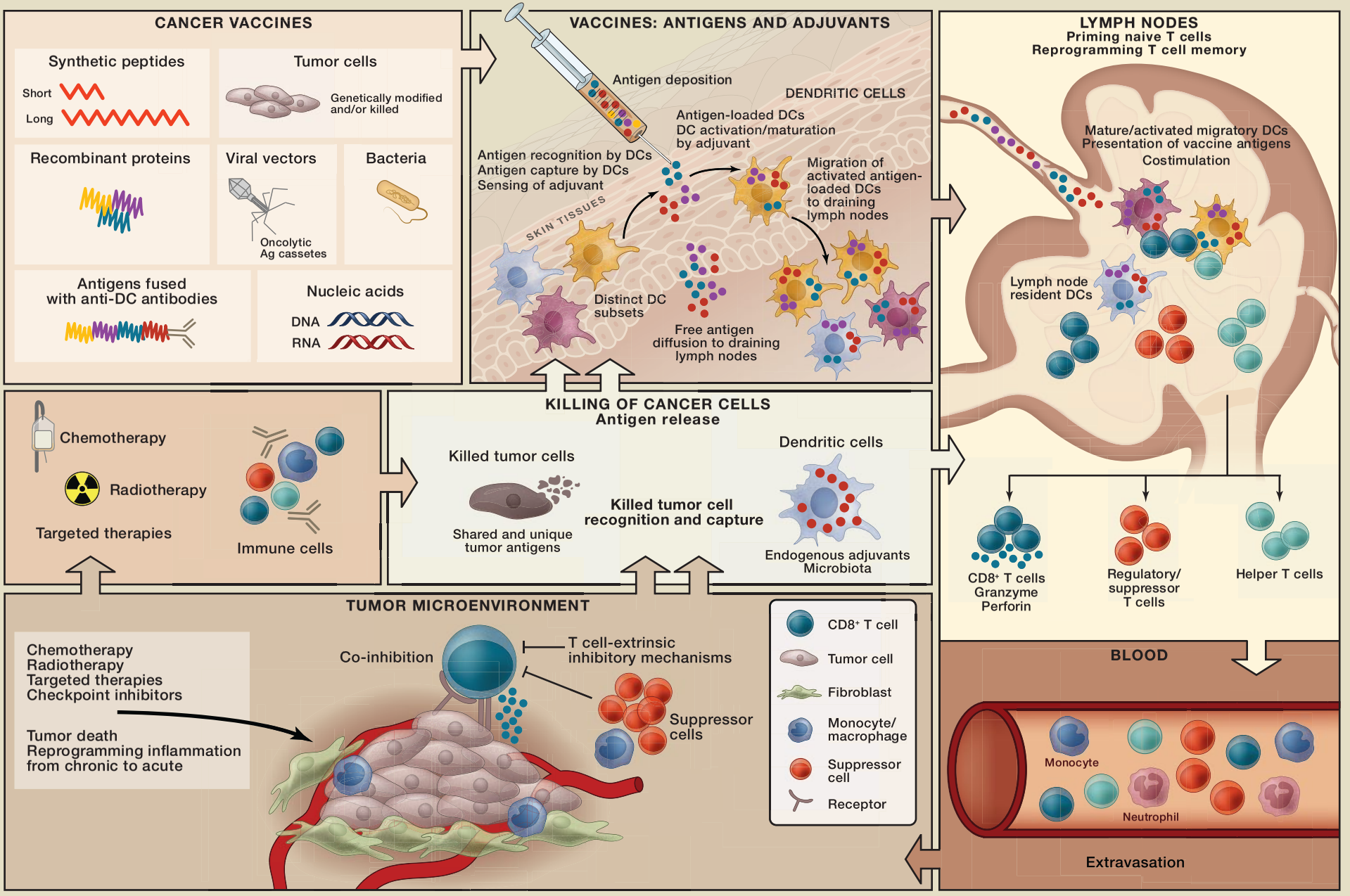

See online version for legend and references

Monochromator. Reinvented!

Microplate reader with revolutionary LVF Monochromator™ technology

Fluorescence, Fluorescence Polarization, TRF, TR-FRET/HTRF®, Luminescence, AlphaTechnology, and Absorbance

Discover the most sensitive monochromator-based microplate reader.

CLARIOstar® - Any Wavelength. Any Bandwidth. Any Assay.

BMG LABTECH

The Microplate Reader Company

www.bmglabtech.com

Cell 159, October 9, 2014 ©2014 Elsevier Inc. DOI http://dx.doi.org/10.1016/j.cell.2014.09.037

SnapShot: Histone Modifications

He Huang,[1] Benjamin R. Sabari,[2] Benjamin A. Garcia,[3] C. David Allis,[2] and Yingming Zhao[1]
[1]Ben May Department of Cancer Research, The University of Chicago, Chicago, IL 60637, USA
[2]Laboratory of Chromatin Biology and Epigenetics, The Rockefeller University, New York, NY 10021, USA
[3]Department of Biochemistry and Biophysics, University of Pennsylvania, Philadelphia, PA 19104, USA

Cell

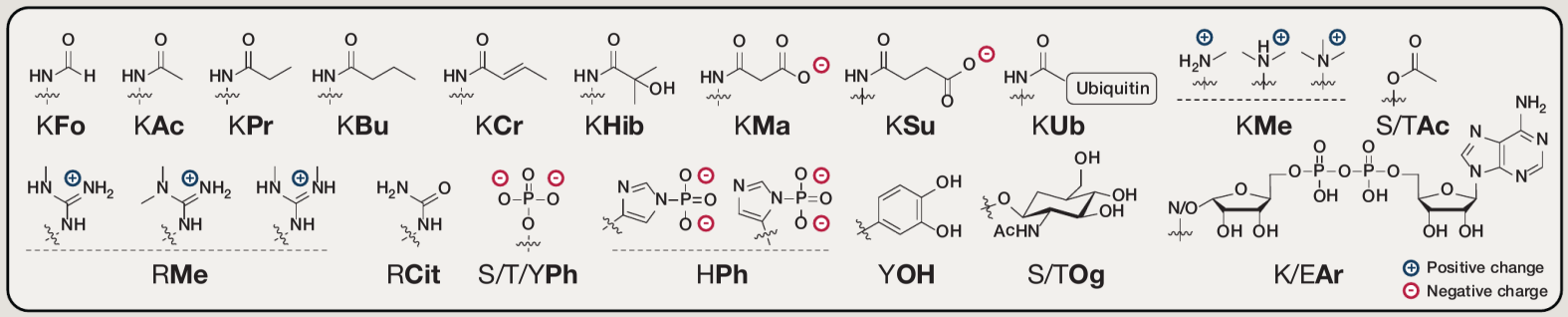

Me	Methylation (K, R)
Ac	Acetylation (K, S, T)
Pr	Propionylation (K)
Bu	Butyrylation (K)
Cr	Crotonylation (K)
Hib	2-Hydroxyisobutyrylation (K)
Ma	Malonylation (K)
Su	Succinylation (K)
Fo	Formylation (K)
Ub	Ubiquitination (K)
Cit	Citrullination (R)
Ph	Phosphorylation (S, T, Y, H)
OH	Hydroxylation (Y)
Og	O-GlcNAcylation (S, T)
Ar	ADP ribosylation (K, E)

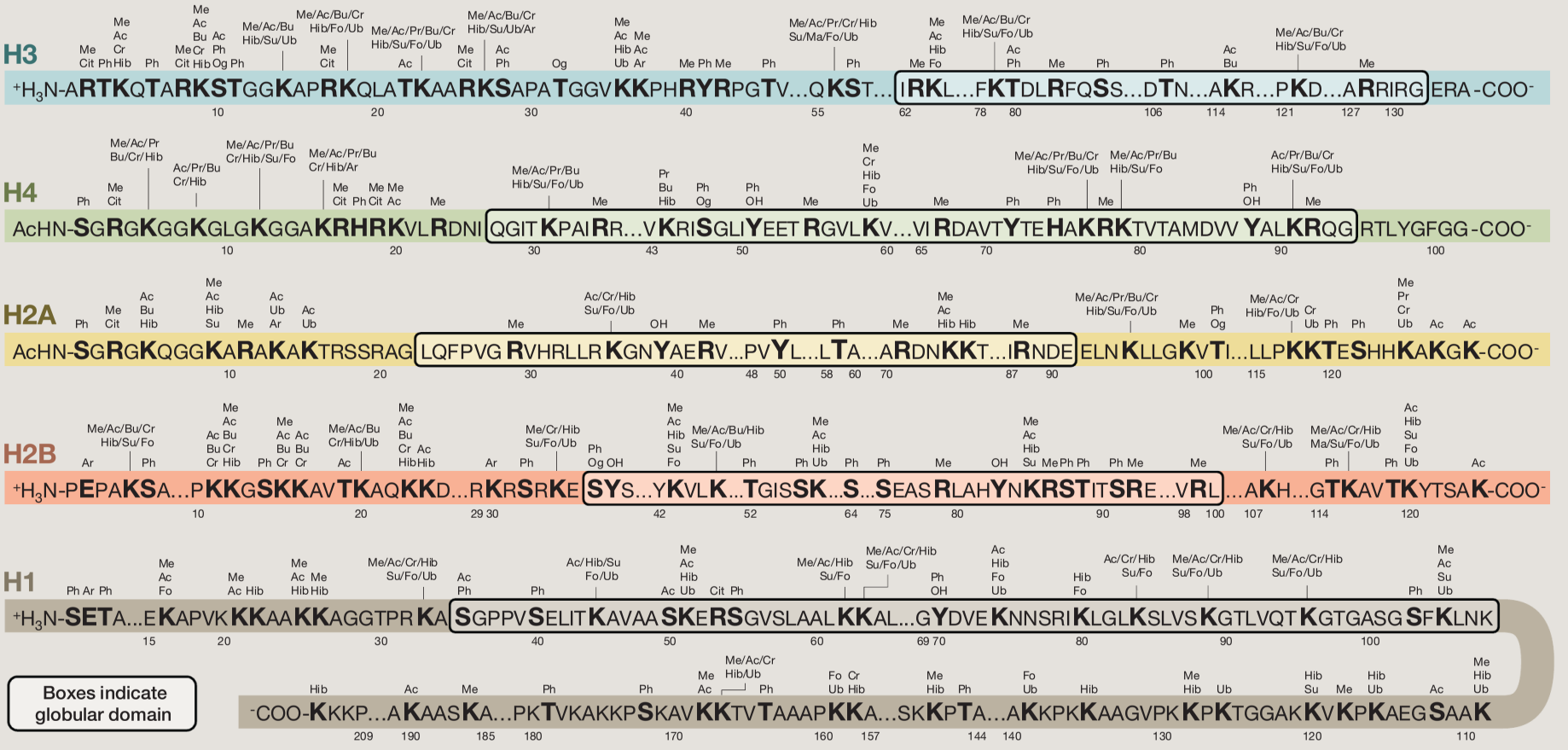

See online version for for legend and references.

Our **LightScanner™ System**

remains the industry standard for

Hi-Res Melting™ and mutation discovery.

With our Master Mix, containing

LCGreen™ Plus Melting Dye,

you will have the sensitivity and

throughput that your lab needs.

Now, more then ever, we remain

committed in providing the industry

with superior products,

unsurpassed customer support

and a solid future of

innovation and design.

BIOFIRE™

DEFENSE

Request a Free Sample of our Hi-Res Melting Master Mix at www.HiResMelting.com

BioFire Defense, LLC, formally known as Idaho Technology, Inc.

SnapShot: *Hox* Gene Regulation

Guillaume Andrey[1] and Denis Duboule[1,2]
[1]School of Life Sciences, Ecole Polytechnique Fédérale, Lausanne 1015, Switzerland
[2]Department of Genetics and Evolution, University of Geneva, Geneva 1211, Switzerland

Cell

The mammalian Hox clusters

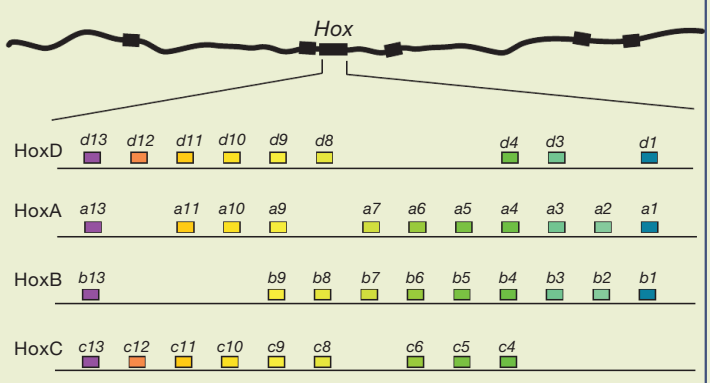

Switch in regulatory controls: the limb model

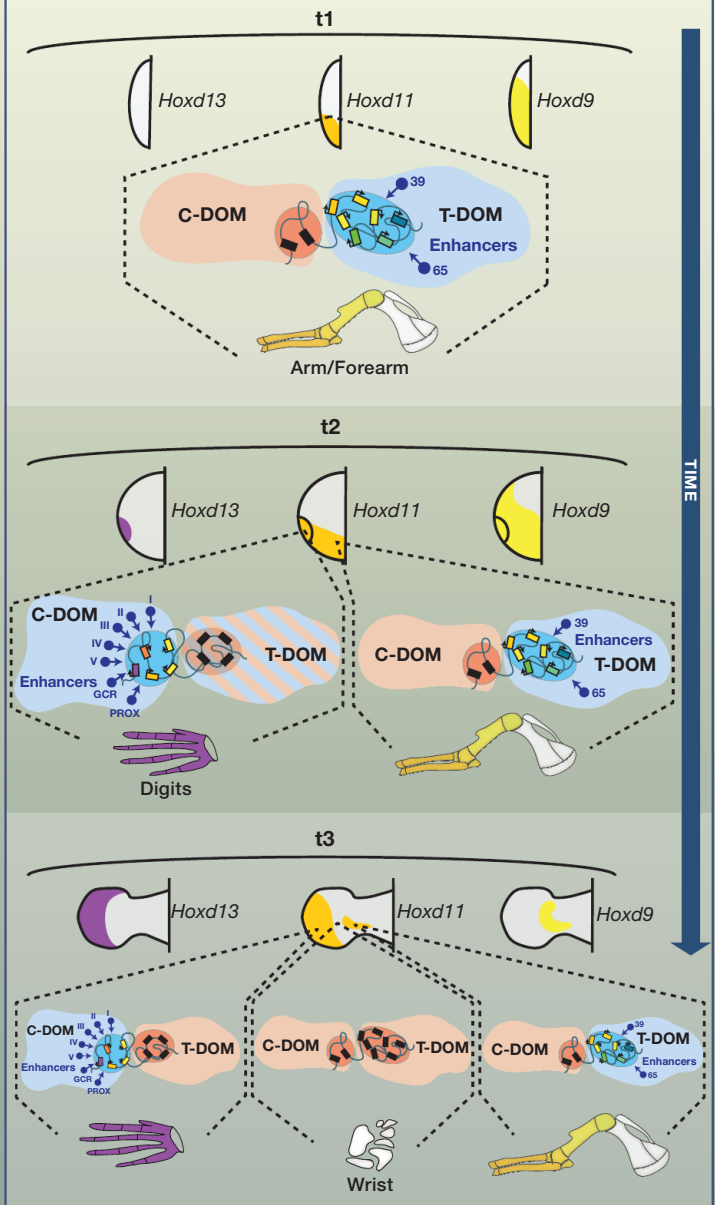

Regulation of *HoxD* gene in primary and secondary axes

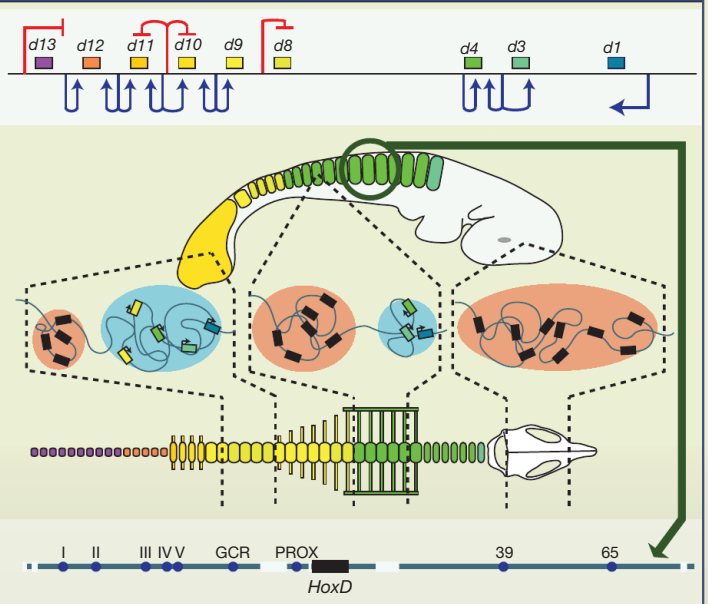

EARLY-PROXIMAL CONTROL OF HOXD EXPRESSION

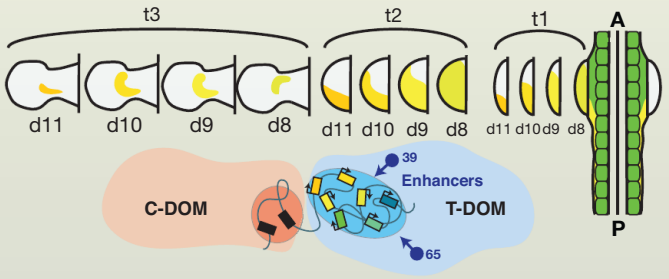

LATE-DISTAL CONTROL OF HOXD EXPRESSION

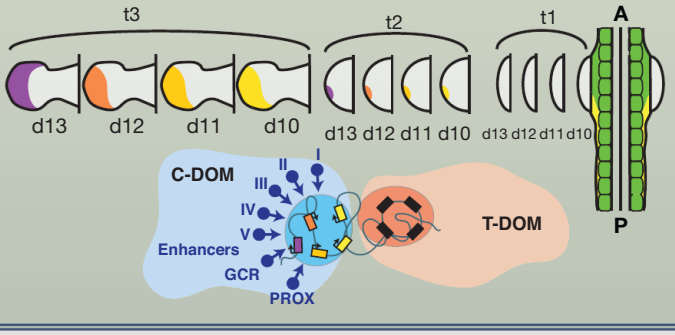

Mechanism of *HoxD* collinear regulation in limbs

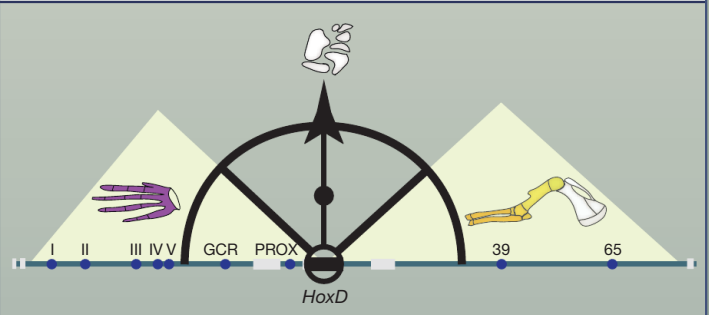

 DOI http://dx.doi.org/10.1016/j.cell.2014.01.060

See online version for legend and references.

BAKER

Environments For Science™

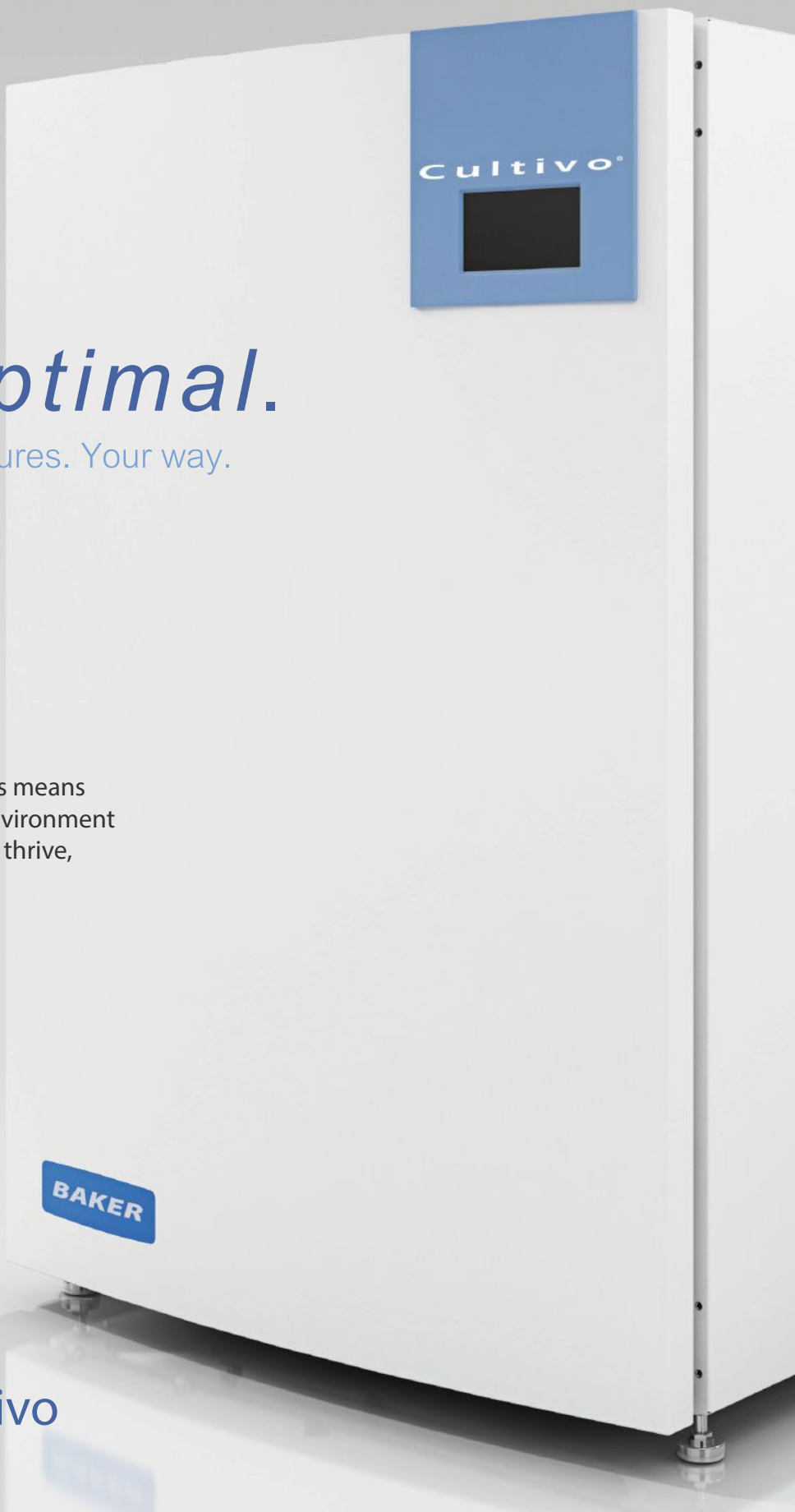

Define *optimal*.

Your work. Your cultures. Your way.

Optimal is never a one-size-fits-all condition.

It's contextual. It's driven by the research or the cell line. But—more importantly—it should be driven by you.

Providing optimal conditions means you control the particular environment where your specific cells will thrive, or be challenged.

You define the variables, not the incubator.

Learn more about Cultivo™ the new CO_2 incubator from Baker.

bakerco.com/cultivo

Cell 156, January 16, 2014 ©2014 Elsevier Inc. DOI http://dx.doi.org/10.1016/j.cell.2014.01.003

SnapShot: Lipid Kinase and Phosphatase Reaction Pathways

Simon A. Rudge and Michael J.O. Wakelam
The Babraham Institute, Babraham Research Campus, Cambridge CB22 3AT, UK

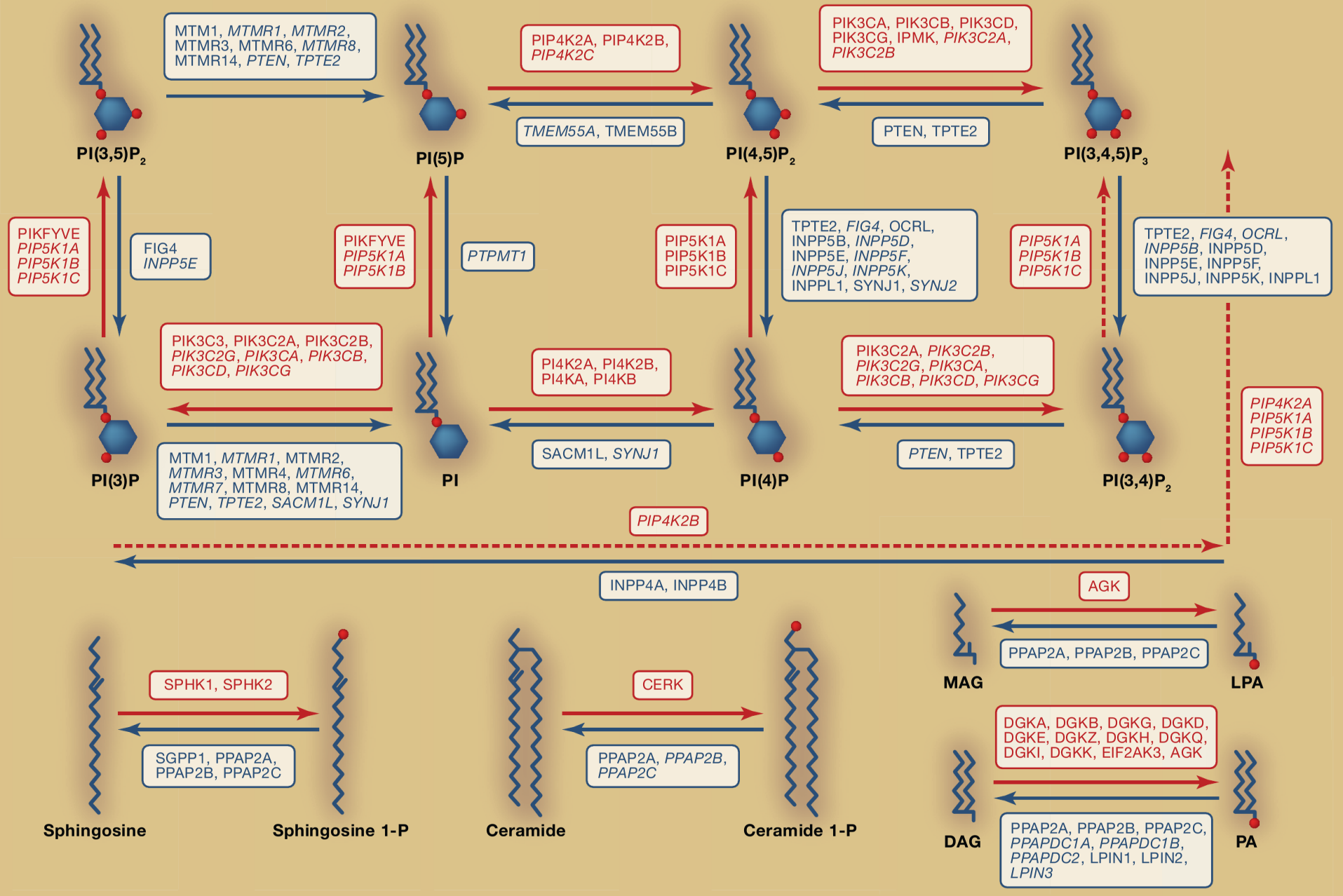

See online version for legend and references.

Data You Can Trust

Class I Tetramers
Class II Tetramers
CD1d Tetramers

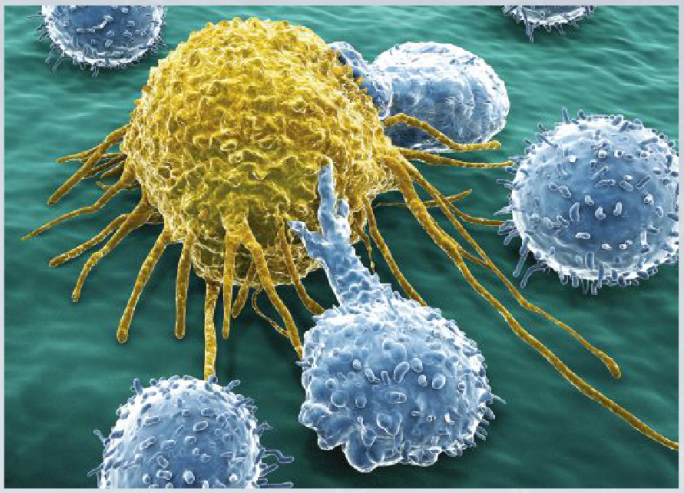

MBL has been providing Tetramer reagents for over a decade and has recently extended its portfolio through the acquisition of the Beckman Coulter iTAg™ MHC Tetramer product line. MBL International is your source for quality reagents for detection of antigen-specific T cells and NKT cells.

- Extensive selection of MHC Class I and Class II alleles for rapid identification and enumeration of antigen-specific CD8+ and CD4+ T cells
- Improved specificity due to a proprietary α3 domain mutation, which reduces non-specific binding
- Maximum stability and minimized lot-to-lot variation
- Human and mouse CD1d Tetramers for identification of NKT cells

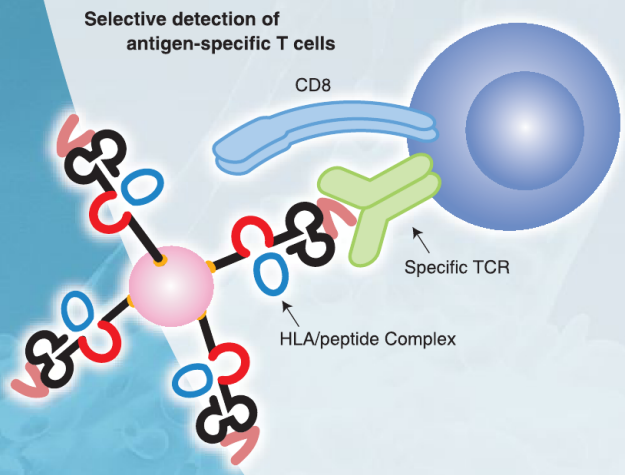

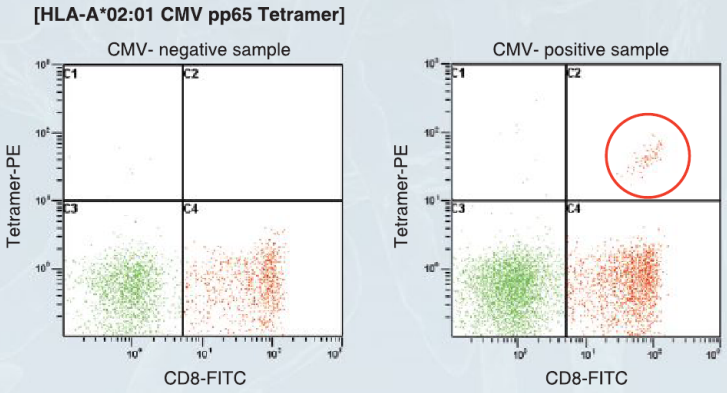

Contact MBL International today to learn more about our other products to help you discover ways to make your science more efficient and effective.

contact us | sales@mblintl.com
www.mblintl.com

MBL® International Corporation

life.science.discovery.™

SnapShot: Necroptosis

Wen Zhou and Junying Yuan
Department of Cell Biology, Harvard Medical School, Boston, MA 02115, USA

Cell

Trigger	Cell Types/Lines	Molecular Mechanism	Chemical Inhibitors
TNF + caspase-8 inhibition (by pan-caspase inhibitor zVAD, caspase-8 inhibitor IETD, caspase-8 knockdown or knockout, overexpression of viral protein CrmA)	MEF, L929, Jurkat, NIH3T3	The stimulation of TNFR1 by TNF leads to the formation of a transient complex associated with the intracellular domain of TNFR1, named complex I, where RIP1 is ubiquitinated by cIAP1/2 and LUBAC. After the dissociation of complex I, RIP1 interacts with RIP3 to form an intracellular amyloid-like complex named complex IIb or necrosome in a RIP1-kinase-dependent manner. Deubiquitination of RIP1 by CYLD promotes the formation of complex IIb. Oligomerization of RIP1 and RIP3 leads to MLKL phosphorylation by RIP3, which is required for MLKL trimerization and translocation to plasma membrane, resulting in Ca^{2+} and/or Na^{+} influx as one of the final execution steps of necroptosis. Necroptosis can be sensitized by inhibitor of protein translation CHX, which suppresses the synthesis of survival factors.	RIP1 kinase inhibitors necrostatin-1, 3, 4, 5; RIP3 kinase inhibitors GSK'843, GSK'872; MLKL inhibitor necrosulfonamide; Ca^{2+} chelator BAPTA-AM
TNF	L929, FADD-deficient Jurkat	These cells are defective in caspase-8 activation in response to TNF so they can undergo necroptosis without caspase inhibition.	Necrostatin-1, 3, 4, 5
FAS ligand + caspase-8 inhibition (by zVAD or caspase-8 knockout)	PHA/IL-2-activated human $CD4^{+}$ T cells, ConA/IL-2-activated murine splenic T cells, Jurkat, CCRF-CEM	RIP1 kinase activity is required for the cell death.	Necrostatin-1
Fas ligand + IAP antagonist + zVAD	HaCaT	The cell death is dependent on RIP1 kinase activity and is protected by $cFLIP_L$ overexpression. TWEAK, which promotes the degradation of cIAP1, can sensitize cells to Fas-ligand-induced cell death with a similar mechanism.	Necrostatin-1
TCR engagement + caspase-8 inhibition (by zVAD, caspase-8 knockout, or FADD death domain overexpression)	Murine CD4+ T cells, murine CD8+ T cells, human peripheral blood lymphocytes	Activation-induced cell death (AICD) of mature T cells is mediated by the induction of Fas ligand. Failure to activate caspase-8 due to chemical inhibition or genetic deficiency of caspase-8 or FADD predisposes T cells to necroptosis in response to the Fas ligand induced by TCR signaling. RIP1 kinase activity and RIP3 are required for the cell death.	Necrostatin-1
TRAIL in acidic condition	HT-29, MEF, HepG2	RIP1 kinase activity, RIP3, and PARP-1 polymerase activity are required for the cell death.	Necrostatin-1, PARP-1 inhibitor PJ-34
TRAIL + zVAD	Jurkat, HaCaT, U937, Mz-ChA-1, BxPC-3, HT-29	The cell death is sensitized by IAP antagonist or by protein synthesis inhibitor CHX. RIP1 kinase activity is required for the cell death.	Necrostatin-1
TNF + cIAP1/2 depletion (by IAP antagonist or cIAP1 knockout) + zVAD	MEF, MDF, Panc-1, Jurkat, U937, CCRF-CEM, L929, macrophage	This combination treatment induces the interaction of RIP1 kinase and RIP3 to form the complex IIb. RIP1 was detected in a complex of ~2 MDa which contains additional components such as caspase-8 and FADD.	Necrostatin-1
LTα + IAP antagonist + pan-caspase inhibitor QVD	MDF	LTα homotrimer binds to TNFR1 and leads to TNFR1 signaling in a similar way to TNF-induced necroptosis.	Necrostatin-1
IAP antagonist + zVAD	HT-29, MDA-MB-231, SKOV3, Kym-1, macrophage	The cell death is dependent on RIP1 kinase activity. Interaction between RIP1 and caspase-8 was detected in a complex of ~2 MDa.	Necrostatin-1
TNF + TAK1 inhibitor 5z-7 or TAK knockdown + zVAD	L929, MEF	The formation of complex I associated with TNFR1 is not affected by TAK1 inhibition, whereas the formation of necrosome (complex IIb) is facilitated by TAK1 inhibition. RIP1 kinase activity is required for the formation of necrosome.	Necrostatin-1
TLR2, TLR5, or TLR9 agonist + zVAD	Macrophage, microglia	The autocrine production of TNF, which is induced by TLR signaling, leads to necroptosis in the absence of caspase-8 activity.	Necrostatin-1
Poly(I:C) agonist + zVAD	Macrophage, microglia	RIP1, RIP3, and TRIF form necrosome independently of autocrine TNF. RIP1 kinase activity, RIP3, TRIF, but not IRF3, are required for the cell death.	Necrostatin-1, RIP3 kinase inhibitor GSK'843, GSK'872
LPS + zVAD	Macrophage, microglia	Both autocrine production of TNF and RIP1-RIP3-TRIF axis contribute to the cell death.	Necrostatin-1
Poly(I:C) + IAP antagonist + zVAD	HaCaT, MET-1	The cell death requires RIP1 kinase activity and RIP3 and is negatively regulated by cFLIP. RIP1 is detected in a ~2 MDa complex named ripoptosome, which also includes $cFLIP_S$ and caspase-8. Ripoptosome forms independently of TNF signaling.	Necrostatin-1
Poly(I:C)	GM-CSF-induced BMDC	The cell death is dependent on RLR adaptor MAVS/IPS-1/VISA/Cardif and the release of lysosomal cathepsin D which in turn cleaves caspase-8. RIP1 kinase activity and RIP3 are required for the cell death.	Cathepsin D inhibitor pepstatin A; Necrostatin-1
IFNα/β	Primary $FADD^{-/-}$ MEF at subconfluency	PKR is transcriptionally upregulated by Type I interferon. The cell death requires the kinase activities of JAK, PKR, and RIP1.	JAK kinase inhibitor I; PKR inhibitor C16 and 2-aminopurine; Necrostatin-1
IFNγ	Primary $FADD^{-/-}$ MEF at subconfluency, $RelA^{-/-}$ MEF, J774A.1	PKR is transcriptionally upregulated by IFNγ. The activation of JAK-STAT1 axis by IFNγ triggers the formation of necrosome consisting of RIP1, RIP3, and PKR. JAK, PKR, and RIP3 are required for cell death. RIP1 kinase inhibition reduces the cell death but does not significantly affect the formation of necrosome.	RNA polymerase II inhibitor Actinomycin D; JAK kinase inhibitor I; PKR inhibitor C16 and 2-aminopurine; Necrostatin-1
Oxygen glucose deprivation	Retinal ganglion cells (RGC)	Oxygen glucose deprivation (OGD), an in vitro condition mimicking ischemic injury, promotes cell death predominantly by necrosis. The necrosis is dependent on RIP1 kinase.	Necrostatin-1
Glutamate, NMDA	HT-22, primary rat cortical cells	Excitotoxicity in neurons is mediated by mitochondrial oxidative stress and MAPK activation and is dependent on RIP1 kinase.	ROS scavenger N-acetyl-cysteine, Necrostatin-1
Salmonella enterica serovar Typhimurium	Macrophage	Type I interferon is required for the cell death, but not inflammasome activation and cytokine secretion. RIP1 is recruited to IFNAR1, leading to necroptosis mediated by RIP1 kinase and RIP3. Caspase-1 also contributes to the cell death.	Necrostatin-1; caspase-1 inhibitor YVAD-CHO
Murine cytomegalovirus (CMV) M45mutRHIM	SVEC4-10, 3T3-Swiss albino, MEF	CMV infection induces DAI interaction with RIP3, leading to RIP3-dependent necroptosis without the requirement for RIP1 kinase. CMV M45-encoded vIRA abrogates DAI-RIP3 interaction. Therefore, CMV can infect cells without causing cell death unless its vIRA is disrupted by mutation.	

See online version for legend and references.

PRE-PACKAGED
LIQUID HANDLING
AUTOMATION SOLUTIONS

So Easy You Can Walk Away!

NGS Workstations

A fully automated compact, flexible and future-proof workstation for library preparation for all common sequencing platforms (Available on STARlet & NIMBUS)

ID STARlet Workstation

Streamlines the entire DNA purification and analysis process using Life Technologies' Human Identification (HID) kits

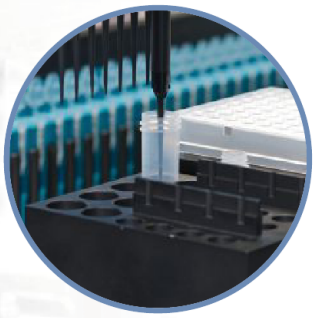

Genomics STARlet

Proven nucleic acid quality with MACHEREY-NAGEL kits are the key to downstream applications like genotyping, sequencing and real-time PCR analysis

HAMILTON®

Contact Hamilton Today

800.648.5950 | www.HamiltonRobotics.com | marketingrequest@hamiltoncompany.com

Cell 157, May 22, 2014 ©2014 Elsevier Inc. DOI http://dx.doi.org/10.1016/j.cell.2014.05.003

SnapShot: Nuclear RNAPII Transcript Modification

Manfred Schmid and Torben Heick Jensen
Centre for mRNP Biogenesis and Metabolism, Department of Molecular Biology and Genetics, Aarhus University, 8000 Aarhus, Denmark

Cell

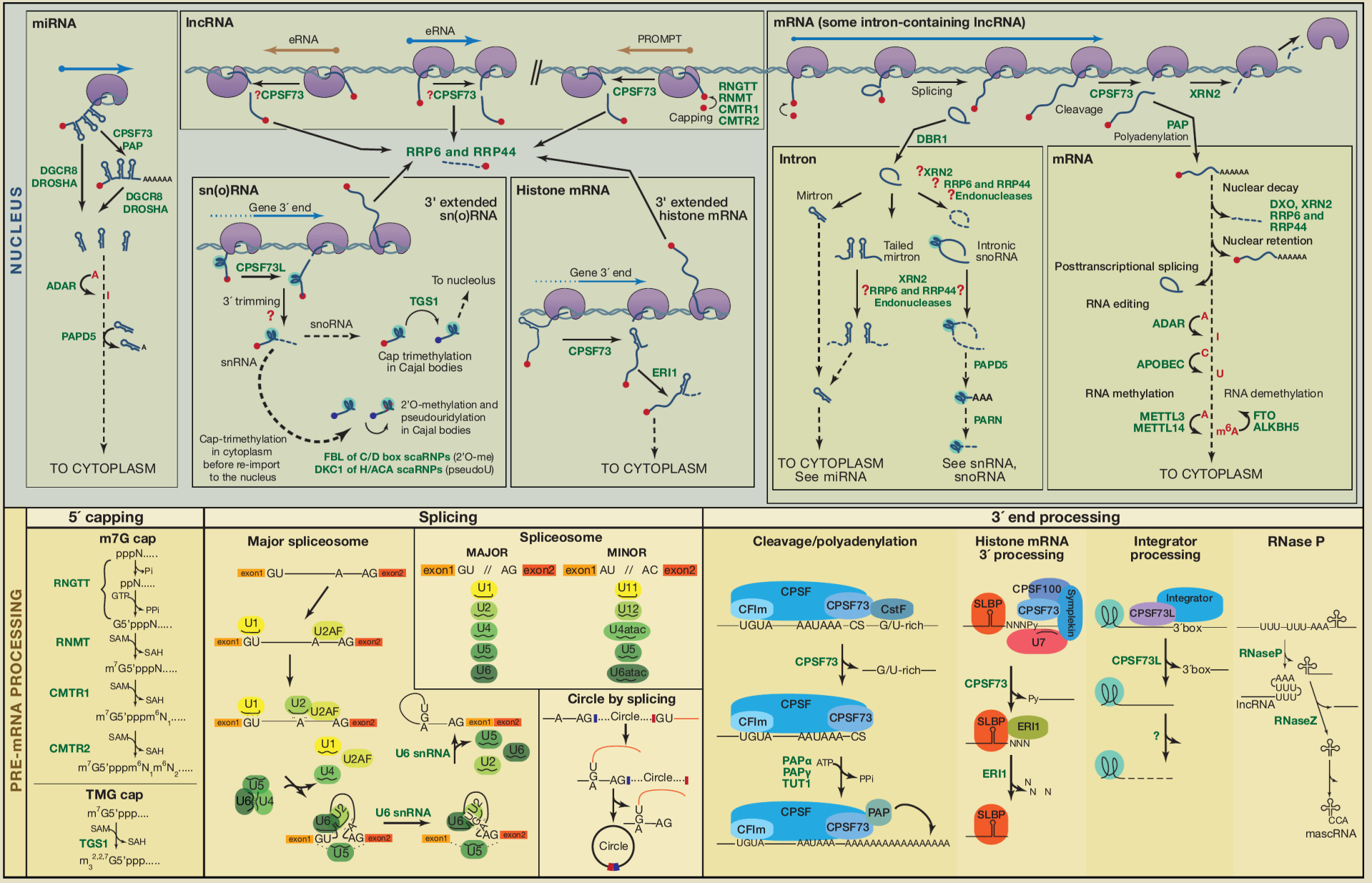

See online version for legend and references.

Dharmacon™
part of GE Healthcare

With Dharmacon, you can confidently silence, express and edit your genes.

In every experiment, you invest time, money and effort. Still, success is not a certainty – that's the nature of science. Fortunately, you can decrease the uncertainty with Dharmacon RNAi, gene expression and gene editing products. As scientists too, we know what you're feeling – and what you're facing – and can help you confidently achieve the best possible results.

Explore our advanced gene editing tools.

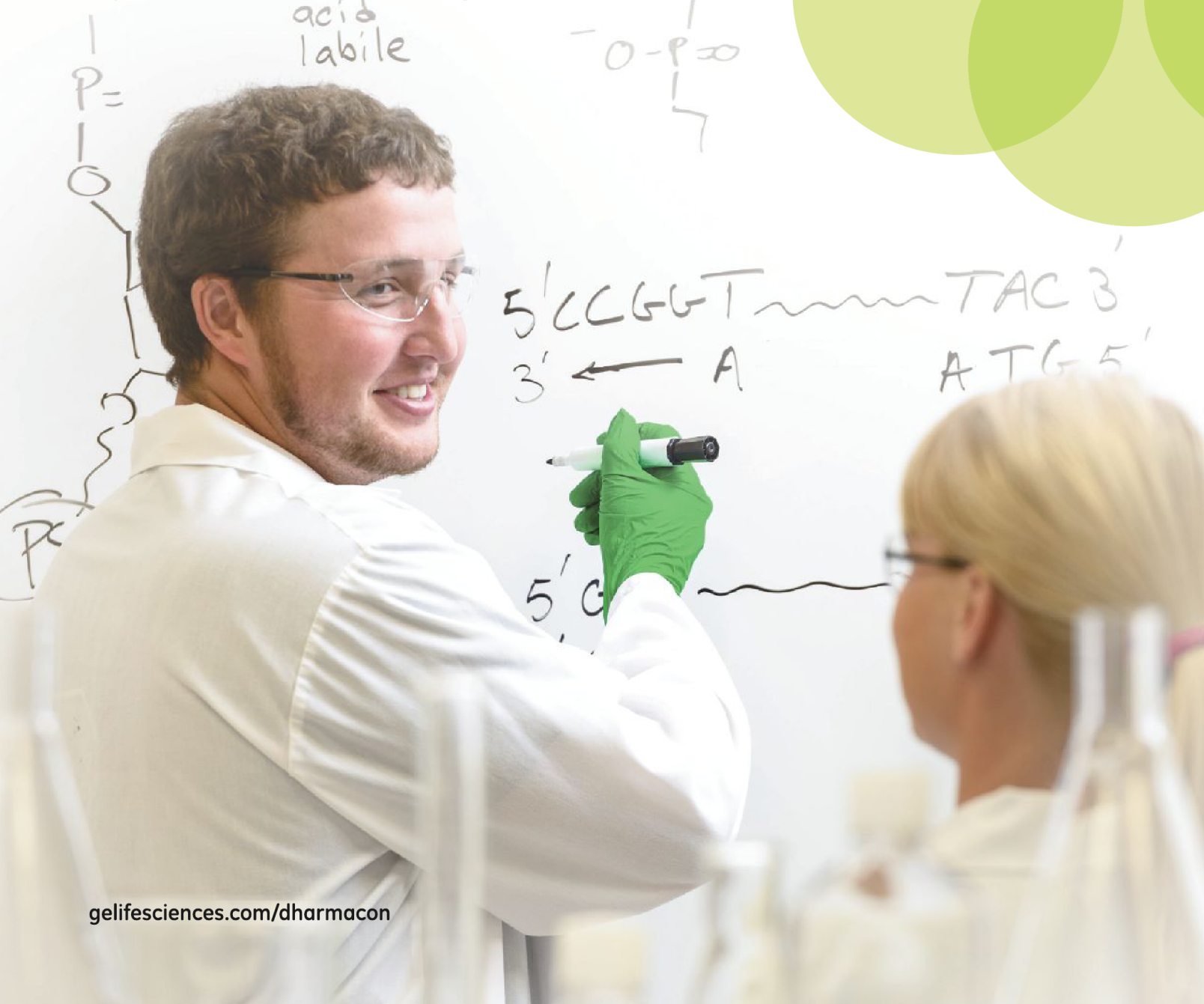

gelifesciences.com/dharmacon

Cell 157, June 19, 2014 ©2014 Elsevier Inc. DOI http://dx.doi.org/10.1016/j.cell.2014.06.002

SnapShot: Receptor Dynamics at Plastic Synapses

Matthias Kneussel,[1] Antoine Triller,[2] and Daniel Choquet[3]
[1]University Medical Center Hamburg Eppendorf, Falkenried 94, 20251 Hamburg, Germany
[2]Ecole Normale Superieure, Institute of Biologie (IBENS) CNRS UMR 8197, Inserm 1024, 46 rue d'Ulm, Paris 75005, France
[3]Interdisciplinary Institute for Neurosciences, CNRS, Bordeaux University, UMR 5297, 146 rue Leo Saignat, 33077 Bordeaux, France

Receptor	Cargo adaptor/ regulator	Motor	Cytoskeletal track
AMPAR GluA2	GRIP1	KIF5A KIF5B KIF5C	Microtubule
AMPAR GluA1	RAB11 RAB11-FIP2	Myosin Vb	Actin filament
AMPAR GluA1 GluA2	βSAP97	Myosin VI	Actin filament
NMDAR GluN2B	LIN2 LIN7 LIN10	KIF17	Microtubule
$GABA_AR$	HAP1	KIF5A KIF5B KIF5C	Microtubule
$GABA_AR$	Muskelin	Myosin VI	Actin filament
$GABA_AR$	Muskelin	Dynein	Microtubule
GlyR	Gephyrin	KIF5A KIF5B KIF5C	Microtubule
GlyR	Gephyrin	Dynein	Microtubule

Latral diffusion in response to ↗ Ca^{2+}	
Mobility	**Confinement**
AMPAR ↘	AMPAR ↗
$GABA_AR$ ↗	$GABA_AR$ ↘
GlyR ↘	GlyR ↗

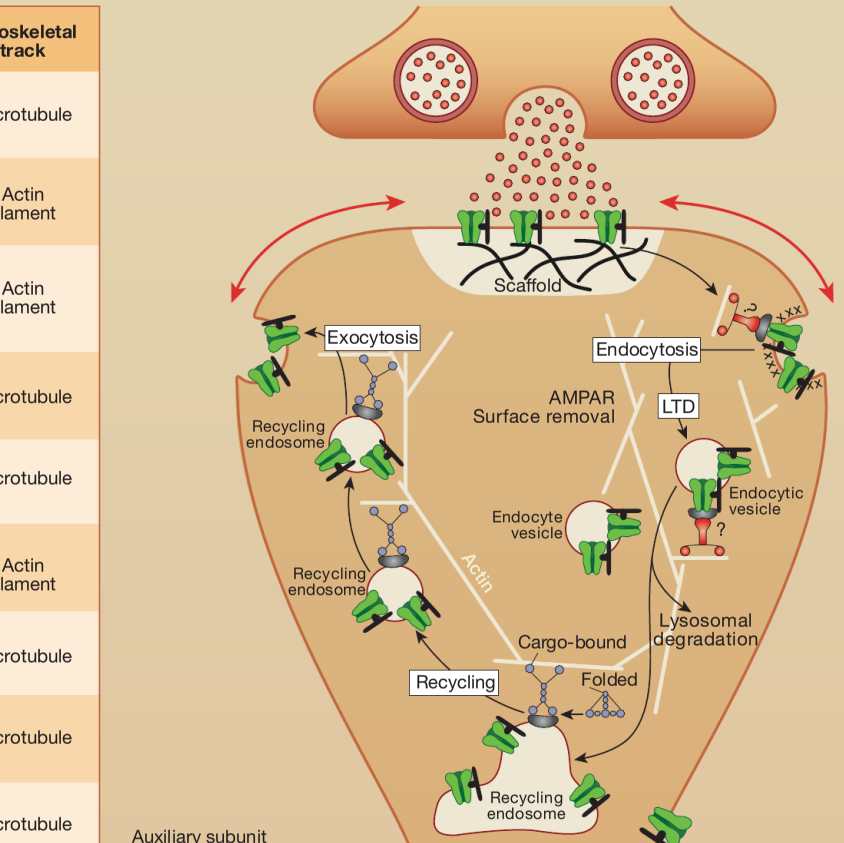

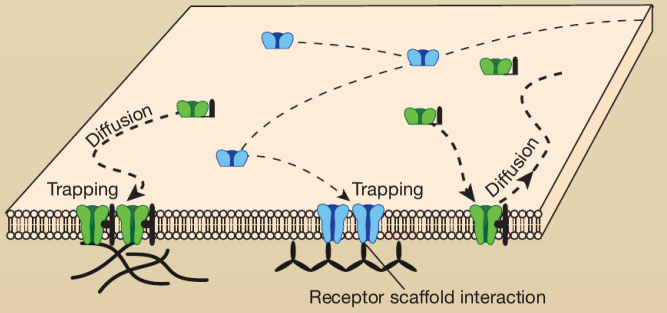

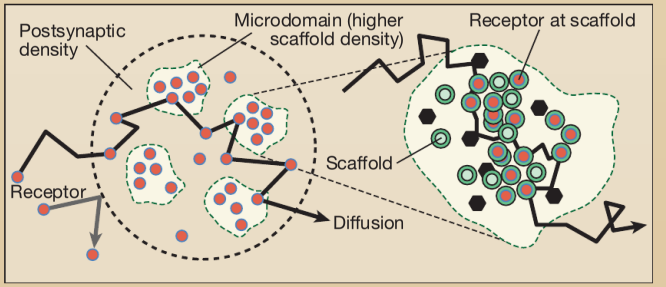

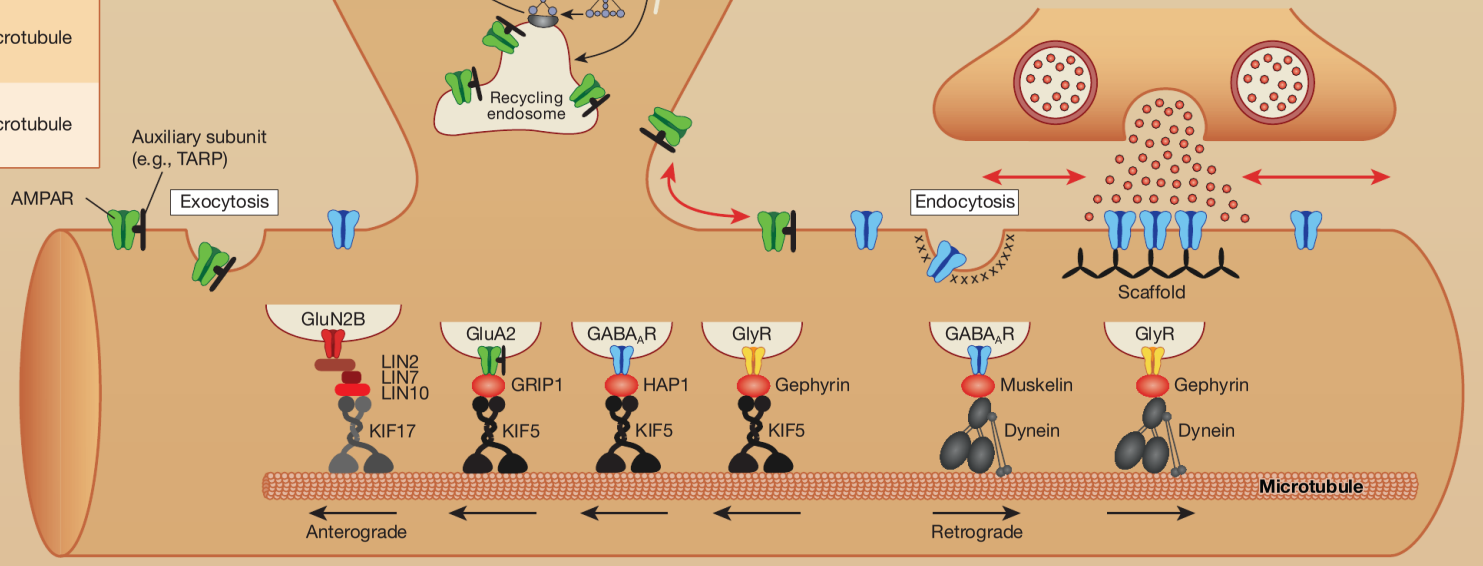

See online version for legend and references.

PROTECT

Detect, eliminate and prevent cell culture contamination

Before mycoplasma contamination compromises your cell cultures, **stop** it. Biological Industries has everything you need.

Disinfect incubators, sterile benches and other surfaces regularly with our pharmacidal spray.

- Prevents contamination and growth of fungi, bacteria, mycoplasma and viruses
- Non-toxic, biodegradable and non-corrosive

Keep water baths clean and clear.

- **Aquaguard-1:** for disinfecting water baths of CO_2 incubators
- **Aquaguard-2:** for disinfecting various kinds of water baths from bacteria and fungi

Detect suspected contamination with our EZ-PCR Mycoplasma Test Kit.

- Complete, ready-to-use—including TAQ polymerase and positive template control cultures
- High sensitivity and selectivity—selective primers for over 20 species of mycoplasma DNA
- Results in less than 5 hours

Treat mycoplasma contamination effectively when it happens.

- **BIOMYC-1:** based on the antibiotic tiamutin
- **BIOMYC-2:** based on the antibiotic minocycline
- **BIOMYC-3:** based on the antibiotic ciprofloxacin

Download brochure

Protect your cell cultures 24/7 with mycoplasma detection and treatment products from Biological Industries. Available in the U.S. from Rainbow Scientific, Inc.

Rainbow Scientific, Inc.

Visit www.shoprainbowscientific.com for easy online ordering or call 860.298.8382.

BI Biological Industries
Culture of Excellence
www.bioind.com

Leading North American supplier of state-of-the-art products

Cell 157, June 5, 2014 ©2014? Elsevier Inc. DOI http://dx.doi.org/10.1016/j.cell.2014.05.026

SnapShot: Resident Memory T Cells

Lalit K. Beura[1,2] and David Masopust[1,2]
[1]Department of Microbiology; [2]Center for Immunology
University of Minnesota Medical School, Minneapolis, MN 55455, USA

Cell

T CELL RECIRCULATION PATTERNS

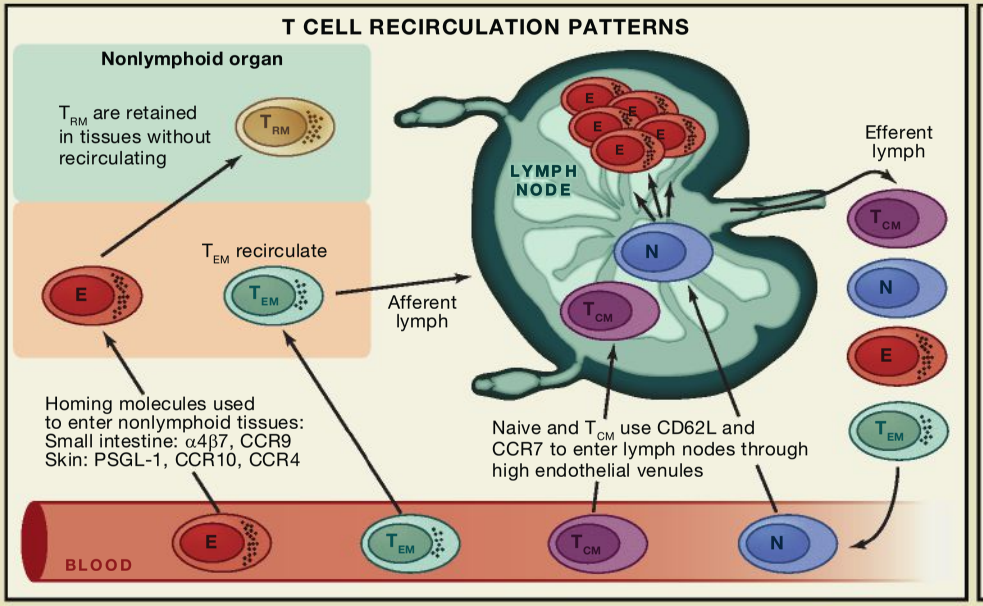

THE TISSUE MILLIEU INDUCES T_{RM} DIFFERENTIATION AND MAINTENANCE

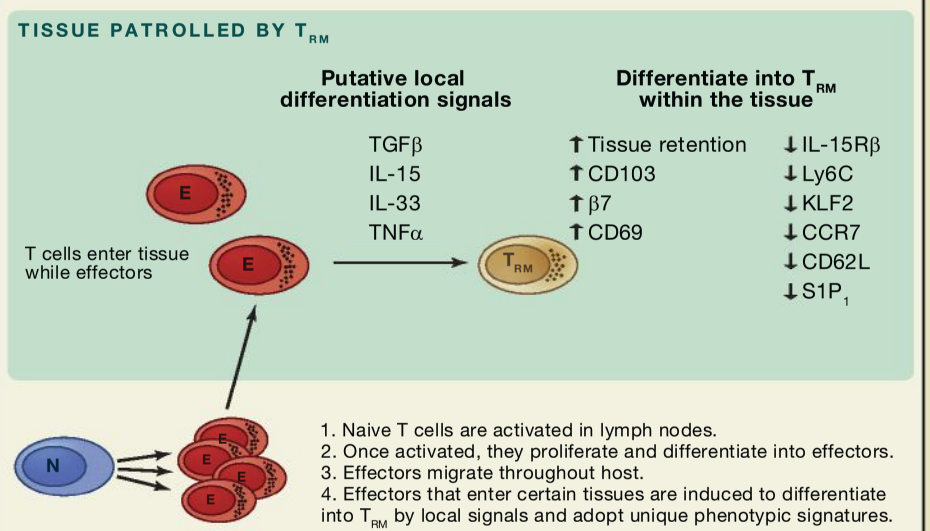

[redacted] OF EXPOSURE

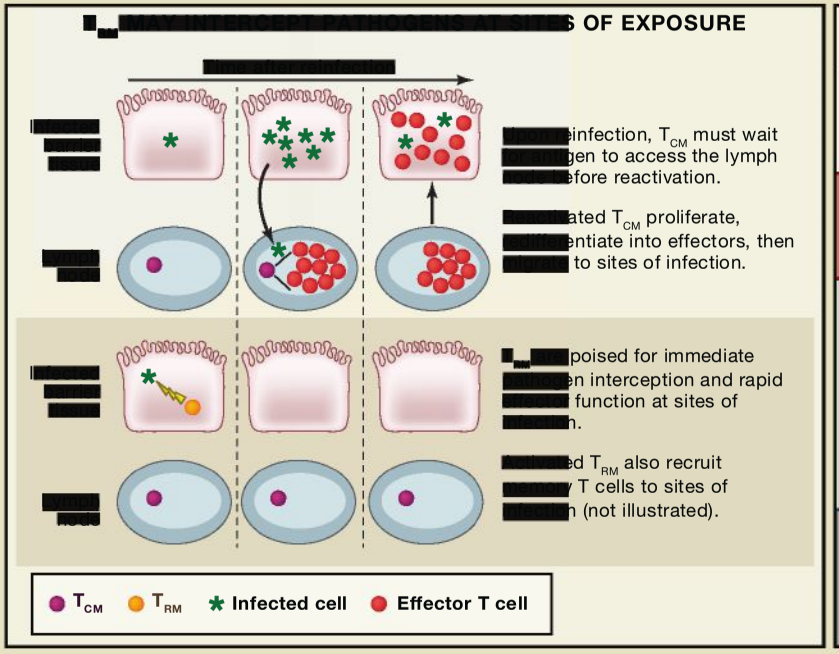

T_{RM} MAINTENANCE VS T_{EM} RECIRCULATION

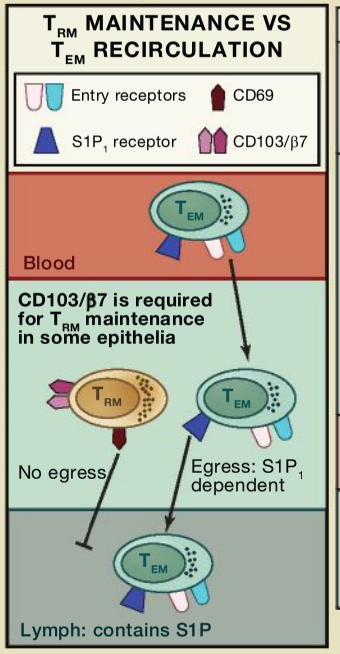

	Markers	N	E	T_{CM}	T_{EM}	T_{RM}
Effector differentiation	Granzyme B	–	+++	–	+	++*
	Eomes	–	+	++	++	+
	Ly6C	±	++	++	++	–
Migration/ retention	L-selectin	++	–	++	–	–
	CCR7	++	–	++	±	–
	CD44	–	+++	+++	+++	++
	CD69	–	–**	–	–	++
	CD103	+	–	–	–	+++*
	$S1P_1$	++	++	++	++	–
	KLF2	++	++	++	++	–
Cytokine receptors	IL-15Rβ	++	+	+++	++	±
	IL-7Rα	++	–	+++	+	++
	Location	SLO, blood, lymph	SLO, blood, non-lymphoid tissues	SLO, blood, lymph	Blood, spleen, red pulp, some nonlymphoid tissues	Barrier tissues

* Varies among different tissues **Effectors transiently express CD69 after stimulation

See online version for legend and references.

Thermo SCIENTIFIC

A Thermo Fisher Scientific Brand

more power to you.

Thermo Scientific™ Pierce™ Power System lets you power through two essential protein detection steps with one efficient system! Save hours in coomassie staining and protein transfer from gels to membranes without compromising the quality of your results. Efficiently stain or transfer protein gels in about 10 minutes with one system. Intuitive, color LCD touchscreen interface and pre-programmed methods make both coomassie staining and protein transfer easy. One power station + two cassettes = powerful possibilities.

- Request a demo at thermoscientific.com/powersystem

Thermo Scientific Pierce Power Stainer
Coomassie staining and destaining of proteins in about 10 minutes

Thermo Scientific Pierce Power Blotter
Transfer proteins in 5-10 minutes

Cell 159, October 23, 2014 ©2014 Elsevier Inc. DOI http://dx.doi.org/10.1016/j.cell.2014.10.012

SnapShot: The Germinal Center Reaction

Gabriel D. Victora
Whitehead Institute for Biomedical Research, Cambridge, MA 02142, USA

Cell

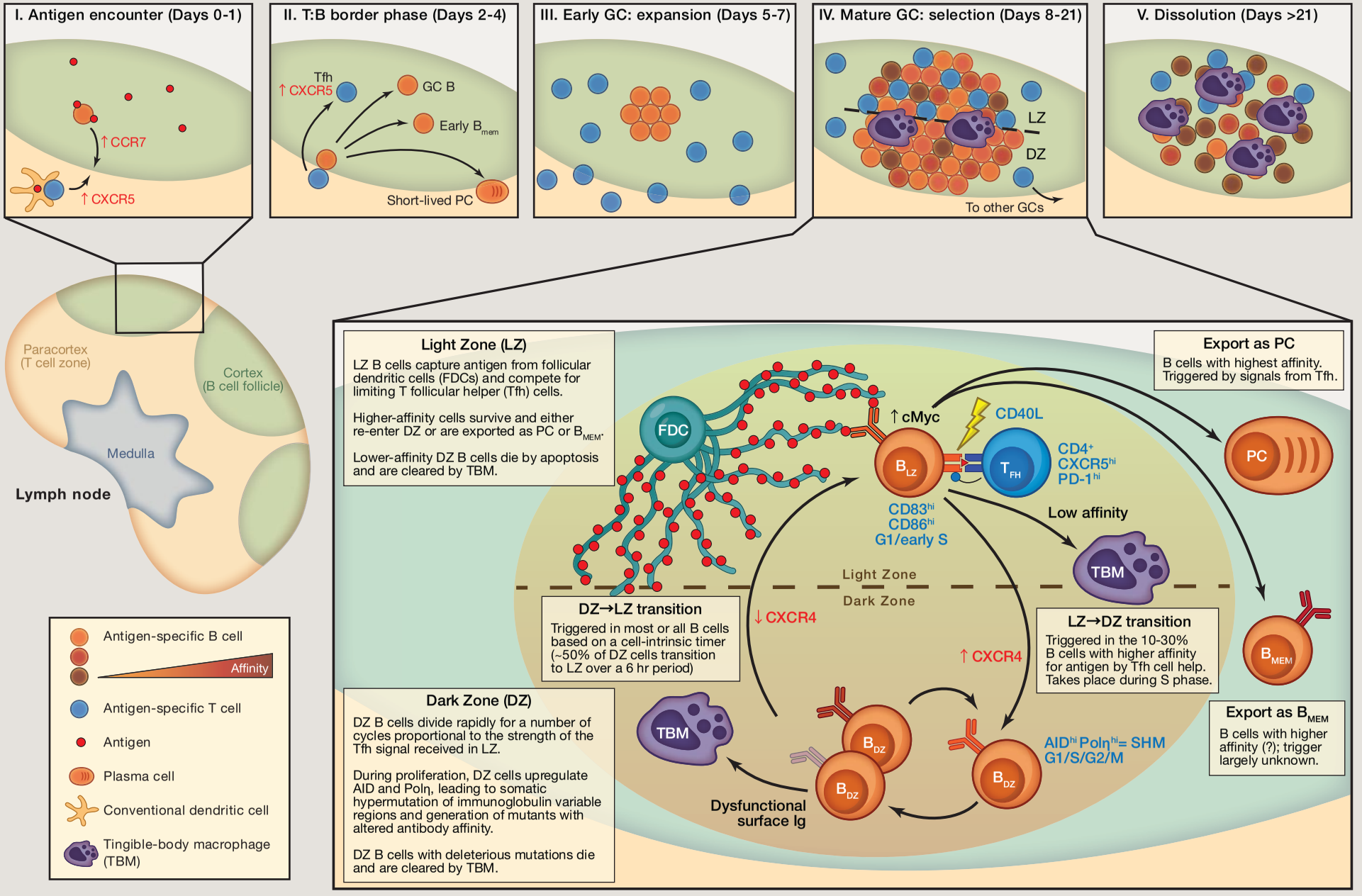

See online version for legend and references.

NEW

Sensor-based shRNA Pooled Screening Libraries

Achieve greater confidence in screen hits

Find shRNA, cDNA and ORFs for your gene of interest using

FETCH my gene

www.transomic.com

PLATINUM *Select* shRNA-mir screening libraries combine superior knockdown efficiency from sensor-based shERWOOD algorithm designs with a stringent equimolar pooling process for more consistent and sensitive hit detection from your pooled screen. Lentiviral pooled shRNA libraries are available targeting the whole genome, epigenome, kinome, cancer metabolism and more.

- ***Powerful and consistent knockdown*** *- drives phenotypic change even at single copy*
- ***Increased confidence in screen hits*** *- more potent shRNA per gene for clearer hit identification*
- ***Flexible format options*** *- high titer lentiviral particles or plasmid DNA pool formats*
- ***Custom Pool Development*** *- Select gene list and vector options*

NEW

Pooled Screening Deconvolution Service - Includes library preparation, sequencing and data analysis from your genomic DNA samples.

Visit **www.transomic.com/pooledscreening/neuron** for more details and to place your order.

transOMIC technologies

www.transomic.com

Enabling Discovery Across the Genome

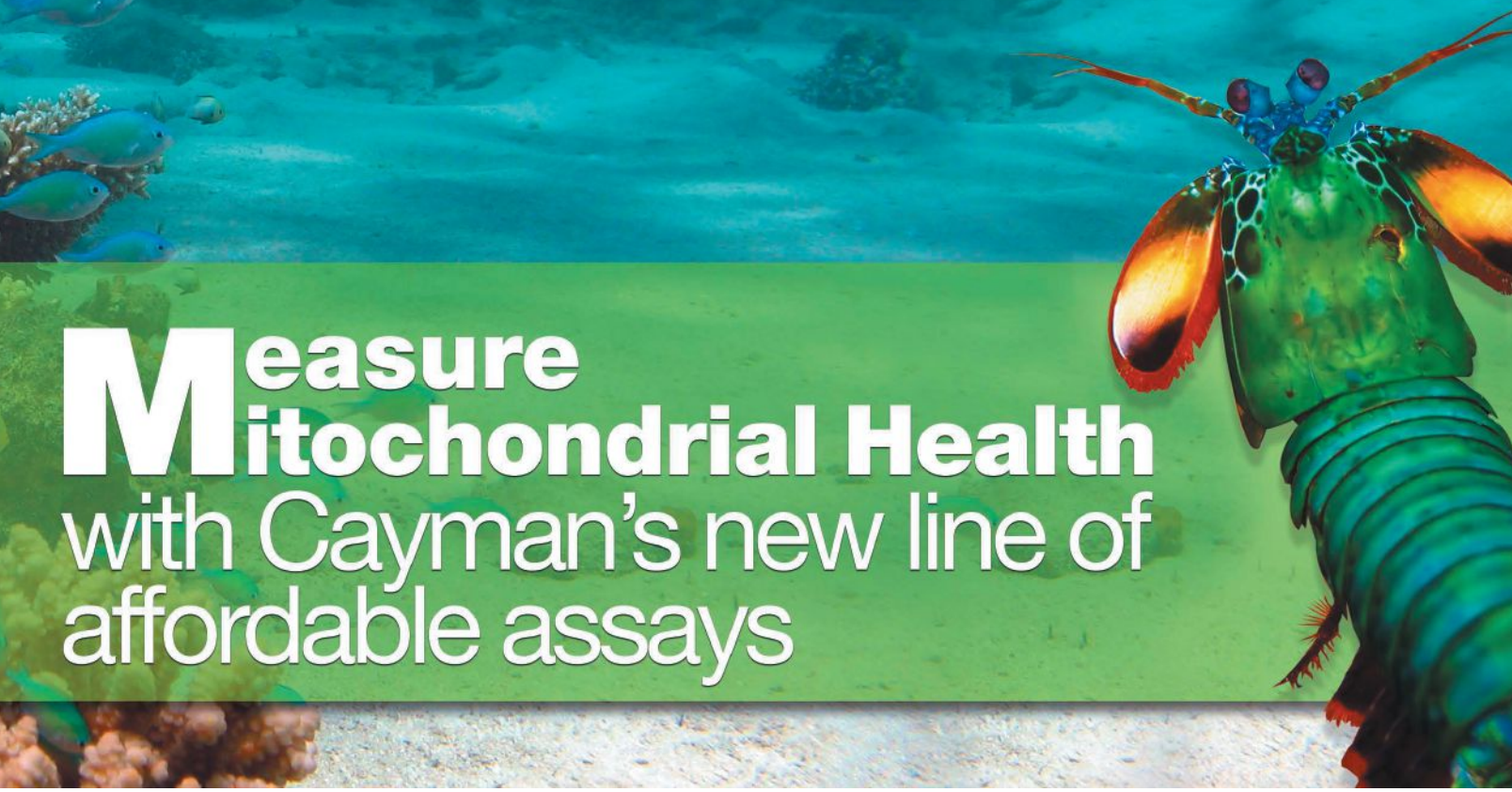

Measure Mitochondrial Health with Cayman's new line of affordable assays

mitoV Assays

Electron Transport Chain Activity Assays
Measure toxicity by screening for inhibition of complexes I, II, II/III, and IV in the electron transport chain

Mitochondrial (Tissue) Isolation Kit
A complete package for easy isolation of mitochondria from fresh tissue

Citrate Synthase Acitvity Assay Kit
Colorimetric assay to accurately quantify mitochondrial citrate synthase activity

Cellular Oxygen Consumption Assays

Measure the oxygen consumption rate in living cells using MitoXpress®-Xtra, a phosphorescent oxygen probe - *does not require expensive equipment*

Oxygen Consumption Rate Assay
Oxygen Consumption/MitoMembrane Potential Dual Assay
Oxygen Consumption/Glycolysis Dual Assay

Our assay kits provide the convenience, reliability, and accuracy your research depends on. Discover the difference more than 30 years of experience makes in assay performance.

Cayman CHEMICAL | *Helping Make Research Possible*

View our line of assay kits and other tools for Mitochondrial Health at **www.caymanchem.com/MitochondrialHealth**

AACR American Association for Cancer Research

ANNUAL MEETING

2015 | PHILADELPHIA

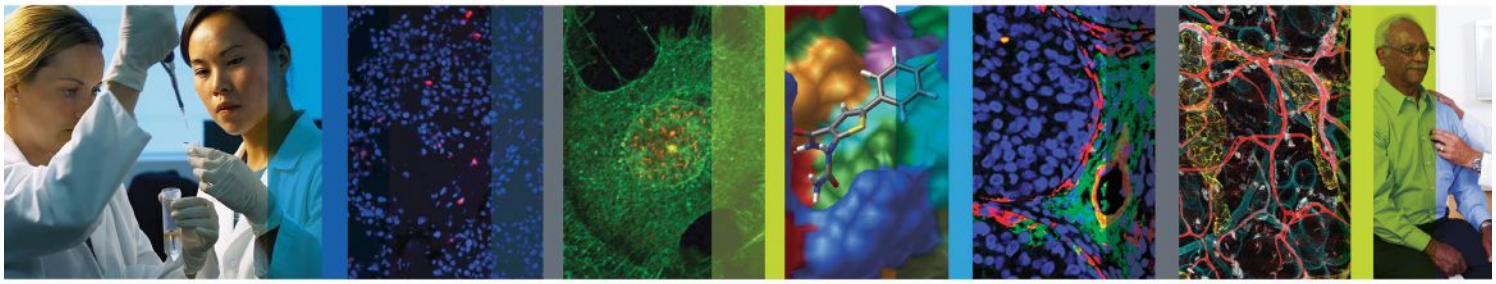

Bringing Cancer Discoveries to Patients

APRIL 18-22, 2015
PENNSYLVANIA CONVENTION CENTER
PHILADELPHIA, PA

Join us in Philadelphia

for the most comprehensive cancer research meeting in the world... the AACR Annual Meeting 2015!

Connect with the international cancer research community to foster new collaborations, learn about cutting-edge advances, and obtain feedback on your research.

This must-attend meeting covers every aspect of cancer – from epidemiology, molecular biology, and clinical studies to prevention, survivorship, and patient advocacy.

Missed the regular abstract deadline?
Submit your late-breaking abstract by January 27, 2015!
Late-breaking abstracts detailing highly significant and timely findings will be considered for presentation at AACR's Annual Meeting 2015.

Register by February 9, 2015 and save!

Become a Member!
Join the AACR and receive a discount on registration.

We look forward to welcoming you to our hometown of Philadelphia, PA!

WWW.AACR.ORG

Leading Edge
Review
Cell

Transgenerational Epigenetic Inheritance: Myths and Mechanisms

Edith Heard[1,2,*] and Robert A. Martienssen[3,4,*]
[1]Mammalian Developmental Epigenetics Group, Institut Curie, CNRS UMR 3215, INSERM U934, 26 rue d'Ulm, 75248 Paris Cedex 05, France
[2]Collège de France, 11 place Marcelin-Berthelot, Paris 75005, France
[3]Howard Hughes Medical Institute and Gordon and Betty Moore Foundation, Cold Spring Harbor Laboratory, Cold Spring Harbor, NY 11724, USA
[4]Chaire Blaise Pascal, IBENS, École Normale Supérieure, Paris 75230, France
*Correspondence: edith.heard@curie.fr (E.H.), martiens@cshl.edu (R.A.M.)
http://dx.doi.org/10.1016/j.cell.2014.02.045

Since the human genome was sequenced, the term "epigenetics" is increasingly being associated with the hope that we are more than just the sum of our genes. Might what we eat, the air we breathe, or even the emotions we feel influence not only our genes but those of descendants? The environment can certainly influence gene expression and can lead to disease, but transgenerational consequences are another matter. Although the inheritance of epigenetic characters can certainly occur—particularly in plants—how much is due to the environment and the extent to which it happens in humans remain unclear.

Introduction

The notion that heredity is influenced by the environment has figured prominently in evolutionary thinking for centuries, as Luther Burbank famously stated, "heredity is only the sum of all past environment" (Burbank, 1906). But, with the rediscovery of genetics, conventional wisdom had it that selection acts on phenotypic variation via genetic variation that is itself blind to environmental cues. Further, according to Weismann's principle of the germplasm (1892), somatic cells are separated from germ cells, and thus, no mechanisms were thought to exist for germ cells to be modified by the environment. Over the last few years, the "rediscovery" of epigenetics and its underlying mechanisms has reopened this old debate, giving rise to the concept of transgenerational inheritance of epigenetic variation and even of acquired traits (Box 1).

In principle, epigenetic inheritance and germline reprogramming are two sides of the same coin. Germline reprogramming facilitates totipotency of the zygote, a cornerstone of developmental biology since the concept of "epigenesis" was first proposed (Aristotle, *On the Generation of Animals*; Harvey, 1651; Wolff, 1759). Reprogramming is required to remove epigenetic signatures acquired during development or imposed by the environment so that subsequent elaboration of the body plan in the embryo properly reflects the genetic blueprint characteristic of each species. If germline reprogramming fails, epigenetic marks can be retained and could be transmitted from one generation to the next. As with classical (i.e., DNA sequence) mutations, most epigenetic "mutations" (epialleles) are either neutral or deleterious, frequently involving the unleashing of transposable elements and other genomic parasites. But transgenerational epigenetic inheritance also has the potential to be adaptive and, in some cases, might even respond to environmental challenges with major implications for heredity, breeding, and evolution.

Epigenetic inheritance is relatively common in plants. The plant germline arises from somatic cells exposed to developmental and environmental cues (Box 2), and many plant species can be propagated clonally with no germline passage at all. It is perhaps no accident that the inheritance of acquired traits was first proposed by botanists, most famously by Jean-Baptiste Lamarck and most infamously by Trofim Denisovich Lysenko. The potential implications for mammalian development and for human health were quickly realized, and in recent years, many potential examples of epigenetic inheritance have been documented. However, such studies often concern inter- rather than transgenerational effects (Figure 1) and rarely exclude DNA sequence changes as the underlying cause for heritability. Although intergenerational effects (such as maternal effects) certainly occur in mammals, the degree to which they can be transmitted in the absence of the initial trigger remains unclear. In mammals, efficient reprogramming occurs in the early embryo and in the germline (Box 2). These two rounds of epigenetic erasure leave little chance for inheritance of epigenetic marks, whether programmed, accidental, or environmentally induced (Figure 2A). Thus, although transmission of acquired states can occur in some animals (such as nematodes), proof that transgenerational inheritance has an epigenetic basis is generally lacking in mammals. Indeed, evolution appears to have gone to great lengths to ensure the efficient undoing of any potentially deleterious bookmarking that a parent's lifetime experience may have imposed.

In this Review, we will examine the mechanisms underlying epigenetic inheritance and germline reprogramming (Box 3). Several comprehensive reviews of epigenetic inheritance in plants (Schmitz and Ecker, 2012; Weigel and Colot, 2012) and animals (Daxinger and Whitelaw, 2012; Jablonka and Raz, 2009; Lim and Brunet, 2013) have been published recently, so we will focus on aspects that are shared and for which parental

Box 1. Definitions of Transgenerational Epigenetics

The term epigenetics was originally coined by Conrad Hal Waddington in 1942 to describe the bridge between genotype and phenotype during development. Subsequently, the definition shifted toward the notion of heritability, in part due to studies on DNA methylation and its potential role as a memory mark for propagating cell identity via control of gene expression states. Although more recent definitions range from the structural adaptation of chromosomal regions so as to register, signal, or perpetuate altered activity states (Bird, 2007), to environmental influences on gene expression and chromatin, here we employ the term in the more conservative sense that concerns the perpetuation of gene expression and function across cell divisions without changes in DNA sequence.

The term transgenerational is often used rather broadly to describe all nonsequence-based effects that can be transmitted from one generation to the next. However, it is important to distinguish parental (or intergenerational) effects, such as the impact of in utero exposure to particular nutritional, hormonal, or stress/toxin environments on the developing embryo and its germline (which will eventually produce grandchildren), from truly transgenerational effects (Figure 1) that are found in generations that were not exposed to the initial signal or environment that triggered the change (Daxinger and Whitelaw, 2012; Lim and Brunet, 2013) (Ferguson-Smith and Patti, 2011).

Box 2. Germline and Early Embryonic Reprogramming in Animals and Plants

Strategies for reprogramming parental epigenomes vary considerably in vertebrates and plants (Figure 2). In the mouse germline and also early postfertilization, the two parental genomes undergo extensive DNA demethylation via both active and passive mechanisms, leading to equivalent hypomethylated states in early cleavage stages accompanied by dynamic changes in histone modification (Hackett and Surani, 2013; Smith et al., 2012). The study of genomic imprinting, which represents a paradigm of epigenetic erasure and resetting in the germline, has revealed sophisticated mechanisms that enable DNA methylation imprints to resist the postfertilization wave of reprogramming (Messerschmidt, 2012) (Figure 2). In early zebrafish embryos, the paternal methylome is stably inherited without changing state during early development, whereas the maternal methylome undergoes demethylation of oocyte-specific hypermethylated regions and de novo methylation of oocyte-specific hypomethylated regions (Jiang et al., 2013; Potok et al., 2013). How the zebrafish paternal methylome is protected from remodeling during development, whereas the maternal epigenome undergoes extensive remodeling, is unclear. In humans and mice, certain genes are protected from protamine replacement in sperm, preserving key histone variants and their modifications (Brykczynska et al., 2010; Hammoud et al., 2009).

In flowering plants, meiocytes (gamete progenitors) differentiate within floral organ primordia that arise from postembryonic stem cells in shoot and floral meristems (Figure 2B). These stem cells remain more or less undifferentiated from early embryogenesis until floral determination but also give rise to somatic branches and leaves and can sometimes be replaced by surrounding cells. For this reason, the plant germline is poorly defined and is potentially subject to somatic modification. Epigenetic inheritance is widespread in plants in part because germline reprogramming of DNA methylation is limited to asymmetric cytosines (or CHH, where H = A, C, T) in sperm cells. CHH methylation is regained after fertilization guided by maternal small RNA and further propagated in the embryo (Calarco et al., 2012; Ibarra et al., 2012). Hence, unlike mammals, there is no overt germline reprogramming of CG methylation. However, reprogramming in germline companion cells (the vegetative nucleus in pollen and the central cell in the ovule) coincides with loss of chromatin remodelers (Figure 2B), and variants of histone H3 largely replace canonical variants in both pollen cell types (Ingouff et al., 2007; Schoft et al., 2009). Some of these variants cannot undergo key posttranslational modifications, which may also contribute to loss of heterochromatin (Jacob et al., 2014; Schoft et al., 2009). Companion cell reprogramming results in transposon activation and the accumulation of small RNA in the gametes (Figure 2B), which reinforces both imprinting and transposon silencing in the germline (Hsieh et al., 2009; Slotkin et al., 2009).

effects and DNA sequence mutations have been excluded as far as possible. We also examine the limited evidence for adaptive inheritance of environmentally induced epigenetic traits and consider the implications for evolution, plant breeding, and human health.

Epigenetic Inheritance of Transposon and Transgene Silencing by DNA Methylation

Long before the terms ''transgenerational'' and ''epigenetic'' were in widespread use (Box 1), the first examples of epigenetic inheritance were described in plants. Following her discovery of transposable elements, Barbara McClintock recognized that *Activator* and *Suppressor Mutator* transposons in maize cycled between active and silent phases and that these phases could be inherited across generations (McClintock, 1961). These transposons sometimes brought nearby color genes under their control, allowing the genetic identification of both *trans*-acting (transposase) and *cis*-acting (transposon) regulatory factors. For this reason, McClintock drew parallels between transposons as ''controlling elements'' and gene control by λ repressor (McClintock, 1961), parallels that are still popular today (Ptashne, 2013).

Subsequently, a variety of molecular mechanisms has emerged that can result in transgenerational epigenetic inheritance of genes, transgenes, and transposons (Box 3). McClintock's ''cycling'' transposons were associated with changes in DNA methylation, as were epialleles at genes located nearby, which resulted in transgenerational leaf and seed color phenotypes (Lisch, 2012; Slotkin and Martienssen, 2007). At around the same time, silencing of transgenes and flower color genes was observed in petunia and tobacco, as well as in the model plant *Arabidopsis*, where genetic screens could be brought to bear (Law and Jacobsen, 2010). Some of the first silencing mutants isolated in *Arabidopsis* were in the maintenance DNA methyltransferase MET1 (DNA methyltransferase 1), the histone deacetylase HDA6, and the Snf2/swi2 chromatin remodeler DDM1 (decrease in DNA methylation 1) (Eun et al., 2012). Mutants in *met1* and *ddm1* had previously been isolated in molecular screens and segregated unmethylated transposable elements (TEs) and repeats in subsequent generations, independently of the causative mutation. Hypomethylated TEs neighboring genes resulted in epimutations such as *BONSAI* and *FWA* (*FLOWERING WAGENINGEN*) (Slotkin and Martienssen, 2007), and the penetrance of phenotypes observed in

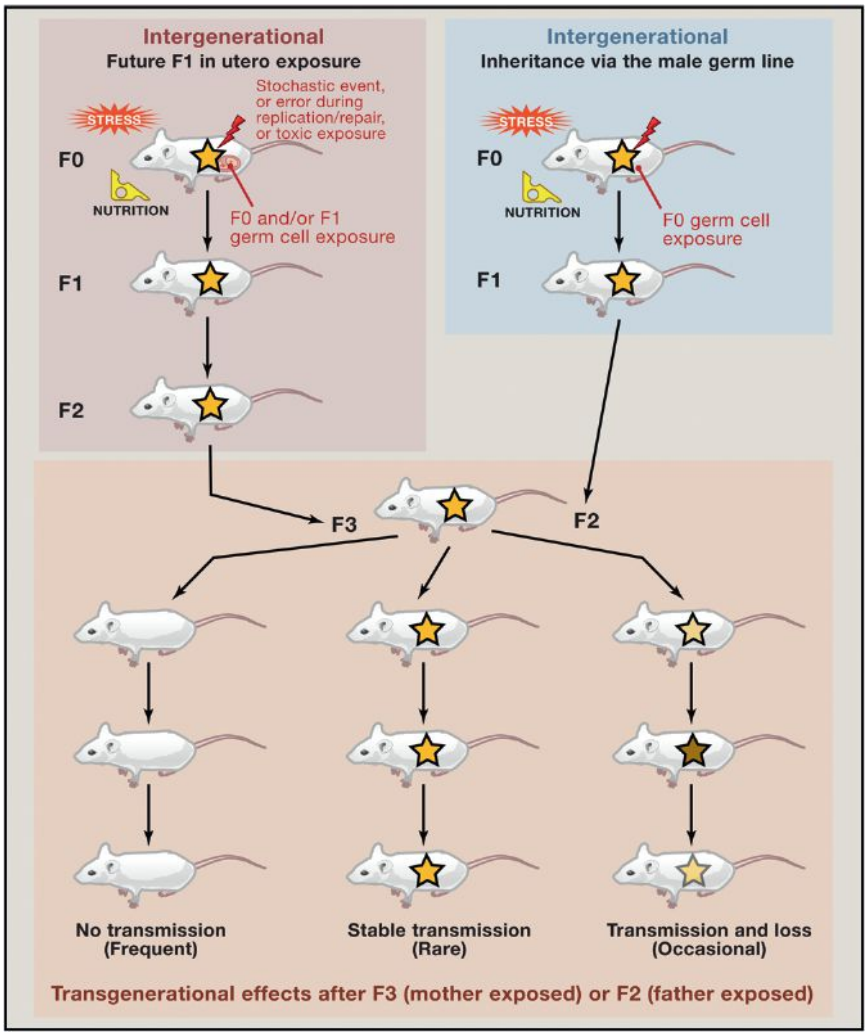

Figure 1. Transgenerational and Intergenerational Epigenetic Effects

Epigenetic changes in mammals can arise sporadically or can be induced by the environment (toxins, nutrition, and stress). In the case of an exposed female mouse, if she is pregnant, the fetus can be affected in utero (F1), as can the germline of the fetus (the future F2). These are considered to be parental effects, leading to intergenerational epigenetic inheritance. Only F3 individuals can be considered as true transgenerational inheritance (see Box 1) in the absence of exposure. In the case of males in which an epigenetic change is induced, the individual (F0) and his germline (future F1) are exposed; the F1 is thus considered as intergenerational. Only F2 and subsequent generations can be considered for evidence of transgenerational inheritance.

ddm1 and *met1* mutants was greatly enhanced in double mutants with histone modification and RNAi (Creasey et al., 2014; Mathieu et al., 2007; Mirouze et al., 2009; Zemach et al., 2013), indicating that these mechanisms can rescue methylation defects to some extent. Epigenetic variants in garden varieties, such as peloric flowers in toad flax and nonripening tomatoes, also have unstable phenotypes associated with methylation changes near genes, in a nearby transposon in at least one case (Cubas et al., 1999; Manning et al., 2006).

In perhaps the most comprehensive studies to date, heritable hypomethylated chromosomal segments have been propagated for eight or more generations in so called "epi RILs" (epigenetic recombinant inbred lines). These are constructed by backcrossing *ddm1* and *met1* mutants and selfing wild-type progeny by single-seed descent (Johannes et al., 2009; Mirouze et al., 2012). Many of these hypomethylated segments are inherited through meiosis and mitosis (Figure 3). By high-throughput phenotyping, quantititative genetics, and epigenetic profiling, the phenotypic consequences of this epigenetic inheritance could be determined, with many phenotypes displaying very high levels of epigenetic heritability (Colomé-Tatché et al., 2012; Cortijo et al., 2014). Several of the differentially methylated regions (DMR) behave as bona fide epigenetic quantitative trait loci (QTL^{epi}) accounting for up to 90% of the heritability for two complex traits, flowering time and primary root length (Cortijo et al., 2014). Up to 30% of these DMR exist in natural populations (Schmitz et al., 2013) suggesting that transposon cycling is more prevalent than originally supposed.

A limited number of epialleles have also been described in mice. The expression of certain transgenes was found to be variable among littermates as was the tendency for active or inactive states to be inherited by the next generation. As the mice used were genetically inbred, it was deduced that the inheritance had an epigenetic basis (Daxinger and Whitelaw, 2012). A few bona fide cases of transgenerational inheritance at endogenous loci in mammals have also been identified. Importantly, these were associated with TEs—for example, at $Agouti^{vy}$ and $Axin^{Fu}$ (axin fused). Transcription originating in an intracisternal A particle (IAP) retrotransposon inserted 100 kb upstream of the agouti gene (*A*) causes ectopic expression of agouti protein, resulting in yellow fur, obesity, diabetes, and increased susceptibility to tumors (Daxinger and Whitelaw, 2012).

Just like cycling transposons in maize, A^{vy} mice are epigenetic mosaics for IAP retrotransposon activity and DNA methylation: isogenic A^{vy} mice have coats varying from full yellow, through variegated yellow/agouti, to full agouti (pseudoagouti). The distribution of phenotypes among offspring is related to the phenotype of the dam; when an A^{vy} dam has the agouti phenotype, her offspring are more likely to be agouti (paternal transmission has no effect on phenotype) (Daxinger and Whitelaw, 2012). This maternal epigenetic effect is not the result of a maternally contributed environment. Rather, it results from incomplete erasure of epigenetic modification when a silenced

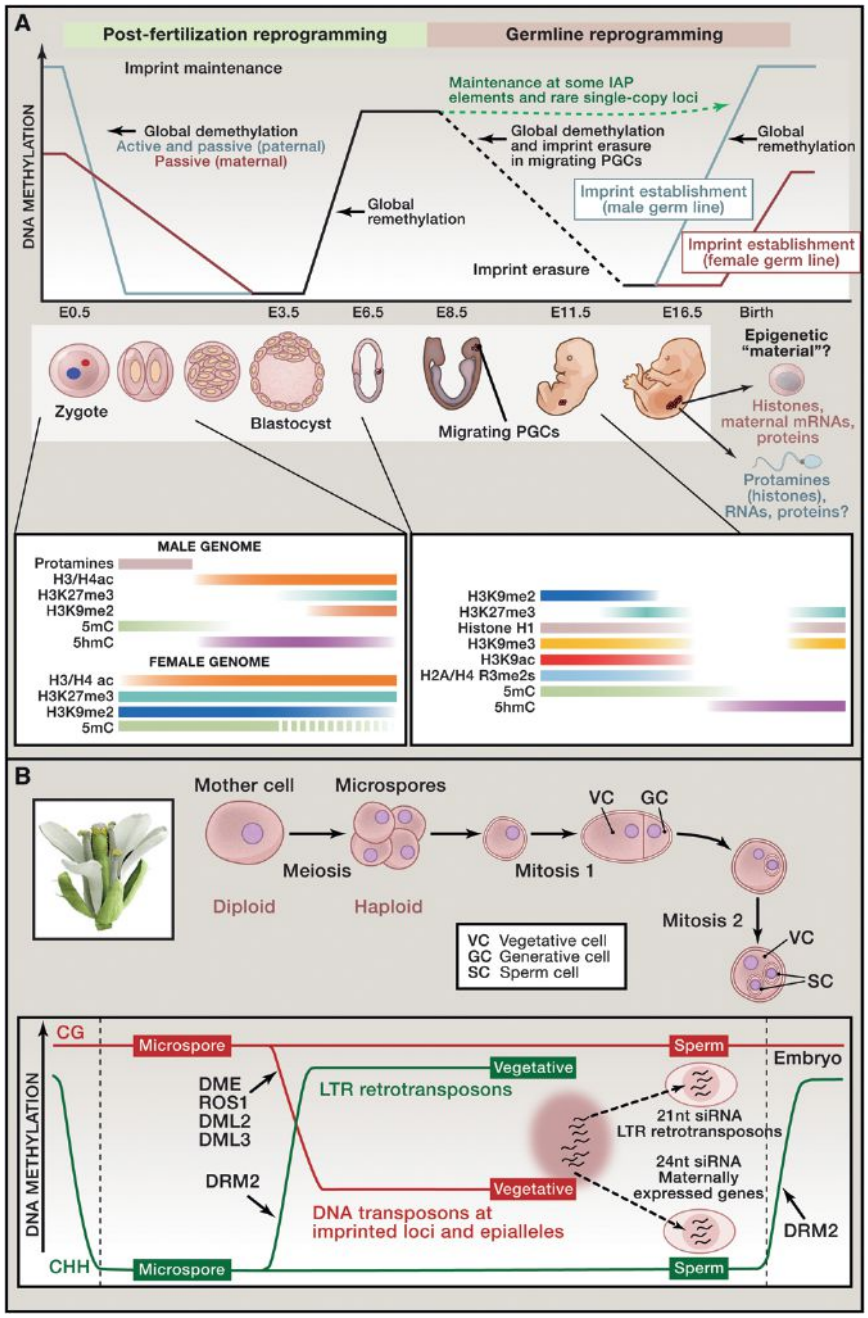

Figure 2. Germline Reprogramming of DNA Methylation in Mice and Plants

(A) In mice, there are at least two rounds of genome-wide DNA methylation reprogramming. The first occurs just after fertilization, in the zygote and early cleavage stages, to erase gametic (sperm and oocyte) epigenomic marks. During this phase of reprogramming, genomic imprints are maintained. The other major reprogramming process occurs in the germline, where the paternal and maternal somatic programs are erased, together with imprints, and the inactive X is reactivated. Subsequent to this, parent-specific imprints are laid down in the germline. In each reprogramming window, a specific set of mechanisms regulates erasure and re-establishment of DNA methylation. Recent studies have uncovered roles for the TET3 hydroxylase and passive demethylation, together with base excision repair (BER) and the elongator complex, in methylation erasure from the zygote (Seisenberger et al., 2013). In the germline, deamination by AID, BER, and passive demethylation has been implicated in reprogramming, but the processes are still poorly understood.

(B) In plants, meiocytes differentiate from somatic cells, and the germline undergoes two to three sterotypical mitotic divisions after formation of the haploid microspore (pollen) and megaspore (ovule) (Gutierrez-Marcos and Dickinson, 2012). In pollen, symmetric CG and CHG methylation (H = A,C,T) is retained in the microspore and sperm cells, but CG methylation is lost from a few hundred imprinted and other genes in the companion vegetative cell nucleus. CHH methylation is sharply reduced in the microspore and sperm cells. 21 nt epigenetically activated siRNA and a subset of 24 nt siRNA arise in the vegetative nucleus but accumulate in sperm cells, where they contribute to imprinting and epigenetic transposon control. Modified from Calarco et al. (2012).

A^{vy} allele is passed through the female germline. Parent-of-origin effects probably arise because the resistance of IAPs to epigenetic reprogramming differs between the male and female germline and also between maternal and paternal genome postfertilization (Figure 2A), but no such difference is found with $Axin^{Fu}$, which otherwise behaves in a similar fashion. Intriguingly, the first mutations found to suppress $Agouti^{vy}$ in the mouse were in similar genes, and in some cases orthologous genes, to those found in similar screens in *Arabidopsis*, including DNA methyltransferases, histone deacetylases, chromatin remodelers, and other ATPases responsible for chromatin compaction (Daxinger and Whitelaw, 2012; Law and Jacobsen, 2010; Eun et al., 2012). In humans, even if transposons are not directly involved, several potential epialleles (e.g., familial predisposition to cancer via the *MLH1* or *DAPK1*loci) also turned out to be dependent on DNA sequence polymorphisms so that aberrant gene silencing (epimutation) is established every generation but is erased in the germline (Hitchins et al., 2011; Raval et al., 2007).

In both plants and animals, epigenetic inheritance of genes controlled by transposons may reflect a predisposition of transposons to DNA methylation and a resistance of transposons to reprogramming, leading to transgenerational epigenetic effects—and, in some cases, parent-of-origin effects—providing a potential basis for the evolution of imprinting (Gehring et al., 2009; Walter et al., 2006). The only case so far in which transposons clearly impact imprinting in mammals is the mouse *Rasgrf1* locus, where noncoding RNA and the PIWI-interacting RNA (piRNA) pathway are required for de novo methylation of the promoter DMR (Watanabe et al., 2011). A retrotransposon sequence

Box 3. Transgenerational Mechanisms

EPIGENETIC MECHANISMS

Self-Sustaining Feedback Loops

The mRNA or protein product of a gene can stimulate its own transcription. Such feedback loops can clearly enable heritable states of altered gene expression without any need to evoke chromatin. However, it is unlikely that such feedback loops alone would enable the propagation of states throughout the length of development and in the germline of complex organisms.

Chromatin-Based Mechanisms

DNA methylation is the best-studied epigenetic mechanism for transgenerational inheritance but is neither universal nor as stable as once thought, with dynamic changes during development and in the germline. Its interplay with RNA interference in plants has provided some detailed mechanistic information on epigenetic inheritance. Histone variants and histone (and protamine) modifications are all potential bearers of epigenetic information, and, together with their "writer" and "reader" complexes, histones can perpetuate chromatin states. Polycomb and Trithorax group proteins (PcG and TrX), underlie ancestral memory strategies for maintaining gene activity in somatic cell lineages, but so far, there is little evidence for PcG complexes as major players in transgenerational inheritance. On the other hand, Trx (COMPASS) complexes, responsible for histone H3 lysine 4 (H3K4) methylation, the lysine-specific demethylase (LSD1) of histone H3K4 and H3K9, and H3K9 methyltransferases, have been implicated in transgenerational inheritance in *C. elegans*.

Noncoding and Coding RNA

RNAs of multiple types have been implicated in epigenetic inheritance across generations. These include maternal stores of mRNAs and long noncoding lncRNAs, as well as small RNAs that interfere with transcription (siRNAs and piRNAs), mRNA stability, or translation (miRNA) via RNAi. Some of these small RNAs are strong candidates for triggering inheritance, as they guide DNA and histone modification in plants, animals, and fungi.

Structural Templating

Prions—proteins that are propagated by changing the structure of normal proteins to match their own—have transgenerational effects in fungi, but so far, there is no evidence in plants or animals that prions can act to transmit information through meiosis. Chaperones such as Hsp90 can also mediate epigenetic variation and may have transgenerational effects.

CONFOUNDING TRANSGENERATIONAL MECHANISMS

Cryptic Genetic Variation

Many examples of transgenerational epigenetic inheritance are, in fact, likely to be DNA sequence based, although it may sometimes be difficult to pinpoint, even in supposedly genetically identical individuals. Several types of such cryptic sequence variation, including copy number variants (CNVs), SNPs, de novo TE insertions, etc., could provide a DNA basis for inheritance that otherwise appears epigenetic.

Behavioral Effects

There are numerous reports of experience-driven heritable changes in the central nervous system (CNS) epigenome involving maternal or paternal behavior, diet, exposure to drugs of abuse, and endocrine disruption. For example, maternal nurturing behavior of newborn pups apparently triggers DNA methylation changes in CNS glucocorticoid receptor genes that persist into adult offspring and result in behavioral changes (Champagne and Curley, 2009). Definitively determining whether experience-driven, acquired epigenetic changes can propagate through the germline and cause behavioral change in subsequent generations is clearly a very seductive but highly controversial topic (Lim and Brunet, 2013). Indeed, recent studies of social defeat phenotypes in males were linked to maternal provisioning (whereby mothers allocate resources to progeny depending on the quality of their mate) rather than epigenetic inheritance (Dietz et al., 2011). Careful experimental design is necessary to define the extent of heritability of experience-driven phenotypic changes, as well as underlying mechanisms. Cross-fostering and in vitro fertilization can circumvent some of the issues in such studies, although they provide confounding factors of their own.

Microbiotic Effects

The intestinal flora—or microbiome—could also be a means of transmitting information across generations. Furthermore, given the recent links between metabolic and neurological diseases with the microbiome, apparent epigenetic inheritance linked with such phenotypes could, in fact, be due to transmission via bacterial populations (Théodorou, 2013).

Metabolites

Metabolites might also be transmitted from one generation to the next and participate in bioenergetic feedback loops. These could be propagated over generations and could also act as cofactors for chromatin modification or RNA processing, for example.

within the noncoding RNA is targeted by piRNAs, which are generated from similar transposons elsewhere. A direct repeat in the DMR, which is required for methylation and imprinting of *Rasgrf1*, serves as a promoter for this noncoding RNA. This mechanism is highly reminiscent of heterochromatic silencing in plants and fission yeast (see below), but the case for this imprinted gene is rather singular, raising the question of why most transposons and retroelement insertions in the mammalian genome do not induce imprinting or epimutations at nearby genes (Rebollo et al., 2012).

RNA Interference and Transcriptional Silencing

What are the factors that specify transposons and transgenes, but not essential genes, for transgenerational silencing? Building on classical work in maize, recent work in *Arabidopsis*, *Drosophila*, and *C. elegans* suggests that small RNA may be an essential component of the trigger that targets heritable silencing. RNAi, which requires transcription, can initiate and maintain a more permanent form of transcriptional silencing, passed from generation to generation in the absence of the small RNA trigger. Many of the clues to this mechanism have come from fission yeast, in which RNAi guides histone modifications, including methylation of histone H3 lysine-9 (H3K9) and the demethylation of H3K4. In fission yeast, histone modification is achieved by cotranscriptional recruitment of

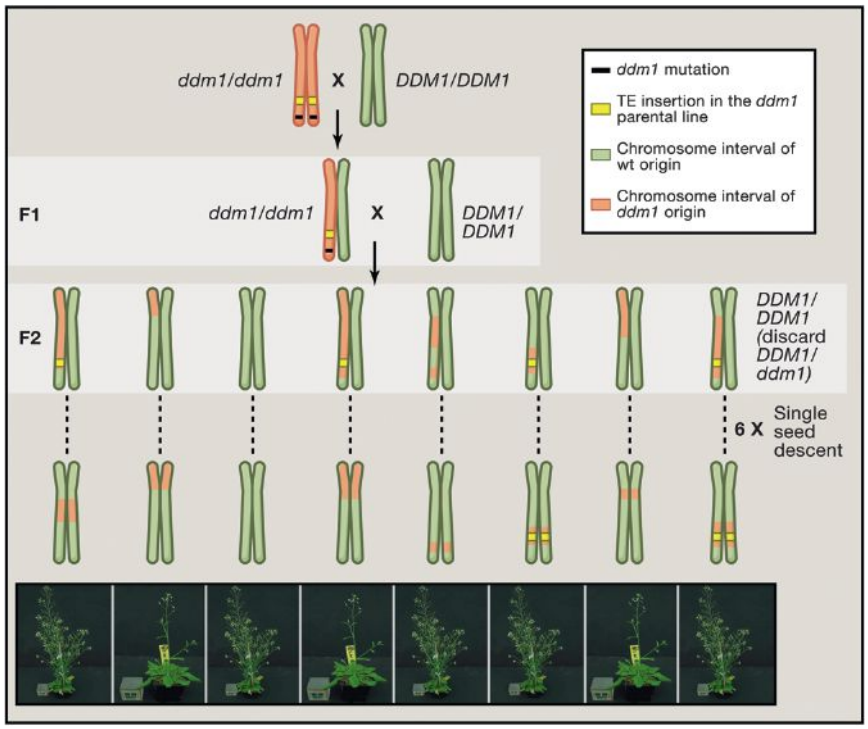

Figure 3. Transgenerational Inheritance of Hypomethylated DNA in Epigenetic Recombinant Inbred Lines, Known as epi-RILs

Arabidopsis plants homozygous for *ddm1* lose heterochromatic (transposon and repeat) methylation in a heritable fashion and were crossed to otherwise-isogenic wild-type plants. Thus, the genome of the *ddm1*/*ddm1* parent is severely hypomethylated (red) relative to that of the wild-type parent (green). Backcrossing of the F1 progeny to the wild-type parental line was used to remove the *ddm1* mutation. Homozygous *DDM1*/*DDM1* lines were then self-crossed for six generations through single-seed descent to generate recombinant inbred lines. Hundreds of parental differences in DNA methylation states across the genome were stably inherited in the epiRIL population and account for most of the heritable variation observed for complex traits, such as flowering time (early and late flowering phenotype, illustrated below each epi-RIL). Adapted from Cortijo et al. (2014).

RNAi transcriptional silencing (RITS) and histone modification complexes via binding of small RNA to PolII-dependent noncoding RNA precursors. Spreading of these complexes along the chromosome occurs by interaction with H3K9me2 itself and by interaction with DNA polymerase and the replisome during S phase. RNAi promotes the release of RNA polymerase II and prevents DNA damage and defects in heterochromatin repair (Castel and Martienssen, 2013; Keller and Bühler, 2013).

RNA-Dependent DNA Methylation

In plants, as in fission yeast, it was also realized that RNAi was linked to transcriptional silencing and was likely responsible for the previously described process of RNA-directed DNA methylation (RdDM) (Eun et al., 2012; Law and Jacobsen, 2010; Slotkin and Martienssen, 2007). In *Arabidopsis*, genes required for RdDM encode factors associated with the large subunits of RNA polymerases PolIV and PolV, which are closely related to PolII (Eun et al., 2012; Haag and Pikaard, 2011; Law and Jacobsen, 2010). For example, RNA-dependent RNA polymerase 2 is required for 24 nt siRNA biogenesis and is associated with PolIV, whereas Argonaute proteins that bind 24 nt siRNA are associated with PolV, as are chromatin remodelers, histone methyltransferases, and DNA-binding proteins, suggesting a link with chromatin as well as RNAi (Haag and Pikaard, 2011; Law and Jacobsen, 2010). The de novo DNA methyltransferases DRM1 and DRM2 (homologs of mammalian Dnmt3), the chromomethyltransferase CMT2, and several histone H3 lysine 9 methyltransferases (SUVH homologs of Su (Var) 3-9) are also required for RdDM, but the direct link between RNAi, DNA, and histone methylation remains unknown (Law and Jacobsen, 2010; Stroud et al., 2014; Zemach et al., 2013). RdDM can correct transgenerational defects in transposon methylation that arise in *ddm1*. These transposons retain or acquire siRNA in *ddm1* mutants, and RNAi is required for restoration of silencing and methylation when DDM1 is reintroduced (Creasey et al., 2014; Ito et al., 2011; Mirouze et al., 2009; Teixeira et al., 2009; Zemach et al., 2013).

Paramutation

Around the same time that McClintock discovered transposable element silencing, R. Alexander Brink, Ed Coe, Jr., and Marcus Rhoades reported the first examples of transgenerational gene silencing by ''paramutation'' in maize (Chandler, 2007; Hollick, 2012). Individual alleles at three different color gene loci gave rise to epialleles with reduced pigmentation. These epialleles silenced other alleles in heterozygotes, more or less permanently. Silencing was allele specific, dose dependent, and temperature dependent and occurred shortly after fertilization. Numerous examples have now been described in plants (Arteaga-Vazquez and Chandler, 2010), and powerful genetic screens in maize uncovered a central role for RNAi (Chandler, 2007; Hollick, 2012): *mop1* (*mediator of paramutation 1*) and *mop2* encode orthologs of *RNA-dependent RNA polymerase 2* and the large subunit of RNA polymerase IV, respectively, whereas *rmr6* (*required to maintain repression6*) encodes the second largest subunit of PolIV. Accessory factors, such as the chromatin remodeler RMR1, the plant-specific RMR2, and the DNA-binding protein CBBP (Barbour et al., 2012; Brzeska et al., 2010) likely interact with paramutated loci. DNA methylation is found at most paramutable loci, and there are up to 2,000 such loci in maize (Eichten et al., 2013; Regulski et al., 2013), but DNA methylation changes are modest and may not be responsible for silencing (Chandler, 2010). The promoters of paramutable genes usually contain transposons and repeats (Chandler, 2007; Erhard et al., 2013; Hollick, 2012), which act in *trans* as the apparent source of small RNA (Arteaga-Vazquez et al., 2010). Inverted repeats can also drive

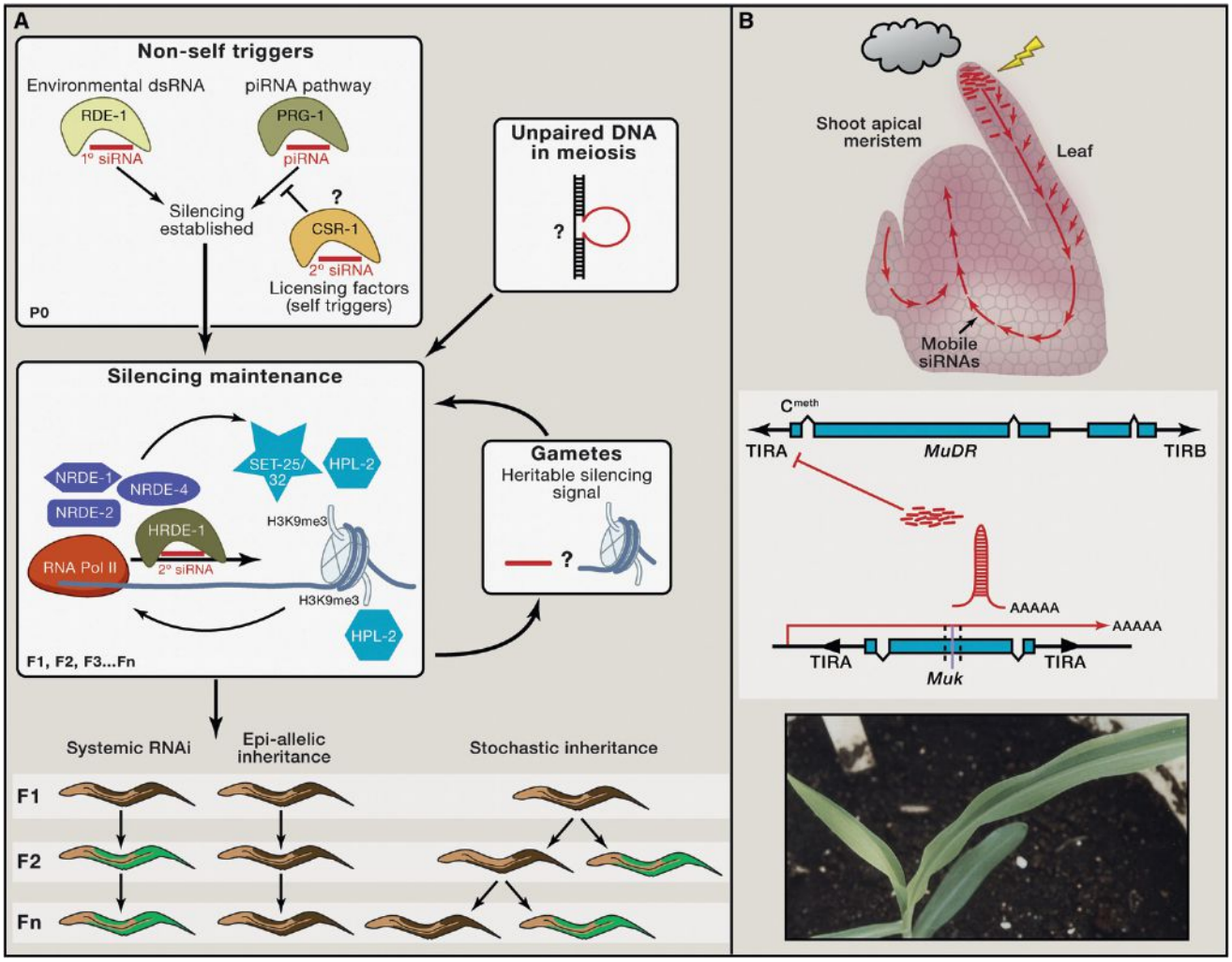

Figure 4. Mechanisms for Transgenerational Inheritance

(A) In *C. elegans*, triggers such as environmental RNAi and endogenous piRNAs lead to the establishment of a nuclear RNAi/chromatin pathway. Maintenance of silencing requires nuclear RNAi factors, including the germline-specific nuclear Argonaute HRDE-1/WAGO-9 and chromatin proteins such as the HP1 ortholog HPL-2 and the putative histone methyltransferases SET-25 and SET- 32. Silencing can be maintained into the F1 for multiple generations (F1–F5) or can become epiallelic with multigenerational, nonstochastic inheritance. Silencing appears to be suppressed by a germline licensing pathway that recognizes bona fide germline transcripts (CSR-1 22G-RNA pathway) and enhanced through the recognition of unpaired DNA during meiosis. Courtesy of Ashe et al. (2012).

(B) In plants, the shoot apical meristem contains stem cells that give rise to leaves and flowers, in which meiocytes and gametes differentiate (Box 2). Small RNAs from roots and leaves are mobile and can re-enter the meristem and, eventually, the flowers. In maize, small RNAs from "Mu-killer" are derived by transcription of a rearranged variant of the 5′ end of the MuDR element. The resulting transcript forms a hairpin, which is processed into small RNAs that target MuDR elements for DNA methylation. When nearby genes are controlled by *Mutator* transposons, MuDR methylation can be visualized as phenotypic sectors inherited by successive leaves, by flowers, and by seeds in the next generation (Lisch, 2012; Slotkin and Martienssen, 2007). Environmental triggers (drought, temperature, and herbivory) can regulate transposon transcription in plants and could hypothetically lead to transgenerational inheritance through similar mechanisms. Modified from Lisch (2012) and Martienssen et al. (1990).

transgenerational silencing of transposons by RdDM in maize (Figure 4B). This coordinate silencing of transposons, reminiscent of paramutation, also depends on *RDR2* (in both maize and *Arabidopsis*) and might operate by a similar mechanism (Lisch, 2012, 2013; Marí-Ordóñez et al., 2013).

RNA interference in *C. elegans* has long-term multigenerational consequences that resemble paramutation (Figure 4A). In worms, inactive transgene arrays containing viral and reporter genes heritably silence active arrays (Rechavi et al., 2011). Resembling paramutation, maintenance of silencing depends on an endogenous RNA-dependent RNA polymerase, encoded by *rrf1*, that is responsible for the generation of 22Gs, which are endogenous 22 nt small RNA that preferentially begin with 5′ guanosine triphosphate (G). piRNA, known as 21Us in *C. elegans*, can trigger endogenous secondary 22Gs that bind nuclear, noncatalytic, worm-specific argonautes (WAGOs). These 22Gs can direct silencing of transgenes and endogenous genes for more than 20 generations (Ashe et al., 2012; Buckley et al., 2012; Burton et al., 2011; Gu et al., 2012; Shirayama et al., 2012). Again, silent transgenes silence other transgenes

in a dominant fashion, resembling paramutation (Ashe et al., 2012).

An important example of paramutation that depends on piRNA was also reported in *Drosophila*. Tandem arrays of P element transposons that contain reporter genes exhibit a *trans*-silencing effect (TSE) in that they can silence similar arrays on other chromosomes but only when transmitted through the maternal germline. Like paramutation in maize, TSE in *Drosophila* is nonallelic and somewhat unstable but is maintained for >50 generations (de Vanssay et al., 2012). TSE requires Aubergine (a metazoan piwi protein), but not RNA-dependent RNA polymerase (which is absent from *Drosophila*) or Dicer-2 (which is required for siRNA biogenesis). Such arrays generate large amounts of piRNA but only when they are silenced, resembling heterochromatic repeat arrays in *S. pombe* (Castel and Martienssen, 2013; Keller and Bühler, 2013) and *Arabidopsis* (Stroud et al., 2014) in this respect. Again, silent target arrays are potent silencers themselves, thus fulfilling the definition of paramutation via maternal piRNA (de Vanssay et al., 2012).

In mammals, very few paramutation-like phenomena have been reported. The best known is the murine Kit^{tm1Alf} allele (Rassoulzadegan et al., 2006), whereby a *LacZ* insertion at the *Kit* locus produces a *Kit-LacZ* fusion (resulting in nonfunctional Kit protein) that leads to melanocyte defects. Wild-type progeny from *Kit* heterozygous parents (and some control progeny) displayed the *Kit* phenotype, but this transmission disappeared after a few generations (F4). The transgenerational phenotype was linked to RNA transmission based on microinjection experiments, and the tRNA methyltransferase Dnmt2 was implicated (Kiani et al., 2013), although the molecular basis for such transgenerational inheritance remains unclear.

Histone Modification

Similarities between RNAi-mediated heterochromatic silencing in *S. pombe* and paramutation in *C. elegans* and *Drosophila*, neither of which have DNA methylation, suggest that histone modifications might also be important for transgenerational inheritance (Castel and Martienssen, 2013). WAGO/NRDE/HRDE-mediated silencing in worms (Figure 4A), Piwi-mediated silencing in *Drosophila*, and RdDM in plants all result in histone H3K9 methylation and depend on it, to some extent, for their transgenerational effects (Burkhart et al., 2011; Gu et al., 2012; Huang et al., 2013; Law and Jacobsen, 2010; Le Thomas et al., 2013; Rozhkov et al., 2013; Shirayama et al., 2012; Sienski et al., 2012). Differences between yeast, plants, and worms include differing dependence of H3K9me2 (and transcriptional silencing) on argonaute catalytic activity (Ashe et al., 2012; Irvine et al., 2006; Qi et al., 2006; Shirayama et al., 2012), reflecting the multiplicity of argonautes in metazoans and plants. Another important difference is that, in addition to histone methylation, plants also deploy DNA methylation downstream of RNAi, although RdDM of transposons can take several generations to take effect (Law and Jacobsen, 2010; Marí-Ordóñez et al., 2013; Teixeira et al., 2009). For example, although RdDM is highly active in pollen (Box 2), it does not silence transposons in the vegetative nucleus (Calarco et al., 2012; Ibarra et al., 2012; Slotkin et al., 2009). It seems likely, therefore, that histone modifications may play an important role in transgenerational inheritance even in plants, especially in the germline.

Screens for loss of transgenerational germline silencing were performed in *C. elegans* (Ashe et al., 2012; Buckley et al., 2012), leading to the identification of *HRDE*-1 (heritable defective RNAi) as *WAGO*-9, an argonaute related to *NRDE*-3, and an H3K9 methyltransferase SET-25, as well as a putative histone methyltransferase, set-32 (Figure 4B). Further, even though the *NRDE* genes were identified in a screen for somatic silencing defects, *NRDE1* to *NRDE4* were also required for transgenerational germline silencing and displayed *hrde* phenotypes. *HRDE*-1 binds 22G secondary endo-siRNA from several thousand genes, pseudogenes, and cryptic loci, resembling *NRDE*-3 in this respect, but only in the germline. Also like *NRDE*-2/3/4, *HRDE*-1 is required for H3K9 methylation at many of these loci in the germline (Buckley et al., 2012).

Remarkably, both *nrde* and *hrde* mutants exhibit progressive loss of fertility of both male and female gametes, as well as loss of gametogenesis itself, after many generations of inbreeding (Buckley et al., 2012). These defects are fully restored when crossed to wild-type, indicating that they are unlikely due to accumulating chromosomal abnormalities. This was not the first time such a phenotype had been observed: mutants in LSD1, the enzyme responsible for demethylation of H3K4, have a very similar progressive loss of fertility, such that later generations have few, if any, offspring compared to early generations (Katz et al., 2009). In another study, mutants in an H3K4 methyltransferase complex caused a heritable increase in longevity for multiple generations after the normal activities of the factors were restored (Greer et al., 2011). In each case, H3K4 methylation, a mark associated with actively transcribed genes, seems to be involved. One idea is that the inability to reprogram this transcriptional histone mark in the germline results in aberrant memory of transcription that increases longevity on the one hand but reduces fertility on the other. Thus, the balance between fertility (germline immortality) and longevity (somatic mortality) may be one of the most profound consequences of epigenetic transgenerational inheritance (Lim and Brunet, 2013).

In some ways, mutants in *ddm1* in *Arabidopsis* resemble mutants in *lsd1* in worms, as they both display elevated levels of H3K4me2, especially in heterochromatin (Lippman et al., 2004). Interestingly, *ddm1* mutants also progressively lose fertility over generations of inbreeding (Kakutani et al., 1996) and lose it much more rapidly in double mutants in which both transcriptional and posttranscriptional silencing are lost (Creasey et al., 2014; Mathieu et al., 2007). Thus, it is possible that RNAi and histone modification also play a role in germline immortality in plants.

Germline Reprogramming and Imprinting

A major barrier to transgenerational epigenetic inheritance is germline reprogramming, during which histone variants and their modifications, as well as small RNAs and DNA methylation, are all reset (Box 2). In mammals, reprogramming occurs both in the germline and in the zygote immediately after fertilization (Figure 2A). Imprinted loci succumb to germline reprogramming but resist the postzygotic phase. The mechanisms that maintain the DNA methylation of imprint control regions (ICRs) in the face of global demethylation in the zygote have recently started to

be unraveled. On the one hand, specific factors (PGC7/Stella/Dppa3) prevent demethylation by binding H3K9me2 and blocking Tet3 activity (which can convert 5-meC to 5-hydroxyl-meC) on the maternal genome, as well as at imprinted loci in the paternal genome (Nakamura et al., 2012). Also, the DNA-binding factor Zfp57, together with Kap1/Trim28, is critical for postfertilization maintenance of maternal and paternal methylation imprints (Li et al., 2008; Messerschmidt et al., 2012). In the germline, where all known imprints appear to be erased, the efficiency of DNA methylation reprogramming of the epigenome has been comprehensively assessed in two recent studies in the mouse (Hackett et al., 2012; Seisenberger et al., 2012). Genome-wide DNA methylation profiling revealed that, although the bulk of the genome (including imprinted loci) becomes demethylated in primordial germ cells, a number of loci (4,730) that escape this demethylation (showing >40% 5 mC) in PGCs were found to be predominately repeat associated—in particular, IAPTR1 elements, which are the most active and mobile (thus potentially mutagenic) repeat elements that may thus need to be silenced even during germline reprogramming. In addition to these IAPs, 233 single-copy loci with >40% 5 mC were found. Why these loci are particularly prone to escape reprogramming is still not clear, but they could represent prime candidates for possible transgenerational inheritance in mammals.

In *C. elegans*, the germline undergoes characteristic alterations in histone modifications that result in meiotic silencing of unpaired DNA, which efficiently silences most transgene arrays in the germline, as well as the X chromosome in males, and depends on the RdRP *ego-1*, which is responsible in part for 22Gs (Kelly and Aramayo, 2007). piRNA, known as 21Us, can also trigger endogenous secondary 22Gs that bind nuclear, noncatalytic WAGOs and silence transposons and some endogenous genes (Ashe et al., 2012; Buckley et al., 2012; Burton et al., 2011; Gu et al., 2012; Shirayama et al., 2012). Germline genes are thought to be protected from silencing by another argonaute, CSR-1, that binds the same 22G siRNA. This has led to the idea that piRNA scan the genome to silence foreign, non-self DNA, whereas CSR-1 22Gs prevent silencing, perhaps by restricting siRNA access to WAGO in the germline (Shirayama et al., 2012). A similar scanning mechanism has been proposed in ciliates that recognize transposons and other insertion sequences that are present in zygotic genomes, but not in the maternal genome, via small RNA (Chalker and Yao, 2011).

In plants, the extent of germline reprogramming of DNA methylation has been examined by whole-genome bisulphite sequencing in pollen cell types (Calarco et al., 2012; Ibarra et al., 2012). In sperm cells and their microspore progenitors, more than 80% of mC residues are retained, including all those in a symmetric (CG or CHG, where H is A,C,T) sequence context, but asymmetric CHH methylation is specifically reduced (Figure 2B). As mCHH is guided by small RNA, this allows for reprogramming of this epigenetic mark after fertilization (Jullien et al., 2012), when the majority of 24 nt heterochromatic siRNA is provided by the maternal genome (Mosher et al., 2009). This results in transgenerational maternal silencing of otherwise-active retrotransposons by RNA-guided DNA methylation (Marí-Ordóñez et al., 2013; Reinders et al., 2013) and may be related to "self-non-self" distinction in *Tetrahymena*, *C. elegans*, and *Drosophila* (Brennecke et al., 2008; Chalker and Yao, 2011; de Vanssay et al., 2012; Shirayama et al., 2012).

24 nt and 21 nt siRNA pathways antagonize each other in plants (Creasey et al., 2014; Jauvion et al., 2012; Marí-Ordóñez et al., 2013), reminiscent of WAGO and CSR-1 22Gs in *C. elegans*, and may participate in scanning for "non-self" transposons in pollen (Slotkin et al., 2009). 21 nt secondary siRNA (epigenetically activated siRNA or easiRNA) are triggered by miRNA (Creasey et al., 2014) and target transposons that are strongly activated in the vegetative nucleus (Figure 2), accompanied by downregulation of DDM1 (Calarco et al., 2012; Ibarra et al., 2012; Slotkin et al., 2009). 21 nt easiRNA accumulate in sperm cells, where they recognize these same transposons in the germline (Slotkin et al., 2009) and could contribute to reduced RdDM. After fertilization, methylation levels are restored in the embryo (Figure 2) but remain low in the endosperm, an extrambryonic tissue in the seed that is the product of fertilization of the central cell nucleus (companion to the egg cell) with a second sperm cell. The endosperm also acts a source of mobile small RNA that may reinforce RdDM in the embryo (Hsieh et al., 2009). Imprinting in flowering plants is largely restricted to the endosperm, and, in sperm cells, maternally expressed imprinted genes are protected from reprogramming by 24 nt siRNA from the vegetative nucleus that triggers RdDM in sperm (Calarco et al., 2012; Ibarra et al., 2012). For this reason, imprinting of a subset of imprinted maternally expressed genes (MEGs) depends on RdDM (Vu et al., 2013). However, small RNA has not yet been implicated in resistance to reprogramming in mammals.

Epigenetic Variation and the Adaptive Inheritance of Acquired Traits

DNA sequence change (mutation) can be a slow process and is therefore not ideal for an organism or population to survive in a dynamic environment. Epigenetic mechanisms, modulated by environmental cues, have been proposed to enable "soft inheritance," permitting adaptation to fluctuating environments and nutrition (Richards, 2006). The question is the following: can epigenetic inheritance truly represent such soft inheritance, given the resetting of epigenetic marks between generations? In plants, evidence for heritable epigenetic variation is more than half a century old and likely reflects the high heritability and limited reprogramming of epigenetic variants in the germline, so that epialleles can be propagated for literally hundreds of years (Cubas et al., 1999). Many, perhaps most, of these epialleles are induced by transposons that bring nearby genes under their control (Slotkin and Martienssen, 2007). In animals, by contrast, there are relatively few examples of heritable epigenetic variation at individual genes, but there are many examples of quantitative epigenetic traits that appear to respond to environmental—and especially nutritional—cues experienced by former generations. For example, in the nematode *C. elegans*, exposure to an olfactory cue early in development affects behavior when encountering the chemical in adulthood, a process known as olfactory imprinting, and this behavior can then be transmitted over more than 40 generations (Remy, 2010). Worms that have been imprinted not only exhibit a more robust ability to migrate toward the chemical but also lay significantly more eggs. Although the mechanisms remain unclear, olfactory

imprinting provides a memory of a favorable environment that can be passed onto multiple generations (Remy, 2010). It is possible, therefore, that the very short generation time, acute exposure to the environment, and the abundance of small RNA have predisposed *C. elegans*, like plants, to dispense with germline reprogramming to some extent and indulge in transgenerational inheritance.

The degree to which germline reprogramming and transgenerational inheritance have contributed to potentially adaptive epigenetic variation in plants has been explored by genome-wide profiling of DNA methylation in natural and inbred populations. These studies have revealed the extent of DNA methylation cycling and paramutation-like behavior and their contribution to epigenetic variation (Becker et al., 2011; Becker and Weigel, 2012; Eichten et al., 2013; Greaves et al., 2012; Li et al., 2013; Regulski et al., 2013; Schmitz et al., 2013; Schmitz et al., 2011). Cycling contributes to the limited epigenetic variation found in individuals (Becker et al., 2011; Schmitz et al., 2011), whereas DNA methylation at most retrotransposons is more faithfully maintained. There are also a few hundred conserved targets of RdDM that never lose methylation in inbred populations (Schmitz et al., 2013), resembling a sort of epigenetic selective sweep (Vaughn et al., 2007). Interestingly, many of these same regions are demethylated in the vegetative nucleus of the pollen grain, along with imprinted genes (Calarco et al., 2012; Ibarra et al., 2012), and reinforce silencing in sperm cells via mobile 24 nt small RNA (Figure 2). Some of these genes are required for pollen tube growth providing a plausible evolutionary origin (Schmitz et al., 2013). Paramutation has also contributed to epigenetic variation in natural populations and sometimes occurs between nonallelic positions, leading to hybrid incompatibility reminiscent of the Dobzhansky-Bateson-Muller effect (Durand et al., 2012). Examples include PAI2, a nonessential gene that is heritably silenced by an unlinked inverted repeat in a subset of *Arabidopsis* accessions (Enke et al., 2011; Schmitz et al., 2013), and AtFOLT1, an essential gene that can be paramutated by nonallelic epialleles, resulting in inviable transgressive phenotypes in hybrids (Durand et al., 2012).

Although heritable epigenetic variation clearly exists in nature, it is very important to distinguish random epivariation acted on by selection from adaptive epigenetic variation induced by the environment. These two forms of transgenerational inheritance may well be related, but this assumption is not yet justified. For example, transgenerational viral reporter gene silencing in *C. elegans* may be related to an adaptive antiviral response, triggered by viral infection, but no such antiviral response has been explicitly demonstrated with this heterotypic virus (Rechavi et al., 2011). Further, it is only when individuals that are truly genetically identical exhibit a range of phenotypes that are heritable that these can truly be attributed to epivariation. When the genes underlying the particular trait are not known, it is almost impossible to rule out DNA sequence mutation. For example, outbred rats exposed to the fungicide vinclozolin in utero exhibited diminished male fertility over three to four generations of offspring, transmitted through the male germline (Anway et al., 2005). However, no effects were observed with another strain of inbred rats, raising the possibility that genetic variation was responsible for the effect (Schneider et al., 2008).

Clearly, epigenetic variation can respond to the environment. However, whether this has any impact on adaptive fitness is far from clear. For example, in *Drosophila* heat shock or osmotic stress-induced *white* gene derepression can be inherited maternally and paternally over several generations before returning to the normal state (Seong et al., 2011). In mice, *Agouti*^{vy} mothers can modulate the coat color phenotype of their progeny through a specific diet of methyl donors, but this effect is only transmitted over two generations and is lost by the third (Daxinger and Whitelaw, 2012), indicating that the influence of diet is not stable or truly transgenerational (Box 1). However, genetic variation at the *Agouti* locus can come under very rapid adaptive selection for coat color ''camouflage'' (Linnen et al., 2013), raising the question as to whether some haplotypes may be prone to epigenetic variation as well.

In plants, there is no question that environmental cues such as temperature can have transgenerational effects on paramutation (Brink et al., 1968) and on transposon activity (Slotkin and Martienssen, 2007), which is often temperature sensitive and can be inherited when remethylation by RdDM is abolished (Ito et al., 2011). Attempts to demonstrate adaptive epigenetic change in plants have focused on biotic and abiotic stress and have proved much more problematic. Plant breeders often note that the introduction of a foreign variety appears to involve a process of adaptation, such that seeds and clonal propagules (cuttings) become progressively more adapted to new climates and new pathogen loads (Holeski et al., 2012). However, attempts to experimentally demonstrate adaptive epigenetic variation in stress tolerance have so far met with very limited success (Slaughter et al., 2012), and intergenerational maternal effects on seeds, similar to maternal effects in mammals (Figure 1), are hard to rule out (Pecinka and Mittelsten Scheid, 2012).

Perhaps the best known epigenetic environmental cue in plants is the influence of temperature and season on flowering time (Andrés and Coupland, 2012; Ream et al., 2012; Song et al., 2012). Some *Arabidopsis* species and related brassicas are known as ''winter annuals'' and encode a floral repressor, the FLC MADS box transcription factor, that prevents flowering in embryos and young plants. Prolonged periods of cold (more than a few weeks) experienced in winter result in stable epigenetic silencing of FLC. This process, called vernalization, involves plant homeodomain (PHD)-containing proteins, Polycomb Repressive Complex 2, and antisense transcription. The cold-induced epigenetic silencing allows flowering to occur when photoperiod is long again in the following spring. Although the mechanism of cold sensing remains unclear, long-term silencing of FLC is achieved through trimethylation of H3K27. In principle, this memory of winter could be retained in the next generation, but instead, it is robustly reset in the germline and early embryo (Sheldon et al., 2008). Upregulation of FLC, even in plants that have not experienced cold, suggests that the resetting process may be part of the genome-wide epigenetic reprogramming that occurs during embryogenesis (Song et al., 2012). This resetting does not seem to involve DNA methylation, but histone modification and replacement undergo drastic changes in the germline and could be responsible (Ingouff et al., 2007; Schoft

et al., 2009). Lysenko contributed significantly to the discovery of this cold-induced phenomenon in wheat and other cereals before the molecular basis of vernalization was known. However, he famously and unfortunately went on to propose that early flowering, induced by prolonged cold, could be inherited as an acquired trait. This led to disastrous attempts to rapidly breed high-yielding wheats that could be planted in the spring.

Thus, although the notion of adaptive epigenetic inheritance retains considerable appeal, concrete evidence from model systems is still lacking. Lysenko and Burbank were both followers of Lamarck in that they believed that the inheritance of acquired traits should underlie evolution, and it is often forgotten that Darwin himself considered Lamarck's hypothesis sound. In *The Variation of Animals and Plants under Domestication* (1868), Darwin even proposed the existence of "gemmules," pieces of information that could arise in somatic cells under environmental challenge, modify the germline, and confer some advantage on the progeny in the next generation. A molecular basis for such signals has long eluded geneticists, but RNA interference is a modern-day candidate with renewed appeal. This is because small RNA signals are highly mobile, being transmitted through the gut in *C. elegans*, through the vasculature and plasmodesmata in plants, and through exosomes and even serum in mammals. At least in *C. elegans*, these small RNAs or their derivatives can enter the germline and mediate heritable transcriptional silencing in subsequent generations using histone modification mechanisms analogous to fission yeast. One can easily imagine a scenario in which, for example, pathogen infection in one generation might give rise to small RNAs that are inherited in the next, conferring some level of resistance. However, such inheritance of adaptive resistance has not yet been demonstrated, despite tantalizing clues in both plants and animals (Hilbricht et al., 2008; Rechavi et al., 2011; Yu et al., 2013).

Implications for Human Health

Given the medical and public health implications (Jirtle and Skinner, 2007), numerous studies have examined the potential for epigenetic inheritance of nutritional metabolic risk in human and mouse populations. It has been proposed that alterations in paternal diet (high-fat or low-protein diets) or else a prior history of intrauterine exposure to maternal caloric restriction can result in increased metabolic risk in offspring (also known as Barker's theory [Hales and Barker, 2013]). Nutritional conditions during uterine development may have effects later in life and may influence the occurrence of adult metabolism and diseases. Thus, under poor nutritional conditions, the fetal environment could modify the development of the embryo to prepare the offspring for a future environment with low resources during adult life ("thrifty" phenotype). For example, during the Dutch famine at the end of WWII, individuals exposed to famine during gestation had a poorer glucose tolerance than those born the year before the famine. Studies have found increased neonatal adiposity among the grandchildren of women who had been undernourished during pregnancy. Furthermore, offspring of prenatally undernourished fathers, but not mothers, were heavier and more obese than offspring of fathers and mothers who had not been undernourished prenatally (Painter et al., 2008; Veenendaal et al., 2013). No evidence of transgenerational effects of grandmaternal undernutrition during gestation was found, but the increased adiposity in the offspring of prenatally undernourished fathers might lead to chronic disease rates in the future.

Recent studies in rodent models have focused on nutritional effects transmitted via the paternal lineage (as this avoids the confounding effects of in utero variations). Mice fed a low-protein diet passed on a high-cholesterol phenotype, with gene expression differences and modest DNA methylation differences to their paternal offspring (Carone et al., 2010; Radford et al., 2012). The sons of mothers calorically restricted during pregnancy transmit metabolic phenotypes to offspring with altered transcript profiles evident prior to onset of disease (Radford et al., 2012). Such paternal-lineage risk is likely to be conferred via sperm, although whether this is via alterations in chromatin, small RNAs, or other agents is currently unclear (Ferguson-Smith and Patti, 2011; Rando, 2012). No global alterations in sperm methylation have been noted so far. Furthermore, most paternal RNAs are thought to be degraded shortly after fertilization, and although some histones may persist in sperm chromatin (Brykczynska et al., 2010; Hammoud et al., 2009), most are rapidly replaced upon fertilization. Another study (Padmanabhan et al., 2013) found that a mutation in folate metabolism (methionine synthase reductase [*Mtrr*]) led to epigenetic instability and transgenerational effects on development. Although epigenetic inheritance may contribute to these effects, as shown by altered DNA methylation profiles, mutations induced under these conditions could not be excluded, as folate metabolism regulates nucleotide biosynthesis pathways and, hence, might have an impact on genetic mutation/DNA repair mechanisms. Furthermore, epigenetic instability might lead to reactivation of TEs and insertional mutations.

Even though epidemiological studies and animal models provide support for the "thrifty phenotype" hypothesis, most of the studies so far concern intergenerational (parental or grandparental exposure) rather than truly transgenerational inheritance (Figure 1), and in most of the epidemiological studies, it has been difficult to rule out other effects (Box 3) such as the influence of postnatal nutritional environment and the use of cohorts where important covariates are missing. Nevertheless, it is clear that different nutritional cues during infancy and childhood can have adverse effects during adult life, and exposure to pollutants, alcohol, and tobacco can affect fetal programming. Such phenomena have now been put under the umbrella of DOHaD "developmental origins of health and disease," which proposes that a wide range of environmental conditions during embryonic development and early life determine susceptibility to disease during adult life (Hochberg et al., 2011). Whether such effects result in bona fide transgenerational epigenetic inheritance over multiple generations seems unlikely given the robust reprogramming found in the mammalian germline. Further investigations will clearly be needed using well-controlled experiments in mammalian models and large, well-characterized cohorts in epidemiological studies.

Conclusions

In conclusion, in plants and in some animals such as nematodes, transgenerational epigenetic inheritance is well documented and relatively common. Epialleles may even form the basis of some

complex traits in plants, where epigenetic inheritance is usually—if not always—associated with transposable elements, viruses, or transgenes and may be a byproduct of aggressive germline defense strategies. In mammals, epialleles can also be found but are extremely rare, presumably due to robust germline reprogramming. How epialleles arise in nature is still an open question, but environmentally induced epigenetic changes are rarely transgenerationally inherited, let alone adaptive, even in plants. Thus, although much attention has been drawn to the potential implications of transgenerational inheritance for human health, so far there is little support. On the other hand, the human transmission of culture and improved habits is clearly Lamarckian. To quote S.J. Gould (Gould, 1980), "human cultural evolution, in strong opposition to our biological history, is Lamarckian in character. What we learn in one generation, we transmit directly by teaching and writing." In this and other respects, perhaps it is premature to compare humans to plants (as Burbank did) in terms of their capacity to recall past environments, in this generation and the next.

ACKNOWLEDGMENTS

We thank Adrian Bird, Vincent Colot, Anne Ferguson-Smith, and Bill Kelly for their comments on the manuscript, and we thank Joe Calarco and Filipe Borges for help with the figures. Research in the authors' laboratories is supported by grants from the National Institutes of Health (GM067014 and GM067014), the National Science Foundation (IOS-1025830), the Howard Hughes Medical Institute and Gordon and Betty Moore Foundation (GBMF3033 to R.A.M.), the "Ligue Nationale contre le cancer," the EpiGeneSys FP7 257082 Network of Excellence, ERC Advanced Investigator award 250367 (to E.H.), EU FP7 MODHEP EU grant 259743 (to E.H.), and the Labex DEEP (ANR-11-LBX-0044) part of the IDEX Idex PSL (ANR-10-IDEX-0001-02 PSL). We apologize to the many authors of important original research articles that could not be cited for lack of space.

REFERENCES

Andrés, F., and Coupland, G. (2012). The genetic basis of flowering responses to seasonal cues. Nat. Rev. Genet. *13*, 627–639.

Anway, M.D., Cupp, A.S., Uzumcu, M., and Skinner, M.K. (2005). Epigenetic transgenerational actions of endocrine disruptors and male fertility. Science *308*, 1466–1469.

Arteaga-Vazquez, M.A., and Chandler, V.L. (2010). Paramutation in maize: RNA mediated trans-generational gene silencing. Curr. Opin. Genet. Dev. *20*, 156–163.

Arteaga-Vazquez, M., Sidorenko, L., Rabanal, F.A., Shrivistava, R., Nobuta, K., Green, P.J., Meyers, B.C., and Chandler, V.L. (2010). RNA-mediated trans-communication can establish paramutation at the b1 locus in maize. Proc. Natl. Acad. Sci. USA *107*, 12986–12991.

Ashe, A., Sapetschnig, A., Weick, E.-M., Mitchell, J., Bagijn, M.P., Cording, A.C., Doebley, A.-L., Goldstein, L.D., Lehrbach, N.J., Le Pen, J., et al. (2012). piRNAs can trigger a multigenerational epigenetic memory in the germline of C. elegans. Cell *150*, 88–99.

Barbour, J.E., Liao, I.T., Stonaker, J.L., Lim, J.P., Lee, C.C., Parkinson, S.E., Kermicle, J., Simon, S.A., Meyers, B.C., Williams-Carrier, R., et al. (2012). required to maintain repression2 is a novel protein that facilitates locus-specific paramutation in maize. Plant Cell *24*, 1761–1775.

Becker, C., and Weigel, D. (2012). Epigenetic variation: origin and transgenerational inheritance. Curr. Opin. Plant Biol. *15*, 562–567.

Becker, C., Hagmann, J., Müller, J., Koenig, D., Stegle, O., Borgwardt, K., and Weigel, D. (2011). Spontaneous epigenetic variation in the Arabidopsis thaliana methylome. Nature *480*, 245–249.

Bird, A. (2007). Perceptions of epigenetics. Nature *447*, 396–398.

Brennecke, J., Malone, C.D., Aravin, A.A., Sachidanandam, R., Stark, A., and Hannon, G.J. (2008). An epigenetic role for maternally inherited piRNAs in transposon silencing. Science *322*, 1387–1392.

Brink, R.A., Styles, E.D., and Axtell, J.D. (1968). Paramutation: directed genetic change. Paramutation occurs in somatic cells and heritably alters the functional state of a locus. Science *159*, 161–170.

Brykczynska, U., Hisano, M., Erkek, S., Ramos, L., Oakeley, E.J., Roloff, T.C., Beisel, C., Schübeler, D., Stadler, M.B., and Peters, A.H. (2010). Repressive and active histone methylation mark distinct promoters in human and mouse spermatozoa. Nat. Struct. Mol. Biol. *17*, 679–687.

Brzeska, K., Brzeski, J., Smith, J., and Chandler, V.L. (2010). Transgenic expression of CBBP, a CXC domain protein, establishes paramutation in maize. Proc. Natl. Acad. Sci. USA *107*, 5516–5521.

Buckley, B.A., Burkhart, K.B., Gu, S.G., Spracklin, G., Kershner, A., Fritz, H., Kimble, J., Fire, A., and Kennedy, S. (2012). A nuclear Argonaute promotes multigenerational epigenetic inheritance and germline immortality. Nature *489*, 447–451.

Burbank, L. (1906). The training of the human plant. The Century Magazine, May, 1906. pp. 127–137.

Burkhart, K.B., Guang, S., Buckley, B.A., Wong, L., Bochner, A.F., and Kennedy, S. (2011). A pre-mRNA-associating factor links endogenous siRNAs to chromatin regulation. PLoS Genet. *7*, e1002249.

Burton, N.O., Burkhart, K.B., and Kennedy, S. (2011). Nuclear RNAi maintains heritable gene silencing in Caenorhabditis elegans. Proc. Natl. Acad. Sci. USA *108*, 19683–19688.

Calarco, J.P., Borges, F., Donoghue, M.T., Van Ex, F., Jullien, P.E., Lopes, T., Gardner, R., Berger, F., Feijó, J.A., Becker, J.D., and Martienssen, R.A. (2012). Reprogramming of DNA methylation in pollen guides epigenetic inheritance via small RNA. Cell *151*, 194–205.

Carone, B.R., Fauquier, L., Habib, N., Shea, J.M., Hart, C.E., Li, R., Bock, C., Li, C., Gu, H., Zamore, P.D., et al. (2010). Paternally induced transgenerational environmental reprogramming of metabolic gene expression in mammals. Cell *143*, 1084–1096.

Castel, S.E., and Martienssen, R.A. (2013). RNA interference in the nucleus: roles for small RNAs in transcription, epigenetics and beyond. Nat. Rev. Genet. *14*, 100–112.

Chalker, D.L., and Yao, M.C. (2011). DNA elimination in ciliates: transposon domestication and genome surveillance. Annu. Rev. Genet. *45*, 227–246.

Champagne, F.A., and Curley, J.P. (2009). Epigenetic mechanisms mediating the long-term effects of maternal care on development. Neurosci. Biobehav. Rev. *33*, 593–600.

Chandler, V.L. (2007). Paramutation: from maize to mice. Cell *128*, 641–645.

Chandler, V.L. (2010). Paramutation's properties and puzzles. Science *330*, 628–629.

Colomé-Tatché, M., Cortijo, S., Wardenaar, R., Morgado, L., Lahouze, B., Sarazin, A., Etcheverry, M., Martin, A., Feng, S., Duvernois-Berthet, E., et al. (2012). Features of the Arabidopsis recombination landscape resulting from the combined loss of sequence variation and DNA methylation. Proc. Natl. Acad. Sci. USA *109*, 16240–16245.

Cortijo, S., Wardenaar, R., Colomé-Tatché, M., Gilly, A., Etcheverry, M., Labadie, K., Caillieux, E., Hospital, F., Aury, J.-M., Wincker, P., et al. (2014). Mapping the epigenetic basis of complex traits. Science. Published online February 6, 2014. http://dx.doi.org/10.1126/science.1248127.

Creasey, K.M., Zhai, J., Borges, F., Van Ex, F., Regulski, M., Meyers, B.C., and Martienssen, R. (2014). miRNAs trigger widespread epigenetically-activated siRNAs from transposons in Arabidopsis. Nature. Published online March 16, 2014. http://dx.doi.org/10.1038/nature13069.

Cubas, P., Vincent, C., and Coen, E. (1999). An epigenetic mutation responsible for natural variation in floral symmetry. Nature *401*, 157–161.

Daxinger, L., and Whitelaw, E. (2012). Understanding transgenerational epigenetic inheritance via the gametes in mammals. Nat. Rev. Genet. *13*, 153–162.

de Vanssay, A., Bougé, A.L., Boivin, A., Hermant, C., Teysset, L., Delmarre, V., Antoniewski, C., and Ronsseray, S. (2012). Paramutation in Drosophila linked to emergence of a piRNA-producing locus. Nature *490*, 112–115.

Dietz, D.M., Laplant, Q., Watts, E.L., Hodes, G.E., Russo, S.J., Feng, J., Oosting, R.S., Vialou, V., and Nestler, E.J. (2011). Paternal transmission of stress-induced pathologies. Biol. Psychiatry *70*, 408–414.

Durand, S., Bouché, N., Perez Strand, E., Loudet, O., and Camilleri, C. (2012). Rapid establishment of genetic incompatibility through natural epigenetic variation. Curr. Biol. *22*, 326–331.

Eichten, S.R., Briskine, R., Song, J., Li, Q., Swanson-Wagner, R., Hermanson, P.J., Waters, A.J., Starr, E., West, P.T., Tiffin, P., et al. (2013). Epigenetic and genetic influences on DNA methylation variation in maize populations. Plant Cell *25*, 2783–2797.

Enke, R.A., Dong, Z., and Bender, J. (2011). Small RNAs prevent transcription-coupled loss of histone H3 lysine 9 methylation in Arabidopsis thaliana. PLoS Genet. *7*, e1002350.

Erhard, K.F., Jr., Parkinson, S.E., Gross, S.M., Barbour, J.E., Lim, J.P., and Hollick, J.B. (2013). Maize RNA polymerase IV defines trans-generational epigenetic variation. Plant Cell *25*, 808–819.

Eun, C., Lorkovic, Z.J., Sasaki, T., Naumann, U., Matzke, A.J., and Matzke, M. (2012). Use of forward genetic screens to identify genes required for RNA-directed DNA methylation in Arabidopsis thaliana. Cold Spring Harb. Symp. Quant. Biol. *77*, 195–204.

Ferguson-Smith, A.C., and Patti, M.E. (2011). You are what your dad ate. Cell Metab. *13*, 115–117.

Gehring, M., Bubb, K.L., and Henikoff, S. (2009). Extensive demethylation of repetitive elements during seed development underlies gene imprinting. Science *324*, 1447–1451.

Gould, S.J. (1980). The Panda's Thumb (New York: W.W. Norton & Company).

Greaves, I.K., Groszmann, M., Ying, H., Taylor, J.M., Peacock, W.J., and Dennis, E.S. (2012). Trans chromosomal methylation in Arabidopsis hybrids. Proc. Natl. Acad. Sci. USA *109*, 3570–3575.

Greer, E.L., Maures, T.J., Ucar, D., Hauswirth, A.G., Mancini, E., Lim, J.P., Benayoun, B.A., Shi, Y., and Brunet, A. (2011). Transgenerational epigenetic inheritance of longevity in Caenorhabditis elegans. Nature *479*, 365–371.

Gu, S.G., Pak, J., Guang, S., Maniar, J.M., Kennedy, S., and Fire, A. (2012). Amplification of siRNA in Caenorhabditis elegans generates a transgenerational sequence-targeted histone H3 lysine 9 methylation footprint. Nat. Genet. *44*, 157–164.

Gutierrez-Marcos, J.F., and Dickinson, H.G. (2012). Epigenetic reprogramming in plant reproductive lineages. Plant Cell Physiol. *53*, 817–823.

Haag, J.R., and Pikaard, C.S. (2011). Multisubunit RNA polymerases IV and V: purveyors of non-coding RNA for plant gene silencing. Nat. Rev. Mol. Cell Biol. *12*, 483–492.

Hackett, J.A., and Surani, M.A. (2013). Beyond DNA: programming and inheritance of parental methylomes. Cell *153*, 737–739.

Hackett, J.A., Zylicz, J.J., and Surani, M.A. (2012). Parallel mechanisms of epigenetic reprogramming in the germline. Trends Genet. *28*, 164–174.

Hales, C.N., and Barker, D.J. (2013). Type 2 (non-insulin-dependent) diabetes mellitus: the thrifty phenotype hypothesis. Int. J. Epidemiol. *42*, 1215–1222.

Hammoud, S.S., Nix, D.A., Zhang, H., Purwar, J., Carrell, D.T., and Cairns, B.R. (2009). Distinctive chromatin in human sperm packages genes for embryo development. Nature *460*, 473–478.

Harvey, W. (1651). Exercitationes de Generatione Animalium (London: Londini, Typis Du-Gardianis; Impensis O. Pulleyn).

Hilbricht, T., Varotto, S., Sgaramella, V., Bartels, D., Salamini, F., and Furini, A. (2008). Retrotransposons and siRNA have a role in the evolution of desiccation tolerance leading to resurrection of the plant Craterostigma plantagineum. New Phytol. *179*, 877–887.

Hitchins, M.P., Rapkins, R.W., Kwok, C.T., Srivastava, S., Wong, J.J., Khachigian, L.M., Polly, P., Goldblatt, J., and Ward, R.L. (2011). Dominantly inherited constitutional epigenetic silencing of MLH1 in a cancer-affected family is linked to a single nucleotide variant within the 5'UTR. Cancer Cell *20*, 200–213.

Hochberg, Z., Feil, R., Constancia, M., Fraga, M., Junien, C., Carel, J.C., Boileau, P., Le Bouc, Y., Deal, C.L., Lillycrop, K., et al. (2011). Child health, developmental plasticity, and epigenetic programming. Endocr. Rev. *32*, 159–224.

Holeski, L.M., Jander, G., and Agrawal, A.A. (2012). Transgenerational defense induction and epigenetic inheritance in plants. Trends Ecol. Evol. *27*, 618–626.

Hollick, J.B. (2012). Paramutation: a trans-homolog interaction affecting heritable gene regulation. Curr. Opin. Plant Biol. *15*, 536–543.

Hsieh, T.F., Ibarra, C.A., Silva, P., Zemach, A., Eshed-Williams, L., Fischer, R.L., and Zilberman, D. (2009). Genome-wide demethylation of Arabidopsis endosperm. Science *324*, 1451–1454.

Huang, X.A., Yin, H., Sweeney, S., Raha, D., Snyder, M., and Lin, H. (2013). A major epigenetic programming mechanism guided by piRNAs. Dev. Cell *24*, 502–516.

Ibarra, C.A., Feng, X., Schoft, V.K., Hsieh, T.F., Uzawa, R., Rodrigues, J.A., Zemach, A., Chumak, N., Machlicova, A., Nishimura, T., et al. (2012). Active DNA demethylation in plant companion cells reinforces transposon methylation in gametes. Science *337*, 1360–1364.

Ingouff, M., Hamamura, Y., Gourgues, M., Higashiyama, T., and Berger, F. (2007). Distinct dynamics of HISTONE3 variants between the two fertilization products in plants. Curr. Biol. *17*, 1032–1037.

Irvine, D.V., Zaratiegui, M., Tolia, N.H., Goto, D.B., Chitwood, D.H., Vaughn, M.W., Joshua-Tor, L., and Martienssen, R.A. (2006). Argonaute slicing is required for heterochromatic silencing and spreading. Science *313*, 1134–1137.

Ito, H., Gaubert, H., Bucher, E., Mirouze, M., Vaillant, I., and Paszkowski, J. (2011). An siRNA pathway prevents transgenerational retrotransposition in plants subjected to stress. Nature *472*, 115–119.

Jablonka, E., and Raz, G. (2009). Transgenerational epigenetic inheritance: prevalence, mechanisms, and implications for the study of heredity and evolution. Q. Rev. Biol. *84*, 131–176.

Jacob, Y., Bergamin, E., Donoghue, M.T., Mongeon, V., Le Blanc, C., Voigt, P., Underwood, C., Brunzelle, J.S., Michaels, S.D., Reinberg, D., et al. (2014). Selective methylation of histone H3 variant H3.1 regulates heterochromatin replication. Science. Published online March 14, 2014. http://dx.doi.org/10.1126/science.1248357.

Jauvion, V., Rivard, M., Bouteiller, N., Elmayan, T., and Vaucheret, H. (2012). RDR2 partially antagonizes the production of RDR6-dependent siRNA in sense transgene-mediated PTGS. PLoS ONE *7*, e29785.

Jiang, L., Zhang, J., Wang, J.J., Wang, L., Zhang, L., Li, G., Yang, X., Ma, X., Sun, X., Cai, J., et al. (2013). Sperm, but not oocyte, DNA methylome is inherited by zebrafish early embryos. Cell *153*, 773–784.

Jirtle, R.L., and Skinner, M.K. (2007). Environmental epigenomics and disease susceptibility. Nat. Rev. Genet. *8*, 253–262.

Johannes, F., Porcher, E., Teixeira, F.K., Saliba-Colombani, V., Simon, M., Agier, N., Bulski, A., Albuisson, J., Heredia, F., Audigier, P., et al. (2009). Assessing the impact of transgenerational epigenetic variation on complex traits. PLoS Genet. *5*, e1000530.

Jullien, P.E., Susaki, D., Yelagandula, R., Higashiyama, T., and Berger, F. (2012). DNA methylation dynamics during sexual reproduction in Arabidopsis thaliana. Curr. Biol. *22*, 1825–1830.

Kakutani, T., Jeddeloh, J.A., Flowers, S.K., Munakata, K., and Richards, E.J. (1996). Developmental abnormalities and epimutations associated with DNA hypomethylation mutations. Proc. Natl. Acad. Sci. USA *93*, 12406–12411.

Katz, D.J., Edwards, T.M., Reinke, V., and Kelly, W.G. (2009). A C. elegans LSD1 demethylase contributes to germline immortality by reprogramming epigenetic memory. Cell *137*, 308–320.

Keller, C., and Bühler, M. (2013). Chromatin-associated ncRNA activities. Chromosome Res. *21*, 627–641.

Kelly, W.G., and Aramayo, R. (2007). Meiotic silencing and the epigenetics of sex. Chromosome Res. *15*, 633–651.

Kiani, J., Grandjean, V., Liebers, R., Tuorto, F., Ghanbarian, H., Lyko, F., Cuzin, F., and Rassoulzadegan, M. (2013). RNA-mediated epigenetic heredity requires the cytosine methyltransferase Dnmt2. PLoS Genet. *9*, e1003498.

Law, J.A., and Jacobsen, S.E. (2010). Establishing, maintaining and modifying DNA methylation patterns in plants and animals. Nat. Rev. Genet. *11*, 204–220.

Le Thomas, A., Rogers, A.K., Webster, A., Marinov, G.K., Liao, S.E., Perkins, E.M., Hur, J.K., Aravin, A.A., and Tóth, K.F. (2013). Piwi induces piRNA-guided transcriptional silencing and establishment of a repressive chromatin state. Genes Dev. *27*, 390–399.

Li, X., Ito, M., Zhou, F., Youngson, N., Zuo, X., Leder, P., and Ferguson-Smith, A.C. (2008). A maternal-zygotic effect gene, Zfp57, maintains both maternal and paternal imprints. Dev. Cell *15*, 547–557.

Li, Q., Eichten, S.R., Hermanson, P.J., and Springer, N.M. (2013). Inheritance patterns and stability of DNA methylation variation in maize near-isogenic lines. Genetics. Published online December 20, 2013. http://dx.doi.org/10.1534/genetics.113.158980.

Lim, J.P., and Brunet, A. (2013). Bridging the transgenerational gap with epigenetic memory. Trends Genet. *29*, 176–186.

Linnen, C.R., Poh, Y.P., Peterson, B.K., Barrett, R.D., Larson, J.G., Jensen, J.D., and Hoekstra, H.E. (2013). Adaptive evolution of multiple traits through multiple mutations at a single gene. Science *339*, 1312–1316.

Lippman, Z., Gendrel, A.-V., Black, M., Vaughn, M.W., Dedhia, N., McCombie, W.R., Lavine, K., Mittal, V., May, B., Kasschau, K.D., et al. (2004). Role of transposable elements in heterochromatin and epigenetic control. Nature *430*, 471–476.

Lisch, D. (2012). Regulation of transposable elements in maize. Curr. Opin. Plant Biol. *15*, 511–516.

Lisch, D. (2013). How important are transposons for plant evolution? Nat. Rev. Genet. *14*, 49–61.

Manning, K., Tör, M., Poole, M., Hong, Y., Thompson, A.J., King, G.J., Giovannoni, J.J., and Seymour, G.B. (2006). A naturally occurring epigenetic mutation in a gene encoding an SBP-box transcription factor inhibits tomato fruit ripening. Nat. Genet. *38*, 948–952.

Marí-Ordóñez, A., Marchais, A., Etcheverry, M., Martin, A., Colot, V., and Voinnet, O. (2013). Reconstructing de novo silencing of an active plant retrotransposon. Nat. Genet. *45*, 1029–1039.

Martienssen, R., Barkan, A., Taylor, W.C., and Freeling, M. (1990). Somatically heritable switches in the DNA modification of Mu transposable elements monitored with a suppressible mutant in maize. Genes Dev. *4*, 331–343.

Mathieu, O., Reinders, J., Caikovski, M., Smathajitt, C., and Paszkowski, J. (2007). Transgenerational stability of the Arabidopsis epigenome is coordinated by CG methylation. Cell *130*, 851–862.

McClintock, B. (1961). Some parallels between gene control systems in maize and in bacteria. Am. Nat. *95*, 265–277.

Messerschmidt, D.M. (2012). Should I stay or should I go: protection and maintenance of DNA methylation at imprinted genes. Epigenetics *7*, 969–975.

Messerschmidt, D.M., de Vries, W., Ito, M., Solter, D., Ferguson-Smith, A., and Knowles, B.B. (2012). Trim28 is required for epigenetic stability during mouse oocyte to embryo transition. Science *335*, 1499–1502.

Mirouze, M., Reinders, J., Bucher, E., Nishimura, T., Schneeberger, K., Ossowski, S., Cao, J., Weigel, D., Paszkowski, J., and Mathieu, O. (2009). Selective epigenetic control of retrotransposition in Arabidopsis. Nature *461*, 427–430.

Mirouze, M., Lieberman-Lazarovich, M., Aversano, R., Bucher, E., Nicolet, J., Reinders, J., and Paszkowski, J. (2012). Loss of DNA methylation affects the recombination landscape in Arabidopsis. Proc. Natl. Acad. Sci. USA *109*, 5880–5885.

Mosher, R.A., Melnyk, C.W., Kelly, K.A., Dunn, R.M., Studholme, D.J., and Baulcombe, D.C. (2009). Uniparental expression of PolIV-dependent siRNAs in developing endosperm of Arabidopsis. Nature *460*, 283–286.

Nakamura, T., Liu, Y.J., Nakashima, H., Umehara, H., Inoue, K., Matoba, S., Tachibana, M., Ogura, A., Shinkai, Y., and Nakano, T. (2012). PGC7 binds histone H3K9me2 to protect against conversion of 5mC to 5hmC in early embryos. Nature *486*, 415–419.

Padmanabhan, N., Jia, D., Geary-Joo, C., Wu, X., Ferguson-Smith, A.C., Fung, E., Bieda, M.C., Snyder, F.F., Gravel, R.A., Cross, J.C., and Watson, E.D. (2013). Mutation in folate metabolism causes epigenetic instability and transgenerational effects on development. Cell *155*, 81–93.

Painter, R.C., Osmond, C., Gluckman, P., Hanson, M., Phillips, D.I., and Roseboom, T.J. (2008). Transgenerational effects of prenatal exposure to the Dutch famine on neonatal adiposity and health in later life. BJOG *115*, 1243–1249.

Pecinka, A., and Mittelsten Scheid, O. (2012). Stress-induced chromatin changes: a critical view on their heritability. Plant Cell Physiol. *53*, 801–808.

Potok, M.E., Nix, D.A., Parnell, T.J., and Cairns, B.R. (2013). Reprogramming the maternal zebrafish genome after fertilization to match the paternal methylation pattern. Cell *153*, 759–772.

Ptashne, M. (2013). Epigenetics: core misconcept. Proc. Natl. Acad. Sci. USA *110*, 7101–7103.

Qi, Y., He, X., Wang, X.-J., Kohany, O., Jurka, J., and Hannon, G.J. (2006). Distinct catalytic and non-catalytic roles of ARGONAUTE4 in RNA-directed DNA methylation. Nature *443*, 1008–1012.

Radford, E.J., Isganaitis, E., Jimenez-Chillaron, J., Schroeder, J., Molla, M., Andrews, S., Didier, N., Charalambous, M., McEwen, K., Marazzi, G., et al. (2012). An unbiased assessment of the role of imprinted genes in an intergenerational model of developmental programming. PLoS Genet. *8*, e1002605.

Rando, O.J. (2012). Daddy issues: paternal effects on phenotype. Cell *151*, 702–708.

Rassoulzadegan, M., Grandjean, V., Gounon, P., Vincent, S., Gillot, I., and Cuzin, F. (2006). RNA-mediated non-mendelian inheritance of an epigenetic change in the mouse. Nature *441*, 469–474.

Raval, A., Tanner, S.M., Byrd, J.C., Angerman, E.B., Perko, J.D., Chen, S.S., Hackanson, B., Grever, M.R., Lucas, D.M., Matkovic, J.J., et al. (2007). Downregulation of death-associated protein kinase 1 (DAPK1) in chronic lymphocytic leukemia. Cell *129*, 879–890.

Ream, T.S., Woods, D.P., and Amasino, R.M. (2012). The molecular basis of vernalization in different plant groups. Cold Spring Harb. Symp. Quant. Biol. *77*, 105–115.

Rebollo, R., Miceli-Royer, K., Zhang, Y., Farivar, S., Gagnier, L., and Mager, D.L. (2012). Epigenetic interplay between mouse endogenous retroviruses and host genes. Genome Biol. *13*, R89.

Rechavi, O., Minevich, G., and Hobert, O. (2011). Transgenerational inheritance of an acquired small RNA-based antiviral response in C. elegans. Cell *147*, 1248–1256.

Regulski, M., Lu, Z., Kendall, J., Donoghue, M.T., Reinders, J., Llaca, V., Deschamps, S., Smith, A., Levy, D., McCombie, W.R., et al. (2013). The maize methylome influences mRNA splice sites and reveals widespread paramutation-like switches guided by small RNA. Genome Res. *23*, 1651–1662.

Reinders, J., Mirouze, M., Nicolet, J., and Paszkowski, J. (2013). Parent-of-origin control of transgenerational retrotransposon proliferation in Arabidopsis. EMBO Rep. *14*, 823–828.

Remy, J.J. (2010). Stable inheritance of an acquired behavior in Caenorhabditis elegans. Curr. Biol. *20*, R877–R878.

Richards, E.J. (2006). Inherited epigenetic variation—revisiting soft inheritance. Nat. Rev. Genet. *7*, 395–401.

Rozhkov, N.V., Hammell, M., and Hannon, G.J. (2013). Multiple roles for Piwi in silencing Drosophila transposons. Genes Dev. *27*, 400–412.

Schmitz, R.J., and Ecker, J.R. (2012). Epigenetic and epigenomic variation in Arabidopsis thaliana. Trends Plant Sci. *17*, 149–154.

Schmitz, R.J., Schultz, M.D., Lewsey, M.G., O'Malley, R.C., Urich, M.A., Libiger, O., Schork, N.J., and Ecker, J.R. (2011). Transgenerational epigenetic instability is a source of novel methylation variants. Science *334*, 369–373.

Schmitz, R.J., Schultz, M.D., Urich, M.A., Nery, J.R., Pelizzola, M., Libiger, O., Alix, A., McCosh, R.B., Chen, H., Schork, N.J., and Ecker, J.R. (2013). Patterns of population epigenomic diversity. Nature *495*, 193–198.

Schneider, S., Kaufmann, W., Buesen, R., and van Ravenzwaay, B. (2008). Vinclozolin—the lack of a transgenerational effect after oral maternal exposure during organogenesis. Reprod. Toxicol. *25*, 352–360.

Schoft, V.K., Chumak, N., Mosiolek, M., Slusarz, L., Komnenovic, V., Brownfield, L., Twell, D., Kakutani, T., and Tamaru, H. (2009). Induction of RNA-directed DNA methylation upon decondensation of constitutive heterochromatin. EMBO Rep. *10*, 1015–1021.

Seisenberger, S., Andrews, S., Krueger, F., Arand, J., Walter, J., Santos, F., Popp, C., Thienpont, B., Dean, W., and Reik, W. (2012). The dynamics of genome-wide DNA methylation reprogramming in mouse primordial germ cells. Mol. Cell *48*, 849–862.

Seisenberger, S., Peat, J.R., Hore, T.A., Santos, F., Dean, W., and Reik, W. (2013). Reprogramming DNA methylation in the mammalian life cycle: building and breaking epigenetic barriers. Philos. Trans. R. Soc. Lond. B Biol. Sci. *368*, 20110330.

Seong, K.H., Li, D., Shimizu, H., Nakamura, R., and Ishii, S. (2011). Inheritance of stress-induced, ATF-2-dependent epigenetic change. Cell *145*, 1049–1061.

Sheldon, C.C., Hills, M.J., Lister, C., Dean, C., Dennis, E.S., and Peacock, W.J. (2008). Resetting of FLOWERING LOCUS C expression after epigenetic repression by vernalization. Proc. Natl. Acad. Sci. USA *105*, 2214–2219.

Shirayama, M., Seth, M., Lee, H.-C., Gu, W., Ishidate, T., Conte, D., and Mello, C.C. (2012). piRNAs initiate an epigenetic memory of nonself RNA in the C. elegans germline. Cell *150*, 65–77.

Sienski, G., Dönertas, D., and Brennecke, J. (2012). Transcriptional silencing of transposons by Piwi and maelstrom and its impact on chromatin state and gene expression. Cell *151*, 964–980.

Slaughter, A., Daniel, X., Flors, V., Luna, E., Hohn, B., and Mauch-Mani, B. (2012). Descendants of primed Arabidopsis plants exhibit resistance to biotic stress. Plant Physiol. *158*, 835–843.

Slotkin, R.K., and Martienssen, R. (2007). Transposable elements and the epigenetic regulation of the genome. Nat. Rev. Genet. *8*, 272–285.

Slotkin, R.K., Vaughn, M., Borges, F., Tanurdzić, M., Becker, J.D., Feijó, J.A., and Martienssen, R.A. (2009). Epigenetic reprogramming and small RNA silencing of transposable elements in pollen. Cell *136*, 461–472.

Smith, Z.D., Chan, M.M., Mikkelsen, T.S., Gu, H., Gnirke, A., Regev, A., and Meissner, A. (2012). A unique regulatory phase of DNA methylation in the early mammalian embryo. Nature *484*, 339–344.

Song, J., Angel, A., Howard, M., and Dean, C. (2012). Vernalization - a cold-induced epigenetic switch. J. Cell Sci. *125*, 3723–3731.

Stroud, H., Do, T., Du, J., Zhong, X., Feng, S., Johnson, L., Patel, D.J., and Jacobsen, S.E. (2014). Non-CG methylation patterns shape the epigenetic landscape in Arabidopsis. Nat. Struct. Mol. Biol. *21*, 64–72.

Teixeira, F.K., Heredia, F., Sarazin, A., Roudier, F., Boccara, M., Ciaudo, C., Cruaud, C., Poulain, J., Berdasco, M., Fraga, M.F., et al. (2009). A role for RNAi in the selective correction of DNA methylation defects. Science *323*, 1600–1604.

Théodorou, V. (2013). Susceptibility to stress-induced visceral sensitivity: a bad legacy for next generations. Neurogastroenterol. Motil. *25*, 927–930.

Vaughn, M.W., Tanurdzić, M., Lippman, Z., Jiang, H., Carrasquillo, R., Rabinowicz, P.D., Dedhia, N., McCombie, W.R., Agier, N., Bulski, A., et al. (2007). Epigenetic natural variation in Arabidopsis thaliana. PLoS Biol. *5*, e174.

Veenendaal, M.V., Painter, R.C., de Rooij, S.R., Bossuyt, P.M., van der Post, J.A., Gluckman, P.D., Hanson, M.A., and Roseboom, T.J. (2013). Transgenerational effects of prenatal exposure to the 1944-45 Dutch famine. BJOG *120*, 548–553.

Vu, T.M., Nakamura, M., Calarco, J.P., Susaki, D., Lim, P.Q., Kinoshita, T., Higashiyama, T., Martienssen, R.A., and Berger, F. (2013). RNA-directed DNA methylation regulates parental genomic imprinting at several loci in Arabidopsis. Development *140*, 2953–2960.

Walter, J., Hutter, B., Khare, T., and Paulsen, M. (2006). Repetitive elements in imprinted genes. Cytogenet. Genome Res. *113*, 109–115.

Watanabe, T., Tomizawa, S.i., Mitsuya, K., Totoki, Y., Yamamoto, Y., Kuramochi-Miyagawa, S., Iida, N., Hoki, Y., Murphy, P.J., Toyoda, A., et al. (2011). Role for piRNAs and noncoding RNA in de novo DNA methylation of the imprinted mouse Rasgrf1 locus. Science *332*, 848–852.

Weigel, D., and Colot, V. (2012). Epialleles in plant evolution. Genome Biol. *13*, 249.

Wolff, C.F. (1759). Theoria Generationis (Germany: Typis et sumtu Io. Christ. Hendel).

Yu, A., Lepère, G., Jay, F., Wang, J., Bapaume, L., Wang, Y., Abraham, A.L., Penterman, J., Fischer, R.L., Voinnet, O., and Navarro, L. (2013). Dynamics and biological relevance of DNA demethylation in Arabidopsis antibacterial defense. Proc. Natl. Acad. Sci. USA *110*, 2389–2394.

Zemach, A., Kim, M.Y., Hsieh, P.H., Coleman-Derr, D., Eshed-Williams, L., Thao, K., Harmer, S.L., and Zilberman, D. (2013). The Arabidopsis nucleosome remodeler DDM1 allows DNA methyltransferases to access H1-containing heterochromatin. Cell *153*, 193–205.

Cytokines & Growth Factors in Cell Culture

- >> Produced in house
- >> Bulks in stock
- >> Multiple species
- >> Save up to 60%

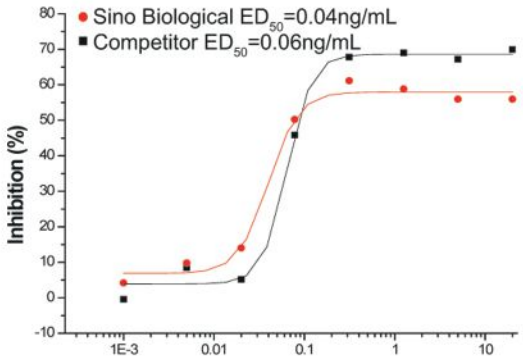

TGF-beta1 Conc.(ng/mL)

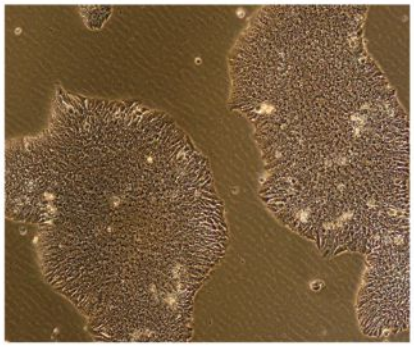

hESC cultured with TGF-β1+bFGF

Sino Biological Inc.
Biological Solution Specialist
ww.sinobiological.com

Leading Edge
Review

Cell

Camouflage and Misdirection: The Full-On Assault of Ebola Virus Disease

John Misasi[1] and Nancy J. Sullivan[2,*]
[1]Boston Children's Hospital, Department of Medicine, Division of Infectious Diseases, Boston, MA 02115, USA
[2]Vaccine Research Center, National Institute of Allergy and Infectious Diseases, National Institutes of Health, Bethesda, MD 20892, USA
*Correspondence: njsull@mail.nih.gov
http://dx.doi.org/10.1016/j.cell.2014.10.006

Ebolaviruses cause a severe hemorrhagic fever syndrome that is rapidly fatal to humans and nonhuman primates. Ebola protein interactions with host cellular proteins disrupt type I and type II interferon responses, RNAi antiviral responses, antigen presentation, T-cell-dependent B cell responses, humoral antibodies, and cell-mediated immunity. This multifaceted approach to evasion and suppression of innate and adaptive immune responses in their target hosts leads to the severe immune dysregulation and "cytokine storm" that is characteristic of fatal ebolavirus infection. Here, we highlight some of the processes by which Ebola interacts with its mammalian hosts to evade antiviral defenses.

Introduction

The *Filoviridae* family consists of three genera: Marburgvirus, Ebolavirus, and the newly identified Cuevavirus. Within the Ebolavirus genus, there are five species, including Zaire ebolavirus, Sudan ebolavirus, Bundibugyo ebolavirus, Taï Forest ebolavirus, and Reston ebolavirus. Filoviruses were first identified as the causative agent of a hemorrhagic fever syndrome in Marburg, Germany in 1967. Nine years later, the first two ebolaviruses were described in the Democratic Republic of Congo (formerly Zaire) and Sudan. Since then, more than 30 Ebola virus disease outbreaks have infected thousands, with a mean case fatality rate of ~65% in humans (Hartman et al., 2010). The recent Ebola virus disease outbreak in West Africa began in March of 2014 and has thus far caused more than 8,000 confirmed and probable cases, with a case fatality rate of about 50% (for the latest information see: http://www.who.int/csr/disease/ebola/en/).

Virus Life Cycle

Ebola particles are enveloped, filamentous, and contain a monopartite negative-sense RNA genome. Though Ebola initially targets macrophages and dendritic cells, it is able to infect almost all cell types, with the exception of lymphocytes (Wool-Lewis and Bates, 1998; Yang et al., 1998). Virus particles have been proposed to attach to host cells through multiple plasma membrane surface-expressed proteins (e.g., C-type lectins, DC-SIGN, integrins, TIM-1, Axl) (Alvarez et al., 2002; Baribaud et al., 2002; Kondratowicz et al., 2011; Lin et al., 2003; Schornberg et al., 2009; Shimojima et al., 2006; Simmons et al., 2003; Takada et al., 2000). Once attached to the plasma membrane, the viral envelope glycoprotein induces particle uptake via macropinocytosis. The induction of macropinocytosis appears to be dependent on the action of cell surface proteins, including TIM-1 and Axl (Aleksandrowicz et al., 2011; Brindley et al., 2011; Hunt et al., 2011; Moller-Tank et al., 2013; Mulherkar et al., 2011; Nanbo et al., 2010; Quinn et al., 2009; Saeed et al., 2010; Shimojima et al., 2007, 2006; Wen et al., 2013). After uptake into macropinosomes, particles travel to low-pH compartments of late endosomes and lysosomes, where the viral envelope glycoprotein (GP) is proteolytically cleaved by endosomal cysteine proteases (i.e., cathepsin B and L). This cleavage removes a heavily glycosylated region from GP (Chandran et al., 2005; Dube et al., 2009; Hood et al., 2010; Misasi et al., 2012; Schornberg et al., 2006) and exposes a domain in GP that binds specifically to the endosomal/lysosomal resident filovirus receptor Niemann-Pick C1 protein (NPC1) (Carette et al., 2011; Côté et al., 2011). Though current evidence suggests that NPC1 binding may be sufficient to trigger fusion of the viral and cellular membranes (Miller et al., 2012), it is as yet unclear whether additional host proteins or intracellular conditions are necessary (e.g., reducing conditions, altered pH, additional protease cleavage) (Brecher et al., 2012; Chandran et al., 2005) (Figure 1, left).

Once the viral and internal cell membranes fuse, the virus particle uncoats and its anti-genome is transcribed into mRNA using nucleocapsid-associated viral proteins. The virus genome consists of seven viral genes—*VP24*, the nucleoprotein (*NP*), *VP30*, *VP35*, the matrix protein (*VP40*), the RNA-dependent RNA polymerase (*L*), and the *glycoprotein*—which are transcribed into mRNA, resulting in the production of at least ten proteins. Transcription of the genome is mediated via a complex of VP30, VP35, and the viral polymerase L bound to an NP-coated genome (Bharat et al., 2012; Hartlieb et al., 2003, 2007; Modrof et al., 2003; Mühlberger et al., 1999; Sanchez and Kiley, 1987; Sanchez et al., 1993). VP30 phosphorylation leads to its dissociation from the VP35/L complex and is the signal to switch from transcription to replication (Biedenkopf et al., 2013; Martinez et al., 2011a). Following this switch, virus genomes are replicated and coated by NP, VP24, VP30, and VP35 (Mühlberger et al., 1999). During assembly, L associates with the ribonucleoprotein complex through an interaction with VP35. The ribonucleoproteins then associate with the matrix

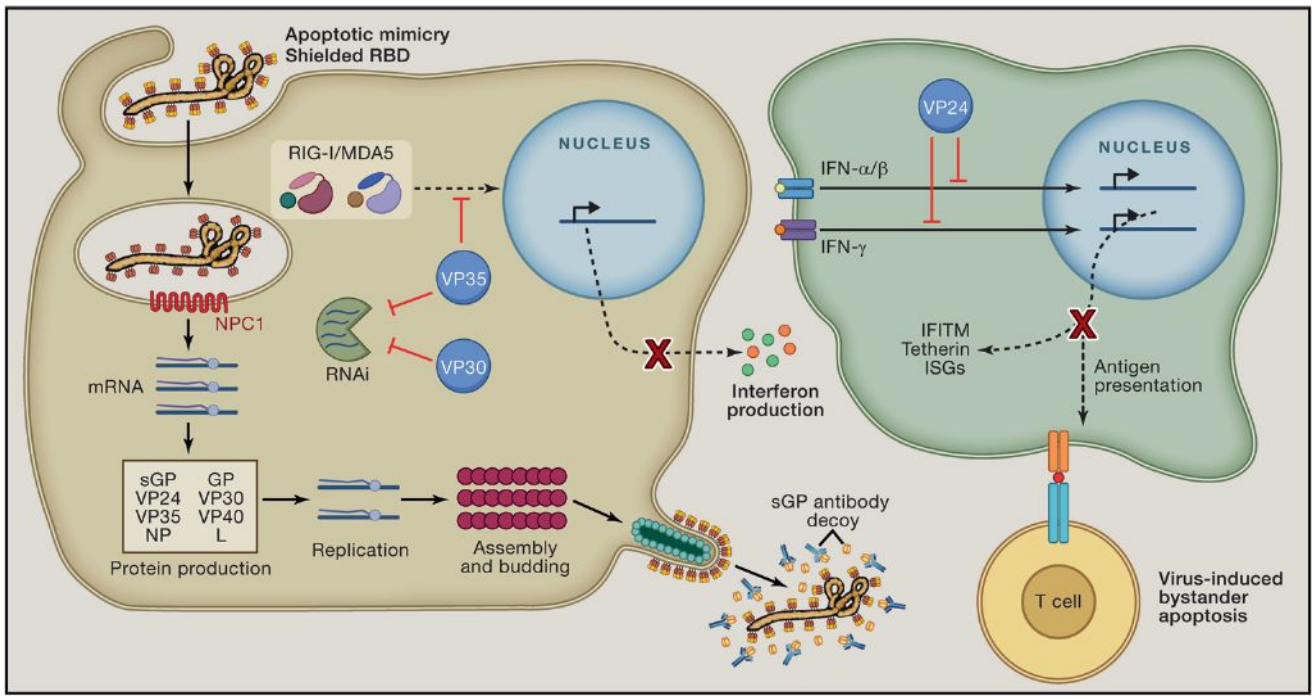

Figure 1. Ebolavirus Life Cycle and Immune Avoidance Mechanisms

(Left) Virus particles attach to cell surface, inducing macropinocytosis and virus uptake, possibly using apoptotic mimicry to suppress inflammatory responses. The particle is brought to a low pH compartment, where it is cleaved by cysteine proteases to reveal its NPC1 receptor-binding domain (RBD). Following fusion and uncoating, the viral genome is transcribed into mRNA and viral proteins produced. Eventually, a signal to begin genome replication occurs, followed by particle assembly and budding.

Expression and secretion of sGP serves as an antibody decoy for antibodies generated against GP. Viral proteins VP35, VP30, and VP24 are expressed and mediate innate immune avoidance in all cell types. (Left) VP35 interferes with RIG-I/MDA-5 signaling and induction of interferon. Additionally, VP35 and VP30 block the RNAi response against viral gene expression. (Right) VP24 acts to inhibit type I and II interferon (IFN) signaling. This prevents interferon-induced gene expression and, in antigen-presenting cells, blocks enhancement of antigen presentation to T cells.

protein VP40, and viral particles are extruded through the plasma membrane within lipid raft microdomain regions (Stahelin, 2014) (Figure 1, left).

Sneaking in with the Trash: Apoptotic Mimicry

Ebolavirus particles can be up to a micron in length, making it difficult for the viruses to enter via classic clathrin- or caveolin-mediated endocytosis pathways, perhaps explaining the requirement for macropinocytotic uptake. Interestingly, an increased amount of phosphatidylserine (PS) may be present on the surface of Ebola-virus-like particles (Jemielity et al., 2013; Moller-Tank et al., 2013). PS is a lipid that is primarily present on the inner leaflet of plasma membranes (Zachowski, 1993). Upon cell death via apoptosis, PS is exposed to the outer leaflets of plasma membranes and apoptotic bodies. This alerts nearby cells, including phagocytic cells, to begin "eating" the debris via macropinocytosis in a process that is mediated by TIM-1 and Axl and does not induce an inflammatory response (Biermann et al., 2013; Morizono and Chen, 2014; Zagórska et al., 2014). This suggests the possibility that, similar to other large viruses such as vaccinia virus (Mercer and Helenius, 2008), Ebola may induce macropinocytic uptake by appearing to be an apoptotic body to phagocytic cells. This "apoptotic mimicry" is anti-inflammatory and induces rapid uptake of a large virus into cells, thus avoiding humoral and cell surface immunity factors.

Snipping the Alarm Wire: Preventing the Interferon Alarm

Evasion of host innate immune responses is of particular importance to viruses, and many have evolved mechanisms to circumvent innate immunity. Ebola inhibits both type I and type II interferon responses in target cells, especially macrophages, monocytes, and dendritic cells. The ultimate result is a defect in dendritic cell maturation and diminished T-cell activation and proliferation along with apoptosis leading to lymphopenia, a key characteristic of Ebola virus disease. Studies in animal models and in tissue culture suggest that both pathogenesis and interferon antagonism are linked to VP35 and VP24 (Cilloniz et al., 2011; Ebihara et al., 2006; Hartman et al., 2008a, 2008b; Mateo et al., 2011; Prins et al., 2010; Reid et al., 2007).

VP35

VP35 is a viral polymerase cofactor that functions in RNA synthesis and has been proposed to link L to NP. In addition to these roles, VP35 plays a prominent role in Ebola's inhibition of α and β interferon induction through multiple mechanisms.

RIG-I and MDA-5 are innate pattern recognition receptors that detect foreign cytosolic RNA. RIG-I recognizes 5′-triphosphates

of blunt-ended RNA, and MDA-5 senses long double-stranded RNA (dsRNA). Both signal via the downstream adaptor IPS-1 (a.k.a. MAVS, VISA, Cardif), resulting in NF-κB, IRF-3, and IRF-7 activation with subsequent expression of type I interferon and proinflammatory cytokines. Activation of IRF-3/7 is the result of a signal cascade through which they are phosphorylated by TANK-binding kinase 1 (TBK-1) and IκB kinase-ε (IKKε) (Chiang et al., 2014). Early experiments determined that VP35 disrupted the RIG-I pathway by preventing IRF-3 phosphorylation (Basler et al., 2000, 2003). Later, VP35 was shown to interact with the N-terminal kinase domain of IKKε in preventing IRF-3 phosphorylation and acting as a decoy substrate for IKKε /TBK-1 kinases. Furthermore, binding of VP35 to IKKε prevents interactions with other proteins, including IRF-7 and IPS-1 (Prins et al., 2009). The net result of these interactions is inhibition of the induction of genes with interferon response promoters.

In addition to these downstream events in the RIG-I pathway, VP35 interacts with dsRNA to prevent RIG-I and MDA-5 responses (Cárdenas et al., 2006). Structural and biochemical studies revealed that VP35 contains a C-terminal interferon inhibitory domain (IID) with two clusters of basic amino acids. One cluster centers on residue R312 and participates in binding to dsRNA. Further analysis revealed that VP35 binds to blunt-ended dsRNA in a manner very similar to that seen with RIG-I (Cárdenas et al., 2006; Leung et al., 2009, 2010a). Structural studies of VP35 dsRNA binding are consistent with the finding that VP35 prevents both RIG-I and MDA-5 responses. Observations from RNA-bound and -unbound structures revealed that VP35 is able to bind both the phosphate backbone of dsRNA and end-capped RNA in VP35 dimers. Mutations of the basic patch centering on R312 abrogate dsRNA binding, and structural analysis suggests that R312 mutations disrupt VP35 dimerization (Kimberlin et al., 2010). Experiments using recombinant viruses incorporating mutant $VP35_{R312A}$ showed attenuation of virulence and impairment of both virus growth and interferon antagonism, suggesting that IID binding to dsRNA and VP35 dimerization play key roles in the virus life cycle and pathogenesis (Hartman et al., 2008a, 2008b; Kimberlin et al., 2010; Prins et al., 2010).

Interestingly, comparisons of VP35 IID from the pathogenic Zaire ebolavirus and Reston ebolavirus—thus far only pathogenic in monkeys—revealed a slight decrease in interferon antagonism and dsRNA binding by Reston. However, these decreases did not appear to contribute significantly to the differences in virulence between the Zaire and Reston viruses (Leung et al., 2010b). Furthermore, comparison of the structures of the Zaire and Reston VP35 did not reveal substantial differences between the dsRNA recognition mechanisms (Kimberlin et al., 2010). Together, these data suggest additional viral factors likely play a role in the differential host responses between these two viruses.

Recently, VP35 was found to interact with the PKR activator (PACT) (Fabozzi et al., 2011). In addition to having activity in RNA silencing and PKR activation, PACT binds to and activates RIG-I. Subsequent work showed that VP35 binding to PACT prevents PACT binding to RIG-I and inhibits RIG-I activation (Luthra et al., 2013). VP35 binding to PACT is mediated by the same central basic patch in IID that abrogates dsRNA binding described above, suggesting a possible role for dsRNA in this interaction. Surprisingly, PACT interaction with VP35 inhibits the binding of VP35 with L, causing a decreased efficiency of viral RNA synthesis and genome replication, a phenotype of "mutual antagonism" (Luthra et al., 2013). Taken together with previous data, these experiments point to the critical importance of VP35 antagonism of the RIG-I pathway during ebolavirus infection.

Additional VP35 interactions with cellular proteins have been explored using a yeast two-hybrid system. These studies found that VP35 interacts with IRF-7, Ubc9, and PIAS1 (Chang et al., 2009). Ubc9 and PIAS1 are key components of the small ubiquitin-related modifier (SUMO) system of posttranslational modification, which regulates a variety of cellular pathways and proteins. During SUMOylation, SUMO proteins are activated by SUMO-specific proteases and are transferred to a SUMO-conjugating E2 enzyme (e.g., Ubc9). Next, an E3 ligase, such as PIAS1, is used to transfer the SUMO domain to a lysine on the target protein (Wimmer et al., 2012). Studies with Ebola VP35 found that it was able to block CpG-induced interferon induction involving the IRF-3/7 pathway. Subsequent investigation revealed that PIAS1 is able to SUMOylate IRF-7. VP35 expression enhanced SUMOylation of IRF-7, leading to suppression of its activity and a decrease in interferon promoter activity. Similar findings were noted with IRF-3 following expression of VP35 (Chang et al., 2009). Thus, VP35-induced SUMOylation of IRF-3 and IRF-7 leads to a further reduction in interferon α/β gene transcription.

Arenaviruses (e.g., Lassa, LCMV) have taken a similar multipronged approach to preventing type I interferon responses. Lassa hemorrhagic fever has many characteristics similar to Ebola virus disease, including the absence of interferon production and lymphoid depletion. On the molecular level, arenaviruses have been shown to suppress interferon production by targeting both upstream (i.e., RIG-I/MDA-5) and downstream signaling events (i.e., IKKε interactions, IRF-3 phosphorylation) (Koma et al., 2013). In this way, each virus disrupts multiple access points in the pathways that lead to increased interferon production. Given the similarity in the clinical syndromes and the common approach to interferon antagonism, further investigations may provide insights into the underlying pathogenic mechanisms of hemorrhagic fever syndromes.

VP24

When innate immunity is intact, the host response to virus infection causes secretion of interferon in order to generate antiviral responses in neighboring cells, signal hematopoietic cell responses, and increase antigen presentation. Secreted interferon binds to type I and II interferon receptors, inducing signaling via adaptor proteins, and results in the phosphorylation and subsequent dimerization of signal transducer and activator of transcription (STAT) proteins (e.g., STAT-1, STAT-2). Next, dimerized phosphorylated STATs are transported to the nucleus where they bind to interferon response elements and induce gene expression (Ivashkiv and Donlin, 2014; Platanias, 2005). Given the importance of these pathways for inducing antiviral gene expression in response to interferon, they are commonly targeted by viruses. For example, Dengue virus blocks STAT-1 phosphorylation and acts to degrade STAT-2 via proteasomal degradation pathways (Green et al., 2014). Early experiments

with Ebola found that the virus not only blocked the production of interferon, but also inhibited cellular responses that normally result from both interferon α/β (type I) and interferon γ (type II) signaling. This signaling block was associated with the expression of the Ebola VP24 protein and later shown to prevent the nuclear accumulation of dimerized phosphorylated STAT-1 (Reid et al., 2006), which participates in both type I (i.e., STAT-1/STAT-2 phosphorylated-dimer) and type II (STAT-1/STAT-1 phosphorylated-dimer) signal propagation cascades (Ivashkiv and Donlin, 2014; Platanias, 2005).

Phosphorylated STAT-1 dimer transport to the nucleus is mediated by interactions with members of the nucleoprotein interactor 1 family (i.e., karyopherin-α1, -α5, or -α6). Karyopherin-α binds to nuclear localization signals (NLS) on cargo destined for the nucleus. Downstream interactions with karyopherin-β and other proteins allow the cargo to cross the nuclear membrane. Unlike most nuclear proteins, dimerized phosphorylated STAT-1 interacts with karyopherin-α through a unique noncanonical NLS, allowing it preferential access to the nucleus. Biochemical and structural studies have shown that VP24 binds to karyopherin-α in the noncanonical NLS-binding domain. This blocks phosphorylated STAT-1 dimer transport to the nucleus. Furthermore, VP24 binding to karyopherin-α does not appear to block access to the canonical NLS-binding site (Mateo et al., 2010; Reid et al., 2007; Xu et al., 2014). Therefore, the virus interfere with both type I and type II interferon signaling without disrupting routine trafficking to the nucleus of the infected cell.

Unphosphorylated STAT-1 is able to enter the nucleus using a karyopherin-α-independent mechanism, where it is able to induce and prolong the expression of interferon-induced immune regulatory genes (Cheon and Stark, 2009; Meyer and Vinkemeier, 2004). Biochemical and structural studies with STAT-1 C-terminal truncation mutant demonstrated that VP24 binds efficiently to STAT-1 lacking the tyrosine target for phosphorylation (Zhang et al., 2012). This suggests an additional mechanism unrelated to phosphorylated STAT-1 dimer nuclear transport by which VP24 is able to inhibit the induction of the interferon response (i.e., by blocking the action of both forms of STAT-1).

In addition to the Jak-STAT pathway, type I interferon receptors signal through the p38 MAP kinase pathway, where a signal cascade of MAP kinases results in the phosphorylation of p38-α (Ivashkiv and Donlin, 2014; Platanias, 2005). One study found that VP24 was able to block the interferon-β-induced phosphorylation of p38-α in HEK293T cells. However, this finding was cell type specific, and the blocking mechanism has yet to be demonstrated or generalized to cells that are primary targets of infection (e.g., macrophages, dendritic cells) (Halfmann et al., 2011).

Like VP35, VP24 has been linked to Ebola pathogenesis. In particular, experiments using mouse- and guinea-pig-adapted variants of Ebola demonstrated that VP24, in conjunction with other proteins such as NP, is critical to virus lethality (Cilloniz et al., 2011; Ebihara et al., 2006; Mateo et al., 2011; Reid et al., 2007). Structural analysis and comparison of Sudan and Reston VP24 identified two conserved structural pockets that contain residues implicated in the pathogenesis of VP24. Solvent exchange studies showed that this region may be near a proposed STAT-1-binding region on VP24, suggesting that it may play a role in STAT-1 binding and pathogenesis (Zhang et al., 2012).

Taken together with previous studies on karyopherin-α, VP24 plays a role in pathogenesis through the disruption of both type I and type II interferon signaling. Thus, Ebola not only diminishes the interferon alarm, but also inhibits the alarm response after it has been heard. This coordinated approach between VP35 and VP24 leads to a highly effective antagonism of the innate immune responses mediated by interferons.

Silence Will Fall: Disrupting the RNAi Response

Infection of cells by RNA viruses activates an RNA-specific inhibition (RNAi) pathway in host cells that silences viral gene expression by cleaving viral RNA into small interfering RNAs (siRNA) that bind and disrupt complementary RNA transcripts. HIV-1 Tat is thought to suppress RNAi responses by blocking Dicer activity, a key component of the RNA silencing complex. Ebola VP35 suppresses cellular RNAi silencing and can complement HIV-1 Tat^{-} mutants. This suppression was lost when mutations were made in the dsRNA-binding domains of VP35, suggesting that VP35 may bind to siRNA or the dsRNA precursors of siRNA (Haasnoot et al., 2007). Though subsequent studies found that the C-terminal domain of VP35 bound to siRNA and not to dsRNA, the RNAi silencing suppression activity of VP35 did not correlate with binding to siRNA. It was hypothesized that suppression via RNA-binding-independent mechanisms could instead occur through binding to the RISC complex or sequestration of RISC complex proteins prior to their incorporation into the complex (Zhu et al., 2012). This theory is supported by prior experiments which found that VP35 interacts with transactivation response RNA-binding protein (TRBP) and PACT (Fabozzi et al., 2011), both components of the RISC RNAi complex and thus proposed to mediate the VP35-dependent RNA-silencing suppressor activity. Interestingly, another Ebola protein, VP30, also binds to components of the RISC complex and acts as a suppressor of RNAi silencing (Fabozzi et al., 2011). Similar to Ebola's tactics for interferon antagonism, the virus uses two different viral proteins to disrupt the mammalian RNAi innate immune response.

Plundering the Factories: Coopting Host Cellular Functions

Protein Translation

Host cells thwart viral infection by decreasing cellular protein synthesis in an effort to prevent or slow viral replication. This is accomplished through the double-stranded RNA-dependent protein kinase, PKR. Upon binding of dsRNA and activation, PKR phosphorylates the α subunit of the eukaryotic translation initiation factor-2 (eIF-2α). Ebola VP35 expression has been shown to block PKR activity and enhance expression of proteins after cells were treated with type I interferons. VP35 blocks PKR by impairing phosphorylation of both PKR and the eIF-2α. Current data suggest that this effect is mediated by the VP35 IID domain; however, further work to elucidate the molecular mechanism is required (Feng et al., 2007; Schümann et al., 2009).

RNA Stability and Replication

The heterogeneous nuclear protein complex C1/C2 proteins (hnRNP C1/C2) are typically found in the nucleus where they bind poly-U regions (>4) in mRNA and assist splicing prior to mRNA export to the cytoplasm. They have also been shown to

participate in cap-independent, IRES-dependent translation in the cytoplasm during mitosis (Shabman et al., 2011). Several viruses, including Dengue and poliovirus, have been found to co-opt this function as a means to enhance viral protein synthesis and replication (Brunner et al., 2005, 2010; Noisakran et al., 2008; Pettit Kneller et al., 2009). Likewise, Ebola VP24 expression causes the relocalization of hnRNP C1/C2 from the nucleus to the cytoplasm. Interestingly, hnRNP C1/C2 also binds to karyopherin-α via the same noncanonical NLS sequence STAT-1 and VP24 use, suggesting a possible mechanism for redistribution. It was hypothesized that, because the Ebola genomic and mRNA sequences contain many poly-U tracts, hnRNP C1/C2 may interact with Ebola RNA to stabilize viral mRNA and enhance genome replication (Shabman et al., 2011). Thus, through PKR inhibition and hnRNP C1/C2 relocalization, ebolaviruses co-opt cellular machinery to optimize translation of gene products and potentially prolong the half-life of viral messenger and genomic RNA.

Escape from Alcatraz: The Tetherin Release Program

Tetherin is a type I interferon-inducible cellular factor that has been shown to prevent enveloped virus budding from plasma membranes. Tetherin contains two membrane-anchored domains and is thought to mediate inhibition of budding by anchoring between the cellular and viral membranes (Neil et al., 2008). Tetherin was first described to antagonize retrovirus and HIV-1 particle budding. These studies found that particle budding was rescued by the expression of HIV-1 Vpu (Neil et al., 2008). When Ebola virus-like particles (VLP) were made with VP40 in the presence of overexpressed tetherin, a similar decrease in VLP release was noted and simultaneous expression of HIV-1 Vpu rescued particle release. VLPs with or without GP expression showed that GP antagonized tetherin activity and coimmunoprecipitated tetherin (Kaletsky et al., 2009). Recent experiments suggest that residues within the transmembrane domain of GP contribute to GP-dependent tetherin antagonism (Gnirß et al., 2014; Kühl et al., 2011). Mechanisms proposed for GP-tetherin antagonism include interference with tetherin integrity, steric hindrance by GP that interferes with the formation of the tetherin connection between the viral and cellular membranes, and GP-dependent exclusion of tetherin from the region of the plasma membrane from which Ebola virus particles bud (Kaletsky et al., 2009). In HIV-1, Vpu mediates cell-surface downregulation, relocalization, and degradation of tetherin (Lopez et al., 2012). However, Ebola GP does not appear to downregulate or alter tetherin localization (Lopez et al., 2010, 2012), suggesting a novel anti-tetherin mechanism.

The Host Strikes Back: Blocking the Entrances and Exits

The trade-off between efficient viral replication and pathogenicity is a delicate balance that, when mismatched, can lead to host demise. Therefore, viruses have evolved to suppress immune responses in a selective and regulated manner that facilitates controlled virus replication and progeny transmission. In this section, we highlight two interferon-inducible genes that, to date, are not known to be directly countered during Ebola infection and lead to decreased virus infectivity.

Interferon-induced transmembrane proteins (IFITMs) are broadly active interferon-responsive restriction factors that were first described as inhibitors of influenza A and have been shown to be active against many enveloped viruses, including Ebola and its cousin Marburg virus (Huang et al., 2011). IFITMs are found in multiple membrane surfaces along cellular uptake pathways and have been proposed to act by blocking virus entry (Huang et al., 2011; Perreira et al., 2013). Several antiviral mechanisms have been proposed, including cholesterol accumulation, inhibition of back fusion of virus containing vesicles in multivesicular bodies, changes to membrane fluid dynamics, or alterations in membrane curvature (i.e., restricting the capacity for fusion between the virus and cellular membranes) (Amini-Bavil-Olyaee et al., 2013; Perreira et al., 2013). Recent experiments with IFITM-3 and influenza A virus suggest that IFITM-3 acts by blocking an as yet undefined step between virus-cell membrane hemi-fusion and fusion pore formation (Desai et al., 2014). Thus, IFITM-3 allows the virus and celluar membrane lipids to mix but does not allow the formation of a complete fusion pore. This prevents the ribonucleoprotein core of the virus from gaining access to the cytoplasm and blocks infection. Future experiments will need to be performed to determine whether this mechanism is applicable to Ebola and how some enveloped viruses (i.e., arenaviruses) are able to avoid restriction by IFITMs.

Another interferon-stimulated gene that blocks Ebola infection is ISG-15, a broadly active antiviral gene product that, when conjugated to a target protein, causes alterations to target protein activity, cellular location, and stability. It has been shown to affect many viruses, including influenza A/B, hepatitis B, HIV-1, herpes simplex type 1, LCMV, and Ebola (Harty et al., 2009). In the case of Ebola, the antiviral activity of ISG-15 was linked to a disruption in VP40-mediated budding using VLP assays. Ebola budding is, in part, mediated by Nedd4 ubiquitination of VP40. Two groups found that ISG-15 interacts with Nedd4 and prevents the ubiquitination of VP40, leading to inefficient particle budding (Liu and Harty, 2010). Thus, together with IFITMs and tetherin, these observations suggest that interferon-stimulated genes have potent antiviral activities targeted against ebolavirus during both entry and egress.

The resistance of freshly isolated monocytes to Ebola illustrates one example in which these factors may be playing a role during infection. Experiments with Ebola GP-pseudotyped VLPs found that particles were able to bind, but not enter, freshly isolated monocytes. However, once the monocytes underwent differentiation, the previously bound VLPs were able to enter the monocytes, a result recapitulated using replicating Ebola viruses (Martinez et al., 2013). Detailed analysis found that, as the monocytes matured, IFITMs were downregulated while both cysteine protease cathepsin B and NPC1 expression were upregulated. These findings demonstrate how IFITM restriction factors might play a role in the relative resistance to infection of interferon-activated cells and also confirm the importance of NPC1 for Ebola infection.

Balancing the Scales of the Immune Response

A paradox in Ebola virus disease is that both survival and mortality are linked to the generation of strong immune signaling responses in the host. Survivors and asymptomatic patients

have increased numbers of T cells and an early cytotoxic T-cell-mediated response (Baize et al., 1999; Sanchez et al., 2004; Wauquier et al., 2010). Rapid uptake of Ebola by macrophages and dendritic cells not only results in translocation to lymphoid and peripheral tissues, but also may explain the deficit in nonsurvivors of inflammatory cytokine secretion needed early after exposure for the control of infection. Experiments using in-vitro-cultured monocyte-derived macrophages found that Ebola infection inhibited the secretion of TNF-α, IL-6, and IL-10, consistent with impairments observed in association with fatal disease outcome (Mahanty et al., 2003). Furthermore, dendritic cells exposed to either live or inactivated virus failed to upregulate molecules needed for T-cell co-stimulation, resulting in an inhibition of CD4 T-cell proliferation. Studies using blood samples obtained from infected human subjects found that IL-6 and TNF-α responses were higher in survivors than nonsurvivors at early time points. At later time points, IL-6 remained higher in survivors, but the difference from nonsurvivors was less dramatic due to increases in the latter group. In contrast to IL-6, TNF-α in nonsurvivors was much higher than survivors late after disease onset. It is interesting to note that IL-10 may play a critical role in modulating these responses. Although IL-10 was mildly elevated in survivors, likely as a feedback mechanism to control the inflammatory response, the increase was short lived, as would be expected once cytokine levels returned to normal. However, IL-10 was 6- to 10-fold higher in fatal cases and remained elevated until death. In addition, monocyte/macrophage activation as measured by neopterin levels was 2- to 10-fold higher and consistently elevated in fatal cases (Baize et al., 2002; Leroy et al., 2000, 2001), suggesting unregulated immune activation. Though more recent studies showed different patterns for specific cytokines (Wauquier et al., 2010), there is a general trend toward survivors having a short-lived, balanced pro- and anti-inflammatory response and nonsurvivors having a delayed and prolonged inflammatory response that leads to ''cytokine storm.''

Together, these observations suggest that subjects able to overcome innate immune response blocking by VP24, VP30, and VP35 are more likely to establish an early, balanced, and beneficial secretion of proinflammatory/anti-inflammatory cytokines. In contrast, when early host antiviral innate responses are blocked, uncontrolled virus replication and lysis of hematopoietic cells leads to late and unbalanced cytokine release, overall dysregulation of immune responses, and the development of advanced Ebola virus disease.

Camouflage and Misdirection: Avoiding Adaptive Immune Responses

A fatal irreversible consequence of hematopoietic cell destruction by Ebola is reduced antigen presentation. This outcome is consistent with the observation of poor IgG responses in fatal infection, whereas high levels of IgG are associated with survival (Baize et al., 1999; Ksiazek et al., 1999). Compounding inhibition of IgG production, Ebola has evolved multiple properties that could circumvent antibody effectiveness. Large filamentous virions containing high-density, stable glycoprotein present a potential obstacle for efficient inhibition by antibodies, and virus filament folding may create ''pockets'' of glycoprotein that are inaccessible to antibody binding. Furthermore, heavy glycosylation in the mucin-like domain of GP may limit access to critical epitopes required for efficient neutralization (Martinez et al., 2011b). Antibody access is restricted further due to rapid virion uptake via macropinocytosis and intracellular receptor binding. Additionally, ebolavirus hides its critical receptor binding domain beneath a glycan cap, with exposure and receptor binding occurring only after cathepsin-mediated removal of the cap. This protection of a critical functional domain is analogous to HIV, in which CD4 engagement of gp120 is required to expose the coreceptor-binding site (Harrison, 2008). Furthermore, the use of an intracellular receptor is a novel immune evasion strategy that may be important for other viruses (e.g., Lassa fever virus [Jae et al., 2014]).

In addition to membrane-anchored GP, the glycoprotein gene of Ebola encodes sGP, a 364 aa protein that is identical to GP in its 205 N-terminal residues but is secreted by infected cells and is not present in virions. The default transcript of the *glycoprotein* gene is surprisingly not the virion-associated GP trimer but instead dimeric sGP; the balance of expression of these two proteins is governed by polymerase stuttering at an RNA-editing site. This has led to speculation that sGP functions to modulate or misdirect host immune responses (Kindzelskii et al., 2000; Yang et al., 1998). The best evidence for this hypothesis comes from a recent paper showing in mice that sGP promotes immune evasion by serving as an antibody decoy for GP or by presenting alternative nonneutralizing antibody epitopes for the humoral immune response (Mohan et al., 2012). Remarkably, evidence suggests that about 80% of glycoprotein gene expression is sGP. This may be due, in part, to selective pressures seeking to balance toxicity due to cytopathic effects of GP with the requirement for GP on virus particles and avoidance of host immune responses directed against GP (Yang et al., 2000, Volchkova et al., 2011). Taken together, these data suggest that Ebola expression of sGP and GP is a tightly regulated process in which immune shielding and virus particle production are balanced via RNA editing.

In addition to immune evasion achieved through virion and GP structural characteristics, GP exhibits direct immunosuppressive properties (Chepurnov et al., 1999). sGP interacts with neutrophils and disrupts the linkage between Fc γ RIIIB and CR3 (Kindzelskii et al., 2000). Furthermore, the Ebola transmembrane glycoprotein, GP2, bears structural similarity to retroviral glycoproteins possessing an immunosuppressive peptide motif (Volchkov et al., 1992) that was found to inhibit lymphocyte activation and proliferation (Yaddanapudi et al., 2006). Of particular interest was the observation that the analogous immunosuppressive peptide from Reston virus was inhibitory only in macaque, but not human, peripheral blood cells, implicating this motif in Ebola pathogenicity.

Studies measuring in vivo antigen-specific T-cell responses are limited by the difficulty of obtaining and preserving viable lymphocyte samples from Ebola-infected subjects and survivors. Nonetheless, data suggest that, over the course of Ebola virus disease, there is a dramatic decrease in the absolute numbers of T cells due to bystander apoptosis. This impairs both direct cell-mediated killing of virus-infected cells and the T-cell-dependent antiviral antibody responses (Sanchez et al., 2004). Indirect measures of T-cell function based on serum

cytokine levels and RNA expression in isolated lymphocytes suggest, as with immunoglobulin levels, an association between intact cell-mediated immunity and survival (Baize et al., 1999; Ksiazek et al., 1999; Sanchez et al., 2004; Wauquier et al., 2010). In macaques, $CD8^+$ T cells are essential for vaccine-induced immune protection (Stanley et al., 2014; Sullivan et al., 2011). Humoral responses clearly play a beneficial role in containing virus but are not required for protection against some Ebola species (Hensley et al., 2010; Stanley et al., 2014; Sullivan et al., 2011). Antibodies participate in effective virus clearance but likely require the presence of intact host cell-mediated responses (Wong et al., 2012). One speculative interpretation of both human and macaque data is that immunoglobulin and innate immune responses participate in containing early viral loads but that cell-mediated immunity is needed for efficient virus clearance. The interplay and necessity of broad immune response mechanisms is also suggested by Ebola evolution of strategies to counteract each of these host antiviral defenses. Taken together, these data suggest a complex interplay between pro- and anti-inflammatory factors, resulting in either a balanced immune response and host survival or dysregulation and death.

Summary

Fatal Ebola infection is marked by a catastrophic failure of innate and adaptive immunity that is mediated by virus-encoded proteins as well as properties associated with virus structure. At the heart of Ebola-induced immune dysregulation is a multipronged attack on host antiviral immunity. Early and coordinated disruption of host innate responses by VP24, VP30, and VP35 leads to elevated levels of virus replication, a cascade of inappropriately timed cytokine release, and death of both antigen-presenting and -responding immune cells (Figure 1). This results in a poorly activated adaptive immune response that is further compromised by the induction of lymphocyte apoptosis and antibody decoy mechanisms. In incidental hosts, this multifaceted approach to subversion of the immune system results in high mortality that would be expected to limit virus persistence in the absence of a distinct reservoir species.

Since first being identified almost 40 years ago, the genome of Ebola has shown remarkable stability, an unusual feature for RNA viruses with an error-prone polymerase. This suggests that Ebola is highly adapted in its reservoir host. One intriguing hypothesis is that additional host restriction factors limit pathogenicity in a natural reservoir species. These factors would play a role in the balance between immunity and sustained viral replication, allowing the virus to propagate and persist over time in the reservoir species. Outside this reservoir, sustained large outbreaks such as the one in West Africa may lead to ebolavirus adaptations being observed longitudinally, resulting in altered pathogenicity as the virus adapts to humans. Overall, the multifaceted approach of Ebola to selectively regulate immune responses and its variable pathogenicity in different host species makes this virus both scientifically interesting and a challenging foe.

ACKNOWLEDGMENTS

The authors thank B. Hartman for graphics and A. Tislerics for editing the manuscript. This work was supported by the Intramural Research Program of the US NIH NIAID Vaccine Research Center, NIH grant K08-AI079381, and a Boston Children's Hospital Faculty Development Fellowship.

REFERENCES

Aleksandrowicz, P., Marzi, A., Biedenkopf, N., Beimforde, N., Becker, S., Hoenen, T., Feldmann, H., and Schnittler, H.-J. (2011). Ebola virus enters host cells by macropinocytosis and clathrin-mediated endocytosis. J. Infect. Dis. *204* (*Suppl 3*), S957–S967.

Alvarez, C.P., Lasala, F., Carrillo, J., Muñiz, O., Corbí, A.L., and Delgado, R. (2002). C-type lectins DC-SIGN and L-SIGN mediate cellular entry by Ebola virus in cis and in trans. J. Virol. *76*, 6841–6844.

Amini-Bavil-Olyaee, S., Choi, Y.J.J., Lee, J.H.H., Shi, M., Huang, I.-C., Farzan, M., and Jung, J.U.U. (2013). The antiviral effector IFITM3 disrupts intracellular cholesterol homeostasis to block viral entry. Cell Host Microbe *13*, 452–464.

Baize, S., Leroy, E.M., Georges-Courbot, M.C., Capron, M., Lansoud-Soukate, J., Debré, P., Fisher-Hoch, S.P., McCormick, J.B., and Georges, A.J. (1999). Defective humoral responses and extensive intravascular apoptosis are associated with fatal outcome in Ebola virus-infected patients. Nat. Med. *5*, 423–426.

Baize, S., Leroy, E.M., Georges, A.J., Georges-Courbot, M.C., Capron, M., Bedjabaga, I., Lansoud-Soukate, J., and Mavoungou, E. (2002). Inflammatory responses in Ebola virus-infected patients. Clin. Exp. Immunol. *128*, 163–168.

Baribaud, F., Pöhlmann, S., Leslie, G., Mortari, F., and Doms, R.W. (2002). Quantitative expression and virus transmission analysis of DC-SIGN on monocyte-derived dendritic cells. J. Virol. *76*, 9135–9142.

Basler, C.F., Wang, X., Mühlberger, E., Volchkov, V., Paragas, J., Klenk, H.D., García-Sastre, A., and Palese, P. (2000). The Ebola virus VP35 protein functions as a type I IFN antagonist. Proc. Natl. Acad. Sci. USA *97*, 12289–12294.

Basler, C.F., Mikulasova, A., Martinez-Sobrido, L., Paragas, J., Mühlberger, E., Bray, M., Klenk, H.-D., Palese, P., and García-Sastre, A. (2003). The Ebola virus VP35 protein inhibits activation of interferon regulatory factor 3. J. Virol. *77*, 7945–7956.

Bharat, T.A., Noda, T., Riches, J.D., Kraehling, V., Kolesnikova, L., Becker, S., Kawaoka, Y., and Briggs, J.A. (2012). Structural dissection of Ebola virus and its assembly determinants using cryo-electron tomography. Proc. Natl. Acad. Sci. USA *109*, 4275–4280.

Biedenkopf, N., Hartlieb, B., Hoenen, T., and Becker, S. (2013). Phosphorylation of Ebola virus VP30 influences the composition of the viral nucleocapsid complex: impact on viral transcription and replication. J. Biol. Chem. *288*, 11165–11174.

Biermann, M., Maueröder, C., Brauner, J.M., Chaurio, R., Janko, C., Herrmann, M., and Muñoz, L.E. (2013). Surface code—biophysical signals for apoptotic cell clearance. Phys. Biol. *10*, 065007.

Brecher, M., Schornberg, K.L., Delos, S.E., Fusco, M.L., Saphire, E.O., and White, J.M. (2012). Cathepsin cleavage potentiates the Ebola virus glycoprotein to undergo a subsequent fusion-relevant conformational change. J. Virol. *86*, 364–372.

Brindley, M.A., Hunt, C.L., Kondratowicz, A.S., Bowman, J., Sinn, P.L., McCray, P.B., Jr., Quinn, K., Weller, M.L., Chiorini, J.A., and Maury, W. (2011). Tyrosine kinase receptor Axl enhances entry of Zaire ebolavirus without direct interactions with the viral glycoprotein. Virology *415*, 83–94.

Brunner, J.E., Nguyen, J.H.C., Roehl, H.H., Ho, T.V., Swiderek, K.M., and Semler, B.L. (2005). Functional interaction of heterogeneous nuclear ribonucleoprotein C with poliovirus RNA synthesis initiation complexes. J. Virol. *79*, 3254–3266.

Brunner, J.E., Ertel, K.J., Rozovics, J.M., and Semler, B.L. (2010). Delayed kinetics of poliovirus RNA synthesis in a human cell line with reduced levels of hnRNP C proteins. Virology *400*, 240–247.

Cárdenas, W.B., Loo, Y.-M., Gale, M., Jr., Hartman, A.L., Kimberlin, C.R., Martínez-Sobrido, L., Saphire, E.O., and Basler, C.F. (2006). Ebola virus

VP35 protein binds double-stranded RNA and inhibits alpha/beta interferon production induced by RIG-I signaling. J. Virol. *80*, 5168–5178.

Carette, J.E., Raaben, M., Wong, A.C., Herbert, A.S., Obernosterer, G., Mulherkar, N., Kuehne, A.I., Kranzusch, P.J., Griffin, A.M., Ruthel, G., et al. (2011). Ebola virus entry requires the cholesterol transporter Niemann-Pick C1. Nature *477*, 340–343.

Chandran, K., Sullivan, N.J., Felbor, U., Whelan, S.P., and Cunningham, J.M. (2005). Endosomal proteolysis of the Ebola virus glycoprotein is necessary for infection. Science *308*, 1643–1645.

Chang, T.-H., Kubota, T., Matsuoka, M., Jones, S., Bradfute, S.B., Bray, M., and Ozato, K. (2009). Ebola Zaire virus blocks type I interferon production by exploiting the host SUMO modification machinery. PLoS Pathog. *5*, e1000493.

Cheon, H., and Stark, G.R. (2009). Unphosphorylated STAT1 prolongs the expression of interferon-induced immune regulatory genes. Proc. Natl. Acad. Sci. USA *106*, 9373–9378.

Chepurnov, A.A., Tuzova, M.N., Ternovoy, V.A., and Chernukhin, I.V. (1999). Suppressive effect of Ebola virus on T cell proliferation in vitro is provided by a 125-kDa GP viral protein. Immunol. Lett. *68*, 257–261.

Chiang, J.J., Davis, M.E., and Gack, M.U. (2014). Regulation of RIG-I-like receptor signaling by host and viral proteins. Cytokine Growth Factor Rev. http://dx.doi.org/10.1016/j.cytogfr.2014.06.005.

Cilloniz, C., Ebihara, H., Ni, C., Neumann, G., Korth, M.J., Kelly, S.M., Kawaoka, Y., Feldmann, H., and Katze, M.G. (2011). Functional genomics reveals the induction of inflammatory response and metalloproteinase gene expression during lethal Ebola virus infection. J. Virol. *85*, 9060–9068.

Côté, M., Misasi, J., Ren, T., Bruchez, A., Lee, K., Filone, C.M., Hensley, L., Li, Q., Ory, D., Chandran, K., and Cunningham, J. (2011). Small molecule inhibitors reveal Niemann-Pick C1 is essential for Ebola virus infection. Nature *477*, 344–348.

Desai, T.M., Marin, M., Chin, C.R., Savidis, G., Brass, A.L., and Melikyan, G.B. (2014). IFITM3 restricts influenza A virus entry by blocking the formation of fusion pores following virus-endosome hemifusion. PLoS Pathog. *10*, e1004048.

Dube, D., Brecher, M.B., Delos, S.E., Rose, S.C., Park, E.W., Schornberg, K.L., Kuhn, J.H., and White, J.M. (2009). The primed ebolavirus glycoprotein (19-kilodalton GP1,2): sequence and residues critical for host cell binding. J. Virol. *83*, 2883–2891.

Ebihara, H., Takada, A., Kobasa, D., Jones, S., Neumann, G., Theriault, S., Bray, M., Feldmann, H., and Kawaoka, Y. (2006). Molecular determinants of Ebola virus virulence in mice. PLoS Pathog. *2*, e73.

Fabozzi, G., Nabel, C.S., Dolan, M.A., and Sullivan, N.J. (2011). Ebolavirus proteins suppress the effects of small interfering RNA by direct interaction with the mammalian RNA interference pathway. J. Virol. *85*, 2512–2523.

Feng, Z., Cerveny, M., Yan, Z., and He, B. (2007). The VP35 protein of Ebola virus inhibits the antiviral effect mediated by double-stranded RNA-dependent protein kinase PKR. J. Virol. *81*, 182–192.

Gnirß, K., Fiedler, M., Krämer-Kühl, A., Bolduan, S., Mittler, E., Becker, S., Schindler, M., and Pöhlmann, S. (2014). Analysis of determinants in filovirus glycoproteins required for tetherin antagonism. Viruses *6*, 1654–1671.

Green, A.M., Beatty, P.R., Hadjilaou, A., and Harris, E. (2014). Innate immunity to dengue virus infection and subversion of antiviral responses. J. Mol. Biol. *426*, 1148–1160. http://dx.doi.org/10.1016/j.jmb.2013.11.023.

Haasnoot, J., de Vries, W., Geutjes, E.-J., Prins, M., de Haan, P., and Berkhout, B. (2007). The Ebola virus VP35 protein is a suppressor of RNA silencing. PLoS Pathog. *3*, e86.

Halfmann, P., Neumann, G., and Kawaoka, Y. (2011). The Ebolavirus VP24 protein blocks phosphorylation of p38 mitogen-activated protein kinase. J. Infect. Dis. *204* (*Suppl 3*), S953–S956.

Harrison, S.C. (2008). Viral membrane fusion. Nat. Struct. Mol. Biol. *15*, 690–698.

Hartlieb, B., Modrof, J., Mühlberger, E., Klenk, H.-D., and Becker, S. (2003). Oligomerization of Ebola virus VP30 is essential for viral transcription and can be inhibited by a synthetic peptide. J. Biol. Chem. *278*, 41830–41836.

Hartlieb, B., Muziol, T., Weissenhorn, W., and Becker, S. (2007). Crystal structure of the C-terminal domain of Ebola virus VP30 reveals a role in transcription and nucleocapsid association. Proc. Natl. Acad. Sci. USA *104*, 624–629.

Hartman, A.L., Ling, L., Nichol, S.T., and Hibberd, M.L. (2008a). Whole-genome expression profiling reveals that inhibition of host innate immune response pathways by Ebola virus can be reversed by a single amino acid change in the VP35 protein. J. Virol. *82*, 5348–5358.

Hartman, A.L., Bird, B.H., Towner, J.S., Antoniadou, Z.-A., Zaki, S.R., and Nichol, S.T. (2008b). Inhibition of IRF-3 activation by VP35 is critical for the high level of virulence of ebola virus. J. Virol. *82*, 2699–2704.

Hartman, A.L., Towner, J.S., and Nichol, S.T. (2010). Ebola and marburg hemorrhagic fever. Clin. Lab. Med. *30*, 161–177.

Harty, R.N., Pitha, P.M., and Okumura, A. (2009). Antiviral activity of innate immune protein ISG15. J. Innate Immun. *1*, 397–404.

Hensley, L.E., Mulangu, S., Asiedu, C., Johnson, J., Honko, A.N., Stanley, D., Fabozzi, G., Nichol, S.T., Ksiazek, T.G., Rollin, P.E., et al. (2010). Demonstration of cross-protective vaccine immunity against an emerging pathogenic Ebolavirus Species. PLoS Pathog. *6*, e1000904.

Hood, C.L., Abraham, J., Boyington, J.C., Leung, K., Kwong, P.D., and Nabel, G.J. (2010). Biochemical and structural characterization of cathepsin L-processed Ebola virus glycoprotein: implications for viral entry and immunogenicity. J. Virol. *84*, 2972–2982.

Huang, I.-C., Bailey, C.C., Weyer, J.L., Radoshitzky, S.R., Becker, M.M., Chiang, J.J., Brass, A.L., Ahmed, A.A., Chi, X., Dong, L., et al. (2011). Distinct patterns of IFITM-mediated restriction of filoviruses, SARS coronavirus, and influenza A virus. PLoS Pathog. *7*, e1001258.

Hunt, C.L., Kolokoltsov, A.A., Davey, R.A., and Maury, W. (2011). The Tyro3 receptor kinase Axl enhances macropinocytosis of Zaire ebolavirus. J. Virol. *85*, 334–347.

Ivashkiv, L.B., and Donlin, L.T. (2014). Regulation of type I interferon responses. Nat. Rev. Immunol. *14*, 36–49.

Jae, L.T., Raaben, M., Herbert, A.S., Kuehne, A.I., Wirchnianski, A.S., Soh, T.K., Stubbs, S.H., Janssen, H., Damme, M., Saftig, P., et al. (2014). Virus entry. Lassa virus entry requires a trigger-induced receptor switch. Science *344*, 1506–1510.

Jemielity, S., Wang, J.J., Chan, Y.K., Ahmed, A.A., Li, W., Monahan, S., Bu, X., Farzan, M., Freeman, G.J., Umetsu, D.T., et al. (2013). TIM-family proteins promote infection of multiple enveloped viruses through virion-associated phosphatidylserine. PLoS Pathog. *9*, e1003232.

Kaletsky, R.L., Francica, J.R., Agrawal-Gamse, C., and Bates, P. (2009). Tetherin-mediated restriction of filovirus budding is antagonized by the Ebola glycoprotein. Proc. Natl. Acad. Sci. USA *106*, 2886–2891.

Kimberlin, C.R., Bornholdt, Z.A., Li, S., Woods, V.L., Jr., MacRae, I.J., and Saphire, E.O. (2010). Ebolavirus VP35 uses a bimodal strategy to bind dsRNA for innate immune suppression. Proc. Natl. Acad. Sci. USA *107*, 314–319.

Kindzelskii, A.L., Yang, Z., Nabel, G.J., Todd, R.F., 3rd, and Petty, H.R. (2000). Ebola virus secretory glycoprotein (sGP) diminishes Fc gamma RIIIB-to-CR3 proximity on neutrophils. J. Immunol. *164*, 953–958.

Koma, T., Huang, C., Kolokoltsova, O.A., Brasier, A.R., and Paessler, S. (2013). Innate immune response to arenaviral infection: a focus on the highly pathogenic New World hemorrhagic arenaviruses. J. Mol. Biol. *425*, 4893–4903.

Kondratowicz, A.S., Lennemann, N.J., Sinn, P.L., Davey, R.A., Hunt, C.L., Moller-Tank, S., Meyerholz, D.K., Rennert, P., Mullins, R.F., Brindley, M., et al. (2011). T-cell immunoglobulin and mucin domain 1 (TIM-1) is a receptor for Zaire Ebolavirus and Lake Victoria Marburgvirus. Proc. Natl. Acad. Sci. USA *108*, 8426–8431.

Ksiazek, T.G., Rollin, P.E., Williams, A.J., Bressler, D.S., Martin, M.L., Swanepoel, R., Burt, F.J., Leman, P.A., Khan, A.S., Rowe, A.K., et al. (1999). Clinical virology of Ebola hemorrhagic fever (EHF): virus, virus antigen, and IgG and IgM antibody findings among EHF patients in Kikwit, Democratic Republic of the Congo, 1995. J. Infect. Dis. *179* (*Suppl 1*), S177–S187.

Kühl, A., Banning, C., Marzi, A., Votteler, J., Steffen, I., Bertram, S., Glowacka, I., Konrad, A., Stürzl, M., Guo, J.-T., et al. (2011). The Ebola virus glycoprotein

and HIV-1 Vpu employ different strategies to counteract the antiviral factor tetherin. J. Infect. Dis. *204* (*Suppl 3*), S850–S860.

Leroy, E.M., Baize, S., Volchkov, V.E., Fisher-Hoch, S.P., Georges-Courbot, M.C., Lansoud-Soukate, J., Capron, M., Debré, P., McCormick, J.B., and Georges, A.J. (2000). Human asymptomatic Ebola infection and strong inflammatory response. Lancet *355*, 2210–2215.

Leroy, E.M., Baize, S., Debre, P., Lansoud-Soukate, J., and Mavoungou, E. (2001). Early immune responses accompanying human asymptomatic Ebola infections. Clin. Exp. Immunol. *124*, 453–460.

Leung, D.W., Ginder, N.D., Fulton, D.B., Nix, J., Basler, C.F., Honzatko, R.B., and Amarasinghe, G.K. (2009). Structure of the Ebola VP35 interferon inhibitory domain. Proc. Natl. Acad. Sci. USA *106*, 411–416.

Leung, D.W., Prins, K.C., Borek, D.M., Farahbakhsh, M., Tufariello, J.M., Ramanan, P., Nix, J.C., Helgeson, L.A., Otwinowski, Z., Honzatko, R.B., et al. (2010a). Structural basis for dsRNA recognition and interferon antagonism by Ebola VP35. Nat. Struct. Mol. Biol. *17*, 165–172.

Leung, D.W., Shabman, R.S., Farahbakhsh, M., Prins, K.C., Borek, D.M., Wang, T., Mühlberger, E., Basler, C.F., and Amarasinghe, G.K. (2010b). Structural and functional characterization of Reston Ebola virus VP35 interferon inhibitory domain. J. Mol. Biol. *399*, 347–357.

Lin, G., Simmons, G., Pöhlmann, S., Baribaud, F., Ni, H., Leslie, G.J., Haggarty, B.S., Bates, P., Weissman, D., Hoxie, J.A., and Doms, R.W. (2003). Differential N-linked glycosylation of human immunodeficiency virus and Ebola virus envelope glycoproteins modulates interactions with DC-SIGN and DC-SIGNR. J. Virol. *77*, 1337–1346.

Liu, Y., and Harty, R.N. (2010). Viral and host proteins that modulate filovirus budding. Future Virol. *5*, 481–491.

Lopez, L.A., Yang, S.J., Hauser, H., Exline, C.M., Haworth, K.G., Oldenburg, J., and Cannon, P.M. (2010). Ebola virus glycoprotein counteracts BST-2/Tetherin restriction in a sequence-independent manner that does not require tetherin surface removal. J. Virol. *84*, 7243–7255.

Lopez, L.A., Yang, S.J., Exline, C.M., Rengarajan, S., Haworth, K.G., and Cannon, P.M. (2012). Anti-tetherin activities of HIV-1 Vpu and Ebola virus glycoprotein do not involve removal of tetherin from lipid rafts. J. Virol. *86*, 5467–5480.

Luthra, P., Ramanan, P., Mire, C.E., Weisend, C., Tsuda, Y., Yen, B., Liu, G., Leung, D.W., Geisbert, T.W., Ebihara, H., et al. (2013). Mutual antagonism between the Ebola virus VP35 protein and the RIG-I activator PACT determines infection outcome. Cell Host Microbe *14*, 74–84.

Mahanty, S., Hutchinson, K., Agarwal, S., McRae, M., Rollin, P.E., and Pulendran, B. (2003). Cutting edge: impairment of dendritic cells and adaptive immunity by Ebola and Lassa viruses. J. Immunol. *170*, 2797–2801.

Martinez, M.J., Volchkova, V.A., Raoul, H., Alazard-Dany, N., Reynard, O., and Volchkov, V.E. (2011a). Role of VP30 phosphorylation in the Ebola virus replication cycle. J. Infect. Dis. *204* (*Suppl 3*), S934–S940.

Martinez, O., Tantral, L., Mulherkar, N., Chandran, K., and Basler, C.F. (2011b). Impact of Ebola mucin-like domain on antiglycoprotein antibody responses induced by Ebola virus-like particles. J. Infect. Dis. *204* (*Suppl 3*), S825–S832.

Martinez, O., Johnson, J.C., Honko, A., Yen, B., Shabman, R.S., Hensley, L.E., Olinger, G.G., and Basler, C.F. (2013). Ebola virus exploits a monocyte differentiation program to promote its entry. J. Virol. *87*, 3801–3814.

Mateo, M., Reid, S.P., Leung, L.W., Basler, C.F., and Volchkov, V.E. (2010). Ebolavirus VP24 binding to karyopherins is required for inhibition of interferon signaling. J. Virol. *84*, 1169–1175.

Mateo, M., Carbonnelle, C., Reynard, O., Kolesnikova, L., Nemirov, K., Page, A., Volchkova, V.A., and Volchkov, V.E. (2011). VP24 is a molecular determinant of Ebola virus virulence in guinea pigs. J. Infect. Dis. *204* (*Suppl 3*), S1011–S1020.

Mercer, J., and Helenius, A. (2008). Vaccinia virus uses macropinocytosis and apoptotic mimicry to enter host cells. Science *320*, 531–535.

Meyer, T., and Vinkemeier, U. (2004). Nucleocytoplasmic shuttling of STAT transcription factors. Eur. J. Biochem. *271*, 4606–4612.

Miller, E.H., Obernosterer, G., Raaben, M., Herbert, A.S., Deffieu, M.S., Krishnan, A., Ndungo, E., Sandesara, R.G., Carette, J.E., Kuehne, A.I., et al. (2012). Ebola virus entry requires the host-programmed recognition of an intracellular receptor. EMBO J. *31*, 1947–1960.

Misasi, J., Chandran, K., Yang, J.-Y., Considine, B., Filone, C.M., Côté, M., Sullivan, N., Fabozzi, G., Hensley, L., and Cunningham, J. (2012). Filoviruses require endosomal cysteine proteases for entry but exhibit distinct protease preferences. J. Virol. *86*, 3284–3292.

Modrof, J., Becker, S., and Mühlberger, E. (2003). Ebola virus transcription activator VP30 is a zinc-binding protein. J. Virol. *77*, 3334–3338.

Mohan, G.S., Li, W., Ye, L., Compans, R.W., and Yang, C. (2012). Antigenic subversion: a novel mechanism of host immune evasion by Ebola virus. PLoS Pathog. *8*, e1003065.

Moller-Tank, S., Kondratowicz, A.S., Davey, R.A., Rennert, P.D., and Maury, W. (2013). Role of the phosphatidylserine receptor TIM-1 in enveloped-virus entry. J. Virol. *87*, 8327–8341.

Morizono, K., and Chen, I.S.Y. (2014). Role of phosphatidylserine receptors in enveloped virus infection. J. Virol. *88*, 4275–4290.

Mühlberger, E., Weik, M., Volchkov, V.E., Klenk, H.D., and Becker, S. (1999). Comparison of the transcription and replication strategies of marburg virus and Ebola virus by using artificial replication systems. J. Virol. *73*, 2333–2342.

Mulherkar, N., Raaben, M., de la Torre, J.C., Whelan, S.P., and Chandran, K. (2011). The Ebola virus glycoprotein mediates entry via a non-classical dynamin-dependent macropinocytic pathway. Virology *419*, 72–83.

Nanbo, A., Imai, M., Watanabe, S., Noda, T., Takahashi, K., Neumann, G., Halfmann, P., and Kawaoka, Y. (2010). Ebolavirus is internalized into host cells via macropinocytosis in a viral glycoprotein-dependent manner. PLoS Pathog. *6*, e1001121.

Neil, S.J.D., Zang, T., and Bieniasz, P.D. (2008). Tetherin inhibits retrovirus release and is antagonized by HIV-1 Vpu. Nature *451*, 425–430.

Noisakran, S., Sengsai, S., Thongboonkerd, V., Kanlaya, R., Sinchaikul, S., Chen, S.-T., Puttikhunt, C., Kasinrerk, W., Limjindaporn, T., Wongwiwat, W., et al. (2008). Identification of human hnRNP C1/C2 as a dengue virus NS1-interacting protein. Biochem. Biophys. Res. Commun. *372*, 67–72.

Perreira, J.M., Chin, C.R., Feeley, E.M., and Brass, A.L. (2013). IFITMs restrict the replication of multiple pathogenic viruses. J. Mol. Biol. *425*, 4937–4955.

Pettit Kneller, E.L., Connor, J.H., and Lyles, D.S. (2009). hnRNPs Relocalize to the cytoplasm following infection with vesicular stomatitis virus. J. Virol. *83*, 770–780.

Platanias, L.C. (2005). Mechanisms of type-I- and type-II-interferon-mediated signalling. Nat. Rev. Immunol. *5*, 375–386.

Prins, K.C., Cárdenas, W.B., and Basler, C.F. (2009). Ebola virus protein VP35 impairs the function of interferon regulatory factor-activating kinases IKKepsilon and TBK-1. J. Virol. *83*, 3069–3077.

Prins, K.C., Delpeut, S., Leung, D.W., Reynard, O., Volchkova, V.A., Reid, S.P., Ramanan, P., Cárdenas, W.B., Amarasinghe, G.K., Volchkov, V.E., and Basler, C.F. (2010). Mutations abrogating VP35 interaction with double-stranded RNA render Ebola virus avirulent in guinea pigs. J. Virol. *84*, 3004–3015.

Quinn, K., Brindley, M.A., Weller, M.L., Kaludov, N., Kondratowicz, A., Hunt, C.L., Sinn, P.L., McCray, P.B., Jr., Stein, C.S., Davidson, B.L., et al. (2009). Rho GTPases modulate entry of Ebola virus and vesicular stomatitis virus pseudotyped vectors. J. Virol. *83*, 10176–10186.

Reid, S.P., Leung, L.W., Hartman, A.L., Martinez, O., Shaw, M.L., Carbonnelle, C., Volchkov, V.E., Nichol, S.T., and Basler, C.F. (2006). Ebola virus VP24 binds karyopherin alpha1 and blocks STAT1 nuclear accumulation. J. Virol. *80*, 5156–5167.

Reid, S.P., Valmas, C., Martinez, O., Sanchez, F.M., and Basler, C.F. (2007). Ebola virus VP24 proteins inhibit the interaction of NPI-1 subfamily karyopherin alpha proteins with activated STAT1. J. Virol. *81*, 13469–13477.

Saeed, M.F., Kolokoltsov, A.A., Albrecht, T., and Davey, R.A. (2010). Cellular entry of ebola virus involves uptake by a macropinocytosis-like mechanism and subsequent trafficking through early and late endosomes. PLoS Pathog. *6*, e1001110.

Sanchez, A., Kiley, M.P., Holloway, B.P., and Auperin, D.D. (1993). Sequence analysis of the Ebola virus genome: organization, genetic elements, and comparison with the genome of Marburg virus. Virus Res. *29*, 215–240.

Sanchez, A.A.J., Lukwiya, M., Bausch, D., Mahanty, S., Sanchez, A.J., Wagoner, K.D., and Rollin, P.E. (2004). Analysis of human peripheral blood samples from fatal and nonfatal cases of Ebola (Sudan) hemorrhagic fever: cellular responses, virus load, and nitric oxide levels. J. Virol. *78*, 10370–10377.

Sanchez, A., and Kiley, M.P. (1987). Identification and analysis of Ebola virus messenger RNA. Virology *157*, 414–420.

Schornberg, K., Matsuyama, S., Kabsch, K., Delos, S., Bouton, A., and White, J. (2006). Role of endosomal cathepsins in entry mediated by the Ebola virus glycoprotein. J. Virol. *80*, 4174–4178.

Schornberg, K.L., Shoemaker, C.J., Dube, D., Abshire, M.Y., Delos, S.E., Bouton, A.H., and White, J.M. (2009). Alpha5beta1-integrin controls ebolavirus entry by regulating endosomal cathepsins. Proc. Natl. Acad. Sci. USA *106*, 8003–8008.

Schümann, M., Gantke, T., and Mühlberger, E. (2009). Ebola virus VP35 antagonizes PKR activity through its C-terminal interferon inhibitory domain. J. Virol. *83*, 8993–8997.

Shabman, R.S., Gulcicek, E.E., Stone, K.L., and Basler, C.F. (2011). The Ebola virus VP24 protein prevents hnRNP C1/C2 binding to karyopherin α1 and partially alters its nuclear import. J. Infect. Dis. *204* (*Suppl 3*), S904–S910.

Shimojima, M., Takada, A., Ebihara, H., Neumann, G., Fujioka, K., Irimura, T., Jones, S., Feldmann, H., and Kawaoka, Y. (2006). Tyro3 family-mediated cell entry of Ebola and Marburg viruses. J. Virol. *80*, 10109–10116.

Shimojima, M., Ikeda, Y., and Kawaoka, Y. (2007). The mechanism of Axl-mediated Ebola virus infection. J. Infect. Dis. *196* (*Suppl 2*), S259–S263.

Simmons, G., Reeves, J.D., Grogan, C.C., Vandenberghe, L.H., Baribaud, F., Whitbeck, J.C., Burke, E., Buchmeier, M.J., Soilleux, E.J., Riley, J.L., et al. (2003). DC-SIGN and DC-SIGNR bind ebola glycoproteins and enhance infection of macrophages and endothelial cells. Virology *305*, 115–123.

Stahelin, R.V. (2014). Membrane binding and bending in Ebola VP40 assembly and egress. Front. Microbiol. *5*, 300.

Stanley, D.A., Honko, A.N., Asiedu, C., Trefry, J.C., Lau-Kilby, A.W., Johnson, J.C., Hensley, L., Ammendola, V., Abbate, A., Grazioli, F., et al. (2014). Chimpanzee adenovirus vaccine generates acute and durable protective immunity against ebolavirus challenge. Nat. Med. Published online September 7, 2014. http://dx.doi.org/10.1038/nm.3702.

Sullivan, N.J., Hensley, L., Asiedu, C., Geisbert, T.W., Stanley, D., Johnson, J., Honko, A., Olinger, G., Bailey, M., Geisbert, J.B., et al. (2011). CD8+ cellular immunity mediates rAd5 vaccine protection against Ebola virus infection of nonhuman primates. Nat. Med. *17*, 1128–1131.

Takada, A., Watanabe, S., Ito, H., Okazaki, K., Kida, H., and Kawaoka, Y. (2000). Downregulation of beta1 integrins by Ebola virus glycoprotein: implication for virus entry. Virology *278*, 20–26.

Volchkov, V.E., Blinov, V.M., and Netesov, S.V. (1992). The envelope glycoprotein of Ebola virus contains an immunosuppressive-like domain similar to oncogenic retroviruses. FEBS Lett. *305*, 181–184.

Volchkova, V.A., Dolnik, O., Martinez, M.J., Reynard, O., and Volchkov, V.E. (2011). Genomic RNA editing and its impact on Ebola virus adaptation during serial passages in cell culture and infection of guinea pigs. J. Infect. Dis. *204* (*Suppl 3*), S941–S946.

Wauquier, N., Becquart, P., Padilla, C., Baize, S., and Leroy, E.M. (2010). Human fatal zaire ebola virus infection is associated with an aberrant innate immunity and with massive lymphocyte apoptosis. PLoS Negl. Trop. Dis. *4*, 4.

Wen, Z., Zhao, B., Song, K., Hu, X., Chen, W., Kong, D., Ge, J., and Bu, Z. (2013). Recombinant lentogenic Newcastle disease virus expressing Ebola virus GP infects cells independently of exogenous trypsin and uses macropinocytosis as the major pathway for cell entry. Virol. J. *10*, 331.

Wimmer, P., Schreiner, S., and Dobner, T. (2012). Human pathogens and the host cell SUMOylation system. J. Virol. *86*, 642–654.

Wong, G., Richardson, J.S., Pillet, S., Patel, A., Qiu, X., Alimonti, J., Hogan, J., Zhang, Y., Takada, A., Feldmann, H., et al. (2012). Immune parameters correlate with protection against ebola virus infection in rodents and nonhuman primates. Sci. Transl. Med. *4*, 158ra146.

Wool-Lewis, R.J., and Bates, P. (1998). Characterization of Ebola virus entry by using pseudotyped viruses: identification of receptor-deficient cell lines. J. Virol. *72*, 3155–3160.

Xu, W., Edwards, M.R.R., Borek, D.M.M., Feagins, A.R.R., Mittal, A., Alinger, J.B.B., Berry, K.N.N., Yen, B., Hamilton, J., Brett, T.J.J., et al. (2014). Ebola virus VP24 targets a unique NLS binding site on karyopherin alpha 5 to selectively compete with nuclear import of phosphorylated STAT1. Cell Host Microbe *16*, 187–200.

Yaddanapudi, K., Palacios, G., Towner, J.S., Chen, I., Sariol, C.A., Nichol, S.T., and Lipkin, W.I. (2006). Implication of a retrovirus-like glycoprotein peptide in the immunopathogenesis of Ebola and Marburg viruses. FASEB J. *20*, 2519–2530.

Yang, Z., Delgado, R., Xu, L., Todd, R.F., Nabel, E.G., Sanchez, A., and Nabel, G.J. (1998). Distinct cellular interactions of secreted and transmembrane Ebola virus glycoproteins. Science *279*, 1034–1037.

Yang, Z.Y., Duckers, H.J., Sullivan, N.J., Sanchez, A., Nabel, E.G., and Nabel, G.J. (2000). Identification of the Ebola virus glycoprotein as the main viral determinant of vascular cell cytotoxicity and injury. Nat. Med. *6*, 886–889.

Zachowski, A. (1993). Phospholipids in animal eukaryotic membranes: transverse asymmetry and movement. Biochem. J. *294*, 1–14.

Zagórska, A., Través, P.G., Lew, E.D., Dransfield, I., and Lemke, G. (2014). Diversification of TAM receptor tyrosine kinase function. Nat. Immunol. *15*, 920–928.

Zhang, A.P.P., Bornholdt, Z.A., Liu, T., Abelson, D.M., Lee, D.E., Li, S., Woods, V.L., Jr., and Saphire, E.O. (2012). The ebola virus interferon antagonist VP24 directly binds STAT1 and has a novel, pyramidal fold. PLoS Pathog. *8*, e1002550.

Zhu, Y., Cherukuri, N.C., Jackel, J.N., Wu, Z., Crary, M., Buckley, K.J., Bisaro, D.M., and Parris, D.S. (2012). Characterization of the RNA silencing suppression activity of the Ebola virus VP35 protein in plants and mammalian cells. J. Virol. *86*, 3038–3049.

Leading Edge
Review
Cell

Individualized Medicine from Prewomb to Tomb

Eric J. Topol[1,*]
[1]The Scripps Translational Science Institute, The Scripps Research Institute and Scripps Health, La Jolla, CA 92037, USA
*Correspondence: etopol@scripps.edu
http://dx.doi.org/10.1016/j.cell.2014.02.012

That each of us is truly biologically unique, extending to even monozygotic, "identical" twins, is not fully appreciated. Now that it is possible to perform a comprehensive "omic" assessment of an individual, including one's DNA and RNA sequence and at least some characterization of one's proteome, metabolome, microbiome, autoantibodies, and epigenome, it has become abundantly clear that each of us has truly one-of-a-kind biological content. Well beyond the allure of the matchless fingerprint or snowflake concept, these singular, individual data and information set up a remarkable and unprecedented opportunity to improve medical treatment and develop preventive strategies to preserve health.

From Digital to Biological to Individualized Medicine

In 2010, Eric Schmidt of Google said "The power of individual targeting—the technology will be so good it will be very hard for people to watch or consume something that has not in some sense been tailored for them" (Jenkins, 2010). Although referring to the capability of digital technology, we have now reached a time of convergence of the digital and biologic domains. It has been well established that 0 and 1 are interchangeable with A, C, T, and G in books and Shakespeare sonnets and that DNA may represent the ultimate data storage system (Church et al., 2012; Goldman et al., 2013b). Biological transistors, also known as genetic logic gates, have now been developed that make a computer from a living cell (Bonnet et al., 2013). The convergence of biology and technology was further captured by one of the protagonists of the digital era, Steve Jobs, who said "I think the biggest innovations of the 21st century will be at the intersection of biology and technology. A new era is beginning" (Issacson, 2011).

With whole-genome DNA sequencing and a variety of omic technologies to define aspects of each individual's biology at many different levels, we have indeed embarked on a new era of medicine. The term "personalized medicine" has been used for many years but has engendered considerable confusion. A recent survey indicated that only 4% of the public understand what the term is intended to mean (Stanton, 2013), and the hackneyed, commercial use of "personalized" makes many people think that this refers to a concierge service of medical care. Whereas "person" refers to a human being, "personalized" can mean anything from having monogrammed stationary or luggage to ascribing personal qualities. Therefore, it was not surprising that a committee representing the National Academy of Sciences proposed using the term "precision medicine" as defined by "tailoring of medical treatment to the individual characteristics of each patient" (National Research Council, 2011). Although the term "precision" denotes the objective of exactness, ironically, it too can be viewed as ambiguous in this context because it does not capture the sense that the information is derived from the individual. For example, many laboratory tests could be made more precise by assay methodology, and treatments could be made more precise by avoiding side effects—without having anything to do with a specific individual. Other terms that have been suggested include genomic, digital, and stratified medicine, but all of these have a similar problem or appear to be too narrowly focused.

The definition of individual is a single human being, derived from the Latin word individu, or indivisible. I propose individualized medicine as the preferred term because it has a useful double entendre. It relates not only to medicine that is particularized to a human being but also the future impact of digital technology on individuals driving their health care. There will increasingly be the flow of one's biologic data and relevant medical information directly to the individual. Be it a genome sequence on a tablet or the results of a biosensor for blood pressure or another physiologic metric displayed on a smartphone, the digital convergence with biology will definitively anchor the individual as a source of salient data, the conduit of information flow, and a—if not the—principal driver of medicine in the future.

The Human GIS

Perhaps the most commonly used geographic information systems (GIS) are Google maps, which provide a layered approach to data visualization, such as viewing a location via satellite overlaid with street names, landmarks, and real-time traffic data. This GIS exemplifies the concept of gathering and transforming large bodies of data to provide exquisite temporal and location information. With the multiple virtual views, it gives one the sense of physically being on site. Although Google has digitized and thus created a GIS for the Earth, it is now possible to digitize a human being. As shown in Figure 1, there are multiple layers of data that can now be obtained for any individual. This includes data from biosensors, scanners, electronic medical records, social media, and the various omics that include

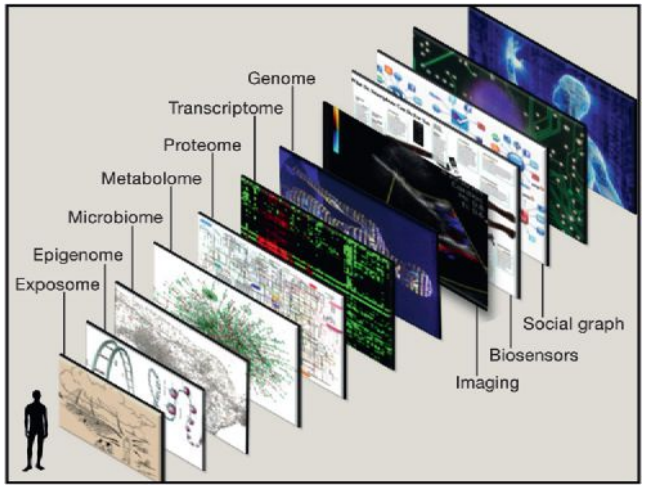

Figure 1. Geographic Information System of a Human Being
The ability to digitize the medical essence of a human being is predicated on the integration of multiscale data, akin to a Google map, which consists of superimposed layers of data such as street, traffic, and satellite views. For a human being, these layers include demographics and the social graph, biosensors to capture the individual's physiome, imaging to depict the anatomy (often along with physiologic data), and the biology from the various omics (genome-DNA sequence, transcriptome, proteome, metabolome, microbiome, and epigenome). In addition to all of these layers, there is one's important environmental exposure data, known as the "exposome."

DNA sequence, transcriptome, proteome, metabolome, epigenome, microbiome, and exposome. Going forward, I will use the term "panoromic" to denote the multiple biologic omic technologies. This term closely resembles and is adopted from panoramic, which refers to a wide-angle view or comprehensive representation across multiple applications and repositories. Or more simply, according to the Merriam-Webster definition of panoramic, it "includes a lot of information and covers many topics." Thus the term panoromic may be well suited for portraying the concept of big biological data.

The first individual who had a human GIS-like construct was Michael Snyder. Not only was his whole genome sequenced, he also collected serial gene expression, autoantibody, proteomic, and metabolomic (Chen et al., 2012) samples. A portion of the data deluge that was generated is represented in the Circos plot of Figure 2 or an adoption of the London Tube map (Shendure and Lieberman Aiden, 2012). The integrated personal omics profiling (iPOP) or "Snyderome," as it became known, proved to be useful for connecting viral infections to markedly elevated glucose levels. With this integrated analysis in hand, Michael Snyder changed his lifestyle, eventually restoring normal glucose homeostasis. Since that report in 2012, Snyder and his team have proceeded to obtain further omic data, including whole-genome DNA methylation data at multiple time points, serial microbiome (gut, urine, nasal, skin, and tongue) sampling, and the use of biosensors for activity tracking and heart rhythm. Snyder also discovered that several extended family members had smoldering, unrecognized glucose intolerance, thereby changing medical care for multiple individuals.

Of note, to obtain the data and process this first panoromic study, it required an armada of 40 experienced coauthors and countless hours of bioinformatics and analytical work. To give context to the digital data burden, it took 1 terabyte (TB) for DNA sequence, 2 TB for the epigenomic data, 0.7 TB for the transcriptome, and 3 TB for the microbiome. Accordingly, this first human GIS can be considered a remarkable academic feat and yielded key diagnostic medical information for the individual. But, it can hardly be considered practical or scalable at this juncture. With the cost of storing information continuing to drop substantially, the bottleneck for scalability will likely be automating the analysis. On the other hand, each omic technology can readily be undertaken now and has the potential of providing meaningful medical information for an individual.

The Omic Tools

Whole-Genome and Exome Sequencing

Perhaps the greatest technologic achievement in the biomedical domain has been the extraordinary progress in our ability to sequence a human genome over the past decade. Far exceeding the pace of Moore's Law for the relentless improvement in transistor capacity, there has been a >4 log order (or 0.00007th) reduction in cost of sequencing (Butte, 2013), with a cost in 2004 of ~$28.8 million compared with the cost as low as $1,000 in 2014 (Hayden, 2014). However, despite this incomparable progress, there are still major limitations to how rapid, accurate, and complete sequencing can be accomplished. High-throughput sequencing involves chopping the DNA into small fragments, which are then amplified by PCR. Currently, it takes 3 to 4 days in our lab to do the sample preparation and sequencing at 30× to 40× coverage of a human genome. The read length of the fragments is now ~250 base pairs for the most cost-effective sequencing methods, but this is still suboptimal in determining maternal versus paternal alleles, or what is known as phasing. Because so much of understanding diseases involves compound heterozygote mutations, *cis*-acting sequence variant combinations, and allele-specific effects, phasing the diploid genome, or what we have called "diplomics" (Tewhey et al., 2011), is quite important. Recently, Moleculo introduced a method for synthetically stitching together DNA sequencing reads yielding fragments as long as 10,000 base pairs. These synthetic long reads are well suited for phasing. Unfortunately, the term "whole-genome sequencing" is far from complete because ~900 genes, or 3%–4% of the genome, are not accessible (Marx, 2013). These regions are typically in centromeres or telomeres. Other technical issues that detract from accuracy include long sequences of repeated bases (homopolymers) and regions rich in guanine and cytosine. Furthermore, the accuracy for medical grade sequencing still needs to be improved. A missed call rate of 1 in 10,000, which may not seem high, translates into a substantial number of errors when considering the 6 billion bases in a diploid genome. These errors obfuscate rare but potentially functional variants. Beyond this issue, the accurate determination of insertions, deletions, and structural variants is impaired, in part due to the relatively short reads that are typically obtained. The Clinical Sequencing Exploratory Research (CSER) program at the National Institutes of Health is aimed at improving the accuracy of sequencing for medical applications (National Human Genome Research Institute, 2013).

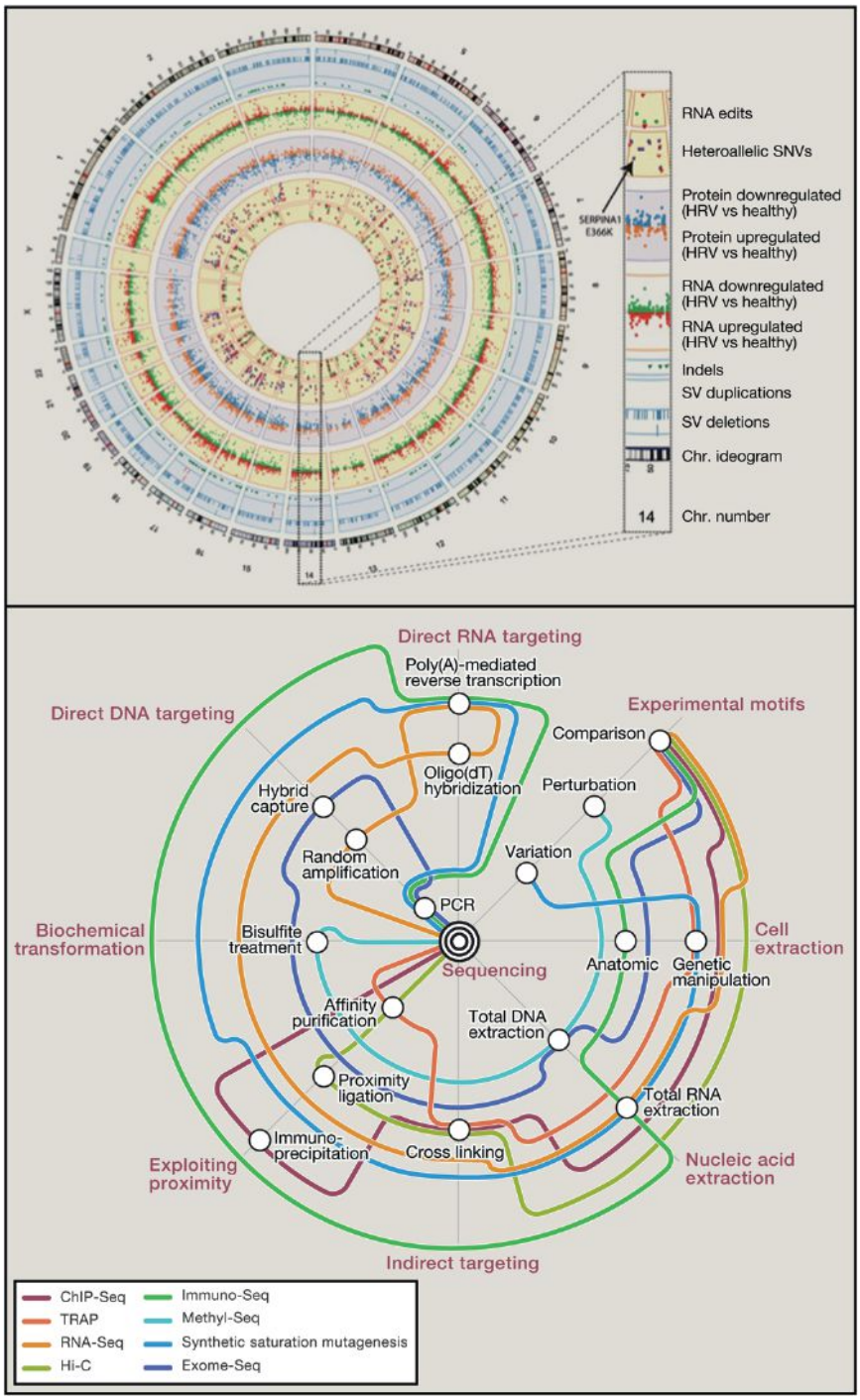

Figure 2. Plots of Panoramic Information

Top: Circos plot of the Snyder genome. From outer to inner rings: chromosome ideogram; genomic data (pale blue ring), structural variants >50 bp (deletions [blue tiles], duplications [red tiles]), indels (green triangles); transcriptomic data (yellow ring), expression ratio of viral infection to healthy states; proteomic data (light purple ring), ratio of protein levels during human rhinovirus (HRV) infection to healthy states; transcriptomic data (yellow ring), differential heteroallelic expression ratio of alternative allele to reference allele for missense and synonymous variants (purple dots) and candidate RNA missense and synonymous edits (red triangles, purple dots, orange triangles, and green dots, respectively). From Chen et al. (2012) with permission.

Bottom: Adopted London Tube model of integrated omics from Shendure and Aiden Integration of the many applications of next-generation DNA sequencing, which include sites of DNA methylation (methyl-seq), protein-DNA interactions (ChIP-seq), 3D genome structure (Hi-C), genetically targeted purification of polysomal mRNAs (TRAP), the B cell and T cell repertoires (immuno-seq), and functional consequences of genetic variation (synthetic saturation mutagenesis) with a small set of core techniques, represented as open circles of "stations." Like subway lines, individual sequencing experiments move from station to station until they ultimately arrive at a common terminal—DNA sequencing.

From Shendure and Lieberman Aiden (2012) with permission.

Despite these shortcomings, the ability to identify rare or low-frequency variants that are pathogenic has been a major outgrowth of high-throughput sequencing. Well beyond the genome scans and genome-wide association studies that identified common variants associated with most complex, polygenic diseases and human traits, sequencing leads to high definition of the uncommon variants that typically have much higher penetrance. For example, rare Mendelian conditions have seen a remarkable surge of definition of their genomic underpinnings (Boycott et al., 2013). In the first half of 2010, the basis for four rare diseases was published, but in the first half of 2012, that number jumped to 68 (Boycott et al., 2013). With the power of sequencing, it is anticipated that the molecular basis for most of the 7,000 known Mendelian diseases will be unraveled in the next few years.

The 1.5% versus 98.5% Genome Sequencing Dilemma

The exome consists of only ~40 Mb, or 1.5% of the human genome. There is continued debate over the use of whole-exome sequencing compared with whole-genome sequencing, given the lower cost of sequencing an exome, that can be readily captured via kits from a few different companies (Agilent SureSelect, Illumina TruSeq, and Roche NimbleGen). Exome sequencing is typically performed at much deeper coverage, >100× (as compared with 30×–40× for whole genome), which enhances accuracy, and the interpretation of variants that affect coding elements is far more advanced compared with the rest of the genome. However, the collective output from genome-wide association studies of complex traits has indicated that ~80% of the

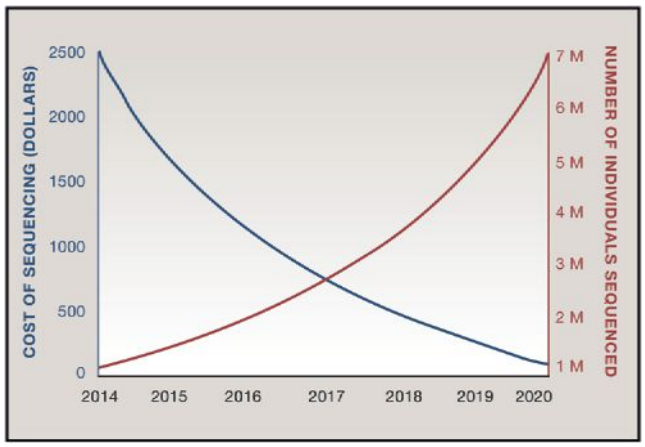

Figure 3. Hypothetical Plot of Cost of Sequencing and Number of Individuals Sequenced over the Next 6 Years

As of early 2014, <100,000 individuals have had whole-genome sequencing, leaving the information difficult to fully interpret (of limited informativeness or value). When millions of people undergo sequencing, with the full gamut of diverse phenotypes and ancestries, and the cost for sequencing continues to drop, a virtuous cycle of informativeness is established. With the new capability in 2014 to have whole-genome sequencing at a cost of $1,000, along with extremely high throughput, it is likely that millions of individuals will be sequenced in the next 3–4 years. The cost of sequencing will continue to drop throughout this time, as increasing numbers of individuals undergo sequencing. Projections suggest that at least 20,000 individuals with each phenotype may be necessary to reliably identify rare, functional genomic variants. Accordingly, once millions of individuals across all main phenotypes and ancestries are sequenced, there is a new set point, or threshold, of informativeness.

incriminated loci are in noncoding regions, outside the confines of genes (Koboldt et al., 2013). It is fair to say that we have long underestimated the importance of the rest of the genome, but its high density of key regulatory features provides intricate and extraordinarily tight control over how genes operate. Recent whole-genome sequencing studies have identified many critical variants in noncoding portions of the genome (Khurana et al., 2013). A typical whole human genome sequence will contain ~3.5 million variants compared with the reference genome, predominantly composed of single-nucleotide polymorphisms but also including insertion-deletions, copy number variants, and other types of structural variants (Frazer et al., 2009). Today, analysis of most of the 3.5 million variants is left with the ''variant of unknown significant'' (VUS) diagnosis. As more people get sequenced with the full range of disease phenotypes, the proportion of VUS will drop, and each sequence will become more informative. Figure 3 provides a theoretical plot of how further reduction of the cost of whole-genome sequencing will also be accompanied by large numbers of individuals undergoing sequencing. In 2014, still well under 100,000 people have had whole-genome sequencing with only a very limited number of phenotypes addressed. At some point in the future, sequence data get progressively more informative at a lower price point, thus establishing particular value of whole-genome sequencing. It is not just about getting a large number of people with diverse medical conditions and diverse ancestries sequenced. The drive to informativeness will clearly be enhanced by incorporating family genomic assessment, especially for determining whether rare variants are meaningful. Here, too much focus on the individual can result in a loss of context, back to our analogy of the Google map of maximal zoom obscuring understanding. By anchoring the genomics of family members, such as was done with the important discovery of PCSK9 rare variants (Hall, 2013) in cholesterol metabolism, progress in genomic medicine will be catalyzed.

At this juncture, however, it appears that exome and whole-genome sequencing provide complementary information. As the cost of whole-genome sequencing is further reduced, along with the availability of enhanced analytical tools for the nongene 98.5% content interpretation, exome sequencing may ultimately become obsolete.

Single-Cell Sequencing

The ability to perform sequencing of individual cells has provided remarkable new insights about human biology and disease (Shapiro et al., 2013; Battich et al., 2013; Owens, 2012). The unexpected heterogeneity in DNA sequence from one cell to another, such as has been well documented in tumor tissue and even in somatic cells in healthy individuals, has enlightened us about intraindividual genomic variation. The concept of ''mosaicism'' has gained rapid acceptance—with multiple mechanisms—ranging from gamete formation, embryonic development, to somatic mutation in cells in adulthood, that account for why each of us has cells with different DNA sequences (Lupski, 2013; Wang et al., 2012; Macosko and McCarroll, 2012; Poduri et al., 2013). It remains unclear whether mosaicism has functional significance beyond being tied to certain congenital conditions and cancers, but this is an active area of research that is capitalizing on single-cell sequencing technology. This is especially the case in neuroscience in order to explain the observed frequent finding of transposons, which appear to involve between 80 and 300 unique insertions for each neuron and are potentially associated with neurologic diseases (Poduri et al., 2013).

Sperm, which tend to swim solo, are particularly well suited for single-cell genomics. This work has quantified recombination rates of ~25 events per sperm, identified the hot spots where these events are most likely to occur, and determined genomic instability as reflected by the rate of de novo mutations (Wang et al., 2012; Poduri et al., 2013). Such de novo mutations, which increase in sperm with paternal age, are associated with autism, schizophrenia, and intellectual disability (Poduri et al., 2013; Kong et al., 2012; Veltman and Brunner, 2012; de Ligt et al., 2012).

Intriguing, and possibly revolutionary, single-cell methods using in situ sequencing protocols are set to offer precise spatial information in addition to linear sequence data. In situ sequencing holds the potential to resolve the spatial distribution of copy number variants, circular DNA, tumor heterogeneity, and RNA localization. A number of methods have been published in the last year, and progress is likely to accelerate in the near future.

Transcriptomics, Proteomics, and Metabolomics

As opposed to the DNA sequence, which is relatively static, RNA reflects the dynamic state of the cell. Gene expression of a particular tissue of the whole genome has been available via microarrays for several years, but RNA sequencing (RNA-seq)

is a relatively new tool that transcends simple expression by capturing data on gene fusions, alternative spliced transcripts, and posttranscriptional changes, along with the whole gamut of RNAs (including microRNA [e.g., miRNAseq], small RNA, lincRNA, ribosomal RNA, and transfer RNA).

A particularly valuable metric related to RNA is the expression quantitative trait locus (eQTL). By having both genome-wide association study (GWAS) data and whole-genome gene expression at baseline with or without particular stimuli, functional genomic assessment has been enabled. For example, Westra et al. (2013) used eQTLs and loci derived from GWAS to provide functional genomic, mechanistic insights for multiple complex traits, including lupus and type 1 diabetes.

The proteome, metabolome, and autoantibody landscape can be assessed for an individual approaching the whole-genome level via recent advances in mass spectrometry and protein arrays. Using these techniques, posttranslational modifications of proteins, protein-protein interactions, or the small-molecule metabolites produced by these proteins can be revealed. Emerging technologies such as RNA-mediated oligonucleotide annealing, selection, and ligation sequencing (RASL-seq), barcoded small hairpin RNA (shRNA) libraries, and combinatorial antibody libraries provide inexpensive and efficient views of biology. Longer read sequencing provides the opportunity to sequence antibodies, which typically have variable and constant regions composed of ~2,000 nucleotides.

Microbiome

Perhaps no area of biology has received more attention in recent years than the microbiome. Just the gut microbiome has orders of magnitude more DNA content than germline human DNA and has markedly heightened diversity. Our commensal bacterial flora has been shown to play an important role in various medical conditions (Cho and Blaser, 2012). From fecal samples using a 16S ribosomal amplicon sequencing method, the gut microbiome has been the subject of intensive prospective clinical assessment. It was determined that there were three major enterotypes of the intestinal microbiome based on the predominant bacterial species, such as Bacteroides, Ruminococcus, or Prevotella (Arumugam et al., 2011). The resident species appear to be quite stable over an extended period of time and to be initially transmitted via the mother at childbirth (Faith et al., 2013). As the interface between genomics and the host's environment, the microbiome clearly plays a pivotal role in defining each individual. The influence of the diet on the gut microbiome, such as the content of fiber, along with the underpinning of malnutrition, has been documented (Gordon et al., 2012; Ridaura et al., 2013). For example, even an individual's response to medications, such as digoxin (Haiser et al., 2013), or multiple drugs used for cancer, has been shown to be linked to the bacterial flora of the gut microbiome (Viaud et al., 2013; Iida et al., 2013).

Epigenome

There has been extraordinary progress in our ability to map the human epigenome from DNA methylation to histone modifications and chromatin structure (Ziller et al., 2013; Rivera and Ren, 2013). The prolific ENCODE project has provided troves of data detailing the role of regulatory elements such as enhancers and insulators and how they are tied to DNA methylation and histone changes (Dawson and Kouzarides, 2012). Like gene expression, epigenomic findings are highly cell-type specific, with more than 200 different cell types in the human body. For methylation, whole-genome bisulphite sequencing has recently been performed for 30 diverse human cell types (Rivera and Ren, 2013). Epigenomic reprogramming has a clear-cut role in cancer, be it via transcription factors or chromatin regulators (Dawson and Kouzarides, 2012; Suvà et al., 2013). Although access to tissue to define epigenomic signatures is a limiting factor outside of the cancer space, it is apparent that many other diseases are affected by epigenomic dynamics, such as complications of diabetes, rheumatoid arthritis, or hypertension (Pirola et al., 2010; Liu et al., 2013; Fratkin et al., 2012). Furthermore, epigenomic changes affect susceptibility to diseases, as has been shown with open chromatin related to the TCF7L2 gene (Groop, 2010) and parental origin of sequence variants for Type 2 diabetes mellitus and breast and prostate cancer (Kong et al., 2009). This parent-of-origin issue may be tied to transgenerational epigenomic instability, as has been well documented in plants, and is certainly a key element of human biology and heritability (Schmitz et al., 2011).

Physiome and Exposome

Understanding and quantifying an individual's physiology and environmental interactions are crucial to digitizing a human being. Through wearable biosensors and smartphones, this has become eminently practical. Continuous tracking is now obtainable for most key physiologic metrics, including blood pressure, heart rhythm, glucose, blood oxygen saturation, brain waves, intraocular eye pressure, and lung function indices. Similarly, there are environmental sensors that connect with smartphones to quantify such indices as air pollution, pollen count, radiation, water quality, ambient humidity, electromagnetic fields, and the presence of pesticides in food.

Bioinformatics

Fundamental to individualized medicine is the ability to analyze the immense data sets and to extract all of the useful, salient information. This is exemplified by the task of sifting through a trio of whole-genome sequences to find a causative mutation in a proband with an undiagnosed disease. Typically, this translates to finding one critical nucleotide variant out of well over one to two million single base variants and simplifying the analysis by only considering variants that change amino acid sequence or lead to obvious splicing defects (Maher, 2011). Identifying the signal from the noise, with the vast majority of variants categorized as ''unknown significance'' (VUS), is the crux of the challenge. Moreover, the tools to assess structural variants and indels are not as extensively developed and validated. So there are considerably more data that come from the sequencer for an individual than can be fully and accurately mined. Beyond this, there is the need for better integration of the multiple GIS layers, such as panoromic and biosensor data, and the ability to provide an integrative multiscale approach to an individual's data set. Although not the comprehensive multilayer as depicted in Figure 2, Zhang et al. (2013) recently used an integrated systems approach, including omics of both human and mice brains to discover genetic networks in Alzheimer's disease. Although in the past there were generally insufficient efforts to understand epistasis, gene-gene interactions have been

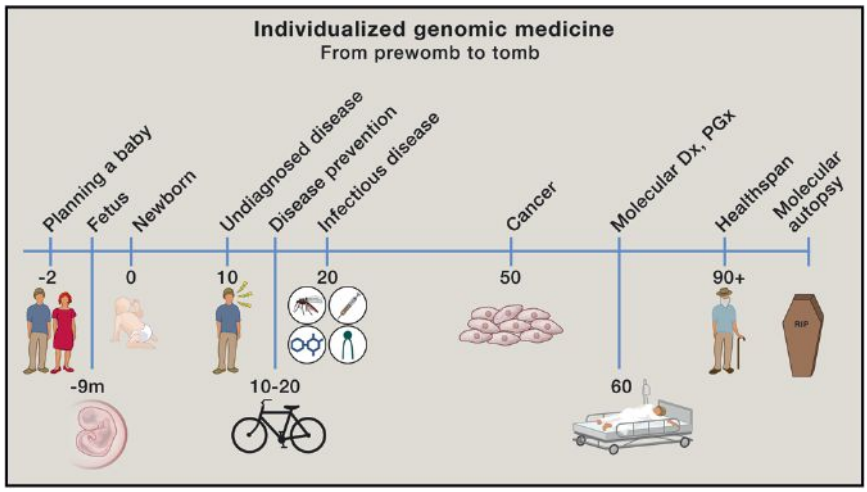

Figure 4. Timeline of Sequencing Applications in Medicine from Prewomb to Tomb

The medical application of genomics is relevant to many points during an individual's lifespan. Prior to conception, a couple can have genomic screening for important recessive alleles. An expectant mother, at 8–12 weeks of pregnancy, can now have single tube of blood used to accurately assess chromosomal abnormalities of the fetus, determine gender, and even have whole-genome sequencing of the fetus performed. At birth, sequencing the genome of the newborn can be used to rapidly diagnosis many critical conditions for which a time delay, which frequently can occur with the present heel stick screening methods, might lead to irrevocable damage. The molecular basis for serious, undiagnosed conditions can often be established by sequencing the individual with parents of siblings. Ultimately, omic information at a young age will be useful by providing susceptibility to various medical conditions that have actionable prevention strategies. Sequencing can be done to define a pathogen for more rapid and accurate approaches to infectious diseases. The driver mutations and key biologic underpinning pathways of an individual's cancer can frequently be pinpointed by omics. The root causes of common polygenic conditions such as diabetes or coronary heart disease may ultimately be defined at the individual level. Specific sequence variants of germline DNA or the gut microbiome have relevance for response to prescription medication (both efficacy and safety). Defining the genomics of healthspan, rather than the traditional focus on diseases, may prove to be especially worthwhile to understand protective alleles and modifier genes. For an individual with sudden death, a molecular autopsy via sequencing can be performed, along with family survivors, to determine the cause of death and potentially prevent untimely or avoidable deaths of members of the family and subsequent generations.

upstaged by the complexity of a higher-order bioinformatics challenge.

How the Omic Tools Reboot Medicine

A Prewomb-to-Tomb Assessment

At many points in the span of a lifetime, the unique biology of the individual will play an increasing role. As depicted in the timeline of Figure 4, I will go through each topic sequentially.

Preconception

The ability to determine carrier mutations for each prospective parent has been greatly enhanced through multiple direct-to-consumer sources, including 23andMe, Counsyl, GenePeeks, and Good Start Genetics. This can be considered the ultimate form of prevention for major recessive conditions and has only received modest attention to date. Counsyl screens for more than 100 recessive Mendelian traits, and 23andMe screens 50 carrier conditions. The carrier rates for many serious conditions are higher than most people would suspect, such as 1 in 35 for spinal muscular atrophy, 1 in 40 for cystic fibrosis, and 1 in 125 individuals for Fragile X syndrome (Test, 2013). GenePeeks uses carrier data from ~100,000 DNA sequence variants for each prospective parent to perform a computer simulation of 10,000 "digital babies," determining the probabilistic odds of significant Mendelian disorders (Couzin-Frankel, 2012). They are already using their analytic methodology to screen sperm from the Manhattan cryobank; until now, sperm banks have been completely unregulated and without genomic assessment (Almeling, 2013; Rincon, 2013). The concept of higher DNA resolution preconception screening is attractive, given that there are many more pathogenic variants in the genes that are implicated in disease, such as cystic fibrosis (~2,000 variants), than are conventionally assessed (Sosnay et al., 2013).

Fetal Sequencing

Whereas the diagnosis of chromosomal aberrations such as trisomy-21, 18, 13 required amniocentesis or chorionic villi sampling, there are now four different maternal blood sampling assays to accomplish the same assessment with extremely high (>99%) accuracy (Morain et al., 2013). Relying on the plasma fetal DNA present in adequate quantity from a maternal blood sample at 8–10 weeks of pregnancy, such testing has been transformative, preempting the need for amniocentesis in all but the rare exception when results are ambiguous. Here is a great example of using plasma-free DNA sequencing to avoid an invasive test that carries a small but important risk of miscarriage. However, with more than 4 million births in the United States each year, only a tiny fraction (<2%) of prenatal maternal blood sampling has yet been performed in clinical practice. Multiple groups have demonstrated the ability to do a fetal whole-exome sequence from a maternal blood sample (Fan et al., 2012) or whole-genome sequencing from both parents' DNA along with the maternal plasma-free DNA (Kitzman et al., 2012; Lo et al., 2010), but this takes a rather extensive computing and bioinformatics effort that is not presently scalable. Undoubtedly, that will be resolved over time but will engender the serious bioethical issues of what constitutes the appropriate reasons for termination of pregnancy. But, at the same time, it will afford the opportunity to make the molecular diagnoses of conditions in utero and facilitate treatment then or at the earliest time after birth.

Neonatal Sequencing

Monogenic diseases, many of which present in the first month of life, are a major cause of neonatal fatality and morbidity (Saunders et al., 2012). Despite routine heel sticks for blood sent out for analysis, with attendant delays of several days to weeks in obtaining results, there has not been any improvement in

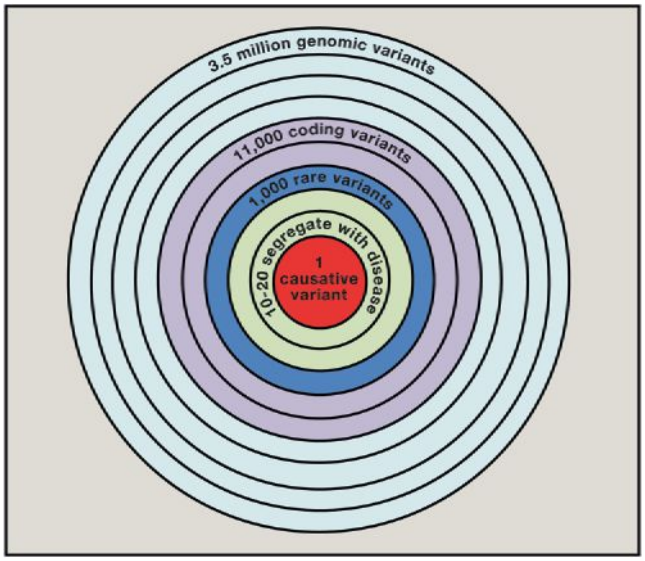

Figure 5. Legend from Whole-Genome Sequencing to Identification of a Causative Variant

Following sequencing, alignment, and annotation, the 3.5 million variants—all genetic variants in the family (unaffected and affected individuals)—are analyzed to identify known disease variants. Then inheritance-based and population-based filters are applied. Phenotype-informed ranking and functional filters are used to then determine the root-cause variant. The timeline for this involves (1) sample preparation of 2 days, (2) sequencing of 2 days in fast output mode, the (3) preliminary analysis in ~24 hr (6 hr for variant calling, 1 hr annotation, 1 hr for each candidate variant), and (4) literature review to exclude and include genes hit by potential candidate variants—an additional ~5 days. The cost for analysis is predominantly personnel and compute time on the cloud, estimated to be ~$300.

reducing neonatal mortality related to genetic disorders in the past 20 years (Kaiser, 2013; Sosnay et al., 2013). Now, it has been shown that whole-genome sequencing of newborns can be accomplished in <48 hr and can lead to highly actionable information for managing a neonate's condition, such as in the classic example of phenylketonuria or galactosemia, whereby irrevocable damage might otherwise occur (Saunders et al., 2012; Kaiser, 2013; Sosnay et al., 2013).

Undiagnosed, Idiopathic, and Rare Diseases

The diagnosis of an XIAP mutation in a child with fulminant pancolitis with successful, curative treatment is often cited as the first case of sequencing to save an individual's life (Worthey et al., 2011). Since that report, there have been several other cases that used whole-genome or exome sequencing, along with other omic tools, for making the molecular diagnosis of idiopathic conditions (Jacob et al., 2013). For example, the National Institutes of Health Undiagnosed Disease Program uses exome sequencing to facilitate the diagnosis (Gahl and Tifft, 2011). Recently, the group at Baylor College of Medicine published a series of 250 individuals, of whom 80% were pediatric and largely affected by neurologic conditions, who underwent whole-exome sequencing. In that cohort, there were many affected patients with a known Mendelian trait but without a specific root cause established. A molecular diagnosis was made in 25% of the cohort (Yang et al., 2013). At the Scripps Health and Scripps Research Institute, we have screened more than 100 individuals for the potential of having an idiopathic disease. This requires review by a multidisciplinary physician panel to assure that a comprehensive evaluation of the patient has been performed before turning to DNA sequencing. The first of 15 individuals who we enrolled into our protocol was 16 years old and had an incapacitating neurologic condition. She and her parents were sequenced, and in Figure 5, the bioinformatics challenge of interpreting the three whole-genome sequences is presented, along with the molecular diagnosis of an ADCY5 mutation that had not been previously described. In our 15 probands at Scripps, we have had a successful molecular diagnosis (using criteria as described by the Baylor group) in 8 individuals. However, establishing the diagnosis represents only the first step of the desired strategy, as providing an effective treatment is the fundamental goal. Unfortunately, the number of individuals for whom that has been achieved is quite limited to date, but strategies using repurposing of existing drugs, drugs that were partially developed but not commercialized, or acceleration of the development of genomically guided therapies are all actively being pursued. With an estimate of at least one million individuals in the United States with a serious medical condition left without a diagnosis, such progress is encouraging (Jacob et al., 2013).

Disease Prevention

At some point in the future, it is hoped that having DNA sequence information will pave the way for prevention of an individual's predisposed conditions. To date, however, that concept has not been actualized for a few principal reasons. First, most of the complex, polygenic traits have not had much more than 10% of their heritability explained by the common variants assessed by GWAS. The "missing" or unsolved heritability detracts from the ability to assign an individual any certainty or risk or protection from a particular condition. There are some notable exceptions, such as age-related macular degeneration or type 1 diabetes mellitus, in which combinations of common and rare variants can provide a well-characterized, quantified risk profile. Second, there is the appropriate question of whether the knowledge of a risk allele is actionable. Prototypic here is the apoε4 allele, which carries an unequivocal high risk for Alzheimer's disease, yet there is no proven strategy to prevent the disease. So, even armed with known risk, there is a lack of knowledge for how to mitigate it. Third, the way data for genomic susceptibility are analyzed via a population approach makes it difficult to extrapolate such average findings to a particular individual. For example, someone may have low-frequency modifier genes for a condition at risk or unusual environmental interactions that markedly affect susceptibility. Notwithstanding these issues, as millions of individuals with diverse phenotypes undergo whole-genome sequencing (Figure 3), the ability to provide meaningful risk data will increase. Having the full GIS of each individual will further enrich the probabilistic approach of providing vulnerability data early in one's life. For example, if one's sequence data indicate a risk for hypertension, that risk may be further modulated by knowledge of his/her proteins, metabolites, microbiome, and epigenomics. The use of a biosensor watch to passively collect continuous blood pressure measurements could make diagnosis at the earliest possible time, avoiding any end-organ damage to the heart or kidney. Specific

treatments could be used that are biologically based from one's GIS. Similarly, for asthma, the panoromic information, coupled with biosensors that track air quality, pollution, forced expiratory volume, and other relevant physiologic metrics, could prove useful to prevent an attack.

A futuristic way in which genomics and biosensors will ultimately converge is through injectable nanosensors that put the blood in continuous surveillance mode (Ferguson et al., 2013). Such sensors have the ability to detect a DNA, RNA, autoantibody, or protein signal and to wirelessly transmit the signal to the individual's smartphone. This sets up the potential for detecting endothelial sloughing from an artery before a heart attack (Damani et al., 2012), plasma tumor DNA in a patient being treated for or in remission from cancer, or a child with known genomic risk of autoimmune diabetes that is developing autoantibodies to pancreatic β-islet cells long before there has been destruction. The blood under continuous surveillance concept highlights the potential ability to temporally detect a risk signal for a major clinical event and to implement true preventive therapy. That could be intensive antiplatelet medication to prevent a heart attack, genomic-guided treatment of cancer recurrence at the earliest possible juncture, or immunomodulation therapy for autoimmune diabetes.

Infectious Diseases

Whole-genome sequencing has proven to be particularly useful for tracking pathogen outbreaks, such as for tuberculosis (Gardy et al., 2011), methicillin-resistant Staphylococcus aureus, antibiotic-resistant Klebsiella pneumonia, and Clostridium difficile (Eyre et al., 2013; Harris et al., 2013; Snitkin et al., 2012). Beyond identifying the particular bacterial or viral strain that accounts for an outbreak's origin and spread, sequencing is likely to prove to be quite useful for rapid, early characterization of the cause of infection and specific, effective antibiotic therapy. For sepsis, the current standard of care is to take blood or other body fluids for culture, which typically takes 2 days to grow out. Additionally, there is at least another day required to determine sensitivities to a range of antibiotics. In the future, with lab-on-a-chip sequencing platforms that attach to or are integrated with a smartphone (Biomeme and QuantuMD), it may be feasible to do rapid sequencing of the pathogen and determination of the optimal treatment. Such a strategy would preempt the need for broad-spectrum antibiotic use, and the rapid diagnosis and targeted treatment would likely have a favorable impact on prognosis in these very high-risk, critically ill patients.

Cancer

With cancer's basis in genomics, there have been extensive efforts to characterize the principal driver mutations and biologic pathways, especially through The Cancer Genome Atlas (TCGA) (Kandoth et al., 2013a, 2013b; Alexandrov et al., 2013). Our understanding of the biology of cancer has expanded exponentially and, with it, so has the appreciation for its extreme complexity. Perhaps the two classical "Hallmarks of Cancer" Reviews in *Cell*, one in 2000 and the sequel in 2011, best exemplify this (Hanahan and Weinberg, 2000; Hanahan and Weinberg, 2011). The diagram to explain the principal mechanisms of cancer was already exceptionally complex in 2000 and became at least a log order more intricate a decade later. In a more recent review of the cancer genome landscape, the Johns Hopkins group provided perspective for the 84 known oncogenes and 54 tumor suppressor genes that have been fully validated (Vogelstein et al., 2013). There will unquestionably be more, but estimates of the total number of genes involved in pivotal mutations may wind up being ~200. Beyond this, the principal pathways involving cell survival, cell fate, and DNA damage repair are recognized. Certain cancers have a relative low burden of mutations per megabase of the tumor genome, such as acute myelogenous leukemia (<1), whereas other are quite high, like lung adenocarcinoma or squamous cell carcinoma (~50) (Kandoth et al., 2013b; Vogelstein et al., 2013). Mutations of certain genes, such as the P53 tumor suppressor, are found in some patients with any of 12 common forms of cancer (Kandoth et al., 2013b). Our old taxonomy of cancer based upon the organ of origin may be considered inapt, for knowledge of the driver mutation(s) and pathway could be more useful for individualizing treatment. "N of 1" case reports with whole-genome sequencing have been particularly illuminating for the clonal origin of an individual's cancer (Brannon and Sawyers, 2013; Haffner et al., 2013). In the past 2 years, the Food and Drug Administration has approved almost 20 new drugs that target a specific mutation for cancer.

So, with these leaps in understanding biology and introduction of new therapies, why has there been relatively little impact in the clinic to date? One major barrier is that we do not have drugs that can target tumor suppressor genes, making up ~40% of mix of principal, driver mutations. Sometimes there are workarounds for this issue, such as the tumor suppressor gene PTEN, which results in PI3-kinase activation, but more often, this is not the case. Even for oncogenes, less than 40% have a specific drug antagonist, as most are part of protein complexes (Vogelstein et al., 2013). A second critical issue is that there is marked heterogeneity in tumors, both within an individual's primary tumor and certainly intermetastatic. This appears to be a foundation for the common occurrence of relapse after an initial marked response, reflecting success directed to an oncogene but also that other undetected mutations become capable of propagating the tumor. The BRAF mutations, which are drivers in a variety of tumors, notably melanoma, thyroid, and colon, can be treated with a specific BRAF inhibitor. In the first 2 weeks of oral therapy, there is usually a marked response, but at 9–12 months, a relapse is quite typical (Sosman et al., 2012). Interestingly, when targeting BRAF for colon cancer, there appears to be primary resistance to these inhibitors (Prahallad et al., 2012) related to EGFR expression and emphasizing that the stroma, microenvironment of the tumor can still exert an important role. The issues of heterogeneity and resistance lend credence to the use of combinations of targeted drugs in the future, but that has yet to be explored at scale in prospective trials. A third largely unaddressed issue in the clinic is the involvement of the epigenome in tumorigenesis. At least 40 epigenome regulator genes are known that have highly recurrent somatic mutations in tumors across a variety of cancers, affecting multiple target genes simultaneously (Kandoth et al., 2013b; Vogelstein et al., 2013; Garraway and Lander, 2013; Shen and Laird, 2013). These are not screened for clinically, nor are there drugs available to modulate their effect.

In the clinic today, the bare bones of mutation screening are typically used, such as HER2 for breast cancer or KRAS for colon cancer. Recently, Foundation Medicine commercialized a targeted gene panel of 287 genes that have an established role in cancer (Frampton et al., 2013). Using predominantly fixed-formalin, paraffin-embedded samples, mutation cell concordance was established compared with mass spectrometric methodology (Sequenom), and the typical driver mutations were identified in a cohort of more than 2,000 individuals, such as TP53, KRAS, CDKN2A, and PIK3CA (Frampton et al., 2013). However, there was a long tail of uncommon mutations that was identified, reflecting the profound diversity of cancers.

This panel represents a step forward compared with a very limited gene mutation screen for commonly occurring drivers, which might even miss other pathogenic mutations within incriminated genes. The 287 genes assessed represent only <15% of genes and only the coding elements. This is in contrast to research studies of whole-genome and whole-exome sequencing, with paired germline DNA for each individual, to more precisely determine driver mutations (Kandoth et al., 2013b). Further, multiple recent studies have highlighted the role of noncoding elements of the genome to play a prominent role, such as TERT promoters in melanoma (Huang et al., 2013), a long, noncoding RNA SChLAP1 for aggressive prostate cancer (Prensner et al., 2013), and identification of ~100 noncoding driver variants for cancer using a new bioinformatics tool known as FunSeq (Khurana et al., 2013). Clearly, even a comprehensive exome would only represent a limited swath of sampling for root causes of cancer in an individual.

Cancer genomic medicine of the future will likely involve a GIS of the tumor with assessment of DNA sequence, gene expression, RNA-seq, microRNAs, proteins, copy number variations, and DNA methylation cross-referenced with the individual's germline DNA. But the issue of addressing heterogeneity still looms (Vogelstein et al., 2013; Bedard et al., 2013), and for that, there are a few possible steps, including deep sequencing of the tumor at multiple locations, single-cell sequencing, or the use of the "liquid biopsy" of cancer (Schwarzenbach et al., 2011; Leary et al., 2010; Forshew et al., 2012).

Cell-free tumor DNA in plasma, which is present in the vast majority of patients with cancer, has been shown to be a useful biomarker for following patients (Schwarzenbach et al., 2011; Leary et al., 2010; Forshew et al., 2012) and appears to have independent prognostic significance (Dawson et al., 2013). It may be that plasma tumor DNA is the best representative of the cancer for targeted treatment because avoidance of metastasis is of utmost concern. The ease of isolating and sequencing cell-free tumor DNA is likely to make this a very attractive and routine in the future. Especially appealing is the ability to sample on a more frequent and even continuous basis using biosensors. Whether the "liquid biopsy" will help override the challenges related to intratumor heterogeneity and recurrence of cancer awaits prospective evaluation. Also of particular interest, at some point, will be screening healthy people for cell-free tumor DNA to determine whether we are constantly facing microscopic tumor burden but are able to effectively keep the disease in check by a variety of homeostatic mechanisms.

Molecular Diagnosis

When a patient receives a diagnosis of a chronic illness today, it is nonspecific and is based on clinical and not molecular features. Take, for example, diabetes mellitus type 2, which could reflect anything from insulin resistance, failure of β-islet cells, or a variety of subtypes, including α-adrenergic receptor (ADRA2A) diabetes (Gribble, 2010) or a zinc transporter subtype (SLC30A8) (Sladek et al., 2007). Common genomic variants have been identified in pathways involving signal transduction, cell proliferation, glucose sensing, and circadian rhythm (Dupuis et al., 2010). Some individuals with a high fasting glucose have a G6PC2 variant that is associated with protection from diabetes (Bouatia-Naji et al., 2008). A genotype score, amalgamating the number of risk variants, has been shown to be helpful for identifying high susceptibility (Meigs et al., 2008). Moreover, there are 13 classes of drugs to treat diabetes, and the treatment could be made considerably more rational with knowledge of the individual's underlying mechanism(s).

This brief summary of the diabetes example reflects the need for a new molecular taxonomy across all diseases. When an individual is diagnosed (or at some point when risk can be defined), the molecular basis will be assessed and, ideally, when possible, the root cause will be established. Clearly, for many common diseases, there are multiple pathways implicated, and this may prove to be difficult. But there has yet to be a systematic attempt of providing such a molecular diagnosis in clinical care. Despite multiple reports of molecular subtypes of asthma (Wenzel, 2012), multiple sclerosis (Ottoboni et al., 2012), and colon (Sadanandam et al., 2013) and uterine cancer (Kandoth et al., 2013a), which appear to be linked with therapy and prognosis, this has yet to be made part of medical practice.

Pharmacogenomics

Just as molecular subtyping of chronic disease is not part of medical practice, pharmacogenomics screening for either assurance of efficacy or avoidance of major side effects is predominantly ignored. With the use of GWAS, there has been an avalanche of discovery of alleles that are pivotal to individual drug response. Unlike polygenic disease, for which the penetrance for a common sequence variant is quite low (approximate odds ratio of 1.15), the typical genotype odds ratio for prescription drugs can be as high as 80, and for many, the range is 3- to 40-fold (reviewed in depth in Harper and Topol [2012]). The likely explanation for this pronounced impact of common variants on individual drug response is based on selection—as compared with diseases, the human genome has had very limited time to adapt to medication exposure. Despite there being more than 100 drugs that carry a genomic "label" by the Food and Drug Administration, meaning that there is a recommendation for genotype assessment before the drug is used, there is rarely any pharmacogenomic assessment in clinical practice. This needs to improve, and perhaps the availability of point-of-care testing will help, along with reduced cost, to eventually promote routine use. Beyond this barrier, there needs to be more genomic sequencing for commonly used drugs, with associated phenotypic determination of efficacy and side effects, along with systematic omic assessment for drugs in development. From the marked success of discovering genomic-drug interactions found to date, there is certainly the sense that, the more you look, the

more you will find. The potential here is to reduce the waste of pharmaceuticals, not just by avoiding drugs that will not provide efficacy for particular individuals but also by avoiding serious toxicity that can be either fatal or life threatening.

Healthspan

The human reference genome is based upon multiple young individuals who had no phenotypic characterization. Accordingly, we know nothing about the reference human's natural history of disease, and one can consider this as a flawed standard for comparison. Ideally, we should have a reference genome that has had rigorous phenotyping. This is especially the case in an era of using sequencing in medical practice but with an inadequate comparator. Perhaps the optimal phenotype would be healthspan. At Scripps, we have defined healthy elderly as age >80 years with no history of chronic illness or use of medications. The cohort (known as "Wellderly") that we have assembled over the past 7 years of 1,400 individuals has an average age of 88, and we have completed whole-genome sequencing for 500 of these individuals. The intent is to provide a more useful reference genome with a clearly defined, uniform, and relevant phenotype.

Moreover, there is another important application of healthspan genomics. Multiple studies have established that a research investment in understanding healthy aging would be more prudent than in any specific disease category (Goldman et al., 2013a). Because the cohort that we have enrolled carries a similar burden of common risk variants for chronic diseases compared with the general population, there are most likely a substantial number of modifier genes and protective alleles that may be ultimately identified. One example is from APP, a gene that has a variant for both high risk of Alzheimer's and another rare variant with marked protection from cognitive impairment of Alzheimer's (De Strooper and Voet, 2012). Unquestionably, there are many more such variants left to be discovered, and therein lies the potential for drug discovery efforts that can follow such findings from nature of particular genes and pathways that prevent diseases.

Molecular Autopsies

Although physical autopsies have lost favor and become exceptionally rare, there is an opportunity to use sequencing to determine the cause of death, particularly when this occurs suddenly. Targeted or whole-genome sequencing for heritable heart disorders implicated in sudden death, including ion channel mutations and hypertrophic cardiomyopathy, can be performed in the deceased individual and family members. This approach is now actively being pursued in New York City for all sudden cardiac deaths (Erdmann, 2013) and may prove helpful in preventing this condition in family members.

Future Directions

This prewomb-to-tomb review has emphasized that there is a disproportionate relationship between knowledge and implementation into clinical practice. For individualized medicine to take hold, it will require intensive, rigorous validation that these new approaches improve patient outcomes and are demonstrated to be cost effective. This proof will be essential for the medical community to embrace the opportunities but will also require educational programs that squarely address the knowledge chasm that currently exists for practicing physicians. A second theme is that our efforts have been largely sequence centric and have not adequately taken into account or integrated the data from other omics, no less biosensors and imaging. Related to this deficiency, there is a profound shortage of data scientists in biomedicine, with unparalleled opportunities to process enormous, high-yield data sets. While we will increasingly rely on algorithms, artificial intelligence, and machine learning, the rate-limiting step necessitates talented biocomputing and bioinformatic human expertise.

One of the most attractive outgrowths of defining each individual's unique biology in an era with unprecedented digital infrastructure is to be able to share the data. By taking the deidentified data from each individual, including panoromic, biosensors, social graph, treatment, and outcomes, an extraordinary resource can now be developed. Such a massive open online medical information (MOOM) repository could provide matching capability to approximate a newly diagnosed individual's data as compared with all of those previously amalgamated. For a patient with cancer, for example, this could provide closest matches to the tumor GIF, demographics, treatment, and outcomes to select an optimal strategy; this would potentially take Bayesian principles to a new, enriched potential. Such a MOOM resource does not need to be confined to cancer, but the first to be announced was with the Leukemia & Lymphoma Society and Oregon Health Sciences University for 900 patients with liquid tumors (Winslow, 2013). Hopefully, this will be one of many data-sharing initiatives in medicine to go forward, now that such rich unique information can be captured at the individual level, and our computing infrastructure is so well suited to perform such functions. Although we are still at the nascent stages of individualized medicine, there has never been more promise and opportunity to reboot the way health care can be rendered. Only with systematic validation of these approaches at the intersection of biology and digital technology can we actualize this more precise, futuristic version of medicine.

ACKNOWLEDGMENTS

I want to express my gratitude to my colleagues Ali Torkamani, PhD, and Erick Scott, MD, who reviewed the manuscript and offered editorial input and to Katrina Schreiber, who helped prepare the typescript and graphics. This work was supported by NIH/NCATS 1 UL1 TR001114. Dr. Topol is an advisor to Illumina, Genapsys, and Edico Genomics and is a cofounder of Cypher Genomics.

REFERENCES

Alexandrov, L.B., Nik-Zainal, S., Wedge, D.C., Aparicio, S.A., Behjati, S., Biankin, A.V., Bignell, G.R., Bolli, N., Borg, A., Børresen-Dale, A.L., et al.; Australian Pancreatic Cancer Genome Initiative; ICGC Breast Cancer Consortium; ICGC MMML-Seq Consortium; ICGC PedBrain (2013). Signatures of mutational processes in human cancer. Nature *500*, 415–421.

Almeling, R. (2013). The unregulated sperm industry. New York Times, November 30, 2013. http://www.nytimes.com/2013/12/01/opinion/sunday/the-unregulated-sperm-industry.html.

Arumugam, M., Raes, J., Pelletier, E., Le Paslier, D., Yamada, T., Mende, D.R., Fernandes, G.R., Tap, J., Bruls, T., Batto, J.M., et al.; MetaHIT Consortium (2011). Enterotypes of the human gut microbiome. Nature *473*, 174–180.

Battich, N., Stoeger, T., and Pelkmans, L. (2013). Image-based transcriptomics in thousands of single human cells at single-molecule resolution. Nat. Methods *10*, 1127–1133.

Bedard, P.L., Hansen, A.R., Ratain, M.J., and Siu, L.L. (2013). Tumour heterogeneity in the clinic. Nature *501*, 355–364.

Bonnet, J., Yin, P., Ortiz, M.E., Subsoontorn, P., and Endy, D. (2013). Amplifying genetic logic gates. Science *340*, 599–603.

Bouatia-Naji, N., Rocheleau, G., Van Lommel, L., Lemaire, K., Schuit, F., Cavalcanti-Proença, C., Marchand, M., Hartikainen, A.L., Sovio, U., De Graeve, F., et al. (2008). A polymorphism within the G6PC2 gene is associated with fasting plasma glucose levels. Science *320*, 1085–1088.

Boycott, K.M., Vanstone, M.R., Bulman, D.E., and MacKenzie, A.E. (2013). Rare-disease genetics in the era of next-generation sequencing: discovery to translation. Nat. Rev. Genet. *14*, 681–691.

Brannon, A.R., and Sawyers, C.L. (2013). "N of 1" case reports in the era of whole-genome sequencing. J. Clin. Invest. *123*, 4568–4570.

Butte, A.J. (2013). Should healthy people have their genomes sequenced at this time? The Wall Street Journal, February 15, 2013. http://online.wsj.com/news/articles/SB10000872396390443884104577645783975993656?KEYWORDS=cost+of+whole+genome+sequencing.

Chen, R., Mias, G.I., Li-Pook-Than, J., Jiang, L., Lam, H.Y., Chen, R., Miriami, E., Karczewski, K.J., Hariharan, M., Dewey, F.E., et al. (2012). Personal omics profiling reveals dynamic molecular and medical phenotypes. Cell *148*, 1293–1307.

Cho, I., and Blaser, M.J. (2012). The human microbiome: at the interface of health and disease. Nat. Rev. Genet. *13*, 260–270.

Church, G.M., Gao, Y., and Kosuri, S. (2012). Next-generation digital information storage in DNA. Science *337*, 1628.

Couzin-Frankel, J. (2012). Genetics. New company pushes the envelope on pre-conception testing. Science *338*, 315–316.

Damani, S., Bacconi, A., Libiger, O., Chourasia, A.H., Serry, R., Gollapudi, R., Goldberg, R., Rapeport, K., Haaser, S., Topol, S., et al. (2012). Characterization of circulating endothelial cells in acute myocardial infarction. Sci. Transl. Med. *4*, 126ra33.

Dawson, M.A., and Kouzarides, T. (2012). Cancer epigenetics: from mechanism to therapy. Cell *150*, 12–27.

Dawson, S.J., Tsui, D.W., Murtaza, M., Biggs, H., Rueda, O.M., Chin, S.F., Dunning, M.J., Gale, D., Forshew, T., Mahler-Araujo, B., et al. (2013). Analysis of circulating tumor DNA to monitor metastatic breast cancer. N. Engl. J. Med. *368*, 1199–1209.

de Ligt, J., Willemsen, M.H., van Bon, B.W., Kleefstra, T., Yntema, H.G., Kroes, T., Vulto-van Silfhout, A.T., Koolen, D.A., de Vries, P., Gilissen, C., et al. (2012). Diagnostic exome sequencing in persons with severe intellectual disability. N. Engl. J. Med. *367*, 1921–1929.

De Strooper, B., and Voet, T. (2012). Alzheimer's disease: A protective mutation. Nature *488*, 38–39.

Dupuis, J., Langenberg, C., Prokopenko, I., Saxena, R., Soranzo, N., Jackson, A.U., Wheeler, E., Glazer, N.L., Bouatia-Naji, N., Gloyn, A.L., et al. (2010). New genetic loci implicated in fasting glucose homeostasis and their impact on type 2 diabetes risk. Nat. Genet. *42*, 105–116.

Erdmann, J. (2013). Telltale hearts. Nat. Med. *19*, 1361–1364.

Eyre, D.W., Cule, M.L., Wilson, D.J., Griffiths, D., Vaughan, A., O'Connor, L., Ip, C.L., Golubchik, T., Batty, E.M., Finney, J.M., et al. (2013). Diverse sources of C. difficile infection identified on whole-genome sequencing. N. Engl. J. Med. *369*, 1195–1205.

Faith, J.J., Guruge, J.L., Charbonneau, M., Subramanian, S., Seedorf, H., Goodman, A.L., Clemente, J.C., Knight, R., Heath, A.C., Leibel, R.L., et al. (2013). The long-term stability of the human gut microbiota. Science *341*, 1237439.

Fan, H.C., Gu, W., Wang, J., Blumenfeld, Y.J., El-Sayed, Y.Y., and Quake, S.R. (2012). Non-invasive prenatal measurement of the fetal genome. Nature *487*, 320–324.

Ferguson, B.S., Hoggarth, D.A., Maliniak, D., Ploense, K., White, R.J., Woodward, N., Hsieh, K., Bonham, A.J., Eisenstein, M., Kippin, et al.. (2013). Real-time, aptamer-based tracking of circulating therapeutic agents in living animals. Sci. Transl. Med. *5*, 213ra165.

Forshew, T., Murtaza, M., Parkinson, C., Gale, D., Tsui, D.W., Kaper, F., Dawson, S.J., Piskorz, A.M., Jimenez-Linan, M., Bentley, D., et al. (2012). Noninvasive identification and monitoring of cancer mutations by targeted deep sequencing of plasma DNA. Sci. Transl. Med. *4*, 136ra68.

Frampton, G.M., Fichtenholtz, A., Otto, G.A., Wang, K., Downing, S.R., He, J., Schnall-Levin, M., White, J., Sanford, E.M., An, P., et al. (2013). Development and validation of a clinical cancer genomic profiling test based on massively parallel DNA sequencing. Nat. Biotechnol. *31*, 1023–1031.

Fratkin, E., Bercovici, S., and Stephan, D.A. (2012). The implications of ENCODE for diagnostics. Nat. Biotechnol. *30*, 1064–1065.

Frazer, K.A., Murray, S.S., Schork, N.J., and Topol, E.J. (2009). Human genetic variation and its contribution to complex traits. Nat. Rev. Genet. *10*, 241–251.

Gahl, W.A., and Tifft, C.J. (2011). The NIH Undiagnosed Diseases Program: lessons learned. JAMA *305*, 1904–1905.

Gardy, J.L., Johnston, J.C., Ho Sui, S.J., Cook, V.J., Shah, L., Brodkin, E., Rempel, S., Moore, R., Zhao, Y., Holt, R., et al. (2011). Whole-genome sequencing and social-network analysis of a tuberculosis outbreak. N. Engl. J. Med. *364*, 730–739.

Garraway, L.A., and Lander, E.S. (2013). Lessons from the cancer genome. Cell *153*, 17–37.

Goldman, D.P., Cutler, D., Rowe, J.W., Michaud, P.C., Sullivan, J., Peneva, D., and Olshansky, S.J. (2013a). Substantial health and economic returns from delayed aging may warrant a new focus for medical research. Health Aff. (Millwood) *32*, 1698–1705.

Goldman, N., Bertone, P., Chen, S., Dessimoz, C., LeProust, E.M., Sipos, B., and Birney, E. (2013b). Towards practical, high-capacity, low-maintenance information storage in synthesized DNA. Nature *494*, 77–80.

Gordon, J.I., Dewey, K.G., Mills, D.A., and Medzhitov, R.M. (2012). The human gut microbiota and undernutrition. Sci. Transl. Med. *4*, 137ps12.

Gribble, F.M. (2010). Alpha2A-adrenergic receptors and type 2 diabetes. N. Engl. J. Med. *362*, 361–362.

Groop, L. (2010). Open chromatin and diabetes risk. Nat. Genet. *42*, 190–192.

Haffner, M.C., Mosbruger, T., Esopi, D.M., Fedor, H., Heaphy, C.M., Walker, D.A., Adejola, N., Gürel, M., Hicks, J., Meeker, A.K., et al. (2013). Tracking the clonal origin of lethal prostate cancer. J. Clin. Invest. *123*, 4918–4922.

Haiser, H.J., Gootenberg, D.B., Chatman, K., Sirasani, G., Balskus, E.P., and Turnbaugh, P.J. (2013). Predicting and manipulating cardiac drug inactivation by the human gut bacterium Eggerthella lenta. Science *341*, 295–298.

Hall, S.S. (2013). Genetics: a gene of rare effect. Nature *496*, 152–155.

Hanahan, D., and Weinberg, R.A. (2000). The hallmarks of cancer. Cell *100*, 57–70.

Hanahan, D., and Weinberg, R.A. (2011). Hallmarks of cancer: the next generation. Cell *144*, 646–674.

Harper, A.R., and Topol, E.J. (2012). Pharmacogenomics in clinical practice and drug development. Nat. Biotechnol. *30*, 1117–1124.

Harris, S.R., Cartwright, E.J., Török, M.E., Holden, M.T., Brown, N.M., Ogilvy-Stuart, A.L., Ellington, M.J., Quail, M.A., Bentley, S.D., Parkhill, J., and Peacock, S.J. (2013). Whole-genome sequencing for analysis of an outbreak of meticillin-resistant Staphylococcus aureus: a descriptive study. Lancet Infect. Dis. *13*, 130–136.

Hayden, E.C. (2014). Is the $1,000 genome for real? Nature News, January 15, 2014. http://www.nature.com/news/is-the-1-000-genome-for-real-1.14530.

Huang, F.W., Hodis, E., Xu, M.J., Kryukov, G.V., Chin, L., and Garraway, L.A. (2013). Highly recurrent TERT promoter mutations in human melanoma. Science *339*, 957–959.

Iida, N., Dzutsev, A., Stewart, C.A., Smith, L., Bouladoux, N., Weingarten, R.A., Molina, D.A., Salcedo, R., Back, T., Cramer, S., et al. (2013). Commensal bacteria control cancer response to therapy by modulating the tumor microenvironment. Science *342*, 967–970.

Issacson, W. (2011). Steve Jobs (New York: Simon & Schuster).

Jacob, H.J., Abrams, K., Bick, D.P., Brodie, K., Dimmock, D.P., Farrell, M., Geurts, J., Harris, J., Helbling, D., Joers, B.J., et al. (2013). Genomics in clinical practice: lessons from the front lines. Sci. Transl. Med. *5*, 194cm5.

Jenkins, H.W. (2010). Google and the search for the future. Wall Street Journal, August 14, 2010. http://ow.ly/qglOu.

Kaiser, J. (2013). Genomics. Researchers to explore promise, risks of sequencing newborns' DNA. Science *341*, 1163.

Kandoth, C., Schultz, N., Cherniack, A.D., Akbani, R., Liu, Y., Shen, H., Robertson, A.G., Pashtan, I., Shen, R., Benz, C.C., et al.; Cancer Genome Atlas Research Network (2013a). Integrated genomic characterization of endometrial carcinoma. Nature *497*, 67–73.

Kandoth, C., McLellan, M.D., Vandin, F., Ye, K., Niu, B., Lu, C., Xie, M., Zhang, Q., McMichael, J.F., Wyczalkowski, M.A., et al. (2013b). Mutational landscape and significance across 12 major cancer types. Nature *502*, 333–339.

Khurana, E., Fu, Y., Colonna, V., Mu, X.J., Kang, H.M., Lappalainen, T., Sboner, A., Lochovsky, L., Chen, J., Harmanci, A., et al.; 1000 Genomes Project Consortium (2013). Integrative annotation of variants from 1092 humans: application to cancer genomics. Science *342*, 1235587.

Kitzman, J.O., Snyder, M.W., Ventura, M., Lewis, A.P., Qiu, R., Simmons, L.E., Gammill, H.S., Rubens, C.E., Santillan, D.A., Murray, J.C., et al. (2012). Noninvasive whole-genome sequencing of a human fetus. Sci. Transl. Med. *4*, 137ra76.

Koboldt, D.C., Steinberg, K.M., Larson, D.E., Wilson, R.K., and Mardis, E.R. (2013). The next-generation sequencing revolution and its impact on genomics. Cell *155*, 27–38.

Kong, A., Steinthorsdottir, V., Masson, G., Thorleifsson, G., Sulem, P., Besenbacher, S., Jonasdottir, A., Sigurdsson, A., Kristinsson, K.T., Jonasdottir, A., et al.; DIAGRAM Consortium (2009). Parental origin of sequence variants associated with complex diseases. Nature *462*, 868–874.

Kong, A., Frigge, M.L., Masson, G., Besenbacher, S., Sulem, P., Magnusson, G., Gudjonsson, S.A., Sigurdsson, A., Jonasdottir, A., Jonasdottir, A., et al. (2012). Rate of de novo mutations and the importance of father's age to disease risk. Nature *488*, 471–475.

Leary, R.J., Kinde, I., Diehl, F., Schmidt, K., Clouser, C., Duncan, C., Antipova, A., Lee, C., McKernan, K., De La Vega, F.M., et al. (2010). Development of personalized tumor biomarkers using massively parallel sequencing. Sci. Transl. Med. *2*, 20ra14.

Liu, Y., Aryee, M.J., Padyukov, L., Fallin, M.D., Hesselberg, E., Runarsson, A., Reinius, L., Acevedo, N., Taub, M., Ronninger, M., et al. (2013). Epigenome-wide association data implicate DNA methylation as an intermediary of genetic risk in rheumatoid arthritis. Nat. Biotechnol. *31*, 142–147.

Lo, Y.M., Chan, K.C., Sun, H., Chen, E.Z., Jiang, P., Lun, F.M., Zheng, Y.W., Leung, T.Y., Lau, T.K., Cantor, C.R., and Chiu, R.W. (2010). Maternal plasma DNA sequencing reveals the genome-wide genetic and mutational profile of the fetus. Sci. Transl. Med. *2*, 61ra91.

Lupski, J.R. (2013). Genetics. Genome mosaicism—one human, multiple genomes. Science *341*, 358–359.

Macosko, E.Z., and McCarroll, S.A. (2012). Exploring the variation within. Nat. Genet. *44*, 614–616.

Maher, B. (2011). Human genetics: Genomes on prescription. Nature *478*, 22–24.

Marx, V. (2013). Next-generation sequencing: The genome jigsaw. Nature *501*, 263–268.

Meigs, J.B., Shrader, P., Sullivan, L.M., McAteer, J.B., Fox, C.S., Dupuis, J., Manning, A.K., Florez, J.C., Wilson, P.W., D'Agostino, R.B., Sr., and Cupples, L.A. (2008). Genotype score in addition to common risk factors for prediction of type 2 diabetes. N. Engl. J. Med. *359*, 2208–2219.

Morain, S., Greene, M.F., and Mello, M.M. (2013). A new era in noninvasive prenatal testing. N. Engl. J. Med. *369*, 499–501.

National Human Genome Research Institute. (2013). Clinical sequencing exploratory research (CSER). http://www.genome.gov/27546194.

National Research Council (2011). Toward precision medicine: building a knowledge network for biomedical research and a new taxonomy of disease (Washington, D.C.: The National Academies Press).

Ottoboni, L., Keenan, B.T., Tamayo, P., Kuchroo, M., Mesirov, J.P., Buckle, G.J., Khoury, S.J., Hafler, D.A., Weiner, H.L., and De Jager, P.L. (2012). An RNA profile identifies two subsets of multiple sclerosis patients differing in disease activity. Sci. Transl. Med. *4*, 153ra131.

Owens, B. (2012). Genomics: The single life. Nature *491*, 27–29.

Pirola, L., Balcerczyk, A., Okabe, J., and El-Osta, A. (2010). Epigenetic phenomena linked to diabetic complications. Nat. Rev. Endocrinol. *6*, 665–675.

Poduri, A., Evrony, G.D., Cai, X., and Walsh, C.A. (2013). Somatic mutation, genomic variation, and neurological disease. Science *341*, 1237758.

Prahallad, A., Sun, C., Huang, S., Di Nicolantonio, F., Salazar, R., Zecchin, D., Beijersbergen, R.L., Bardelli, A., and Bernards, R. (2012). Unresponsiveness of colon cancer to BRAF(V600E) inhibition through feedback activation of EGFR. Nature *483*, 100–103.

Prensner, J.R., Iyer, M.K., Sahu, A., Asangani, I.A., Cao, Q., Patel, L., Vergara, I.A., Davicioni, E., Erho, N., Ghadessi, M., et al. (2013). The long noncoding RNA SChLAP1 promotes aggressive prostate cancer and antagonizes the SWI/SNF complex. Nat. Genet. *45*, 1392–1398.

Ridaura, V.K., Faith, J.J., Rey, F.E., Cheng, J., Duncan, A.E., Kau, A.L., Griffin, N.W., Lombard, V., Henrissat, B., Bain, J.R., et al. (2013). Gut microbiota from twins discordant for obesity modulate metabolism in mice. Science *341*, 1241214.

Rincon, P. (2013). Genepeeks firm to offer 'digital baby' screen for sperm donors. BBC News, October 4, 2014. http://ow.ly/qi9wm.

Rivera, C.M., and Ren, B. (2013). Mapping human epigenomes. Cell *155*, 39–55.

Sadanandam, A., Lyssiotis, C.A., Homicsko, K., Collisson, E.A., Gibb, W.J., Wullschleger, S., Ostos, L.C., Lannon, W.A., Grotzinger, C., Del Rio, M., et al. (2013). A colorectal cancer classification system that associates cellular phenotype and responses to therapy. Nat. Med. *19*, 619–625.

Saunders, C.J., Miller, N.A., Soden, S.E., Dinwiddie, D.L., Noll, A., Alnadi, N.A., Andraws, N., Patterson, M.L., Krivohlavek, L.A., Fellis, J., et al. (2012). Rapid whole-genome sequencing for genetic disease diagnosis in neonatal intensive care units. Sci. Transl. Med. *4*, 154ra135.

Schmitz, R.J., Schultz, M.D., Lewsey, M.G., O'Malley, R.C., Urich, M.A., Libiger, O., Schork, N.J., and Ecker, J.R. (2011). Transgenerational epigenetic instability is a source of novel methylation variants. Science *334*, 369–373.

Schwarzenbach, H., Hoon, D.S., and Pantel, K. (2011). Cell-free nucleic acids as biomarkers in cancer patients. Nat. Rev. Cancer *11*, 426–437.

Shapiro, E., Biezuner, T., and Linnarsson, S. (2013). Single-cell sequencing-based technologies will revolutionize whole-organism science. Nat. Rev. Genet. *14*, 618–630.

Shen, H., and Laird, P.W. (2013). Interplay between the cancer genome and epigenome. Cell *153*, 38–55.

Shendure, J., and Lieberman Aiden, E. (2012). The expanding scope of DNA sequencing. Nat. Biotechnol. *30*, 1084–1094.

Sladek, R., Rocheleau, G., Rung, J., Dina, C., Shen, L., Serre, D., Boutin, P., Vincent, D., Belisle, A., Hadjadj, S., et al. (2007). A genome-wide association study identifies novel risk loci for type 2 diabetes. Nature *445*, 881–885.

Snitkin, E.S., Zelazny, A.M., Thomas, P.J., Stock, F., Henderson, D.K., Palmore, T.N., and SEGRE, J.A.; NISC Comparative Sequencing Program Group (2012). Tracking a hospital outbreak of carbapenem-resistant Klebsiella pneumoniae with whole-genome sequencing. Sci. Transl. Med. *4*, 148ra116.

Sosman, J.A., Kim, K.B., Schuchter, L., Gonzalez, R., Pavlick, A.C., Weber, J.S., McArthur, G.A., Hutson, T.E., Moschos, S.J., Flaherty, K.T., et al. (2012). Survival in BRAF V600-mutant advanced melanoma treated with vemurafenib. N. Engl. J. Med. *366*, 707–714.

Sosnay, P.R., Siklosi, K.R., Van Goor, F., Kaniecki, K., Yu, H., Sharma, N., Ramalho, A.S., Amaral, M.D., Dorfman, R., Zielenski, J., et al. (2013). Defining

the disease liability of variants in the cystic fibrosis transmembrane conductance regulator gene. Nat. Genet. *45*, 1160–1167.

Stanton, D. (2013). GFK survey. GFK, August 22, 2013. http://www.gfk.com/us/news-and-events/press-room/press-releases/Pages/Only-27-of-US-Consumers-Have-Heard-of-Personalized-Medicine.aspx.

Suvà, M.L., Riggi, N., and Bernstein, B.E. (2013). Epigenetic reprogramming in cancer. Science *339*, 1567–1570.

Test, T.C. (2013). The Counsyl Test. https://www.counsyl.com/.

Tewhey, R., Bansal, V., Torkamani, A., Topol, E.J., and Schork, N.J. (2011). The importance of phase information for human genomics. Nat. Rev. Genet. *12*, 215–223.

Veltman, J.A., and Brunner, H.G. (2012). De novo mutations in human genetic disease. Nat. Rev. Genet. *13*, 565–575.

Viaud, S., Saccheri, F., Mignot, G., Yamazaki, T., Daillère, R., Hannani, D., Enot, D.P., Pfirschke, C., Engblom, C., Pittet, M.J., et al. (2013). The intestinal microbiota modulates the anticancer immune effects of cyclophosphamide. Science *342*, 971–976.

Vogelstein, B., Papadopoulos, N., Velculescu, V.E., Zhou, S., Diaz, L.A., Jr., and Kinzler, K.W. (2013). Cancer genome landscapes. Science *339*, 1546–1558.

Wang, J., Fan, H.C., Behr, B., and Quake, S.R. (2012). Genome-wide single-cell analysis of recombination activity and de novo mutation rates in human sperm. Cell *150*, 402–412.

Wenzel, S.E. (2012). Asthma phenotypes: the evolution from clinical to molecular approaches. Nat. Med. *18*, 716–725.

Westra, H.J., Peters, M.J., Esko, T., Yaghootkar, H., Schurmann, C., Kettunen, J., Christiansen, M.W., Fairfax, B.P., Schramm, K., Powell, J.E., et al. (2013). Systematic identification of trans eQTLs as putative drivers of known disease associations. Nat. Genet. *45*, 1238–1243.

Winslow, R. (2013). Patients share DNA for cures. Wall Street Journal, September 16, 2013. http://online.wsj.com/news/articles/SB10001424127887323342404579079453190552312?KEYWORDS=Patients+SHare+DNA+for+CUres.

Worthey, E.A., Mayer, A.N., Syverson, G.D., Helbling, D., Bonacci, B.B., Decker, B., Serpe, J.M., Dasu, T., Tschannen, M.R., Veith, R.L., et al. (2011). Making a definitive diagnosis: successful clinical application of whole exome sequencing in a child with intractable inflammatory bowel disease. Genet. Med. *13*, 255–262.

Yang, Y., Muzny, D.M., Reid, J.G., Bainbridge, M.N., Willis, A., Ward, P.A., Braxton, A., Beuten, J., Xia, F., Niu, Z., et al. (2013). Clinical whole-exome sequencing for the diagnosis of mendelian disorders. N. Engl. J. Med. *369*, 1502–1511.

Zhang, B., Gaiteri, C., Bodea, L.G., Wang, Z., McElwee, J., Podtelezhnikov, A.A., Zhang, C., Xie, T., Tran, L., Dobrin, R., et al. (2013). Integrated systems approach identifies genetic nodes and networks in late-onset Alzheimer's disease. Cell *153*, 707–720.

Ziller, M.J., Gu, H., Müller, F., Donaghey, J., Tsai, L.T., Kohlbacher, O., De Jager, P.L., Rosen, E.D., Bennett, D.A., Bernstein, B.E., et al. (2013). Charting a dynamic DNA methylation landscape of the human genome. Nature *500*, 477–481.

THE 2015 KEYSTONE SYMPOSIA MEETINGS

Precision Genome Engineering and Synthetic Biology (A1)
January 11–16, 2015 | Big Sky, Montana | USA

Viral Immunity (A2)
January 11–16, 2015 | Breckenridge, Colorado | USA

The Biological Code of Signaling – A Tribute to Tony Pawson (F1)
January 11–16, 2015 | Steamboat Springs, Colorado | USA

Integrating Metabolism and Tumor Biology (J1)
joint with **PI 3-Kinase Signaling Pathways in Disease (J2)**
January 13–18, 2015 | Vancouver, British Columbia | Canada

Immunity to Veterinary Pathogens: Informing Vaccine Development (A3)
January 20–25, 2015 | Keystone, Colorado | USA

Host Response in Tuberculosis (J3)
joint with **Granulomas in Infectious and Non-Infectious Diseases (J4)**
January 22–27, 2015 | Santa Fe, New Mexico | USA

Epigenetics and Cancer (A4)
January 25–30, 2015 | Keystone, Colorado | USA

Neuroinflammation in Diseases of the Central Nervous System (A5)
January 25–30, 2015 | Taos, New Mexico | USA

Mitochondria, Metabolism and Heart Failure (J5)
joint with **Diabetes and Metabolic Dysfunction (J6)**
January 27–Feb 1, 2015 | Santa Fe, New Mexico | USA

Autoimmunity and Tolerance (B1)
February 3–8, 2015 | Keystone, Colorado | USA

Endoderm Lineages in Development and Disease (B2)
February 8–13, 2015 | Keystone, Colorado | USA

Plant Receptor Kinases: From Molecules to Environment (B3)
February 8–13, 2015 | Taos, New Mexico | USA

Tumor Immunology:
Multidisciplinary Science Driving Combination Therapy (J7)
joint with **Antibodies as Drugs: Immunological Scaffolds as Therapeutics (J8)**
February 8–13, 2015 | Banff, Alberta | Canada

Systems Biology of Lipid Metabolism (B4)
February 9–13, 2015 | Breckenridge, Colorado | USA

RNA Silencing in Plants (G1)
February 17–22, 2015 | Keystone, Colorado | USA

Neuroepigenetics (B5)
February 22–26, 2015 | Santa Fe, New Mexico | USA

Hematopoiesis (B6)
February 22–27, 2015 | Keystone, Colorado | USA

Gut Microbiota Modulation of Host Physiology:
The Search for Mechanism (C1)
March 1–6, 2015 | Keystone, Colorado | USA

Heart Disease and Regeneration: Insights from Development (X1)
joint with **Cell Biology of the Heart: Beyond the Myocyte-Centric View (X2)**
March 1–6, 2015 | Copper Mountain, Colorado | USA

DNA Replication and Recombination (X3)
joint with **Genomic Instability and DNA Repair (X4)**
March 1–6, 2015 | Whistler, British Columbia | Canada

Hybrid Methods in Structural Biology (C2)
March 4–8, 2015 | Tahoe City, California | USA

Biology of Sirtuins (C3)
March 8–12, 2015 | Santa Fe, New Mexico | USA

Dendritic Cells and Macrophages Reunited (C4)
March 8–13, 2015 | Montreal, Quebec | Canada

Optogenetics (C5)
March 12–16, 2015 | Denver, Colorado | USA

Co-Infection: A Global Challenge for Disease Control (C6)
March 15–20, 2015 | Ouro Preto, Minas Gerais | Brazil

Long Noncoding RNAs: From Evolution to Function (C7)
March 15–20, 2015 | Keystone, Colorado | USA

Pathways of Neurodevelopmental Disorders (C8)
March 16–20, 2015 | Tahoe City, California | USA

HIV Vaccines (X5)
joint with **The Golden Anniversary of B Cell Discovery (X6)**
March 22–27, 2015 | Banff, Alberta | Canada

Obesity and the Metabolic Syndrome:
Mitochondria and Energy Expenditure (X7)
joint with **Liver Metabolism and Nonalcoholic Fatty Liver Disease (NAFLD) (X8)**
March 22–27, 2015 | Whistler, British Columbia | Canada

Transcriptional and Epigenetic Influences on Stem Cell States (C9)
March 23–28, 2015 | Steamboat Springs, Colorado | USA

Gram-Negative Resistance (D1)
March 29–April 2, 2015 | Tahoe City, California | USA

Viruses and Human Cancer (D2)
March 29–April 3, 2015 | Big Sky, Montana | USA

T Cells: Regulation and Effector Function (D3)
March 29–April 3, 2015 | Snowbird, Utah | USA

DNA Methylation (Z1)
joint with **Epigenomics (Z2)**
March 29–April 3, 2015 | Keystone, Colorado | USA

Neural Control of Metabolic Physiology and Diseases (D4)
April 12–17, 2015 | Snowbird, Utah | USA

Beige and Brown Fat:
Basic Biology and Novel Therapeutics (D5)
April 17–22, 2015 | Snowbird, Utah | USA

The Crossroads of Lipid Metabolism and Diabetes (D6)
April 19–24, 2015 | Copenhagen | Denmark

Innate Immunity and Determinants of Microbial Pathogenesis (Z3)
joint with **Mechanisms of Pro-Inflammatory Diseases (Z4)**
April 19–24, 2015 | Olympic Valley, California | USA

The Human Proteome (D7)
April 24–29, 2015 | Stockholm | Sweden

Mechanisms of HIV Persistence: Implications for a Cure (E1)
April 26–May 1, 2015 | Boston, Massachusetts | USA

The Arthropod Vector: The Controller of Transmission (E2)
May 12–17, 2015 | Taos, New Mexico | USA

Hypoxia: From Basic Mechanisms to Therapeutics (E3)
May 12–17, 2015 | Dublin | Ireland

The Hippo Pathway: Signaling, Development and Disease (E4)
May 17–21, 2015 | Taos, New Mexico | USA

MicroRNAs and Noncoding RNAs in Cancer (E5)
June 7–12, 2015 | Keystone, Colorado | USA

Autophagy (E6)
June 19–24, 2015 | Breckenridge, Colorado | USA

KEYSTONE SYMPOSIA™
on Molecular and Cellular Biology
Accelerating Life Science Discovery

*Discounted Abstract and Scholarship Deadlines precede meetings by four months and Discounted Registration Deadlines by two months. Visit keystonesymposia.org/meetings for more details. You can also view each meeting's program by adding 15 and then the program code (in parentheses after each meeting name) after keystonesymposia.org/ (e.g., **keystonesymposia.org/15A1**).*

Leading Edge
Review

Cell

Mechanisms and Functions of Inflammasomes

Mohamed Lamkanfi[1,2,*] and Vishva M. Dixit[3,*]
[1]Department of Medical Protein Research, VIB, Ghent 9000, Belgium
[2]Department of Biochemistry, Ghent University, Ghent 9000, Belgium
[3]Department of Physiological Chemistry, Genentech, South San Francisco, CA 94080, USA
*Correspondence: mohamed.lamkanfi@vib-ugent.be (M.L.), dixit.vishva@gene.com (V.M.D.)
http://dx.doi.org/10.1016/j.cell.2014.04.007

Recent studies have offered a glimpse into the sophisticated mechanisms by which inflammasomes respond to danger and promote secretion of interleukin (IL)-1β and IL-18. Activation of caspases 1 and 11 in canonical and noncanonical inflammasomes, respectively, also protects against infection by triggering pyroptosis, a proinflammatory and lytic mode of cell death. The therapeutic potential of inhibiting these proinflammatory caspases in infectious and autoimmune diseases is raised by the successful deployment of anti-IL-1 therapies to control autoinflammatory diseases associated with aberrant inflammasome signaling. This Review summarizes recent insights into inflammasome biology and discusses the questions that remain in the field.

Introduction

From the primitive lamprey to humans, vertebrates use innate and adaptive immune systems to defend against pathogens (Boehm et al., 2012). In mammals, the innate immune system mounts the initial response to threats. Concomitantly, dendritic cells and other antigen-presenting cells (APCs) relay information about the harmful agent to B and T lymphocytes of the adaptive immune system. Lymphocytes have diverse antigen receptors, and clonal expansion of the cells that recognize the foreign material culminates in its targeted removal (Koch and Radtke, 2011). Antigen receptor gene rearrangements in lymphocytes enable the adaptive immune system to recognize seemingly any antigen, but innate immune cells detect pathogens with a fixed number of germline-encoded "pattern recognition receptors" (PRRs) (Takeuchi and Akira, 2010). PRRs detect unique microbial structures termed pathogen-associated molecular patterns (PAMPs). Microbial nucleic acids, bacterial secretion systems, and components of the microbial cell wall are examples of the conserved microbial factors that are sensed by PRRs. Damaged host cells can also trigger PRRs by releasing danger-associated molecular patterns (DAMPs) such as uric acid crystals, ATP, high-mobility group box 1 (HMGB1), and the heat-shock proteins hsp70 and hsp90.

PRRs can be subdivided into two major classes based on their subcellular localization. Toll-like receptors (TLRs) and C-type lectin receptors (CLRs) are transmembrane proteins found in the plasma membrane and endosomes, where they can survey PAMPs and DAMPs in the extracellular milieu. A second class of PRRs resides in intracellular compartments and includes the RIG-I-like receptor (RLR), the AIM2-like receptor (ALR), and the nucleotide-binding domain and leucine-rich repeat-containing (NLR) proteins (Takeuchi and Akira, 2010). We would add to this second class of PRRs the proteins that sense cytosolic DNA and trigger the production of type I interferon (Paludan and Bowie, 2013).

Many PRRs encountering PAMPs and DAMPs trigger signaling cascades that promote gene transcription by nuclear factor-κB (NF-κB), activator protein 1 (AP1), and interferon regulatory factors (IRFs). Target genes encode cytokines, interferons, and other proinflammatory or microbicidal proteins (Takeuchi and Akira, 2010). A subset of NLRs and ALRs triggers a distinct defense mechanism. These proteins assemble cytosolic protein complexes called inflammasomes to activate proinflammatory caspases 1 and 11 (Kayagaki et al., 2011; Martinon et al., 2002). Rapid conversion of procaspase zymogens into enzymatically active proteases results in: (1) the production of proinflammatory IL-1β and IL-18 and (2) the death of the cell.

Here, we review recent progress in our understanding of inflammasome signaling, the consequences of aberrant inflammasome signaling in human disease, and the therapeutic potential of inflammasome modulation in inflammatory diseases.

Canonical and Noncanonical Inflammasomes: Platforms for Caspase-1 and -11 Activation

Canonical inflammasomes convert procaspase-1 into the catalytically active enzyme, whereas an undefined noncanonical inflammasome promotes activation of procaspase-11 (Figure 1). Caspases 1 and 11 belong to a family of aspartate-specific cysteine proteases conserved through evolution. Like caspases 8, 9, and 10, which initiate apoptotic cell death, caspases 1 and 11 have large prodomains that mediate interactions with other proteins. Interaction motifs belonging to the "death domain" superfamily bring the zymogens into the activating protein complex (Lamkanfi and Dixit, 2012; Riedl and Salvesen, 2007). These homotypic interaction domains typically consist of six or seven antiparallel α helices, the relative orientation of which determines their classification as a caspase activation and recruitment

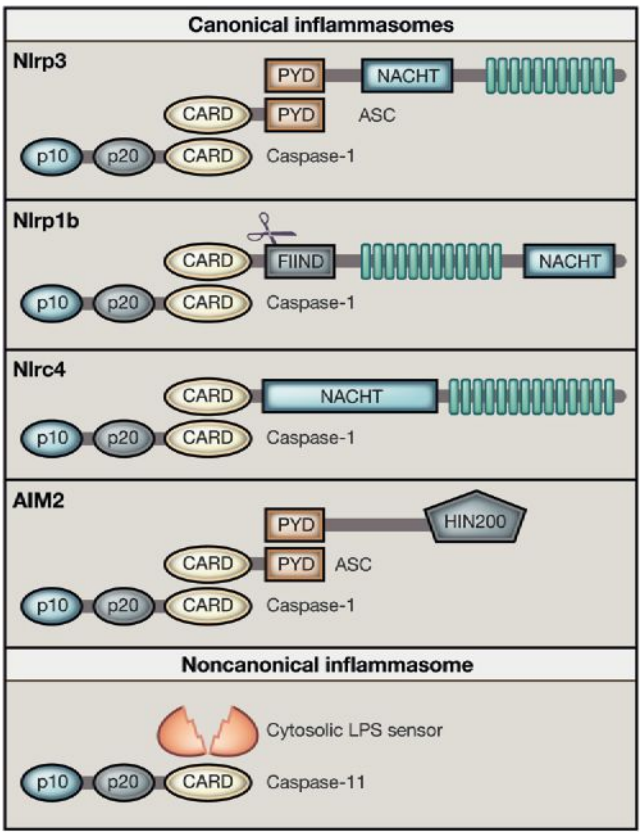

Figure 1. Composition of Canonical and Noncanonical Inflammasomes

The murine NLRs Nlrp3, Nlrp1b, and Nlrc4 and the ALR member absent in melanoma 2 (AIM2) assemble canonical inflammasomes that promote activation of the cysteine protease caspase-1. NLRs are characterized by the combined presence of a NACHT domain and a variable number of LRRs. Most NLRs further contain either a CARD or PYD motif in their amino-terminus. AIM2 is composed of an amino-terminal PYD and a carboxy-terminal DNA-binding HIN200 domain. Note that murine Nlrp1b lacks the amino-terminal PYD motif found in human NLRP1 and is autocatalytically cleaved in its central FIIND domain. Nlrp1b and Nlrc4 recruit caspase-1 via their CARD motifs. The bipartite PYD-CARD adaptor protein ASC may stabilize these interactions and is required for assembly of the AIM2 and Nlrp3 inflammasomes. A currently unknown cytosolic LPS sensor mediates activation of caspase-11 in the noncanonical inflammasome. CARD, caspase recruitment domain; FIIND, domain with function to find; LRR, leucine-rich repeat; NACHT, nucleotide-binding and oligomerization domain; NLR, Nod-like receptor; PYD, pyrin.

domain (CARD), pyrin domain (PYD), death domain (DD), or death effector domain (DED).

The structural rearrangements that occur when procaspases 1 and 11 are activated have not been characterized in detail, but activation is thought to mirror the proximity-induced activation of caspases 8 and 9 (Riedl and Salvesen, 2007). Activation of caspase-9 within the "apoptosome" has several features in common with activation of caspase-1 within canonical inflammasomes. First, the apoptosome and canonical inflammasomes are large, cytosolic, multiprotein complexes that recruit and promote the activation of a CARD-containing initiator caspase. Second, each complex consumes ATP and may have a double-ringed wheel structure with 7- or 8-fold symmetry (Duncan et al., 2007; Faustin et al., 2007; Riedl and Salvesen, 2007). Third, recruitment of procaspases 1 and 9 to their respective complexes is sufficient for them to acquire enzymatic activity (Broz et al., 2010a; Riedl and Salvesen, 2007; Van Opdenbosch et al., 2014), although their maturation into heterotetramers by autoprocessing may lock the proteases into an enzymatically active state. Finally, the intracellular K^+ concentration appears to set the threshold for assembly of the apoptosome and several inflammasomes (Arlehamn et al., 2010; Cain et al., 2001; Muñoz-Planillo et al., 2013). It is possible that cellular stress or damage associated with K^+ efflux relieves a checkpoint safeguarding the cell against unwarranted activation of these lethal caspases.

Caspases 1 and 11 in Immunity and Host Defense

Inflammasomes modulate host defense responses through the production of eicosanoids (von Moltke et al., 2012) and other mechanisms (Lamkanfi, 2011), but the induction of pyroptosis and secretion of proinflammatory IL-1β and IL-18 are considered the prominent outcomes of inflammasome signaling. Pyroptosis is a nonhomeostatic and lytic mode of cell death that requires the enzymatic activity of caspase-1 or -11 (Kayagaki et al., 2011). Cells dying by pyroptosis exhibit cytoplasmic swelling and rupture of the plasma membrane, features that are shared with caspase-independent necroptotic cell death (Lamkanfi, 2011). The molecular events underlying these changes remain obscure, but the application of sophisticated proteomic approaches may illuminate these phenomena in the future. Despite such gaps in our knowledge, pyroptosis has emerged as a key defense against microbial infections (Aachoui et al., 2013; Case et al., 2013; Casson et al., 2013; Kayagaki et al., 2011; Miao et al., 2010a). It is thought to halt the replication of intracellular pathogens by eliminating infected immune cells while simultaneously promoting destruction of surviving bacteria by exposing them to circulating phagocytes and neutrophils. Moreover, pyroptosis may influence adaptive immunity against the infectious agent by releasing antigens into the extracellular milieu, with DAMPs such as IL-1α and HMGB1 acting as potential adjuvants. Further characterization of the in vivo roles of pyroptosis will depend on the identification of markers that are specific for this type of cell death. Biomarkers may also unveil potential differences between caspase-1- versus caspase-11-induced pyroptosis.

Caspases 1 and 11 both induce pyroptosis, but only caspase-1 processes IL-1β and IL-18 (Figure 2). IL-1β is a pyrogenic cytokine that also promotes adaptive T helper 1 (Th_1), Th_{17}, and humoral immunity. IL-18 is important for IL-17 expression by Th_{17} cells and may polarize T cells toward Th_1 or Th_2 profiles in combination with other cytokines (Dinarello, 2009). Unlike most cytokines, IL-1β and IL-18 are not secreted through the classical endoplasmic reticulum-Golgi route but are produced as biologically inactive precursor proteins that are cleaved prior to their secretion as bioactive cytokines (Lamkanfi, 2011). Pro-IL-18 is expressed constitutively in macrophages, whereas expression of pro-IL-1β is regulated by NF-κB-mediated transcription.

Although caspase-11 is required for macrophages to secrete IL-1β and IL-18 after infection with *Escherichia coli*, *Citrobacter rodentium*, or *Vibrio cholerae*, caspase-1 must be activated too (Gurung et al., 2012; Kayagaki et al., 2011). In contrast, pyroptosis in response to these bacteria requires caspase-11, but not

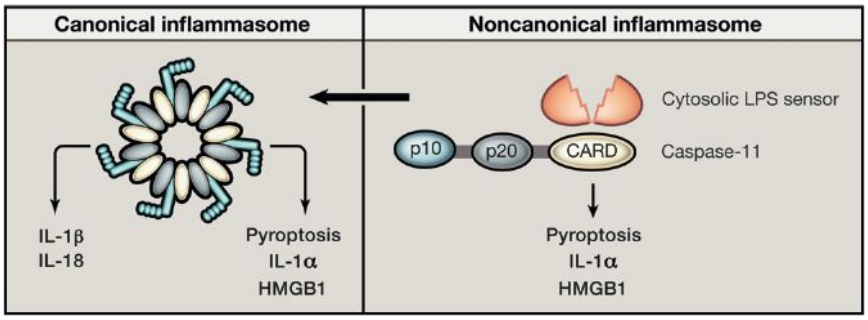

Figure 2. Major Effector Mechanisms of the Canonical and Noncanonical Inflammasomes

Assembly of the canonical inflammasome complexes promotes the proximity-induced autoactivation of caspase-1. Caspase-1 subsequently converts its substrates proIL-1β and proIL-18 into the secreted bioactive cytokines and triggers pyroptosis through an unknown mechanism. A hypothetical noncanonical inflammasome that is activated in response to the detection of cyotosolic LPS triggers activation of caspase-11 in macrophages infected with *Escherichia coli*, *Citrobacter rodentium*, *Vibrio cholera*, and other Gram-negative bacteria that enter the cytosol. Caspase-11 mediates pyroptosis and extracellular release of IL-1α and HMGB1 directly and induces secretion of mature IL-1β and IL-18 indirectly through engagement of the canonical Nlrp3 inflammasome.

caspase-1 (Figure 2). Further evidence of a unique role for caspase-11 is provided by the resistance of caspase-11-deficient mice, but not caspase-1-deficient mice, in a model of endotoxic shock (Kayagaki et al., 2011; Wang et al., 1998). Like caspase-1 deficiency, combined loss of the caspase-1 substrates IL-1β and IL-18 does not provide significant protection in this model of endotoxic shock (Kayagaki et al., 2011; Lamkanfi et al., 2010). Pyroptosis to excess might promote sepsis by inducing immunosuppression while amplifying the inflammatory response. In this regard, activation of caspase-1 and pyroptosis in quiescent $CD4^+$ T cells was recently proposed to underlie the immunosuppressive and chronic inflammatory condition of HIV-infected individuals (Doitsh et al., 2014).

Caspase-11 responds to most intracellular Gram-negative bacteria (Broz et al., 2012; Case et al., 2013; Casson et al., 2013; Gurung et al., 2012; Rathinam et al., 2012), with those invading the cytosol being detected earlier than those remaining in vacuoles (Aachoui et al., 2013). In contrast, Gram-positive pathogens do not activate caspase-11 (Rathinam et al., 2012). The explanation for these observations is that activation of caspase-11 is triggered by acylated lipid A, a component of the LPS found in many Gram-negative bacteria (Hagar et al., 2013; Kayagaki et al., 2013). Of note, intracellular LPS or acylated lipid A activated caspase-11 in macrophages lacking the LPS receptor TLR4. Indeed, TLR4-deficient mice treated first with a TLR3 agonist to induce expression of caspase-11 were susceptible to a lethal dose of LPS, whereas the majority of caspase-11-deficient mice survived this regimen (Hagar et al., 2013; Kayagaki et al., 2013). These observations argue that there is another LPS receptor besides TLR4 whose role is to activate caspase-11 upon binding to intracellular LPS. Identification of this receptor and the substrates of the noncanonical inflammasome should shed light on the roles of human caspases 4 and 5. These caspases share highest sequence homology with mouse caspase-11, but whether they represent true functional orthologs will require further study.

Canonical Inflammasome Subtypes and Their Activation Mechanisms

Although the composition of the noncanonical inflammasome remains unknown, several canonical inflammasomes that activate caspase-1 in response to endogenous and exogenous danger signals have been characterized. Each is named after its NLR or ALR protein scaffold (Lamkanfi and Dixit, 2012). Human NLRP2, NLRP6, NLRP7, NLRP12, and the ALR protein IFI16 may assemble inflammasomes, but additional studies are needed to understand their importance for caspase-1 activation. In contrast, the role of ALR AIM2 and the NLRs NLRP1, NLRP3, and NLRC4 in inflammasome signaling is firmly established (Figure 1). In the following section, we discuss the activation mechanisms of these inflammasomes in additional detail.

The Nlrp1a and Nlrp1b Inflammasomes

Humans have a single *NLRP1* gene, whereas mice have *Nlrp1a*, *Nlrp1b*, and *Nlrp1c* genes. An important difference between human NLRP1 and its murine orthologs is that the latter lack a PYD motif at the N terminus (Boyden and Dietrich, 2006). *Nlrp1b* is highly polymorphic between mouse strains. Macrophages from 129S1 mice produce functional Nlrp1b but lack mRNA expression of the other two isoforms (Boyden and Dietrich, 2006; Sastalla et al., 2013). In contrast, C57BL/6 mice express Nlrp1a and Nlrp1c but have mutations in *Nlrp1b* that render the Nlrp1b protein nonfunctional. The role of Nlrp1c remains to be discovered, but genetic data support a role in inflammasome signaling for Nlrp1a and Nlrp1b.

Mice homozygous for an activating Q593P point mutation in Nlrp1a succumb to a systemic neutrophilic inflammatory disease at 3–5 months of age (Masters et al., 2012). Neutrophilia is caused by excessive IL-1β production and pyroptosis of hematopoietic progenitor cells. The mice exhibit profound cytopenia after chemotherapy or infection with lymphocytic choriomeningitis virus (LCMV). Biochemical studies may clarify what triggers Nlrp1a activation and why the Q593P mutation in its function-to-find (FIIND) domain renders the protein constitutively active.

The Nlrp1b inflammasome is an important defense mechanism against *Bacillus anthracis* because defective activation of the Nlrp1b inflammasome hampers host defense in mice infected with live *B. anthracis* spores (Moayeri et al., 2010; Terra et al., 2010). *Nlrp1b* is the key locus determining whether macrophages undergo pyroptosis in response to *B. anthracis* lethal toxin (LeTx) (Boyden and Dietrich, 2006). Thus, macrophages from Nlrp1b-deficient mice fail to activate caspase-1 and are defective at IL-1β secretion and pyroptosis in response to LeTx (Kovarova et al., 2012). Nlrp1b recruits caspase-1 directly

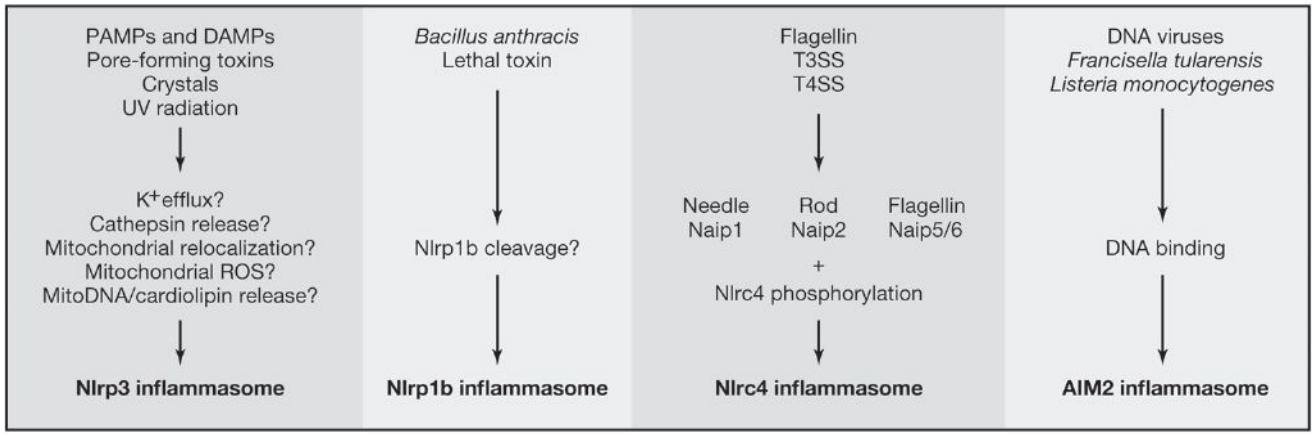

Figure 3. Schematic Overview of Proposed Inflammasome Activation Mechanisms

The different inflammasomes recruit and activate caspase-1 in response to a variety of triggers. PAMPs, DAMPs, pore-forming toxins, crystals, and UV radiation are thought to activate the Nlrp3 inflammasome by reducing intracellular K^+ concentrations, by promoting cytosolic release of lysosomal cathepsins, by relocating Nlrp3 to the mitochondrial outer membrane, and by inducing mitochondrial damage, which may be sensed by Nlrp3 via the production of ROS or the cytosolic release of oxidized mitochondrial DNA and cardiolipin. The presence of *Bacillus anthracis* lethal toxin in the cytosol might be detected through the cleavage of Nlrp1b. Cells exposed to bacteria expressing flagellin or a type III (T3SS) or IV (T4SS) secretion system indirectly activate the Nlrc4 inflammasome through Naip proteins. Mouse Naip1 and human NAIP bind the T3SS needle, while mouse Naip2 detects the rod component of T3SS and T4SS. Finally, mouse Naip5 and -6 detect bacterial flagellin in the cytosol. These bacterial factors also induce PKCδ-mediated phosphorylation of Nlrc4 on Ser533, which is required for activation of the Nlrc4 inflammasome. AIM2 is activated by the presence of dsDNA in the cytosol of cells infected with *Francisella tularensis*, *Listeria monocytogenes*, and the DNA viruses cytomegalovirus and vaccinia virus.

via its CARD motif, although the bipartite PYD-CARD adaptor protein ASC may stabilize these interactions. Indeed, ASC is critical for Nlrp1b-induced caspase-1 autoprocessing but dispensable for LeTx-induced pyroptosis and IL-1β secretion (Van Opdenbosch et al., 2014).

LeTx is a two-component toxin in which the ''protective antigen'' subunit provides the metalloprotease effector subunit ''lethal factor'' (LF) access to the cytosol. Initially, Nlrp1b was assumed to just physically associate with cytosolic LF, but it was then shown that LF metalloprotease activity was needed for its recognition (Fink et al., 2008). Subsequent studies showed that LeTx cleaves Nlrp1b close to its N terminus (Chavarría-Smith and Vance, 2013; Hellmich et al., 2012). How removal of a short (4 kDa) peptide from the N terminus promotes inflammasome activation requires further analysis (Figure 3).

The Nlrc4 Inflammasome

Similar to Nlrp1b, Nlrc4 contains a CARD motif through which it interacts with caspase-1, and this probably explains why ASC is dispensable for Nlrc4-induced pyroptosis (Figure 1). Nevertheless, ASC may amplify Nlrc4 inflammasome activity because it is critical for Nlrc4-induced caspase-1 autoprocessing and secretion of mature IL-1β and IL-18 (Broz et al., 2010b; Mariathasan et al., 2004; Van Opdenbosch et al., 2014). Nlrc4 responds to two critical components of pathogenic bacteria: flagellin, the building block of their locomotion machinery, and proteins from the type III and IV bacterial secretion systems that inject virulence factors into the host cell (Amer et al., 2006; Franchi et al., 2006; Miao et al., 2006; Miao et al., 2010b). Consequently, the Nlrc4 inflammasome is a major component of host defense against facultative intracellular pathogens such as *Salmonella* Typhimurium, *Shigella flexneri*, *Pseudomonas aeruginosa*, *Burkholderia thailandensis*, and *Legionella pneumophila* (Lamkanfi and Dixit, 2012). Activation of Nlrc4 involves members of the Naip subfamily of NLRs (Kofoed and Vance, 2011; Rayamajhi et al., 2013; Yang et al., 2013; Zhao et al., 2011). Naip proteins have BIR motifs at their N terminus, whereas most NLRs carry a CARD or PYD motif (Lamkanfi and Dixit, 2012). The murine *Naip* locus is highly polymorphic. C57BL/6J mice express four Naip proteins: Naip1 binds to the needle of the type III secretion system (Rayamajhi et al., 2013; Yang et al., 2013), Naip2 binds to the basal rod component (Kofoed and Vance, 2011; Zhao et al., 2011), and Naip5 and Naip6 recognize flagellin (Kofoed and Vance, 2011; Zhao et al., 2011). Humans express only one NAIP homolog, and it binds to the needle structure of the type III secretion system (Yang et al., 2013; Zhao et al., 2011). Once Naip proteins have bound their ligands, they may bind to Nlrc4 to promote activation of caspase-1. Posttranslational modification of Nlrc4 also contributes to inflammasome activation, with Ser^{533} in Nlrc4 being phosphorylated after infection with *S.* Typhimurium (Qu et al., 2012). This phosphorylation site appears conserved through evolution because a mouse Nlrc4 truncation mutant lacking its CARD and an internal peptide was phosphorylated at Ser^{533} when it was expressed in insect cells (Hu et al., 2013). In crystals, CARD-less Nlrc4 adopted a solenoid shape in which the LRRs folded back onto the NACHT domain (Hu et al., 2013). Further investigation of the relationship between Naip detection of bacterial components and Nlrc4 phosphorylation may illuminate how this inflammasome is activated.

The Nlrp3 Inflammasome

The Nlrp3 inflammasome is assembled when the amino-terminal PYD of Nlrp3 engages in homotypic interactions with the PYD of ASC to recruit caspase-1. However, the mechanisms associated with activation of the Nlrp3 inflammasome continue to be debated. This inflammasome is activated by bacterial, viral,

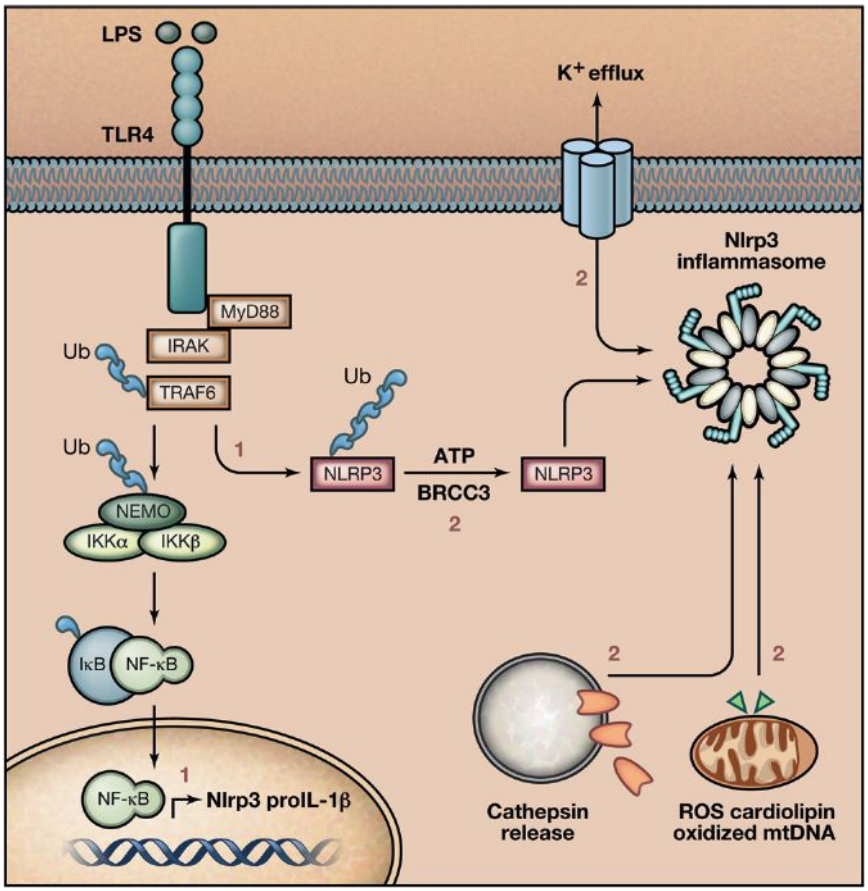

Figure 4. Priming and Activation Signals of the Nlrp3 Inflammasome

Although the exact molecular mechanisms of NLRP3 inflammasome assembly are incompletely understood, it is well-established that Nlrp3 activation requires two signals. Binding of the TLR4 ligand LPS to its receptor provides the first signal by triggering NF-κB-mediated upregulation of Nlrp3 along with proIL-1β. Alternatively, TLR4 may provide signal 1 through an incompletely understood pathway involving its adaptor molecules MyD88, IRAK1, and IRAK4 without the need for new protein synthesis. BRCC3-mediated K63-deubiquitination of Nlrp3 is required for Nlrp3 inflammasome assembly and activation by extracellular ATP and other Nlrp3-activating stimuli. These agents provide a second signal in the form of K^+ efflux, cytosolic release of lysosomal cathepsins, relocalization of Nlrp3 from the cytosol to mitochondria, or cytosolic release of mitochondria-derived factors such as reactive oxygen species (ROS), cardiolipin, and oxidized mitochondrial DNA (mtDNA).

and fungal pathogens, pore-forming toxins, crystals, aggregates such as β-amyloid, and DAMPs such as ATP and hyaluronan (Lamkanfi and Dixit, 2012). It is generally agreed that detection of such a diversity of agents cannot be direct. Instead, Nlrp3 is thought to monitor some host-derived factor that is altered by these agents. Several hypotheses for Nlrp3 activation have been formulated. They can be summarized as follows: Nlrp3 is activated by: (1) K^+ efflux (Muñoz-Planillo et al., 2013), (2) translocation to mitochondria (Misawa et al., 2013; Subramanian et al., 2013; Zhou et al., 2011), (3) the production of mitochondrial reactive oxygen species (Zhou et al., 2011), (4) the release of mitochondrial DNA or the mitochondrial phospholipid cardiolipin (Iyer et al., 2013; Nakahira et al., 2011; Shimada et al., 2012), and (5) the cytosolic release of lysosomal cathepsins (Hornung et al., 2008). A single unifying event has not emerged because some of these events do not occur with all Nlrp3-activating agents, or they are associated with multiple inflammasomes, or their occurrence is contested (Bauernfeind et al., 2011; Muñoz-Planillo et al., 2013; Pétrilli et al., 2007). There is disagreement too as to whether PKR (Lu et al., 2012), TXNIP (Zhou et al., 2010), and MAVS (Subramanian et al., 2013) have important roles in the Nlrp3 pathway (Ermler et al., 2014; He et al., 2013; Masters et al., 2010; Muñoz-Planillo et al., 2013).

What is clear is that activation of the Nlrp3 inflammasome requires two signals (Figure 4). First, an NF-κB-activating stimulus is required for cells to express pro-IL-1β and optimal Nlrp3 (Bauernfeind et al., 2009). Actual assembly of the Nlrp3 inflammasome occurs when a second signal is provided by an Nlrp3-activating agent (Lamkanfi and Dixit, 2012). Although Nlrp3 induction certainly contributes to inflammasome activation, brief TLR stimulation that doesn't increase the amount of Nlrp3 is sufficient to prime the pathway for activation by ATP (Juliana et al., 2012; Schroder et al., 2012). This alternative signal 1 is provided by TLR4 and is relayed by its adaptors MyD88, IRAK1, and IRAK4 independently of new protein synthesis (Fernandes-Alnemri et al., 2013; Juliana et al., 2012; Lin et al., 2014). Intriguingly, Nlrp3 deubiquitination is required for inflammasome assembly and activation (signal 2) (Juliana et al., 2012; Lopez-Castejon et al., 2013; Py et al., 2013). The K63-specific deubiquitinase BRCC3 was proposed to remove ubiquitin chains from the Nlrp3 leucine-rich repeat (LRR) motifs at this step (Py et al., 2013). Whether this triggers Nlrp3 relocalization, induces conformational changes, or serves other purposes that promote Nlrp3 inflammasome assembly is not known. Also the identity of the E3 ubiquitin ligase that modifies Nlrp3 in the basal state is unclear.

The AIM2 Inflammasome

The ALR protein AIM2 assembles a canonical inflammasome that recruits ASC to activate caspase-1. It does so when its DNA-binding HIN200 domain detects DNA from intracellular pathogens such as *Francisella tularensis*, cytomegalovirus, and vaccinia virus (Alnemri, 2010; Kanneganti, 2010). Mice lacking AIM2 or caspase-1 fail to clear infections with *F. tularensis*, the causative agent of tularaemia, illustrating the critical role that the AIM2 inflammasome plays in host defense against microbial pathogens (Alnemri, 2010). In association with Nlrp3 and Nlrc4, AIM2 also contributes to caspase-1 activation by *Listeria monocytogenes* (Rathinam et al., 2010; Sauer et al., 2010; Wu et al.,

2010). It was suggested that AIM2 may be linked to the pathology of autoimmune disorders such as systemic lupus erythematosus where DNA-autoantibodies are abundant (Zhang et al., 2013). If proven true, the pathway becomes a candidate for targeted therapies.

Of note, AIM2 inflammasome activation in macrophages coincides with the formation of a single large perinuclear aggregate or "speck" (Jones et al., 2010). Specks are also seen upon activation of the Nlrp1b, Nlrc4, and Nlrp3 inflammasomes (Broz et al., 2010a; Broz et al., 2010b; Van Opdenbosch et al., 2014). Speck formation is explained by the tendency of the ASC PYD domain to polymerize into star-shaped, branched filaments that serve as platforms for caspase-1 clustering (Cai et al., 2014; Lu et al., 2014). AIM2 and Nlrp3 nucleate ASC fibers through their PYD domains (Cai et al., 2014; Lu et al., 2014). The CARD of Nlrc4 triggers formation of similar ASC fibers, and again, the PYD of ASC is important (Cai et al., 2014). Of note, however, speck formation is not an absolute requirement for inflammasome activity because *S.* Typhimurium activates caspase-1 and induces pyroptosis even in the absence of ASC (Broz et al., 2010b; Van Opdenbosch et al., 2014). Nlrp1b-induced pyroptosis and IL-1β secretion also have been reported to occur in the absence of ASC (Van Opdenbosch et al., 2014).

Therapeutic Potential of Inflammasome Modulation

Aberrant inflammasome signaling contributes to pathology in a large number of infectious (Lamkanfi and Dixit, 2011) and autoimmune diseases (Lamkanfi and Dixit, 2012; Strowig et al., 2012). Recent work implicated inappropriate inflammasome signaling in graft-versus-host disease (Jankovic et al., 2013), type 2 diabetes (Jourdan et al., 2013; Masters et al., 2010), obesity-induced asthma (Kim et al., 2014), and insulin resistance (Stienstra et al., 2011; Vandanmagsar et al., 2011; Wen et al., 2011). Moreover, the NLRP3 inflammasome is activated during age-related macular degeneration (AMD) (Marneros, 2013; Tarallo et al., 2012). The accumulation of drusen and retinal damage in AMD is the leading cause of central vision loss in the elderly. Nlrp3 inflammasome blockade augmented retinal damage in an acute laser-induced wound-healing model (Doyle et al., 2012), but chronic NLRP3-driven IL-1β production may contribute to AMD-associated chorioretinal pathology in patients. This hypothesis is supported by studies demonstrating that deletion of Nlrp3 and caspase-1 reduced AMD pathology in two mouse models that resemble age-dependent aspects of human AMD (Marneros, 2013; Tarallo et al., 2012).

Alzheimer's disease is another age-related degenerative disorder that is exacerbated by NLRP3 inflammasome activity. Fibrillar β-amyloid deposits engage the NLRP3 inflammasome in cultured microglia and recruit activated microglia to β-amyloid plaques in the brain in vivo (Halle et al., 2008). More recently, deletion of Nlrp3 or caspase-1 was demonstrated to reduce memory loss and the accumulation of chronic β-amyloid deposits in transgenic mouse models of Alzheimer's disease (Heneka et al., 2013). In keeping with these observations, microglia in the vicinity of β-amyloid plaques in either Alzheimer's patients or mouse models of the disease were shown to express more IL-1β (Kim and de Vellis, 2005; Simard et al., 2006). In addition, mice lacking IL-1 receptor antagonist (IL-1Ra) exhibited more neuronal damage when exposed to exogenous β-amyloid (Craft et al., 2005).

Anti-IL-1 therapies have proven successful in several of the aforementioned ailments, including type 2 diabetes and juvenile rheumatoid arthritis (Dinarello et al., 2012; Larsen et al., 2007). Clinical studies may establish the therapeutic validity of inflammasome inhibition in additional inflammatory disorders in the future. To highlight a number of possible therapeutic approaches, we will elaborate on inflammasome blockade in autoinflammatory syndromes, which are often associated with mutations in inflammasome-related genes.

Inherited autoinflammatory diseases are characterized by recurrent episodes of inflammation in the absence of high-titer autoantibodies and antigen-specific T cells. These criteria differentiate them from autoimmune disorders in which autoreactive antibodies and lymphocytes play a central role in pathogenesis. Several autoinflammatory disorders are caused by mutations in genes mediating or modulating inflammasome activation. Well-studied examples are the cryopyrin-associated periodic fever syndromes (CAPS), which include familial cold autoinflammatory syndrome (FCAS), Muckle-Wells syndrome (MWS), and chronic infantile neurological cutaneous and articular syndrome/neonatal onset multisystem inflammatory disease (CINCA/NOMID) (Feldmann et al., 2002; Hoffman et al., 2001). These diseases produce urticarial skin rashes and prolonged episodes of fever, and a significant number of patients have gain-of-function mutations in *NLRP3* (Feldmann et al., 2002; Hoffman et al., 2001). The CAPS-associated mutations probably produce conformational changes in NLRP3 that render the protein constitutively active, thereby causing persistent caspase-1 activation and disproportionate production of IL-1β and IL-18 (Dowds et al., 2004).

Inhibition of IL-1 signaling has proven remarkably beneficial in CAPS patients (Ter Haar et al., 2013). Several other autoinflammatory disorders, including tumor necrosis factor receptor-associated periodic syndrome (TRAPS), in which disease is causally linked with mutations in TNF-R1, have also benefited from anti-IL-1 therapy. In fact, TRAPS patients respond significantly better to IL-1 inhibition than to TNF blockade (Ter Haar et al., 2013). Anti-IL-1 molecules currently approved for these syndromes include rilonacept (Hoffman et al., 2012), anakinra (Goldbach-Mansky et al., 2006), and canakinumab (Kuemmerle-Deschner et al., 2011). Anakinra is a non-glycosylated human IL-1 receptor antagonist, and rilonacept contains the ligand-binding domains of human IL-1 receptor (IL-1R1) and IL-1 receptor accessory protein (IL-1RAcP) fused to the Fc portion of a human immunoglobulin G1 (IgG1). The interaction of anakinra and rilonacept with the IL-1 receptor prevents IL-1α and IL-1β from binding to the IL-1 receptor and exerting their biological functions. In contrast, canakinumab is a humanized monoclonal antibody that neutralizes IL-1β in circulation and does not interfere with binding of IL-1α to the IL-1 receptor. Several other molecules targeting either IL-1β or IL-1R are currently under development (Dinarello et al., 2012).

Despite their remarkable efficacy, anti-IL-1 therapies do not resolve all CAPS-associated symptoms (Neven et al., 2010). One possible explanation is that the caspase-1-dependent

cytokine IL-18 still promotes disease. In mice expressing CAPS-associated *Nlrp3* mutations, IL-18 was important early in disease development, whereas the effects of IL-1 dominated at later stages (Brydges et al., 2013). Of note, however, a number of CAPS mice lacking both IL-18 and the IL-1 receptor still succumbed to disease, whereas caspase-1 deficiency provided full protection. Therefore, other caspase-1-mediated pathways, such as pyroptosis, may contribute to CAPS pathology. These findings highlight the potential benefits of blocking the NLRP3 inflammasome directly over inhibiting its downstream cytokines. It is possible that CAPS and other patients might benefit from pharmacologic inhibitors of caspase-1 such as VX-765, which is presently being tested in epilepsy. This compound prevented IL-1β secretion from LPS-stimulated peripheral blood mononuclear cells of FCAS patients in vitro (Stack et al., 2005), suggesting therapeutic potential in CAPS disease. Continued development of this and other caspase-1 inhibitors could potentially offer patients with autoinflammatory and related immune disorders additional options for improving their quality of life.

Conclusion and Perspectives

This Review has provided a discussion of the key advances that have been made in understanding the roles and activation mechanisms of inflammasomes and illustrated their increasingly appreciated roles in infectious, autoimmune, and autoinflammatory diseases. The existence of a noncanonical inflammasome that responds to intracellular LPS and Gram-negative bacteria has been proposed, the importance of posttranslational modifications in the activation of Nlrc4 and Nlrp1b demonstrated, and the contribution of pyroptosis in host defense against microbes and its role in autoinflammation clarified. These recent developments have raised some fascinating new questions for the field nonetheless. For instance, how does deubiquitination modulate Nlrp3 activation, what is the identity of the LPS sensor activating caspase-11, and how do caspases 1 and 11 trigger pyroptosis?

ACKNOWLEDGMENTS

The authors apologize to those whose citations were omitted owing to space limitations. M.L. is supported, in part, by the Ghent University Concerted Research Actions (BOF14/GOA/013), the European Research Council (Grant 281600), and the Fund for Scientific Research (FWO)-Flanders (grant G030212N). V.M.D. is a shareholder and employee of Genentech, Inc.

REFERENCES

Aachoui, Y., Leaf, I.A., Hagar, J.A., Fontana, M.F., Campos, C.G., Zak, D.E., Tan, M.H., Cotter, P.A., Vance, R.E., Aderem, A., and Miao, E.A. (2013). Caspase-11 protects against bacteria that escape the vacuole. Science *339*, 975–978.

Alnemri, E.S. (2010). Sensing cytoplasmic danger signals by the inflammasome. J. Clin. Immunol. *30*, 512–519.

Amer, A., Franchi, L., Kanneganti, T.D., Body-Malapel, M., Ozören, N., Brady, G., Meshinchi, S., Jagirdar, R., Gewirtz, A., Akira, S., and Núñez, G. (2006). Regulation of Legionella phagosome maturation and infection through flagellin and host Ipaf. J. Biol. Chem. *281*, 35217–35223.

Arlehamn, C.S., Pétrilli, V., Gross, O., Tschopp, J., and Evans, T.J. (2010). The role of potassium in inflammasome activation by bacteria. J. Biol. Chem. *285*, 10508–10518.

Bauernfeind, F.G., Horvath, G., Stutz, A., Alnemri, E.S., MacDonald, K., Speert, D., Fernandes-Alnemri, T., Wu, J., Monks, B.G., Fitzgerald, K.A., et al. (2009). Cutting edge: NF-kappaB activating pattern recognition and cytokine receptors license NLRP3 inflammasome activation by regulating NLRP3 expression. J. Immunol. *183*, 787–791.

Bauernfeind, F., Bartok, E., Rieger, A., Franchi, L., Núñez, G., and Hornung, V. (2011). Cutting edge: reactive oxygen species inhibitors block priming, but not activation, of the NLRP3 inflammasome. J. Immunol. *187*, 613–617.

Boehm, T., Iwanami, N., and Hess, I. (2012). Evolution of the immune system in the lower vertebrates. Annu. Rev. Genomics Hum. Genet. *13*, 127–149.

Boyden, E.D., and Dietrich, W.F. (2006). Nalp1b controls mouse macrophage susceptibility to anthrax lethal toxin. Nat. Genet. *38*, 240–244.

Broz, P., Newton, K., Lamkanfi, M., Mariathasan, S., Dixit, V.M., and Monack, D.M. (2010a). Redundant roles for inflammasome receptors NLRP3 and NLRC4 in host defense against Salmonella. J. Exp. Med. *207*, 1745–1755.

Broz, P., von Moltke, J., Jones, J.W., Vance, R.E., and Monack, D.M. (2010b). Differential requirement for Caspase-1 autoproteolysis in pathogen-induced cell death and cytokine processing. Cell Host Microbe *8*, 471–483.

Broz, P., Ruby, T., Belhocine, K., Bouley, D.M., Kayagaki, N., Dixit, V.M., and Monack, D.M. (2012). Caspase-11 increases susceptibility to Salmonella infection in the absence of caspase-1. Nature *490*, 288–291.

Brydges, S.D., Broderick, L., McGeough, M.D., Pena, C.A., Mueller, J.L., and Hoffman, H.M. (2013). Divergence of IL-1, IL-18, and cell death in NLRP3 inflammasomopathies. J. Clin. Invest. *123*, 4695–4705.

Cai, X., Chen, J., Xu, H., Liu, S., Jiang, Q.X., Halfmann, R., and Chen, Z.J. (2014). Prion-like polymerization underlies signal transduction in antiviral immune defense and inflammasome activation. Cell *156*, 1207–1222.

Cain, K., Langlais, C., Sun, X.M., Brown, D.G., and Cohen, G.M. (2001). Physiological concentrations of K+ inhibit cytochrome c-dependent formation of the apoptosome. J. Biol. Chem. *276*, 41985–41990.

Case, C.L., Kohler, L.J., Lima, J.B., Strowig, T., de Zoete, M.R., Flavell, R.A., Zamboni, D.S., and Roy, C.R. (2013). Caspase-11 stimulates rapid flagellin-independent pyroptosis in response to Legionella pneumophila. Proc. Natl. Acad. Sci. USA *110*, 1851–1856.

Casson, C.N., Copenhaver, A.M., Zwack, E.E., Nguyen, H.T., Strowig, T., Javdan, B., Bradley, W.P., Fung, T.C., Flavell, R.A., Brodsky, I.E., and Shin, S. (2013). Caspase-11 activation in response to bacterial secretion systems that access the host cytosol. PLoS Pathog. *9*, e1003400.

Chavarría-Smith, J., and Vance, R.E. (2013). Direct proteolytic cleavage of NLRP1B is necessary and sufficient for inflammasome activation by anthrax lethal factor. PLoS Pathog. *9*, e1003452.

Craft, J.M., Watterson, D.M., Hirsch, E., and Van Eldik, L.J. (2005). Interleukin 1 receptor antagonist knockout mice show enhanced microglial activation and neuronal damage induced by intracerebroventricular infusion of human beta-amyloid. J. Neuroinflammation *2*, 15.

Dinarello, C.A. (2009). Immunological and inflammatory functions of the interleukin-1 family. Annu. Rev. Immunol. *27*, 519–550.

Dinarello, C.A., Simon, A., and van der Meer, J.W. (2012). Treating inflammation by blocking interleukin-1 in a broad spectrum of diseases. Nat. Rev. Drug Discov. *11*, 633–652.

Doitsh, G., Galloway, N.L., Geng, X., Yang, Z., Monroe, K.M., Zepeda, O., Hunt, P.W., Hatano, H., Sowinski, S., Muñoz-Arias, I., and Greene, W.C. (2014). Cell death by pyroptosis drives CD4 T-cell depletion in HIV-1 infection. Nature *505*, 509–514.

Dowds, T.A., Masumoto, J., Zhu, L., Inohara, N., and Núñez, G. (2004). Cryopyrin-induced interleukin 1beta secretion in monocytic cells: enhanced activity of disease-associated mutants and requirement for ASC. J. Biol. Chem. *279*, 21924–21928.

Doyle, S.L., Campbell, M., Ozaki, E., Salomon, R.G., Mori, A., Kenna, P.F., Farrar, G.J., Kiang, A.S., Humphries, M.M., Lavelle, E.C., et al. (2012). NLRP3 has a protective role in age-related macular degeneration through the induction of IL-18 by drusen components. Nat. Med. *18*, 791–798.

Duncan, J.A., Bergstralh, D.T., Wang, Y., Willingham, S.B., Ye, Z., Zimmermann, A.G., and Ting, J.P. (2007). Cryopyrin/NALP3 binds ATP/dATP, is an ATPase, and requires ATP binding to mediate inflammatory signaling. Proc. Natl. Acad. Sci. USA *104*, 8041–8046.

Ermler, M.E., Traylor, Z., Patel, K., Schattgen, S.A., Vanaja, S.K., Fitzgerald, K.A., and Hise, A.G. (2014). Rift Valley fever virus infection induces activation of the NLRP3 inflammasome. Virology *449*, 174–180.

Faustin, B., Lartigue, L., Bruey, J.M., Luciano, F., Sergienko, E., Bailly-Maitre, B., Volkmann, N., Hanein, D., Rouiller, I., and Reed, J.C. (2007). Reconstituted NALP1 inflammasome reveals two-step mechanism of caspase-1 activation. Mol. Cell *25*, 713–724.

Feldmann, J., Prieur, A.M., Quartier, P., Berquin, P., Certain, S., Cortis, E., Teillac-Hamel, D., Fischer, A., and de Saint Basile, G. (2002). Chronic infantile neurological cutaneous and articular syndrome is caused by mutations in CIAS1, a gene highly expressed in polymorphonuclear cells and chondrocytes. Am. J. Hum. Genet. *71*, 198–203.

Fernandes-Alnemri, T., Kang, S., Anderson, C., Sagara, J., Fitzgerald, K.A., and Alnemri, E.S. (2013). Cutting edge: TLR signaling licenses IRAK1 for rapid activation of the NLRP3 inflammasome. J. Immunol. *191*, 3995–3999.

Fink, S.L., Bergsbaken, T., and Cookson, B.T. (2008). Anthrax lethal toxin and Salmonella elicit the common cell death pathway of caspase-1-dependent pyroptosis via distinct mechanisms. Proc. Natl. Acad. Sci. USA *105*, 4312–4317.

Franchi, L., Amer, A., Body-Malapel, M., Kanneganti, T.D., Ozören, N., Jagirdar, R., Inohara, N., Vandenabeele, P., Bertin, J., Coyle, A., et al. (2006). Cytosolic flagellin requires Ipaf for activation of caspase-1 and interleukin 1beta in salmonella-infected macrophages. Nat. Immunol. *7*, 576–582.

Goldbach-Mansky, R., Dailey, N.J., Canna, S.W., Gelabert, A., Jones, J., Rubin, B.I., Kim, H.J., Brewer, C., Zalewski, C., Wiggs, E., et al. (2006). Neonatal-onset multisystem inflammatory disease responsive to interleukin-1beta inhibition. N. Engl. J. Med. *355*, 581–592.

Gurung, P., Malireddi, R.K., Anand, P.K., Demon, D., Vande Walle, L., Liu, Z., Vogel, P., Lamkanfi, M., and Kanneganti, T.D. (2012). Toll or interleukin-1 receptor (TIR) domain-containing adaptor inducing interferon-β (TRIF)-mediated caspase-11 protease production integrates Toll-like receptor 4 (TLR4) protein- and Nlrp3 inflammasome-mediated host defense against enteropathogens. J. Biol. Chem. *287*, 34474–34483.

Hagar, J.A., Powell, D.A., Aachoui, Y., Ernst, R.K., and Miao, E.A. (2013). Cytoplasmic LPS activates caspase-11: implications in TLR4-independent endotoxic shock. Science *341*, 1250–1253.

Halle, A., Hornung, V., Petzold, G.C., Stewart, C.R., Monks, B.G., Reinheckel, T., Fitzgerald, K.A., Latz, E., Moore, K.J., and Golenbock, D.T. (2008). The NALP3 inflammasome is involved in the innate immune response to amyloid-beta. Nat. Immunol. *9*, 857–865.

He, Y., Franchi, L., and Núñez, G. (2013). The protein kinase PKR is critical for LPS-induced iNOS production but dispensable for inflammasome activation in macrophages. Eur. J. Immunol. *43*, 1147–1152.

Hellmich, K.A., Levinsohn, J.L., Fattah, R., Newman, Z.L., Maier, N., Sastalla, I., Liu, S., Leppla, S.H., and Moayeri, M. (2012). Anthrax lethal factor cleaves mouse nlrp1b in both toxin-sensitive and toxin-resistant macrophages. PLoS ONE *7*, e49741.

Heneka, M.T., Kummer, M.P., Stutz, A., Delekate, A., Schwartz, S., Vieira-Saecker, A., Griep, A., Axt, D., Remus, A., Tzeng, T.C., et al. (2013). NLRP3 is activated in Alzheimer's disease and contributes to pathology in APP/PS1 mice. Nature *493*, 674–678.

Hoffman, H.M., Mueller, J.L., Broide, D.H., Wanderer, A.A., and Kolodner, R.D. (2001). Mutation of a new gene encoding a putative pyrin-like protein causes familial cold autoinflammatory syndrome and Muckle-Wells syndrome. Nat. Genet. *29*, 301–305.

Hoffman, H.M., Throne, M.L., Amar, N.J., Cartwright, R.C., Kivitz, A.J., Soo, Y., and Weinstein, S.P. (2012). Long-term efficacy and safety profile of rilonacept in the treatment of cryopryin-associated periodic syndromes: results of a 72-week open-label extension study. Clin. Ther. *34*, 2091–2103.

Hornung, V., Bauernfeind, F., Halle, A., Samstad, E.O., Kono, H., Rock, K.L., Fitzgerald, K.A., and Latz, E. (2008). Silica crystals and aluminum salts activate the NALP3 inflammasome through phagosomal destabilization. Nat. Immunol. *9*, 847–856.

Hu, Z., Yan, C., Liu, P., Huang, Z., Ma, R., Zhang, C., Wang, R., Zhang, Y., Martinon, F., Miao, D., et al. (2013). Crystal structure of NLRC4 reveals its autoinhibition mechanism. Science *341*, 172–175.

Iyer, S.S., He, Q., Janczy, J.R., Elliott, E.I., Zhong, Z., Olivier, A.K., Sadler, J.J., Knepper-Adrian, V., Han, R., Qiao, L., et al. (2013). Mitochondrial cardiolipin is required for Nlrp3 inflammasome activation. Immunity *39*, 311–323.

Jankovic, D., Ganesan, J., Bscheider, M., Stickel, N., Weber, F.C., Guarda, G., Follo, M., Pfeifer, D., Tardivel, A., Ludigs, K., et al. (2013). The Nlrp3 inflammasome regulates acute graft-versus-host disease. J. Exp. Med. *210*, 1899–1910.

Jones, J.W., Kayagaki, N., Broz, P., Henry, T., Newton, K., O'Rourke, K., Chan, S., Dong, J., Qu, Y., Roose-Girma, M., et al. (2010). Absent in melanoma 2 is required for innate immune recognition of Francisella tularensis. Proc. Natl. Acad. Sci. USA *107*, 9771–9776.

Jourdan, T., Godlewski, G., Cinar, R., Bertola, A., Szanda, G., Liu, J., Tam, J., Han, T., Mukhopadhyay, B., Skarulis, M.C., et al. (2013). Activation of the Nlrp3 inflammasome in infiltrating macrophages by endocannabinoids mediates beta cell loss in type 2 diabetes. Nat. Med. *19*, 1132–1140.

Juliana, C., Fernandes-Alnemri, T., Kang, S., Farias, A., Qin, F., and Alnemri, E.S. (2012). Non-transcriptional priming and deubiquitination regulate NLRP3 inflammasome activation. J. Biol. Chem. *287*, 36617–36622.

Kanneganti, T.D. (2010). Central roles of NLRs and inflammasomes in viral infection. Nat. Rev. Immunol. *10*, 688–698.

Kayagaki, N., Warming, S., Lamkanfi, M., Vande Walle, L., Louie, S., Dong, J., Newton, K., Qu, Y., Liu, J., Heldens, S., et al. (2011). Non-canonical inflammasome activation targets caspase-11. Nature *479*, 117–121.

Kayagaki, N., Wong, M.T., Stowe, I.B., Ramani, S.R., Gonzalez, L.C., Akashi-Takamura, S., Miyake, K., Zhang, J., Lee, W.P., Muszyński, A., et al. (2013). Noncanonical inflammasome activation by intracellular LPS independent of TLR4. Science *341*, 1246–1249.

Kim, S.U., and de Vellis, J. (2005). Microglia in health and disease. J. Neurosci. Res. *81*, 302–313.

Kim, H.Y., Lee, H.J., Chang, Y.J., Pichavant, M., Shore, S.A., Fitzgerald, K.A., Iwakura, Y., Israel, E., Bolger, K., Faul, J., et al. (2014). Interleukin-17-producing innate lymphoid cells and the NLRP3 inflammasome facilitate obesity-associated airway hyperreactivity. Nat. Med. *20*, 54–61.

Koch, U., and Radtke, F. (2011). Mechanisms of T cell development and transformation. Annu. Rev. Cell Dev. Biol. *27*, 539–562.

Kofoed, E.M., and Vance, R.E. (2011). Innate immune recognition of bacterial ligands by NAIPs determines inflammasome specificity. Nature *477*, 592–595.

Kovarova, M., Hesker, P.R., Jania, L., Nguyen, M., Snouwaert, J.N., Xiang, Z., Lommatzsch, S.E., Huang, M.T., Ting, J.P., and Koller, B.H. (2012). NLRP1-dependent pyroptosis leads to acute lung injury and morbidity in mice. J. Immunol. *189*, 2006–2016.

Kuemmerle-Deschner, J.B., Hachulla, E., Cartwright, R., Hawkins, P.N., Tran, T.A., Bader-Meunier, B., Hoyer, J., Gattorno, M., Gul, A., Smith, J., et al. (2011). Two-year results from an open-label, multicentre, phase III study evaluating the safety and efficacy of canakinumab in patients with cryopyrin-associated periodic syndrome across different severity phenotypes. Ann. Rheum. Dis. *70*, 2095–2102.

Lamkanfi, M. (2011). Emerging inflammasome effector mechanisms. Nat. Rev. Immunol. *11*, 213–220.

Lamkanfi, M., and Dixit, V.M. (2011). Modulation of inflammasome pathways by bacterial and viral pathogens. J. Immunol. *187*, 597–602.

Lamkanfi, M., and Dixit, V.M. (2012). Inflammasomes and their roles in health and disease. Annu. Rev. Cell Dev. Biol. *28*, 137–161.

Lamkanfi, M., Sarkar, A., Vande Walle, L., Vitari, A.C., Amer, A.O., Wewers, M.D., Tracey, K.J., Kanneganti, T.D., and Dixit, V.M. (2010). Inflammasome-dependent release of the alarmin HMGB1 in endotoxemia. J. Immunol. *185*, 4385–4392.

Larsen, C.M., Faulenbach, M., Vaag, A., Vølund, A., Ehses, J.A., Seifert, B., Mandrup-Poulsen, T., and Donath, M.Y. (2007). Interleukin-1-receptor antagonist in type 2 diabetes mellitus. N. Engl. J. Med. *356*, 1517–1526.

Lin, K.M., Hu, W., Troutman, T.D., Jennings, M., Brewer, T., Li, X., Nanda, S., Cohen, P., Thomas, J.A., and Pasare, C. (2014). IRAK-1 bypasses priming and directly links TLRs to rapid NLRP3 inflammasome activation. Proc. Natl. Acad. Sci. USA *111*, 775–780.

Lopez-Castejon, G., Luheshi, N.M., Compan, V., High, S., Whitehead, R.C., Flitsch, S., Kirov, A., Prudovsky, I., Swanton, E., and Brough, D. (2013). Deubiquitinases regulate the activity of caspase-1 and interleukin-1β secretion via assembly of the inflammasome. J. Biol. Chem. *288*, 2721–2733.

Lu, B., Nakamura, T., Inouye, K., Li, J., Tang, Y., Lundbäck, P., Valdes-Ferrer, S.I., Olofsson, P.S., Kalb, T., Roth, J., et al. (2012). Novel role of PKR in inflammasome activation and HMGB1 release. Nature *488*, 670–674.

Lu, A., Magupalli, V.G., Ruan, J., Yin, Q., Atianand, M.K., Vos, M.R., Schröder, G.F., Fitzgerald, K.A., Wu, H., and Egelman, E.H. (2014). Unified polymerization mechanism for the assembly of ASC-dependent inflammasomes. Cell *156*, 1193–1206.

Mariathasan, S., Newton, K., Monack, D.M., Vucic, D., French, D.M., Lee, W.P., Roose-Girma, M., Erickson, S., and Dixit, V.M. (2004). Differential activation of the inflammasome by caspase-1 adaptors ASC and Ipaf. Nature *430*, 213–218.

Marneros, A.G. (2013). NLRP3 inflammasome blockade inhibits VEGF-A-induced age-related macular degeneration. Cell Rep. *4*, 945–958.

Martinon, F., Burns, K., and Tschopp, J. (2002). The inflammasome: a molecular platform triggering activation of inflammatory caspases and processing of proIL-beta. Mol. Cell *10*, 417–426.

Masters, S.L., Dunne, A., Subramanian, S.L., Hull, R.L., Tannahill, G.M., Sharp, F.A., Becker, C., Franchi, L., Yoshihara, E., Chen, Z., et al. (2010). Activation of the NLRP3 inflammasome by islet amyloid polypeptide provides a mechanism for enhanced IL-1β in type 2 diabetes. Nat. Immunol. *11*, 897–904.

Masters, S.L., Gerlic, M., Metcalf, D., Preston, S., Pellegrini, M., O'Donnell, J.A., McArthur, K., Baldwin, T.M., Chevrier, S., Nowell, C.J., et al. (2012). NLRP1 inflammasome activation induces pyroptosis of hematopoietic progenitor cells. Immunity *37*, 1009–1023.

Miao, E.A., Alpuche-Aranda, C.M., Dors, M., Clark, A.E., Bader, M.W., Miller, S.I., and Aderem, A. (2006). Cytoplasmic flagellin activates caspase-1 and secretion of interleukin 1beta via Ipaf. Nat. Immunol. *7*, 569–575.

Miao, E.A., Leaf, I.A., Treuting, P.M., Mao, D.P., Dors, M., Sarkar, A., Warren, S.E., Wewers, M.D., and Aderem, A. (2010a). Caspase-1-induced pyroptosis is an innate immune effector mechanism against intracellular bacteria. Nat. Immunol. *11*, 1136–1142.

Miao, E.A., Mao, D.P., Yudkovsky, N., Bonneau, R., Lorang, C.G., Warren, S.E., Leaf, I.A., and Aderem, A. (2010b). Innate immune detection of the type III secretion apparatus through the NLRC4 inflammasome. Proc. Natl. Acad. Sci. USA *107*, 3076–3080.

Misawa, T., Takahama, M., Kozaki, T., Lee, H., Zou, J., Saitoh, T., and Akira, S. (2013). Microtubule-driven spatial arrangement of mitochondria promotes activation of the NLRP3 inflammasome. Nat. Immunol. *14*, 454–460.

Moayeri, M., Crown, D., Newman, Z.L., Okugawa, S., Eckhaus, M., Cataisson, C., Liu, S., Sastalla, I., and Leppla, S.H. (2010). Inflammasome sensor Nlrp1b-dependent resistance to anthrax is mediated by caspase-1, IL-1 signaling and neutrophil recruitment. PLoS Pathog. *6*, e1001222.

Muñoz-Planillo, R., Kuffa, P., Martínez-Colón, G., Smith, B.L., Rajendiran, T.M., and Núñez, G. (2013). K^+ efflux is the common trigger of NLRP3 inflammasome activation by bacterial toxins and particulate matter. Immunity *38*, 1142–1153.

Nakahira, K., Haspel, J.A., Rathinam, V.A., Lee, S.J., Dolinay, T., Lam, H.C., Englert, J.A., Rabinovitch, M., Cernadas, M., Kim, H.P., et al. (2011). Autophagy proteins regulate innate immune responses by inhibiting the release of mitochondrial DNA mediated by the NALP3 inflammasome. Nat. Immunol. *12*, 222–230.

Neven, B., Marvillet, I., Terrada, C., Ferster, A., Boddaert, N., Couloignier, V., Pinto, G., Pagnier, A., Bodemer, C., Bodaghi, B., et al. (2010). Long-term efficacy of the interleukin-1 receptor antagonist anakinra in ten patients with neonatal-onset multisystem inflammatory disease/chronic infantile neurologic, cutaneous, articular syndrome. Arthritis Rheum. *62*, 258–267.

Paludan, S.R., and Bowie, A.G. (2013). Immune sensing of DNA. Immunity *38*, 870–880.

Pétrilli, V., Papin, S., Dostert, C., Mayor, A., Martinon, F., and Tschopp, J. (2007). Activation of the NALP3 inflammasome is triggered by low intracellular potassium concentration. Cell Death Differ. *14*, 1583–1589.

Py, B.F., Kim, M.S., Vakifahmetoglu-Norberg, H., and Yuan, J. (2013). Deubiquitination of NLRP3 by BRCC3 critically regulates inflammasome activity. Mol. Cell *49*, 331–338.

Qu, Y., Misaghi, S., Izrael-Tomasevic, A., Newton, K., Gilmour, L.L., Lamkanfi, M., Louie, S., Kayagaki, N., Liu, J., Kömüves, L., et al. (2012). Phosphorylation of NLRC4 is critical for inflammasome activation. Nature *490*, 539–542.

Rathinam, V.A., Jiang, Z., Waggoner, S.N., Sharma, S., Cole, L.E., Waggoner, L., Vanaja, S.K., Monks, B.G., Ganesan, S., Latz, E., et al. (2010). The AIM2 inflammasome is essential for host defense against cytosolic bacteria and DNA viruses. Nat. Immunol. *11*, 395–402.

Rathinam, V.A., Vanaja, S.K., Waggoner, L., Sokolovska, A., Becker, C., Stuart, L.M., Leong, J.M., and Fitzgerald, K.A. (2012). TRIF licenses caspase-11-dependent NLRP3 inflammasome activation by gram-negative bacteria. Cell *150*, 606–619.

Rayamajhi, M., Zak, D.E., Chavarria-Smith, J., Vance, R.E., and Miao, E.A. (2013). Cutting edge: Mouse NAIP1 detects the type III secretion system needle protein. J. Immunol. *191*, 3986–3989.

Riedl, S.J., and Salvesen, G.S. (2007). The apoptosome: signalling platform of cell death. Nat. Rev. Mol. Cell Biol. *8*, 405–413.

Sastalla, I., Crown, D., Masters, S.L., McKenzie, A., Leppla, S.H., and Moayeri, M. (2013). Transcriptional analysis of the three Nlrp1 paralogs in mice. BMC Genomics *14*, 188.

Sauer, J.D., Witte, C.E., Zemansky, J., Hanson, B., Lauer, P., and Portnoy, D.A. (2010). Listeria monocytogenes triggers AIM2-mediated pyroptosis upon infrequent bacteriolysis in the macrophage cytosol. Cell Host Microbe *7*, 412–419.

Schroder, K., Sagulenko, V., Zamoshnikova, A., Richards, A.A., Cridland, J.A., Irvine, K.M., Stacey, K.J., and Sweet, M.J. (2012). Acute lipopolysaccharide priming boosts inflammasome activation independently of inflammasome sensor induction. Immunobiology *217*, 1325–1329.

Shimada, K., Crother, T.R., Karlin, J., Dagvadorj, J., Chiba, N., Chen, S., Ramanujan, V.K., Wolf, A.J., Vergnes, L., Ojcius, D.M., et al. (2012). Oxidized mitochondrial DNA activates the NLRP3 inflammasome during apoptosis. Immunity *36*, 401–414.

Simard, A.R., Soulet, D., Gowing, G., Julien, J.P., and Rivest, S. (2006). Bone marrow-derived microglia play a critical role in restricting senile plaque formation in Alzheimer's disease. Neuron *49*, 489–502.

Stack, J.H., Beaumont, K., Larsen, P.D., Straley, K.S., Henkel, G.W., Randle, J.C., and Hoffman, H.M. (2005). IL-converting enzyme/caspase-1 inhibitor VX-765 blocks the hypersensitive response to an inflammatory stimulus in monocytes from familial cold autoinflammatory syndrome patients. J. Immunol. *175*, 2630–2634.

Stienstra, R., van Diepen, J.A., Tack, C.J., Zaki, M.H., van de Veerdonk, F.L., Perera, D., Neale, G.A., Hooiveld, G.J., Hijmans, A., Vroegrijk, I., et al. (2011). Inflammasome is a central player in the induction of obesity and insulin resistance. Proc. Natl. Acad. Sci. USA *108*, 15324–15329.

Strowig, T., Henao-Mejia, J., Elinav, E., and Flavell, R. (2012). Inflammasomes in health and disease. Nature *481*, 278–286.

Subramanian, N., Natarajan, K., Clatworthy, M.R., Wang, Z., and Germain, R.N. (2013). The adaptor MAVS promotes NLRP3 mitochondrial localization and inflammasome activation. Cell *153*, 348–361.

Takeuchi, O., and Akira, S. (2010). Pattern recognition receptors and inflammation. Cell *140*, 805–820.

Tarallo, V., Hirano, Y., Gelfand, B.D., Dridi, S., Kerur, N., Kim, Y., Cho, W.G., Kaneko, H., Fowler, B.J., Bogdanovich, S., et al. (2012). DICER1 loss and Alu RNA induce age-related macular degeneration via the NLRP3 inflammasome and MyD88. Cell *149*, 847–859.

Ter Haar, N., Lachmann, H., Özen, S., Woo, P., Uziel, Y., Modesto, C., Koné-Paut, I., Cantarini, L., Insalaco, A., Neven, B., et al.; Paediatric Rheumatology International Trials Organisation (PRINTO) and the Eurofever/Eurotraps Projects (2013). Treatment of autoinflammatory diseases: results from the Eurofever Registry and a literature review. Ann. Rheum. Dis. *72*, 678–685.

Terra, J.K., Cote, C.K., France, B., Jenkins, A.L., Bozue, J.A., Welkos, S.L., LeVine, S.M., and Bradley, K.A. (2010). Cutting edge: resistance to Bacillus anthracis infection mediated by a lethal toxin sensitive allele of Nalp1b/Nlrp1b. J. Immunol. *184*, 17–20.

Van Opdenbosch, N., Gurung, P., Vande Walle, L., Fossoul, A., Kanneganti, T.D., and Lamkanfi, M. (2014). Activation of the NLRP1b inflammasome independently of ASC-mediated caspase-1 autoproteolysis and speck formation. Nat. Commun. *5*, 3209.

Vandanmagsar, B., Youm, Y.H., Ravussin, A., Galgani, J.E., Stadler, K., Mynatt, R.L., Ravussin, E., Stephens, J.M., and Dixit, V.D. (2011). The NLRP3 inflammasome instigates obesity-induced inflammation and insulin resistance. Nat. Med. *17*, 179–188.

von Moltke, J., Trinidad, N.J., Moayeri, M., Kintzer, A.F., Wang, S.B., van Rooijen, N., Brown, C.R., Krantz, B.A., Leppla, S.H., Gronert, K., and Vance, R.E. (2012). Rapid induction of inflammatory lipid mediators by the inflammasome in vivo. Nature *490*, 107–111.

Wang, S., Miura, M., Jung, Y.K., Zhu, H., Li, E., and Yuan, J. (1998). Murine caspase-11, an ICE-interacting protease, is essential for the activation of ICE. Cell *92*, 501–509.

Wen, H., Gris, D., Lei, Y., Jha, S., Zhang, L., Huang, M.T., Brickey, W.J., and Ting, J.P. (2011). Fatty acid-induced NLRP3-ASC inflammasome activation interferes with insulin signaling. Nat. Immunol. *12*, 408–415.

Wu, J., Fernandes-Alnemri, T., and Alnemri, E.S. (2010). Involvement of the AIM2, NLRC4, and NLRP3 inflammasomes in caspase-1 activation by Listeria monocytogenes. J. Clin. Immunol. *30*, 693–702.

Yang, J., Zhao, Y., Shi, J., and Shao, F. (2013). Human NAIP and mouse NAIP1 recognize bacterial type III secretion needle protein for inflammasome activation. Proc. Natl. Acad. Sci. USA *110*, 14408–14413.

Zhang, W., Cai, Y., Xu, W., Yin, Z., Gao, X., and Xiong, S. (2013). AIM2 facilitates the apoptotic DNA-induced systemic lupus erythematosus via arbitrating macrophage functional maturation. J. Clin. Immunol. *33*, 925–937.

Zhao, Y., Yang, J., Shi, J., Gong, Y.N., Lu, Q., Xu, H., Liu, L., and Shao, F. (2011). The NLRC4 inflammasome receptors for bacterial flagellin and type III secretion apparatus. Nature *477*, 596–600.

Zhou, R., Tardivel, A., Thorens, B., Choi, I., and Tschopp, J. (2010). Thioredoxin-interacting protein links oxidative stress to inflammasome activation. Nat. Immunol. *11*, 136–140.

Zhou, R., Yazdi, A.S., Menu, P., and Tschopp, J. (2011). A role for mitochondria in NLRP3 inflammasome activation. Nature *469*, 221–225.

Cell

Broadly Neutralizing Antibodies and Viral Inducers Decrease Rebound from HIV-1 Latent Reservoirs in Humanized Mice

Ariel Halper-Stromberg,[1] Ching-Lan Lu,[1,2] Florian Klein,[1] Joshua A. Horwitz,[1] Stylianos Bournazos,[3] Lilian Nogueira,[1] Thomas R. Eisenreich,[1] Cassie Liu,[1] Anna Gazumyan,[1] Uwe Schaefer,[4] Rebecca C. Furze,[5] Michael S. Seaman,[6] Rab Prinjha,[5] Alexander Tarakhovsky,[4] Jeffrey V. Ravetch,[3] and Michel C. Nussenzweig[1,7,*]

[1]Laboratory of Molecular Immunology, The Rockefeller University, New York, NY 10065, USA
[2]Weill Cornell Medical College, New York, NY 10065, USA
[3]Laboratory of Molecular Genetics and Immunology, The Rockefeller University, New York, NY 10065, USA
[4]Laboratory of Lymphocyte Signaling, The Rockefeller University, New York, NY 10065, USA
[5]Epinova DPU, Immuno-Inflammation Therapy Area, Medicines Research Centre, GlaxoSmithKline, Stevenage SG1 2NY, UK
[6]Beth Israel Deaconess Medical Center, Boston, MA 02215, USA
[7]Howard Hughes Medical Institute
*Correspondence: nussen@rockefeller.edu
http://dx.doi.org/10.1016/j.cell.2014.07.043

SUMMARY

Latent reservoirs of HIV-1-infected cells are refractory to antiretroviral therapies (ART) and remain the major barrier to curing HIV-1. Because latently infected cells are long-lived, immunologically invisible, and may undergo homeostatic proliferation, a "shock and kill" approach has been proposed to eradicate this reservoir by combining ART with inducers of viral transcription. However, all attempts to alter the HIV-1 reservoir in vivo have failed to date. Using humanized mice, we show that broadly neutralizing antibodies (bNAbs) can interfere with establishment of a silent reservoir by Fc-FcR-mediated mechanisms. In established infection, bNAbs or bNAbs plus single inducers are ineffective in preventing viral rebound. However, bNAbs plus a combination of inducers that act by independent mechanisms synergize to decrease the reservoir as measured by viral rebound. Thus, combinations of inducers and bNAbs constitute a therapeutic strategy that impacts the establishment and maintenance of the HIV-1 reservoir in humanized mice.

INTRODUCTION

HIV-1 infection can be suppressed with combination antiretroviral therapy (ART). However, therapy must be maintained for the life of the individual because even years of ART does not eliminate a reservoir of latently infected cells harboring replication-competent provirus (Siliciano et al., 2003). As a result, ART interruption produces rapid viral rebound (Davey et al., 1999). One strategy proposed to eliminate latent viruses involves reversing their latent state using agents that induce HIV-1 RNA synthesis under the cover of ART (Deeks, 2012). However, all attempts to alter the reservoir by intensifying ART with additional antiretroviral drugs (Dinoso et al., 2009; Gandhi et al., 2010) or by administering viral inducers in the presence of ART have failed to date (Archin et al., 2014; Dybul et al., 2002; Lafeuillade et al., 2001; Prins et al., 1999).

Like ART, broadly neutralizing antibodies (bNAbs) against HIV-1 can completely suppress viremia in HIV-1-infected humanized mice (hu-mice) (Horwitz et al., 2013; Klein et al., 2012b) and SHIV-infected macaques (Barouch et al., 2013; Shingai et al., 2013). Although the composition of the reservoir is ill defined and may differ between ART and antibody treatments, discontinuation of ART or bNAb therapy in hu-mice and macaques results in viral rebound, indicating persistence of a functionally silent pool of cells harboring replication-competent virus. Moreover, the relative frequency of latently infected $CD4^+$ T cells as measured by ex vivo reactivation is similar in ART-suppressed hu-mice and humans (Chun et al., 1997; Denton et al., 2012; Finzi et al., 1997; Marsden et al., 2012; Wong et al., 1997). Thus, antibodies and ART control HIV-1 infection in hu-mice but allow persistence of a latent reservoir.

Unlike ART, however, antibodies can engage the host immune system by virtue of their Fc effector domains (Nimmerjahn and Ravetch, 2008) and thereby accelerate clearance of cell-free virus (Igarashi et al., 1999), induce antibody-dependent cytotoxicity to kill infected cells (Bonsignori et al., 2012; Chung et al., 2011; Forthal et al., 2013; Forthal et al., 2001; Jost and Altfeld, 2013; Sun et al., 2011), and produce immune complexes that activate dendritic cells to become potent antigen-presenting cells (Dhodapkar et al., 2005). Finally, some classes of bNAbs can prevent cell-cell transmission of HIV-1(Abela et al., 2012; Malbec et al., 2013), whereas ART's activity in this regard is still debated (Agosto et al., 2014; Schiffner et al., 2013; Sigal et al., 2011).

Here, we examine the effects of bNAbs on the establishment of the reservoir and on its maintenance in the presence of inducers of viral transcription by measuring viral rebound. We find that bNAbs can interfere with the establishment of the

reservoir by a mechanism that depends on their ability to bind to Fc receptors and that bNAbs plus a combination of inducers can reduce viral rebound from the reservoir in established infections in hu-mice.

RESULTS

Postexposure Prophylaxis with bNAbs

The ART-resistant reservoir is established early in infection, as evidenced by postexposure prophylaxis experiments in humans and macaques (Landovitz and Curry, 2009; Lifson et al., 2000; Tsai et al., 1998; Tsai et al., 1995; Whitney et al., 2014). Postexposure prophylaxis with ART or previous-generation bNAbs is only effective when administered within 24 hr of intravenous exposure (Ferrantelli et al., 2007; Landovitz and Curry, 2009; Lifson et al., 2000; Nishimura et al., 2003; Tsai et al., 1995, 1998). To determine whether the current generation of more potent bNAbs can abort the establishment of a latent HIV-1 reservoir at later time points, we performed postexposure prophylaxis experiments in hu-mice (Figure 1A). Mice were infected with HIV-1_{YU2} (150 ng p24) by intraperitoneal injection and were treated with either ART (raltegravir, emtricitabine, tenofovir) (Denton et al., 2012; Nischang et al., 2012) or a tri-mix of bNAbs (3BNC117, 10-1074, and PG16) (Horwitz et al., 2013) 4 or 8 days after infection, when viremia was already detectable in 51 of 70 mice. Plasma viremia varied from undetectable to 2.70×10^6 viral RNA copies/ml at 4 days after infection (Figures 1B–1E and Data S1 available online). In the absence of therapy, 14 out of 15 mice in the control group developed sustained plasma viremia, ranging from 2.48×10^3 to 4.19×10^6 copies/ml (Figure 1B).

Doses of ART and antibodies were chosen on the basis of their therapeutic efficacy in chronic HIV-1 infection in hu-mice (Denton et al., 2012; Horwitz et al., 2013; Klein et al., 2012b; Nischang et al., 2012). ART was administered in the food for up to 40 days, starting 4 days after infection (Denton et al., 2012; Nischang et al., 2012). Antibodies were administered subcutaneously with a loading dose of 3 mg per mouse and three to five subsequent doses of 1.5 mg each, spaced 3–4 days apart (Figure 1A). Consistent with human and macaque studies, 18 of 22 mice treated with ART showed viremia after ART termination, demonstrating that this form of therapy is relatively ineffective at preventing reservoir development in hu-mice when administered 4 days after infection (Figure 1C). Among the 18 viremic mice, viremia was first detected 28–84 days after ART termination (Figures 1C and S1). In contrast, 10 of 21 hu-mice treated with antibodies 4 days after infection showed viremia by the terminal point ($p = 0.027$, Figure 1F), and for 9 of these 10 viremic mice, the first detectable viremia occurred 74–107 days after the last antibody injection (Figures 1D and S1 and Data S1A). The delay in viral rebound observed for mice treated with antibody at day 4 was statistically significant compared to ART-treated mice (Figure S1). The mice that rebounded showed a geometric mean antibody concentration at rebound of 0.46 μg/ml. However, sustained inhibitory antibody levels did not account for the 11 mice that did not rebound, all of which had antibody levels $\leq$ 0.50 μg/ml by termination (Data S1C). In contrast to bNAb treatment at day 4, bNAb treatment after 8 days was far less effective, resulting in viremia in 10 of the 11 treated mice 44–58 days after the last antibody injection (Figures 1E and 1F and Data S1B).

Mice in the early treatment group that failed to show detectable plasma viremia were further examined for the presence of human $CD4^+$ T cells and cell-associated HIV-1 RNA and DNA in the spleen. We found that mice that failed to develop sustained plasma viremia had similar percentages of $CD4^+$ T cells relative to infected controls, which correlated with absolute $CD4^+$ T cell levels (Figures 1G and S2). Therefore, differences in $CD4^+$ T cell levels are unlikely to account for the observed differences between viremic and aviremic mice (Figure 1G). Moreover, T-cell-associated HIV-1 RNA levels were consistent with plasma viral loads, with mice that remained aviremic having either undetectable or lower cell-associated HIV-1 RNA than mice that developed sustained viremia (Figure 1H).

We measured cell-associated viral DNA as an imperfect surrogate of the HIV-1 reservoir. HIV-1 DNA is thought to overestimate the reservoir because it fails to exclude damaged or incomplete viral sequences that cannot be reactivated (Ho et al., 2013). In addition, the overall number of cells assayed in mice is limited and therefore the assay is not very sensitive. Nevertheless, we found HIV-1 DNA measurements to be consistent with each mouse's rebound status (Figure 1I). We conclude that bNAbs can interfere with the establishment of the latent HIV-1 reservoir in hu-mice, as determined by the significant delay in viral rebound.

Fc Receptor Binding Is Required for bNAb Activity

To determine whether the efficacy of bNAbs is dependent on the antibodies' ability to engage components of the immune system through their Fc domains, we repeated the day 4 postexposure prophylaxis experiments using the same tri-mix of bNAbs carrying Fc region mutations that abrogate both human and mouse Fc-receptor binding (G236R/L328R; GRLR, herein referred to as FcR^{null}) (Horton et al., 2010). Despite equivalent neutralizing activity in TZM-bl assays (Pietzsch et al., 2012), FcR^{null} antibodies were far less potent than controls in vivo (Figure 2 and Data S2). Mice treated with FcR^{null} tri-mix initially suppressed viremia at the same rate as the wild-type antibody-treated mice (Figure 2A). However, 9 of 15 mice receiving postexposure prophylaxis with the FcR^{null} tri-mix showed viral rebound by 44 days after the last antibody injection. In contrast, 44 days after the last injection of control antibodies, only 1 of 21 mice showed rebound viremia ($p = 0.0004$). Not only was the delay in viral rebound significantly reduced for FcR^{null} antibodies, but the antibody levels at the time of viral rebound were ~50-fold higher for mice receiving FcR^{null} tri-mix compared to wild-type tri-mix ($p = 0.0007$, Figure 2B). This suggests that FcR^{null} antibodies have reduced activity in vivo, and thus Fc function enhances antibody activity but is not an absolute requirement.

The escape variants to the individual bNAbs in the tri-mix used in these experiments have been documented extensively (Horwitz et al., 2013; Klein et al., 2012b). However, we have never observed HIV-1 escape by mutation to the bNAb tri-mix. Rather, viral rebound is usually due to a drop in antibody concentrations to subtherapeutic levels (Horwitz et al., 2013; Klein et al., 2012b). Because mice receiving FcR^{null} tri-mix

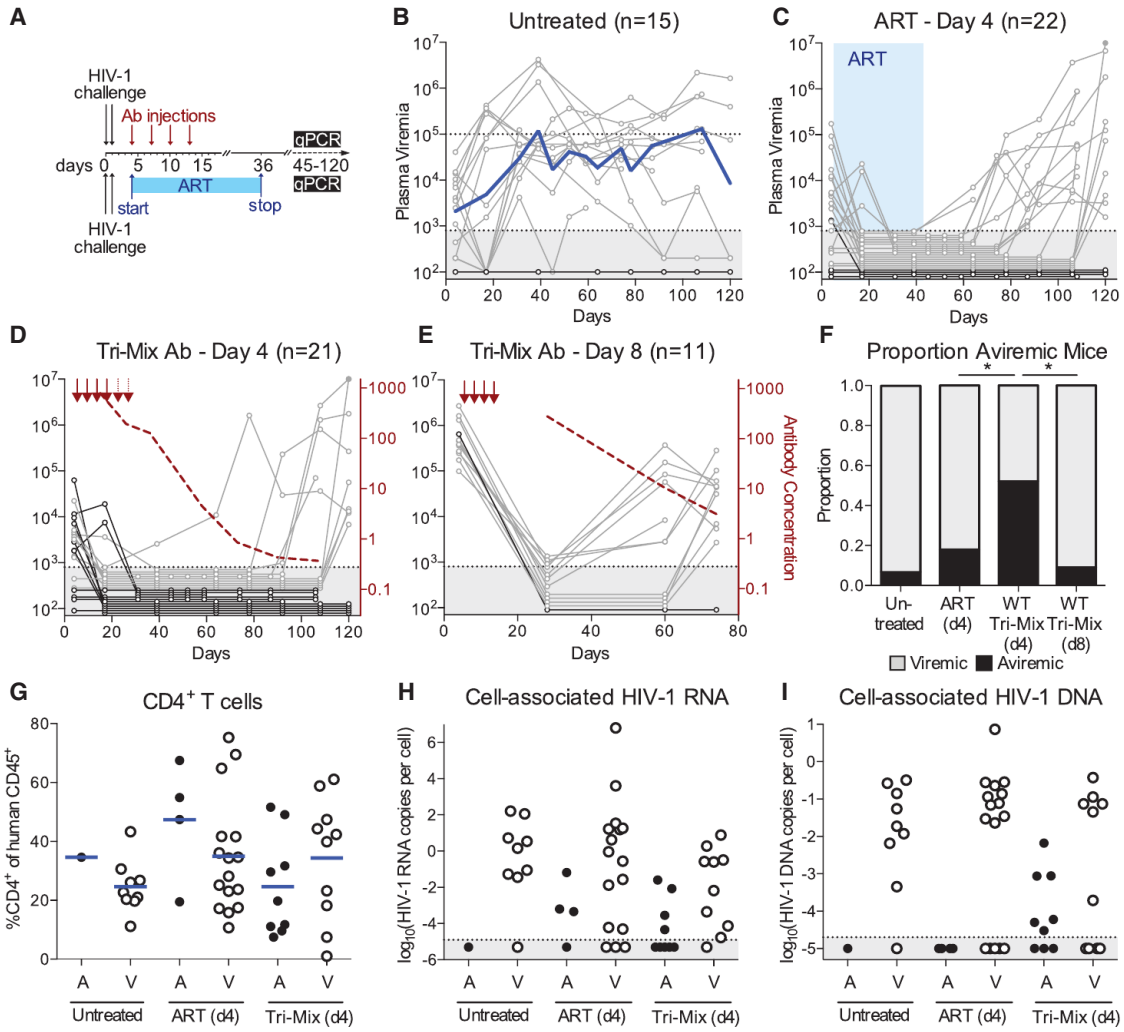

Figure 1. Postexposure Prophylaxis with bNAbs

(A) Schematic timeline for the bNAb (top) and ART (bottom) experiments.

(B) Plasma viremia for untreated mice. The x axis is days post HIV-1 challenge. The y axis is viral RNA copies/ml. Gray shading indicates values beneath the detection limit of 800 copies/ml. The blue line indicates the geometric mean of plasma viremia.

(C) Plasma viremia for ART-treated mice. Graph as in (B). The blue shading indicates the treatment period with ART.

(D) Plasma viremia for antibody-treated mice. The red arrows indicate antibody tri-mix injections. The dashed red line shows average plasma antibody concentration (μg/ml) for all mice in the group.

(E) Graph as in (D) for mice treated with antibody starting 8 days after HIV-1 challenge.

(F) The proportion of mice that were aviremic at the terminal point for each treatment group (*$p < 0.05$; Fisher's exact test).

(G) Percentage of $CD4^+$ T cells in the spleen at the terminal point measured by flow cytometry, organized by treatment group. A, aviremic; V, viremic.

(H) Cell-associated HIV-1 RNA measured in spleen T cells at the terminal point, plotted as the ratio of HIV-1 RNA to CCR5 copies for each mouse. Gray shading indicates the detection limit of 1.25×10^{-5} copies per cell.

(I) Cell-associated HIV-1 DNA measured in spleen T cells at the terminal point, plotted as the ratio of HIV-1 DNA to CCR5 copies for each mouse. Gray shading indicates the detection limit of 2.0×10^{-5} copies per cell.

Mice that died prematurely are not included in Figures 1G–1I. See also Figures S1, S2, and Data S1.

showed viral rebound in the presence of antibody concentrations far higher than the therapeutic threshold for wild-type antibodies (Figure 2B), we cloned and sequenced gp120 from the 9 mice that rebounded by day 44 to examine the mechanism for viral breakthrough in the presence of FcR^{null} tri-mix (Figure 2C). Among all 40 clones sequenced, not a single clone had the triple combination of signature mutations that confer escape to the antibody-tri-mix. We conclude that viral rebound in FcR^{null} tri-mix-treated mice is not attributable to antibody escape but, rather, reduced antibody potency. Thus, FcR^{null} mutant antibodies, which cannot engage Fc receptors, are less active in suppressing infection than their wild-type counterparts, and optimal postexposure prophylaxis by bNAbs requires engagement of Fc receptors.

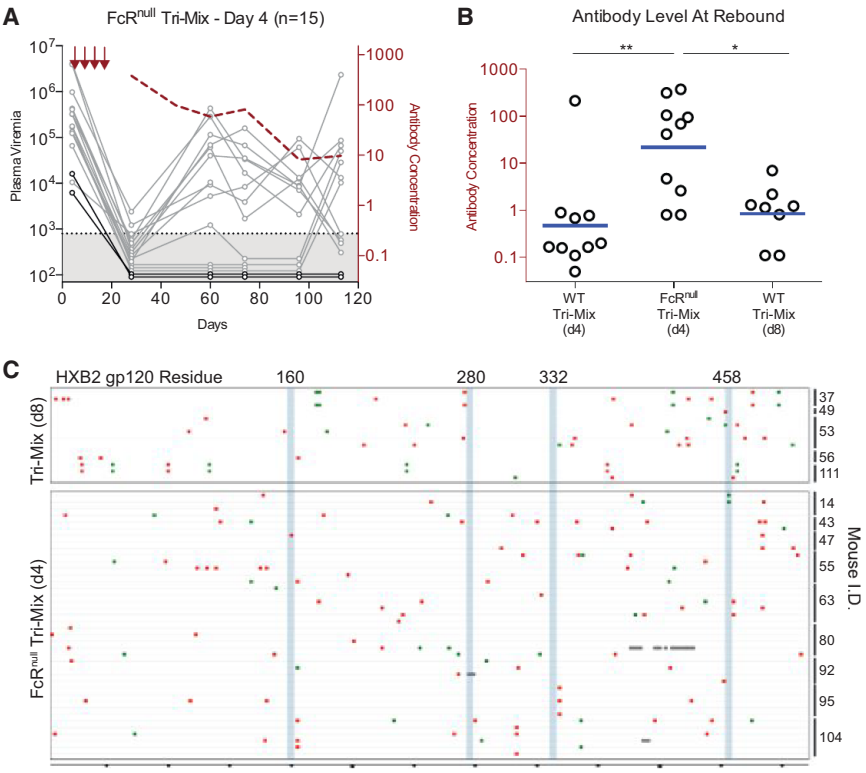

Figure 2. FcR^{null} Antibodies Suppress Viremia but Do Not Prevent Rebound

(A) Plasma viremia as in Figure 1D for mice treated with FcR^{null} tri-mix.

(B) For all viremic mice, plasma antibody concentration (μg/ml) on the day of viral rebound. Antibody levels were significantly higher in FcR^{null} tri-mix-treated mice compared to wild-type tri-mix-treated mice (*p < 0.05; **p < 0.01; Mann-Whitney U test).

(C) Sequences of gp120 cloned from plasma. Horizontal lines denote individual clones, grouped by mouse, shown on the right. Red ticks and green ticks indicate nonsynonymous and synonymous substitutions relative to gp120$_{YU2}$, respectively. Blue shading highlights sites of mutations that confer escape to the antibody tri-mix.

See also Data S2.

Combination Therapy with bNAbs and Inducers

A small number (~15%) of chronically infected hu-mice and macaques treated with antibodies fail to show rebound viremia after therapy is discontinued (Barouch et al., 2013; Horwitz et al., 2013; Klein et al., 2012a; Shingai et al., 2013). This suggests that antibodies may be able to decrease the size of the reservoir or interfere with its maintenance in established infections. To determine whether agents that induce viral transcription from latently infected cells can enhance this effect, we combined antibody therapy with viral inducers (Figure 3 and Data S3).

Hu-mice with established HIV-1$_{YU2}$ infections (viremia ranging from 4.70 × 10^3–7.96 × 10^5 copies/ml at 2–3 weeks after infection; Figures 3B–3E) were treated with tri-mix bNAbs. When plasma viremia and cell-associated HIV RNA dropped below detection, they were co-administered a viral inducer for 5–14 days and monitored for viral rebound for an additional 47–85 days (Figures 3B–3E and S3). The inducers tested were vorinostat, an HDAC inhibitor (Archin et al., 2009a; Archin et al., 2009b; Contreras et al., 2009); I-BET151, a BET protein inhibitor (Boehm et al., 2013b; Dawson et al., 2011); and CTLA, a T cell inhibitory pathway blocker (Alegre et al., 2001; Krummel and Allison, 1995). They were selected because of their documented abilities to induce HIV-1 transcription in vitro, as well as their safety and established pharmacokinetic properties in mice (Krejsgaard et al., 2010; Kwon et al., 1997; Nicodeme et al., 2010).

Hu-mice receiving antibodies plus vorinostat showed no significant differences in viral rebound compared to hu-mice receiving antibody alone (Figures 3B and 3C and Data S3). The same result was seen for hu-mice treated with antibodies plus I-BET151 or CTLA (Figures 3D and 3E and Data S3). All 10 mice that received antibody therapy plus vorinostat showed viral rebound when the antibody dropped below therapeutic levels. Of 12 mice that received antibody therapy plus I-BET151, 11 had viral rebound, and 10 of 11 mice that received antibody plus CTLA showed viral rebound. In total, of 33 mice that received antibody plus a single inducer, 31 showed viral rebound. In comparison, of 25 mice that received antibody therapy alone, 22 rebounded after the level of passively administered antibody decayed below the therapeutic threshold (p = 0.64, Fisher's exact test).

To determine whether a combination of inducers might be more effective than a single inducer, we administered all three inducers simultaneously (Figure 4 and Data S4). In the absence of antibody therapy, the combination of all three inducers did not alter the human graft and did not abort or noticeably alter active infection (Figure S4). Additionally, the human graft did not differ between groups of mice that received antibody alone versus antibody plus the combination of inducers (Figure S4). 23 mice that initially suppressed viremia on antibody therapy were treated with the inducers combination and followed for 62–105 days after the last antibody injection (Figure 4A). Only 10 of the 23 mice (43%) showed viral rebound, and the remaining 57% of mice failed to rebound, a significant decrease in rebound frequency compared to antibody alone (p = 0.0018, Fisher's exact test) or to antibody plus a single inducer (p = 0.0001, Fisher's exact test) (Figures 4B and S5).

Importantly, when compared to antibody alone, neither single inducers nor combination inducers measurably altered the frequency of CD4$^+$ T cells remaining at the end of the experiment (Figure 5A). Additionally, cell-associated viral RNA measured in splenic T cells at the terminal point supported the results from the plasma viremia levels, with mice that failed to show viral rebound in the plasma also having undetectable cell-associated viral RNA (Figure 5B).

Finally, when compared to controls, hu-mice that failed to rebound after combination antibody and inducer therapy

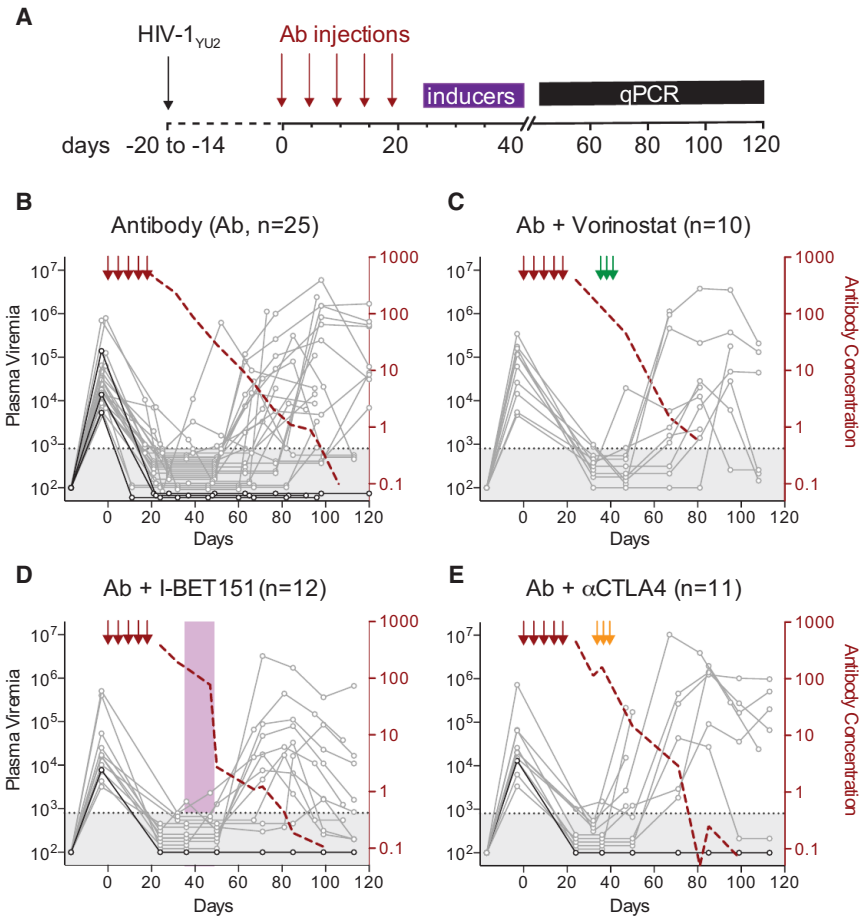

Figure 3. Rebound Viremia after Therapy with Single Inducers

(A) Schematic timeline of the experiment.

(B–D) Graphs show plasma viremia for individual mice on the left y axis and geometric mean antibody level (μg/ml) on the right y axis among all mice in the group (red). The x axis represents days relative to the first antibody injection. Antibody injections are indicated with red arrows. Mice that had rebound plasma viremia are shown in gray. Mice that failed to rebound are shown in black.

(B) Mice that received tri-mix antibodies but no inducers.

(C) Mice that received tri-mix antibodies and vorinostat (green arrows).

(D) Mice that received tri-mix antibodies and I-BET151 (purple shading).

(E) Mice that received tri-mix antibodies and CTLA (orange arrows).

See also Data S3 and Figures S3 and S5.

showed similar initial plasma viremias to mice that rebounded across all experimental groups (Figure 5C). Therefore, neither initial viremia levels nor $CD4^+$ T cell levels can account for the differences between the experimental groups.

To determine whether antibody persistence or premature termination accounted for differing viral rebound outcomes, we calculated antibody levels at the time of rebound and at the terminal point for 59 of the 63 rebounding mice. The average plasma antibody concentration at the time of viral rebound was 2.97 μg/ml (Figure 5D). Because the antibody concentrations decayed to 2.97 μg/ml at different rates in individual mice, we calculated the number of days that elapsed from when each individual mouse's antibody levels reached 2.97 μg/ml to when the mouse showed rebound viremia. Of 59 mice, 50 rebounded within 10 days (Figure 5E). Of the 18 nonrebounding mice, the average antibody concentration at the terminal point was 0.44 μg/ml, with 15 out of 18 mice having antibody concentrations <2.97 μg/ml. Furthermore, in nonrebounding mice, an average of 20.2 days elapsed from the time antibody concentrations reached 2.97 μg/ml to termination (Figure 5F). Thus, failure to rebound cannot be explained by antibody persistence or premature termination.

Finally, we could not detect viral DNA at the terminal point in the majority of mice that did not rebound, whereas the majority of mice that did rebound had detectable HIV-1 DNA, with an average of 0.09 copies per T cell (Figure 5G). We conclude that combining vorinostat, I-BET151, and CTLA with immunotherapy decreases the frequency of viral rebound in hu-mice.

DISCUSSION

Eliminating the HIV-1 reservoir in chronic infection is essential to curing the disease, but direct measurement of the latent reservoir to evaluate therapeutic eradication strategies remains difficult (Siliciano and Siliciano, 2013). Quantitative viral outgrowth assays and PCR-based assays of integrated DNA yield disparate results (Eriksson et al., 2013), in part because PCR cannot distinguish between inactive and permanently disabled proviruses, whereas outgrowth assays underestimate reservoir size (Ho et al., 2013). Indeed, the best way to determine whether a persistent reservoir exists is to measure viral rebound after discontinuing therapy in vivo.

Because the precise cellular and molecular nature of the HIV-1 reservoir is debated, it is not possible to know with certainty how its composition might differ between humans, macaques, and hu-mice. Hu-mice resemble infected humans in that they contain human cells that are infected with authentic HIV-1 (Brehm et al., 2014; Hatziioannou and Evans, 2012). In addition, the kinetics of viral rebound in hu-mice after suppression of viremia with ART resembles infected humans (Horwitz et al., 2013; Nischang et al., 2012). However, human hematopoietic reconstitution in mice is incomplete; thus, important cellular elements of the reservoir may be absent in hu-mice. Additionally, the human graft and the infection can only be maintained in mice for a limited time, making it impossible to distinguish between integrated and unintegrated forms of HIV-1 latency (Bukrinsky et al., 1991).

The macaque model is valuable because it represents an immunologically intact host that may harbor reservoirs found in

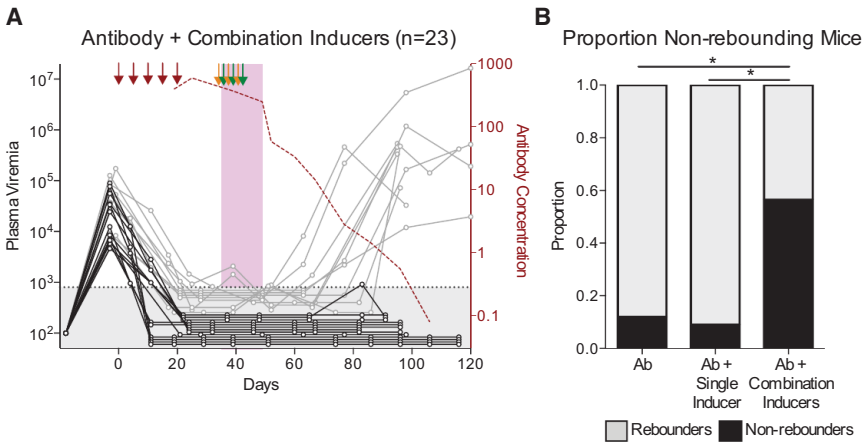

Figure 4. Combination Inducers Decrease the Incidence of Rebound Viremia

(A) Mice treated with tri-mix of antibodies and a combination of three inducers. Graph, arrows, and shading are as in Figure 3.

(B) Graph shows the proportion of mice that showed rebound viremia for each treatment group, where all mice that received antibody tri-mix and any one of the three single inducers (shown in Figures 3C–3E) are pooled together (*p < 0.05; Fisher's exact test).

See also Data S4 and Figures S3, S4, and S5.

humans, but not in mice. However, the infection in macaques involves nonhuman primate cells with SHIV or SIV, which differ significantly from HIV-1 molecularly and in their response to drug therapy. Thus, neither of the two model systems is entirely faithful to the human infection. Nevertheless, the two models have produced very similar results in both immunotherapy and prevention experiments to date (West et al., 2014). Whether our results with inducers will translate to infected humans can only be determined in clinical studies.

Despite the potential differences between available models, our experiments indicate that bNAbs can interfere with the establishment of the reservoir in humanized mice when administered early in the infection. One of the key differences between antibodies and ART is that antibodies can engage a variety of host immune effector pathways by way of their Fc receptors (Nimmerjahn and Ravetch, 2008). Consistent with this important difference, our experiments show that the mechanism by which antibodies suppress active infection is dependent on their ability to engage components of the immune system by binding to Fc receptors. Engagement of these receptors is also implicated in antibody-mediated protection against infection in mice and macaques (Hessell et al., 2007; Pietzsch et al., 2012). However, in contrast to the relatively modest effect of FcR engagement on prophylaxis against initial infection (Hessell et al., 2007; Pietzsch et al., 2012), the ~50-fold effect on the dose of antibody required to suppress viral rebound after early therapy is impressive. One potential explanation for the difference in relative antibody potency for prevention versus suppression of rebound viremia is that the effects on the latter are compounded over a far longer period of antibody therapy (McMichael et al., 2010).

One of the strategies proposed to eliminate latent viruses involves inducing their expression under the cover of ART. In theory, this would kill actively infected cells while preventing the spread of infection (Deeks, 2012). In vitro experiments indicate that silent proviruses can, in fact, be induced to become active by a variety of different agents that impact viral transcription (Bullen et al., 2014; Ho et al., 2013). However, whether reactivated cells will die by the cytopathic effect in the presence of ART has recently been called into question (Shan et al., 2012). Of the three inducers that we tested, vorinostat is the only one that has been studied in HIV-1-infected humans for this purpose. Infected individuals treated with vorinostat plus ART showed a transient increase in resting $CD4^+$ T cell-associated HIV-1 RNA but no change in plasma viremia or in the frequency of replication-competent HIV-1 within resting $CD4^+$ T cells (Archin et al., 2014; Archin et al., 2012). Our results in hu-mice are consistent with the human studies and extend them to additional candidate inducers, demonstrating that administration of a single inducer has no significant effect on the ability of the latent reservoir to produce rebound viremia. Although we could not detect an increase in viremia following administration of either single or combination inducers, antibodies were still present and may have interfered with our ability to detect the virus (Igarashi et al., 1999).

Antibody and inducer combinations have not been optimized, and we cannot explain why 43% of mice receiving antibodies plus combination inducers continue to rebound. Nor have we addressed the mechanism that would explain the difference between single and combination inducers. However, experiments using cell lines that contain artificial indicators of HIV-1 latency indicate that HDAC and BET protein inhibitors show synergy with transcriptional activators in reactivating HIV-1 in vitro (Boehm et al., 2013a; Dar et al., 2014; Quivy et al., 2002; Reuse et al., 2009). Consistent with the in vitro experiments, the combination of inducers appears to be synergistic in vivo because single inducers had no measurable effect above the background controls, whereas ~57% of the hu-mice treated with antibodies plus combination inducers failed to rebound. Irrespective of the mechanism, the reduction in viral rebound suggests that the reservoir of HIV-1-infected cells remaining after combination inducer and antibody therapy in hu-mice is significantly decreased, establishing the principle that the HIV-1 reservoir can be altered by combination therapy with antibodies and inducers in vivo.

EXPERIMENTAL PROCEDURES

Mice

NOD Rag1$^{-/-}$Il2rg^{NULL} (NOD.Cg-*Rag1^{tm1Mom} Il2rg^{tm1Wjl}*/SzJ, NRG) mice were purchased from The Jackson Laboratory. All mice were bred and maintained at the Comparative Bioscience Center of The Rockefeller University according to guidelines established by the Institutional Animal Committee. All experiments were performed with authorization from the Institutional Review Board and the IACUC at The Rockefeller University.

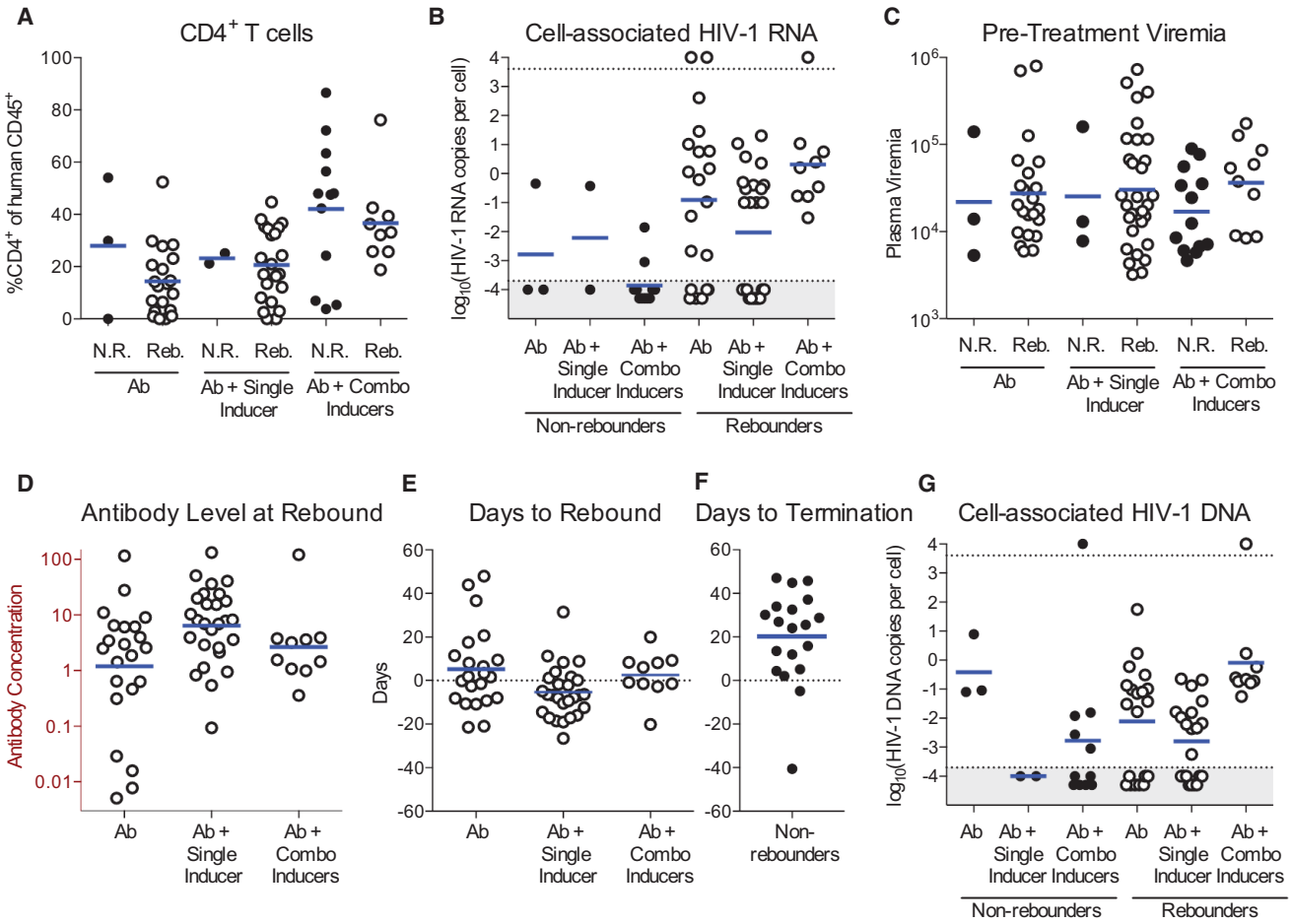

Figure 5. Antibody Persistence and Premature Termination Do Not Account for Nonrebounding

(A) Percentage of $CD4^+$ T cells at the terminal point measured in the spleen by flow cytometry, organized by treatment group and rebound status (N.R., non-rebounder; Reb., viral rebounder).

(B) Cell-associated HIV-1 RNA measured in spleen cells at terminal point, plotted as the ratio of HIV-1 RNA to CCR5 DNA copies for each mouse. Mice that had measureable HIV-1 RNA but undetectable CCR5 DNA are plotted as 10^4 copies per cell.

(C) Plasma viremia before therapy was initiated for each mouse. There was no significant difference for any individual group (Kruskal-Wallis test).

(D) The plasma antibody level (μg/ml) at the time of viral rebound for each mouse that rebounded, organized by treatment group. The mean plasma antibody level at the time of rebound was 2.97 μg/ml for all groups.

(E) For each mouse that rebounded, the number of days that elapsed from when the antibody level dropped below 2.97 μg/ml to the time of rebound.

(F) For mice that did not rebound, the number of days that elapsed from when each mouse's antibody levels dropped below 2.97 μg/ml to the terminal point.

(G) Cell-associated HIV-1 DNA measured in spleen T cells at the terminal point, plotted as the ratio of HIV-1 DNA to CCR5 DNA copies for each mouse. Mice that had measureable HIV-1 DNA but undetectable CCR5 DNA are plotted as 10^4 copies per cell.

Mice that died prematurely are not included in Figures 5A, 5B, and 5G.

Humanized Mice

Humanized mice were generated as previously described (Klein et al., 2012b). In brief, human fetal livers were obtained from Advanced Bioscience Resources (ABR). Fetal livers were homogenized and incubated in HBSS media with 0.1% collagenase IV (Sigma-Aldrich), 40 mM HEPES, 2 mM $CaCl_2$, and 2 U ml^{-1} DNAase I (Roche) for 30 min at 37°C. Hematopoietic stem cells (HSCs) were isolated from digested liver using $CD34^+$ HSC isolation kit (Stem Cell Technologies). Neonatal NRG mice (1–5 days old) were sublethally irradiated with 100 cG and injected intrahepatically with 2×10^5 human $CD34^+$ HSCs 6 hr after irradiation.

Mouse Screening for Humanization

Eight or more weeks after HSC injection, mice were screened for the presence of human lymphocytes in peripheral blood by flow cytometry. 200 μl whole blood was collected by facial vein bleed and peripheral blood mononuclear cells (PBMCs) were isolated by density gradient centrifugation using Ficoll-Paque Plus (GE Healthcare Life Sciences). PBMCs were stained with antibodies to mouse CD45-PECy7, human CD45-Pacific Orange, human CD3-Pacific Blue, human CD19-APC, human CD4-PE, human CD8-FITC, and human CD16-Alexa700 for 25 min at 4°C. Cells were washed and fixed using Cytofix/Cytoperm (BD Biosciences). Flow cytometry analysis was performed with a LSRFortessa (BD) and FlowJo software (Tree Star). For each mouse, the percentage of human lymphocytes ([100 × human $CD45^+$] / [human $CD45^+$ + mouse $CD45^+$]), termed huCD45$^+$ %, and the percentage of human $CD4^+$ T cells (100 × human $CD45^+CD3^+CD4^+$ / human $CD45^+$), termed huCD4$^+$ %, was calculated. Mice with at least 10% huCD45$^+$ and 10% huCD4$^+$ were selected for postexposure prophylaxis experiments and were infected with two doses of HIV-1_{YU2} (150 ng p24) by i.p. injections, 24 hr apart. Pretreatment

viremia was measured at 72–96 hr following the first HIV-1_{YU2} injection, and treatment was initiated 4 days following the first injection. For experiments assessing the effects of bNAbs and inducers on established infections, mice with measurable human $CD4^+$ cells by FACS were injected with two doses of HIV-1_{YU2} (150 ng p24), and pre-treatment viremia was measured 14–20 days after the first injection. Mice with plasma viral loads >3,000 RNA copies/ml were selected to receive antibody therapy. After five subcutaneous antibody injections (see below), posttreatment viremias were measured. Only mice with completely suppressed plasma viremias were selected for further analysis and to receive viral inducers.

Plasma Viral Load Measurements

300–500 μl of whole blood was collected from mice at each time point by facial vein bleed. Whole blood was spun at 300 × *g* for 10 min to separate plasma from the cellular fraction. Total RNA was extracted from 100 μl plasma using QIAmp MinElute Virus Spin Kit (QIAGEN) in combination with RNase-free DNase (QIAGEN), eluted in a 50 μl volume. HIV-1 RNA was quantified by qRT-PCR. The reaction mixture was prepared using TaqMan RNA-to-Ct 1-Step kit (Applied Biosystems), with 20 μl of eluted RNA, and a sequence specific probe targeting a conserved region of the HIV-1 *pol* gene (/HEX/5′-CCCACCAACARGCRGCCTTAACTG-3′/ZenDQ, HXB2 nt 4603 to 4626) (Integrated DNA Technologies). Forward and reverse primer sequences were 5′-TAATGGCAGCAATTTCACCA-3′ (HXB2 nt 4577-4596) and 5′-GAATGCCAAATTCCTGCTTGA-3′ (HXB2 nt 4633 to 4653), respectively. Cycle threshold (Ct) values were calibrated using standard samples with known amounts of absolute viral RNA copies. The quantitation limit was previously determined to be 800 copies/ml (Klein et al., 2012b).

Gp120 Sequencing

Gp120 cloning and sequencing was performed as previously described (Klein et al., 2012a). In brief, cDNA was synthesized from viral RNA using SuperScript III reverse transcriptase (Invitrogen Life Technologies). cDNA was amplified with Expand Long Template PCR System (Roche) with nested PCR. Primers for the first round of PCR were 5′-GGCTTAGGCATCTCCTATGGCAGGAAGAA-3′ and 5′-GGTGTGTAGTTCTGCCAATCAGGGAAGWAGCCTTGTG-3′. Primers for the second round of PCR were 5′-TAGAAAGAGCAGAAGACAGTGGCAATGA-3′ and 5′-TCATCAATGGTGGTGATGATGATGTTTTTCTCTCTGCACCACTCTTCT-3′. Gel-purified PCR amplicons were ligated into pCR4-TOPO (Invitrogen) and transformed into One Shot TOP10 cells. Individual colonies were sequenced using M13F and M13R primers. Sequences were aligned to $gp120_{YU2}$ (accession number M93258) and analyzed for mutations using Los Alamos Highlighter tool (http://www.hiv.lanl.gov/content/sequence/HIGHLIGHT/HIGHLIGHT_XYPLOT/highlighter.html).

Cell-Associated HIV-1 RNA

The cellular fraction of whole blood was resuspended in 400 μl PBS, and PBMCs were isolated by density gradient centrifugation as described above. Lymphocytes were split into two samples, one for cell-associated HIV-1 RNA measurements and one for cell-associated HIV-1 DNA measurements. Cell-associated RNA was extracted and quantified by the same procedures as described above for plasma viral RNA. The lower limit of detection was determined to be ten copies of viral RNA per qRT-PCR reaction. Cell-associated HIV-1 RNA is reported as the ratio of HIV-1 RNA copies per sample to CCR5 genomic DNA copies per equivalent sample measured in DNA extract. For terminal point measurements, spleen tissue was isolated, homogenized, and filtered through 40 μm mesh. Splenocytes were used to isolate HIV-1 RNA as described above.

Cell-Associated HIV-1 DNA

PBMCs were isolated from whole blood as described above. Splenocytes were isolated from spleen as described above. Total DNA was extracted using QIAmp DNA Blood Mini Kit (QIAGEN) and eluted in 80 μl volume. Purified DNA was quantified for HIV-1 DNA by qPCR using the primers and probe for HIV-1 RNA quantification mentioned above. Genomic human CCR5 DNA was quantified with primers 5′-GTTGGACCAAGCTATGCAGGT-3′ (forward) and 5′-AGAAGCGTTTGGCAATGTGC-3′ (reverse) and the sequence-specific probe /HEX/5′-TTGGGATGACGCACTGCTGCATCAACCCCA-3′/ZenDQ. All qPCR reactions contained 25 μl AmpliTaq Gold PCR master mix (Applied Biosystems) in 50 μl reaction volume. Reaction mixtures were as previously described (Horwitz et al., 2013). HIV-1 DNA is reported as copies per sample to CCR5 genomic copies per equivalent sample.

Terminal Graft

The presence of human lymphocytes at the terminal point was quantified from the spleen and PBMCs by flow cytometry. Isolation of PBMCs and splenocytes were as described above. Staining procedures were as described above.

Antibody Concentrations

Plasma levels of passively administered antibodies were quantified by two independent methods. gp120-specific ELISA was as previously described (Klein et al., 2012b), using 10-1074 and 3BNC117 monoclonal antibodies as standard controls. The detection limit was 0.05 μg/ml. Because PG16 does not bind gp120 and endogenously produced gp120-reactive antibodies could confound the ELISA measurement, plasma antibody levels were also quantified by TZM-bl neutralization using the Tier 2 envelopes 3301.v1.c24 and YU2. A mixture with known amounts of 3BNC117, 10-1074, and PG16 was used as standard for calibration.

Day of Viral Rebound and Antibody Level at Rebound

Plasma viremias immediately preceding and following viral rebound were plotted on a semi-log-y axis versus days postinitial antibody injection (x axis) for each individual mouse. The linear portion of viremia was fit to a line by least-squares linear regression. The day that viremia crossed the 800 copies/ml quantitation limit, termed rebound day, was calculated from the viremia fit. The antibody concentrations (as determined by TZM-bl neutralization) spanning before and after viral rebound were plotted on a semi-log-y axis versus days postinitial antibody injection. The linear portion of antibody concentrations was fit to a line by least-squares linear regression, and the antibody concentration on the rebound day was calculated from the fit.

Antiretroviral Therapy

Individual tablets of tenofovir disproxil-fumarate (TDF; Gilead Sciences), emtricitabine (FTC; Gilead Sciences), and raltegravir (RAL; Merck) were crushed into fine powder and manufactured with TestDiet 5B1Q feed (Modified LabDiet 5058 with 0.12% amoxicillin) into 1/2" irradiated pellets. Final concentrations of ART drugs in the food were 720 mg/kg TFV, 520 mg/kg FTC, and 4800 mg/kg RAL. Doses were chosen based on suppression of viremia in humanized mice as previously published (Denton et al., 2012; Nischang et al., 2012) and by pharmacokinetic analysis of these drugs in humanized mice (Roberto F. Speck, personal communication). To test potential toxicity or reduced preference for drug-supplemented food, mice were weighed daily on normal diet and then switched to ART feed and weighed daily. There were no visible signs of toxicity, and mice maintained their weights. Assuming that mice weigh 25 g and eat 4 g of food per day, the drug doses correspond to 2.88 mg/kg TFV, 83 mg/kg FTC, and 768 mg/kg RAL daily.

Antibody Therapy

Plasmids encoding 10-1074 or PG16 heavy- and light-chain Ig genes were transfected into HEK293E cells. Antibodies were isolated from tissue-culture supernatant using Protein G Sepharose 4 Fast-Flow (GE Healthcare). Antibodies were then buffer exchanged into PBS and sterile filtered using Ultrafree-CL centrifugal filters (0.22 μm; Millipore). Endotoxin was removed from antibody preparations using Triton X-114 (Sigma-Aldrich) as previously described (Aida and Pabst, 1990), and antibodies were concentrated to 10 mg/ml. Sterile, endotoxin-free 3BNC117 (20 mg/ml) was obtained from CellDex Therapeutics. All antibodies were injected subcutaneously as described.

Inducers

Vorinostat (Selleckchem) was suspended in sterile water or sterile water plus 0.5% methylcellulose, 0.1% Tween (v/v) and administered by oral gavage at doses of 60 mg/kg (Krejsgaard et al., 2010). For each mouse, three total doses were administered, spaced 48 hr apart. 100 μg doses of αCTLA4 were injected intraperitoneally (i.p.). Three total doses were administered, spaced 48 hr apart. I-BET 151 was obtained from GlaxoSmithKline and dissolved in 10%

beta-cyclodextrin, 5% DMSO in 0.9% saline and injected daily for 14 days at doses of 30 mg/kg (Dawson et al., 2011).

Statistical Analysis

Statistical analyses were performed using GraphPad Prism 6.0 for Mac OS X.

SUPPLEMENTAL INFORMATION

Supplemental Information includes five figures and four data files and can be found with this article online at http://dx.doi.org/10.1016/j.cell.2014.07.043.

AUTHOR CONTRIBUTIONS

A.H.-S. planned and performed experiments and wrote the manuscript. C.-L.L., F.K., J.A.H., and U.S. helped plan and perform experiments. S.B., L.N., and T.R.E. performed experiments. C.L. and A.G. produced monoclonal antibodies and proteins. M.S.S. performed TZM-bl neutralization measurements. R.P. and R.F. helped with experiments using I-BET151. A.T. and J.V.R. planned experiments. M.C.N. planned experiments and wrote the manuscript.

ACKNOWLEDGMENTS

We thank Roberto Speck and Renier Myburgh for help manufacturing ART feed; CellDex Therapeutics for providing 3BNC117; and all members of the Nussenzweig Laboratory for helpful discussion and advice. This work was supported by the National Institutes of Health (NIH) Medical Scientist Training Program grant T32GM07739 to the Weill Cornell/Rockefeller/Sloan-Kettering Tri-Institutional MD-PhD Program (A.H.-S.); Bill and Melinda Gates Foundation with Comprehensive Antibody Vaccine Immune Monitoring Consortium Grant 1032144 (M.S.S.); and Collaboration for AIDS Vaccine Discovery Grant OPP1033115 (M.C.N. and J.V.R.). This work was also supported, in part, by grant # 8 UL1 TR000043 from the National Center for Advancing Translational Sciences (NCATS), National Institutes of Health (NIH) Clinical and Translational Science Award (CTSA) program, Center for HIV/AIDS Vaccine Immunology and Immunogen Discovery AI100663-02 (M.C.N.), and National Institute Of Allergy and Infectious Diseases of the NIH Grants AI100148-02 and AI081677-05 (M.C.N. and J.V.R.). The content is solely the responsibility of the authors and does not necessarily represent the official views of the NIH. S.B. receives fellowship support from the American Heart Association. M.C.N. is a Howard Hughes Medical Institute Investigator. R.P. and R.F. are employees of GlaxoSmithKline (GSK).

Received: June 23, 2014
Revised: July 17, 2014
Accepted: July 29, 2014
Published: August 14, 2014

REFERENCES

Abela, I.A., Berlinger, L., Schanz, M., Reynell, L., Günthard, H.F., Rusert, P., and Trkola, A. (2012). Cell-cell transmission enables HIV-1 to evade inhibition by potent CD4bs directed antibodies. PLoS Pathog. *8*, e1002634.

Agosto, L.M., Zhong, P., Munro, J., and Mothes, W. (2014). Highly active antiretroviral therapies are effective against HIV-1 cell-to-cell transmission. PLoS Pathog. *10*, e1003982.

Aida, Y., and Pabst, M.J. (1990). Removal of endotoxin from protein solutions by phase separation using Triton X-114. J. Immunol. Methods *132*, 191–195.

Alegre, M.L., Frauwirth, K.A., and Thompson, C.B. (2001). T-cell regulation by CD28 and CTLA-4. Nat. Rev. Immunol. *1*, 220–228.

Archin, N.M., Espeseth, A., Parker, D., Cheema, M., Hazuda, D., and Margolis, D.M. (2009a). Expression of latent HIV induced by the potent HDAC inhibitor suberoylanilide hydroxamic acid. AIDS Res. Hum. Retroviruses *25*, 207–212.

Archin, N.M., Keedy, K.S., Espeseth, A., Dang, H., Hazuda, D.J., and Margolis, D.M. (2009b). Expression of latent human immunodeficiency type 1 is induced by novel and selective histone deacetylase inhibitors. AIDS *23*, 1799–1806.

Archin, N.M., Liberty, A.L., Kashuba, A.D., Choudhary, S.K., Kuruc, J.D., Crooks, A.M., Parker, D.C., Anderson, E.M., Kearney, M.F., Strain, M.C., et al. (2012). Administration of vorinostat disrupts HIV-1 latency in patients on antiretroviral therapy. Nature *487*, 482–485.

Archin, N.M., Bateson, R., Tripathy, M., Crooks, A.M., Yang, K.H., Dahl, N.P., Kearney, M.F., Anderson, E.M., Coffin, J.M., Strain, M.C., et al. (2014). HIV-1 expression within resting CD4 T cells after multiple doses of Vorinostat. J. Infect. Dis. Published online April 24, 2014. http://dx.doi.org/10.1093/infdis/jiu155.

Barouch, D.H., Whitney, J.B., Moldt, B., Klein, F., Oliveira, T.Y., Liu, J., Stephenson, K.E., Chang, H.W., Shekhar, K., Gupta, S., et al. (2013). Therapeutic efficacy of potent neutralizing HIV-1-specific monoclonal antibodies in SHIV-infected rhesus monkeys. Nature *503*, 224–228.

Boehm, D., Calvanese, V., Dar, R.D., Xing, S., Schroeder, S., Martins, L., Aull, K., Li, P.-C., Planelles, V., Bradner, J.E., et al. (2013a). BET bromodomain-targeting compounds reactivate HIV from latency via a Tat-independent mechanism. Cell Cycle *12*, 452–462.

Boehm, D., Calvanese, V., Dar, R.D., Xing, S., Schroeder, S., Martins, L., Aull, K., Li, P.C., Planelles, V., Bradner, J.E., et al. (2013b). BET bromodomain-targeting compounds reactivate HIV from latency via a Tat-independent mechanism. Cell Cycle *12*, 452–462.

Bonsignori, M., Pollara, J., Moody, M.A., Alpert, M.D., Chen, X., Hwang, K.K., Gilbert, P.B., Huang, Y., Gurley, T.C., Kozink, D.M., et al. (2012). Antibody-dependent cellular cytotoxicity-mediating antibodies from an HIV-1 vaccine efficacy trial target multiple epitopes and preferentially use the VH1 gene family. J. Virol. *86*, 11521–11532.

Brehm, M.A., Wiles, M.V., Greiner, D.L., and Shultz, L.D. (2014). Generation of improved humanized mouse models for human infectious diseases. J. Immunol. Methods. Published online March 4, 2014. http://dx.doi.org/10.1016/j.jim.2014.02.011.

Bukrinsky, M.I., Stanwick, T.L., Dempsey, M.P., and Stevenson, M. (1991). Quiescent T lymphocytes as an inducible virus reservoir in HIV-1 infection. Science *254*, 423–427.

Bullen, C.K., Laird, G.M., Durand, C.M., Siliciano, J.D., and Siliciano, R.F. (2014). New ex vivo approaches distinguish effective and ineffective single agents for reversing HIV-1 latency in vivo. Nat. Med. *20*, 425–429.

Chun, T.W., Stuyver, L., Mizell, S.B., Ehler, L.A., Mican, J.A., Baseler, M., Lloyd, A.L., Nowak, M.A., and Fauci, A.S. (1997). Presence of an inducible HIV-1 latent reservoir during highly active antiretroviral therapy. Proc. Natl. Acad. Sci. USA *94*, 13193–13197.

Chung, A.W., Isitman, G., Navis, M., Kramski, M., Center, R.J., Kent, S.J., and Stratov, I. (2011). Immune escape from HIV-specific antibody-dependent cellular cytotoxicity (ADCC) pressure. Proc. Natl. Acad. Sci. USA *108*, 7505–7510.

Contreras, X., Schweneker, M., Chen, C.S., McCune, J.M., Deeks, S.G., Martin, J., and Peterlin, B.M. (2009). Suberoylanilide hydroxamic acid reactivates HIV from latently infected cells. J. Biol. Chem. *284*, 6782–6789.

Dar, R.D., Hosmane, N.N., Arkin, M.R., Siliciano, R.F., and Weinberger, L.S. (2014). Screening for noise in gene expression identifies drug synergies. Science *344*, 1392–1396.

Davey, R.T., Bhat, N., Yoder, C., Chun, T.W., Metcalf, J.A., Dewar, R., Natarajan, V., Lempicki, R.A., Adelsberger, J.W., Miller, K.D., et al. (1999). HIV-1 and T cell dynamics after interruption of highly active antiretroviral therapy (HAART) in patients with a history of sustained viral suppression. Proc. Natl. Acad. Sci. USA *96*, 15109–15114.

Dawson, M.A., Prinjha, R.K., Dittmann, A., Giotopoulos, G., Bantscheff, M., Chan, W.I., Robson, S.C., Chung, C.W., Hopf, C., Savitski, M.M., et al. (2011). Inhibition of BET recruitment to chromatin as an effective treatment for MLL-fusion leukaemia. Nature *478*, 529–533.

Deeks, S.G. (2012). HIV: Shock and kill. Nature *487*, 439–440.

Denton, P.W., Olesen, R., Choudhary, S.K., Archin, N.M., Wahl, A., Swanson, M.D., Chateau, M., Nochi, T., Krisko, J.F., Spagnuolo, R.A., et al. (2012). Generation of HIV latency in humanized BLT mice. J. Virol. *86*, 630–634.

Dhodapkar, K.M., Kaufman, J.L., Ehlers, M., Banerjee, D.K., Bonvini, E., Koenig, S., Steinman, R.M., Ravetch, J.V., and Dhodapkar, M.V. (2005). Selective blockade of inhibitory Fcgamma receptor enables human dendritic cell maturation with IL-12p70 production and immunity to antibody-coated tumor cells. Proc. Natl. Acad. Sci. USA *102*, 2910–2915.

Dinoso, J.B., Kim, S.Y., Wiegand, A.M., Palmer, S.E., Gange, S.J., Cranmer, L., O'Shea, A., Callender, M., Spivak, A., Brennan, T., et al. (2009). Treatment intensification does not reduce residual HIV-1 viremia in patients on highly active antiretroviral therapy. Proc. Natl. Acad. Sci. USA *106*, 9403–9408.

Dybul, M., Hidalgo, B., Chun, T.W., Belson, M., Migueles, S.A., Justement, J.S., Herpin, B., Perry, C., Hallahan, C.W., Davey, R.T., et al. (2002). Pilot study of the effects of intermittent interleukin-2 on human immunodeficiency virus (HIV)-specific immune responses in patients treated during recently acquired HIV infection. J. Infect. Dis. *185*, 61–68.

Eriksson, S., Graf, E.H., Dahl, V., Strain, M.C., Yukl, S.A., Lysenko, E.S., Bosch, R.J., Lai, J., Chioma, S., Emad, F., et al. (2013). Comparative analysis of measures of viral reservoirs in HIV-1 eradication studies. PLoS Pathog. *9*, e1003174.

Ferrantelli, F., Buckley, K.A., Rasmussen, R.A., Chalmers, A., Wang, T., Li, P.L., Williams, A.L., Hofmann-Lehmann, R., Montefiori, D.C., Cavacini, L.A., et al. (2007). Time dependence of protective post-exposure prophylaxis with human monoclonal antibodies against pathogenic SHIV challenge in newborn macaques. Virology *358*, 69–78.

Finzi, D., Hermankova, M., Pierson, T., Carruth, L.M., Buck, C., Chaisson, R.E., Quinn, T.C., Chadwick, K., Margolick, J., Brookmeyer, R., et al. (1997). Identification of a reservoir for HIV-1 in patients on highly active antiretroviral therapy. Science *278*, 1295–1300.

Forthal, D.N., Landucci, G., and Daar, E.S. (2001). Antibody from patients with acute human immunodeficiency virus (HIV) infection inhibits primary strains of HIV type 1 in the presence of natural-killer effector cells. J. Virol. *75*, 6953–6961.

Forthal, D., Hope, T.J., and Alter, G. (2013). New paradigms for functional HIV-specific nonneutralizing antibodies. Curr. Opin. HIV AIDS *8*, 393–401.

Gandhi, R.T., Zheng, L., Bosch, R.J., Chan, E.S., Margolis, D.M., Read, S., Kallungal, B., Palmer, S., Medvik, K., Lederman, M.M., et al.; AIDS Clinical Trials Group A5244 team (2010). The effect of raltegravir intensification on low-level residual viremia in HIV-infected patients on antiretroviral therapy: a randomized controlled trial. PLoS Med. *7*, 7.

Hatziioannou, T., and Evans, D.T. (2012). Animal models for HIV/AIDS research. Nat. Rev. Microbiol. *10*, 852–867.

Hessell, A.J., Hangartner, L., Hunter, M., Havenith, C.E., Beurskens, F.J., Bakker, J.M., Lanigan, C.M., Landucci, G., Forthal, D.N., Parren, P.W., et al. (2007). Fc receptor but not complement binding is important in antibody protection against HIV. Nature *449*, 101–104.

Ho, Y.C., Shan, L., Hosmane, N.N., Wang, J., Laskey, S.B., Rosenbloom, D.I., Lai, J., Blankson, J.N., Siliciano, J.D., and Siliciano, R.F. (2013). Replication-competent noninduced proviruses in the latent reservoir increase barrier to HIV-1 cure. Cell *155*, 540–551.

Horton, H.M., Bernett, M.J., Peipp, M., Pong, E., Karki, S., Chu, S.Y., Richards, J.O., Chen, H., Repp, R., Desjarlais, J.R., and Zhukovsky, E.A. (2010). Fc-engineered anti-CD40 antibody enhances multiple effector functions and exhibits potent in vitro and in vivo antitumor activity against hematologic malignancies. Blood *116*, 3004–3012.

Horwitz, J.A., Halper-Stromberg, A., Mouquet, H., Gitlin, A.D., Tretiakova, A., Eisenreich, T.R., Malbec, M., Gravemann, S., Billerbeck, E., Dorner, M., et al. (2013). HIV-1 suppression and durable control by combining single broadly neutralizing antibodies and antiretroviral drugs in humanized mice. Proc. Natl. Acad. Sci. USA *110*, 16538–16543.

Igarashi, T., Brown, C., Azadegan, A., Haigwood, N., Dimitrov, D., Martin, M.A., and Shibata, R. (1999). Human immunodeficiency virus type 1 neutralizing antibodies accelerate clearance of cell-free virions from blood plasma. Nat. Med. *5*, 211–216.

Jost, S., and Altfeld, M. (2013). Control of human viral infections by natural killer cells. Annu. Rev. Immunol. *31*, 163–194.

Klein, F., Halper-Stromberg, A., Horwitz, J.A., Gruell, H., Scheid, J.F., Bournazos, S., Mouquet, H., Spatz, L.A., Diskin, R., Abadir, A., et al. (2012a). HIV therapy by a combination of broadly neutralizing antibodies in humanized mice. Nature *492*, 118–122.

Klein, F., Halper-Stromberg, A., Horwitz, J.A., Gruell, H., Scheid, J.F., Bournazos, S., Mouquet, H., Spatz, L.A., Diskin, R., Abadir, A., et al. (2012b). HIV therapy by a combination of broadly neutralizing antibodies in humanized mice. Nature *492*, 118–122.

Krejsgaard, T., Kopp, K., Ralfkiaer, E., Willumsgaard, A.E., Eriksen, K.W., Labuda, T., Rasmussen, S., Mathiesen, A.M., Geisler, C., Lauenborg, B., et al. (2010). A novel xenograft model of cutaneous T-cell lymphoma. Exp. Dermatol. *19*, 1096–1102.

Krummel, M.F., and Allison, J.P. (1995). CD28 and CTLA-4 have opposing effects on the response of T cells to stimulation. J. Exp. Med. *182*, 459–465.

Kwon, E.D., Hurwitz, A.A., Foster, B.A., Madias, C., Feldhaus, A.L., Greenberg, N.M., Burg, M.B., and Allison, J.P. (1997). Manipulation of T cell costimulatory and inhibitory signals for immunotherapy of prostate cancer. Proc. Natl. Acad. Sci. USA *94*, 8099–8103.

Lafeuillade, A., Poggi, C., Chadapaud, S., Hittinger, G., Chouraqui, M., Pisapia, M., and Delbeke, E. (2001). Pilot study of a combination of highly active antiretroviral therapy and cytokines to induce HIV-1 remission. J. Acquir. Immune Defic. Syndr. *26*, 44–55.

Landovitz, R., and Curry, J. (2009). Clinical practice. Postexposure Prophylaxis for HIV Infection. N. Engl. J. Med. *361*, 1768–1775.

Lifson, J.D., Rossio, J.L., Arnaout, R., Li, L., Parks, T.L., Schneider, D.K., Kiser, R.F., Coalter, V.J., Walsh, G., Imming, R.J., et al. (2000). Containment of simian immunodeficiency virus infection: Cellular immune responses and protection from rechallenge following transient postinoculation antiretroviral treatment. J. Virol. *74*, 2584–2593.

Malbec, M., Porrot, F., Rua, R., Horwitz, J., Klein, F., Halper-Stromberg, A., Scheid, J.F., Eden, C., Mouquet, H., Nussenzweig, M.C., and Schwartz, O. (2013). Broadly neutralizing antibodies that inhibit HIV-1 cell to cell transmission. J. Exp. Med. *210*, 2813–2821.

Marsden, M.D., Kovochich, M., Suree, N., Shimizu, S., Mehta, R., Cortado, R., Bristol, G., An, D.S., and Zack, J.A. (2012). HIV latency in the humanized BLT mouse. J. Virol. *86*, 339–347.

McMichael, A.J., Borrow, P., Tomaras, G.D., Goonetilleke, N., and Haynes, B.F. (2010). The immune response during acute HIV-1 infection: clues for vaccine development. Nat. Rev. Immunol. *10*, 11–23.

Nicodeme, E., Jeffrey, K.L., Schaefer, U., Beinke, S., Dewell, S., Chung, C.W., Chandwani, R., Marazzi, I., Wilson, P., Coste, H., et al. (2010). Suppression of inflammation by a synthetic histone mimic. Nature *468*, 1119–1123.

Nimmerjahn, F., and Ravetch, J.V. (2008). Fcgamma receptors as regulators of immune responses. Nat. Rev. Immunol. *8*, 34–47.

Nischang, M., Sutmuller, R., Gers-Huber, G., Audigé, A., Li, D., Rochat, M.-A., Baenziger, S., Hofer, U., Schlaepfer, E., Regenass, S., et al. (2012). Humanized mice recapitulate key features of HIV-1 infection: A novel concept using long-acting anti-retroviral drugs for treating HIV-1. PloS One *7*, e38853.

Nishimura, Y., Igarashi, T., Haigwood, N.L., Sadjadpour, R., Donau, O.K., Buckler, C., Plishka, R.J., Buckler-White, A., and Martin, M.A. (2003). Transfer of neutralizing IgG to macaques 6 h but not 24 h after SHIV infection confers sterilizing protection: implications for HIV-1 vaccine development. Proc. Natl. Acad. Sci. USA *100*, 15131–15136.

Pietzsch, J., Gruell, H., Bournazos, S., Donovan, B.M., Klein, F., Diskin, R., Seaman, M.S., Bjorkman, P.J., Ravetch, J.V., Ploss, A., and Nussenzweig, M.C. (2012). A mouse model for HIV-1 entry. Proc. Natl. Acad. Sci. USA *109*, 15859–15864.

Prins, J.M., Jurriaans, S., van Praag, R.M., Blaak, H., van Rij, R., Schellekens, P.T., ten Berge, I.J., Yong, S.L., Fox, C.H., Roos, M.T., et al. (1999). Immunoactivation with anti-CD3 and recombinant human IL-2 in HIV-1-infected patients on potent antiretroviral therapy. AIDS *13*, 2405–2410.

Quivy, V., Adam, E., Collette, Y., Demonte, D., Chariot, A., Vanhulle, C., Berkhout, B., Castellano, R., de Launoit, Y., Burny, A., et al. (2002). Synergistic activation of human immunodeficiency virus type 1 promoter activity by NF-kappaB and inhibitors of deacetylases: potential perspectives for the development of therapeutic strategies. J. Virol. *76*, 11091–11103.

Reuse, S., Calao, M., Kabeya, K., Guiguen, A., Gatot, J.S., Quivy, V., Vanhulle, C., Lamine, A., Vaira, D., Demonte, D., et al. (2009). Synergistic activation of HIV-1 expression by deacetylase inhibitors and prostratin: implications for treatment of latent infection. PLoS ONE *4*, e6093.

Schiffner, T., Sattentau, Q.J., and Duncan, C.J. (2013). Cell-to-cell spread of HIV-1 and evasion of neutralizing antibodies. Vaccine *31*, 5789–5797.

Shan, L., Deng, K., Shroff, N.S., Durand, C.M., Rabi, S.A., Yang, H.C., Zhang, H., Margolick, J.B., Blankson, J.N., and Siliciano, R.F. (2012). Stimulation of HIV-1-specific cytolytic T lymphocytes facilitates elimination of latent viral reservoir after virus reactivation. Immunity *36*, 491–501.

Shingai, M., Nishimura, Y., Klein, F., Mouquet, H., Donau, O.K., Plishka, R., Buckler-White, A., Seaman, M., Piatak, M., Jr., Lifson, J.D., et al. (2013). Antibody-mediated immunotherapy of macaques chronically infected with SHIV suppresses viraemia. Nature *503*, 277–280.

Sigal, A., Kim, J.T., Balazs, A.B., Dekel, E., Mayo, A., Milo, R., and Baltimore, D. (2011). Cell-to-cell spread of HIV permits ongoing replication despite antiretroviral therapy. Nature *477*, 95–98.

Siliciano, J.D., and Siliciano, R.F. (2013). HIV-1 eradication strategies: design and assessment. Curr. Opin. HIV AIDS *8*, 318–325.

Siliciano, J.D., Kajdas, J., Finzi, D., Quinn, T.C., Chadwick, K., Margolick, J.B., Kovacs, C., Gange, S.J., and Siliciano, R.F. (2003). Long-term follow-up studies confirm the stability of the latent reservoir for HIV-1 in resting CD4+ T cells. Nat. Med. *9*, 727–728.

Sun, Y., Asmal, M., Lane, S., Permar, S.R., Schmidt, S.D., Mascola, J.R., and Letvin, N.L. (2011). Antibody-dependent cell-mediated cytotoxicity in simian immunodeficiency virus-infected rhesus monkeys. J. Virol. *85*, 6906–6912.

Tsai, C.-C., Follis, K., Sabo, A., Beck, T., Grant, R., Bischofberger, N., Benveniste, R., and Black, R. (1995). Prevention of SIV infection in macaques by (R)-9-(2-phosphonylmethoxypropyl) adenine. Science *270*, 1197–1199.

Tsai, C.-C., Emau, P., Follis, K., Beck, T., Benveniste, R., Bischofberger, N., Lifson, J., and Morton, W. (1998). Effectiveness of postinoculation (R)-9-(2-phosphonylmethoxypropyl) adenine treatment for prevention of persistent simian immunodeficiency virus SIV infection depends critically on timing of initiation and duration of treatment. J. Virol. *72*, 4265–4273.

West, A.P., Jr., Scharf, L., Scheid, J.F., Klein, F., Bjorkman, P.J., and Nussenzweig, M.C. (2014). Structural insights on the role of antibodies in HIV-1 vaccine and therapy. Cell *156*, 633–648.

Whitney, J.B., Hill, A.L., Sanisetty, S., Penaloza-MacMaster, P., Liu, J., Shetty, M., Parenteau, L., Cabral, C., Shields, J., Blackmore, S., et al. (2014). Rapid seeding of the viral reservoir prior to SIV viraemia in rhesus monkeys. Nature. Published online July 20, 2014. http://dx.doi.org/10.1038/nature13594.

Wong, J.K., Hezareh, M., Günthard, H.F., Havlir, D.V., Ignacio, C.C., Spina, C.A., and Richman, D.D. (1997). Recovery of replication-competent HIV despite prolonged suppression of plasma viremia. Science *278*, 1291–1295.

Cell

Discovery of a Class of Endogenous Mammalian Lipids with Anti-Diabetic and Anti-inflammatory Effects

Mark M. Yore,[1,5] Ismail Syed,[1,5] Pedro M. Moraes-Vieira,[1] Tejia Zhang,[3,7] Mark A. Herman,[1] Edwin A. Homan,[3] Rajesh T. Patel,[2] Jennifer Lee,[1] Shili Chen,[3,7] Odile D. Peroni,[1] Abha S. Dhaneshwar,[1] Ann Hammarstedt,[4] Ulf Smith,[4] Timothy E. McGraw,[2] Alan Saghatelian,[3,6,7,*] and Barbara B. Kahn[1,6,*]

[1]Division of Endocrinology, Diabetes and Metabolism, Department of Medicine, Beth Israel Deaconess Medical Center and Harvard Medical School, Boston, MA 02215, USA

[2]Department of Biochemistry, Weill Cornell Medical College, New York, NY 10065, USA

[3]Department of Chemistry and Chemical Biology, Harvard University, Cambridge, MA 02138, USA

[4]Department of Molecular and Clinical Medicine, the Sahlgrenska Academy, University of Gothenburg, Gothenburg 41345, Sweden

[5]Co-first author

[6]Co-senior author

[7]Present address: Salk Institute for Biological Studies, Torrey Pines Road, La Jolla, CA 92037

*Correspondence: asaghatelian@salk.edu (A.S.), bkahn@bidmc.harvard.edu (B.B.K.)

http://dx.doi.org/10.1016/j.cell.2014.09.035

SUMMARY

Increased adipose tissue lipogenesis is associated with enhanced insulin sensitivity. Mice overexpressing the Glut4 glucose transporter in adipocytes have elevated lipogenesis and increased glucose tolerance despite being obese with elevated circulating fatty acids. Lipidomic analysis of adipose tissue revealed the existence of branched *f*atty *a*cid esters of *h*ydroxy *f*atty *a*cids (FAHFAs) that were elevated 16- to 18-fold in these mice. FAHFA isomers differ by the branched ester position on the hydroxy fatty acid (e.g., *p*almitic-*a*cid-9-*h*ydroxy-stearic-*a*cid, 9-PAHSA). PAHSAs are synthesized in vivo and regulated by fasting and high-fat feeding. PAHSA levels correlate highly with insulin sensitivity and are reduced in adipose tissue and serum of insulin-resistant humans. PAHSA administration in mice lowers ambient glycemia and improves glucose tolerance while stimulating GLP-1 and insulin secretion. PAHSAs also reduce adipose tissue inflammation. In adipocytes, PAHSAs signal through GPR120 to enhance insulin-stimulated glucose uptake. Thus, FAHFAs are endogenous lipids with the potential to treat type 2 diabetes.

INTRODUCTION

Obesity and type 2 diabetes (T2D) are at epidemic proportions worldwide (Hu, 2011). The major pathogenic factors underlying T2D are resistance to insulin action in peripheral tissues and dysregulated insulin secretion. The Glut4 glucose transporter is the major insulin-regulated glucose transporter and mediates glucose uptake into skeletal muscle, heart, and adipocytes in response to rising insulin after a meal (Shepherd and Kahn, 1999). In humans and rodents with obesity or T2D, Glut4 is downregulated selectively in adipose tissue (AT) and not in muscle (Shepherd and Kahn, 1999). This alters AT biology leading to systemic insulin resistance (Abel et al., 2001). Glut4 knockdown selectively in adipocytes in mice results in insulin resistance and increased T2D risk (Abel et al., 2001), whereas adipose-selective overexpression of Glut4 (AG4OX) lowers fasting glycemia and enhances glucose tolerance (Carvalho et al., 2005; Shepherd et al., 1993). These effects in AG4OX mice are mediated by glucose-dependent induction of lipogenesis in AT driven by ChREBP (Herman et al., 2012), a transcription factor that regulates both glycolysis and lipogenesis (Iizuka et al., 2004; Ma et al., 2005). ChREBP knockout in AG4OX mice completely reverses the enhanced glucose tolerance (Herman et al., 2012). Expression of ChREBP and lipogenic genes in AT is highly associated with insulin sensitivity in humans and rodents (Herman et al., 2012; Roberts et al., 2009) and increased de novo lipogenesis in AT has favorable metabolic effects including potentially increasing longevity (Bruss et al., 2010).

Elevated circulating fatty acids are generally associated with insulin resistance and glucose intolerance (Boden and Shulman, 2002). However, certain fatty acids such as dietary omega-3 fatty acids (Oh et al., 2010; Virtanen et al., 2014) and the endogenously produced palmitoleate (Cao et al., 2008) have favorable metabolic effects. Furthermore, large epidemiological studies show that an increased ratio of unsaturated to saturated fatty acids in serum triacylglycerols is associated with a reduced risk of T2D (Rhee et al., 2011; Risérus et al., 2009). Similarly, an increased ratio of monounsaturated to saturated fatty acids in the liver is associated with insulin sensitivity even with extensive hepatic steatosis (Benhamed et al., 2012). AG4OX mice have elevated circulating fatty acids and increased adiposity,

yet have lower fasting glycemia and profoundly enhanced glucose tolerance compared to controls (Carvalho et al., 2005; Herman et al., 2012; Shepherd et al., 1993). This raised the possibility that enhanced AT lipogenesis in response to Glut4 overexpression might drive the production of lipids which have favorable metabolic effects. Since Glut4 (Carvalho et al., 2005; Shepherd and Kahn, 1999) and ChREBP (Herman et al., 2012) expression are downregulated in AT in insulin-resistant humans and rodents, the production of these metabolically favorable lipids may be low in these states. To test these hypotheses, we performed lipidomic analysis of AT from wild-type (WT) and AG4OX mice.

RESULTS

Identification of a Class of Glut4-Regulated Lipids

Using a quantitative mass spectrometry (MS) lipidomics platform (Saghatelian et al., 2004), we detected more than 1,400 ions in AT, 6% of which had a 2- to 4-fold difference between AG4OX and WT mice. A cluster of ions in AG4OX AT was elevated $\geq$16-fold (Figure 1A). The measured accurate mass of these ions enabled us to calculate their molecular formulas as $C_{32}H_{61}O_4$ (509.4575), $C_{34}H_{63}O_4$ (535.4732), $C_{34}H_{65}O_4$ (537.4888), and $C_{36}H_{67}O_4$ (563.5045). These formulas all contain a unique signature of four oxygen atoms indicating that these ions are members of a single lipid class. These formulas do not correspond to any known metabolite in the Metlin (Smith et al., 2005) and Lipid Maps (Sud et al., 2007) metabolite databases. We hypothesized these lipids might contribute to glucose-insulin homeostasis because of their abundance in AG4OX mice, in which improved glucose tolerance depends on enhanced AT lipogenesis (Herman et al., 2012). Therefore, we proceeded to determine the molecular structures and biologic effects of these lipids.

The mass differences among these ions suggested they contain fatty acids. Fragmentation of the 537 ion generated several product ions with masses of 255, 281, and 299 (Figure 1B), which correspond to palmitic acid (PA), octadecenoic acid, and hydroxy-stearic acid (HSA), respectively. The molecular formula of the 537 ion ($C_{34}H_{65}O_4$) does not contain any double bonds. This indicates that octadecenoic acid, which contains a double bond, results from fragmentation in the MS and is not part of the natural metabolite. Based on the chemical formula and the fact that this metabolite ionized only in the negative mode, the most reasonable structure for the 537 ion is an ester that combines PA and HSA to yield *p*almitic *a*cid-*h*ydroxy *s*tearic *a*cid (PAHSA) (Figures 1B and 1C). Based on this structural model and the masses detected for the other elevated ions, their structures are: *p*almitic *a*cid-*h*ydroxy *p*almitic *a*cid (PAHPA, m/z 509), *o*leic *a*cid-*h*ydroxy *s*tearic *a*cid (OAHSA, m/z 563), and the 535 ion is a mixture of *p*almitoleic acid-*h*ydroxy *s*tearic *a*cid (POHSA), and *o*leic *a*cid-*h*ydroxy *p*almitic *a*cid (OAHPA) (Figure 1C). We refer to this class of natural-occurring lipids as *f*atty *a*cid-*h*ydroxy *f*atty *a*cids (Figures 1C and 1D), abbreviated as FAHFAs. An additional ion, detected in positive ionization mode, was also upregulated in AG4OX AT (Figure 1A) but the molecular formula indicated it is not a FAHFA, and therefore we did not characterize it further.

Using a targeted MS approach, we identified 16 FAHFA family members in mouse serum that consisted of four fatty acids and four hydroxy-fatty acids in different combinations (Figure 1D). FAHFAs with PO, PA, or OA as the fatty acid moiety and HPA or HSA as the hydroxy-fatty acid moiety were most highly increased in AG4OX compared to WT mice (Figure 1D). Because PAHSAs were the most highly upregulated family member in AT of AG4OX (Figure 1A), we investigated their biologic effects.

Tissue Distribution of Total PAHSAs in WT and AG4OX Mice and Regulation by ChREBP

Targeted MS revealed PAHSAs in all tissues analyzed. In WT mice, total PAHSA levels are highest in brown adipose tissue (BAT) followed by subcutaneous (SQ) white adipose tissue (WAT), perigonadal (PG) WAT, and liver (Figure 1E). Total PAHSA levels are very low in heart and gastrocnemius muscle (data not shown). PAHSA levels vary >7-fold among tissues in WT mice (Figure 1E). In WT serum, total PAHSA levels are ~7 nM (Figure 1E). In AG4OX mice, total PAHSA levels are 16- to 18-fold elevated in SQ and PG WAT, 3-fold in BAT and ~2-fold in serum compared to WT mice (Figure 1E). In contrast, PAHSA levels in liver of AG4OX mice are ~30% lower than WT. Thus, Glut4 overexpression in AT results in broad systemic regulation of PAHSAs with tissue-specific alterations.

Because ChREBP regulates AT lipogenesis in AG4OX, we tested whether ChREBP regulates PAHSA levels in vivo. ChREBP knockout in normal mice reduces total PAHSA levels ~75% in PG- and SQ-WAT with no change in serum (Figure 1F). Knocking out ChREBP in AG4OX completely reverses the marked elevation in PAHSA levels in PG- and SQ-WAT and serum.

Tissue Distribution of Specific PAHSA Isomers and Regulation in WT and AG4OX Mice

We observed multiple peaks in the chromatograms that correspond to different PAHSA isomers with the ester connected to a different carbon of the hydroxy-fatty acid resulting in a branched lipid. Fragmentation of PAHSAs from AT using high collisional energy tandem MS (Moe et al., 2004) produced two ions at 127 and 155 (Figure 1B) indicating that the ester is at the 9th carbon of the HSA (Figure 1C). We refer to this isomer as 9-PAHSA, which was confirmed by chemical synthesis and coelution with ^{13}C-9-PAHSA (Figure 2A). We also discovered PAHSAs with branched esters at carbons 5, 7, 8, 10, 11, 12, and 13 verified by comparison to synthetic standards (Figure 2A). Thus, there are at least eight PAHSA isomers. We achieved complete separation of all isomers except 13- and 12-PAHSA (Figure 2A), which we quantify together in all data sets.

We sought to determine which PAHSA isomers are upregulated in WAT and serum of AG4OX mice as an initial clue to which ones may have biologic activities that could affect glucose homeostasis. In WT serum, 13/12-, 11-, 10-, 9-, and 5-PAHSA are present at 0.4–2.5 nM, which is the range for signaling lipids such as prostacyclins, prostaglandins, steroids, and endocannabinoids. In WT WAT and BAT, 9-PAHSA is the most abundant isomer (Figure 2B). 13/12-, 11-, and 10-PAHSA are present at 20%–30% of 9-PAHSA levels and 8-, 7-, and 5-PAHSA are present at substantially lower concentrations (Figure 2B). Surprisingly, liver which is also a lipogenic tissue, has only

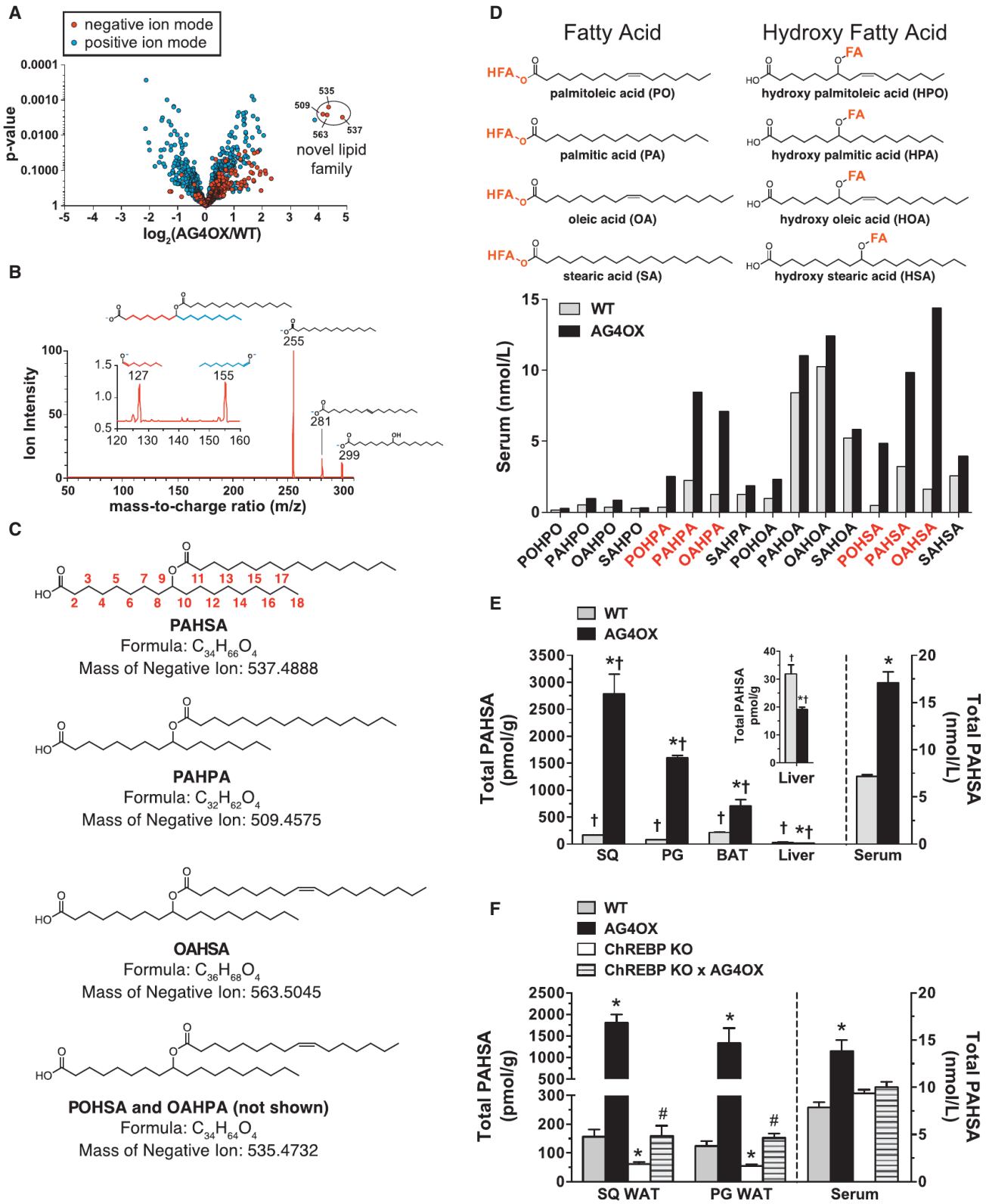

Figure 1. Discovery and Characterization of a Class of Lipids (FAHFAs)

(A) Comparative lipidomics of SQ white adipose tissue (WAT) from AG4OX and WT mice reveals the presence of a group of ions at m/z 509 (PAHPA), 535 (POHSA/OAHPA), 563 (OAHSA), and 537 (PAHSA) that are elevated 16- to 18-fold in AG4OX mice.

(legend continued on next page)

13/12- and 9-PAHSAs (Figure 2B). In AG4OX mice, all PAHSA isomers are elevated in serum, SQ and PG WAT and BAT with 9-PAHSA being the most highly upregulated. In contrast, in AG4OX liver, PAHSA isomers are reduced compared to WT. These data reveal that individual PAHSA isomers are coordinately upregulated in AG4OX WAT and BAT which may result from the effect of increased Glut4 to induce ChREBP and lipogenesis in these tissues (Herman et al., 2012; Tozzo et al., 1995). However, PAHSAs are reduced in AG4OX liver indicating tissue-specific mechanisms for regulating uptake, synthesis, degradation or release.

This is further indicated by the tissue distribution of specific PAHSA isomers in WT mice. 13/12- and 9-PAHSAs are present in all WT tissues examined (Figure 2C). 9-PAHSA is more abundant in AT than liver while 13/12-PAHSA is not. In contrast to 13/12- and 9-PAHSA, 5-PAHSA is restricted to AT, kidney, and serum (Figure 2C).

Physiologic Regulation of PAHSAs with Fasting

We examined PAHSA regulation with fasting (Figure 2D). In the fed state, total PAHSA levels are highest in BAT; slightly lower in SQ and PG WAT; and substantially lower in liver, pancreas, and kidney (Figure 2D). Fasting increases PAHSAs 2- to 3-fold in WAT and kidney and 65% in pancreas but does not alter the levels in BAT, liver, or serum (Figure 2D). Hence, PAHSAs undergo tissue-specific regulation with fasting (Figure 2D). The fasting-induced increase in PAHSAs in WAT is surprising since one would expect synthesis to be lower due to reduced lipogenesis and ChREBP with fasting. Indeed, in spite of elevated PAHSA levels, biosynthetic activity (described below) was not increased in WAT from fasted mice (data not shown). This may reflect inhibition of degradation or release. To better understand the mechanism, we determined fasting effects on PAHSA levels in AG4OX mice. Fasting further elevated PAHSAs in WAT but not in BAT or serum (Figure S1 available online). Since PAHSA levels in AG4OX WAT are regulated by ChREBP-driven lipogenesis (Figure 1E) and lipogenesis is not increased with fasting, these data demonstrate an additional level of regulation and support the possibility that fasting inhibits PAHSA degradation or release.

We also investigated regulation of individual PAHSA isomers with fasting (Figure 2E). Although total PAHSA levels are unchanged in serum of fasted mice (Figure 2D), specific isomers (10-, 9- and 5-PAHSA) are modestly decreased (Figure 2E). In SQ and PG WAT, most of the isomers (13/12-, 11-, 10-, 9-, and 8-PAHSA) including the more abundant ones are increased with fasting while 7- and 5-PAHSA are unchanged (Figure 2E). Fasting had no effect on any PAHSA isomer in BAT or liver while all isomers were upregulated in kidney. In pancreas, 11- and 9-PAHSA are increased with fasting while 13/12- and 7-PAHSA are unchanged. Thus, PAHSA isomer levels undergo tissue-specific and isomer-specific regulation with fasting (Figure 2E). The abundance of different PAHSA isomers in the fasted state differs by 60-fold in a given tissue (compare 9- with 5-PAHSA in SQ WAT) (Figure 2E). These results suggest that fasting regulates pathways involved in synthesis, degradation, and/or release of specific PAHSA isomers in a tissue- and isomer-specific manner.

Regulation of PAHSAs in Obesity and Insulin Resistance

We investigated PAHSA levels in insulin-resistant mice with high-fat-diet (HFD)-induced obesity (Figure 3A). After 9 weeks of HFD, mice were obese and diabetic (determined by GTT) (Figure S2A). HFD had differential effects on specific PAHSA isomers. 5- and 13/12-PAHSAs were downregulated in HFD mice in serum, PG and SQ WAT and BAT (Figure 3A) although the difference did not reach significance for 13/12-PAHSA in PG WAT. Strikingly, 10-, 9-, 8-, and 7-PAHSA were increased in PG WAT of HFD-fed mice. Most of these isomers were decreased in SQ WAT and BAT and unchanged in serum (Figure 3A). Total lipid ion signal measured in SQ WAT was unchanged between chow- and HFD-fed mice (Figure S2B). 13/12- and 9-PAHSA were also decreased in liver (Figure 3A). These studies demonstrate: (1) 5-PAHSA and 13/12-PAHSA are consistently reduced in AT depots with HFD while other PAHSA isomers have opposite regulation among the depots (PG WAT versus SQ WAT and BAT) (Figure 3A); and (2) Only two of the five isomers in serum are reduced with HFD (Figure 3A). Thus, PAHSAs undergo isomer-specific and tissue-specific regulation under insulin-resistant conditions in WT mice.

PAHSAs Are Present in Food

To determine whether the changes in PAHSA levels in altered metabolic states could result from differences in dietary intake, we measured PAHSA levels in rodent and human foods. In chow and HFD, we found five of the seven isomers that are present in mouse AT, 13/12-, 11-, 10-, 9-, and 8-PAHSA, but not 7- and 5-PAHSA. However, the relative abundance among isomers was strikingly different from AT or serum with 10-PAHSA being most abundant in both diets (Figure 3B). Levels of all these isomers were substantially lower in HFD than chow (Figure 3B). Given that PAHSAs increase in WAT during fasting (Figures 2D and 2E), regulation of tissue PAHSA levels does not simply reflect dietary intake. Similarly, the abundance of PAHSA isomers in serum and tissues (Figure 2C) does not correlate with predominant isomers

(B) Structural analysis of the 537 ion from AG4OX WAT by tandem MS demonstrates that it is composed of palmitic acid (m/z 255) and hydroxy stearic acid (m/z 299). Octadecanoic acid (m/z 281) results from the dehydration of hydroxy stearic acid. Fragmentation at high collision energies produces two ions at m/z 127 and 155, identifying carbon 9 as the position of the hydroxyl group on hydroxy-stearic acid, confirming the structure to be 9-PAHSA.

(C) Acyl chain carbon numbering scheme, molecular formula, mass and names of FAHFAs from the m/z 537 (PAHSA), m/z 509 (PAHPA), m/z 563 (OAHSA), and m/z 535 (POHSA or OAHPA) ions.

(D) Constituent fatty acid and hydroxy-fatty acid components of FAHFAs. Quantification of 16 FAHFA family members identified in serum of WT and AG4OX mice.

(E) Total PAHSA levels in serum and tissues of WT and AG4OX mice. Inset, liver total PAHSA levels. n = 3–5/group, *$p < 0.05$ versus WT (t test), $^{\dagger}p < 0.05$ versus all other tissues within the same genotype (ANOVA).

(F) Total PAHSA levels in SQ-WAT, PG-WAT, and serum of WT, AG4OX, ChREBP KO, and AG4OX/ChREBP KO mice. n = 3–5/group, *$p < 0.05$ versus all other genotypes within same tissue or serum (ANOVA), # $p < 0.05$ versus AG4OX and ChREBP-KO.

Data are means ± SEM. MRM transitions for detection of different FAHFAs can be found in Table S1.

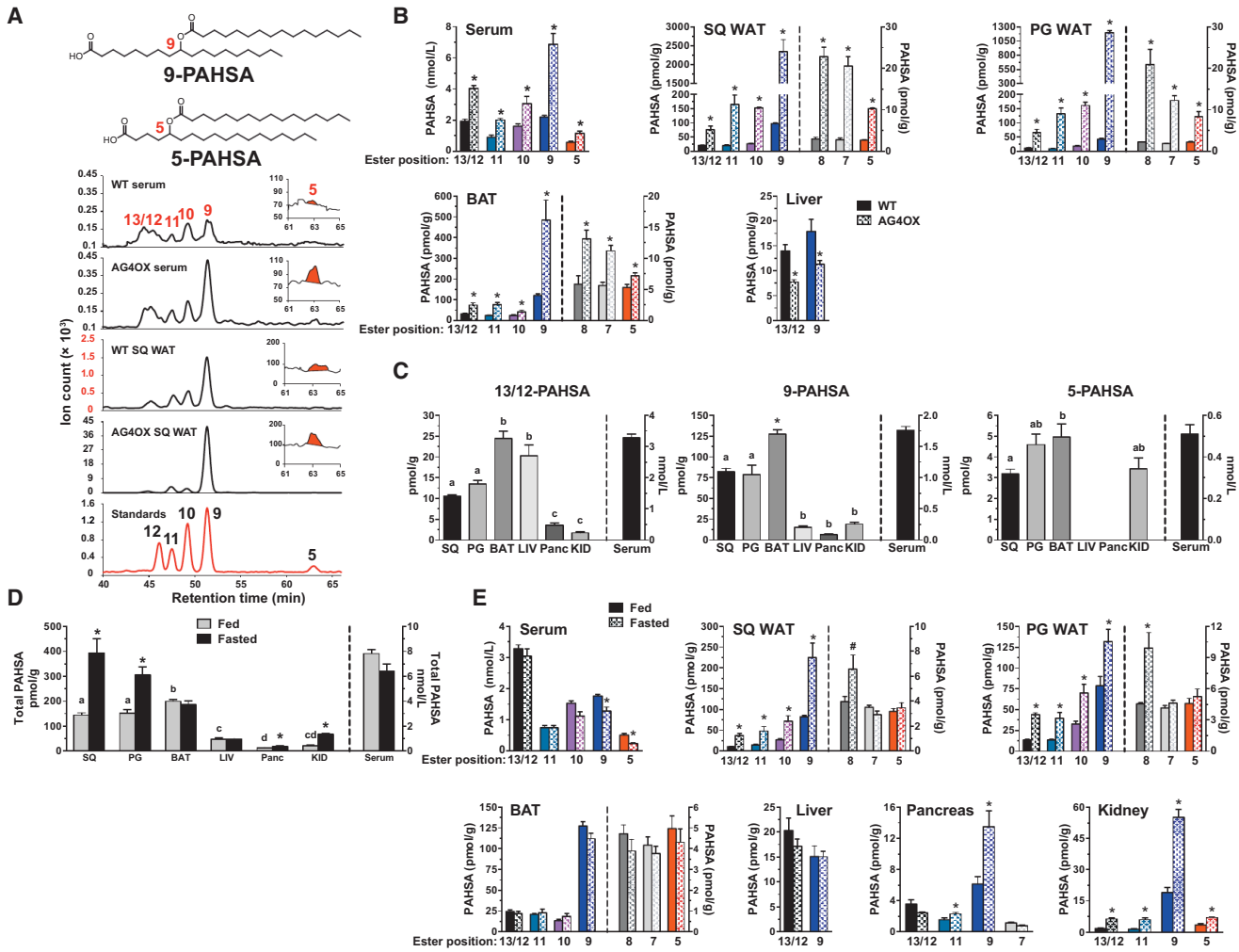

Figure 2. Identification and Quantification of PAHSA Isomers in Mouse Serum and Tissues

(A) Coelution of PAHSA isomers from serum and SQ WAT of WT and AG4OX mice with synthetic standards for individual PAHSA isomers. The peak for 5-PAHSA is shown in red in the inset. Note: different y axis scale for WT SQ WAT (Red numbers) versus AG4OX SQ WAT.

(B) Distribution and quantification of PAHSA isomers in serum and tissues of WT and AG4OX mice. "Ester position" refers to the location of the ester bond in PAHSA isomers. n = 3–5/group, *p < 0.05 versus WT (t test).

(C) Distribution and quantification of 13/12-, 9-, and 5-PAHSA isomers in serum and tissues of WT female FVB mice. n = 3–5/group, [a,b,c] Tissues with different letters are different from each other within the same isomer panel (p < 0.05, ANOVA).

(D and E) Total PAHSA levels (D) and PAHSA isomer levels (E) in serum and tissues of WT mice in fed or fasted (16 hr) states. "Ester position" refers to the location of the ester bond in PAHSA isomers. n = 3–5/group, *p < 0.05, # < 0.07 versus fed (t test) [a,b,c,d]Tissues with different letters are different from each other for the fed state (p < 0.05, ANOVA).

Data are means ± SEM. See also Figure S1.

in chow (Figure 3B), suggesting that PAHSAs present in tissues are synthesized endogenously. The fact that 5-PAHSA is not present in mouse chow or HFD (Figure 3B) but is present in WAT, BAT, kidney, and serum (Figures 2A–2C, 2E and 3A) further supports this notion. We also found PAHSAs in all human foods tested with different isomer distributions and abundance (Figure S2C).

PAHSAs Are Synthesized in Mammalian Tissues

To determine whether PAHSAs are synthesized endogenously, we investigated PAHSA biosynthesis in liver and WAT lysates of normal mice. We detected PAHSA biosynthetic activity in both tissues, and it was markedly reduced by heat denaturation (Figure 3C). We also detected PAHSA biosynthesis in vivo. Gavage of mice with 9-hydroxy heptadecanoic acid (9-HHA), a hydroxy fatty acid not normally found in mammalian tissues resulted in synthesis of full-length FAHFAs containing a 9-HHA acyl chain indicating that FAHFAs can be synthesized in vivo (Figure 3D).

PAHSAs Are Present in Humans and Levels Are Reduced with Insulin Resistance

To determine if PAHSAs are present in humans and are regulated in disease states, we measured PAHSA isomers in serum and SQ

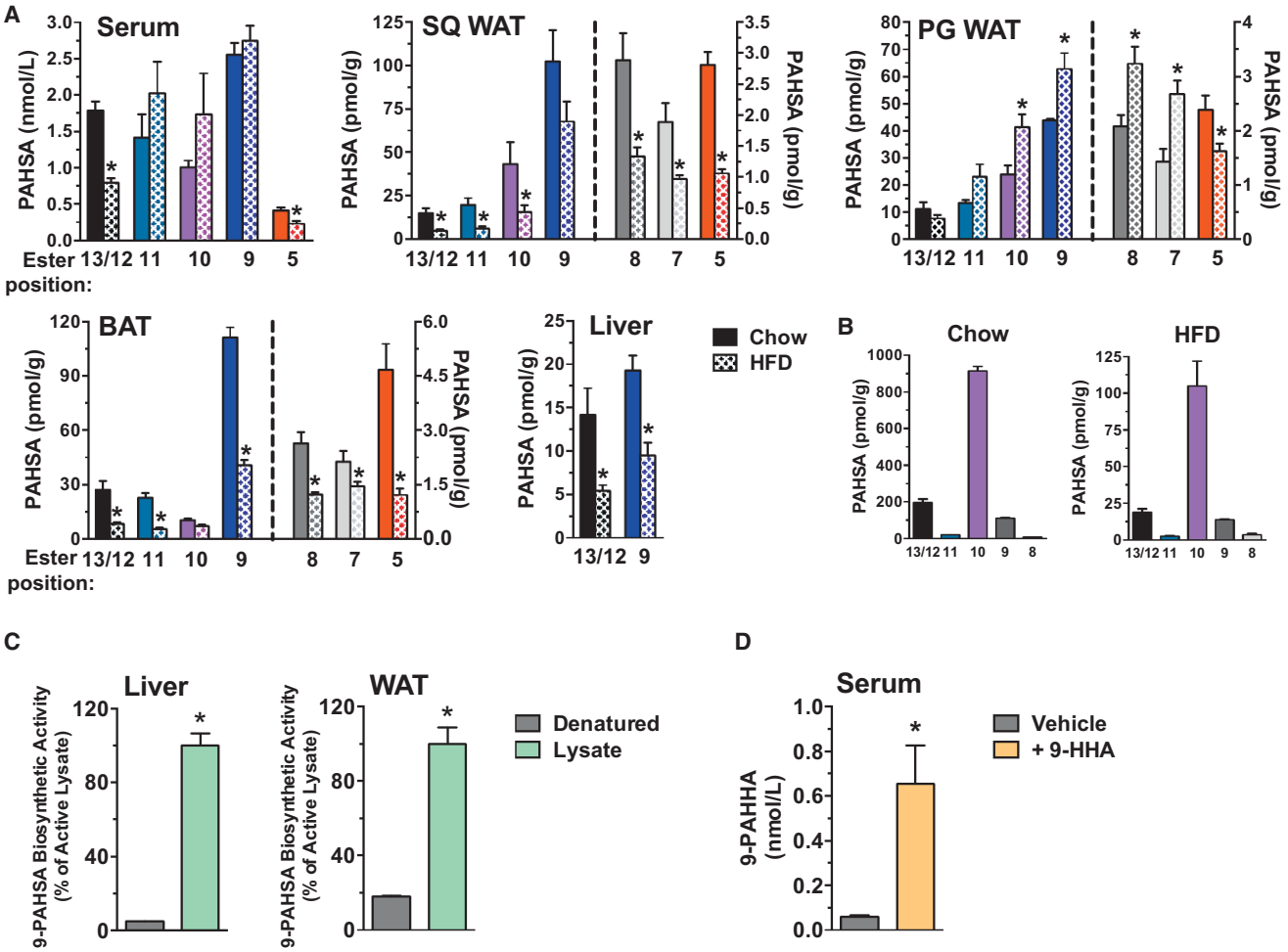

Figure 3. PAHSA Isomer Levels in Tissues of Mice on Chow or HFD, PAHSA Isomer Levels in Food, and PAHSA Biosynthesis In Vivo and in Tissues In Vitro

(A) Quantification of PAHSA isomers in serum, SQ WAT, PG WAT, BAT, and liver of WT female FVB mice fed on chow or HFD for 9 weeks. "Ester position" refers to the location of the ester bond in PAHSA isomers. n = 3–6/group, *p < 0.05 versus chow (t test).

(B) Quantification of PAHSA isomers in mouse chow and HFD. n = 3/group.

(C) 9-PAHSA levels in liver and PG-WAT lysates incubated with palmitoyl-CoA and 9-hydroxy stearic acid and heat-denatured Controls. n = 3/group, *p < 0.05 versus heat-denatured Controls (t test).

(D) 9-palmitic-acid-hydroxy-heptadecanoic-acid (9-PAHHA) serum levels in mice 3 hr postgavage with 9-hydroxy-heptadecanoic-acid (9-HHA) or vehicle control. n = 3/group, *p < 0.05 versus vehicle (t test).

Data are means ± SEM. See also Figure S2.

WAT from insulin-sensitive and insulin-resistant nondiabetic humans. Subjects were middle-aged. BMI was increased in five out of six insulin-resistant participants (Table S2). Insulin resistance was demonstrated by a 61% reduction in glucose infusion rate during a euglycemic hyperinsulinemic clamp (Table S2). Serum triglycerides and free fatty acids in the fasting state were not different between groups (Table S2). Total PAHSA levels are reduced ~40% in serum of insulin-resistant humans (Figure 4A). In serum of both insulin-sensitive and insulin-resistant humans, 9- and 10-PAHSA are most abundant and 13/12- and 5-PAHSAs are present at ~1/5 of these concentrations (Figure 4A). In insulin-resistant people, serum levels of all PAHSAs except 9-PAHSA are reduced by 40%–55% compared to insulin-sensitive people (Figure 4A). Serum concentrations of total PAHSAs and all isomers correlated remarkably strongly with insulin sensitivity measured by clamp (Figure 4B). Serum PAHSA levels did not correlate with levels of nonesterified fatty acids or triglycerides (data not shown) suggesting that PAHSA levels are regulated by different mechanisms.

In human SQ WAT, total PAHSAs are reduced ~70% (Figure 4C). We detected 13/12-, 11-, 10-, 9-, and 5-PAHSA isomers in these biopsies (Figure 4C). However, for technical reasons we were unable to quantify the levels of 11-PAHSA. 9-PAHSA levels were higher than all other isomers (Figure 4C) similar to mouse SQ WAT (Figures 2B, 2E and 3A). 13/12-, 10-, 9-, and 5-PAHSA concentrations in SQ WAT of insulin-resistant people were 60%–73% lower than in insulin-sensitive people (Figure 4C). Concentrations of total PAHSAs and of 9- and 5-PAHSA isomers

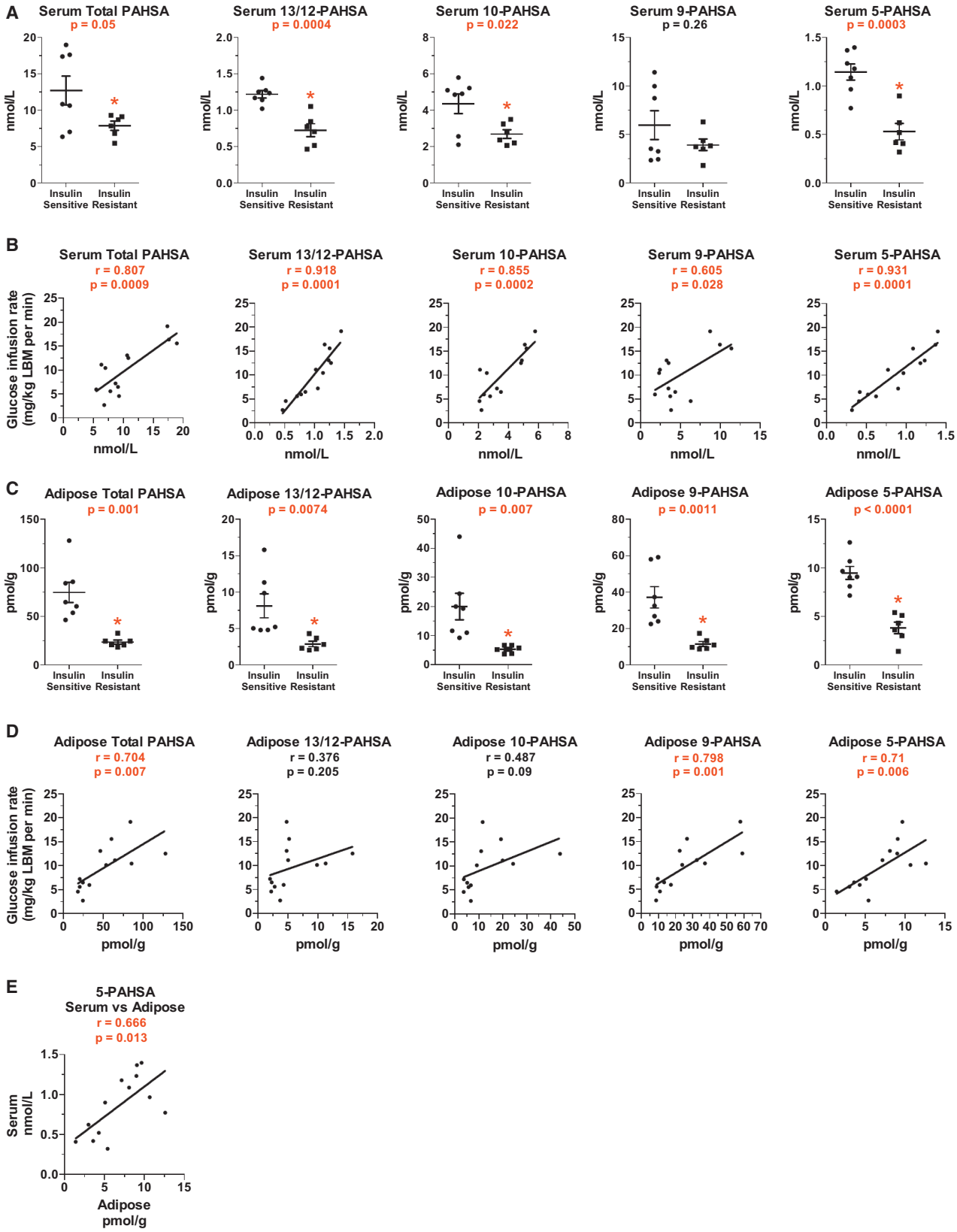

(legend on next page)

in WAT correlate highly with insulin sensitivity (Figure 4D). Serum PAHSA levels correlated with WAT PAHSA levels only for 5-PAHSA (Figure 4E).

In summary, all PAHSA isomers detected are reduced in SQ WAT in insulin-resistant subjects and all but one are reduced in serum. Furthermore, PAHSA levels in serum and WAT correlate highly with whole-body insulin sensitivity. These effects parallel the effects in diet-induced obese mice in which all PAHSA isomers are reduced in SQ WAT, and 13/12- and 5-PAHSA are lower in serum compared to chow-fed mice (Figure 3A). Thus, the regulation of PAHSAs and their inverse correlation with insulin resistance is conserved between mice and humans.

PAHSAs Acutely Improve Glucose Tolerance and Ambient Glycemia

Since levels of PAHSA isomers correlate with insulin sensitivity (Figures 4B and 4D), we tested whether administration of PAHSAs could improve glucose homeostasis in obese, diabetic mice. We selected 9-PAHSA and 5-PAHSA because: (1) 9-PAHSA was the most abundant form in WAT and BAT in WT mice (Figure 2B) and in SQ WAT of humans (Figure 4C). (2) 9-PAHSA is the most strongly upregulated in serum and WAT of insulin-sensitive AG4OX mice (Figure 2B) and was downregulated (with other isomers) in WAT of insulin-resistant humans (Figure 4C). (3) 5-PAHSA was the most consistently downregulated in all adipose depots and in serum of insulin-resistant mice (Figure 3A) and in WAT and serum of insulin-resistant humans. Oral gavage of 5-PAHSA increased serum levels 3- to 5-fold in mice on chow and HFD (Figure S3). As shown in Figure 3A, baseline 5-PAHSA levels were 50%–80% lower in HFD-fed mice compared to chow-fed mice and 5-PAHSA gavage more than restored the levels (Figure S3). The elevation of serum 5-PAHSA levels after gavage in both chow and HFD-fed mice was similar to the elevation in serum of AG4OX mice (Figures 2B and S2). This indicated that PAHSAs are absorbed orally and this route of administration can be used to increase PAHSA concentrations for in vivo metabolic studies.

Acute oral administration of 5- or 9-PAHSA in insulin-resistant HFD-fed mice lowered basal glycemia at 30 min after PAHSA administration (Figure 5A, −30 to 0 min). Subsequently, glucose was administered and we observed improved glucose tolerance in PAHSA-treated mice with reduced area under the glucose excursion curve (Figure 5A). Because of the significant effect of PAHSAs on the baseline glucose levels in HFD-fed mice at 30 min after administration, we tested whether PAHSA action to lower baseline glycemia was sustained. 5-PAHSA or 9-PAHSA had a greater glucose-lowering effect than vehicle treatment in HFD-fed mice also at 2.5–3 hr after administration (Figure 5B). There was no difference in plasma insulin levels at this time in PAHSA-treated compared to vehicle-treated mice (data not shown). Since no food was available during this study, calorie absorption was not a variable and the results suggest that oral PAHSA administration enhances insulin sensitivity. An insulin tolerance test showed lower glucose levels in PAHSA-treated mice compared to vehicle-treated mice for the study duration (120 min after insulin administration) which was largely because of the PAHSA effect to lower baseline glycemia (data not shown).

PAHSAs Stimulate Insulin and GLP-1 Secretion

To determine whether enhanced insulin secretion might contribute to the PAHSA-induced improvement in glucose tolerance (Figure 5A), we tested PAHSA effects on glucose-stimulated insulin secretion (GSIS) in vivo in aged chow-fed mice. 5-PAHSA improved glucose tolerance (Figure 5C) concurrent with acute enhancement of insulin secretion at 5 min after glucose administration (Figure 5D). This may result from direct effects on insulin secretion or from stimulation of incretin secretion since GLP-1 levels were also increased in PAHSA-treated mice at 5 min after glucose administration (Figure 5E). Thus, PAHSAs augment the acute stimulation of GLP-1 and insulin secretion in response to glucose and these effects most likely have an important role in the enhanced glucose tolerance following a single PAHSA dose.

To determine whether the stimulation of insulin secretion is a direct effect of PAHSAs on pancreatic beta cells, we incubated islets from human donors (Table S3, donors' metabolic parameters) with 5-PAHSA and measured GSIS. 5-PAHSA had no effect on insulin secretion at 2.5 mM glucose but augmented the insulin secretion response at 20 mM glucose (Figure 5F). These data demonstrate that 5-PAHSA directly enhances GSIS in human islets. To determine whether PAHSAs directly stimulate GLP-1 secretion, we used the enteroendocrine cell line STC-1. Both 5- and 9-PAHSA rapidly stimulated GLP-1 secretion from STC-1 cells in a dose-dependent manner (Figure 5G). The effects are similar to those with the omega-3 fatty acid, α-linolenic acid, and a synthetic GPR120 ligand (Figure 5G). Thus, the rapid effects of PAHSAs to augment GSIS may be both direct effects on pancreatic beta cells and indirect effects through stimulation of GLP-1 secretion.

PAHSAs Enhance Insulin-Stimulated Glucose Transport and Glut4 Translocation by Activating GPR120

To further understand the mechanism(s) by which PAHSAs improve glucose homeostasis, we tested their effects on glucose transport in adipocytes. PAHSAs increased glucose transport at submaximal and maximal insulin concentrations (Figure 6A). Neither of the fatty acids that form the parent PAHSA structure,

Figure 4. PAHSA Levels Are Decreased in Insulin-Resistant Humans and Levels Correlate with Insulin Sensitivity

(A) Quantification of total PAHSAs and individual PAHSA isomers in serum of insulin-sensitive and insulin-resistant nondiabetic humans (see Table S2 for metabolic characteristics). n = 6–7/group.

(B) Correlation between insulin-sensitivity (clamp glucose infusion rate) and serum total PAHSA and individual PAHSA isomers. n = 13.

(C) Quantification of total PAHSA and individual PAHSA isomers in SQ WAT of insulin-sensitive and insulin-resistant humans. n = 6–7/group.

(D) Correlation between insulin-sensitivity (clamp glucose infusion rate) and SQ WAT total PAHSA and individual PAHSA isomers. n = 13.

(E) Correlation between SQ WAT and serum 5-PAHSA levels. LBM: lean body mass. Individual p values are shown on graphs, *$p < 0.05$ versus insulin-sensitive (t test, A and C).

Data are means ± SEM for (A and C). Correlations were determined by linear regression analysis for (B, D, and E).

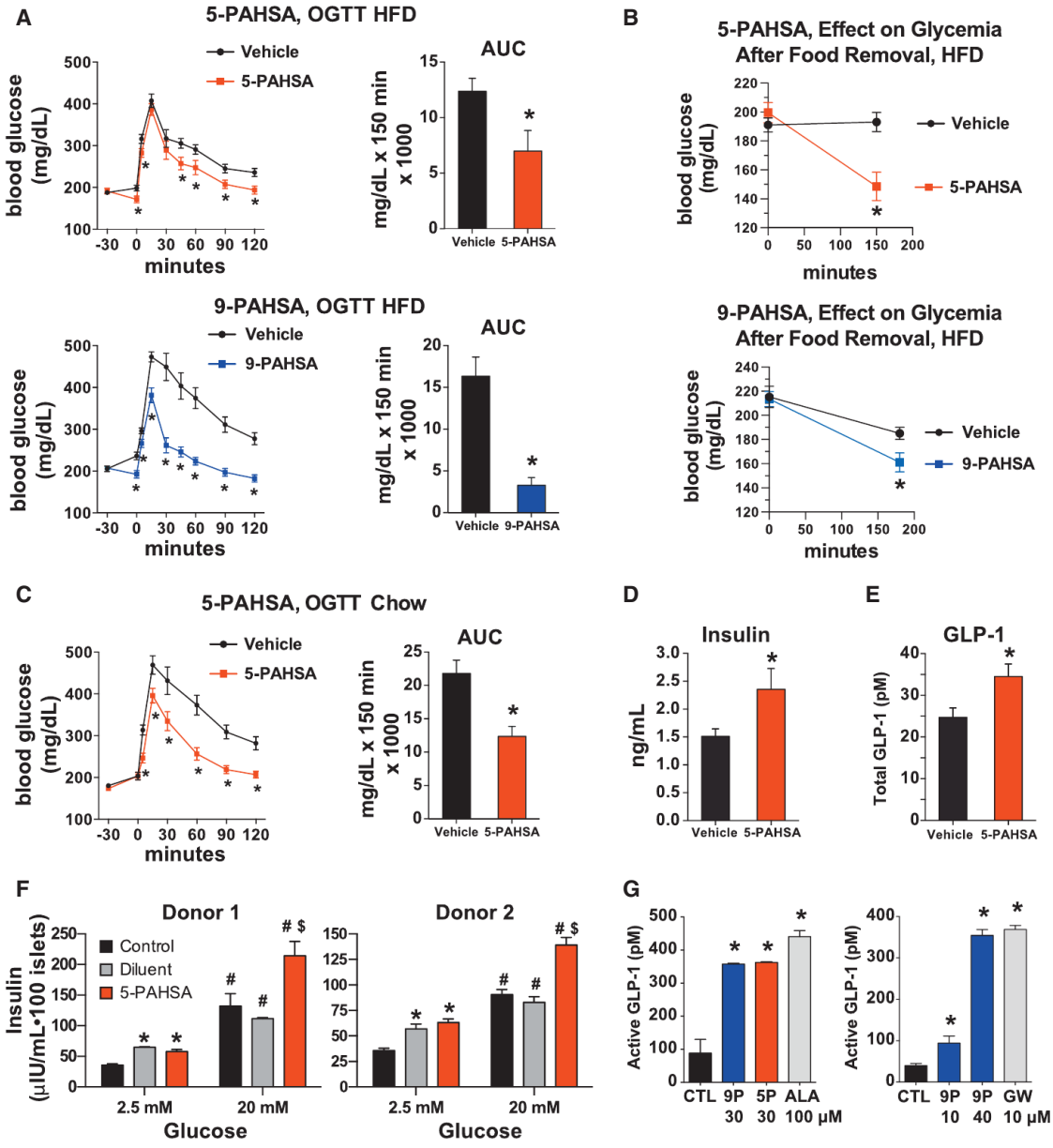

Figure 5. PAHSAs Improve Glucose Tolerance and Ambient Glycemia In Vivo and Augment Insulin and GLP-1 Secretion

(A) 4.5 hr after food removal, HFD-fed mice were gavaged with 5-PAHSA (top), 9-PAHSA (bottom) or vehicle control. 30 min later an oral glucose tolerance test (OGTT) was performed. n = 12–14/group, mice were on HFD for 42–52 weeks. *p < 0.05 versus vehicle at same time (t test). Area under the curve (AUC) was calculated from −30 to 120 min. *p < 0.05 versus vehicle (t test).

(B) 2.5 hr after food removal, HFD-fed mice were gavaged with 5-PAHSA (top), 9-PAHSA (bottom) or vehicle control. Glycemia was measured immediately before (time 0) and at 2.5 hr (5-PAHSA) or 3 hr (9-PAHSA) after PAHSA gavage. n = 12–14/group. *p < 0.05 versus vehicle (t test).

(C) 4.5 hr after food removal, aged, chow-fed mice (45-week-old) were gavaged with 5-PAHSA 30 min prior to an OGTT. n = 12–14/group. *p < 0.05 versus vehicle at same time (t test). Area under the curve (AUC) was calculated from −30 to 120 min. *p < 0.05 versus vehicle (t test).

(D and E) Serum insulin levels (D) and serum GLP-1 levels (E) 5 min postglucose challenge in chow-fed mice gavaged with 5-PAHSA or vehicle (glucose values shown in C). n = 12–14/group, *p < 0.05 versus vehicle (t test).

(F) Insulin secretion from primary human islets from two independent donors. Islets were incubated with low (2.5 mM) or high (20 mM) glucose ex vivo in the presence of 5-PAHSA (20 µM) or Control (KRB buffer). Diluent for 5-PAHSA was methanol (0.25%). n = 100 islets/condition, *p < 0.05 versus control 2.5 mM glucose (t test), #p < 0.05 versus all treatments at 2.5 mM glucose (t test), $p < 0.05 versus control and diluent at 20 mM glucose (t test).

(G) Active GLP-1 secretion from STC-1 cells in response to 5-PAHSA (5P), 9-PAHSA (9P), α-Linolenic Acid (ALA), GW9508 (GW), or vehicle control (CTL, DMSO). n = 4/group, *p < 0.05 versus vehicle (CTL) (t test).

Data are means ± SEM. See also Table S3 and Figure S3.

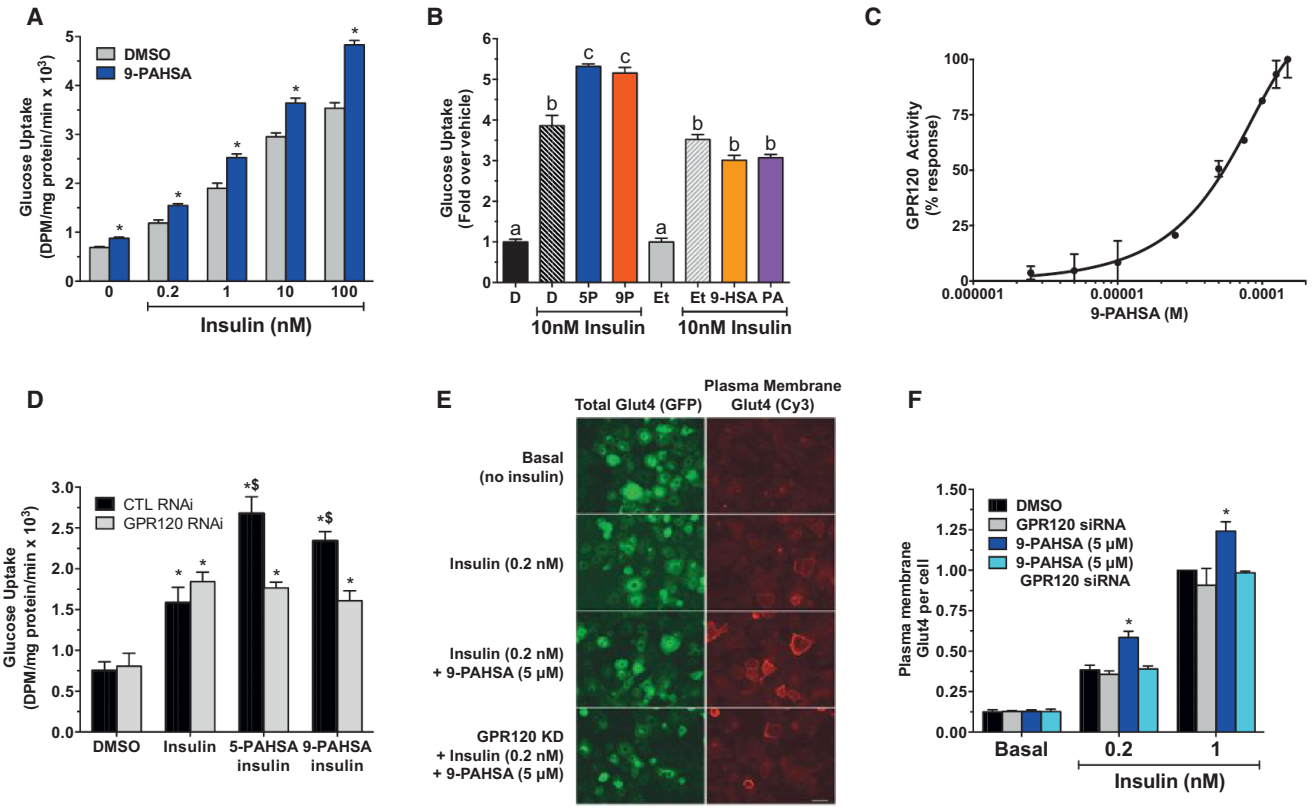

Figure 6. PAHSAs Regulate Glucose Uptake and Glut4 Translocation via GPR120

(A) Insulin-stimulated glucose transport in 3T3-L1 adipocytes treated with 9-PAHSA (20 μM) or vehicle (DMSO) control for 6 days. n = 6/group, *p < 0.001 versus vehicle (DMSO) at the same insulin concentration (ANOVA).

(B) Glucose transport in 3T3-L1 adipocytes treated for 48 hr with 9-PAHSA, 5-PAHSA, palmitic acid (PA), 9-hydroxy stearic acid (HSA) at 20 μM or their respective vehicle controls (DMSO for 9- and 5-PAHSA. Ethanol for PA and HSA). n = 6/group. [a,b,c]groups with different letters are different from each other p < 0.05 (ANOVA).

(C) Dose response of 9-PAHSA on GPR120 binding and receptor activation. n = 3 wells/condition.

(D) Insulin (10 nM)-stimulated glucose transport in 3T3-L1 adipocytes transfected with control siRNA (CTL) or GPR120 siRNA and treated with 5-PAHSA (10 μM), 9-PAHSA (10 μM) or vehicle (DMSO) control for 2 days. n = 3/group, *p < 0.05 versus control siRNA or GPR120 siRNA with DMSO without insulin (ANOVA), [$]p < 0.05 versus all other conditions except each other (ANOVA).

(E) Glut4 plasma membrane translocation in 3T3-L1 adipocytes transfected with control siRNA or GPR120 siRNA and treated with 9-PAHSA in the presence or absence of insulin. Scale bar = 50 μm.

(F) Quantification of Glut4 translocation in (E). Bars show means of six independent experiments without siRNA knockdown and three with siRNA knockdown. Each experiment had an n ≥ 50 cells/condition.*p < 0.05 versus everything else at same insulin concentration (ANOVA). All data are means ± SEM. See also Figure S4.

palmitic acid or hydroxystearic acid, alone improved insulin-stimulated glucose transport (Figure 6B). The effects of PAHSAs on insulin-stimulated glucose transport occurred with both acute (30 min) and chronic (2–6 day) treatment and at concentrations as low as 500 nM (Figure S4A). PAHSAs did not alter total cellular Glut1 or Glut4 protein levels in adipocytes even after 6 days of incubation (data not shown).

Bioactive lipids can influence biology through binding to cell surface receptors such as G protein-coupled receptors (GPCRs) (Hara et al., 2013). The effects of PAHSAs on GLP-1 secretion and glucose transport are consistent with possible activation of GPCRs (Hirasawa et al., 2005). To determine whether PAHSAs activate GPCRs, we screened a panel of known lipid-activated GPCRs. Both 9-PAHSA (Figure 6C) and 5-PAHSA (data not shown) dose-dependently bind to and activate GPR120 which is also activated by ω-3 fatty acids and monounsaturated fatty acids (Hirasawa et al., 2005; Oh et al., 2010). Activation of GPR120 increases glucose transport and Glut4 translocation in adipocytes (Oh et al., 2010). To test whether GPR120 mediates the effects of PAHSAs, we knocked it down >95% in adipocytes with siRNA (Figure S4B). This completely reversed the enhanced effects of PAHSAs on insulin-stimulated glucose transport (Figure 6D). These data demonstrate that GPR120 mediates the effects of PAHSAs on insulin-stimulated glucose transport.

To determine the mechanism for enhancement of glucose transport with PAHSAs, we analyzed the effects on insulin-induced Glut4 translocation to the plasma membrane in adipocytes. In the absence of insulin, PAHSAs had no effect on Glut4 translocation (Figure 6F). However, PAHSAs enhanced Glut4 translocation at submaximal and maximal insulin

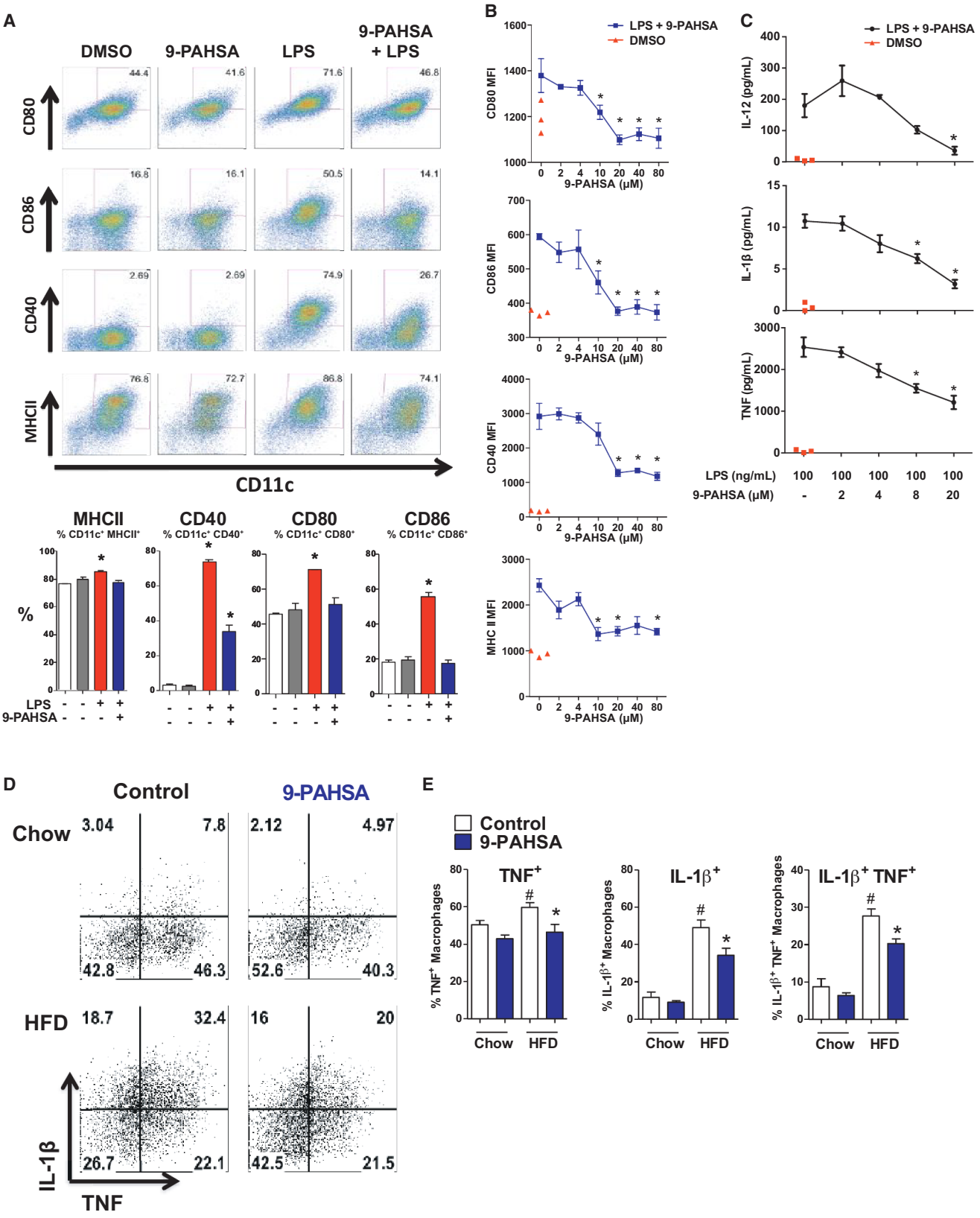

(legend on next page)

concentrations (Figures 6E and 6F). These data indicate that PAHSAs augment insulin-stimulated glucose transport by enhancing Glut4 translocation. Knockdown of GPR120 in adipocytes completely blocked the effect of PAHSAs to augment insulin-stimulated Glut4 translocation (Figures 6E and 6F). We obtained this effect with two different GPR120 siRNAs indicating that it is a specific "on target" effect. These data together demonstrate that PAHSAs bind to and activate GPR120 (Figure 6C), which mediates the effects of PAHSAs on insulin-stimulated glucose transport and Glut4 translocation (Figures 6D–6F).

PAHSAs Exert Anti-Inflammatory Effects

Fatty acids, such as ω-3 fatty acids, can elicit anti-inflammatory effects through GPR120 (Oh et al., 2010). GPR120 is expressed in bone-marrow-derived dendritic cells (BMDCs), which are initial antigen-presenting cells in the innate immune response. Innate immunity is activated in WAT in obesity and may contribute to the insulin-resistant state (Lumeng and Saltiel, 2011). Saturated fatty acids such as palmitic acid and pathogen-derived molecules, such as lipopolysaccharide (LPS), promote BMDC maturation by activating Toll-like receptors (TLRs) (Lumeng and Saltiel, 2011). This induces expression of proinflammatory cytokines, major histocompatibility complex II (MHC II), and costimulatory molecules (CD40, CD80, and CD86) required for antigen presentation and T cell activation. LPS addition to BMDCs robustly increased CD80, CD86, CD40, and MHC II expression, demonstrating the expected activation of BMDCs (Figure 7A). 9-PAHSA blocked the LPS effect on BMDC activation as evidenced by inhibition of LPS-induced CD80, CD86, CD40, and MHC II expression (Figures 7A and 7B). Neither palmitic acid which is a component of the PAHSA molecule, nor the mono-unsaturated fatty acid, oleic acid, exerted these effects at a concentration (20 μM) (Figure S5) at which 9-PAHSA had strong anti-inflammatory effects (Figure 7B). 9-PAHSA completely blocked LPS-induced IL-12 secretion in a dose-dependent manner (Figure 7C) and substantially reduced IL-1β and TNFα at doses as low as 8 μM (Figure 7C). These data indicate that 9-PAHSA has anti-inflammatory effects.

To test whether PAHSAs exert anti-inflammatory effects in vivo, we measured TNFα and IL-1β in AT macrophages (ATMs) from HFD-fed mice gavaged with 9-PAHSA or vehicle for 3 days. The percentage of ATMs expressing TNFα, IL-1β, or both was elevated in HFD-fed mice compared to chow. Administration of 9-PAHSA normalized the percentage of TNFα positive ATMs and reduced the percentage of IL-1β positive and double-positive ATMs (Figure 7D). Total ATM number was not reduced due to the short treatment duration (data not shown). This demonstrates that PAHSAs have anti-inflammatory effects in vivo. Therefore, reduced PAHSA levels in insulin-resistant states (Figures 3A and 4) could contribute to activation of the innate immune system, thus playing a role in AT inflammation and systemic insulin-resistance.

DISCUSSION

Adipose-Glut4 levels in humans are tightly associated with insulin sensitivity and lower Glut4 levels confer increased T2D risk (Carvalho et al., 2001; Shepherd and Kahn, 1999). Adipose-specific Glut4 overexpression in mice (AG4OX) causes beneficial metabolic effects which result from enhanced ChREBP-driven de novo lipogenesis in adipose tissue (AT) (Herman et al., 2012; Tozzo et al., 1995). Because this occurs even in the setting of obesity and elevated serum fatty acids (Herman et al., 2012; Tozzo et al., 1995), we sought to determine whether the augmented lipogenesis in AG4OX mice leads to production of lipid species that have favorable metabolic effects. Here we report the discovery of a class of mammalian lipids characterized by a branched ester linkage between a fatty-acid and a hydroxy-fatty acid or FAHFAs. The closest reported structures are (O-acyl)-omega hydroxy-fatty acids in the eye (Butovich et al., 2009), which are not branched.

Of the 16 FAHFA family members we report here, we extensively characterized the biology of PAHSA isomers that are present in many, if not all, tissues and in serum in normal mice and in human WAT and serum (Figures 1, 2, 3, and 4). Total PAHSA levels are highest in WAT and BAT that also have the greatest number of PAHSA isomers (Figure 2). Furthermore, PAHSA levels are highly elevated in serum, WAT and BAT of AG4OX mice that are obese but have markedly enhanced glucose tolerance (Herman et al., 2012; Shepherd et al., 1993). In parallel, nearly all PAHSA isomers are higher in serum and SQ WAT of insulin-sensitive humans compared to insulin-resistant humans.

In insulin-resistant, obese mice, PAHSA isomer levels show adipose-depot-specific regulation and all PAHSA isomers are lower in SQ WAT of obese compared to lean mice (Figure 3). These results in SQ WAT are similar to those in insulin-resistant

Figure 7. 9-PAHSA Inhibits LPS-Induced Dendritic Cell Maturation In Vitro and Proinflammatory Cytokine Production from Adipose Tissue Macrophages In Vivo

(A) LPS induces dendritic cell (DC) maturation (increased percentage of $CD11c^+$ cells expressing costimulatory molecules, CD80, CD86, CD40, and MHCII). This LPS effect is reduced in the presence of 9-PAHSA (40 μM) compared to vehicle (DMSO) control. Quantification of $CD11c^+$ cells which are positive for costimulatory molecules from the panel above. n = 3 mice/group.

(B) LPS-induced DC maturation is inhibited by increasing concentrations of 9-PAHSA. Red triangles represent vehicle for 9-PAHSA (DMSO) without LPS. MFI: median fluorescence intensity. n = 3 mice/group.

(C) LPS–induced cytokine secretion from DC's is inhibited by increasing concentrations of 9-PAHSA compared to vehicle for 9-PAHSA (DMSO, "-") control. Red triangles represent vehicle for 9-PAHSA (DMSO, "-") without LPS. n = 3 mice/group.

(D) Flow cytometry representation of AT macrophages expressing TNFα and IL-1β. Mice fed on HFD or chow mice were gavaged for 3 days with 9-PAHSA (30 mg/kg for chow mice and 45 mg/kg for HFD mice) or vehicle control. PG-WAT was harvested on day 4 and the stromal vascular cells were incubated in vitro with PMA, ionomycin and brefeldin for 5 hr. AT macrophages ($CD45^+CD11b^+F4/80^+$) were stained intracellularly for TNFα and IL-1β.

(E) Quantification D-percentage of AT macrophages expressing TNFα, IL-1β or both. n = 5 mice/group. LPS concentration is 100 ng/ml for all panels.

*$p < 0.05$ versus LPS-activated cells without PAHSA treatment (A–C) or control cells, same diet (E) by one-way (A–C) and two-way ANOVA (D). #$p < 0.05$ versus all other groups by two-way ANOVA. Data are means ± SEM. See also Figure S5.

people (Figure 4). 5-PAHSA is consistently reduced in all adipose depots studied and in serum in insulin-resistant mice and humans. In insulin-resistant people, most PAHSA isomers are reduced in serum and AT and correlate highly with insulin sensitivity (Figure 4). ChREBP is required to maintain normal PAHSA levels in WT mice and elevated levels in AG4OX mice (Figure 1F). In humans, ChREBP and lipogenic enzyme expression correlate strongly with insulin-sensitivity. Thus, the reduction in PAHSAs in insulin-resistant people may be mediated by suppressed ChREBP expression.

This class of lipids has multiple effects that improve glucose-insulin homeostasis which suggests that restoring PAHSA levels in insulin-resistant people could have beneficial metabolic effects. Oral PAHSA administration in insulin-resistant mice on a HFD rapidly lowers ambient glucose and also improves glucose tolerance (Figures 5A and 5B). This may result, at least in part, from enhanced glucose transport since PAHSAs augment insulin-stimulated glucose transport and Glut4 translocation directly in adipocytes in vitro (Figure 6). In addition, PAHSAs stimulate both insulin and GLP-1 secretion (Figures 5D–5G). Importantly, the effects of PAHSAs on insulin secretion are observed only under hyperglycemic conditions (Figure 5F). The enhanced GSIS in vivo most likely results from both direct effects on islet cells and indirect effects though GLP-1-stimulated insulin secretion.

Total PAHSA levels in tissues and serum are similar to concentrations of signaling lipids such as prostacyclins, prostaglandins, steroids, and endocannabinoids. PAHSAs are signaling lipids that directly bind to and activate GPR120 in a cell-based GPCR activity assay (Figure 6C). GPR120 activation appears to explain the effects on insulin-induced Glut4 translocation and glucose uptake in adipocytes (Figures 6B–6D) and may explain the effects on GLP-1 secretion and inhibition of inflammatory responses in immune cells. Thus, PAHSAs are endogenous GPR120 ligands and may also exert effects through other lipid-activated GPCRs.

PAHSAs have striking anti-inflammatory effects and largely block LPS-stimulated dendritic cell activation and cytokine production (Figure 7). Chronic, low-grade inflammation in AT plays an important role in obesity-related insulin resistance (Lumeng and Saltiel, 2011; Olefsky and Glass, 2010). Three days of PAHSA gavage in HFD-fed mice reduced the percentage of ATMs that express proinflammatory cytokines (Figure 7D). Therefore, anti-inflammatory effects of PAHSAs may promote insulin sensitivity and ameliorate other inflammatory diseases.

Insulin-sensitizing and anti-inflammatory effects and GLP-1 secretion are also observed with ω-3 fatty acids (Hirasawa et al., 2005; Oh et al., 2010). However, a major difference between ω-3 fatty acids and PAHSAs is that PAHSAs are synthesized endogenously as evidenced by PAHSA biosynthetic activity in adipose and liver lysates and incorporation of modified precursors into FAHFAs in vivo (Figures 3C and 3D). The potential importance of identifying an endogenous GPR120 ligand is demonstrated by the fact that loss of function mutations in GPR120 in humans promote obesity and insulin resistance (Ichimura et al., 2012). Thus, GPR120 is an important control point in the integration of anti-inflammatory and systemic insulin-sensitizing responses and is emerging as an important regulator of whole-body glucose-insulin homeostasis (Mo et al., 2013). It is the subject of ongoing preclinical investigation for the treatment of obesity-related insulin resistance, T2D, and inflammatory diseases (Mo et al., 2013; Oh et al., 2014).

Reduced PAHSA levels may contribute to diabetes risk since many PAHSA isomers are reduced in SQ WAT and serum of insulin-resistant rodents (Figure 3A) and humans (Figure 4). In humans, PAHSA levels in both serum and SQ WAT correlate highly with whole-body insulin-sensitivity (Figures 4B and 4D). Thus, reduced circulating PAHSA levels may serve as a biomarker for insulin resistance and T2D risk. PAHSAs lower glycemia, improve glucose tolerance and stimulate GLP-1 and insulin secretion in mice (Figure 5). This raises the possibility that restoring the reduced PAHSA levels in insulin-resistant humans could have therapeutic effects to prevent or ameliorate insulin resistance and T2D. The discovery of the FAHFAs is important also because their presence suggests uncharacterized biochemical pathways and enzymes that may be important in human physiology and disease. Changes in the levels of these metabolites and in their signaling pathways may provide important insights and new treatment avenues for metabolic and inflammatory diseases.

EXPERIMENTAL PROCEDURES

Materials and Reagents

All chemicals were purchased from Sigma-Aldrich (St. Louis, MO) unless otherwise stated.

Culture and Differentiation of Cells

3T3-L1 fibroblasts were cultured and differentiated as described (Norseen et al., 2012). STC-1 cells were maintained in DMEM supplemented with 10% FCS, pen/strep and maintained at 37°C and 5% CO_2.

Pancreatic Islets, GSIS, and GLP-1 Secretion Studies

Human islets from nondiabetic donors were obtained from Prodo Laboratories (Irvine, CA). GSIS studies (Kowluru et al., 2010) and GLP-1 secretion from STC-1 cells (Hirasawa et al., 2005) were performed as described.

Generation and Treatment of Bone-Marrow-Derived Dendritic Cells

BMDCs were generated as described (Moraes-Vieira et al., 2014). Cells were incubated with 9-PAHSA 10 min prior to LPS (100 ng/ml) stimulation. CD11c, MHC II, CD40, CD80 and CD86 (all Biolegend) were detected by flow cytometry as described (Moraes-Vieira et al., 2014). Cytokine levels were measured by ELISA (Biolegend).

9-PAHSA Biosynthetic Activity Assay

Liver and PG-WAT tissue was Dounce homogenized in buffer A (10 mM Tris-HCL (pH 7.4), 250 mM Sucrose containing protease inhibiters (Roche)). Lysates were centrifuged at 1,200 g to remove incompletely lysed cells and debris. Lysates were then adjusted to 1 mg/ml protein and 100 μl was incubated with 100 μM palmitoyl-CoA and 100 μM 9-hydroxy stearic acid (PAHSA substrates) for 2 hr at 37°C. Control samples were heat denatured by boiling for 10 min prior to incubation with PAHSA substrates. After 2 hr the reaction was stopped by the addition of 300 μl cold buffer A followed by 400 μl of methanol (MeOH) and 800 μl of chloroform. Samples were vortexed and centrifuged at 1,200 g for 5 min. 9-PAHSA levels in the organic layer were measured by LC-MS.

FAHFA Synthesis In Vivo

Two hours postfood removal C57B6/J mice were gavaged with 25 mg/Kg of 9-hydroxy heptadecanoic acid or vehicle. Three hours later mice were sacrificed and serum was collected. Serum lipids were extracted and 9-PAHHA levels measured by LC-MS.

Animal Studies and Measurement of Metabolic Parameters

Female AG4OX mice and WT FVB littermate controls (Shepherd et al., 1993) at 8–14 weeks old were used for FAHFA tissue distribution and regulation with fasting and HFD studies. ChREBP-KO, ChREBP-KO/AG4OX and control females (Herman et al., 2012) were used at 16–18 weeks old. Mice were fed on chow (Lab Diet, 5008) or HFD (Harlan Teklad, TD.93075) for 9 weeks (female FVB) or 42–52 weeks (male C57BL6/J). OGTT's were performed as described (Moraes-Vieira et al., 2014) after 5 hr food removal.

Anti-Inflammatory Effects of 9-PAHSA In Vivo

Male C57BL6/J mice on chow or HFD described above were gavaged once a day for 3 days with 30 mg/kg (chow) or 45 mg/kg (HFD) of 9-PAHSA or an equivalent volume of vehicle. On the 4th day PG stromal vascular fraction (SVF) cells were harvested and cultured for 5 hr with ionomycin, PMA and brefeldin at 37°C and the intracellular cytokine content was measured in gated CD45$^+$, CD11b$^+$, and F4/80$^+$ cells as described (Moraes-Vieira et al., 2014).

Human Studies

Hyperinsulinemic-euglycemic clamp was performed in 13 nondiabetic subjects. SQ WAT biopsies were obtained from the peri-umbilical, abdominal region after an overnight fast.

Lipid Extraction

Lipid extraction was performed as described (Bligh and Dyer, 1959; Saghatelian et al., 2004). Tissues (60–150 mg) were Dounce homogenized on ice in a mixture of 1.5 ml MeOH, 1.5 ml chloroform and 3 ml citric acid buffer. PAHSA standards were added to chloroform prior to extraction. The resulting mixture was centrifuged and the organic phase containing extracted lipids was dried under N_2 and stored at −80°C prior to solid phase extraction.

Lipidomic Analysis

Lipidomic analysis was performed using an Agilent 6220 ESI-TOF fitted with an electrospray ionization source with a capillary voltage of 3,500 kV and fragmentor voltage of 100 V. A Gemini C18 reversed phase column (Phenomenex) and a C18 reversed phase guard column (Western Analytical) was used for LC-MS analysis in negative mode. In positive mode, a Luna C5 reversed phase column (Phenomenex) was used together with a C4 reversed phase guard column (Western Analytical). Drying gas temperature was 350°C, flow rate 10 l/min and nebulizer pressure 45 psi. Untargeted data were collected using an m/z of 100–1,500.

ADD

Structural characterization of the FAHFAs by MS/MS was carried out on an Agilent 6510 quadrupole-time of flight MS.

Synthesis of PAHSAs and PAHSA Standards

Detailed information on synthesis of PAHSAs and PAHSA standards is outlined in the Supplemental Information.

Targeted LC/MS Analysis of FAHFAs

FAHFAs were measured on an Agilent 6410 Triple Quad LC/MS via Multiple Reaction Monitoring in negative ionization mode. Extracted and fractionated samples were reconstituted in 25 μl MeOH; 10 μl was injected for analysis. A Luna C18(2) (Phenomenex) column was used with an in-line filter (Phenomenex). Distinct PAHSA species were resolved via isocratic flow at 0.2 ml/min for 120 min using 93:7 MeOH:H_2O with 5 mM ammonium acetate and 0.01% ammonium hydroxide as solvent. Transitions for endogenous PAHSAs were m/z 537.5 → m/z 255.2 (Collision Energy [CE] = 30 V), m/z 537.5 → m/z 281.2 (CE = 25 V), and m/z 537.5 → m/z 299.3 (CE = 23 V), and the transition for ^{13}C-9-PAHSA was m/z 553.5 → m/z 271.3 (CE = 30 V), all FAHFA transitions are listed in Supplemental Information.

Data Analysis

All values are means ± SEM. Differences between groups were assessed using unpaired two-tailed Student's t tests and/or ANOVA with Fisher's LSD multiple comparisons as specified in figure legends. All statistical analyses were performed with GraphPad Prism 5.

SUPPLEMENTAL INFORMATION

Supplemental Information includes Extended Experimental Procedures, four figures, four tables, and one data file and can be found with this article online at http://dx.doi.org/10.1016/j.cell.2014.09.035.

AUTHOR CONTRIBUTIONS

M.M.Y. and I.S. conceived of, designed, performed, and interpreted experiments and made figures. P.M.M.-V. designed, performed and interpreted the immunology experiments and made the figures. M.A.H. conceived of the untargeted lipidomics experiment and E.A.H. and M.A.H. designed and performed the untargeted lipidomics experiment. E.A.H. designed, performed and interpreted the data from the structure elucidation studies. E.A.H. and A.S. designed and performed chemical synthesis of the lipids. T.Z., I.S., E.A.H. and S.C. developed and applied new targeted lipidomics methods. J.L., A.S.D., O.D.P. assisted with animal studies. B.B.K., I.S., U.S., and A.H. designed, performed and interpreted the data from human studies. R.T.P, T.E.M. designed and performed Glut4 translocation assays. B.B.K. and A.S. conceived of, designed and supervised the experimental plan and interpreted experiments. B.B.K., A.S., M.M.Y. and I.S. wrote the manuscript. M.A.H., P.M.M.V., O.D.P., T.E.M., and J.L. edited the manuscript.

ACKNOWLEDGMENTS

We thank Dr. Thue Schwartz for stimulating discussions; Drs. Anna Greka and Dequan Tian for performing functional assays; Pratik Aryal, Marlee Jackson, Kerry Wellenstein, and Peter Dwyer for technical assistance; and Dr. Douglas Hanahan for the STC1 cells. Supported by grants from the NIH R37DK43051 and P30 DK57521 (B.B.K.); R01 DK098002 (B.B.K. and T.E.M.); a grant from the JPB foundation (B.B.K.). Searle Scholars Award, Burroughs Welcome Fund CABS, and Sloan Foundation Fellowship (A.S.); Harvard Training Program in Nutrition and Metabolism, 2T32HD052961 (M.M.Y.); 5T32DK007516 (B.B.K., M.M.Y., and J.L.); K08 DK076726 (M.A.H.); P30 DK046200 (M.A.H.). B.B.K., M.A.H., A.S., and E.A.H. are inventors on a patent related to the fatty acid hydroxy-fatty acids.

Received: March 23, 2014
Revised: July 15, 2014
Accepted: September 18, 2014
Published: October 9, 2014

REFERENCES

Abel, E.D., Peroni, O., Kim, J.K., Kim, Y.B., Boss, O., Hadro, E., Minnemann, T., Shulman, G.I., and Kahn, B.B. (2001). Adipose-selective targeting of the GLUT4 gene impairs insulin action in muscle and liver. Nature *409*, 729–733.

Benhamed, F., Denechaud, P.D., Lemoine, M., Robichon, C., Moldes, M., Bertrand-Michel, J., Ratziu, V., Serfaty, L., Housset, C., Capeau, J., et al. (2012). The lipogenic transcription factor ChREBP dissociates hepatic steatosis from insulin resistance in mice and humans. J. Clin. Invest. *122*, 2176–2194.

Bligh, E.G., and Dyer, W.J. (1959). A rapid method of total lipid extraction and purification. Can. J. Biochem. Physiol. *37*, 911–917.

Boden, G., and Shulman, G.I. (2002). Free fatty acids in obesity and type 2 diabetes: defining their role in the development of insulin resistance and beta-cell dysfunction. Eur. J. Clin. Invest. *32* (*Suppl 3*), 14–23.

Bruss, M.D., Khambatta, C.F., Ruby, M.A., Aggarwal, I., and Hellerstein, M.K. (2010). Calorie restriction increases fatty acid synthesis and whole body fat oxidation rates. Am. J. Physiol. Endocrinol. Metab. *298*, E108–E116.

Butovich, I.A., Wojtowicz, J.C., and Molai, M. (2009). Human tear film and meibum. Very long chain wax esters and (O-acyl)-omega-hydroxy fatty acids of meibum. J. Lipid Res. *50*, 2471–2485.

Cao, H., Gerhold, K., Mayers, J.R., Wiest, M.M., Watkins, S.M., and Hotamisligil, G.S. (2008). Identification of a lipokine, a lipid hormone linking adipose tissue to systemic metabolism. Cell *134*, 933–944.

Carvalho, E., Jansson, P.A., Nagaev, I., Wenthzel, A.M., and Smith, U. (2001). Insulin resistance with low cellular IRS-1 expression is also associated with low GLUT4 expression and impaired insulin-stimulated glucose transport. FASEB J. *15*, 1101–1103.

Carvalho, E., Kotani, K., Peroni, O.D., and Kahn, B.B. (2005). Adipose-specific overexpression of GLUT4 reverses insulin resistance and diabetes in mice lacking GLUT4 selectively in muscle. Am. J. Physiol. Endocrinol. Metab. *289*, E551–E561.

Hara, T., Kimura, I., Inoue, D., Ichimura, A., and Hirasawa, A. (2013). Free fatty acid receptors and their role in regulation of energy metabolism. Rev. Physiol. Biochem. Pharmacol. *164*, 77–116.

Herman, M.A., Peroni, O.D., Villoria, J., Schön, M.R., Abumrad, N.A., Blüher, M., Klein, S., and Kahn, B.B. (2012). A novel ChREBP isoform in adipose tissue regulates systemic glucose metabolism. Nature *484*, 333–338.

Hirasawa, A., Tsumaya, K., Awaji, T., Katsuma, S., Adachi, T., Yamada, M., Sugimoto, Y., Miyazaki, S., and Tsujimoto, G. (2005). Free fatty acids regulate gut incretin glucagon-like peptide-1 secretion through GPR120. Nat. Med. *11*, 90–94.

Hu, F.B. (2011). Globalization of diabetes: the role of diet, lifestyle, and genes. Diabetes Care *34*, 1249–1257.

Ichimura, A., Hirasawa, A., Poulain-Godefroy, O., Bonnefond, A., Hara, T., Yengo, L., Kimura, I., Leloire, A., Liu, N., Iida, K., et al. (2012). Dysfunction of lipid sensor GPR120 leads to obesity in both mouse and human. Nature *483*, 350–354.

Iizuka, K., Bruick, R.K., Liang, G., Horton, J.D., and Uyeda, K. (2004). Deficiency of carbohydrate response element-binding protein (ChREBP) reduces lipogenesis as well as glycolysis. Proc. Natl. Acad. Sci. USA *101*, 7281–7286.

Lumeng, C.N., and Saltiel, A.R. (2011). Inflammatory links between obesity and metabolic disease. J. Clin. Invest. *121*, 2111–2117.

Ma, L., Tsatsos, N.G., and Towle, H.C. (2005). Direct role of ChREBP.Mlx in regulating hepatic glucose-responsive genes. J. Biol. Chem. *280*, 12019–12027.

Mo, X.L., Wei, H.K., Peng, J., and Tao, Y.X. (2013). Free fatty acid receptor GPR120 and pathogenesis of obesity and type 2 diabetes mellitus. Prog. Mol. Biol. Transl. Sci. *114*, 251–276.

Moe, M.K., Strøm, M.B., Jensen, E., and Claeys, M. (2004). Negative electrospray ionization low-energy tandem mass spectrometry of hydroxylated fatty acids: a mechanistic study. Rapid Commun. Mass Spectrom. *18*, 1731–1740.

Moraes-Vieira, P.M., Yore, M.M., Dwyer, P.M., Syed, I., Aryal, P., and Kahn, B.B. (2014). RBP4 activates antigen-presenting cells, leading to adipose tissue inflammation and systemic insulin resistance. Cell Metab. *19*, 512–526.

Norseen, J., Hosooka, T., Hammarstedt, A., Yore, M.M., Kant, S., Aryal, P., Kiernan, U.A., Phillips, D.A., Maruyama, H., Kraus, B.J., et al. (2012). Retinol-binding protein 4 inhibits insulin signaling in adipocytes by inducing proinflammatory cytokines in macrophages through a c-Jun N-terminal kinase- and toll-like receptor 4-dependent and retinol-independent mechanism. Mol. Cell. Biol. *32*, 2010–2019.

Oh, D.Y., Talukdar, S., Bae, E.J., Imamura, T., Morinaga, H., Fan, W., Li, P., Lu, W.J., Watkins, S.M., and Olefsky, J.M. (2010). GPR120 is an omega-3 fatty acid receptor mediating potent anti-inflammatory and insulin-sensitizing effects. Cell *142*, 687–698.

Oh, Y., Walenta, E., Akiyama, T.E., Lagakos, W.S., Lackey, D., Pessentheiner, A.R., Sasik, R., Hah, N., Chi, T.J., Cox, J.M., et al. (2014). A Gpr120-selective agonist improves insulin resistance and chronic inflammation in obese mice. Nat. Med. *20*, 942–947.

Olefsky, J.M., and Glass, C.K. (2010). Macrophages, inflammation, and insulin resistance. Annu. Rev. Physiol. *72*, 219–246.

Rhee, E.P., Cheng, S., Larson, M.G., Walford, G.A., Lewis, G.D., McCabe, E., Yang, E., Farrell, L., Fox, C.S., O'Donnell, C.J., et al. (2011). Lipid profiling identifies a triacylglycerol signature of insulin resistance and improves diabetes prediction in humans. J. Clin. Invest. *121*, 1402–1411.

Risérus, U., Willett, W.C., and Hu, F.B. (2009). Dietary fats and prevention of type 2 diabetes. Prog. Lipid Res. *48*, 44–51.

Roberts, R., Hodson, L., Dennis, A.L., Neville, M.J., Humphreys, S.M., Harnden, K.E., Micklem, K.J., and Frayn, K.N. (2009). Markers of de novo lipogenesis in adipose tissue: associations with small adipocytes and insulin sensitivity in humans. Diabetologia *52*, 882–890.

Saghatelian, A., Trauger, S.A., Want, E.J., Hawkins, E.G., Siuzdak, G., and Cravatt, B.F. (2004). Assignment of endogenous substrates to enzymes by global metabolite profiling. Biochemistry *43*, 14332–14339.

Shepherd, P.R., and Kahn, B.B. (1999). Glucose transporters and insulin action—implications for insulin resistance and diabetes mellitus. N. Engl. J. Med. *341*, 248–257.

Shepherd, P.R., Gnudi, L., Tozzo, E., Yang, H., Leach, F., and Kahn, B.B. (1993). Adipose cell hyperplasia and enhanced glucose disposal in transgenic mice overexpressing GLUT4 selectively in adipose tissue. J. Biol. Chem. *268*, 22243–22246.

Smith, C.A., O'Maille, G., Want, E.J., Qin, C., Trauger, S.A., Brandon, T.R., Custodio, D.E., Abagyan, R., and Siuzdak, G. (2005). METLIN: a metabolite mass spectral database. Ther. Drug Monit. *27*, 747–751.

Sud, M., Fahy, E., Cotter, D., Brown, A., Dennis, E.A., Glass, C.K., Merrill, A.H., Jr., Murphy, R.C., Raetz, C.R., Russell, D.W., and Subramaniam, S. (2007). LMSD: LIPID MAPS structure database. Nucleic Acids Res. *35* (Database issue), D527–D532.

Tozzo, E., Shepherd, P.R., Gnudi, L., and Kahn, B.B. (1995). Transgenic GLUT-4 overexpression in fat enhances glucose metabolism: preferential effect on fatty acid synthesis. Am. J. Physiol. *268*, E956–E964.

Virtanen, J.K., Mursu, J., Voutilainen, S., Uusitupa, M., and Tuomainen, T.P. (2014). Serum omega-3 polyunsaturated fatty acids and risk of incident type 2 diabetes in men: the Kuopio Ischemic Heart Disease Risk Factor study. Diabetes Care *37*, 189–196.

Cell

Epigenetic Priming of Memory Updating during Reconsolidation to Attenuate Remote Fear Memories

Johannes Gräff,[1,2,3,6,7] Nadine F. Joseph,[1,2,3,6] Meryl E. Horn,[1,2,8] Alireza Samiei,[1] Jia Meng,[1,2,9] Jinsoo Seo,[1,2] Damien Rei,[1,2] Adam W. Bero,[1,2] Trongha X. Phan,[1,2] Florence Wagner,[3] Edward Holson,[3] Jinbin Xu,[4] Jianjun Sun,[4] Rachael L. Neve,[1] Robert H. Mach,[4] Stephen J. Haggarty,[3,5] and Li-Huei Tsai[1,2,3,*]

[1]Picower Institute for Learning and Memory, Department of Brain and Cognitive Sciences, Massachusetts Institute of Technology, Cambridge, MA 02139, USA

[2]Howard Hughes Medical Institute, Department of Brain and Cognitive Sciences, Massachusetts Institute of Technology, Cambridge, MA 02139, USA

[3]Broad Institute of Harvard University and Massachusetts Institute of Technology, Cambridge, MA 02142, USA

[4]Mallinckrodt Institute of Radiology, Department of Radiology, Washington University School of Medicine, St. Louis, MO 63110, USA

[5]Center for Human Genetic Research, Departments of Neurology and Psychiatry, Massachusetts General Hospital, Harvard Medical School, Boston, MA 02114, USA

[6]These authors contributed equally to this work

[7]Present address: Brain Mind Institute, School of Life Sciences, Swiss Federal Institute of Technology (EPFL), CH-1015 Lausanne, Switzerland

[8]Present address: Neuroscience Graduate Program, University of California, San Francisco, San Francisco, CA 94158, USA

[9]Present address: Department of Biological Sciences, Xi'an Jiaotong-Liverpool University, Suzhou, Jiangsu 215123, China

*Correspondence: lhtsai@mit.edu

http://dx.doi.org/10.1016/j.cell.2013.12.020

SUMMARY

Traumatic events generate some of the most enduring forms of memories. Despite the elevated lifetime prevalence of anxiety disorders, effective strategies to attenuate long-term traumatic memories are scarce. The most efficacious treatments to diminish recent (i.e., day-old) traumata capitalize on memory updating mechanisms during reconsolidation that are initiated upon memory recall. Here, we show that, in mice, successful reconsolidation-updating paradigms for recent memories fail to attenuate remote (i.e., month-old) ones. We find that, whereas recent memory recall induces a limited period of hippocampal neuroplasticity mediated, in part, by S-nitrosylation of HDAC2 and histone acetylation, such plasticity is absent for remote memories. However, by using an HDAC2-targeting inhibitor (HDACi) during reconsolidation, even remote memories can be persistently attenuated. This intervention epigenetically primes the expression of neuroplasticity-related genes, which is accompanied by higher metabolic, synaptic, and structural plasticity. Thus, applying HDACis during memory reconsolidation might constitute a treatment option for remote traumata.

INTRODUCTION

Fear and other anxiety disorders develop after the experience of a traumatic event such as grave physical or psychological harm. Because of a strong emotional underpinning, traumatic memories are extraordinarily robust and difficult to treat, evidenced by an estimated lifetime prevalence of close to 29% (Kessler et al., 2005). Among the most efficacious treatments for anxiety disorders are exposure-based therapies (Cukor et al., 2010; Foa, 2000; Foa and Kozak, 1986), during which a patient is repeatedly confronted with the original fear-eliciting stimulus in a safe environment so that the once fearful stimulus can be newly interpreted as neutral or safe (Foa and Kozak, 1986). A fundamental element for successful exposure-based therapies is the reactivation of the traumatic memory (Foa and Kozak, 1986), which initiates a time-limited process called memory reconsolidation, during which a memory becomes susceptible to modification (Misanin et al., 1968; Nader et al., 2000).

In the context of exposure-based therapies, reconsolidation-updating approaches have proven effective to attenuate the response to fearful stimuli in humans and rodents alike (Monfils et al., 2009; Schiller et al., 2010), and similar paradigms have been successfully used to prevent drug craving and relapse (Xue et al., 2012). Based on the assumption of a period of updating or learning during memory reconsolidation (McKenzie and Eichenbaum, 2011; Nader and Hardt, 2009; Tronson and Taylor, 2007), several other studies have referred to pharmacological means in order to enhance this process (Kaplan and Moore, 2011). Among those, histone deacetylase inhibitors (HDACis)

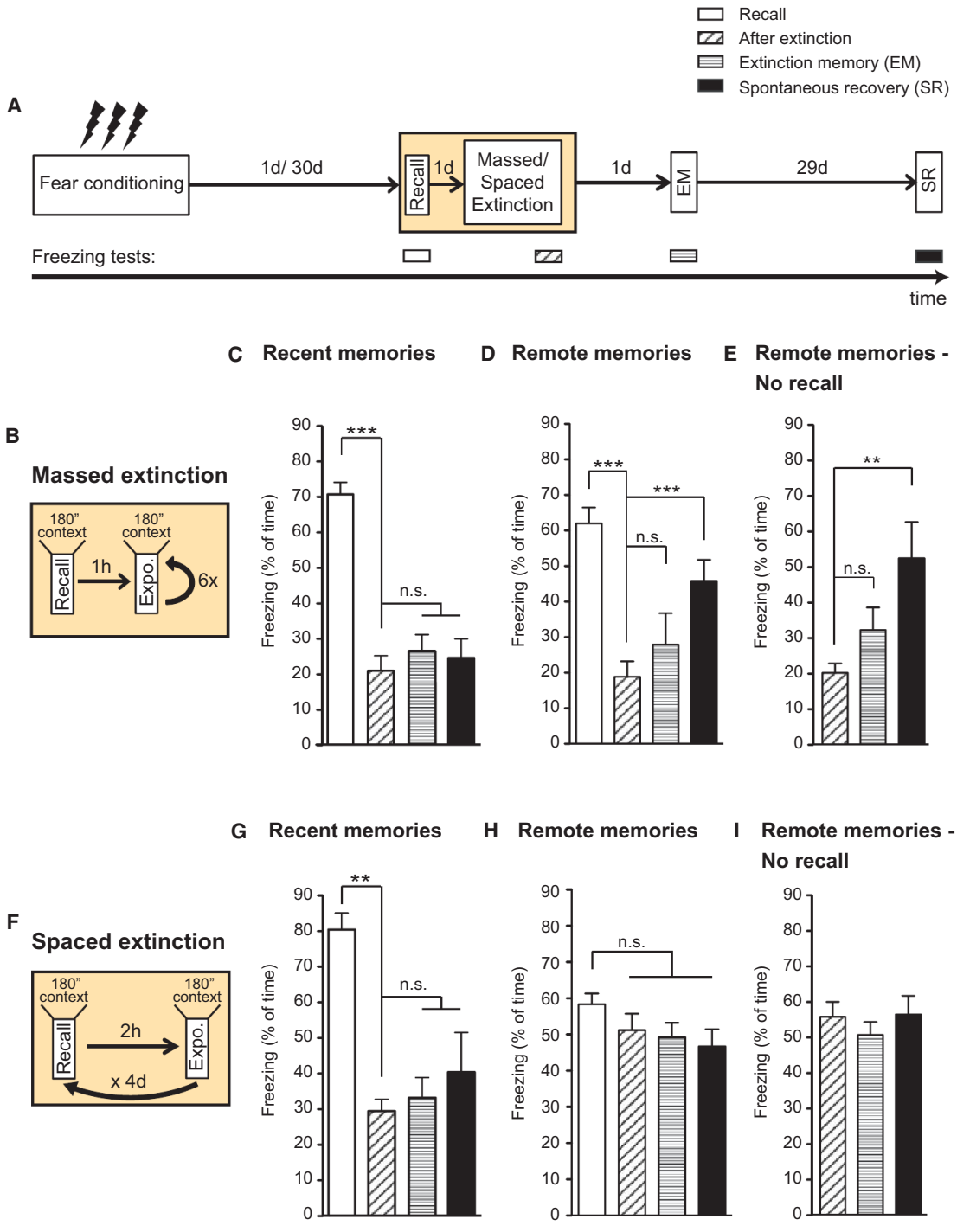

Figure 1. Remote Fear Memories Are Resistant to Attenuation despite Using Reconsolidation-Updating Mechanisms

(A) Schematic of the experimental paradigm. For details, see text.

(B) Schematic of the massed extinction paradigm.

(C) Using the massed extinction paradigm for contextual fear memories, recent memories show no signs of spontaneous recovery (n = 10; repeated-measurements ANOVA; $p \leq 0.0001$).

(D) Using the same massed extinction paradigm, remote memories spontaneously recover (n = 9; repeated-measurements ANOVA; $p \leq 0.0001$).

(E) Using the same paradigm but without memory recall, remote memories spontaneously recover (n = 10; repeated-measurements ANOVA; $p \leq 0.0001$).

(F) Schematic of the spaced extinction paradigm.

(legend continued on next page)

might be a particularly promising candidate to permanently modify fearful memories (Lattal and Wood, 2013) for two reasons. First, by modifying chromatin compaction, epigenetic mechanisms can have potentially stable and long-lasting effects on gene expression (Levenson and Sweatt, 2005), a required feature of long-term memories (Kandel, 2001); second, epigenetic mechanisms per se can target a vast variety of nuclear processes involved in neuronal plasticity (Gräff et al., 2011), such that their effect is not restricted to a particular signaling pathway.

Remarkably, almost all of these either purely behavioral or pharmacologically supported approaches to attenuate fearful responses have exclusively focused on recent, i.e., day-old, memories—leaving it unclear whether they would also be effective for remote, i.e., month-old, memories. As traumatic memories are oftentimes not readily amenable to immediate treatments (Kearns et al., 2012) and because remote memories are more stable than recent ones (Frankland et al., 2006; Inda et al., 2011; Milekic and Alberini, 2002; Suzuki et al., 2004), there is a clear need to investigate options to overcome remote fear memories.

RESULTS

Despite Using Reconsolidation-Updating Paradigms, Remote Memories Cannot Be Persistently Attenuated

To test whether exposure-therapy-based approaches can be used to attenuate remote traumatic memories, we used Pavlovian fear conditioning in mice, a commonly employed method to study fear responses underlying traumatic memories such as posttraumatic stress disorder (PTSD) (Mahan and Ressler, 2012). In fear conditioning, an unconditioned stimulus (US)—an electrical footshock—is paired with a conditioned stimulus (CS)—either a specific tone or context for cued and contextual fear conditioning, respectively. When the animals are later tested for their fear memory by exposing them to the CS, the CS alone will elicit the conditioned response (CR), freezing. Specifically, we trained mice for either cued or contextual fear conditioning, 1 day and 30 days after which we attempted to attenuate their CR by different fear extinction paradigms (Figure 1A, Experimental Procedures, and Figure S1A available online). All of these paradigms take advantage of a transient period of memory lability, the reconsolidation window, that occurs between 1 and 6 hr following the memory recall (Monfils et al., 2009).

The first protocol aimed at extinguishing the CR to a tone (the CS) by employing a massed extinction paradigm for cued fear conditioning (Figure S1B, expo.). We found that, for recent memories, this paradigm persistently attenuated the CR immediately and 1 day after extinction (Figures S1C and S1F). Importantly, there were no signs of spontaneous recovery (SR) or reinstatement (RI) of the fear (Figures S1C and S1F), the presence of which is indicative of incomplete fear extinction (Bouton, 1993, 2004; Bouton and Bolles, 1979; Pavlov, 1927; Rescorla, 2004; Rescorla and Heth, 1975). For remote memories, in contrast, we found that, although this paradigm was effective in decreasing the freezing response after the extinction session, there were significant RI (Figure S1D) and SR (Figure S1G), indicating persistence of the original memory. This finding is consistent with the occurrence of both RI and SR upon remote memory extinction without memory recall (Figures S1E and S1H).

The second protocol aimed at attenuating the CR to a context (the CS) by a massed extinction paradigm adopted for contextual fear conditioning (Figure 1B) (Sananbenesi et al., 2007). By using this paradigm, recent fear memories could be successfully and permanently attenuated (Figure 1C), but remote fear memories showed significant SR (Figure 1D). Similar results were obtained when no recall was presented (Figure 1E).

Furthermore, because increasing the intertrial interval during fear extinction training has been shown to facilitate fear extinction of recent memories (Urcelay et al., 2009), we reasoned that such spacing would also help in attenuating remote memories (Figure 1F). This paradigm significantly attenuated recent fear memories, and there were no signs of SR (Figure 1G). However, when applied to remote memories, the same paradigm failed to even temporarily reduce fear, and when tested for SR, freezing levels were comparable to those during memory recall (Figure 1H). Similar results were obtained in the absence of memory recall (Figure 1I).

Together, these results indicate that three different behavioral paradigms that successfully extinguish recent fear memories were not capable of doing so for remote fear memories, despite taking advantage of the transient period of memory lability induced by memory recall. The question arises as to why remote fear memories are more difficult to extinguish.

Recalling Remote Memories Is Not Salient Enough to Induce Histone Acetylation-Mediated Neuronal Plasticity in the Hippocampus

By definition, the reconsolidation window opened by memory recall allows previously acquired memories to be updated with new information and is thereby thought to initiate a new period of neuronal plasticity (Hartley and Phelps, 2010; McKenzie and Eichenbaum, 2011). We hypothesized that the same memory recall might not induce the same extent of neuronal plasticity for remote as for recent memories. For the subsequent analyses, we focused on contextual fear memories, the formation of which depends on the hippocampus, a brain area crucial for memory-related neuronal plasticity (Kandel et al., 2013) that is activated upon remote memory recall (Debiec et al., 2002). One fundamental mechanism that governs neuronal plasticity is the epigenetic modification of gene expression by acetylation of histone proteins (Levenson and Sweatt, 2005). Histone acetylation promotes a chromatin structure that is more permissive for

(G) Using the spaced extinction paradigm for contextual fear memories, recent memories show significant attenuation of fear and no signs of spontaneous recovery (n = 12; repeated-measurements ANOVA; $p = 0.0038$).

(H) Using the same spaced extinction paradigm, remote memories show no signs of attenuation (n = 16).

(I) Using the spaced extinction paradigm without memory recall, remote memories show no signs of attenuation (n = 12).

Error bars indicate ± SEM. *$p \leq 0.05$, **$p \leq 0.01$, ***$p \leq 0.001$ for Tukey's posthoc analysis. See also Figure S1 for results of remote cued fear memories.

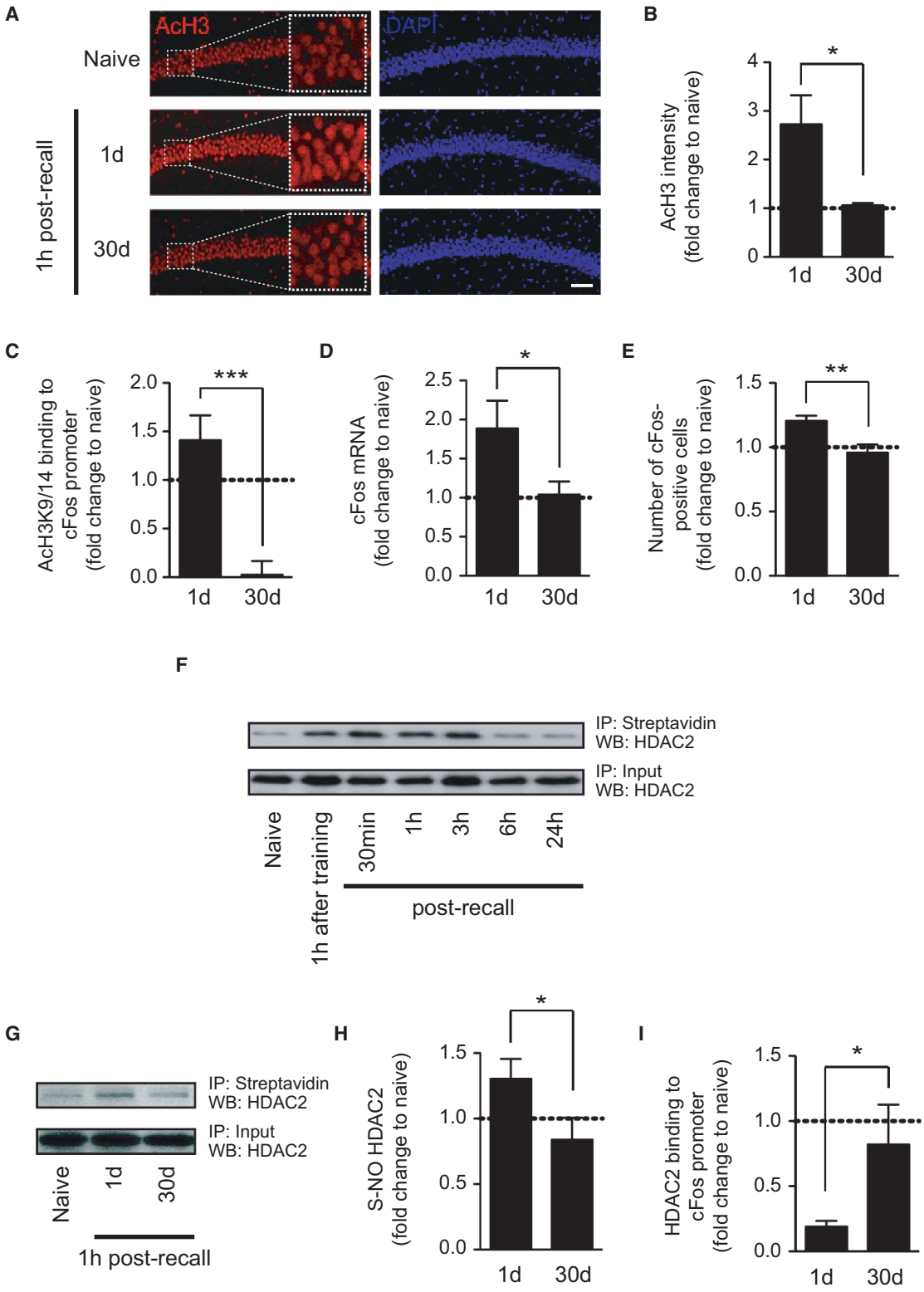

Figure 2. The Recall of Remote Memories Is Not Salient Enough to Induce Neuroplasticity-Permitting Histone Acetylation Changes

(A) Representative images of immunohistochemical labelings of acetylated H3K9/14 ("AcH3") in hippocampal area CA1 1 hr after recent and remote memory recall as compared to behaviorally naive animals. Scale bar, 100 μm.

(B) Quantification thereof (n = 3–4 animals each).

(legend continued on next page)

gene transcription (Brownell and Allis, 1996) and thereby positively regulates transcription-dependent long-lasting forms of neuronal plasticity.

To test whether the same memory recall leads to differences in histone acetylation between remote and recent memories, we first used immunohistochemical analyses to assess the acetylation of histone 3 on lysine residues 9 and 14 (H3K9/14), a modification associated with facilitated neuronal plasticity (Gräff et al., 2011). We found that, 1 hr post memory recall, hippocampal H3K9/14 acetylation of remote memories was indistinguishable from behaviorally naive animals but was significantly smaller than that of recent memories (Figures 2A and 2B). Next, we carried out chromatin immunoprecipitation (ChIP) to determine the abundance of H3K9/14 acetylation at the promoter region of *cFos*, an immediate early gene regulated by neuronal activity and critical for neuronal plasticity (Tischmeyer and Grimm, 1999). Consistent with the overall histone acetylation pattern, we found the *cFos* promoter to be hypoacetylated after remote memory recall compared to after recent memory recall (Figure 2C). Accordingly, the expression of *cFos* was significantly reduced after remote memory recall (Figure 2D), an effect that was also observed at the protein level evidenced by the number cFos-positive cells (Figure 2E), as reported previously (Frankland et al., 2004).

Increments in histone acetylation are dependent on neuronal activity (Levenson and Sweatt, 2005), and one pathway shown to mediate these changes in cultured neurons involves the dissociation of histone deacetylase 2 (HDAC2) from the chromatin following its nitrosylation on Cys262 and Cys274 (Nott et al., 2008). We therefore investigated whether the lack of increased histone acetylation following remote memory recall might be due to a lack of hippocampal HDAC2 nitrosylation. Using a biotin-switch assay, we found that, for recent memories, HDAC2 becomes nitrosylated between 30 and 60 min following memory recall, a state that lasted for no longer than 6 hr (Figure 2F). Thus, HDAC2 nitrosylation correlated with the limited period of memory lability during the reconsolidation window (Monfils et al., 2009). In contrast, we detected no increase in HDAC2 nitrosylation following remote memory recall (Figures 2G and 2H). Consistent with its nitrosylation status, the binding of HDAC2 to the promoter of *cFos* was reduced following recent memory recall, whereas HDAC2 was still bound to the chromatin after the recall of remote memories (Figure 2I). Importantly, memory recall was necessary to elicit all of the changes described above (Figure S2). Together, these results indicate that, in contrast to recent memories, the recall of remote memories fails to install HDAC2 nitrosylation and histone acetylation-mediated neuronal plasticity in the hippocampus.

S-Nitrosylation of HDAC2 in the Hippocampus Is Critical for Memory Updating during Reconsolidation

To further assess the role of nitrosylated HDAC2 in mediating such neuroplasticity, we treated fear-conditioned mice with N_{ω}-Nitro-L-arginine methyl ester (L-NAME), an inhibitor of nitric oxide (NO) synthase, before the recall of recent memories and extinction training (Figure 3A). We reasoned that, if nitrosylation plays a role in facilitating the update of recent memories, its inhibition would prevent it. We found that, although L-NAME-treated animals showed significant attenuation of fear after extinction training, their fear spontaneously recovered (Figure 3B). In contrast, VEH-treated animals showed no SR (Figure 3B). L-NAME treatment did not affect the overall behavior of the animals (Figures S3A–S3D). Interestingly, L-NAME treatment also abolished the recall-induced nitrosylation of HDAC2 1 hr after memory recall (Figure 3C), suggesting that HDAC2 nitrosylation might be critical for recall-induced memory updating during reconsolidation.

Then, to prove a causal implication of HDAC2 nitrosylation in memory updating, we used the following strategy. We treated mice before remote memory recall with the nitric oxide donor molsidomine (MOL), which should facilitate memory updating of even remote memories, and simultaneously overexpressed a non-nitrosylateable form of HDAC2, the double-alanine mutant $HDAC2^{C262/274A}$(Nott et al., 2008), which should prevent remote memories from being updated in the presence of MOL. To this end, we injected short-term herpes simplex viral (HSV) vectors carrying either $HDAC2^{WT}$ or $HDAC2^{C262/274A}$ (Figure S3E) into hippocampal area CA1 (Figure S3F) 3 days before remote memory recall to assure maximal expression at the time of recall. Then, 1 hr prior to recall and subsequent extinction training, we administered MOL or its vehicle to both groups (Figure 3D). We found that, whereas MOL-administration increased HDAC2 nitrosylation in HSV-$HDAC2^{WT}$-injected animals 1 hr after remote memory recall, HSV-$HDAC2^{C262/274A}$-injected mice showed no HDAC2 nitrosylation despite MOL treatment (Figure 3E), indicating that, in $HDAC2^{C262/274A}$-injected animals, HDAC2 is predominantly present in its non-nitrosylateable form. When tested for fear extinction, MOL-treated HSV-$HDAC2^{WT}$-injected animals showed significant fear reduction after memory extinction and no signs of SR (Figure 3F), suggesting that the NO donor allowed for successful memory updating. In contrast, MOL-treated $HDAC2^{C262/274A}$-injected animals showed significant SR despite successful memory extinction immediately and 1 day after extinction training (Figure 3F). Importantly, MOL treatment did not affect the animals' general behavior (Figures S3G–S3J). Together, these results indicate that nitrosylation of HDAC2 following memory recall is a critical event for remote

(C) Quantitative PCR results of the abundance of acetylated H3K9/14 in the promoter region of cFos at the same time points (n = 8 animals each).
(D) Quantitative RT-PCR results of the expression of *cFos* in the hippocampus at the same time points (n = 4–5 animals each).
(E) Quantification of the number of cFos-positive cells in the hippocampus at the same time points (n = 3 animals each).
(F) Western blot analysis of S-nitrosylation of HDAC2 using the biotin-switch assay and streptavidin precipitation 1 hr after contextual fear conditioning and at different intervals after recent memory recall.
(G) Representative pictures of western blot analysis of S-nitrosylation of HDAC2 1 hr after recent and remote memory recall.
(H) Quantification thereof (n = 3–4 animals each).
(I) Quantitative PCR results of HDAC2 binding to the promoter region of cFos at the same time points (n = 8 animals each).
Error bars indicate ± SEM. *$p \leq 0.05$, **$p \leq 0.01$, ***$p \leq 0.001$ by Student's t test. See also Figure S2.

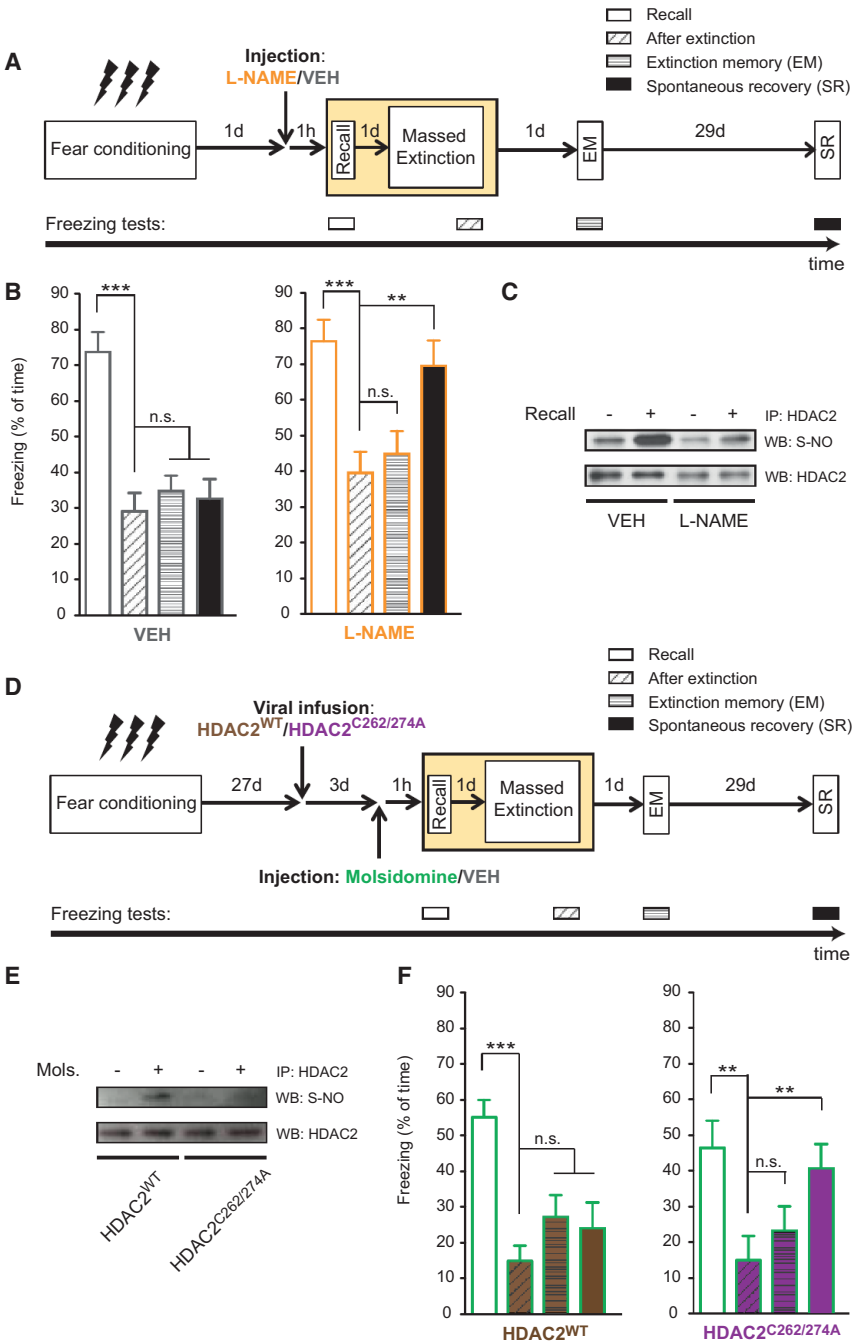

Figure 3. Nitrosylation of HDAC2 Is Critical for Memory Updating during Reconsolidation

(A) Schematic of the experimental paradigm. 1 hr before recent memory recall, L-NAME or its VEH was administered i.p.

(B) Using the massed extinction paradigm for contextual fear memories, L-NAME-treated animals show significant spontaneous recovery, whereas VEH-treated ones do not (n = 8 for each treatment; repeated-measurements ANOVA; $p \leq 0.0001$ for VEH, $p = 0.0034$ for L-NAME).

(C) Representative pictures of western blot analysis of S-nitrosylation of HDAC2 1 hr after or without recall of recent memories in L-NAME and VEH-treated animals.

(D) Schematic of the experimental paradigm. For details, see text.

(E) Representative pictures of western blot analysis of S-nitrosylation of HDAC2 1 hr after remote memory recall in molsidomine- or VEH-treated $HDAC2^{WT}$ or $HDAC2^{C262/274A}$-injected animals.

(F) Using the massed extinction paradigm for contextual fear memories, $HDAC2^{WT}$-treated animals show no signs of spontaneous recovery, whereas $HDAC2^{C262/274A}$-injected animals do (n = 7–10 for both groups; repeated-measurements ANOVA; $p \leq 0.0001$ for $HDAC2^{WT}$, $p = 0.01$ for $HDAC2^{C262/274A}$).

Error bars indicate ± SEM. *$p \leq 0.05$, **$p \leq 0.01$, ***$p \leq 0.001$ by Tukey's posthoc. See also Figure S3.

memories to become amenable for effective updating during reconsolidation.

By Using HDAC2-Targeting HDAC Inhibitors, Remote Fear Memories Can Be Attenuated

Because MOL cannot be targeted to HDAC2 alone, we hypothesized that, by using an HDAC2-targeting HDACi, it might also be possible to overcome the lack of neuroplasticity-related histone hyperacetylation for remote memories and, consequently, to enable memory-updating mechanisms. For this, we used the benzamide-based HDACi CI-994 (Figure 4A), a selective inhibitor of class I HDACs, including HDAC2 (Figure 4B). Systemic, intraperitoneal administration of 30 mg per kg resulted in high (C_{max} = 12.3 μM) and long-lasting ($T_{1/2}$ = 3.7 hr) levels of CI-994 in the brain (Figure 4C) and did not affect overall behavior (Figures S4A–S4D). To confidently target the memory-updating mechanisms during the reconsolidation window, we administered CI-994 or its vehicle (VEH) to fear-conditioned animals 1 hr post memory recall and then performed the extinction paradigms used previously (Figure 4D).

For the massed extinction paradigm, we found that, whereas VEH-treated animals showed significant SR (Figure 4E), CI-994-treated animals showed no signs thereof (Figure 4F). Furthermore, the fear-attenuating effect of the HDACi depended on memory recall, as we also observed SR when the HDACi was given without recall (Figure 4G). Next, when using the spaced extinction paradigm, which did not reduce remote fear memories (Figures 1H and 4H), we observed a significant reduction of the CR with CI-994, indicating memory extinction (Figure 4I). Importantly, we also observed a complete absence of SR, reflecting persistent memory extinction. This effect again depended on memory recall (Figure 4J). Of note, we observed the same

beneficial effects with the HDACi for remote cued fear memories (data not shown).

Importantly, HDACi administration did not generalize fear extinction. When mice were both cued and contextual fear conditioned yet only the context as a CS underwent extinction (using the spaced extinction paradigm), fearful memories associated with the cue were still present after successful extinction of the context (Figures S4E–S4G). Together, these results suggest that, by using an HDACi in combination with extinction training during the reconsolidation window, even remote contextual fear memories become amenable to persistent and specific attenuation.

HDAC Inhibitors Epigenetically Prime the Hippocampal Transcriptome for Reinstated Neuroplasticity

Next, we investigated the mechanisms by which the HDACi operates, hypothesizing that extinction training in conjunction with CI-994 would allow for increased histone acetylation-mediated neuroplasticity. We focused on the spaced extinction paradigm (Figure 1F), as this paradigm was the only one in which VEH- and CI-994-treated animals showed different fear responses immediately following the extinction procedure (Figures 4H and 4I). We first measured hippocampal histone acetylation using immunohistochemistry 1 hr after the end of the extinction procedure. We found that, compared to the histone acetylation of VEH-treated animals and that of 1 hr after remote memory recall, CI-994-treated animals showed significantly higher acetylation levels (Figures 5A and 5B). This was consistent with reduced hippocampal HDAC2 activity upon HDACi-treatment (Figure 5C). In the prefrontal cortex, where remote memories are primarily stored (Bontempi et al., 1999; Frankland and Bontempi, 2005; Frankland et al., 2004), histone acetylation following extinction training in combination with CI-994 was also elevated relative to VEH-treated animals and was comparable to levels 1 hr after remote memory recall (Figure S5), which may indicate persistent engagement of cortical areas in HDACi-treated animals. For the following analyses, we nevertheless focused exclusively on the hippocampus, as this brain area is critical for the incorporation of new information into a given memory trace during reconsolidation of contextual fear memories (Debiec et al., 2002).

Alongside histone acetylation, another critical aspect of neuroplasticity is the transcription of genes related to synaptic plasticity, learning, and memory (Kandel, 2001). To investigate those, we performed RNA sequencing of hippocampal extracts of both VEH and CI-994-treated animals 1 hr after completion of remote memory extinction. At an expression fold change cutoff of 1.4, we found 475 differentially expressed genes (DEGs) between CI-994 and VEH-treated animals, among which 199 genes showed higher expression in CI-994-treated animals (Figure 5D and Table S1). Upon generation of pathway and gene ontology analyses, we noticed these DEGs to be implicated in biological processes related to neuronal plasticity, such as learning or memory, regulation of transmission of nerve impulse, cell morphogenesis and projection, cation transport, and synaptic transmission (Figure 5E). These findings suggest that, by using CI-994 in combination with extinction training, neuroplasticity at the level of gene expression was enhanced.

Moreover, we detected several key regulators of neuronal plasticity to be significantly upregulated in CI-994-treated animals (Figure 5D). These genes include the immediate-early genes *Arc* and *cFos*, which are both critically involved in synaptic plasticity and memory-related processes (Korb and Finkbeiner, 2011; Shepherd and Bear, 2011; Tischmeyer and Grimm, 1999), *Adcy6*, an adenylate cyclase regulating neurite extension (Wu et al., 2011), *Npas4*, a transcription factor regulating contextual memory formation (Ramamoorthi et al., 2011; Lin et al., 2008), and *Igf2* (insulin-like growth factor 2), which facilitates memory retention (Chen et al., 2011) and extinction of recent fear memories (Agis-Balboa et al., 2011). qRT-PCR analysis of independent CI-994 and VEH-treated samples confirmed the expression changes of these genes (Figure 5F). Importantly, no such expression changes were detected when the HDACi was administered without extinction training (Figure 5G), in line with the observation that the HDACi alone had no behavioral effect (Figure 4J).

The genes with higher expression also showed higher acetylation in their promoter region (Figure 5H). Intriguingly, such increased histone acetylation occurred despite HDAC2 being bound to their promoter (Figure 5I). These findings suggest that the HDACi treatment following remote memory recall can compensate for the absence of HDAC2 nitrosylation and its persistent binding to the chromatin, thereby increasing histone acetylation-mediated neuroplasticity at the level of gene expression.

HDAC Inhibitors Lead to Increased Neuroplasticity during Memory Extinction

Lastly, we conducted a series of experiments to assess whether such increased expression of neuroplasticity-related genes would also result in facilitated synaptic plasticity. We first measured hippocampal glucose utilization 1 hr after completion of remote memory extinction by means of radiolabeled [^{3}H]2-deoxyglucose ([^{3}H]2-DG) uptake, which reflects neuronal activity (Magistretti, 2006). We found that CI-994-treated animals showed higher hippocampal [^{3}H]2-DG uptake compared to VEH-treated animals, depicting increased metabolic engagement of this brain area following memory extinction (Figures 6A and 6B). In contrast, [^{3}H]2-DG measurements did not differ between VEH- and CI-994-treated animals in the piriform cortex, a brain region implicated in olfactory memories and thus unrelated to the formation of contextual memories (Figure S6A).

Next, to test whether such increased metabolic activity was indicative of increased neuronal plasticity, we assessed long-term potentiation (LTP) at Schaffer collaterals by electrophysiological recordings at the same time point. Using triple theta-burst stimulation (3 × TBS), we observed that CI-994-treated animals displayed facilitated LTP compared to VEH-treated ones (Figure 6C). In contrast, we found no difference in basal synaptic transmission, as the slope of field excitatory postsynaptic potential (fEPSP) elicited by a given presynaptic fiber volley did not differ between the two groups (Figure S6B). Likewise, we detected no significant difference in paired-pulse facilitation (Figure S6C). These results suggest that a combination of extinction training and CI-994 administration leads to increased synaptic plasticity.

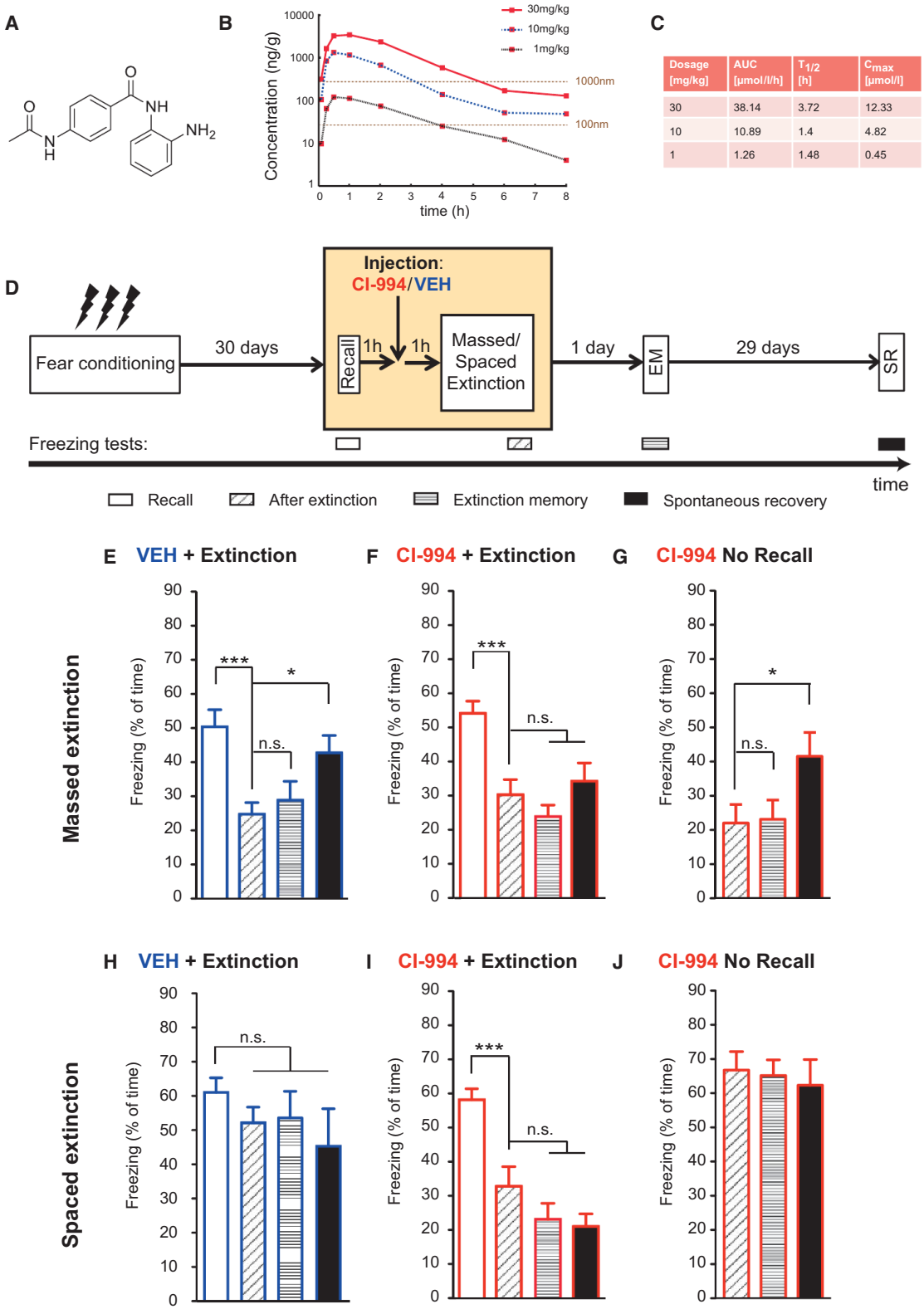

Figure 4. Remote Fear Memories Become Amenable to Attenuation by CI-994

(A) Chemical structure of CI-994, a benzamide-based HDAC inhibitor.

(B) Concentration-time curve of CI-994 in C57BL/6 mouse brain after a 30/10/1mg/kg i.p. dose.

(legend continued on next page)

Finally, we investigated whether such increased synaptic plasticity might also be accompanied by increased structural plasticity. For this, we measured the number of dendrites by microtubule-associated protein 2 (MAP2) immunohistochemistry, dendritic branching and the number of dendritic spines by Golgi staining, and the density of synapses by transmission electron microscopy and synaptophysin immunohistochemistry, a presynaptic marker, 1 hr after completion of memory extinction. These measurements reflect the degree of neuronal connectivity and thereby synaptic strength (Fiala et al., 2002). We found that CI-994-treated animals displayed an elevated number of MAP2-stained dendrites compared to VEH-treated ones in the stratum radiatum layer of the hippocampus (Figures 6D and 6E). Similarly, we detected a significant enhancement of dendritic branching between 120 and 170 μm from the soma as measured by Sholl analysis (Figures 6F and 6G), as well as a greater number of spines in CI-994-treated animals (Figures 6H and 6I). Of note, when analyzing the fine structure of these spines, we noticed a greater number of mushroom-like than thin spines upon HDACi-treatment (Figures 6H and 6J), an indicator of a more pronounced spine maturation process (Bourne and Harris, 2007). Lastly, the density of functional synapses was also markedly increased following CI-994 treatment (Figures 6K, 6L, and S6D, and S6E). Taken together, our findings demonstrate that, in addition to epigenetically enhancing neuroplasticity-related gene expression, the HDACi-treatment also resulted in increased synaptic and structural plasticity.

DISCUSSION

To our knowledge, this is the first report successfully attempting to attenuate remote fear responses in an animal model of traumatic memories. Using different behavioral protocols, a previous study also found that, despite using reconsolidation-updating paradigms that successfully extinguish recent fear memories, remote memories are resistant to attenuation (Costanzi et al., 2011). One potential mechanism behind such resilience of remote memories to be attenuated by behavioral interventions alone might be the lack of histone acetylation-mediated hippocampal neuroplasticity for remote memories presented here. Whereas recent memory recall allows for histone hyperacetylation and the expression of neuroplasticity-related genes such as *cFos* by stimulating HDAC2 nitrosylation and its subsequent dissociation from the chromatin, remote memory recall fails to do so (Figures 7A and 7B). Interestingly, learning itself is known to be accompanied by increased NO signaling in the hippocampus (Harooni et al., 2009), whereas mice lacking the enzyme neuronal NO synthase (nNOS) display contextual fear memory deficits (Itzhak et al., 2012). Thus, as per yet to be determined mechanisms, reduced hippocampal NO signaling toward HDAC2 might prevent a phase of learning that is crucial for remote memory updating.

While our molecular analyses focused primarily on the hippocampus, we do not exclude a possible contribution of similar or different mechanisms in other brain regions such as the amygdala (see Clem and Huganir, 2010) or cortical areas (see Figure S5) to the attenuation of remote memories. This latter brain area in particular would warrant further studies, as it is widely acknowledged that, as a memory matures, it becomes increasingly represented in and dependent on cortical areas (Nadel and Moscovitch, 1997; Frankland and Bontempi, 2005). Our finding of a lack of hippocampal neuroplasticity upon remote memory recall indeed supports this concept of hippocampal disengagement for remote memories (Figure 7B). However, it has also been known that, upon memory recall, even supposedly cortex-dependent remote memories re-enter a phase of hippocampus dependency (Debiec et al., 2002), and artificially inhibiting hippocampal activity (in area CA1) during memory recall in effect abolishes the capacity to recall remote memories (Goshen et al., 2011). The present results extend these findings by showing that recalling remote fear in conjunction with extinction training alone does not lead to a level of neuroplasticity that is sufficient for fear memory updating. Rather, it is the combined use of HDAC2-targeting HDACis and extinction training during memory reconsolidation that reinstates hippocampal neuroplasticity and permits updating of even remote traumatic memories (Figure 7C). This finding is reminiscent of an fMRI study in humans showing that subjects with persisting traumatic memories display lower hippocampal activation upon memory recall than those for whom fear memory extinction training was successful (Milad et al., 2009).

We found the HDACi treatment to trigger the upregulation of a key set of neuroplasticity-related genes, which was accompanied by increased histone acetylation in their respective promoter region. This observation indicates that the HDACi may epigenetically prime the chromatin into a transcriptionally permissive state, thereby allowing for enhanced neuroplasticity. Of the genes that exhibited increased expression following remote memory extinction, *cFos*, *Arc*, and *Igf2* were also found to be increased after the extinction of recent fear memories

(C) Pharmacokinetic parameters of CI-994 in C57BL/6 mouse brain (see Extended Experimental Procedures for additional details).
(D) Schematic of the experimental paradigm. 1 hr post remote memory recall, either CI-994 or its VEH was administered i.p., and 1 hr later, the different extinction procedures were applied.
(E) Using the massed extinction paradigm to the context, VEH-treated animals show significant spontaneous recovery of fear (n = 11; repeated-measurements ANOVA; $p = 0.0001$).
(F) Using the same paradigm, HDACi-treated animals show no spontaneous recovery (n = 16; repeated-measurements ANOVA; $p \leq 0.0053$).
(G) Using the same paradigm but without memory recall, HDACi-treated animals show significant spontaneous recovery (n = 17; repeated-measurements ANOVA; $p \leq 0.0001$).
(H) Using the spaced extinction paradigm to the context, VEH-treated animals do not show any attenuation in their fear response (n = 15).
(I) Using the same paradigm, HDACi-treated animals show significant reduction in their freezing response immediately and 1 day after extinction and show no signs of spontaneous recovery (n = 16; repeated-measurements ANOVA, $p \leq 0.0001$).
(J) Using the same paradigm but without memory recall, HDACi-treated animals do not show any attenuation in their fear response (n = 12).
Error bars indicate ± SEM. *$p \leq 0.05$, **$p \leq 0.01$, ***$p \leq 0.001$ by Tukey's posthoc. See also Figure S4.

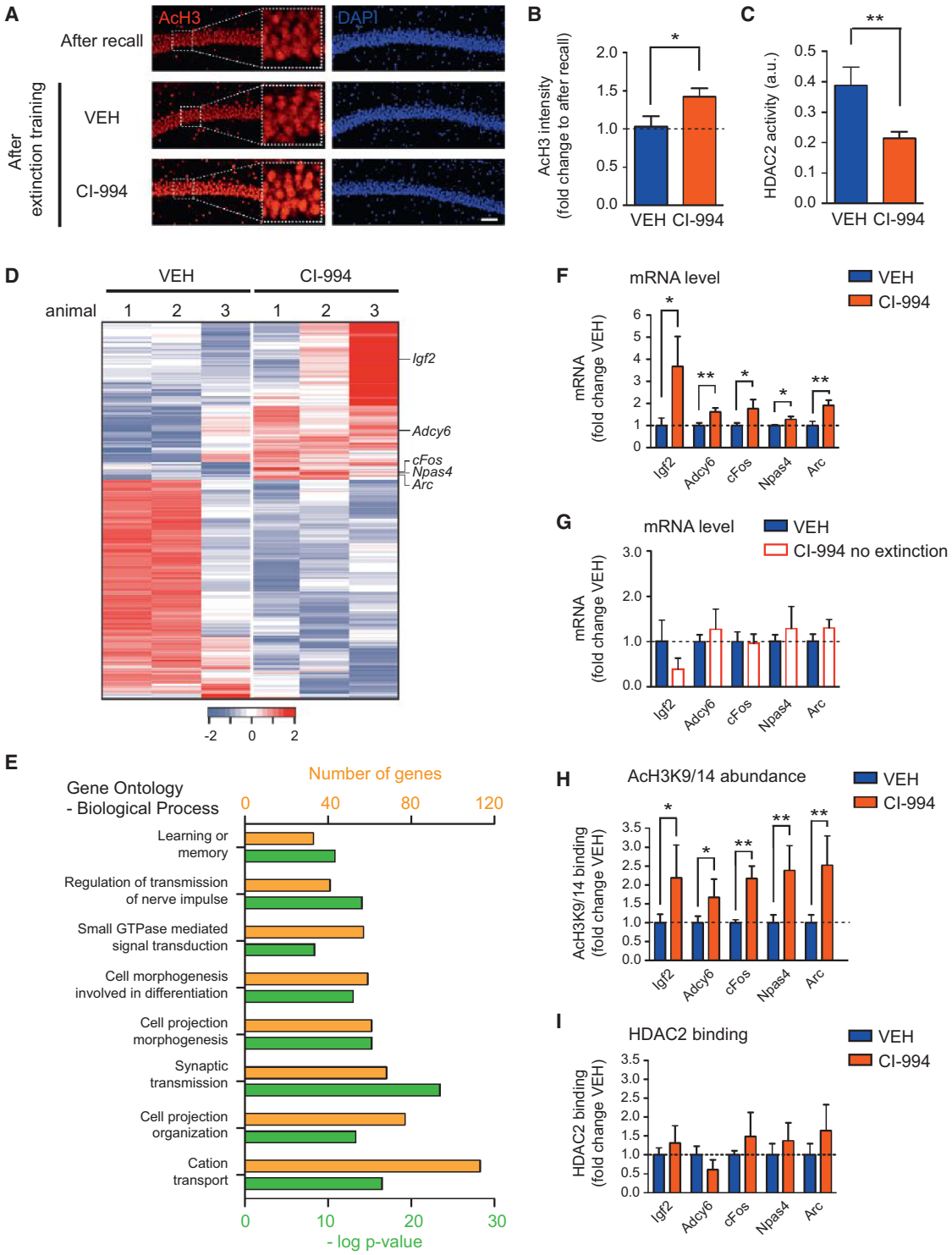

Figure 5. HDACis Prime a Transcriptional Program for Increased Neuroplasticity

(A) Representative images of immunohistochemical labelings of acetylated H3K9/14 ("AcH3") in hippocampal area CA1 1 hr after recall and 1 hr after completion of extinction in VEH- and HDACi-treated animals. Scale bar, 100 μm.

(B) Quantification thereof (n = 3–4 animals each).

(C) HDAC2 activity assay showing that CI-994 effectively inhibited hippocampal HDAC2 activity (n = 4 animals each).

(legend continued on next page)

(Agis-Balboa et al., 2011), and conclusive evidence exists that—at least for recent fear memories—hippocampal *Igf2* is necessary for successful contextual extinction (Agis-Balboa et al., 2011). However, the precise contribution of each of these genes to remote memory attenuation remains to be determined.

Previous studies have already demonstrated the usefulness of other HDACis in extinguishing recent memories (Bredy and Barad, 2008; Bredy et al., 2007; Fujita et al., 2012; Itzhak et al., 2012; Lattal et al., 2007; Stafford et al., 2012). Interestingly, in none of these studies were the extinction paradigms applied during the reconsolidation window, a procedure that by itself is sufficient to successfully attenuate fearful memories (Monfils et al., 2009). Together with our own observation that combining the HDACi treatment with successful reconsolidation-updating mechanisms for recent memories does not lead to further attenuation of the fear (data not shown), it seems that HDACis can facilitate memory updating in situations when extinction training alone is insufficient.

HDACi-supported extinction training led to increased neuroplasticity on a functional and structural level. For instance, we observed that hippocampal metabolic activity and LTP were enhanced. This is consistent with fMRI studies in humans, which show that successful extinction memory correlates with higher hippocampal activity (Milad et al., 2009). On a structural level, we found that memory extinction in combination with HDACi treatment was accompanied by increased synaptic density and dendritic branching and an elevated number of spines. These observations are consistent with a finding of increased spine numbers following recent memory extinction (Lai et al., 2012) and with earlier reports showing that HDACi treatment alone can lead to increased dendritic branching (Fischer et al., 2007). Therefore, the structural changes here are most likely the combined result of extinction training together with the HDACi application.

By extension, our finding of regained neuroplasticity strongly speaks in favor of a new period of learning during memory extinction (Bouton, 2004). Such learning has been postulated to either constitute a new memory trace of safety being laid over the original memory trace of fear or a re-learning of the original memory trace such that the association context-fear becomes re-associated toward one of context-safety (McKenzie and Eichenbaum, 2011; Nader and Hardt, 2009; Tronson and Taylor, 2007). It has been argued that, if the former is the case, the original memory of fear can still persist, which would become manifest in its SR, RI, or renewal, when the CS is presented outside of the extinction context (Bouton, 1993, 2004; Bouton and Bolles, 1979; Rescorla, 2004; Rescorla and Heth, 1975). Based on these purely behavioral results (Figures 4F and 4I) and the finding that the HDACi treatment in the absence of memory recall had no beneficial behavioral effect (Figures 4G and 4J), our results would therefore not only argue in favor of a permanent attenuation of the fear response, but also that it is the original memory trace that has been modified.

EXPERIMENTAL PROCEDURES

All experiments were performed by a person unaware of treatment groups, whenever possible.

Animals

C57Bl/6 male mice were used for all experiments. Animals were 12–14 weeks old at the time of training. All animal work was performed in accordance with the guidelines of the Massachusetts Institute of Technology's Division of Comparative Medicine.

Behavior

Fear Conditioning

Freezing behavior was defined as the complete absence of movement except breathing.

Contextual Fear Conditioning and Extinction

Training consisted of a 3 min habituation of mice to the conditioning chamber (TSE systems) followed by three 2 s foot shocks (0.8 mA) with an intertrial interval (ITI) of 28 s. After the shocks, the animals remained in the chamber for an additional 15 s. 1 or 30 days later, the following extinction paradigms were used. For massed extinction, mice were re-exposed to the same chamber for 3 min without receiving the foot shock to recall the memory (expo.). One hour later (spent in the home cage), the animals were put back in the same chamber without shock for an additional 18 min (for a total of 6 × 3 min exposure), the last 3 min of which were employed to measure the animals' extinction memory (after extinction). For spaced extinction, mice were re-exposed to the same chamber for 3 min without receiving the foot shock to recall the memory and were returned to their home cage for 2 hr, after which they were once again exposed to the training chamber for 3 min. This procedure was repeated on three subsequent days, for a total of 4 days of spaced extinction. The second session of the fourth day was employed to measure freezing at the end of extinction (after extinction). For both paradigms, 24 hr after extinction, animals were exposed for 3 min to the context again to assess their 24 hr extinction memory (EM).

Spontaneous Recovery

Thirty days following massed or spaced extinction, mice were tested for spontaneous recovery of fear by exposing them to the training chamber for 3 min. See Extended Experimental Procedures for cued fear conditioning and extinction.

Open-Field Behavior

Open-field behavior was examined using the VersaMax system (Accuscan) during 20 min.

Experimental Manipulations

Drug Administration

L-NAME (10 mg/kg, Sigma), molsidomine (20 mg/kg, Sigma), and CI-994 (30 mg/kg, synthesized at the Broad Institute) was given intraperitoneally. CI-994 was synthesized at the Broad Institute with a purity of >95% by HPLC analysis.

(D) Heatmap depicting 475 differentially expressed genes (DEGs) determined by RNA-sequencing in the hippocampus between VEH-treated and HDACi-treated animals after remote memory attenuation. Each line represents a DEG, each row the gene expression per animal. Blue and red indicate low and high levels of expression, respectively.

(E) Histogram showing the biological processes to which the DEGs belong (orange, number of DEGs per biological process; green, significance of enrichment).

(F) Quantitative RT-PCR confirmation of the expression of several neuroplasticity-related genes detected under (D) (n = 5–9 animals each).

(H) Quantitative PCR results showing the abundance of AcH3K9/14 at the promoter region of the genes under (F) (n = 5–11 animals each).

(I) Quantitative PCR results showing the binding of HDAC2 to the promoter region of the genes under (F) (n = 5–6 animals each).

Error bars are ± SEM. *$p \leq 0.05$, **$p \leq 0.01$ by Student's t test. See also Figure S5 and Table S1.

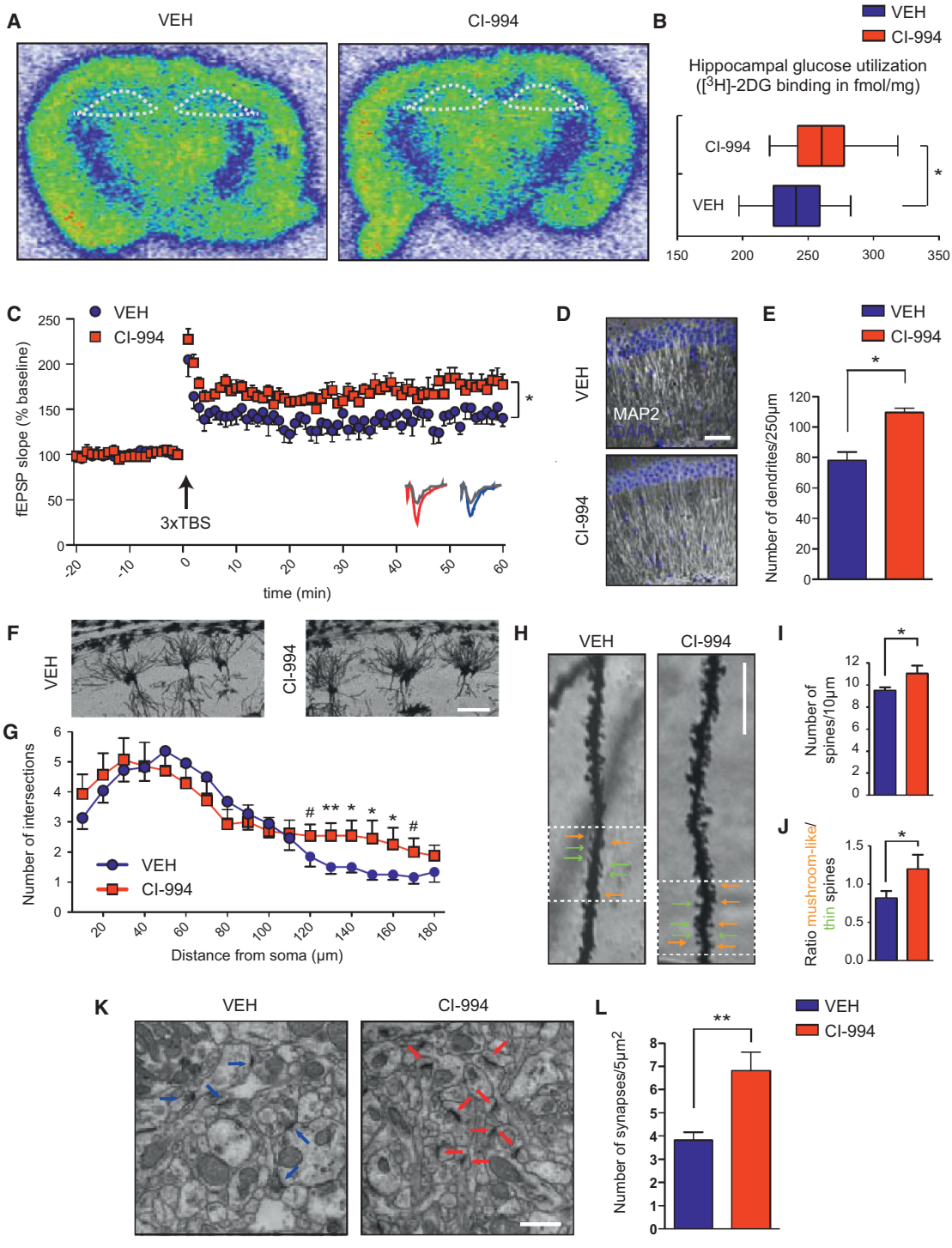

Figure 6. HDACis Increase Neuroplasticity after Remote Memory Attenuation

(A) Representative scans of [^{3}H]-2DG uptake in coronal brain sections depicting higher metabolic activity in the hippocampus (outlined by white dotted lines) for CI-994-treated animals.

(B) Quantification thereof (n = 10 animals each).

(C) Field excitatory postsynaptic potential (fEPSP) slopes in hippocampal area CA1 of VEH- and CI-994-treated animals (n = 6 slices from four mice each); sample traces below the point chart represent fEPSPs at 1 min before (gray) and 1 hr after (colored) theta-burst stimulation (TBS).

(D) Representative images of MAP2-labeled hippocampal sections. Scale bar, 200 µm.

(E) Quantification thereof (n = 3 animals each).

(legend continued on next page)

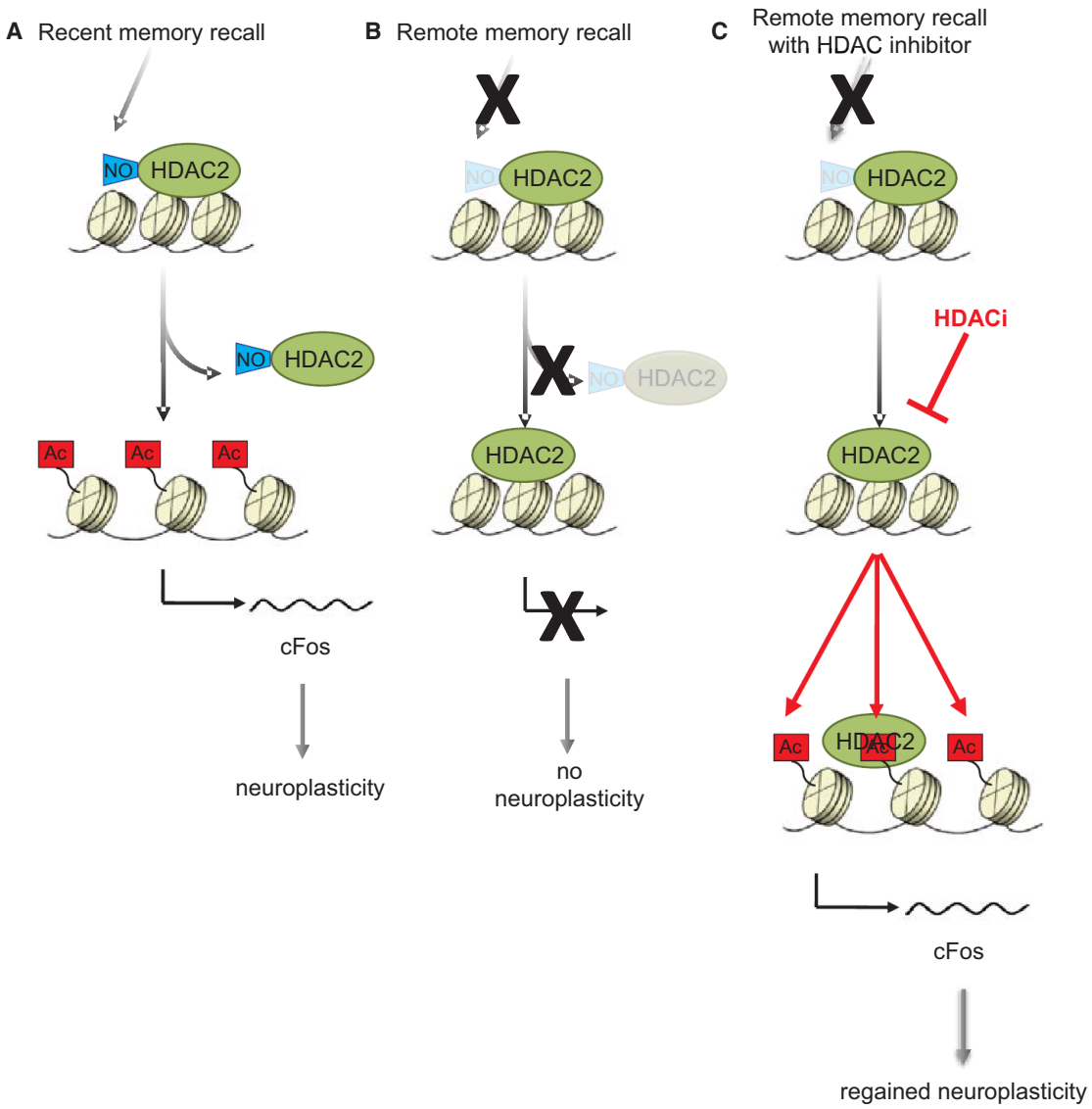

Figure 7. Working Model

HDACis epigenetically prime the expression of neuroplasticity-related genes (e.g., *cFos*) to overcome the absence of hippocampal neuroplasticity upon remote memory recall and thereby the resilience of remote fear memories to successful extinction (for details, see text).

Viral Administration

Mouse HDAC2^{WT} or HDAC2$^{C262/274A}$ cDNAs were subcloned under the HSV IE 4/5 promoter into a short-term HSV p1005 vector that coexpresses GFP driven by a CMV promoter. 1 μl of high-titer (4 × 10^8 particles/ml) HSVs were stereotaxically introduced into both hemispheres of hippocampal area CA1 (see Extended Experimental Procedures).

Immunohistochemistry

Coronal brain slices (40 μm thickness) were incubated with AcH3K9/14 (Millipore), cFos (Santa Cruz), synaptophysin, MAP2 (Sigma-Aldrich), and GFP (Aves Labs) and were visualized (LSM 510, Zeiss) with fluorescently conjugated secondary antibodies (Molecular Probes). Images were quantified using ImageJ 1.42q (see Extended Experimental Procedures for additional details).

(F) Representative images of Golgi-stained hippocampal pyramidal neurons used for Sholl analysis. Scale bar, 100 μm.
(G) Quantification of the number of dendritic branches per given distance from the soma (n = 8–12 neurons of 3 animals each).
(H) Representative images of Golgi-stained hippocampal pyramidal neurons. Scale bar, 10 μm.
(I) Quantification of (H) in terms of number of spines (n = 3 animals each).
(J) Quantification of (H) in terms of number of mature versus immature spines (n = 3 animals each).
(K) Representative images of hippocampal brain section (stratum radiatum) used for transmission electron microscopy. Arrows point to synapses. Scale bar, 1 μm.
(L) Quantification thereof (n = 3–4 animals each).
Error bars indicate ± SEM. #$p \leq 0.1$, *$p \leq 0.05$, **$p \leq 0.01$ by Student's t test. See also Figure S6.

Chromatin Immunoprecipitation

Whole hippocampi (1 hemisphere) were crosslinked using formaldehyde, following which chromatin immunoprecipitation was performed using standard procedures with HDAC2 (Abcam) and AcH3K9/14 (Millipore) antibodies. The fluorescent signal of the amplified DNA (SYBR green, Biorad) was normalized to input with promoter-specific primers (Extended Experimental Procedures).

Detection of Protein S-Nitrosylation

To determine HDAC2 S-nitrosylation, a biotin-switch assay (Cayman Chemical Company), which visualizes nitrosylated cysteine residues, was performed essentially as per the manufacturer's instructions (Extended Experimental Procedures).

HDAC Activity Assay

HDAC2 activity was measured by a Fluor-de-Lys fluorometric enzymatic assay (Enzo Life Sciences; see Extended Experimental Procedures). HDAC2 activity was normalized to total HDAC2 protein levels as determined by western blotting with an HDAC2 (Abcam) antibody.

Gene Expression Analyses

For RNA sequencing, total mRNA was extracted (QIAGEN), quality controlled (Bioanalyzer, Agilent), prepared for sequencing (Illumina) as per the manufacturers' instructions, and sequenced at high-throughput (Illumina HiSeq 2000 platform). Three biological replicates per condition were used. Sequence reads were aligned and quality controlled (see Extended Experimental Procedures). A gene was considered differentially expressed with a fold change of $\geq$1.4 and a significance of $p \leq 0.05$. For gene ontology analyses (http://www.geneontology.org), only biological pathways from hierarchical level 7 were compared with each other. Statistical tests were performed using Student's t test and the Benjamini-Hochberg false discovery rate to account for multiple comparisons. qRT-PCR was performed using standard procedures with exon-specific primers (Extended Experimental Procedures).

[^{3}H]-2DG Autoradiography

Immediately after the last extinction session, animals were injected with 2 μCi/kg of radioactive 2-deoxyglucose ([^{3}H]-2DG, PerkinElmer) and were returned to their home cage. One hour postinjection, animals were sacrificed using cervical dislocation and their brain dissected in 2-methylbutane (Sigma), stored at −80°C, and coronally cut at 30 μm thickness using a cryostat (Leica). Slides were air dried, made conductive by coating the free side with a copper foil tape, and placed into a gaseous chamber containing a mixture of argon and triethylamine (Sigma-Aldrich) as part of the Beta Imager 2000Z Digital Beta Imaging System (Biospace). Exposure for 20 hr yielded high-quality images. A [^{3}H]-Microscale (American Radiolabeled Chemicals) was counted simultaneously as a reference for total radioactivity quantitative analysis. Quantitative analysis was performed with the program Beta-Vision Plus (BioSpace) for each anatomical region of interest. At least six brain sections of the same rostrocaudal position were used to obtain an average [^{3}H]-2DG uptake per mouse.

Electrophysiology

To record field excitatory postsynaptic potentials, transverse hippocampal slices were prepared using standard procedures (Extended Experimental Procedures), and CA1 field potentials evoked by Schaffer collateral stimulation were measured. After recording of a stable baseline (at least 20 min), long-term potentiation was induced by three episodes of theta-burst stimulation (TBS) with 10 s intervals. TBS consisted of ten bursts (each with four pulses at 100 Hz) of stimuli delivered every 200 ms. Quantification was carried out with the average slopes of fEPSP during the last 10 min of recording.

Golgi Staining

Mice were perfused with 10% paraformaldehyde, and their entire brains were Golgi-Cox stained using the Rapid Golgistain Kit (FD NeuroTechnologies) as per the manufacturer's instructions (see also Extended Experimental Procedures). Mushroom spines were defined as having a clear round stubby head. An experimenter blind to treatment group counted the number and defined the types of apical and basal spines on hippocampal CA1 pyramidal neurons.

Sholl Analysis

z stack images from Golgi-Cox stained and isolated pyramidal neurons were acquired with 1 μm steps using a Zeiss LSM510 confocal microscope. Sholl analysis was performed by drawing concentric equidistant (10 μm) circles around the neuronal soma using Adobe Illustrator CS5 and by counting the number of intersecting branches per circle. Per condition, 8–12 neurons from 3 animals were analyzed.

Electron Microscopy

Electron microscopy on hippocampal brain sections was performed as described previously (Gräff et al., 2013). Fifteen distinct apical regions (stratum radiatum) of CA1 ~50–100 uM from the cell body layer of the hippocampus were imaged per animal. A synapse was defined as an electron dense postsynaptic density area juxtaposed to a presynaptic terminal filled with synaptic vesicles.

Statistics

Statistical analyses were performed using GraphPad Prism 5. Repeated-measurements ANOVAs followed by Tukey's posthoc analyses or by one-tailed Student's t tests were used. All data are represented as mean ± SEM. Statistical significance was set at $p \leq 0.05$.

ACCESSION NUMBERS

The RNA sequencing data has been deposited in the GEO Data Bank under ID code GSE53794.

SUPPLEMENTAL INFORMATION

Supplemental Information includes Extended Experimental Procedures, six figures, and one table and can be found with this article online at http://dx.doi.org/10.1016/j.cell.2013.12.020.

ACKNOWLEDGMENTS

We thank MIT's BioMicroCenter for the RNA sequencing, Martin Kahn for help with the qRT-PCR and IHC experiments, and Theo Elfers for critical comments on the manuscript. This work was partially supported by NIH NINDS/NIA (NS078839) to L.-H.T. and NIH/NIDA (R01DA028301) to S.J.H., the Picower Neurological Disorder Fund (PNDRF), the Stanley Medical Foundation, HHMI, and a Bard Richmond fellowship to J.G.

Received: April 25, 2013
Revised: August 22, 2013
Accepted: December 23, 2013
Published: January 16, 2014

REFERENCES

Agis-Balboa, R.C., Arcos-Diaz, D., Wittnam, J., Govindarajan, N., Blom, K., Burkhardt, S., Haladyniak, U., Agbemenyah, H.Y., Zovoilis, A., Salinas-Riester, G., et al. (2011). A hippocampal insulin-growth factor 2 pathway regulates the extinction of fear memories. EMBO J. *30*, 4071–4083.

Bontempi, B., Laurent-Demir, C., Destrade, C., and Jaffard, R. (1999). Time-dependent reorganization of brain circuitry underlying long-term memory storage. Nature *400*, 671–675.

Bourne, J., and Harris, K.M. (2007). Do thin spines learn to be mushroom spines that remember? Curr. Opin. Neurobiol. *17*, 381–386.

Bouton, M.E. (1993). Context, time, and memory retrieval in the interference paradigms of Pavlovian learning. Psychol. Bull. *114*, 80–99.

Bouton, M.E. (2004). Context and behavioral processes in extinction. Learn. Mem. *11*, 485–494.

Bouton, M.E., and Bolles, R.C. (1979). Role of conditioned contextual stimuli in reinstatement of extinguished fear. J. Exp. Psychol. Anim. Behav. Process. *5*, 368–378.

Bredy, T.W., and Barad, M. (2008). The histone deacetylase inhibitor valproic acid enhances acquisition, extinction, and reconsolidation of conditioned fear. Learn. Mem. *15*, 39–45.

Bredy, T.W., Wu, H., Crego, C., Zellhoefer, J., Sun, Y.E., and Barad, M. (2007). Histone modifications around individual BDNF gene promoters in prefrontal cortex are associated with extinction of conditioned fear. Learn. Mem. *14*, 268–276.

Brownell, J.E., and Allis, C.D. (1996). Special HATs for special occasions: linking histone acetylation to chromatin assembly and gene activation. Curr. Opin. Genet. Dev. *6*, 176–184.

Chen, D.Y., Stern, S.A., Garcia-Osta, A., Saunier-Rebori, B., Pollonini, G., Bambah-Mukku, D., Blitzer, R.D., and Alberini, C.M. (2011). A critical role for IGF-II in memory consolidation and enhancement. Nature *469*, 491–497.

Clem, R.L., and Huganir, R.L. (2010). Calcium-permeable AMPA receptor dynamics mediate fear memory erasure. Science *330*, 1108–1112.

Costanzi, M., Cannas, S., Saraulli, D., Rossi-Arnaud, C., and Cestari, V. (2011). Extinction after retrieval: effects on the associative and nonassociative components of remote contextual fear memory. Learn. Mem. *18*, 508–518.

Cukor, J., Olden, M., Lee, F., and Difede, J. (2010). Evidence-based treatments for PTSD, new directions, and special challenges. Ann. N Y Acad. Sci. *1208*, 82–89.

Debiec, J., LeDoux, J.E., and Nader, K. (2002). Cellular and systems reconsolidation in the hippocampus. Neuron *36*, 527–538.

Fiala, J.C., Spacek, J., and Harris, K.M. (2002). Dendritic spine pathology: cause or consequence of neurological disorders? Brain Res. Brain Res. Rev. *39*, 29–54.

Fischer, A., Sananbenesi, F., Wang, X., Dobbin, M., and Tsai, L.H. (2007). Recovery of learning and memory is associated with chromatin remodelling. Nature *447*, 178–182.

Foa, E.B. (2000). Psychosocial treatment of posttraumatic stress disorder. J. Clin. Psychiatry *61* (*Suppl 5*), 43–48, discussion 49–51.

Foa, E.B., and Kozak, M.J. (1986). Emotional processing of fear: exposure to corrective information. Psychol. Bull. *99*, 20–35.

Frankland, P.W., and Bontempi, B. (2005). The organization of recent and remote memories. Nat. Rev. Neurosci. *6*, 119–130.

Frankland, P.W., Bontempi, B., Talton, L.E., Kaczmarek, L., and Silva, A.J. (2004). The involvement of the anterior cingulate cortex in remote contextual fear memory. Science *304*, 881–883.

Frankland, P.W., Ding, H.K., Takahashi, E., Suzuki, A., Kida, S., and Silva, A.J. (2006). Stability of recent and remote contextual fear memory. Learn. Mem. *13*, 451–457.

Fujita, Y., Morinobu, S., Takei, S., Fuchikami, M., Matsumoto, T., Yamamoto, S., and Yamawaki, S. (2012). Vorinostat, a histone deacetylase inhibitor, facilitates fear extinction and enhances expression of the hippocampal NR2B-containing NMDA receptor gene. J. Psychiatr. Res. *46*, 635–643.

Goshen, I., Brodsky, M., Prakash, R., Wallace, J., Gradinaru, V., Ramakrishnan, C., and Deisseroth, K. (2011). Dynamics of retrieval strategies for remote memories. Cell *147*, 678–689.

Gräff, J., Kim, D., Dobbin, M.M., and Tsai, L.H. (2011). Epigenetic regulation of gene expression in physiological and pathological brain processes. Physiol. Rev. *91*, 603–649.

Gräff, J., Kahn, M., Samiei, A., Gao, J., Ota, K.T., Rei, D., and Tsai, L.H. (2013). A dietary regimen of caloric restriction or pharmacological activation of SIRT1 to delay the onset of neurodegeneration. J. Neurosci. *33*, 8951–8960.

Harooni, H.E., Naghdi, N., Sepehri, H., and Rohani, A.H. (2009). The role of hippocampal nitric oxide (NO) on learning and immediate, short- and long-term memory retrieval in inhibitory avoidance task in male adult rats. Behav. Brain Res. *201*, 166–172.

Hartley, C.A., and Phelps, E.A. (2010). Changing fear: the neurocircuitry of emotion regulation. Neuropsychopharmacology *35*, 136–146.

Huang, W., Sherman, B.T., and Lempicki, R.A. (2009). Systematic and integrative analysis of large gene lists using DAVID bioinformatics resources. Nat. Protoc. *4*, 44–57.

Inda, M.C., Muravieva, E.V., and Alberini, C.M. (2011). Memory retrieval and the passage of time: from reconsolidation and strengthening to extinction. J. Neurosci. *31*, 1635–1643.

Itzhak, Y., Anderson, K.L., Kelley, J.B., and Petkov, M. (2012). Histone acetylation rescues contextual fear conditioning in nNOS KO mice and accelerates extinction of cued fear conditioning in wild type mice. Neurobiol. Learn. Mem. *97*, 409–417.

Kandel, E.R. (2001). The molecular biology of memory storage: a dialogue between genes and synapses. Science *294*, 1030–1038.

Kandel, E.R., Schwartz, J.H., Jessell, T.M., Siegelbaum, S.A., and Hudspeth, A.J. (2013). Principles of Neural Science (New York: McGraw Hill).

Kaplan, G.B., and Moore, K.A. (2011). The use of cognitive enhancers in animal models of fear extinction. Pharmacol. Biochem. Behav. *99*, 217–228.

Kearns, M.C., Ressler, K.J., Zatzick, D., and Rothbaum, B.O. (2012). Early interventions for PTSD: a review. Depress. Anxiety *29*, 833–842.

Kessler, R.C., Berglund, P., Demler, O., Jin, R., Merikangas, K.R., and Walters, E.E. (2005). Lifetime prevalence and age-of-onset distributions of DSM-IV disorders in the National Comorbidity Survey Replication. Arch. Gen. Psychiatry *62*, 593–602.

Korb, E., and Finkbeiner, S. (2011). Arc in synaptic plasticity: from gene to behavior. Trends Neurosci. *34*, 591–598.

Lai, C.S., Franke, T.F., and Gan, W.B. (2012). Opposite effects of fear conditioning and extinction on dendritic spine remodelling. Nature *483*, 87–91.

Langmead, B., Trapnell, C., Pop, M., and Salzberg, S.L. (2009). Ultrafast and memory-efficient alignment of short DNA sequences to the human genome. Genome Biol. *10*, R25.

Lattal, K.M., and Wood, M.A. (2013). Epigenetics and persistent memory: implications for reconsolidation and silent extinction beyond the zero. Nat. Neurosci. *16*, 124–129.

Lattal, K.M., Barrett, R.M., and Wood, M.A. (2007). Systemic or intrahippocampal delivery of histone deacetylase inhibitors facilitates fear extinction. Behav. Neurosci. *121*, 1125–1131.

Levenson, J.M., and Sweatt, J.D. (2005). Epigenetic mechanisms in memory formation. Nat. Rev. Neurosci. *6*, 108–118.

Li, H., Handsaker, B., Wysoker, A., Fennell, T., Ruan, J., Homer, N., Marth, G., Abecasis, G., and Durbin, R.; 1000 Genome Project Data Processing Subgroup (2009). The Sequence Alignment/Map format and SAMtools. Bioinformatics *25*, 2078–2079.

Lin, Y., Bloodgood, B.L., Hauser, J.L., Lapan, A.D., Koon, A.C., Kim, T.K., Hu, L.S., Malik, A.N., and Greenberg, M.E. (2008). Activity-dependent regulation of inhibitory synapse development by Npas4. Nature *455*, 1198–1204.

Livak, K.J., and Schmittgen, T.D. (2001). Analysis of relative gene expression data using real-time quantitative PCR and the 2(-Delta Delta C(T)) Method. Methods *25*, 402–408.

Magistretti, P.J. (2006). Neuron-glia metabolic coupling and plasticity. J. Exp. Biol. *209*, 2304–2311.

Mahan, A.L., and Ressler, K.J. (2012). Fear conditioning, synaptic plasticity and the amygdala: implications for posttraumatic stress disorder. Trends Neurosci. *35*, 24–35.

McKenzie, S., and Eichenbaum, H. (2011). Consolidation and reconsolidation: two lives of memories? Neuron *71*, 224–233.

Milad, M.R., Pitman, R.K., Ellis, C.B., Gold, A.L., Shin, L.M., Lasko, N.B., Zeidan, M.A., Handwerger, K., Orr, S.P., and Rauch, S.L. (2009). Neurobiological basis of failure to recall extinction memory in posttraumatic stress disorder. Biol. Psychiatry *66*, 1075–1082.

Milekic, M.H., and Alberini, C.M. (2002). Temporally graded requirement for protein synthesis following memory reactivation. Neuron *36*, 521–525.

Misanin, J.R., Miller, R.R., and Lewis, D.J. (1968). Retrograde amnesia produced by electroconvulsive shock after reactivation of a consolidated memory trace. Science *160*, 554–555.

Monfils, M.H., Cowansage, K.K., Klann, E., and LeDoux, J.E. (2009). Extinction-reconsolidation boundaries: key to persistent attenuation of fear memories. Science *324*, 951–955.

Nadel, L., and Moscovitch, M. (1997). Memory consolidation, retrograde amnesia and the hippocampal complex. Curr. Opin. Neurobiol. *7*, 217–227.

Nader, K., and Hardt, O. (2009). A single standard for memory: the case for reconsolidation. Nat. Rev. Neurosci. *10*, 224–234.

Nader, K., Schafe, G.E., and Le Doux, J.E. (2000). Fear memories require protein synthesis in the amygdala for reconsolidation after retrieval. Nature *406*, 722–726.

Neve, R.L., and Lim, F. (2013). Generation of high-titer defective HSV-1 vectors. Curr. Protoc. Neurosci. *Chapter 4*, Unit 13.

Nott, A., Watson, P.M., Robinson, J.D., Crepaldi, L., and Riccio, A. (2008). S-Nitrosylation of histone deacetylase 2 induces chromatin remodelling in neurons. Nature *455*, 411–415.

Pavlov, I. (1927). Conditioned reflexes (Oxford, UK: Oxford University Press).

Ramamoorthi, K., Fropf, R., Belfort, G.M., Fitzmaurice, H.L., McKinney, R.M., Neve, R.L., Otto, T., and Lin, Y. (2011). Npas4 regulates a transcriptional program in CA3 required for contextual memory formation. Science *334*, 1669–1675.

Rescorla, R.A. (2004). Spontaneous recovery. Learn. Mem. *11*, 501–509.

Rescorla, R.A., and Heth, C.D. (1975). Reinstatement of fear to an extinguished conditioned stimulus. J. Exp. Psychol. Anim. Behav. Process. *1*, 88–96.

Sananbenesi, F., Fischer, A., Wang, X., Schrick, C., Neve, R., Radulovic, J., and Tsai, L.H. (2007). A hippocampal Cdk5 pathway regulates extinction of contextual fear. Nat. Neurosci. *10*, 1012–1019.

Schiller, D., Monfils, M.H., Raio, C.M., Johnson, D.C., Ledoux, J.E., and Phelps, E.A. (2010). Preventing the return of fear in humans using reconsolidation update mechanisms. Nature *463*, 49–53.

Shepherd, J.D., and Bear, M.F. (2011). New views of Arc, a master regulator of synaptic plasticity. Nat. Neurosci. *14*, 279–284.

Stafford, J.M., Raybuck, J.D., Ryabinin, A.E., and Lattal, K.M. (2012). Increasing histone acetylation in the hippocampus-infralimbic network enhances fear extinction. Biol. Psychiatry *72*, 25–33.

Suzuki, A., Josselyn, S.A., Frankland, P.W., Masushige, S., Silva, A.J., and Kida, S. (2004). Memory reconsolidation and extinction have distinct temporal and biochemical signatures. J. Neurosci. *24*, 4787–4795.

Tischmeyer, W., and Grimm, R. (1999). Activation of immediate early genes and memory formation. Cell. Mol. Life Sci. *55*, 564–574.

Trapnell, C., Hendrickson, D.G., Sauvageau, M., Goff, L., Rinn, J.L., and Pachter, L. (2013). Differential analysis of gene regulation at transcript resolution with RNA-seq. Nat. Biotechnol. *31*, 46–53.

Tronson, N.C., and Taylor, J.R. (2007). Molecular mechanisms of memory reconsolidation. Nat. Rev. Neurosci. *8*, 262–275.

Urcelay, G.P., Wheeler, D.S., and Miller, R.R. (2009). Spacing extinction trials alleviates renewal and spontaneous recovery. Learn. Behav. *37*, 60–73.

Wu, C.S., Lin, J.T., Chien, C.L., Chang, W.C., Lai, H.L., Chang, C.P., and Chern, Y. (2011). Type VI adenylyl cyclase regulates neurite extension by binding to Snapin and Snap25. Mol. Cell. Biol. *31*, 4874–4886.

Xue, Y.X., Luo, Y.X., Wu, P., Shi, H.S., Xue, L.F., Chen, C., Zhu, W.L., Ding, Z.B., Bao, Y.P., Shi, J., et al. (2012). A memory retrieval-extinction procedure to prevent drug craving and relapse. Science *336*, 241–245.

Cell

The Bacterial Cytoplasm Has Glass-like Properties and Is Fluidized by Metabolic Activity

Bradley R. Parry,[1,9] Ivan V. Surovtsev,[1,2,9] Matthew T. Cabeen,[1,10] Corey S. O'Hern,[3,4,5] Eric R. Dufresne,[4,5,6,7] and Christine Jacobs-Wagner[1,2,8,*]

[1]Department of Molecular, Cellular, and Developmental Biology, Yale University, New Haven, CT 06520, USA
[2]Howard Hughes Medical Institute, Yale University, New Haven, CT 06520, USA
[3]Department of Applied Physics, Yale University, New Haven, CT 06520, USA
[4]Department of Physics, Yale University, New Haven, CT 06520, USA
[5]Department of Mechanical Engineering and Materials Science, Yale University, New Haven, CT 06520, USA
[6]Department of Chemical and Environmental Engineering, Yale University, New Haven, CT 06520, USA
[7]Department of Cell Biology, Yale University, New Haven, CT 06520, USA
[8]Department of Microbial Pathogenesis, Yale School of Medicine, New Haven, CT 06510, USA
[9]These authors contributed equally to this work
[10]Present address: Department of Molecular and Cellular Biology, Harvard University, Cambridge, MA 02138, USA
*Correspondence: christine.jacobs-wagner@yale.edu
http://dx.doi.org/10.1016/j.cell.2013.11.028

SUMMARY

The physical nature of the bacterial cytoplasm is poorly understood even though it determines cytoplasmic dynamics and hence cellular physiology and behavior. Through single-particle tracking of protein filaments, plasmids, storage granules, and foreign particles of different sizes, we find that the bacterial cytoplasm displays properties that are characteristic of glass-forming liquids and changes from liquid-like to solid-like in a component size-dependent fashion. As a result, the motion of cytoplasmic components becomes disproportionally constrained with increasing size. Remarkably, cellular metabolism fluidizes the cytoplasm, allowing larger components to escape their local environment and explore larger regions of the cytoplasm. Consequently, cytoplasmic fluidity and dynamics dramatically change as cells shift between metabolically active and dormant states in response to fluctuating environments. Our findings provide insight into bacterial dormancy and have broad implications to our understanding of bacterial physiology, as the glassy behavior of the cytoplasm impacts all intracellular processes involving large components.

INTRODUCTION

In eukaryotes, active transport (including ATP-dependent diffusive-like motion) involves protein motors and cytoskeletal filaments. In the absence of cytoskeletal motor proteins, (micrometer-sized) bacteria are thought to primarily rely on diffusion for molecular transport and cytoplasmic mixing. Diffusion is therefore considered an integral part of bacterial life; it determines the mobility of cytoplasmic constituents and hence sets the limits at which molecular interactions (and thereby biological reactions) can occur. Diffusion is also essential for cell proliferation by promoting a homogeneous distribution of cytoplasmic components and the equal partitioning of solutes between daughter cells. Although diffusion in general has been extensively studied theoretically and experimentally, the bacterial cytoplasm bears little resemblance to the simple liquids usually considered. First, the bacterial cytoplasm is an aqueous environment that is extremely crowded (Cayley et al., 1991; Zimmerman and Trach, 1991). Second, the cytoplasm is highly polydisperse, with constituent sizes spanning several orders of magnitude, from subnanometer (ions and metabolites) to nanometers (proteins) to tens and hundreds of nanometers (ribosomes, plasmids, enzymatic megacomplexes, granules, and microcompartments) to micrometers (protein filaments and chromosomes). Third, metabolic activities drive the cytoplasm far from thermodynamic equilibrium. Furthermore, as a resistance mechanism, the cell can reversibly shut down metabolism in response to environmental stresses. How these features affect the physical properties of the cytoplasm is poorly understood. Such an understanding is critical because the physical nature of the cytoplasm determines the dynamics of cytoplasmic components and therefore impacts all intracellular processes.

Both normal and anomalous diffusive motions have been reported for cytoplasmic components (Bakshi et al., 2011; Coquel et al., 2013; English et al., 2011; Golding and Cox, 2006; Niu and Yu, 2008; Weber et al., 2010), and a unifying picture about the physical nature of the cytoplasm has yet to emerge. We show here that the bacterial cytoplasm exhibits physical properties typically associated with glass-forming liquids approaching the glass transition. Glass-forming liquids, which are intensively studied in condensed matter physics, encompass

many materials, including molecular glasses (vitreous glass) and dense suspensions of colloidal particles (colloidal glasses) (Hunter and Weeks, 2012). We found that the glassy behavior of the bacterial cytoplasm affects the mobility of cytoplasmic components in a size-dependent fashion, providing an explanation for the previous seemingly conflicting reports. Strikingly, metabolic activity abates this glassy behavior such that, in response to environmental cues, cytoplasmic fluidity and dynamics are dramatically altered through modulation of cellular metabolism.

RESULTS

The Motion of Crescentin-GFP Structures and PhaZ-GFP-Labeled Storage Granules Is Reduced in Metabolically Inactive *Caulobacter crescentus* Cells

Our study began with a serendipitous observation while studying the bacterial intermediate filament protein crescentin. Under native conditions, crescentin self-associates to form a stable (i.e., having no detectable subunit exchange) membrane-bound filamentous structure that generates the namesake curvature of the bacterium *Caulobacter crescentus* (Ausmees et al., 2003). A specific modification of the cell envelope (Cabeen et al., 2010) or addition of a bulky tag (e.g., GFP) to crescentin (Ausmees et al., 2003) causes the crescentin structure to detach from the membrane; these nonfunctional structures display random motion in the cytoplasm (Cabeen et al., 2009). While imaging GFP-labeled crescentin structures in a filamentous mutant strain growing on an agarose pad made with nutrient-containing medium (M2G), we observed, to our surprise, that crescentin-GFP structure movement suddenly stopped when the cells simultaneously arrested growth (Movie S1 available online). The reason for the abrupt growth arrest was unknown, but the ensuing drop in crescentin-GFP structure mobility raised the intriguing possibility that metabolic activity may play a role in the motion of freely diffusing cytoplasmic components.

A possible link between metabolism and cytoplasmic dynamics would be important to investigate, as bacteria in the wild are able to shift between metabolically active and dormant states in response to changing environments (Lennon and Jones, 2011). Dormancy is a survival strategy that can be triggered by many external insults, including nutrient limitation and late stationary phase. To examine whether dormancy can affect cytoplasmic dynamics, we first tracked crescentin-GFP structures (replacing wild-type crescentin structures) in otherwise wild-type cells (using custom two-dimensional tracking methods for non-diffraction-limited objects; see Supplemental Information and Figures S1A–S1F), and compared their mobility in actively growing cells to their mobility in cells subjected to prolonged carbon starvation. In cells actively growing on M2G medium, crescentin-GFP structures displayed motion and were able to sample the cytoplasm in minutes (Figure 1A and Movie S2) by taking large, seemingly random steps (Figure 1B). In contrast, carbon-starved cells were unable to grow, and crescentin-GFP structures rarely left their original locations (Figures 1A and 1B and Movie S3) for the entire duration of the experiment (up to 9 hr; data not shown). We observed similar spatial confinement in late-stationary-phase cells (Figure 1B) and under treatment with 2,4-dinitrophenol (DNP; Figure 1B and Movie S4), an oxidative phosphorylation uncoupling agent that rapidly depletes cells of ATP and GTP.

To quantitatively analyze crescentin-GFP structure mobility at the population level, we calculated the mean square displacement (MSD) over large numbers of trajectories (n = 718–1,943). The MSD averages, over all objects, the square of the distance between an object's current position and its original position (see Supplemental Information). Comparison of one-dimensional (along cell length) MSDs between experimental conditions confirmed the dramatic loss of mobility in metabolically reduced cells (carbon-starved, stationary-phase, and DNP-treated populations; Figure 1C). Thus, the metabolic state of the cell had a dramatic effect on crescentin-GFP structure mobility.

Crescentin-GFP forms large structures, with an average apparent length of 900 nm (Figure S1G). To test whether the motion of other large cytoplasmic components is affected, we tracked the motion of polyhydroxyalkanoate (PHA) granules labeled with PhaZ-mCherry. PhaZ is a PHA depolymerase that binds to PHA storage granules (Maehara et al., 2002; Qi and Rehm, 2001). Consistent with this binding, PhaZ-mCherry formed fluorescent foci (1–2 per cell) that moved inside active (untreated) *C. crescentus* cells (Figure S2A). Metabolic depletion by DNP treatment dramatically reduced motion (Figure S2A), similar to what we observed with crescentin-GFP structures.

Plasmid Motion Is Also Reduced in *Escherichia coli* when Cellular Energy Is Depleted

To examine whether this metabolism-dependent motion is unique to *C. crescentus*, we switched to *E. coli* and examined the motion of engineered low-copy-number mini-RK2 plasmids. These plasmids have an estimated radius of gyration of 150 nm based on measurements of plasmids with similar base-pair lengths (Latulippe and Zydney, 2010). Mini-RK2 lacks a partitioning system and hence is not actively partitioned or constrained in space (Derman et al., 2008). This plasmid also contains a *lacO* array for visualization via GFP-LacI labeling. Mini-RK2 plasmids were imaged every 30 s on agarose pads containing M9-glycerol (M9G) medium to sustain cellular activity. Under these conditions, mini-RK2 plasmids were able to travel the cell length within 1 min, leaving their previous location from frame to frame (Figure 1D and Movie S5), as previously observed (Derman et al., 2008). In contrast, depletion of cellular energy by DNP treatment drastically limited their spatial exploration (Figure 1D and Movie S6), which was confirmed at the population level in MSD plots (Figure 1E; n = 488–497 trajectories). Thus, mini-RK2 plasmids exhibit metabolism-dependent motion in *E. coli*, similar to crescentin-GFP structures and PHA granules in *C. crescentus*. As *E. coli* and *C. crescentus* diverged over one billion years ago, the effect of metabolism on cytoplasmic dynamics is likely to be an ancient and common feature of the bacterial cytoplasm.

Development of a Genetically Encoded Probe to Study Cytoplasmic Dynamics

Specific interactions with other cellular components are known to affect the motion of components endogenous to the cytoplasm, altering motion in an unpredictable manner (Nenninger et al., 2010) and making normal diffusion appear anomalous

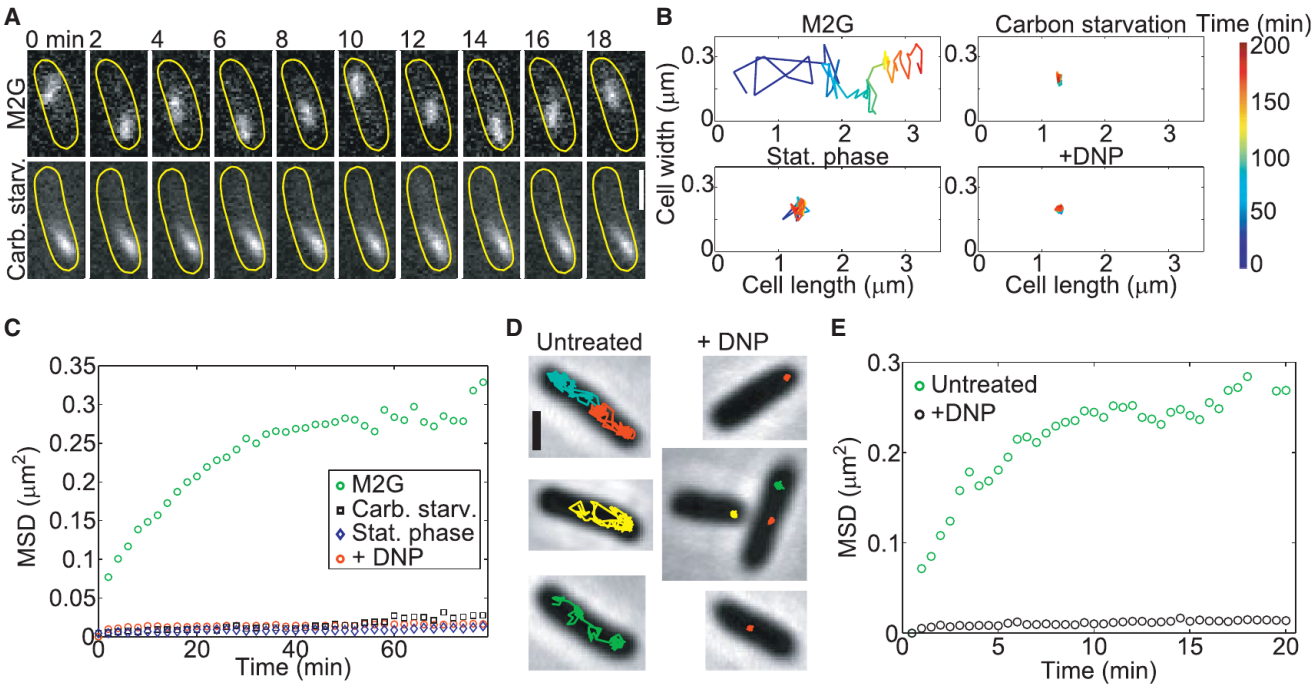

Figure 1. The Mobility of Crescentin-GFP Structures and GFP-LacI-Labeled Mini-RK2 Plasmids Is Affected by Metabolism

(A) Time-lapse montages of crescentin-GFP structures acquired under conditions of growth (M2G) and carbon source depletion. *C. crescentus* cells (CJW1265) were grown and imaged in M2G, a glucose-based medium (top). For carbon starvation, cells were washed into M2 buffer (lacking glucose) and incubated for 3 hr before imaging (bottom). Scale bar, 1 μm.

(B) Two-dimensional trajectories representing 200 min of crescentin-GFP tracking from single *C. crescentus* cells (CJW1265) under metabolically active (M2G) and metabolically depleted (carbon starvation, late stationary phase, + DNP) conditions.

(C) MSD of crescentin-GFP structures in metabolically active (M2G, n = 1,796 trajectories) and energy-depleted (carbon starvation, n = 861 trajectories; stationary phase, n = 718 trajectories; and +DNP, n = 1,943 trajectories) conditions. *C. crescentus* cells (CJW1265) from late stationary-phase cell cultures ($OD_{660} \geq 1.7$) were imaged on agarose pads made with stationary-phase culture supernatant instead of M2G.

(D) Two-dimensional trajectories of GFP-LacI-labeled mini-RK2 plasmids overlaid on corresponding phase-contrast images of metabolically active and DNP-treated *E. coli* cells (JP924). Scale bar, 1 μm.

(E) MSD of mini-RK2 plasmids under metabolically active (untreated, n = 497 trajectories) and energy-depleted (+DNP, n = 488 trajectories) conditions.

See also Figures S1 and S2 and Movies S1–S6.

(Dix and Verkman, 2008). Therefore, to characterize the physical nature of metabolism-dependent motion, we needed a probe that is completely foreign to the cell (unlike crescentin, PHA granules, and plasmids) and is thus unlikely to make any specific interactions with components of the bacterial cytoplasm. As the direct injection methods used in eukaryotic cells cannot be used with micron-sized bacteria, we attempted to introduce nonbiological probes (quantum dots, dextrans, or gold particles) into the bacterial cytoplasm with biolistic and electroporation techniques. None of these attempts were successful. As an alternative, we sought a genetically encoded probe that is foreign to the bacterial cytoplasm and is capable of self-assembly into particles. Several eukaryotic viruses are known to replicate in cytoplasmic factories that require a matrix made of self-assembling viral proteins. The avian reovirus protein μNS is an example of such a self-assembling protein (Broering et al., 2002), and a C-terminal fragment is sufficient to form globular cytoplasmic particles, even when fused to GFP (Broering et al., 2005). These GFP-labeled particles, referred to as GFP-μNS particles here, are unlikely to make specific interactions with components of the bacterial cytoplasm, given the evolutionary divergence between bacteria and the avian reovirus host.

Induction of GFP-μNS synthesis in *E. coli* usually resulted in a single fluorescent focus per cell (Figure S3A). The foci exhibited significant motion in metabolically active cells but became spatially confined with DNP treatment (Figures 2A–2C and Movie S7), recapitulating our results with plasmids, PHA granules, and crescentin-GFP structures. Depletion of cellular energy through treatment with carbonylcyanide-*m*-chlorophenylhydrazone (CCCP) instead of DNP had the same negative effect on GFP-μNS mobility (data not shown). Collectively, these results further support the notion that metabolism-dependent motion is a general property of the bacterial cytoplasm.

Metabolism-Dependent Motion Is Not Driven by Known Motor-like Activity or Chromosome Dynamics

The observation that the motion of cytoplasmic components depends on metabolic activity was surprising, as it appeared inconsistent with diffusion, which is a passive process. ATP-dependent motion was recently reported for chromosomal loci in *E. coli* (Weber et al., 2012). However, chromosomal loci are

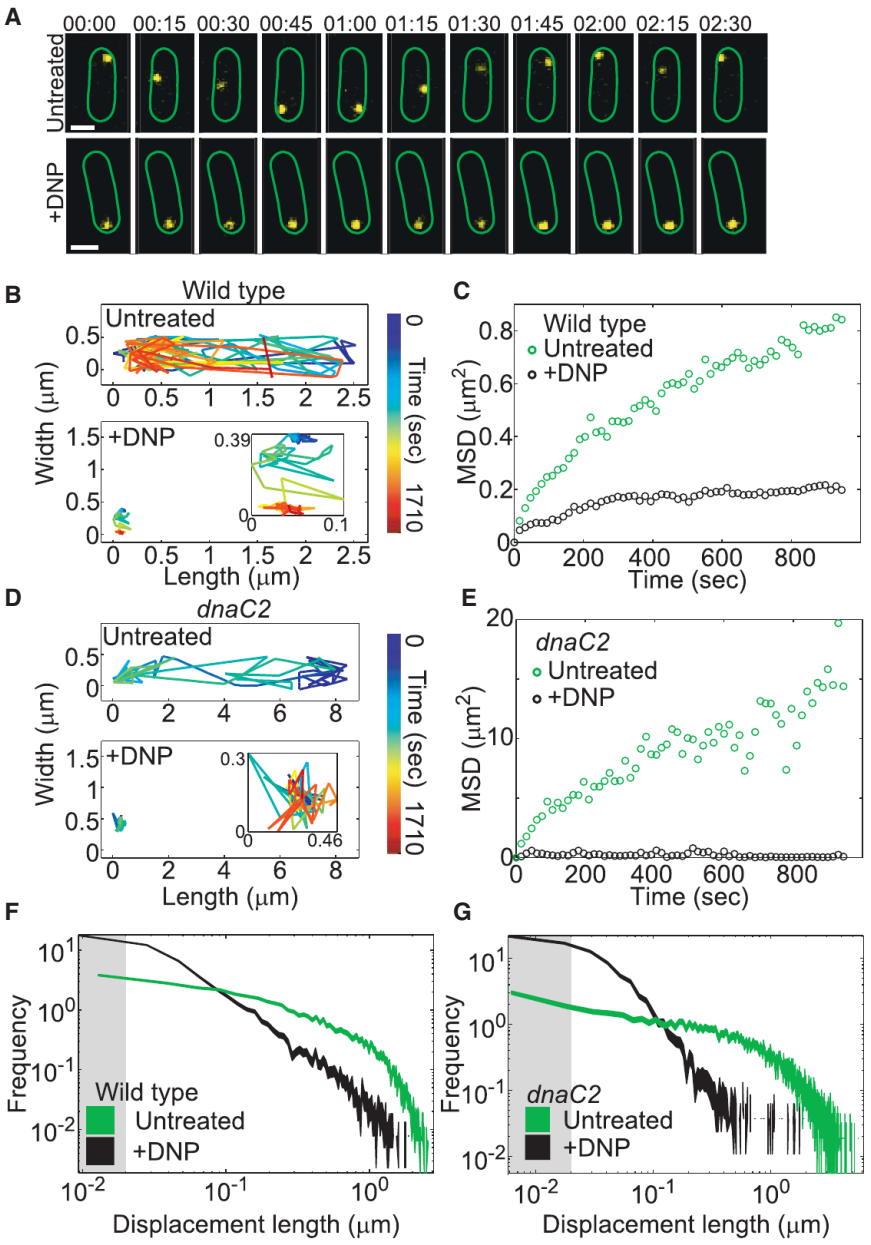

Figure 2. GFP-μNS Probe Dynamics Are Affected by Cellular Metabolism

(A) Representative time-lapse montages of GFP-μNS particles (yellow) in *E. coli* cells (CJW4617) acquired under untreated and DNP-treated conditions (+DNP). Scale bar, 1 μm. Time is min:sec.

(B) An example of a two-dimensional trajectory of a GFP-μNS particle in an *E. coli* cell (CJW4617), with or without DNP treatment.

(C) MSD of GFP-μNS particles in metabolically active (untreated, n = 729 trajectories) and DNP-treated (+DNP, n = 643 trajectories) *E. coli* cells (CJW4617).

(D) Two-dimensional trajectory of a GFP-μNS particle in a filamentous *E. coli dnaC2* cell (CJW4619) at the restrictive temperature (37°C) with or without DNP treatment.

(E) MSD of GFP-μNS particles in filamentous *E. coli dnaC2* cells (CJW4619) at their restrictive temperature with (+DNP, n = 118 trajectories) or without (untreated, n = 192 trajectories) DNP treatment.

(F) Histogram of GFP-μNS particle displacements in *E. coli* cells (CJW4617) with or without DNP treatment. Line width indicates Poisson counting error, and the gray shading delineates the estimated tracking error. Displacements were measured over 15 s intervals.

(G) Histogram of GFP-μNS particle displacements in *E. coli dnaC2* cells (CJW4619) at the restrictive temperature (37°C) with or without DNP treatment. Line width indicates Poisson counting error, and the gray shading delineates the estimated tracking error. Displacements were measured over 15 s intervals.

See also Figures S2–S5 and Movie 7.

distinct from free cytoplasmic components, as they remain confined within a small space (where they "jiggle") by virtue of their attachment to the rest of the chromosome. As a consequence, the motion of chromosomal loci depends not only on the cytosolic environment, but also on the DNA structure. Using DAPI staining, we found that energy depletion by DNP treatment has a strong effect on the shape and hence the structure of the chromosome (Figures S4A and S4B) and likely contributes to the change in chromosomal locus dynamics. Consistent with this notion, the mobility of chromosomal loci is also ATP dependent in eukaryotic nuclei (Heun et al., 2001; Levi et al., 2005), and this ATP dependence has been attributed to reduced activity of DNA-remodeling proteins (Soutoglou and Misteli, 2007).

Although our cytoplasmic probes do not associate with the chromosome, it remained possible that their metabolism-dependent motion results from a change in chromosome structure and dynamics (for example, through probe entrapment; see Supplemental Information). We found that the chromosome affected the spatial distribution of GFP-μNS particles (see Supplemental Information). However, experiments with *dnaC2* mutant cells, which produce large DNA-free regions, showed that metabolism-dependent motion occurs independently of the DNA (see Supplemental Information and Figures 2D, 2E, and S2B). These experiments exclude a predominant role for the chromosome in the metabolism-dependent motion of free cytoplasmic components.

In eukaryotes, agitation of the pervasive cytoskeletal meshwork by the activity of motor proteins can produce diffusive-like motion in the cytoplasm in an ATP-dependent manner (Brangwynne et al., 2009). This process is often referred to as "active diffusion." However, bacteria lack motor proteins like dyneins, myosins, and kinesins, and their cytoskeletal elements are primarily membrane associated. Furthermore,

metabolism-dependent motion still occurred when the polymerization of MreB (bacterial actin homolog) or FtsZ (tubulin homolog) was disrupted (see Supplemental Information and Figures S3B, 2E, 2D, and S2B note that FtsZ rings do not form in filamentous *dnaC2* cells). Thus, the mechanism producing the metabolism-dependent motion in bacteria appears different from the cytoskeletal motor-based "active diffusion" observed in eukaryotes.

Through drug inactivation of transcription, translation, or peptidoglycan wall synthesis, we also showed that metabolism-dependent motion does not originate from the sole (motor-like) action of RNA polymerases, ribosomes, or penicillin-binding proteins on their DNA, mRNA, or peptidoglycan substrates (see Supplemental Information and Figures S3C–S3E).

Increase in Frequency of Large Displacements Contributes to Metabolism-Dependent Motion

To gain insight into the origin of metabolism-dependent motion, we sought to characterize this motion more precisely. An interesting characteristic of energy-depleted cells is that, although GFP-μNS particles remained largely confined in space in these cells, they still appeared to display small displacements over the imaging interval (15 s); this was true in wild-type and *dnaC2* cells (see Figures 2B and 2D for example trajectories). Through control experiments and simulations (see Supplemental Information and Figure S5), we determined that our single-particle tracking method can distinguish small (>20 nm) displacements. Therefore, even after accounting for potential localization errors, GFP-μNS particles displayed discernible motion in DNP-treated cells, as shown by the distributions of displacement lengths (Figure 2F for wild-type cells and Figure 2G for *dnaC2* cells, with gray shading denoting our estimated tracking error; see Supplemental Information). Under both untreated and DNP-treated conditions, small displacements were more frequent than large ones (Figures 2F and 2G). However, the frequency of long displacements was much greater in metabolically active cells. This higher frequency of long displacements is likely responsible for the ability of GFP-μNS particles to explore more cytoplasmic area in active cells. In other words, GFP-μNS particles are able to sample the cytoplasm of active cells with large displacements, though they remain spatially confined in inactive cells because the largest displacements disappear.

The Effect of Metabolism on Cytoplasmic Dynamics Depends on Particle Size

Recent fluorescence recovery after photobleaching (FRAP) measurements from our laboratory have shown only a nominal difference in the diffusion coefficient of free GFP between untreated and DNP-treated *C. crescentus* cells (Montero Llopis et al., 2012). Because GFP (size ≈3 nm) is smaller than mini-RK2 plasmids, PHA granules, and crescentin-GFP filaments, this observation raised the possibility that the influence of metabolism on motion may depend on particle size. To examine this possibility, we took advantage of our titratable GFP-μNS system in which GFP-μNS synthesis can be tuned to different levels by varying the inducer (IPTG) concentration and the induction time. By doing so, we obtained GFP-μNS particles with a wide range of fluorescence intensities and hence sizes (Figure S6A and S6B). We then plotted MSDs of particles binned by fluorescence intensities (bins 1–9) and found that MSDs of both untreated and DNP-treated cell are inversely correlated with fluorescence intensity (Figures 3A and 3B show selected bins on a log-log scale for clarity), as anticipated. When we compared the distribution of displacement lengths between untreated and DNP-treated conditions across discrete bins of particle fluorescence intensities, we found that the difference between the two conditions is accentuated with fluorescence intensity and hence particle size (Figures 3C and S7).

To estimate the absolute size of particles from their fluorescence intensity, we measured the diffusion coefficients of GFP-μNS particles in solution after cell lysis and compared these values to those of fluorescent beads of known size (see Supplemental Information and Figures S6C and S6D). From these measurements, we obtained a calibration curve (see Supplemental Information), which we used to estimate the particle size (in nm). We then characterized the relationship between particle size and metabolism-dependent motion by calculating the radius of gyration (R_g; along the long axis of the cell) of each trajectory. R_g is the root-mean-square distance from the center of the trajectory (see Supplemental Information) and measures the average space that a particle explores. R_g analysis showed that both cellular energy depletion (+DNP) and increasing particle size leads to increasing spatial confinement (Figure 3D). By calculating the ratio $(R_g^{untreated} - R_g^{+DNP})/R_g^{+DNP}$ (which compares the difference in space explored in metabolically active conditions relative to energy-depleted conditions) as a function of particle size (Figure 3E), we found that the ratio is significantly greater than zero and increases with increasing particle size (except perhaps for the largest size bin, possibly because these particles may be too big to move even in active cells). This trend supports a size dependence for metabolism-dependent motion. Of equal interest, the ratio $(R_g^{untreated} - R_g^{+DNP})/R_g^{+DNP}$ decreased toward 0 as size decreased (Figure 3E), with an estimated intercept near 30–40 nm assuming a linear relationship. This finding suggests that cytoplasmic components smaller than this estimated size are not affected by metabolism-dependent motion.

The Distribution of Displacements Is Non-Gaussian

In normal diffusion, the diffusing particles will exhibit a Gaussian distribution of displacements. In contrast, the displacement distributions of GFP-μNS particles under both untreated and DNP-treated conditions diverged from the expected Gaussian distribution (Figure 4A shows bin 5 as an example), as signified by long tails. We quantified deviations from a Gaussian distribution by calculating the non-Gaussian parameter α_2 (see Supplemental Information). The α_2 value of a Gaussian distribution is zero and grows as the tail of the measured distribution increases. First, we found that, in metabolically active cells, the α_2 values of GFP-μNS displacement distributions grew with increasing GFP-μNS particle size (Figure 4B), indicating that non-Gaussian behavior increases with particle size. Second, the non-Gaussian behavior was dramatically stronger for particles in metabolically inactive cells, wherein α_2 grew much faster with particle size than in active cells (Figure 4B).

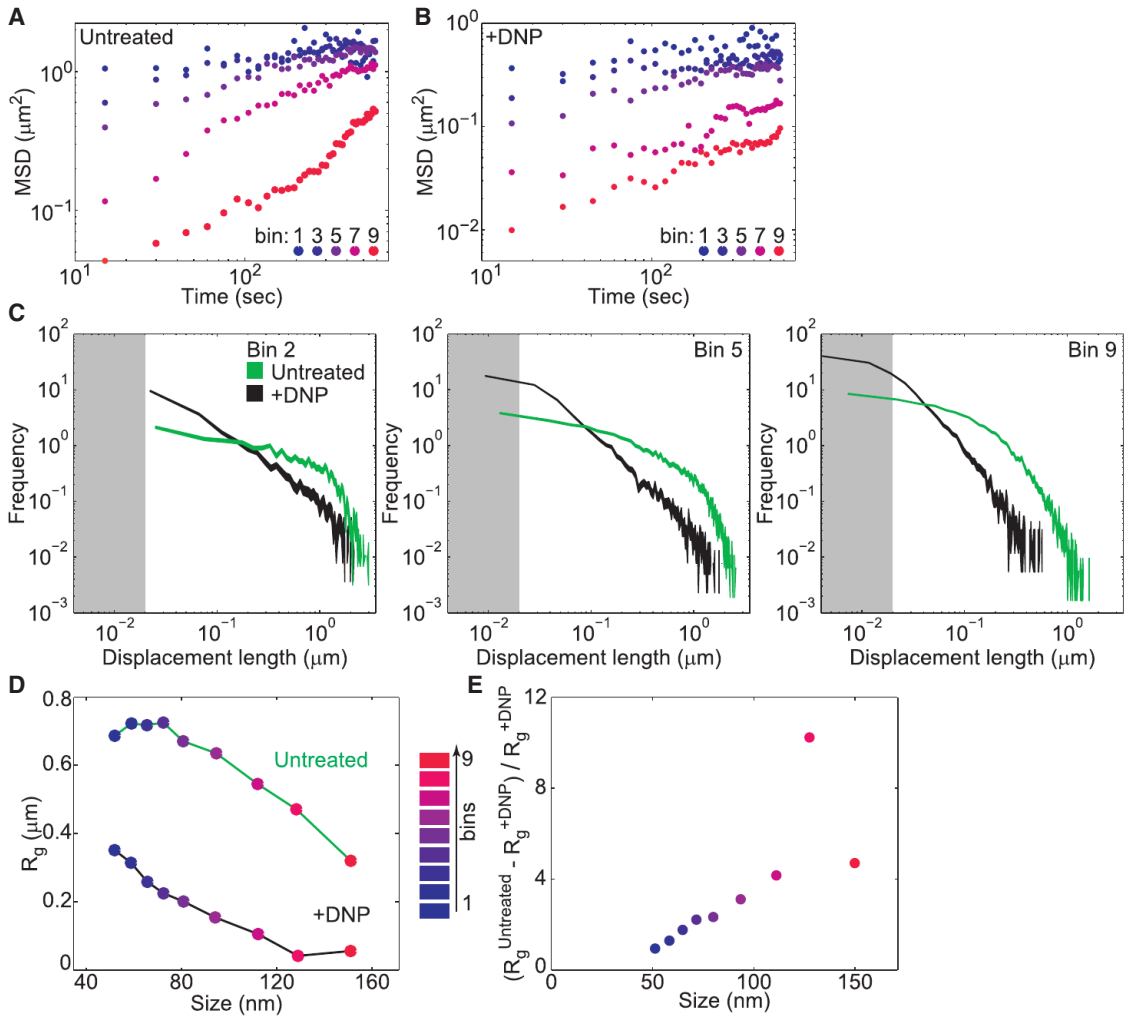

Figure 3. Effect of Metabolism on Cytoplasmic Motion Depends on Particle Size

(A) MSD of GFP-μNS particles of varying binned fluorescence intensities in *E. coli* cells (CJW4617) under normal growth conditions (M2G).

(B) Same as (A) but for GFP-μNS particles in *E. coli* cells (CJW4617) under DNP treatment.

(C) Histograms of GFP-μNS particle displacements under untreated and DNP-treated conditions for selected bins. Displacements were measured over 15 s intervals. Line width indicates Poisson counting error, and the gray shading delineates the estimated tracking error.

(D) Mean radius of gyration (R_g) of all trajectories from GFP-μNS particles of a given binned size is plotted as a measure of spatial exploration for untreated and DNP-treated cells.

(E) The ratio $(R_g^{untreated} - R_g^{+DNP})/R_g^{+DNP}$ is plotted as a function of particle size.

See also Figures S6 and S7.

Nonergodicity Increases with Energy Depletion and Particle Size

Notably, deviations from Gaussian statistics for particle displacements have been reported in various nonliving physical systems, including glass-forming liquids near the glass transition. Colloidal suspensions have proven to be instructive model systems to characterize the dynamics of glass-forming liquids (Hunter and Weeks, 2012). Dense colloidal suspensions (also known as colloidal glasses) are metastable near the glass transition, changing from liquids to amorphous solids with small changes in colloid concentration. At low concentration (low crowding), colloidal particles exhibit diffusive behavior. Increasing the concentration of particles results in a strong increase in viscosity and a decrease in particle mobility, ultimately driving the system through the glass transition to a disordered solid-like state (Pusey and van Megen, 1986). The approach to the glass transition is accompanied by several distinct features. For example, the non-Gaussian parameter α_2 increases as the system approaches the glass transition (Kegel and van Blaaderen, 2000; Marcus et al., 1999; Weeks et al., 2000). Additionally, the system becomes nonergodic (Cipelletti and Ramos, 2005). In ergodic systems, time averages are equivalent to ensemble averages. For example, to measure probe diffusion in cells, one could either track a probe in a single cell over a very long time and average over all times or track many probes in different cells over a short time and average over all probes. The two methods produce the same

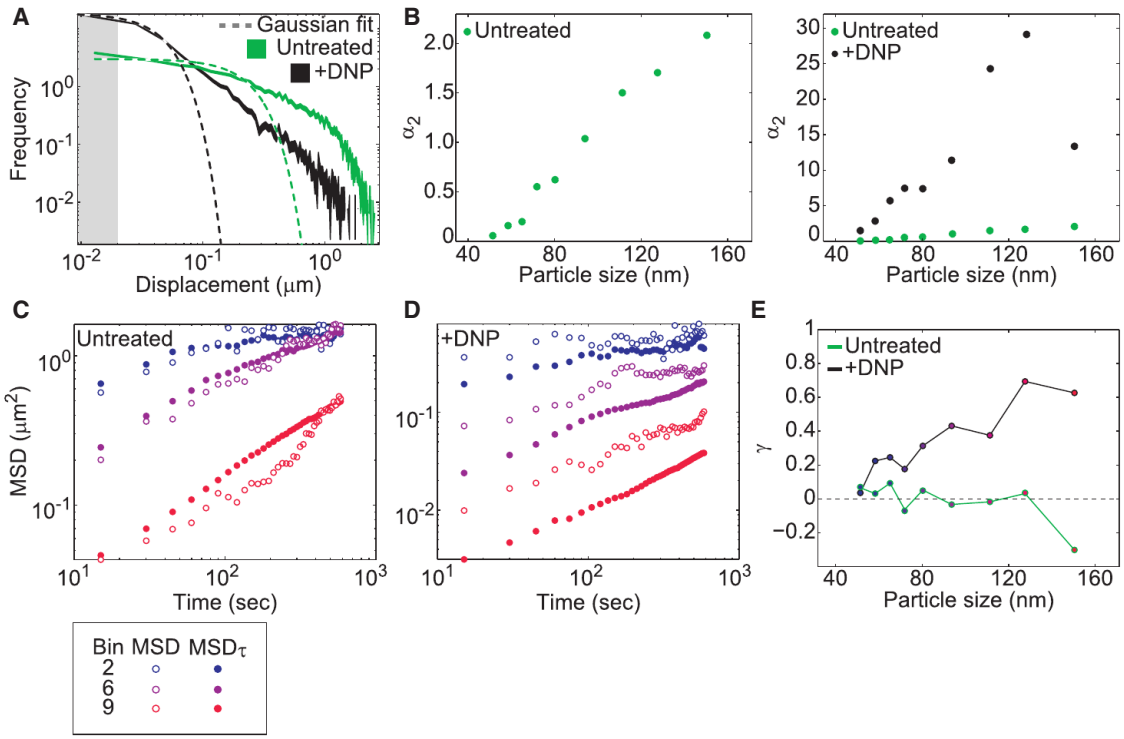

Figure 4. GFP-μNS Particles Display Non-Gaussian and Nonergodic Behavior in the Cytoplasm

(A) Experimental distributions of GFP-μNS particle displacements for *E. coli* cells (CJW4617) under untreated and DNP-treated conditions for a selected size bin (bin 5). Dashed lines are the best fit to a Gaussian distribution. Line width indicates Poisson counting error, and the gray shading delineates the estimated tracking error. Time interval is 15 s.

(B) Non-Gaussian parameter α_2 of particle displacement distributions is plotted as a function of particle size for *E. coli* cells (CJW4617) with or without DNP treatment.

(C) Comparison of MSD and MSD_τ for selected size bins for cells under untreated conditions.

(D) Same as (C) but for cells under DNP treatment.

(E) The parameter γ is plotted as a function of particle size for cells with or without DNP treatment.

result if the system is ergodic. Nonergodicity can arise from caging or aging phenomena, whereby the probe becomes trapped in a given region or the system slowly moves from one region of configuration space to another.

If the cytoplasm were ergodic, we would expect ensemble-averaged MSDs of many GFP-μNS trajectories to coincide with the time-averaged MSD of a single trajectory. Obtaining the time-averaged MSD of a trajectory in a single cell with sufficient statistics for this comparison requires acquisition of an extremely long trajectory, which was not possible for GFP-μNS particles due to technical limitations (photobleaching and phototoxicity). Instead, we compared ensemble-averaged MSDs with an MSD (MSD_τ) that is both time and ensemble averaged (see Supplemental Information). If the system were ergodic, MSD and MSD_τ would be equivalent. We found relatively close agreement between the MSD and its corresponding MSD_τ for GFP-μNS particles in untreated cells (Figure 4C), except perhaps for the largest particles. However, in DNP-treated cells, MSD and MSD_τ were significantly different for all particle sizes, and this difference was greatest for the largest GFP-μNS particles (Figure 4D). We defined a parameter γ to measure the difference between the MSD and MSD_τ (see Supplemental Information), with $\gamma = 0$ indicating equivalency between MSD and MSD_τ. For GFP-μNS particles in metabolically active cells, γ fluctuated near zero except for GFP-μNS particles of the largest size bin (Figure 4E). However, under metabolic depletion, γ grew in response to increasing GFP-μNS particle size (Figure 4E). These differences cannot be explained by the finite number of trajectories or by their limited duration (see Supplemental Information). These results suggest that the bacterial cytoplasm becomes increasingly nonergodic with both energy depletion and increasing particle size.

The Cytoplasm Displays Dynamic Heterogeneity

Although non-Gaussian statistics and ergodicity breaking are consistent with glassy dynamics, a hallmark of glassy systems is dynamic heterogeneity, which is characterized by regions of high particle mobility coexisting with regions of low particle mobility (Berthier, 2011). Due to crowding, particles in colloidal suspensions can become trapped by their nearest neighbors, resulting in small random displacements of the particles. Over longer times, the "cage" formed by their neighbors can spontaneously rearrange through collective motion, allowing the particles to escape with large displacements. Particles in regions

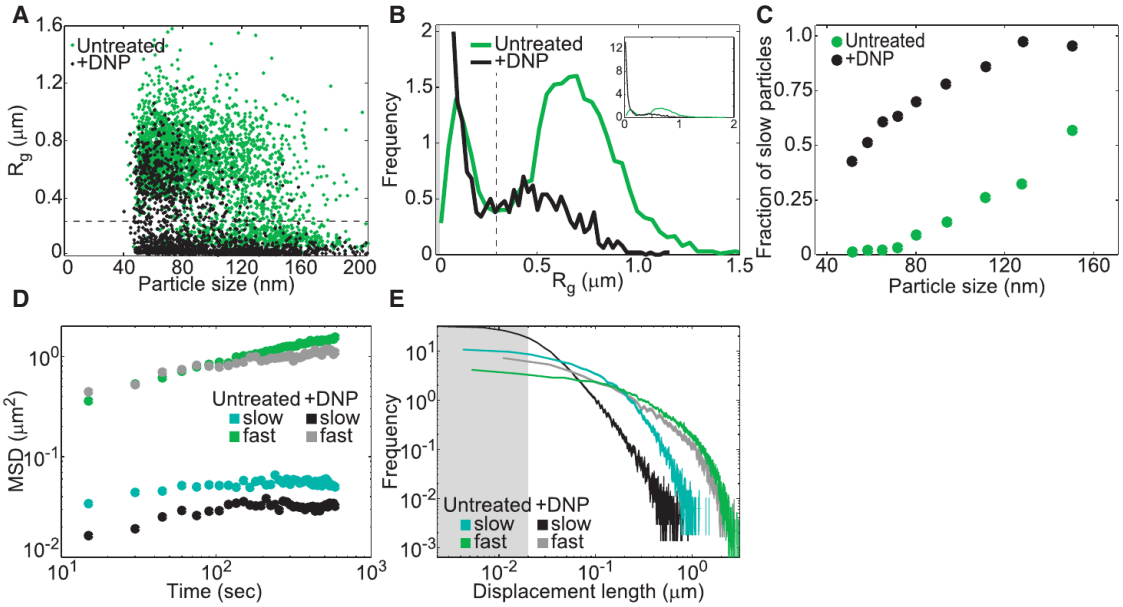

Figure 5. Two Subpopulations of GFP-μNS Particles Exist in Both Active and Inactive Cells

(A) Radius of gyration (R_g) of individual trajectories is plotted as a function of GFP-μNS particle size for *E. coli* cells (CJW4617) under untreated and DNP-treated conditions. The horizontal dashed line delimits slow (R_g < 0.3 μm) and fast (R_g > 0.3 μm) particles.

(B) Histogram of R_g for cells under untreated and DNP-treated conditions. The vertical dashed line delimits slow (R_g < 0.3 μm) and fast (R_g > 0.3 μm) particles. The gray shading delineates the estimated tracking error.

(C) Fraction of slow particles (R_g < 0.3 μm) for trajectories in each size bin for cells with or without DNP treatment.

(D) MSD of slow (R_g < 0.3 μm) and fast (R_g > 0.3 μm) GFP-μNS particles.

(E) Distribution of displacements for slow (R_g < 0.3 μm) and fast (R_g > 0.3 μm) GFP-μNS particles under untreated and DNP-treated conditions. The line width indicates Poisson counting error, and the gray shading delineates the estimated tracking error.

with different cage rearrangement times will exhibit different dynamics.

To examine whether heterogeneity in particle dynamics exists in the GFP-μNS tracking experiments, we plotted R_g measurements of individual GFP-μNS trajectories as a function of particle size (Figure 5A). Interestingly, the R_g values split GFP-μNS particles into two distinct subpopulations at an R_g value of 0.3 μm, irrespective of particle size or metabolic state of the cell. This can be easily seen in the distributions of R_g (Figure 5B). Because R_g is a measure of how much space a particle explores on average, we will refer to the two populations as "slow" (R_g < 0.3 μm) and "fast" (R_g > 0.3 μm) particles. Though fast and slow particles were found in both active and inactive cell populations, their fraction differed, with the fraction of slow particles being low in the active (untreated) cell population and high in the inactive (+DNP) cell population (Figure 5B). This trend was observed across the nine bins of particle sizes (Figure 5C). Thus, the fraction of slow and fast particles appears to be the primary reason for the difference in dynamics between active and inactive cells. Note that the presence of fast particles in the DNP-treated cell population was not due to cell growth by DNP-resistant cells, as no DNP-treated cells (out of 4×10^9 cells) were able to form a colony after overnight incubation.

The slow and fast particle populations from both active and inactive cells exhibited markedly different behavior, as evident from their MSDs (Figure 5D) and displacement distributions (Figure 5E). Fast particles not only explored more cytoplasmic space on average but did so with displacements from distributions shifted toward longer lengths. Most striking was the observation that fast particles from both untreated and DNP-treated conditions behave similarly, with virtually overlapping MSDs and displacement length distributions (Figures 5D and 5E). Although not to the same degree, the behavior of slow particles was also close between metabolically active and energy-depleted conditions. This suggests that particles from the fast population and, to a lesser extent, particles from the slow population experience a similar local environment regardless of metabolic status.

The difference in particle dynamics (slow and fast) may reflect dynamic heterogeneity within the cytoplasm. Similar to glass-forming liquids, the slow particles would be caged by neighboring macromolecules and have a low probability of escape, whereas the probability of escape through collective rearrangement of neighboring macromolecules would be greatly increased for fast particles. The collective effect of all ongoing metabolic activities in active cells would facilitate cage turnover, which would explain the observed higher fraction of fast particles in active cells (Figures 5B and 5C). Alternatively, the two populations in particle dynamics may stem from heterogeneity among cells: some cells would have slow particles, whereas others would have fast particles. In this latter case, two particles in the same cell would always behave similarly (slow or fast), whereas in the first scenario (heterogeneity within the cytoplasm), slow and fast dynamics could coexist in a single cell. To test this, we sought to identify instances of cells containing

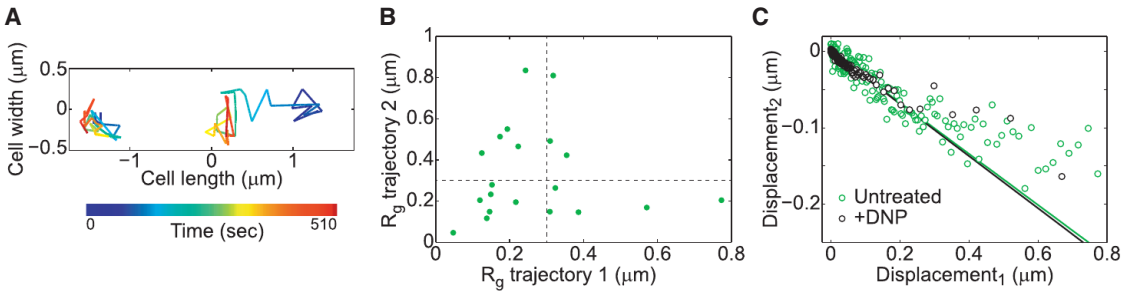

Figure 6. Double-Particle Tracking and Correlation of Displacements Are Consistent with Dynamic Heterogeneity in the Cytoplasm

(A) Example of two-dimensional trajectories of two GFP-μNS particles in a single *E. coli* cell (CJW4617). The trajectory of the left particle has a radius of gyration R_g = 0.12 μm, and the particle has an estimated size d = 144 nm; for the right particle, R_g = 0.43 μm and d = 158 nm.

(B) Radius of gyration (R_g) of individual trajectories for pairs of GFP-μNS particles in individual *E. coli* cells (CJW4617) under metabolically active conditions. Only the results for particle pairs with a difference of particle size of less than 10% are shown. The horizontal dashed line delimits slow (R_g < 0.3 μm) and fast (R_g > 0.3 μm) particles.

(C) Plot showing the average displacement length (displacement$_2$) following an initial displacement (displacement$_1$) of a given length for GFP-μNS particles in *E. coli* cells (CJW4617) under untreated and DNP-treated conditions. The second displacement was signed positive if it was in the same direction as the initial displacement and negative otherwise. Each point represents the average of 700 displacements. Solid lines represent the best fit (displacement$_2$ = −0.34 displacement$_1$) to the data where displacement$_1$ < 0.2 μm. The time interval is 15 s.

two particles of similar size (within 10%). Cells with two GFP-μNS foci were rare and tended to be observed only under greater induction conditions of GFP-μNS synthesis, which led to larger and thus slower particles. Despite the bias toward slower particles, we still found that fast (R_g > 0.3 μm) particles could coexist with slow (R_g < 0.3 μm) particles (Figures 6A and 6B), arguing that the difference in dynamics primarily comes from dynamic heterogeneity within the cytoplasm of individual cells.

Local Caging Is Mitigated by Cellular Metabolism

In dense colloidal suspensions, local caging is evident in correlation analysis of consecutive displacements (Doliwa and Heuer, 1998; Weeks and Weitz, 2002). For small displacements, the local caging results in a negative linear correlation between consecutive displacements. The linear relationship does not hold for longer displacements, which indicates the escape of the particle from its cage, presumably through collective rearrangement of its neighbors. To examine whether the dynamics of GFP-μNS particles are linked to caging, we calculated the average displacement length following an initial displacement of a given length (signed positive if the second displacement was in the same direction as the initial displacement and negative otherwise). An object trapped in a container with perfectly reflecting walls exhibits an apparent negative correlation between two subsequent steps with a correlation coefficient c = −0.5 (Doliwa and Heuer, 1998). If the object has a nonzero probability of escaping the cage, the correlation coefficient is expected to be between 0 and −0.5. For small initial displacements (<200 nm), we observed a strong negative correlation (c = −0.34 for both untreated and DNP-treated cells; Figure 6C), in agreement with local caging. Around 250 nm, this linear relationship breaks, consistent with cage escape. The break in linearity provides an estimation of the cage size (Weeks and Weitz, 2002). The higher number of displacements above 250 nm in untreated cells rather than in DNP-treated cells (reflected by the greater number of data points greater than 250 nm in Figure 6C) suggests more frequent cage escape and thus higher cage turnover under metabolically active conditions, consistent with the greater proportion of fast particles in the active cell population (Figures 5B and 5C). This result suggests that cellular metabolism facilitates long-distance motion by increasing cage rearrangement (see Discussion).

DISCUSSION

Our findings fundamentally alter the way that we view the bacterial cytoplasm. We show that, above a certain size scale (~30 nm), the bacterial cytoplasm behaves differently from a simple (viscous) fluid. Instead, it displays striking features (such as non-Gaussian distributions of displacements with long tails, nonergodicity, caging, and dynamic heterogeneity; Figures 4B, 4E, 5A, and 6) that are characteristic of colloidal glasses (Cipelletti and Ramos, 2005; Hunter and Weeks, 2012). The cytoplasm behaves as a liquid for small particles while it increasingly behaves as a glass-forming liquid approaching the glass transition with increasing particle size. This size dependence provides an explanation for previous seemingly conflicting reports of normal and anomalous diffusion (see Supplemental Information and Figures S6E–S6G). In dense colloidal suspensions containing particles of two sizes, the smaller particle can be mobile, perceiving the environment as a liquid, while the larger one can display glassy dynamics (Zaccarelli et al., 2005). This is in line with the size-dependent dynamics that we observed for GFP-μNS particles. As their size increases, GFP-μNS particles would become increasingly constrained by other surrounding components of the cytoplasm.

Remarkably, the glassy dynamics are partially suppressed by metabolic activity in a size-dependent manner. In other words, our data suggest that cellular metabolism enhances the motion of cytoplasmic components by "fluidizing" the cytoplasm, and this effect increases with component size.

What Is the Origin of the Glassy Behavior?

Aspects of glassiness have been reported in eukaryotic cells but have been attributed to the mechanical response of their

extensive cytoskeletal network (Fabry et al., 2001). Bacteria lack such a pervasive cytoskeletal meshwork and its associated motors. However, the bacterial cytoplasm is more similar to colloidal glasses by being more crowded than the eukaryotic cytoplasm based on the diffusion coefficient of free GFP being about three times smaller in *E. coli* than in eukaryotic cells (Elowitz et al., 1999; Swaminathan et al., 1997). Because crowding in dense colloidal suspensions is responsible for their glassy dynamics, it is likely that the glassy behavior of the bacterial cytoplasm originates from its extreme crowding (Cayley et al., 1991; Zimmerman and Trach, 1991). While measuring crowding inside bacterial cells is technically difficult and is subject to uncertainties, estimates suggest that macromolecules occupy 20%–40% of the bacterial cytoplasm (Cayley et al., 1991; Zimmerman and Trach, 1991). An additional ~20% of the cytoplasm consists of "bound" water, presumably as a hydration layer to macromolecules (Cayley et al., 1991), suggesting that the total excluded volume may range between 40%–60%. Colloidal suspensions can exhibit glassy dynamics over a wide range of volume fractions depending on the properties of the system. For example, monodisperse suspensions of noninteractive colloidal particles vitrify at volume fractions near 58% (Hunter and Weeks, 2012). Importantly, elements of glassy dynamics are observable at lower (e.g., 45%) volume fractions (Kegel and van Blaaderen, 2000; Weeks et al., 2000). If the colloidal particles are interacting, glassy dynamics can occur at even lower volume fractions (Dawson, 2002). Furthermore, glass transition occurs at a lower density in a confined geometry (Fehr and Löwen, 1995).

How Can Cellular Metabolism Fluidize the Cytoplasm to Enhance Motion?

The nucleoid affects the distribution of large components (Coquel et al., 2013), and the dynamics of individual chromosomal loci change with ATP depletion (Weber et al., 2012). However, we found that metabolic depletion results in the confinement of both GFP-μNS particles and mini-RK2 plasmids, even when they are located in the large DNA-depleted regions of filamentous *dnaC2* cells (Figures 2D, 2E, and S2B). Thus, DNA dynamics, DNA-related processes (e.g., transcription), or agitation of the DNA mesh from DNA-associated activities cannot be the driving factor underlying metabolism-dependent motion and the proposed increase in cage turnover in active cells. We also ruled out a predominant role for MreB (Figure S3B) or FtsZ (Figures 2D, 2E, and S2B; note that filamentous *dnaC2* cells do not make FtsZ rings). Inhibiting translation or peptidoglycan synthesis had little, if any, measurable effect on metabolism-dependent motion (Figures S3C and S3E). This suggests that any of these processes cannot alone account for the observed metabolism-dependent motion. However, there are a multitude of cellular processes occurring simultaneously inside of metabolically active cells. We envision that these processes collectively promote cage turnover, as opposed to a single process being solely responsible.

How could cellular activities collectively increase cage turnover? Spitzer and Poolman argued that, from a physical chemistry perspective, hydrophobic and screened electrostatic interactions, together with macromolecular crowding, must result in the formation of overcrowded regions of macromolecules separated by a more fluid phase of less-crowded cytosol (nanopools) (Spitzer, 2011; Spitzer and Poolman, 2009). Their theory also stipulates that metabolic reactions, by altering the hydrophobicity and charge of molecules, would continuously remodel the topology of nanopools and overcrowded regions within the cytoplasm. Following this view, it is conceivable that large particles would become caged in the overcrowded regions or nanopools and that the metabolism-dependent rearrangement of these domains would promote their long-range motion. A second, nonexclusive way by which metabolism could promote cage turnover does not require microphase separation and is based on the notion that cellular activities cause agitations to the system. A remarkable property of liquids near a glass transition is that small changes in the system can dramatically modify its fluidity. In a colloidal glass, particles are caged by surrounding neighbors. However, agitation can fluidize the system by increasing the rate of cage rearrangements (Petekidis et al., 2002). We provide evidence that cellular metabolism promotes cytoplasmic fluidization (Figures 1, 2, 3, 4, and 5) and uncaging (Figure 6C). Metabolic activity can cause a variety of perturbations (conformational changes, fluid displacements, nonequilibrium fluctuations, etc.) that may collectively influence cage rearrangement, allowing cage escape and long-distance motion. When all metabolic activities are abolished, rearrangement of the local domain (cage) would become rare (as in nonliving glassy materials), leading to particle confinement.

What Are the Biological Implications?

Current models of bacterial processes generally consider the cytoplasm as a simple fluid. However, even in active cells, the cytoplasm retains glassy features in a component-size-dependent manner (Figures 4B, 5A–5C, and 6C). Based on our rough critical size estimation, we expect that cytoplasmic constituents $\geq$30 nm will be subject to metabolism-dependent motion. This implies that proteins, which typically have a size <10 nm, will not be affected, consistent with the minimal effect of DNP on the apparent diffusion of free GFP in *C. crescentus* (Montero Llopis et al., 2012). However, larger cellular components such as plasmids (Figures 1D and 1E), protein filaments (Figures 1A–1C), storage granules (Figure S2A), and the multitude of other large components populating the cytoplasm (e.g., polyribosomes, chromosomes, enzymatic megacomplexes, intracellular organelles, phage capsids and genomes, microcompartments, etc.) will be impacted by the glassy behavior of the cytoplasm and the metabolic state of the cell. Many of these large components are involved in processes that are essential for life and fitness in natural environments, and their functions depend on their ability to move in the cytoplasm. For example, although the origin region of the chromosome segregates via an active mechanism, the bulk of the chromosome has been proposed to partition passively through an entropy-driven mechanism (Jun and Wright, 2010) that implies diffusion. Similarly, multicopy plasmids and some storage granules require motion for their partitioning (which is essential for their propagation). Low-copy plasmids typically have a dedicated partitioning system, but even then, some plasmid partitioning systems have been proposed to rely on an active diffusion-ratchet mechanism (Hwang et al., 2013; Vecchiarelli et al., 2013) in which plasmid diffusion is

an essential element. We even expect phages to be impacted by the physical nature of the cytoplasm, as the assembly of their genomes and capsids depends on their ability to interact.

Our data suggest that cellular metabolism fluidizes the cytoplasm, allowing larger cellular components to escape local environments and sample cytoplasmic space that they otherwise could not. This metabolism-induced fluidization may help the cell to achieve the delicate balance of attaining extremely high concentrations of biomolecules (to increase metabolism and cell proliferation) without severely compromising macromolecular motion. Ultimately, during the course of evolution, the glassy properties of the cytoplasm may have set upper limits to the size of molecular components and the degree of molecular crowding a cell can have. Higher crowding could result in particles of smaller sizes (such as proteins) "perceiving" the cytoplasm as more glass like, severely impacting biochemical reactions. Consistent with this idea, the mobility of free GFP becomes disproportionally reduced compared to a smaller molecule (e.g., glucose derivative) when high osmotic stress increases cytoplasmic crowding (Mika et al., 2010).

Another interesting outcome of the metabolic effect on cytoplasmic fluidity is that fluctuations in the environment can modulate cytoplasmic dynamics by affecting metabolism. Metabolic dormancy is widespread in the wild; for example, the fraction of quiescent cells ranges from 20% in the human gut to >80% in soil samples (Lennon and Jones, 2011). Dormancy has generated considerable interest in the scientific community, notably because of its links to both pathogenesis and antibiotic resistance (Coates, 2003). Dormancy is a survival strategy that bacteria in both environmental and clinical settings use to respond to stress such as starvation, antibiotic exposure, and high cell density (Lennon and Jones, 2011). We show that the motion of large components drops under metabolic depletion, and this occurs under natural conditions such as prolonged carbon starvation and late stationary phase (Figures 1B and 1C). This implies that the fluidity of the cytoplasm in dormant cells is very different compared to active cells, a difference that has not, to our knowledge, been considered. It would be interesting to examine in the future whether the vitrification of the dormant cytoplasm helps to preserve subcellular architecture during quiescent periods while still allowing diffusion of proteins and metabolites to permit a quick restart of growth when conditions improve.

EXPERIMENTAL PROCEDURES

Procedures used for imaging, strains construction, single-particle tracking, trajectory analysis, tracking precision estimation, image analysis, parameter determination (R_g, MSD, MSD_τ, α_2, γ), and particle size estimation are described in the Extended Experimental Procedures.

Strains, Plasmids, and Growth Conditions

A list of strains is provided in Table S1. Exponentially growing cell cultures were used in all experiments ($OD_{600} \leq 0.3$ for *E. coli* and $OD_{660} \leq 0.25$ for *C. crescentus*), except where noted.

C. crescentus strains were grown at 30°C in defined minimal M2G medium (Ely, 1991) and were supplemented with antibiotics when appropriate.

E. coli strain JP924 was grown at 30°C in M9 glycerol medium supplemented with casamino acids (M9G), 50 μg/ml of ampicillin, and 2 μg/ml of chloramphenicol. GFP-LacI expression was accomplished by spotting cells on agarose pads containing a concentration gradient of L-arabinose prior to imaging. CJW4386 (carrying *dnaC2*) was grown at 30°C in M9G, 50 μg/ml ampicillin, and 2 μg/ml chloramphenicol. Ninety minutes prior to imaging, the culture was shifted to 37°C, and L-arabinose was added (to a final concentration of 0.02%) 45 min prior to imaging.

E. coli strains CJW4617 and CJW4619 were grown at 30°C in M9G supplemented with 50 μg/ml kanamycin. GFP-μNS synthesis was induced by addition of isopropyl β-D-1-thiogalactopyranoside (IPTG) to 50–200 μM. After 30–120 min at 30°C, induction was stopped by washing cells into IPTG-free M9G medium. CJW4619 (carrying *dnaC2*) cells were incubated at 37°C for 2–3 hr to obtain filamentous cells.

Light Microscopy

Cells were imaged on agarose-padded slides supplemented with indicated media; see Extended Experimental Procedures for further details. Cell outlines were obtained from phase contrast images using open-source software MicrobeTracker (Sliusarenko et al., 2011). Fluorescent spots were detected and tracked using SpotFinder (Sliusarenko et al., 2011) and custom-built scripts in Matlab (The MathWorks), as described in the Extended Experimental Procedures.

SUPPLEMENTAL INFORMATION

Supplemental Information includes Extended Results, Extended Experimental Procedures, one table, and seven movies and can be found with this article online at http://dx.doi.org/10.1016/j.cell.2013.11.028.

ACKNOWLEDGMENTS

We are grateful to Jason Hocking for the construction of strains CJW4617 and CJW4619. We thank Dr. Anuradha Janakiraman, Dr. Max Nibert, and Dr. Cammie Lesser for providing the template for the construction of the IPTG-inducible allele that encodes GFP-μNS. We also thank Dr. Joe Pogliano for providing JP924 strain and Dr. Manuel Campos for sharing the information about nucleoid expansion in response to DNP treatment. We also thank all members of the Jacobs-Wagner lab for critical reading of the manuscript and for fruitful discussions. B.R.P. was, in part, supported by the National Institutes of Health (T32HG 003198). This work was supported by the National Institutes of Health (GM065835 to C.J.-W.). C.J.-W. is a Howard Hughes Medical Institute investigator.

Received: June 14, 2013
Revised: July 31, 2013
Accepted: November 5, 2013
Published: December 19, 2013

REFERENCES

Ausmees, N., Kuhn, J.R., and Jacobs-Wagner, C. (2003). The bacterial cytoskeleton: an intermediate filament-like function in cell shape. Cell *115*, 705–713.

Bakshi, S., Bratton, B.P., and Weisshaar, J.C. (2011). Subdiffraction-limit study of Kaede diffusion and spatial distribution in live Escherichia coli. Biophys. J. *101*, 2535–2544.

Berthier, L. (2011). Dynamic heterogeneity in amorphous materials. Physics *4*, 42.

Brangwynne, C.P., Koenderink, G.H., MacKintosh, F.C., and Weitz, D.A. (2009). Intracellular transport by active diffusion. Trends Cell Biol. *19*, 423–427.

Broering, T.J., Parker, J.S., Joyce, P.L., Kim, J., and Nibert, M.L. (2002). Mammalian reovirus nonstructural protein microNS forms large inclusions and colocalizes with reovirus microtubule-associated protein micro2 in transfected cells. J. Virol. *76*, 8285–8297.

Broering, T.J., Arnold, M.M., Miller, C.L., Hurt, J.A., Joyce, P.L., and Nibert, M.L. (2005). Carboxyl-proximal regions of reovirus nonstructural protein muNS necessary and sufficient for forming factory-like inclusions. J. Virol. *79*, 6194–6206.

Cabeen, M.T., Charbon, G., Vollmer, W., Born, P., Ausmees, N., Weibel, D.B., and Jacobs-Wagner, C. (2009). Bacterial cell curvature through mechanical control of cell growth. EMBO J. *28*, 1208–1219.

Cabeen, M.T., Murolo, M.A., Briegel, A., Bui, N.K., Vollmer, W., Ausmees, N., Jensen, G.J., and Jacobs-Wagner, C. (2010). Mutations in the Lipopolysaccharide biosynthesis pathway interfere with crescentin-mediated cell curvature in Caulobacter crescentus. J. Bacteriol. *192*, 3368–3378.

Cayley, S., Lewis, B.A., Guttman, H.J., and Record, M.T., Jr. (1991). Characterization of the cytoplasm of Escherichia coli K-12 as a function of external osmolarity. Implications for protein-DNA interactions in vivo. J. Mol. Biol. *222*, 281–300.

Cipelletti, L., and Ramos, L. (2005). Slow dynamics in glassy soft matter. J. Phys. Condens. Matter *17*, R253–R285.

Coates, A.R.M. (2003). Dormancy and low-growth states in microbial disease (Cambridge, New York: Cambridge University Press).

Coquel, A.S., Jacob, J.P., Primet, M., Demarez, A., Dimiccoli, M., Julou, T., Moisan, L., Lindner, A.B., and Berry, H. (2013). Localization of protein aggregation in Escherichia coli is governed by diffusion and nucleoid macromolecular crowding effect. PLoS Comp. Biol. *9*, e1003038.

Dawson, K.A. (2002). The glass paradigm for colloidal glasses, gels, and other arrested states driven by attractive interactions. Curr. Opin. Coll. Int. Sci. *7*, 218–227.

Derman, A.I., Lim-Fong, G., and Pogliano, J. (2008). Intracellular mobility of plasmid DNA is limited by the ParA family of partitioning systems. Mol. Microbiol. *67*, 935–946.

Dix, J.A., and Verkman, A.S. (2008). Crowding effects on diffusion in solutions and cells. Annu Rev Biophys *37*, 247–263.

Doliwa, B., and Heuer, A. (1998). Cage effect, local anisotropies, and dynamic heterogeneities at the glass transition: A computer study of hard spheres. Phys. Rev. Lett. *80*, 4915–4918.

Elowitz, M.B., Surette, M.G., Wolf, P.E., Stock, J.B., and Leibler, S. (1999). Protein mobility in the cytoplasm of Escherichia coli. J. Bacteriol. *181*, 197–203.

Ely, B. (1991). Genetics of Caulobacter crescentus. Methods Enzymol. *204*, 372–384.

English, B.P., Hauryliuk, V., Sanamrad, A., Tankov, S., Dekker, N.H., and Elf, J. (2011). Single-molecule investigations of the stringent response machinery in living bacterial cells. Proc. Natl. Acad. Sci. USA *108*, E365–E373.

Fabry, B., Maksym, G.N., Butler, J.P., Glogauer, M., Navajas, D., and Fredberg, J.J. (2001). Scaling the microrheology of living cells. Phys. Rev. Lett. *87*, 148102.

Fehr, T., and Löwen, H. (1995). Glass transition in confined geometry. Phys. Rev. E *52*, 4016–4025.

Golding, I., and Cox, E.C. (2006). Physical nature of bacterial cytoplasm. Phys. Rev. Lett. *96*, 098102.

Heun, P., Laroche, T., Shimada, K., Furrer, P., and Gasser, S.M. (2001). Chromosome dynamics in the yeast interphase nucleus. Science *294*, 2181–2186.

Hunter, G.L., and Weeks, E.R. (2012). The physics of the colloidal glass transition. Rep. Prog. Phys. *75*, 066501.

Hwang, L.C., Vecchiarelli, A.G., Han, Y.W., Mizuuchi, M., Harada, Y., Funnell, B.E., and Mizuuchi, K. (2013). ParA-mediated plasmid partition driven by protein pattern self-organization. EMBO J. *32*, 1238–1249.

Jun, S., and Wright, A. (2010). Entropy as the driver of chromosome segregation. Nat. Rev. Microbiol. *8*, 600–607.

Kegel, W.K., and van Blaaderen, A. (2000). Direct observation of dynamical heterogeneities in colloidal hard-sphere suspensions. Science *287*, 290–293.

Latulippe, D.R., and Zydney, A.L. (2010). Radius of gyration of plasmid DNA isoforms from static light scattering. Biotechnol. Bioeng. *107*, 134–142.

Lennon, J.T., and Jones, S.E. (2011). Microbial seed banks: the ecological and evolutionary implications of dormancy. Nat. Rev. Microbiol. *9*, 119–130.

Levi, V., Ruan, Q., Plutz, M., Belmont, A.S., and Gratton, E. (2005). Chromatin dynamics in interphase cells revealed by tracking in a two-photon excitation microscope. Biophys. J. *89*, 4275–4285.

Maehara, A., Taguchi, S., Nishiyama, T., Yamane, T., and Doi, Y. (2002). A repressor protein, PhaR, regulates polyhydroxyalkanoate (PHA) synthesis via its direct interaction with PHA. J. Bacteriol. *184*, 3992–4002.

Marcus, A.H., Schofield, J., and Rice, S.A. (1999). Experimental observations of non-Gaussian behavior and stringlike cooperative dynamics in concentrated quasi-two-dimensional colloidal liquids. Phys. Rev. E *60* (5 Pt B), 5725–5736.

Mika, J.T., van den Bogaart, G., Veenhoff, L., Krasnikov, V., and Poolman, B. (2010). Molecular sieving properties of the cytoplasm of Escherichia coli and consequences of osmotic stress. Mol. Microbiol. *77*, 200–207.

Montero Llopis, P., Sliusarenko, O., Heinritz, J., and Jacobs-Wagner, C. (2012). In vivo biochemistry in bacterial cells using FRAP: insight into the translation cycle. Biophys. J. *103*, 1848–1859.

Nenninger, A., Mastroianni, G., and Mullineaux, C.W. (2010). Size dependence of protein diffusion in the cytoplasm of Escherichia coli. J. Bacteriol. *192*, 4535–4540.

Niu, L., and Yu, J. (2008). Investigating intracellular dynamics of FtsZ cytoskeleton with photoactivation single-molecule tracking. Biophys. J. *95*, 2009–2016.

Petekidis, G., Moussaïd, A., and Pusey, P.N. (2002). Rearrangements in hard-sphere glasses under oscillatory shear strain. Phys. Rev. E Stat. Nonlin. Soft Matter Phys. *66*, 051402.

Pusey, P.N., and van Megen, W. (1986). Phase-behavior of concentrated suspensions of nearly hard colloidal spheres. Nature *320*, 340–342.

Qi, Q.S., and Rehm, B.H.A. (2001). Polyhydroxybutyrate biosynthesis in Caulobacter crescentus: molecular characterization of the polyhydroxybutyrate synthase. Microbiology *147*, 3353–3358.

Sliusarenko, O., Heinritz, J., Emonet, T., and Jacobs-Wagner, C. (2011). High-throughput, subpixel precision analysis of bacterial morphogenesis and intracellular spatio-temporal dynamics. Mol. Microbiol. *80*, 612–627.

Soutoglou, E., and Misteli, T. (2007). Mobility and immobility of chromatin in transcription and genome stability. Curr. Opin. Genet. Dev. *17*, 435–442.

Spitzer, J. (2011). From water and ions to crowded biomacromolecules: in vivo structuring of a prokaryotic cell. Microbiol. Mol. Biol. Rev. *75*, 491–506.

Spitzer, J., and Poolman, B. (2009). The role of biomacromolecular crowding, ionic strength, and physicochemical gradients in the complexities of life's emergence. Microbiol. Mol. Biol. Rev. *73*, 371–388.

Swaminathan, R., Hoang, C.P., and Verkman, A.S. (1997). Photobleaching recovery and anisotropy decay of green fluorescent protein GFP-S65T in solution and cells: cytoplasmic viscosity probed by green fluorescent protein translational and rotational diffusion. Biophys. J. *72*, 1900–1907.

Vecchiarelli, A.G., Hwang, L.C., and Mizuuchi, K. (2013). Cell-free study of F plasmid partition provides evidence for cargo transport by a diffusion-ratchet mechanism. Proc. Natl. Acad. Sci. USA *110*, E1390–E1397.

Weber, S.C., Spakowitz, A.J., and Theriot, J.A. (2010). Bacterial chromosomal loci move subdiffusively through a viscoelastic cytoplasm. Phys. Rev. Lett. *104*, 238102.

Weber, S.C., Spakowitz, A.J., and Theriot, J.A. (2012). Nonthermal ATP-dependent fluctuations contribute to the in vivo motion of chromosomal loci. Proc. Natl. Acad. Sci. USA *109*, 7338–7343.

Weeks, E.R., and Weitz, D.A. (2002). Properties of cage rearrangements observed near the colloidal glass transition. Phys. Rev. Lett. *89*, 095704.

Weeks, E.R., Crocker, J.C., Levitt, A.C., Schofield, A., and Weitz, D.A. (2000). Three-dimensional direct imaging of structural relaxation near the colloidal glass transition. Science *287*, 627–631.

Zaccarelli, E., Mayer, C., Asteriadi, A., Likos, C.N., Sciortino, F., Roovers, J., Iatrou, H., Hadjichristidis, N., Tartaglia, P., Löwen, H., and Vlassopoulos, D. (2005). Tailoring the flow of soft glasses by soft additives. Phys. Rev. Lett. *95*, 268301.

Zimmerman, S.B., and Trach, S.O. (1991). Estimation of macromolecule concentrations and excluded volume effects for the cytoplasm of *Escherichia coli*. J. Mol. Biol. *222*, 599–620.

FORWARD FROM

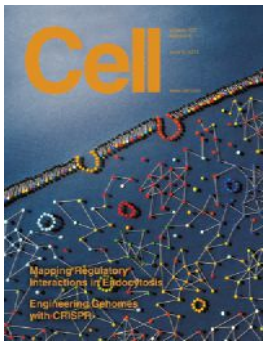

As we commemorate 40 years of publishing exciting biology we're also embracing the future. We will continue to lead the way with best-in-class editorial service, innovations in publishing, and new technology to address the evolving needs of scientists. Here's to the next 40 years!

www.cell.com/40/home

Cell

Cell

Resource

Generation of Gene-Modified Cynomolgus Monkey via Cas9/RNA-Mediated Gene Targeting in One-Cell Embryos

Yuyu Niu,[1,5,7] Bin Shen,[2,7] Yiqiang Cui,[3,7] Yongchang Chen,[1,5,7] Jianying Wang,[2] Lei Wang,[3] Yu Kang,[1,5] Xiaoyang Zhao,[4] Wei Si,[1,5] Wei Li,[4] Andy Peng Xiang,[6] Jiankui Zhou,[2] Xuejiang Guo,[3] Ye Bi,[3] Chenyang Si,[1,5] Bian Hu,[2] Guoying Dong,[3] Hong Wang,[1,5] Zuomin Zhou,[3] Tianqing Li,[1,5] Tao Tan,[1,5] Xiuqiong Pu,[1,5] Fang Wang,[1,5] Shaohui Ji,[1,5] Qi Zhou,[4] Xingxu Huang,[2,*] Weizhi Ji,[1,5,*] and Jiahao Sha[3,*]

[1]Yunnan Key Laboratory of Primate Biomedical Research, Kunming 650500, China

[2]MOE Key Laboratory of Model Animal for Disease Study, Model Animal Research Center of Nanjing University, National Resource Center for Mutant Mice, Nanjing 210061, China

[3]State Key Laboratory of Reproductive Medicine, Department of Histology and Embryology, Nanjing Medical University, Nanjing 210029, China

[4]State Key Laboratory of Reproductive Biology, Institute of Zoology, Chinese Academy of Sciences, Beijing 100101, China

[5]Kunming Biomed International and National Engineering Research Center of Biomedicine and Animal Science, Kunming 650500, China

[6]Center for Stem Cell Biology and Tissue Engineering, Key Laboratory for Stem Cells and Tissue Engineering, Sun Yat-Sen University, Guangzhou 510080, China

[7]These authors contributed equally to this work

*Correspondence: shajh@njmu.edu.cn (J.S.), wji@kbimed.com (W.J.), xingxuhuang@mail.nju.edu.cn (X.H.)

http://dx.doi.org/10.1016/j.cell.2014.01.027

SUMMARY

Monkeys serve as important model species for studying human diseases and developing therapeutic strategies, yet the application of monkeys in biomedical researches has been significantly hindered by the difficulties in producing animals genetically modified at the desired target sites. Here, we first applied the CRISPR/Cas9 system, a versatile tool for editing the genes of different organisms, to target monkey genomes. By coinjection of Cas9 mRNA and sgRNAs into one-cell-stage embryos, we successfully achieve precise gene targeting in cynomolgus monkeys. We also show that this system enables simultaneous disruption of two target genes (*Ppar-γ* and *Rag1*) in one step, and no off-target mutagenesis was detected by comprehensive analysis. Thus, coinjection of one-cell-stage embryos with Cas9 mRNA and sgRNAs is an efficient and reliable approach for gene-modified cynomolgus monkey generation.

INTRODUCTION

Monkeys have served as one of the most valuable models for modeling human diseases and developing therapeutic strategies due to their close similarities to humans in terms of genetic and physiological features (Chan, 2013). The genetic modification is invaluable for generation of monkey models. Although several transgenic monkeys have been successfully generated using retroviral or lentiviral vectors (Chan et al., 2001; Niu et al., 2010; Sasaki et al., 2009; Yang et al., 2008), precise genomic targeting in monkeys is the most desired for generating human disease models and has not been achieved so far (Chan, 2013; Shen, 2013). The recently described clustered regularly interspaced short palindromic repeats (CRISPR)/CRISPR-associated (Cas) 9 system confers targeted gene editing by small RNAs that guide the Cas9 nuclease to the target site through base pairing (Jinek et al., 2012). The CRISPR/Cas9 system has been demonstrated as an easy-handle, highly specific, efficient, and multiplexable approach for engineering eukaryotic genomes (Mali et al., 2013a). By now, this system has been successfully used to target genomic loci in the mammalian cell lines (Cho et al., 2013; Cong et al., 2013; Mali et al., 2013b; Wang et al., 2013) and several species, including mice and rat (Li et al., 2013a; Li et al., 2013b; Ma et al., 2014; Shen et al., 2013; Wang et al., 2013). But whether it's feasible in primates is still unclear.

By taking the advantages of CRISPR/Cas9, we achieved efficient gene targeting in mice and rats by coinjection of one-cell-stage embryos with Cas9 mRNA and sgRNAs (Li et al., 2013b; Shen et al., 2013; Ma et al., 2014). Encouraged by our successes in CRISPR/Cas9-mediated gene targeting, as well as gene manipulation in early-cleavage-stage embryos of monkeys (Niu et al., 2010), here, we have extended the application of the CRISPR/Cas9 system to multiplex genetic engineering in one-cell-stage embryos of monkeys and successfully obtained founder animals harboring two gene modifications.

RESULTS AND DISCUSSION

Cas9/RNA Effectively Mediates Gene Disruptions in Monkey Cell Line

We selected cynomolgus monkey (*Macaca fascicularis*) as the model animal because of its body size, availability, similar

menstrual cycle to human, and efficient reproduction ability (Sun et al., 2008). Three genes, namely *Nr0b1* (*Nuclear Receptor Subfamily 0 Group B Member 1*), *Ppar-γ* (*Peroxisome Proliferator-Activated Receptor Gamma*), and *Rag1* (*Recombination Activating Gene 1*), were selected as the target genes. Two sgRNAs separated by 117 bp for *Nr0b1*, 2 sgRNAs separated by 49 bp for *Ppar-γ*, and 1 sgRNA targeting *Rag1* (Figure 1A), were designed as described (Mali et al., 2013b). The efficiency of all sgRNAs was first tested by cotransfection with Cas9 into the COS-7 cell line derived from African green monkey kidney. Genomic DNA was isolated from cells harvested 72 hr after transient transfection and screened for the presence of site-specific gene modification by PCR amplification of regions surrounding the target sites as well as T7EN1 cleavage assay (Figure 1B). The cleavage bands were visible in all target genes. Further characterization of the cleavage by sequencing showed, different indels were detected at all five target sites with various mutation sizes (−336 ∼+1 bp) at the efficiency of 22.2% for *Nr0b1*-sgRNA1, 20% for *Nr0b1*-sgRNA2, 10% for *Ppar-γ*-sgRNA1, 25% for *Ppar-γ*-sgRNA2, and 23.8% for *Rag1*-sgRNA (Figure 1C). These data demonstrated that the selected sgRNAs worked effectively with Cas9 on monkey genomes.

Cas9/RNA Induces Efficient Genomic Targeting in Monkey Embryos

Although microinjection of ZFN or TALEN mRNA into embryo has been successfully used for creation of gene target animals, but they have not been feasible in monkeys so far (Chan, 2013). To test whether the CRISPR/Cas9 system works in monkey embryos, the Cas9 (Addgene No. 44758) and sgRNAs were transcribed by T7 RNA polymerase in vitro as described (Shen et al., 2013). Twenty nanogram/μl Cas9 mRNA and 25 nanogram/μl of mixtures containing equal amount of each 5 sgRNAs were pooled and microinjected into 22 one-cell fertilized eggs of cynomolgus monkeys. The eggs were further cultured at 37°C in 5% CO_2. A total of 15 embryos with normal development to morula or blastocyst stages were collected and examined for the presence of site-specific genome modification analysis by PCR, T7EN1 cleavage assay, and sequencing as described above. The results showed (Figures 2 and S1 available online), different sgRNAs function by different efficiency. Targeted modification with a range of sizes (−30 ∼+6 bp) in monkey embryos occurred at all three target genes with efficiency of 4/15 for *Nr0b1*, 7/15 for *Ppar-γ*, and 9/15 for *Rag1*. Intriguingly, 6 of 15 embryos (embryos 2, 5, 8, 10, 11, and 13) harbored simultaneously mutations in both *Ppar-γ* and *Rag1*; whereas 2 of 15 embryos (embryos 3 and 4) harbored simultaneously mutations in both *Nr0b1* and *Rag1*, demonstrating that the CRISPR/Cas9 system functions well in monkey embryos.

Cas9/RNA Enables One-Step Multiple Gene Modifications in Monkeys

With these successes, we set out to generate genetic modified cynomolgus monkeys. A total of 198 MII oocytes were collected. After fertilization by intracytoplasmic sperm injection (ICSI), Cas9 mRNA and sgRNA mixtures of five sgRNAs were injected as described above. A total 83 out of 186 injected zygotes were transferred into 29 surrogate females. Of the recipient mothers, ten pregnancies were established (34.5%; 10 out of 29), one of which was miscarried 36 days after embryo transfer. Among the pregnancies, three were twins, three were triplets, and the remaining four were single pregnancies (Table 1). So far, a set of twin female babies (A and B) were successfully delivered at full term (155 days) by caesarean section (Figure 3A). The other eight surrogate females are still in the gestation period. The noninvasively available tissues of the two infant monkeys, including placenta, umbilical cord, and ear punch tissues, were collected. Cas9/RNA-mediated genome modifications were first screened using genomic DNA from umbilical cord as described above. An additional band with smaller molecular size was observed by PCR amplification of the target region of *Rag1* in infant B (Figure 3B), suggesting that the genomic modification occurred in this founder animal. Next, all the PCR products were subjected to the T7EN1 cleavage assay (Figure 3C). Cleavage products were detected in both infants in *Rag1* and around the second sgRNA target site of *Ppar-γ*, indicating the presence of multiple genomic modifications in the founder monkeys. As expected, different kinds of indels (one for *Ppar-γ*, four for *Rag1*) were detected by sequencing of the PCR products (Figure 3D), further confirming the occurrence of multiple genomic modifications in the founder monkeys. Of note, no cleavage band was detected at *Nr0b1* (Figure S2), which may be due to the lowest mutation efficiency of this gene in the embryonic test described above.

The presence of gene modification was further analyzed using genomic DNA from ear punch tissues and placenta. The same PCR bands, cleavage bands, and modifications were detected in *Rag1* and *Ppar-γ* genes in both monkeys (Figure 4), further demonstrating the targeting success and confirming that CRISPR/Cas9 induces global genome modification in monkey embryos. Very impressively, no wild-type *Rag1* sequence was detected in the ear punch of founder B (Figure 4C), demonstrating that the target modification has been ubiquitously and efficiently integrated into different tissues, most likely including the germline.

We also further substantiated the allelic targeting effects by tagging single-nucleotide polymorphisms (SNPs) of parent monkeys. A 3.8 kb fragment harboring *Rag1*-sgRNA target site was PCR amplified from ear genomic DNA of the parents and sequenced. Two different combinations of 4 SNPs tagging the parents derivation were detected downstream of the target site of *Rag1*-sgRNA (Figure S3A, Tables S1 and S5). The tagging SNP combinations of the parents and the founder twins were further determined by TA cloning and sequencing (Figures S3B and S3C). The results showed that two tagging SNP combinations segregate in accordance with Mendel's laws. The *Rag1*-sgRNA target site in the ear of founder B showed high target efficiency was further sequenced. The results (Figure S3D) showed that both alleles identified by tagging SNPs harbored target modifications, indicating two alleles from both parents could be modified by Cas9/RNA-mediated targeting in monkeys.

Surprisingly, only one genotype with a single-nucleotide insertion for *Ppar-γ* at different tissues of both founder animals was detected (Figures 3D and 4C). To exclude the possibility that this single-nucleotide insertion was a SNP rather than a real mutation, the target sites of the parents and surrogate mother were amplified to perform T7EN1 cleavage assay and sequencing (Figure S4).

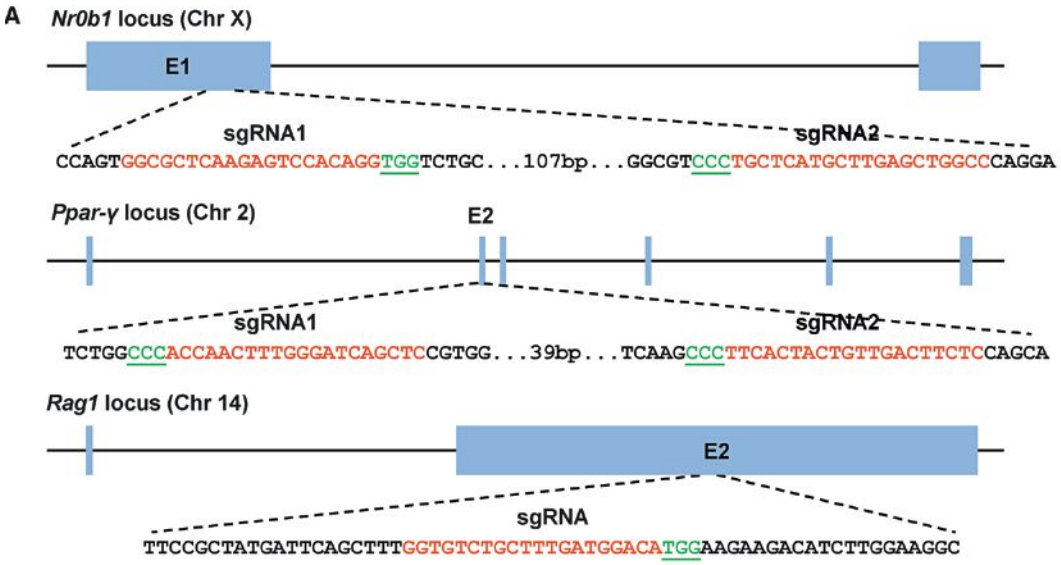

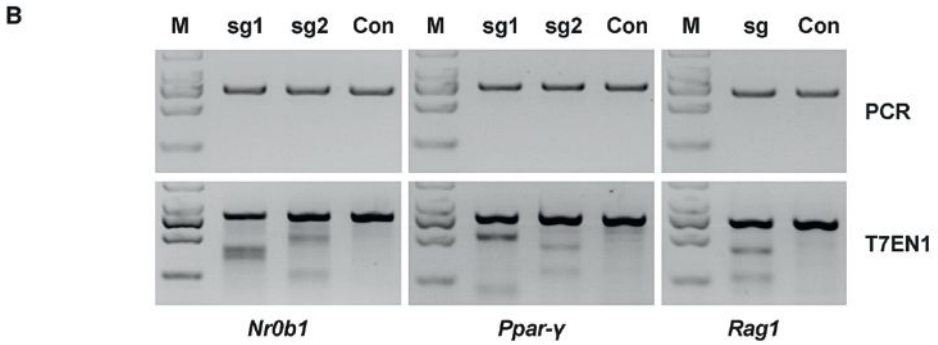

C

```
Nr0b1   TCTGGTGCGCTGCGGCCAGTGGCGCTCAAGAGTCCACAGGTGGTCTGCGAGGCAGCCTCAGCT (WT)
sg1     TCTGGTGCGCTGCGGCCAGTGGCGCTCAAGAGTCCACA:GTGGTCTGCGAGGCAGCCTCAGCT (-1,1/18)
        TCTGGTGCGCTGCGGCCAGTGGCGCT::::::::::CAGGTGGTCTGCGAGGCAGCCTCAGCT (-10,1/18)
        TCTGGTGCGCTGCGGCCAGTGGC::::::::::::::::::::::::::::::::::::::: (-43,1/18)
        :::::::::::::::::::::::::cctggtgggacacc::::::::::::::::::::::: (-336,+14,1/18)

Nr0b1   GGTGCGCAACTGCTGGGCGTCCCTGCTCATGCTTGAGCTGGCCCAGGACCGCTTGCAGTTCGA (WT)
sg2     GGTGCGCAACTGCTGGGCGTCCCTGCT::TGCTTGAGCTGGCCCAGGACCGCTTGCAGTTCGA (-2,1/15)
        GGTGCGCAACTGCTGGGCGTCCCTGCTCATGCTTGAGCTGGCCCAGGACCGCTTGCAGTTCGA (+1,1/15)
                                  ^c
        :::::::::::::tcctaaattgccc:::::CTTGAGCTGGCCCAGGACCGCTTGCAGTTCGA (-49,1/15)

Ppar-γ  ACACAGAGATGCCATTCTGGCCCACCAACTTTGGGATCAGCTCCGTGGATCTCTCCGTAATGG (WT)
sg1     ACACAGAGATGCCATTCTGGC:tc:::ACTTTGGGATCAGCTCCGTGGATCTCTCCGTAATGG (-6,+2,1/20)
        ACACAGAGATGCCATTCTGGCCCACC::::::GGGATCAGCTCCGTGGATCTCTCCGTAATGG (-6,1/20)

Ppar-γ  CCCACTCCTTTGACATCAAGCCCTTCACTACTGTTGACTTCTCCAGCATTTCTGCTCCACATT (WT)
sg2     CCCACTCCTTTGACATCAAGCCCTTCACTACTGTTGACTTCTCCAGCATTTCTGCTCCACATT (+1,5/20)
                                  ^a

Rag1    TTCCGCTATGATTCAGCTTTGGTGTCTGCTTTGATGGACATGGAAGAAGACATCTTGGAAGGC (WT)
sg      TTCCGCTATGATTCAGCTTTGGTGTCTGCTTTGATG:ACATGGAAGAAGACATCTTGGAAGGC (-1,3/21)
        TTCCGCTATGATTCAGCTTTGGTGTCTGCTTTGAT::ACATGGAAGAAGACATCTTGGAAGGC (-2,1/21)
        TTCCGCTATGATTCAGCTTTGGTGTCTG::::::::GACATGGAAGAAGACATCTTGGAAGGC (-8,1/21)
```

(legend on next page)

The results excluded the presence of the same single nucleotide, confirming that the insertion was indeed caused by CRISPR/Cas9 modification to the *Ppar-γ* gene. Taken together, we have successfully achieved Cas9/RNA-mediated site-specific modifications in monkey genome by one-cell embryo microinjection.

Mosaicism

It is worth notifying that the sequence data of both cultured embryos and founder animals showed multiple genotypes (Figures 2B, 3D, and 4C), suggesting the CRISPR/Cas9-mediated cleavage had occurred multiple times at different stages of monkey embryogenesis and resulted in mosaicism of the modification, as have been observed in other species (Sung et al., 2013; Tesson et al., 2011). Currently, the founder babies are housed in dedicated facilities and developing normally. Due to the limited access of tissues from the founder infants, more thorough characterization of the genomic modifications as well as phenotype remains to be performed. This has to be awaited until the founder monkeys have developed into adulthood. In addition, more full-term founders will be born and provide more samples for further assessment of CRISPR/Cas9-mediated genome modification in monkeys.

Off-Target Analysis

The off-target effect is of a major concern for the CRISPR/Cas9 system (Fu et al., 2013; Hsu et al., 2013; Pattanayak et al., 2013). We observed CRISPR/Cas9 induced heritable off-target mutation in mice (B.S., W. Zhang, J. Zhang, J. Zhou, J.W., L. Chen, L. Wang, A. Hodgkins, V. Iyer, X.H., and W.C. Skarnes, unpublished data). To test whether off target occurred in these genetic modified monkeys, we screened the monkey genome and predicted a total of 84 potential off-target sites (OTS), including 9 for site 1 of *Nr0b1*, 20 for site 2 of *Nr0b1*, 14 for site 1 of *Ppar-γ*, 20 for site 2 of *Ppar-γ*, and 21 for *Rag1*, respectively (Table S2). The off-target effects were comprehensively assessed as on-target effect analysis using genomic DNA from umbilical cord. The fragments around all the potential off-target loci were PCR amplified, then subjected to T7EN1 cleavage assay. Seventeen PCR products yielded cleavage bands were precisely examined by TA sequencing. Surprisingly, all the cleavage were caused by SNP or repeat sequences, and no authentic mutation was detected (Table S3). These results demonstrated that Cas9/RNA does not induce detectable off-target mutation in our study. Considering that the off-target effect is site-dependent, and more specific strategies using mutated Cas9 have already been established (Ran et al., 2013), the off-target mutagenesis can be minimized by optimizing the procedure, suggesting CRISPR/Cas9 could be a reliable genome target tool for monkeys.

In summary, our current studies demonstrate that site-specific gene modification can be effectively achieved in monkeys by coinjection of Cas9 mRNA and sgRNAs into the one-cell fertilized eggs. We also demonstrate that the multiple genetic mutations can be established at once without detectable off-target effects, providing the success of creating genome engineered primates and confirming the CRISPR/Cas9 system is applicable for monkey genome targeting.

EXPERIMENTAL PROCEDURES

Animals

Healthy female cynomolgus monkeys (*Macaca fascicularis*), ranging in age from 5 to 8 years and having body weights of 3.62 to 5.90 kg, were selected for use in this study. All animals were housed at the Kunming Biomed International (KBI). The KBI is an Association for Assessment and Accreditation of Laboratory Animal Care accredited facility. All animal protocols are approved in advance by the Institutional Animal Care and Use Committee of Kunming Biomed International.

Embryo Collection

Embryo collection and transfer were performed as previously described (Niu et al., 2010). In brief, 11 healthy female cynomolgus monkeys aged 5–8 years with regular menstrual cycles were selected as oocyte donors for superovulation, which were performed by intramuscular injection with rhFSH (recombinant human follitropin alfa, GONAL-F, Merck Serono) for 8 days, then rhCG (recombinant human chorionic gonadotropin alfa, OVIDREL, Merck Serono) on day 9. Oocytes were collected by laparoscopic follicular aspiration 32–35 hr after rhCG administration. MII (first polar body present) oocytes were used to perform intracytoplasmic sperm injection (ICSI) and the fertilization was confirmed by the presence of two pronuclei.

Cas9/sgRNA Injection of One-Cell Embryos

The zygotes were injected with a mixture of Cas9 mRNA (20 ng/μl) and five sgRNAs (5 ng/μl each). Microinjections were performed in the cytoplasm of zygotes using a Nikon microinjection system under standard conditions. The zygotes then were cultured in the chemically defined, protein-free hamster embryo culture medium-10 (HECM-10) containing 10% fetal calf serum (Hyclone Laboratories, SH30088.02) at 37°C in 5% CO_2. The cleaved embryos with high quality at two-cell to blastocyst stage were transferred into the oviduct of the matched recipient monkeys. Twenty-nine monkeys were used as surrogate recipient, and typically, three embryos were transferred into each female. The earliest pregnancy diagnosis was performed by ultrasonography about 20–30 days after the embryo transfer. Both clinical pregnancy and number of fetuses were confirmed by fetal cardiac activity and presence of a yolk sac as detected by ultrasonography (Chen et al., 2012).

DNA Constructs

Codon optimized Cas9 expression construct, Cas9-N-NLS-flag-linker (Addgene No. 44758), was synthesized and inserted into pST1374 vector as described before (Shen et al., 2013). The pUC57-sgRNA expression vector used for in vitro transcription of sgRNAs was described as before (Zhou et al., 2014). pGL3-U6-sgRNA-PGK-Puro vector, containing the U6-PGK-Puro fragment amplified from pLKO.1 (Addgene No. 8453), sgRNA scaffold amplified from pUC57-sgRNA, and pGL3-Basic plasmid backbone (Promega,

Figure 1. sgRNA:Cas9-Mediated Modifications of *Nr0b1*, *Ppar-γ*, and *Rag1* in COS-7 Cells

(A) Schematic diagram of sgRNAs targeting at *Nr0b1*, *Ppar-γ*, and *Rag1* loci. PAM sequences are underlined and highlighted in green. sgRNA targeting sites are highlighted in red.

(B) Detection of sgRNA1:Cas9-mediated cleavage of *Nr0b1*, *Ppar-γ*, and *Rag1* by PCR and T7EN1 cleavage assay. M, DNA marker; sg1, sgRNA1; sg2, sgRNA2; Con, control.

(C) Sequences of modified *Nr0b1*, *Ppar-γ*, and *Rag1* loci detected in COS-7 cells. At least 15 TA clones of the PCR products were analyzed by DNA sequencing. The PAM sequences are underlined and highlighted in green; the targeting sequences in red; the mutations in blue, lower case; deletions (–), insertions (+). N/N indicates positive colonies out of total sequenced.

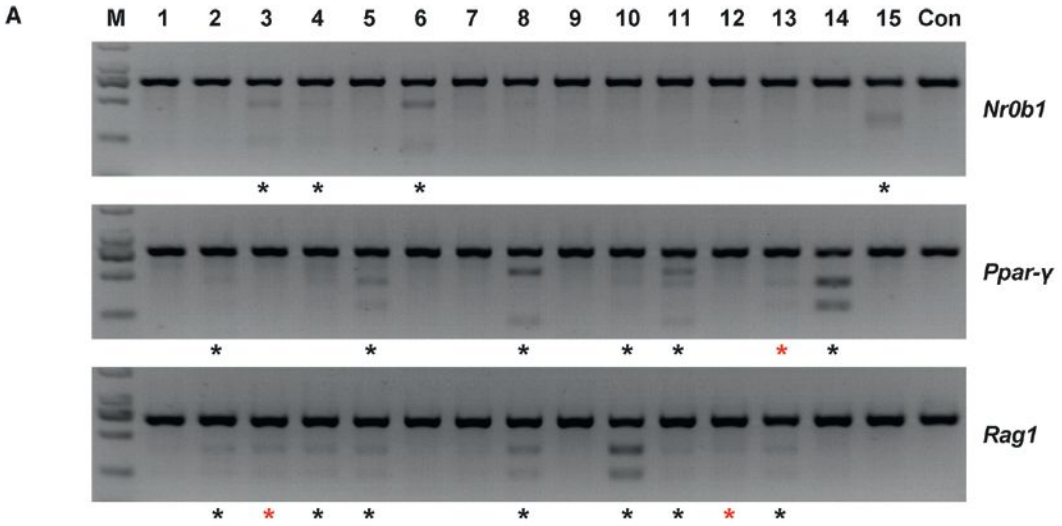

B

```
Nr0b1 CCAGTGGCGCTCAAGAGTCCACAGGTGGTC...GTCCCTGCTCATGCTTGAGCTGGCCCAGGA (WT)
  #3  CCAGTGGCGCTCAAGAGTCCACAGGTGGTC...GTCCCTGCTCATGCTTGAGCTGGCCCAGGA (+1,4/14)
                                          ^t
  #4  CCAGTGGCGCTCAAGAGTCCACAGGTGGTC...GTCCCTGCTCATGCTTGAGCTGGCCCAGGA (+1,2/17)
                                          ^t
  #6  CCAGTGGCGCTCAAGAGTCCACAGGTGGTC...GTCCCTGC:::::::::::::::::::::: (-30,3/21)
 #15  CCAGTGGCGCTCAAGAGTCCA:AGGTGGTC...GTCCCTGCTCATGCTTGAGCTGGCCCAGGA (-1,7/20)

Ppar-γ TCTGGCCCACCAACTTTGGGATCAGCTCCG...AGCCCTTCACTACTGTTGACTTCTCCAGCA (WT)
  #2  TCTGGCCCACCAACTTTGGGATCAGCTCCG...AGCCCTTCA:TACTGTTGACTTCTCCAGCA (-1,2/13)
  #5  TCTGGCCCACCAACTTTGGGATCAGCTCCG...AGCCCTTCACTACTGTTGACTTCTCCAGCA (+1,2/11)
                                          ^a
  #8  TCTGGCCCACC:::TTTGGGATCAGCTCCG...AGCCCTTCACTACTGTTGACTTCTCCAGCA (-3,8/36)
 #10  TCTGGCCCACCAACTTTGGGATCAGCTCCG...AGCCCTTCACTACTGTTGACTTCTCCAGCA (+1,3/29)
                                          ^a
 #11  TCTGGCCCACCAACTTTGGGATCAGCTCCG...AGCCCTTCACTACTGTTGACTTCTCCAGCA (+1,1/9)
                                          ^a
      TCTGGCCCA:::ACTTTGGGATCAGCTCCG...AGCCCTTCACTACTGTTGACTTCTCCAGCA (-3,1/9)
 #14  TCTGGCCCACCAACTTTGGGATCAGCTCCG...AGCCCTTC:::::TGTTGACTTCTCCAGCA (-5,4/9)
      TCTGGCCCACCAACTTTGGGATCAGCTCCG...AGCCCTTCACTACTGTTGACTTCTCCAGCA (+1,1/9)
                                          ^a
Rag1  TTCCGCTATGATTCAGCTTTGGTGTCTGCTTTGATGGACATGGAAGAAGACATCTTGGAAGGC (WT)
  #2  TTCCGCTATGATTCAGCTTTGGTGTCTGCTTTG::::::ATGGAAGAAGACATCTTGGAAGGC (-6,1/19)
  #4  TTCCGCTATGATTCAGCTTTGGTGTCTGCTTTGATG:ACATGGAAGAAGACATCTTGGAAGGC (-1,4/9)
  #5  TTCCGCTATGATTCAGCTTTGGTGTCTGCTTTG::::::::::::::::ACATCTTGGAAGGC (-16,1/30)
  #8  TTCCGCTATGATTCAGCTTTGGTGTCTGCTTTGATGGACATGGAAGAAGACATCTTGGAAGGC (+6,1/8)
                                       ^aagaag
 #10  TTCCGCTATGATTCAGCTTTGGTGTCTGCTTTGAT:GACATGGAAGAAGACATCTTGGAAGGC (-1,2/11)
      TTCCGCTATGATTCAGCTTTGGTGTCTGCTTT::::GACATGGAAGAAGACATCTTGGAAGGC (-4,3/11)
      TTCCGCTATGATTCAGCTTT::::::::::::::::ACATGGAAGAAGACATCTTGGAAGGC (-17,2/11)
 #11  TTCCGCTATGATTCAGCTTTGGTGTCTGCTTTGA::::::::::::::::CATCTTGGAAGGC (-16,2/14)
 #13  TTCCGCTATGATTCAGCTTTGGTGTCTG::::::::::CATGGAAGAAGACATCTTGGAAGGC (-10,1/17)
      TTCCGCTATGATTCAGCTTTGGTGTCTGCTTTGATGG:CATGGAAGAAGACATCTTGGAAGGC (-1,1/17)
```

Figure 2. sgRNA:Cas9-Mediated Modifications of *Nr0b1*, *Ppar-γ*, and *Rag1* in Cultured Embryos

(A) Detection of sgRNA1:Cas9-mediated on-target cleavage of *Nr0b1*, *Ppar-γ*, and *Rag1* by T7EN1 cleavage assay. PCR products were amplified and subjected to T7EN1 cleavage assay. Samples with cleavage bands were marked with an asterisk "*."

(B) DNA sequences of marked samples. TA clones from the PCR products were analyzed by DNA sequencing. Mutations in three PCR products (labeled with red asterisk) indentified by T7EN1 cleavage assay were not detected by TA sequencing because of limited amount of colonies. The PAM sequences are underlined and highlighted in green; the targeting sequences in red; the mutations in blue, lower case; deletions (−), and insertions (+). N/N indicates positive colonies out of total sequenced. See also Figure S1.

Table 1. Summary of Embryo Microinjection of Cas9 mRNA and sgRNAs

MII Oocyte	Injected Embryos	Embryos for ET	Pregnancies /Surrogates	Single Pregnancy	Multiple Pregnancy	Fetuses
198	186	83	34.5% (10/29)	4[a]	3 twins, 3 triplets	19

[a]One miscarried 36 days after embryo transfer.

E1751) was used for expression of sgRNAs in cells. Oligos for the generation of sgRNA expression plasmids (Table S4) were annealed and cloned into the BsaI sites of pUC57-sgRNA or pGL3-U6-sgRNA-PGK-Puro. pGL3-U6-sgRNA-PGK-Puro was deposited in Addgene (Addgene NO. 51133).

Cell Culture and Electroporation

COS-7 cells (ATCC, CRL-1651) were cultured in DMEM/high glucose (HyClone) with 10% FBS, penicillin (100 U/ml) and streptomycin (100 μg/ml); 2×10^6 cells were electroporated (BioRad Gene Pulser XL) with four micrograms of Cas9 expression plasmids and two micrograms of pGL3-U6-sgRNA-PGK-Puro. Empty pGL3-U6-sgRNA-PGK-Puro plasmid was used as control. Cells were collected 72 hr postelectroporation.

In Vitro Transcription

In vitro transcription was performed as described (Zhou et al., 2014). Briefly, the pST1374-Cas9-N-NLS-flag-linker vector was linearized by Age1 enzyme and in vitro transcribed using T7 Ultra Kit (Ambion, AM1345). Cas9-N-NLS-flag-linker mRNA was purified by RNeasy Mini Kit (QIAGEN, 74104). sgRNA oligos were annealed into pUC57-sgRNA expression vector with T7 promoter. Then expression vectors were linearized by Dra I and transcribed by MEGAshortscript Kit (Ambion, AM1354) in vitro. The sgRNAs were purified by MEGAclear Kit (Ambion, AM1908) and recovered by alcohol precipitation.

T7EN1 Cleavage Assay and Sequencing

Different samples, including cells, placenta, umbilical cord, and ear punch tissues, were collected and digested in lysis buffer (10 μM Tris-HCl, 0.4 M NaCl, 2 μM EDTA, 1% SDS, and 100 μg/ml Proteinase K). The genomic DNA was extracted from lysate by phenol-chloroform recovered by alcohol precipitation. Genomic DNA from cultured embryos was amplified by REPL1-g Single Cell Kit (QIAGEN, 150343) according to the manufacturer's instructions. T7EN1 cleavage assay was performed as described (Shen et al., 2013). In brief, targeted fragments were amplified by PrimerSTAR HS DNA polymerase (Takara, DR010A) from extracted DNA, and purified with PCR cleanup kit (Axygen, AP-PCR-50). Purified PCR product was denatured and reannealed in NEBuffer 2 (NEB) using a thermocycler. Hybridized PCR products were digested with T7EN1 (NEB, M0302L) for 30 min and separated by 2.5% agarose gel. To detect T7EN cleavage products of *Nr0b1* (localized on chromosome X) in

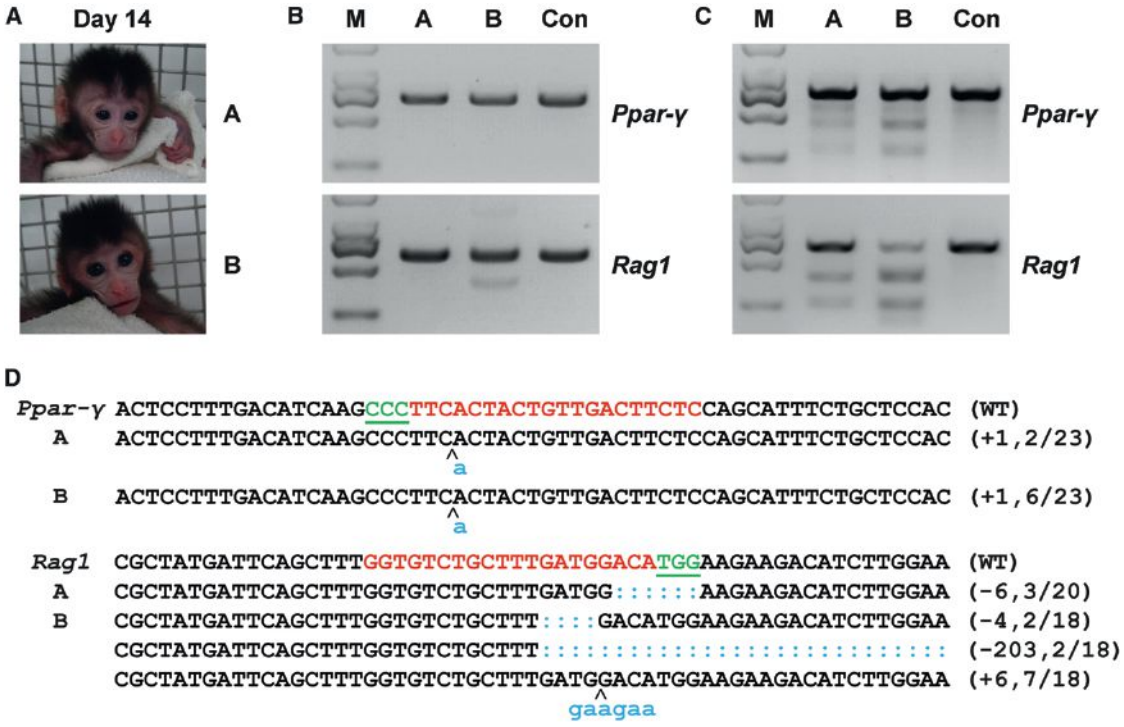

Figure 3. sgRNA:Cas9-Mediated Modifications of *Ppar-γ* and *Rag1* in Founder Cynomolgus Monkeys

(A) Photographs of 14-day-old founder infants A and B.

(B) PCR products of the target region of *Ppar-γ* and *Rag1* in founders. Targeted region of *Ppar-γ* and *Rag1* loci were PCR amplified from the umbilical cord genomic DNA of A and B founders. M, DNA marker; Con, control umbilial cord from wild-type cynomolgus monkey, which was born 9 days after birth of A and B.

(C) Detection of sgRNA:Cas9-mediated on-target cleavage of *Ppar-γ* and *Rag1* by T7EN1 cleavage assay. PCR products from (B) were subjected to T7EN1 cleavage assay.

(D) Sequences of modified *Ppar-γ* and *Rag1* loci detected in founders. At least 18 TA clones of the PCR products were analyzed by DNA sequencing. The PAM sequences are underlined and highlighted in green; the targeting sequences in red; the mutations in blue, lower case; deletions (–), and insertions (+). N/N indicates positive colonies out of total sequenced. See also Figure S2 and S4.

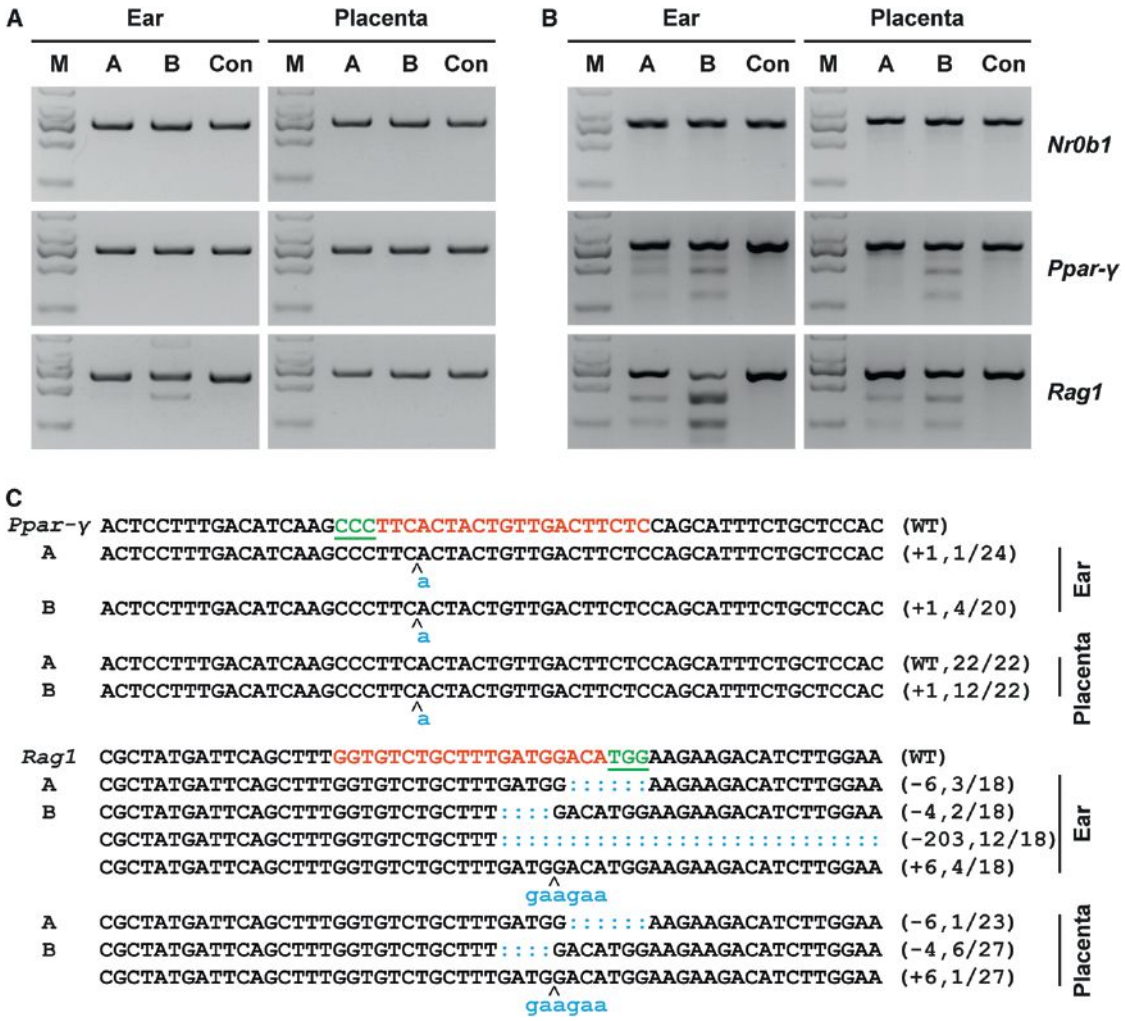

Figure 4. sgRNA:Cas9-Mediated Modifications of *Nr0b1*, *Ppar-γ*, and *Rag1* in Ear and Placenta of Founders

(A) PCR products of the targeted region of *Nr0b1*, *Ppar-γ*, and *Rag1* in founders. Target regions of *Nr0b1*, *Ppar-γ*, and *Rag1* loci were PCR amplified from the ear and placenta genomic DNA of A and B founders. M, DNA marker; Con, wild-type control.

(B) Detection of sgRNA1:Cas9-mediated on-target cleavage of *Nr0b1*, *Ppar-γ*, and *Rag1* by T7EN1 cleavage assay.

(C) DNA sequences of *Nr0b1*, *Ppar-γ*, and *Rag1* loci. The PCR products were analyzed by DNA sequencing. The PAM sequence are underlined and highlighted in green; the targeting sequences in red; the mutations in blue, lower case; deletions (−), and insertions (+). N/N indicates positive colonies out of total sequenced. See also Figure S3 and S4.

cultured embryos, 50 ng of PCR fragment from wild-type control embryos was mixed with 150 ng of PCR fragments from embryos injected with Cas9 mRNA and sgRNAs. PCR products with mutations detected by T7EN1 cleavage assay were sub-cloned into T vector (Takara, D103A). For each sample, colonies were picked up randomly and sequenced by M13-47 primer. Primers for amplifying *Nr0b1*, *Pparg*, and *Rag1* targeted fragments are listed in Table S5.

Off-Target Assay

All potential off-target sites with homology to the 23 bp sequence (sgRNA+PAM) were retrieved by a base-by-base scan of the whole rhesus genome (BGI CR_1.0/rheMac3), allowing for ungapped alignments with up to four mismatches in the sgRNA target sequence. In the output of the scan, potential off-target sites with less than three mismatches in the seed sequence (1 to 7 base) were selected to PCR amplification using umbilical cord genomic DNA as templates. The PCR products were first subject to T7EN1 cleavage assay. The potential off-target sites yielding typical cleavage bands were considered as candidates, then the PCR products of the candidates were cloned and sequenced to confirm the off-target effects. The primers for amplifying the off-target sites are listed in Table S6.

SUPPLEMENTAL INFORMATION

Supplemental Information includes four figures and six tables and can be found with this article online at http://dx.doi.org/10.1016/j.cell.2014.01.027.

AUTHOR CONTRIBUTIONS

J.S., W.J., X.H., and Q.Z. initiated the project, designed the experiments, and wrote the manuscript. J.S. organized and supervised the whole project. W.J. organized and supervised all monkey work; X.H. organized and supervised all genome manipulation and analysis; Q.Z. organized the teams and provided guidance on the whole project. Y.N. and Y. Chen performed monkey work,

including superovulation, microinjection, embryo transfer, animal care, etc. B.S. and Y. Cui performed genome manipulation and analysis, including Cas9 and sgRNA design and construct, in vitro transcription, genome modification analysis, off-target assay, etc. Y.K., X.Z., W.S., W.L., A.P.X., C.S., H.W., T.L., T.T., X.P., F.W., and S.J. assisted in monkey work. J.W, L.W., J.Z., X.G., Y.B., B.H., G.D., and Z.Z. assisted in genome manipulation and analysis.

ACKNOWLEDGMENTS

We thank Dr. Dangsheng Li from Shanghai Information Center for Life Sciences, Shanghai Institutes for Biological Sciences, Chinese Academy of Sciences for helpful discussions and insightful comments on this manuscript. We thank Dr. Xiujie Wang from Institutes of Genetics and Developmental Biology, Chinese Academy of Sciences for careful reading and editing of the manuscript. We also thank Lu Wang from CAS Key Laboratory of Genome Sciences and Information, Beijing Institute of Genomics, Chinese Academy of Sciences for help with the computational analysis of off-target sites. This study was supported by grants from the National Basic Research Program of China (2011CB944300 and 2012CBA01300), the National High Technology Research and Development Program of China (2012AA020701).

Received: December 13, 2013
Revised: January 9, 2014
Accepted: January 14, 2014
Published: January 30, 2014

REFERENCES

Chan, A.W. (2013). Progress and prospects for genetic modification of nonhuman primate models in biomedical research. ILAR J. *54*, 211–223.

Chan, A.W., Chong, K.Y., Martinovich, C., Simerly, C., and Schatten, G. (2001). Transgenic monkeys produced by retroviral gene transfer into mature oocytes. Science *291*, 309–312.

Chen, Y., Niu, Y., Yang, S., He, X., Ji, S., Si, W., Tang, X., Xie, Y., Wang, H., Lu, Y., et al. (2012). The available time window for embryo transfer in the rhesus monkey (Macaca mulatta). Am. J. Primatol. *74*, 165–173.

Cho, S.W., Kim, S., Kim, J.M., and Kim, J.S. (2013). Targeted genome engineering in human cells with the Cas9 RNA-guided endonuclease. Nat. Biotechnol. *31*, 230–232.

Cong, L., Ran, F.A., Cox, D., Lin, S., Barretto, R., Habib, N., Hsu, P.D., Wu, X., Jiang, W., Marraffini, L.A., and Zhang, F. (2013). Multiplex genome engineering using CRISPR/Cas systems. Science *339*, 819–823.

Fu, Y., Foden, J.A., Khayter, C., Maeder, M.L., Reyon, D., Joung, J.K., and Sander, J.D. (2013). High-frequency off-target mutagenesis induced by CRISPR-Cas nucleases in human cells. Nat. Biotechnol. *31*, 822–826.

Hsu, P.D., Scott, D.A., Weinstein, J.A., Ran, F.A., Konermann, S., Agarwala, V., Li, Y., Fine, E.J., Wu, X., Shalem, O., et al. (2013). DNA targeting specificity of RNA-guided Cas9 nucleases. Nat. Biotechnol. *31*, 827–832.

Jinek, M., Chylinski, K., Fonfara, I., Hauer, M., Doudna, J.A., and Charpentier, E. (2012). A programmable dual-RNA-guided DNA endonuclease in adaptive bacterial immunity. Science *337*, 816–821.

Li, D., Qiu, Z., Shao, Y., Chen, Y., Guan, Y., Liu, M., Li, Y., Gao, N., Wang, L., Lu, X., et al. (2013a). Heritable gene targeting in the mouse and rat using a CRISPR-Cas system. Nat. Biotechnol. *31*, 681–683.

Li, W., Teng, F., Li, T., and Zhou, Q. (2013b). Simultaneous generation and germline transmission of multiple gene mutations in rat using CRISPR-Cas systems. Nat. Biotechnol. *31*, 684–686.

Ma, Y., Zhang, X., Shen, B., Lu, Y., Chen, W., Ma, J., Bai, L., Huang, X., and Zhang, L. (2014). Generating rats with conditional alleles using CRISPR/Cas9. Cell Res. *24*, 122–125.

Mali, P., Esvelt, K.M., and Church, G.M. (2013a). Cas9 as a versatile tool for engineering biology. Nat. Methods *10*, 957–963.

Mali, P., Yang, L., Esvelt, K.M., Aach, J., Guell, M., DiCarlo, J.E., Norville, J.E., and Church, G.M. (2013b). RNA-guided human genome engineering via Cas9. Science *339*, 823–826.

Niu, Y., Yu, Y., Bernat, A., Yang, S., He, X., Guo, X., Chen, D., Chen, Y., Ji, S., Si, W., et al. (2010). Transgenic rhesus monkeys produced by gene transfer into early-cleavage-stage embryos using a simian immunodeficiency virus-based vector. Proc. Natl. Acad. Sci. USA *107*, 17663–17667.

Pattanayak, V., Lin, S., Guilinger, J.P., Ma, E., Doudna, J.A., and Liu, D.R. (2013). High-throughput profiling of off-target DNA cleavage reveals RNA-programmed Cas9 nuclease specificity. Nat. Biotechnol. *31*, 839–843.

Ran, F.A., Hsu, P.D., Lin, C.Y., Gootenberg, J.S., Konermann, S., Trevino, A.E., Scott, D.A., Inoue, A., Matoba, S., Zhang, Y., and Zhang, F. (2013). Double nicking by RNA-guided CRISPR Cas9 for enhanced genome editing specificity. Cell *154*, 1380–1389.

Sasaki, E., Suemizu, H., Shimada, A., Hanazawa, K., Oiwa, R., Kamioka, M., Tomioka, I., Sotomaru, Y., Hirakawa, R., Eto, T., et al. (2009). Generation of transgenic non-human primates with germline transmission. Nature *459*, 523–527.

Shen, H. (2013). Precision gene editing paves way for transgenic monkeys. Nature *503*, 14–15.

Shen, B., Zhang, J., Wu, H., Wang, J., Ma, K., Li, Z., Zhang, X., Zhang, P., and Huang, X. (2013). Generation of gene-modified mice via Cas9/RNA-mediated gene targeting. Cell Res. *23*, 720–723.

Sun, Q., Dong, J., Yang, W., Jin, Y., Yang, M., Wang, Y., Wang, P.L., Hu, Y., and Tsien, J.Z. (2008). Efficient reproduction of cynomolgus monkey using pronuclear embryo transfer technique. Proc. Natl. Acad. Sci. USA *105*, 12956–12960.

Sung, Y.H., Baek, I.J., Kim, D.H., Jeon, J., Lee, J., Lee, K., Jeong, D., Kim, J.S., and Lee, H.W. (2013). Knockout mice created by TALEN-mediated gene targeting. Nat. Biotechnol. *31*, 23–24.

Tesson, L., Usal, C., Ménoret, S., Leung, E., Niles, B.J., Remy, S., Santiago, Y., Vincent, A.I., Meng, X., Zhang, L., et al. (2011). Knockout rats generated by embryo microinjection of TALENs. Nat. Biotechnol. *29*, 695–696.

Wang, H., Yang, H., Shivalila, C.S., Dawlaty, M.M., Cheng, A.W., Zhang, F., and Jaenisch, R. (2013). One-step generation of mice carrying mutations in multiple genes by CRISPR/Cas-mediated genome engineering. Cell *153*, 910–918.

Yang, S.H., Cheng, P.H., Banta, H., Piotrowska-Nitsche, K., Yang, J.J., Cheng, E.C., Snyder, B., Larkin, K., Liu, J., Orkin, J., et al. (2008). Towards a transgenic model of Huntington's disease in a non-human primate. Nature *453*, 921–924.

Zhou, J., Shen, B., Zhang, W., Wang, J., Yang, J., Chen, L., Zhang, N., Zhu, K., Xu, J., Hu, B., et al. (2014). One-step generation of different immunodeficient mice with multiple gene modifications by CRISPR/Cas9 mediated genome engineering. Int. J. Biochem. Cell Biol *46*, 49–55.

Cell

Resource

Neural Networks of the Mouse Neocortex

Brian Zingg,[1,4] Houri Hintiryan,[2,4] Lin Gou,[2] Monica Y. Song,[2] Maxwell Bay,[2] Michael S. Bienkowski,[2] Nicholas N. Foster,[2] Seita Yamashita,[2] Ian Bowman,[2] Arthur W. Toga,[2,3] and Hong-Wei Dong[2,3,*]

[1]Zilkha Neurogenetic Institute

[2]Institute for Neuroimaging and Informatics

[3]Department of Neurology

Keck School of Medicine of USC, University of Southern California, Los Angeles, CA 90032, USA

[4]These authors contributed equally to this work

*Correspondence: Hongwei.Dong@loni.usc.edu

http://dx.doi.org/10.1016/j.cell.2014.02.023

SUMMARY

Numerous studies have examined the neuronal inputs and outputs of many areas within the mammalian cerebral cortex, but how these areas are organized into neural networks that communicate across the entire cortex is unclear. Over 600 labeled neuronal pathways acquired from tracer injections placed across the entire mouse neocortex enabled us to generate a cortical connectivity atlas. A total of 240 intracortical connections were manually reconstructed within a common neuroanatomic framework, forming a cortico-cortical connectivity map that facilitates comparison of connections from different cortical targets. Connectivity matrices were generated to provide an overview of all intracortical connections and subnetwork clusterings. The connectivity matrices and cortical map revealed that the entire cortex is organized into four somatic sensorimotor, two medial, and two lateral subnetworks that display unique topologies and can interact through select cortical areas. Together, these data provide a resource that can be used to further investigate cortical networks and their corresponding functions.

INTRODUCTION

Decades of research have converged on the idea that cognition and behavior are network-level phenomena (Bressler and Menon, 2010; Sporns, 2010; Swanson and Bota, 2010). The expression of complex behaviors requires the integration of various sensory inputs, the synchronization of multiple motor outputs, and the coordination of activity within large-scale networks that link the two. Therefore, constructing a brain-wide connectivity diagram for all well-defined gray matter regions, i.e., the macro- or meso-connectome (Sporns et al., 2005; Bohland et al., 2009; Bota et al., 2012) that captures the organizational principles of neural networks will help inform a multitude of testable hypotheses regarding the neural underpinnings of cognitive function and motivated behavior.

Unlike the recently assembled connectome of the *C. elegans* (White et al., 1986; Jarrell et al., 2012), wiring diagrams for mammalian species have been assembled on substantially smaller scales and for specific functional systems (Felleman and Van Essen, 1991; Saleem et al., 2008). For the cerebral cortex, a brain structure involved in regulating cognition, motivation, and emotion, it remains largely unclear how different areas across the entire structure communicate at the network level to guide its complex functions. Recently, significant progress has been made in assembling structural and functional cortical networks in the human brain using functional MRI and diffusion tensor imaging (DTI) with graph theoretical analysis (Andrews-Hanna et al., 2010; Behrens and Sporns, 2012; Toga et al., 2012). These efforts have advanced our understanding of how neural network disruptions may be associated with neurological and neuropsychiatric diseases. Nevertheless, it is necessary to validate these networks using reliable neural tract tracing methods in animal models at a higher resolution, which will facilitate exploration of the molecular and cellular etiologies of these disorders.

As part of the effort to chart long-range connectivity in the mouse brain (Marx, 2012; Osten and Margrie, 2013; Pollock et al., 2014), we launched the Mouse Connectome Project (MCP, www.MouseConnectome.org). We generated a cortical connectivity atlas, which accommodates over 600 labeled neural pathways from tracer injections applied across the entire neocortex. Two hundred and forty pathways were then manually reconstructed onto a common neuroanatomic frame to create an online interactive cortico-cortical connectivity map to ease comparison of connectivity patterns across injections. We report the development of this resource and identify three major cortical subnetworks: the somatic sensorimotor, medial, and lateral subnetworks, each of which displays unique network topologies. We also provide evidence for how these relatively segregated networks may interact through highly associative regions like the prefrontal cortex, entorhinal cortex, and the claustrum.

RESULTS

Data Production and Collection

The MCP neuronal connectivity data were produced using double coinjection tract tracing (Thompson and Swanson, 2010), which simultaneously reveals four types of information for a given region (i.e., A): its (1) inputs (A←B), (2) outputs (A→B), (3) reciprocal or recurrent connections (A⇔ B), and (4) intermediate stations, which bridge brain structures that are not directly

connected (A→C→B). In one animal, two confined, nonoverlapping coinjections are placed into different brain regions (Figures 1A and 1B and Figure S1A available online). Each coinjection consists of one anterograde (*Phaseolus vulgaris* leucoagglutinin [PHAL] or biotinylated dextran amine [BDA]) and one retrograde (cholera toxin subunit b [CTb] or Fluorogold [FG]) tracer. Anterograde tracers label axons arising from coinjection sites and their terminals in targeted regions and retrograde tracers label upstream neurons that innervate the coinjection sites, thus simultaneously revealing four pathways (Figures 1A–1C and S1A).

The size of coinjections are ~250–500 μm and mostly confined within individual cortical areas (Figure 1B), although when images are adjusted to reveal fine fibers, injection sites are overexposed, misrepresenting their actual size (Figure S1A). The confinement of the injections can be verified from the cytoarchitectural background provided by a Nissl stain of the same section (Figures 1B and S1B) and by observing their unique thalamic labeling (Figures S1A and S1B). The specificity of injections are cross-validated by the application of retrograde tracers to regions targeted by anterogradely labeled axon terminals and vice versa (Figure S1 for details on data validation). All images were processed through informatics pipelines and presented on the MCP website through an interactive visualization tool, the iConnectome (www.MouseConnectome.org; Figure S2A). The fluorescent connectivity data are presented in four different channels: PHAL (green), BDA (red), FG (yellow), and CTb (pink). Two additional channels aid in data analysis: the inverted fluorescent Nissl of the same section and the corresponding atlas level from a standard mouse atlas, the Allen Reference Atlas (ARA; Dong, 2007). Currently, a total of ~600 pathways (304 efferent and 296 afferent) associated with ~317 coinjections are available (Figure S3 for injections; Table S1 for list of selected cases; Table S2 for abbreviations). Injections span the entire neocortex and selected regions of the entorhinal cortex, hippocampus, amygdala, and olfactory areas. Although this report focuses on intracortical pathways, the subcortical connections of all injections also are available.

Connectivity Matrices

To begin building cortical networks, data within all regions was annotated by manually recording the distribution of anterograde and retrograde labeling. Using the annotation data, two label-based weighted directional connectivity matrices were created (Figures 2A–2D). Iterating through each matrix entry, 89% of connections exhibited mutual labeling by both anterograde and retrograde labeling methods, suggesting that the data sets were significantly similar. To reveal subnetworks, a composite matrix was constructed in which the nodes (ROIs) were reordered via a clustering algorithm (Figure 2E; Supplemental Information for annotation and analysis details). The clustering orders nodes into modules that maximize the connectivity and arrange highly interconnected nodes such that they are clustered along the matrix diagonal, facilitating visualization of grouped regions that can be considered subnetworks. The number of connections within these groupings near the diagonal reflects the density of intraconnectivity within a subnetwork, while connections farther from the diagonal demonstrate a subnetwork's interconnectivity with other subnetworks. The clustering demonstrated that all nodes fall into a few relatively distinct cortico-cortical subnetwork modules (Figures 2C–2E). Each of the four somatic sensorimotor modules (orofaciopharyngeal, upper limb, lower limb/trunk, and whisker) formed distinct subnetworks. The medial, visual, and auditory modules formed one big network that was also highly connected with the lower limb/trunk and whisker subnetworks. The insular and temporal areas along the lateral aspect of the cortex formed two distinct clusters and the broad and unique intracortical connections of the claustrum and lateral entorhinal area suggested they may serve as hubs or regions of high network interaction (Sporns, 2010).

Cortico-Cortical Connectivity Map

The matrices provide a condensed view of cortical connectivity patterns, but exclude details like projection routes, laminar specificity of projections, and topographical and topological connectivity patterns, which are critical features of networks. Consequently, labeled pathways were manually reconstructed onto corresponding atlas levels to create a comprehensive cortico-cortical connectivity map available through the iConnectome map viewer (Figures 1D, S2B, and S4A; http://www.MouseConnectome.org/CorticalMap/).

This map includes 80 anterograde (PHAL) and 160 retrograde pathways (CTb and FG). The coinjection sites are represented by circles, PHAL pathways by shaded regions, and retrograde labeling by small dots that reflect regional and laminar distribution patterns (Figures 1D and S4A). Each of these pathways was assigned a unique RGB value and rendered into an individually layered document such that multiple layers representing multiple injection sites could be viewed simultaneously within the same anatomic frame (ARA), thus revealing topographic trends and interactions between regions. Within the connectivity map, when nodes within the same module of the connectivity matrix are viewed together (e.g., anteromedial and anterolateral visual areas), intermixed and overlapping cortical connectivity patterns are observed, suggesting a high degree of integration within the same subnetwork (Figures S4B and S4C). Conversely, nodes of different modules show divergent cortical connections.

The Somatic Sensorimotor Subnetworks

To build the somatic sensorimotor subnetworks, four general primary somatosensory (SSp) domains were defined based on their subcortical and intracortical connections (Figures 3A and 3B): the mouth and nose (SSp-m/n), upper limb (SSp-ul), lower limb and trunk (SSp-ll/tr), and barrel field (SSp-bfd). The specificities of these domains were validated by examining their specific somatotopic projections in sensory and motor related nuclei in the lower brainstem (Figures S5A and S5B). Each of these SSp domains displays unique connectional patterns with other somatic sensorimotor areas like the primary (MOp) and secondary (MOs) somatomotor areas, and the secondary somatosensory area (SSs) (Figures 3A, 3B, and S5C). These distinct connections provided a structural basis for delineating related subdomains within each of these sensorimotor areas, which are largely unknown in the mouse. Parcellations were confirmed by the application of coinjections into the corresponding body subfield domains of the somatic sensorimotor cortical areas (i.e., SSp-ll/tr, MOp-ll/tr, MOs-ll/tr; Figure 3C).

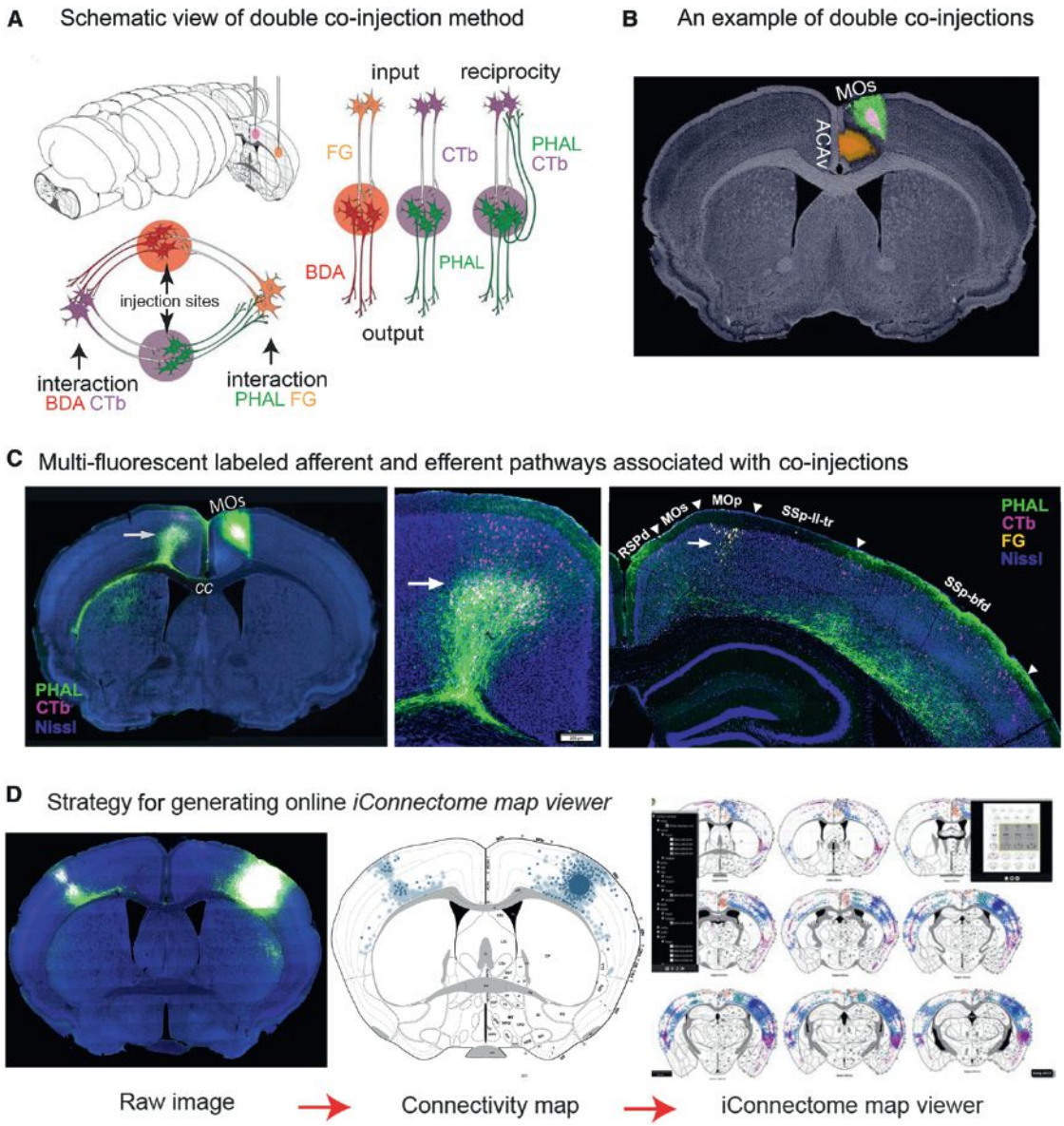

Figure 1. Strategy for Generating the Cortical Connectivity Atlas

(A) Schematic illustrating a PHAL/CTb and BDA/FG double coinjection in two different structures labeling both input to, and output from each injection site. Reciprocal interactions between brain regions and circuit interactions between each injection site may also be revealed.

(B) A coronal section showing coinjections made into the MOs and ACAv viewed with Nissl background to reveal cytoarchitecture. Scale bar, 1 mm.

(C) Intermixed anterogradely labeled axons (green, PHAL) and retrogradely labeled neurons (pink, CTb) in the MOs following a coinjection in the contralateral hemisphere (first two panels, arrows). Note: the PHAL/CTb coinjection is the same as pictured in B. Image histogram was adjusted differently for the two hemispheres so that PHAL/CTb labeling on the left side can be viewed properly without over exposing the injection site on the right side. Last panel, comparison of retrogradely labeled neurons from injection in ACAv (arrow, yellow, Fluorogold [FG]) and fibers and cells from injection in MOs (PHAL/CTb). Fluorescent Nissl in blue; scale bar, 200 μm.

(D) Strategy for mapping fluorescent labeling from a raw image (left, scale bar, 1 mm) onto the corresponding level of the ARA (middle) to generate a comprehensive map of projection pathways for all injection sites (right). Note: anterogradely labeled pathways were rendered as layer and regional-specific shading, while retrogradely labeled neurons were represented by individual dots. The large circle on the right hemisphere represents an injection site (see corresponding region on raw image).

See Figures S1, S2, S4, and Table S1 for more information.

These somatic sensorimotor areas formed four distinct subnetworks. The orofaciopharyngeal subnetwork is composed of five major nodes (Figures 2 and 3B): (1) SSp-m/n, (2) the orofacial region of the MOp (MOp-orf; Yamada et al., 2005), (3) the rostrodorsolateral MOs (MOs-rdl), (4) anterolateral SSp-bfd (SSp-bfd.al), and (5) the rostral and caudoventral SSs (SSs-r and cv).

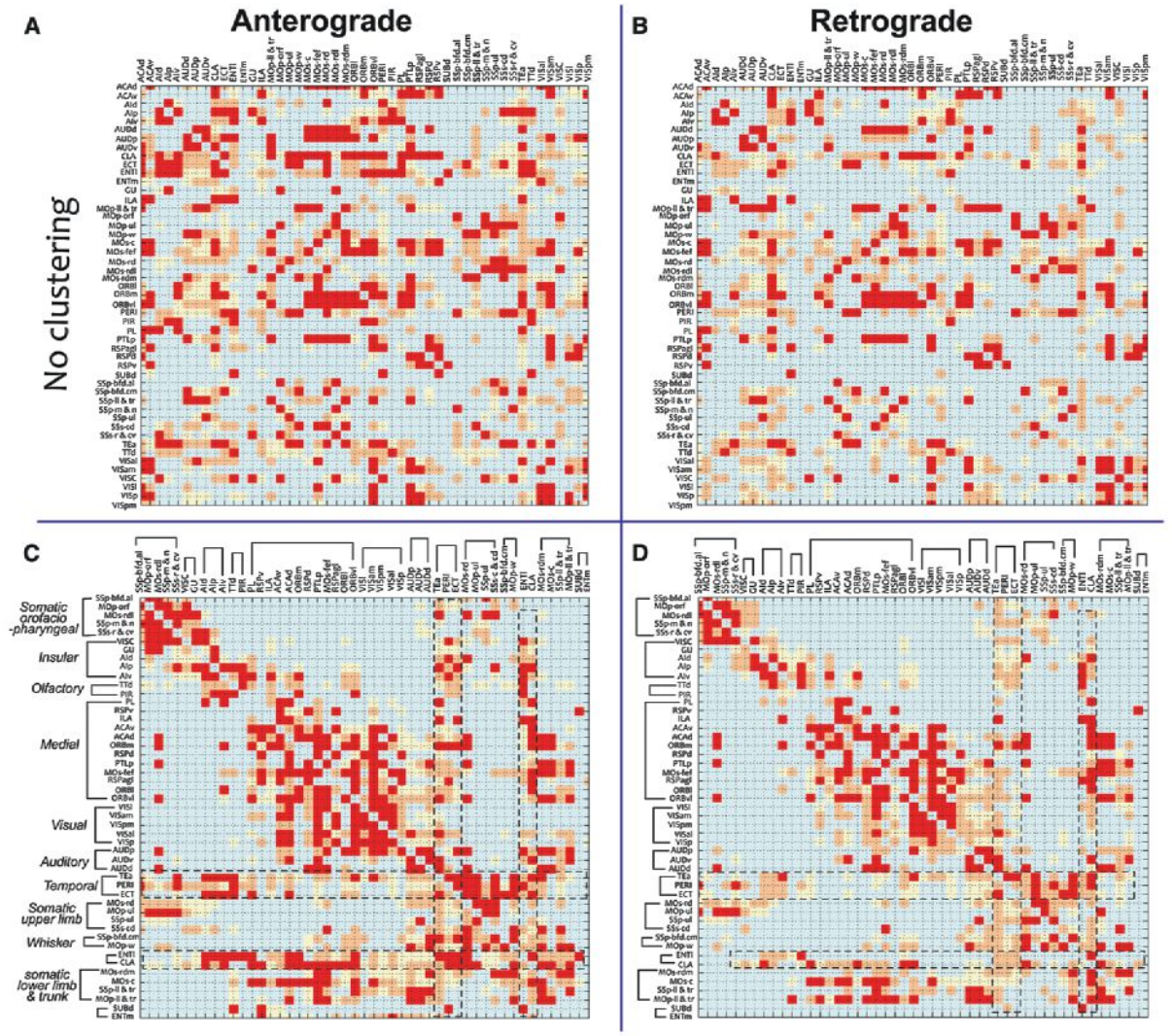

Abbreviations of cortical areas and their subdivisions

ACA: *anterior cingulate area (dorsal,* ACAd; *ventral,* ACAv); AI, *agranular insular area (dorsal,* AId; *ventral,* AIv; *posterior,* AIp); AUD, *auditory area (dorsal,* AUDd; *primary,* AUDp; *ventral,* AUDv); CLA, *claustrum;* ECT, *ectorhinal area;* ENT, *entorhinal area (lateral,* ENTl; *medial,* ENTm); GU, *gustatory area;* ILA, *infralimbic area;* MOp, *primary somatomotor area (*MOp-ll & tr, *lower limb and trunk domains;* MOp-orf, *orofacial domain;* MOp-ul, *upper limb domain;* MOp-w, *whisker domain);* MOs, *secondary somatomotor area (*MOs-c, *caudal domain;* MOs-fef, *frontal eye field;* MOs-rd, *rostrodorsal domain;* MOs-rdl, *rostrodorsolateral domain;* MOs-rdm, *rostrodorsomedial domain);* ORB, *orbitofrontal area (lateral,* ORBl; *medial,* ORBm; *ventrolateral,* ORBvl); PERI, *perirhinal area;* PIR, *piriform cortex;* PL, *prelimbic area;* PTLp, *posterior parietal association area;* RSP, *retrosplenial area (agranular,* RSPagl; *dorsal,* RSPd; *ventral,* RSPv); SUBd, *dorsal subiculum;* SSp, *primary somatosensory area (*SSp-ll & tr, *lower limb & trunk domains;* SSp-m & n, *mouth & nose domains;* SSp-ul, *upper limb domain);* SSp-bfd, *barrel field of the primary somatosensory area (*SSp-bfd.al, *anterolateral domain;* SSp-bfd.cm, *caudomedial domain);* SSs, *supplemental somatosensory area (*SSs-cd, *caudodorsal domain;* SSs-r & cv, *rostral and caudoventral domains);* TEa, *temporal association area;* TTd, *dorsal taenia tecta area;* VIS, *visual area (anterolateral,* VISal; *anteromedial,* VISam; *lateral,* VISl; *primary,* VISp; *posteromedial,* VISpm); VISC, *visceral area.*

Somatic sensorimotor subnetworks (four disctinct modules: orofaciopharyngeal, upper limb, lower limb/trunk, and whisker)

Medial subnetworks (also including the visual and auditory modules as indicated in boxed grids)

Lateral subnetworks (two distinct modules: insular and temoporal)

Claustrum and entorhinal modules

(legend on next page)

Coinjections into each of these orofaciopharyngeal nodes showed they are all heavily reciprocally interconnected (Figure 3D). The gustatory (GU), visceral (VISC), and dorsal agranular (AId) areas also connect with this subnetwork (Figures 2 and 3D), which could contribute relevant information (i.e., gustation and food safety; Carleton et al., 2010; Maffei et al., 2012).

Following the same topological organization (i.e., reciprocity among all nodes), the upper limb subnetwork is composed of four somatic sensorimotor nodes: (1) the SSp-ul, (2) caudodorsal SSs caudodorsal (SSs-cd), (3) MOp-ul, and (4) rostrodorsal MOs (MOs-rd) (Figures 3D and S5B). The lower limb/trunk subnetwork includes the SSp-ll/tr, MOp-ll/tr, and rostrodorsomedial MOs (MOs-rdm) (Figures 3B–3D). Finally, the whisker subnetwork is composed of the caudomedial SSp-bfd (SSp-bfd.cm), MOp-w, which corresponds to the vibrissal primary motor cortex (vM1) (Mao et al., 2011; Gerdjikov et al., 2013), and the caudodorsal SSs (SSs-cd; Figures 3B and 3D). The upper limb, lower limb/trunk, and whisker subnetworks also share connections with lateral subnetwork nodes like the temporal association (TEa), perirhinal (PERI), and ectorhinal (ECT) areas. Relevant information for the lower limb/trunk subnetwork also may be provided by inputs from the visual (VIS), auditory (AUD), and several areas within the medial networks (Figures 2 and 3D).

Finally, a specific frontal eye field MOs domain (MOs-fef, Figure S5D; Reep et al., 1990) was identified, which shares dense reciprocal connections with the visual, auditory, posterior parietal, anterior cingulate, and restrosplenial areas of the medial subnetworks.

The Medial Subnetworks

Cortical areas along the medial bank of the cortex cluster to form two parallel medial subnetworks (Figures 2 and 4A). The first medial subnetwork is organized for transferring visual, auditory, and somatic sensory information to the ORBvl. ORBvl coinjections showed its direct reciprocal connections with the primary (VISp) and secondary visual (anteromedial, VISam; anterolateral, VISal) and auditory areas (AUD), as well as the SSp-ll/tr and SSp-bfd.cm (Figures 2 and 4A–4C). Coinjections into each of these areas confirmed these connections (Figure S4B–S4C for VISam and VISal; Figure S6A for VISp and AUD; Figure 3B for SSp-ll/tr). Further, multiple retrograde tracers injected into different visual areas revealed dense ORBvl neuronal labeling that was intermixed but mostly not colocalized, suggesting multiple parallel ORBvl→VIS pathways (Figures 4E–4F).

These VIS and AUD areas also reciprocally connect with areas along the cortical medial bank, including the posterior parietal (PTLp), three subdivisions of the retrosplenial area (dorsal, RSPd; agranular, RSPagl; and ventral, RSPv), and two subdivisions of the anterior cingulate area (dorsal, ACAd; ventral, ACAv) (Figures 2, 4A–4C, 4F, S6A, and S6B). The PTLp is another critical area that integrates inputs from the VIS, AUD, and SSp-ll/tr (Figures 2, 3B, and S6A). The RSPd and RSPagl receive much stronger visual inputs, but only sparse AUD and SSp projections (Figures 2 and S6A). In the ACA, axons from different VIS and AUD areas intermix in layer 1 (Figure S6A), while neurons that project to the VISp and VISam form different clusters in deeper layers (Figure 4E).

Moreover, the ORBvl and all of these higher-order association areas (PTLp, RSP, ACA) heavily interconnect with regional and laminar specificity (Figures 4A–4C, 4F, and S6B). For example, in the PTLp, the densest labeling from ORB injections are distributed in layer 5 (Figures 4B and 4C); ACAd axons are distributed primarily in PTLp layers 1 and 6 and retrogradely labeled neurons across layers 2 to 6 (Figure S6B). Projections from these areas to lower-order sensory areas also are laminar specific with ORBvl axons primarily distributing in layers 1 and 5 of visual areas, while ACAd axons reside in layers 1 and 6 (Figures 4C, 4D, and S6B).

Interestingly, this medial subnetwork provides an interface for direct interactions between different sensory modalities via reciprocal connections among the visual and auditory areas and the SSp-ll/tr and SSp-bfd.cm (Figures 2, 3B, S6C, and S6D). This supports the concept of crossmodal modulation, which challenges the idea that mammalian primary sensory cortices are strictly unisensory (Driver and Noesselt, 2008; Stein and Stanford, 2008). Finally, this medial network may be important for translating sensory information into motor action since the ORBvl, ACAd, and PTLp connect with the entire MOs including the MOs-fef and the ORBvl and PTLp further connect with the MOp-ll/tr (Figures 4B, 4C, 4F, and S5D).

The second medial subnetwork successively relays information from the dorsal subiculum (SUBd) to the medial prefrontal cortex (Figure S6E). The RSPv is the only neocortical recipient of dense inputs from the SUBd, through which information processed in the dorsal hippocampus can reach the neocortex (Fanselow and Dong, 2010). The RSPv shares massive reciprocal connections with the ACAv. It in turn projects to medial prefrontal cortical areas like the infralimbic (ILA), prelimbic (PL), and medial orbitofrontal areas (ORBm) (Figure S6E), each of which receive only sparse inputs from the RSPv (Figure 4F).

Importantly, the two medial networks can interact (Figure 4F) since the RSPv and ACAv are connected with the ORBvl, ACAd, RSPd, RSPagl, and PTLp. Finally, these medial subnetwork areas are all connected with the CLA (Figures 2, 4B, 4F, and S6B).

The Lateral Subnetworks

Cortical areas in the lateral aspect of the neocortex form two distinctive, highly interconnected networks (Figures 2 and 5A): the anterolateral insular and posterolateral temporal subnetworks. Distinguishing the lateral networks from the medial and

Figure 2. Weighted and Directed Cortico-Cortical Connectivity Matrices

(A–E) Connectivity matrices were constructed based on either anterograde (PHAL, A) or retrograde (FG/CTb, B) tract tracing data. In both matrices, connection origin is listed along the row while targets are listed across the columns (sorted alphabetically). The weighting of each connection is indicated by red (strong), orange (moderate), and yellow (light) coloring. In (C) and (D), the anatomical data in (A) and (B) has been reordered, illustrating a total of 12 distinct modules in different cortical subnetworks. Combining retrograde and anterograde tracing methods formed the composite matrix (E), a consensus perspective of cortico-cortical subnetwork connectivity. See Extended Experimental Procedures for details regarding construction of the matrices, Figure S3 for injection cases, and Table S2 for list of abbreviations.

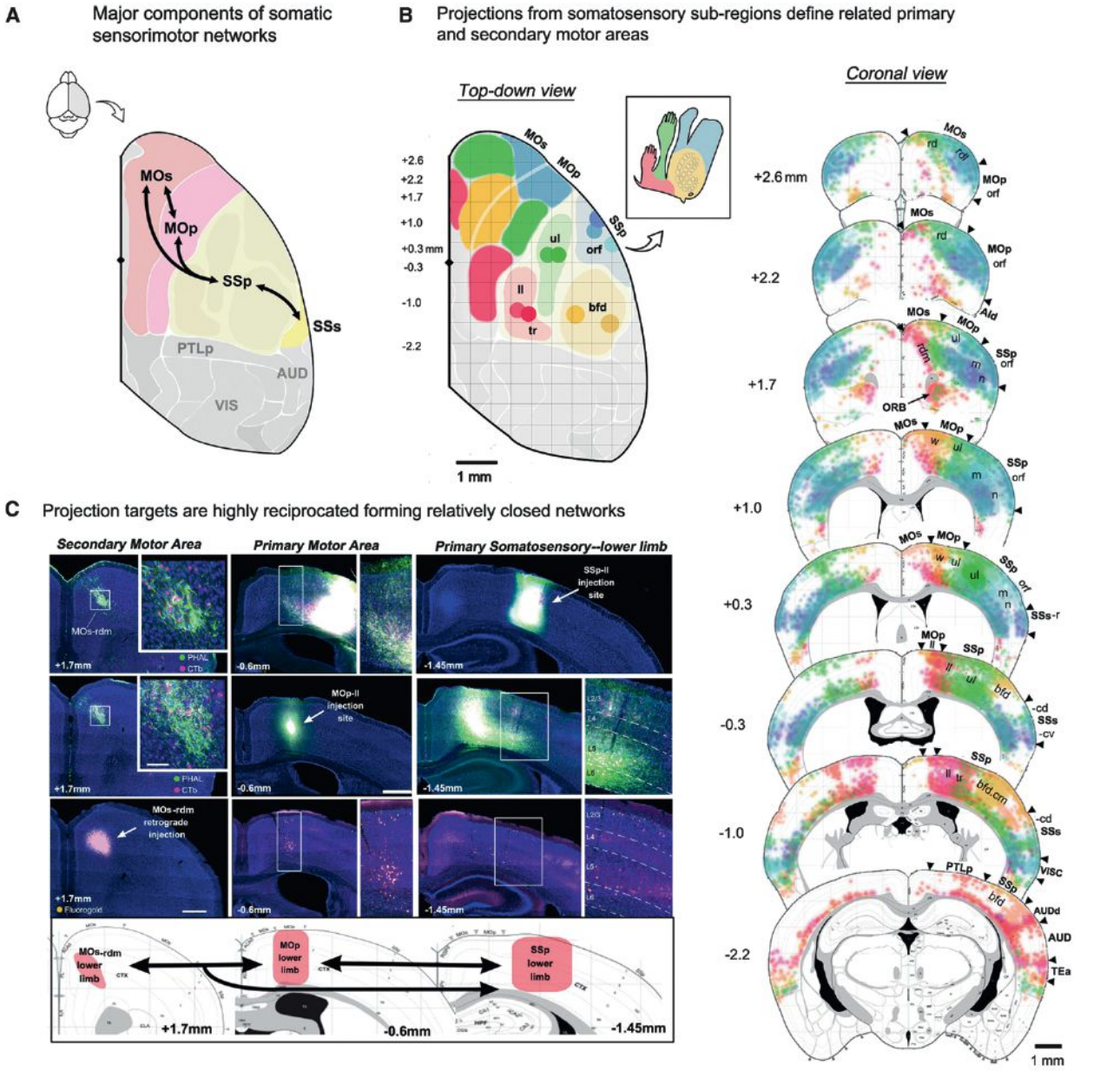

(legend on next page)

somatic sensorimotor subnetworks is the fact that the lateral subnetworks share connections with olfactory cortical areas (piriform cortex, endopiriform nucleus, dorsal taenia tecta), basolateral amygdalar nucleus, and ventral hippocampus.

The anterolateral insular subnetwork is composed of the three agranular insular areas: the dorsal (AId), ventral (AIv), and posterior (AIp). The neural connections of the rat AI have been investigated (e.g., Saper, 1982; Allen et al., 1991; Jasmin et al., 2004), but their functional and structural differences remains controversial. Our data show that these subdivisions are substantially interconnected, but generate distinguishable cortical projections (Figure 2). First, connections between these three areas and the medial prefrontal cortex display a rough topography (Figures 5B and S1E): the AIp is heavily connected with the poorly defined dorsal peduncular area (DP) (all layers) and its dorsally adjacent ILA (layers 1 and 6) but relatively sparsely connected with the PL. The AIv has the densest reciprocal connections with the PL, ILA, and DP. The AId is interconnected with the PL but sparsely connected with the ILA and not at all with the DP. An ILA coinjection validated this preferential interaction between AIv and ILA (Figure S1E). Second, all three AI areas connect with the VISC, but only AId and AIp are significantly connected with the GU. The VISC receives visceral inputs from the parvicellular part of the ventral posterolateral thalamic nucleus (VPLpc), while the GU shares massive reciprocal connections with the parvicellular part of the ventral posteromedial thalamic nucleus (VPMpc; Figure S1B) (Jones, 2007). Third, the AId also is connected with the orofaciopharyngeal (MOp-orf and MOs-rdl) and upper limb (MOs-rd) subnetworks, while the AIp receives significant inputs from the SSs and SSp-bfd (Figure S7A).

Caudally, these AI subdivisions preferentially connect with three components of the posterolateral temporal subnetwork (Figure 5B): the perirhinal (PERI) receives dense inputs from the AId and AIv, while the ectorihinal (ECT) is more heavily innervated by inputs from the AIp. Finally, all three generate dense inputs specifically to layers 3–5 of the lateral entorhinal cortex (ENTl; Figures 5B and S1B).

Three areas located in the vicinity of the rhinal fissure, namely the temporal association area (TEa), ECT, and PERI form the highly interconnected posterolateral temporal subnetwork (Figures 2, 5A, and 5C). A retrograde tracer injection in all three structures back labeled neurons in layers 2 and 5a of the entire neocortex with the exception of the ACAv, RSP, and VISp (Figures 5C and 5D), suggesting that this subnetwork receives input from nearly the entire neocortex. Complementarily, the TEa, ECT, and PERI collectively project back to nearly the entire neocortical mantle including the VISp (Figures 5C and 5E).

Injections in all other cortical areas revealed heterogeneous zones within the TEa (Figure S7B). The rostral TEa shares bidirectional connections with areas in the orofaciopharyngeal network; the middle TEa and its adjacent PERI and ECT share stronger connectivity with somatic sensorimotor areas of the upper limb and lower limb/trunk subnetworks and visual and auditory areas, as well as the PTLp; the caudal TEa more specifically connects with the medial prefrontal areas and ventral hippocampus.

Finally, coinjections in the TEa, PERI, and ECT result in dense labeling in layers 3-5 of the ENTl (Figure 5C).

ENTl and CLA

The ENTl and CLA are two reciprocally connected structures that both share connections with the medial prefrontal (ILA, PL, ORBm) and orbitofrontal areas (ORBvl, ORBl) (Figures 2, 6A, 6E, and 6G). The CLA further shares massive connections with cortical areas within the medial (ACAv, ACAd, PTLp, RSPd, RSPagl) and lateral subnetworks (AId, AIv, AIp, TEa, PERI, ECT), as well as with the entire MOs and MOp (Figures 6A–6D). Dense CLA axons travel through layers 5 and 6 of all sensory areas (SSp, AUD, VIS), although these cortical areas contain relatively few neurons that project back to the CLA. The intracortical connectivity of the CLA displays a unique asymmetric pattern: cortical inputs to the CLA are bilateral, but outputs from CLA are almost exclusively ipsilateral (Figures 6B and 6C).

Figure 3. The Somatic Sensorimotor Subnetworks

(A) Overview of the four major components of somatic sensorimotor areas (SSp, SSs, MOp, MOs). Each region is extensively interconnected with all others. Parcellation of cortical areas in map based on ARA and drawn to scale. Diamond shape on midline indicates bregma.

(B) Projections from representative injection sites (colored dots) in each of four basic body representations in primary somatosensory cortex: orofaciopharyngeal (orf, blue), upper limb (ul, green), lower limb and trunk (ll/tr, red), and whisker-related caudomedial barrel field (bfd.cm, yellow). A cartoon (inset) shows approximate size and location of the four body areas defined here (inspired from Brecht et al., 2004). Top-down view (left) shows topographic organization of projections from each area to corresponding primary and secondary motor areas (MOp, MOs). ARA defined boundary between MOs and MOp added for reference. Projection data in top-down view were drawn to scale using coronal sections (right) and shaded regions represent the areal extent of the most dense projections from each of the injected regions. Representative coronal sections also show projection trends to supplemental somatosensory area (SSs). Numbers indicate position of sections relative to bregma (mm).

(C) Projections from each of the somatosensory subregions define presumably functionally related MOs and MOp subregions, which are tightly reciprocated, as indicated by closely overlapped axonal fibers and retrogradely labeled cell bodies following coinjection. Here, coinjections of PHAL (green)/CTb (pink) in either SSp-ll (top, right) or a corresponding MOp region (middle, middle) reveal intermixed labeling in other corresponding domains of the somatic sensorimotor region, confirming their strong reciprocal connectivity. Both coinjections reveal intermixed labeling in the same MOs domain (left images on the top and middle). Retrograde injection in the same MOs domain (left image on the bottom) confirms the specificity of this interaction, showing retrogradely labeled neurons in the former two areas (middle and right images). Their anatomical locations and interactions are summarized in corresponding atlas levels in the bottom panel. Scale bars, 500 μm and 100 μm (inset).

(D) Building on these observations, four network graphs were created using each of the defined somatosensory regions as starting points. Each subnetwork is distinct and all components within it share a high degree of interconnection. Each are composed of several somatic sensorimotor "nodes" (color coded to match anatomically defined functional domains in (B) that are reciprocally connected (as indicated with red arrows). Each of these subnetworks also includes other nonsomatic "peripheral" nodes (gray circles) and their connections are shown with gray arrows.

See also Figure S5. For abbreviations of nomenclatures, please see Figure 2 and Table S2.

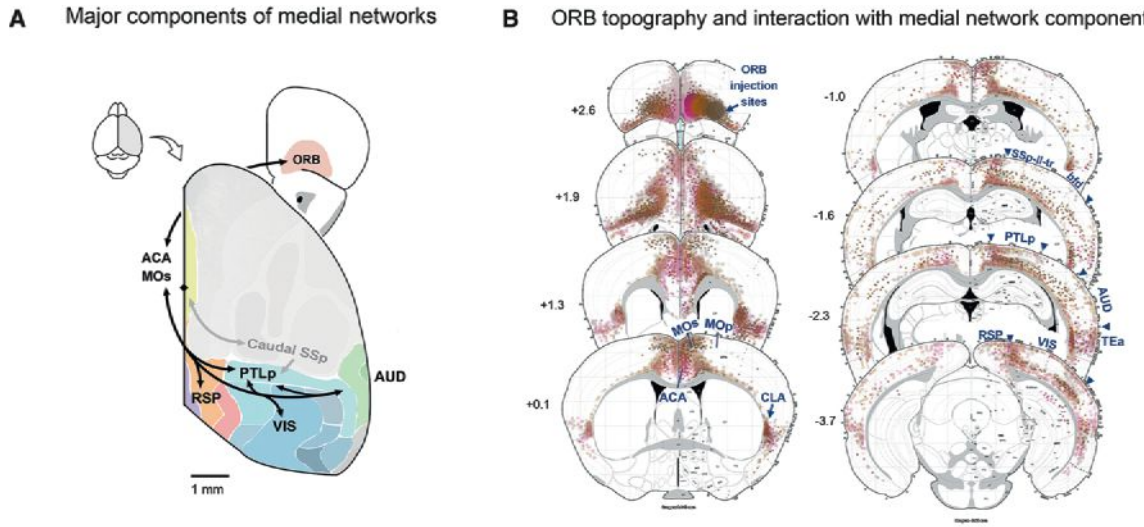

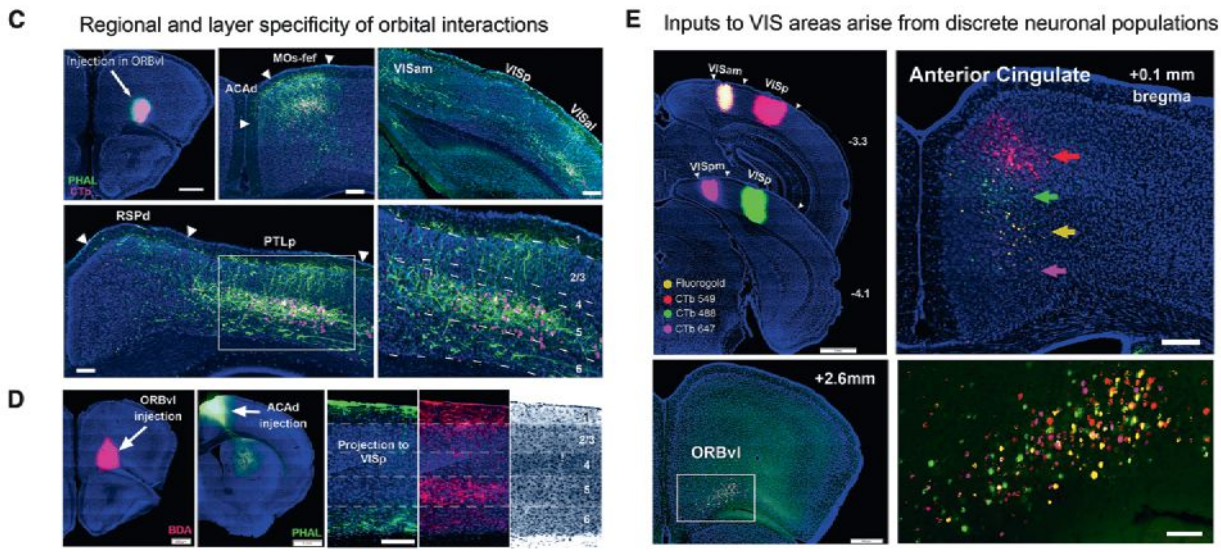

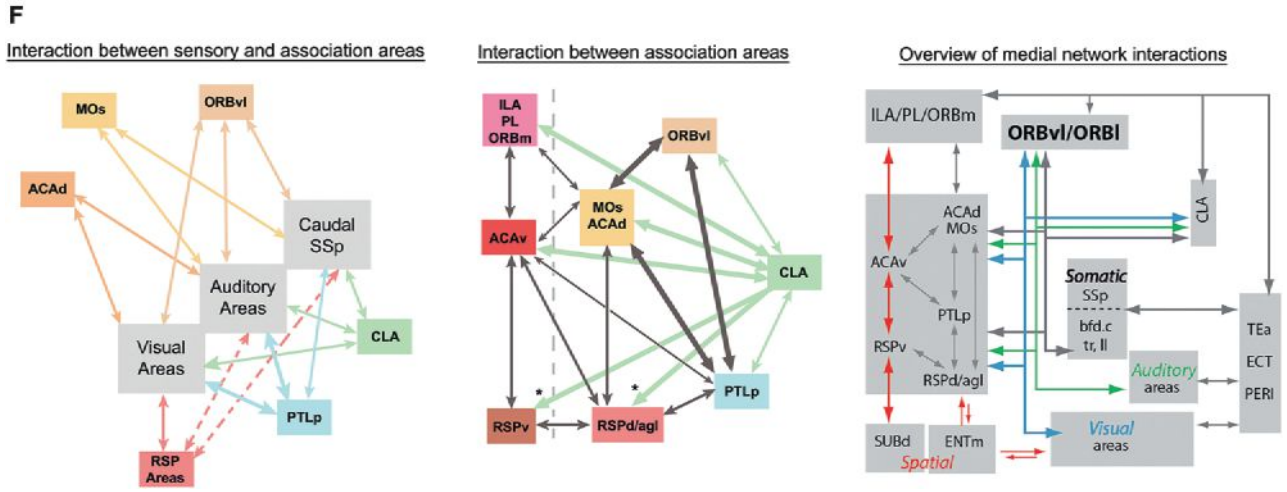

(legend on next page)

The ENTl shares much stronger reciprocal connections with all areas of the lateral subnetworks (Figures 5A, 6C and 6F), amygdala (basomedial and anterior basolateral nuclei), and the ventral and intermediate CA1 and SUBd (data not shown). The ENTl receives direct inputs from the main olfactory bulb (Hintiryan et al., 2012) and shares massive reciprocal connections with olfactory cortical areas like the piriform and taenia tecta (Figure 6E). These data suggest that the ENTl is not only a gateway for neocortical information to the hippocampus (de Curtis and Paré, 2004), but may also be a site of interaction for various cortical areas and between these neocortical areas and the amygdala, hippocampus, and olfactory cortical areas.

Compared to the CLA, the ENTl receives very sparse or no direct inputs from regions within the medial subnetworks (ACA, RSP, PTLp) and somatic sensorimotor subnetworks; however, coinjections into layers 4/5 of the rostrodorsal ENTl revealed dense axons throughout layer 1 of almost the entire neocortex (Figure 6E) with a few exceptions—the RSPv and areas within the orofaciopharyngeal subnetwork. Notably, the ENTl layer 1 axons are denser in the contralateral visual, auditory, and SSp-bfd areas.

Interactions with the Prefrontal Cortex

Projections from each of the identified subnetworks topographically converge onto discrete regions of the prefrontal cortex. The somatic sensorimotor subnetworks primarily converge onto the dorsolateral, dorsal, and dorsomedial sectors of the rostral-most MOs (Figures 3B, 7A, and 7B). Together, these three neighboring zones occupy the dorsolateral half of the prefrontal cortex (PFCdl, Figures 7A and 7B).

The ventromedial half of the prefrontal cortex (PFCvm) is also composed of three distinct zones: the medial prefrontal (ILA, PL, ACAd, ORBm), orbitofrontal (ORBvl, ORBl), and the anterior-most part of the agranular insular areas (AId, AIv). The medial prefrontal zone reciprocally connects with the AI and caudal TEa of the lateral subnetworks potentially acting as a site for medial and lateral subnetwork integration. This information arrives at the medial prefrontal zone via two routes (Figure 7A). The dorsal route links the dorsomedial corner of the prefrontal cortex (PL, ACAd) with the ventrolaterally located AId. The axons through this route make a 45° cut that demarcates the border between the dorsolateral and ventromedial halves of the prefrontal cortex. The ventral route links the medial (ILA) and lateral (AIv) areas across the orbitofrontal areas.

Overall, most components of the medial subnetwork communicate with the orbitofrontal zone. The ORBvl and ORBl are targets of projections from the VIS, AUD, and PTLp. The orbitofrontal zone also receives input from the TEa (lateral subnetwork), suggesting that, like the medial prefrontal cortex, it may also serve as a site of integration for the medial and lateral subnetworks.

Aside from the strong interaction between the medial prefrontal and insular zones, very little interaction is observed among the other neighboring structures of the prefrontal cortex. For example, coinjections in the ORBvl show no projections to or from the PFCdl and medial prefrontal areas. The relative segregation of these prefrontal zones combined with their specific cortical inputs and subcortical targets may help define their unique processing role and contribution to behavior.

DISCUSSION

The iConnectome: An Open Resource of Multiformat Connectivity Data

Open resources providing access to neurohistological images are revolutionizing neuroanatomy (Jones et al., 2011). The iConnectome is an online resource that presents high-resolution whole-brain images of neural connectivity in several different formats. Imaging data are presented in which labeled axonal pathways and neurons can be viewed with their own Nissl background or their corresponding anatomic ARA map. Cortico-cortical connectivity matrices (Figure 2) provide an overview of intracortical connections. Cortical connectivity matrices that comprise virtually all of the neocortex have been generated in

Figure 4. The Medial Subnetworks

(A) Major components of the medial subnetworks, which mediate transduction of information between sensory areas (VIS, AUD, and caudal-most SSp) and higher-order association areas along the medial bank of the neocortex, such as the retrosplenial (RSP), parietal (PTLp), anterior cingulate (ACA), and orbital (ORB) areas.

(B) Connectivity pathways of the medial subnetwork revealed by coinjections in the ORB (note: these are aggregated pathways for three different cases, see three coinjection sites in ORB, colored pink, light brown, and dark brown, medial to lateral).

(C) Representative raw images from an ORBvl coinjection. PHAL-labeled axons and CTb-labeled neurons are found in other medial network components such as the ACAd and adjacent MOs-fef, PTLp, RSPd, and primary and secondary VIS areas (VISp, VISal, and VISam). Scale bars, 500 μm (first panel) and 200 μm.

(D) Laminar-specific differences in axonal projections to primary visual cortex (VISp) arising from either ORBvl (red, BDA labeling) or ACAd (green, PHAL). Injection sites in the same brain, left panels, scale bars, 500 μm (left) and 1 mm. Projections to different layers of the same section of VISp (right). Underlying fluorescent Nissl was inverted to aid visualization of layers (right-most panel). Scale bar, 200 μm.

(E) Four different retrograde tracers were injected into the VISp (two), VISam, and VISpm within the same brain, resulting in distinct, topographically arranged clusters of neurons in the ACA and adjacent MOs-fef. In the ORBvl, these retrogradely labeled neurons are intermixed, but mostly not colocalized (bottom right, 5% colocalization for any combination of tracers in ORBvl, 436 cells counted, 21 had two or more tracers present). Scale bars, 1 mm (top left), 500 μm (bottom left), 200 μm (top right), 100 μm (bottom right).

(F) Summary of interactions among the medial subnetworks. Left, interaction between sensory and association areas. Dashed lines indicate sparse connection. Claustrum (CLA) is included due to high degree of interconnection with medial network. Middle, connections between the association areas. Thicker arrows indicate dense projection patterns between regions. Dashed line separates a direct pathway to medial prefrontal region along the ventro-medial bank of the cortex (second medial subnetwork). Asterisks indicate a unidirectional connection between CLA and RSP. Right panel, overview of medial network interactions including TEa and parahippocampal structures (i.e., SUBd, ENTm), which project to RSP (red arrows). Reciprocal connections of visual (blue) and auditory (green) areas with all major medial network components shown. Caudal-most somatosensory areas (SSp-ll/tr; SSp-bfd.cm) are included as well (gray arrows).
See also Figure S6.

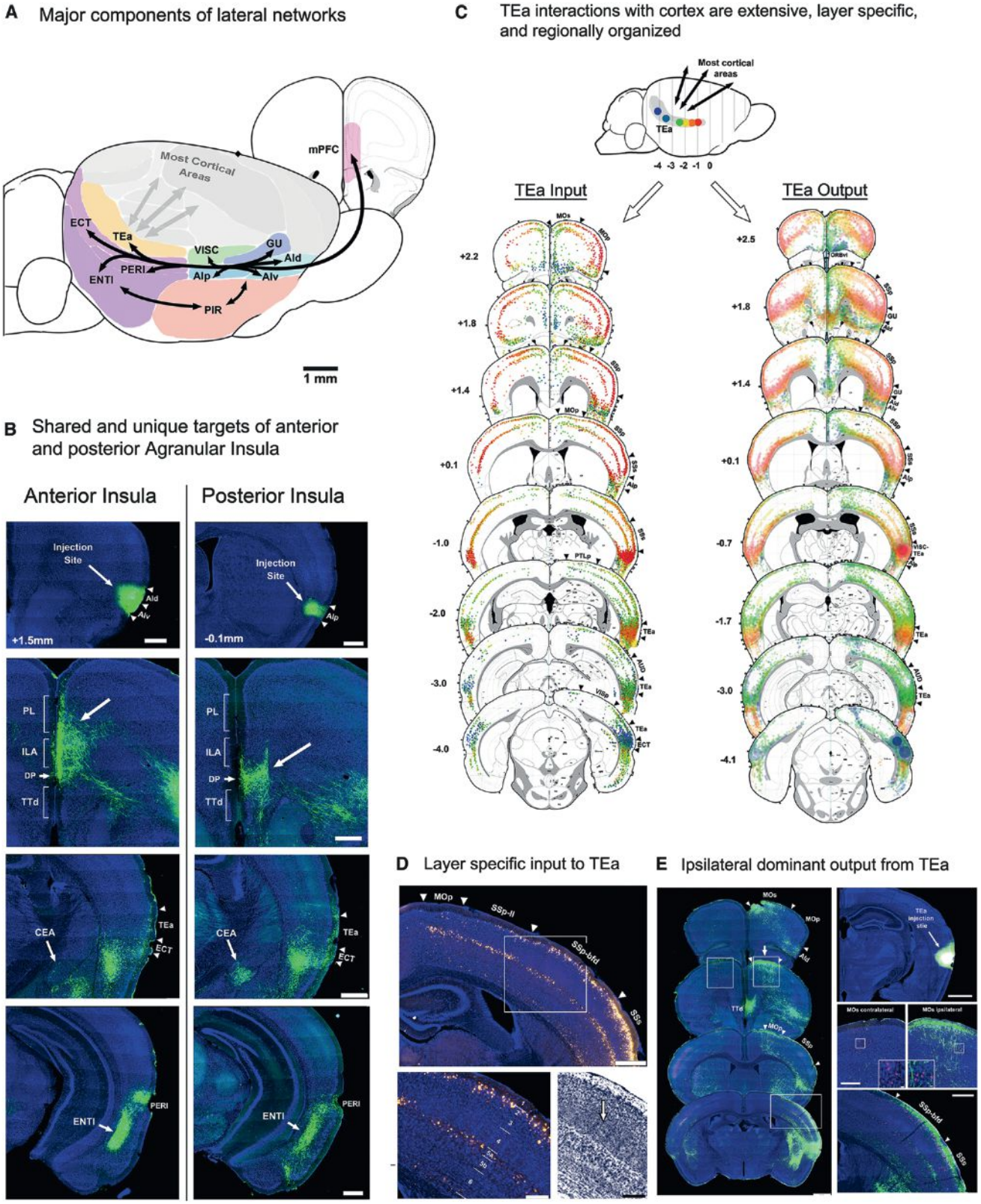

(legend on next page)

different species using data available in the literature (Honey et al., 2007; Sporns et al., 2007; Markov et al., 2011; for rat see BAMS: http://brancusi.usc.edu/). In contrast, the networks reported here are based on data collected and analyzed in a homogenous fashion rather than gathered piecemeal from the literature. The cortical connectivity map allows users to directly compare connectivity patterns of different cortical areas within the same neuroanatomic framework. Taken together, these resources allow researchers to conceptualize any cortical region of interest in the context of larger network interactions.

The Cortical Subnetworks

Examination of the full data set revealed that the neocortex is organized into several subnetworks that display unique topological organization, perhaps reflecting different information processing strategies for each. Within the somatic sensorimotor network, all main somatic nodes within the four subnetworks are heavily and reciprocally connected. This organization allows direct interactions between sensory and motor areas in the absence of higher-order association areas. This pattern could enable rapid integration of different sensory modalities for dynamically regulating motor actions, such as the integration of tactile information in the oral cavity and proprioception of the jaw for initiation, maintenance, or termination of rhythmic jaw movements throughout the masticatory period (Yamada et al., 2005).

Unlike direct sensorimotor interactions that occur within the somatic sensorimotor subnetworks, the medial subnetworks primarily mediate interactions between the sensory and higher-order association areas. The first medial subnetwork serves to transmit sensory information from the visual, auditory, and somatic sensory (SSp-ll /tr and SSp-bfd.cm) areas to the ORBvl and is organized differently than the sensorimotor subnetworks. All of the sensory areas directly connect with the ORBvl through multiple parallel pathways. Each of these areas is also connected with higher-order association areas like the RSPd, RSPagl, RSPv, PTLp, ACAd, and ACAv, within which sensory inputs can be integrated prior to reaching the ORBvl. Almost all cortical areas in this network (ORBvl, ACA, RSP, PTLp) have been implicated in orientating and coordinating movements of the eyes, head, and body in object searching tasks and spatial navigation (Feierstein et al., 2006; Bucci, 2009; Vann et al., 2009; Weible, 2013).

The second medial subnetwork is topologically distinct from the first in that it successively transmits information from the SUBd to the RSPv to the ACAv and then to the ILA, PL, and ORBm. This multisynaptic subnetwork may provide a structural basis for relaying information processed in the dorsal hippocampus and SUBd, perhaps regarding spatial orientation, navigation, and episodic memory, to the medial prefrontal cortex (Vann et al., 2009; Fanselow and Dong, 2010; Weible, 2013).

The lateral subnetworks represent a point of massive convergence in the cortex. Interactions are centered on two major components: the AI in the anterolateral insula subnetwork, and the TEa/PERI/ECT complex in the posterolateral temporal subnetwork. Each receives input from, and projects back to, an extensive number of cortical areas. For example, the anterolateral insular subnetwork integrates gustatory, visceral, and olfactory information, while the posterolateral temporal subnetwork processes more visual, auditory, somatosensory, and motor information. Both subnetworks then transfer this information rostrally to the medial prefrontal cortex and caudally to the ENTl. These connectivity patterns may support the proposed role of the AI in self-awareness of internal states (Craig, 2009) and the role of the TEa/PERI/ECT in perception, object recognition, and contextual memory associated with emotion (Winters et al., 2008; Aggleton et al., 2010).

Interactions among the Subnetworks

Importantly, several regions of the cortex potentially serve as sites for subnetwork interaction. The PFCdl receives a confluence of information from all four somatic sensorimotor subnetworks. The PFCvm receives convergent inputs from the medial and lateral subnetworks and provides an interface for integrating or communicating information regarding external stimuli (such as visual, auditory, somatic sensory) and internal stimuli (such as visceral and gustatory information). The CLA provides another means by which the medial, lateral, and even the somatic sensory subnetworks may directly interact. Both the PFCvm and CLA are directly interconnected with the ENTl, which further receives massive, highly integrated sensory information from the two lateral subnetworks. Through the ENTl, this information

Figure 5. The Lateral Subnetworks

(A) Sagittal view of the major components of two lateral subnetworks: the anterolateral insular (including the AId, AIv, AIp, VISC, GU) and posterior temporal (including TEa, ECT, PERI). These two interconnected subnetworks are also connected with olfactory (e.g., PIR) and medial prefrontal (mPFC) areas and with the ENTl. TEa in particular forms extensive connections with much of the rest of the neocortex (gray arrows).

(B) Distinct projection patterns of the anterior agranular areas (PHAL injections involved both AId and AIv, left panel) and AIp (right panel) with the mPFC areas (PL, ILA, DP), posterior temporal areas (TEa, ECT, PERI), and ENTl. The AIp targets more ventral structures in mPFC and more heavily innervates the central nucleus of the amygdala (CEA). Scale bars, 500 μm.

(C) Map of neuronal inputs to (left) and output from (right) the TEa, which are arranged topographically along the rostrocaudal direction. Note: these pathways are aggregated from six coinjections made into different parts of the TEa from rostral (red) to caudal (blue) direction (top most sagittal image, numbers relative to bregma in mm). Retrogradely labeled neurons are indicated as colored dots and demonstrate the layer-specific origin of cortical projections to TEa. Axonal pathways arising from TEa (outputs) are rendered as shaded areas of color.

(D) Raw image of retrograde labeling (FG, yellow) following injection in TEa. Cells are distributed extensively across numerous cortical regions following a single, small injection, suggesting a high level of convergence. Bottom left panel shows close up of layer specificity in somatosensory barrel field, with most cell bodies residing in layers 2/3, 5a, and some layer 6. Fluorescent Nissl inverted (right) to aid in discriminating layers. Layer 4 "barrels" indicated with arrow. Scale bars, 500 μm (top) and 200 μm (bottom).

(E) Raw image of coinjection in TEa. Fibers are predominately ipsilateral, but retrogradely labeled inputs are evenly distributed across both hemispheres. See right panel, middle, comparing labeling in contralateral and ipsilateral MOs.

Scale bars, 1 mm (top right), 200 μm (middle), 500 μm (bottom). See also Figure S7.

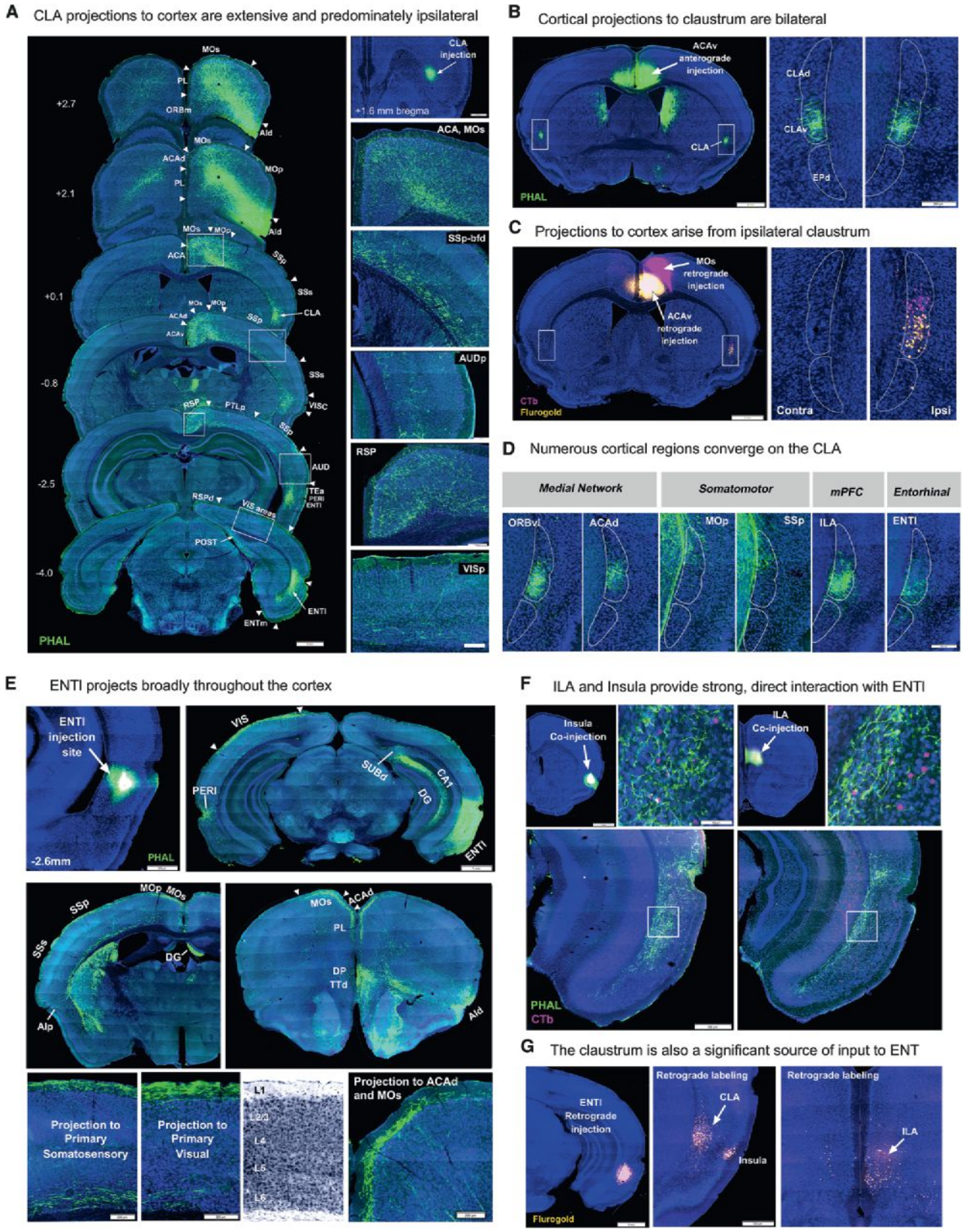

(legend on next page)

may reach the hippocampus, amygdala, and olfactory cortical areas, or be routed directly back to the medial prefrontal cortex (Figure 7C). In addition, the ENTl is also the starting point of the classic trisynaptic circuit that transfers information to the hippocampus, which may ultimately reach one of its main output targets, the SUBd (Witter, 2007), to re-enter the medial network through its projections to RSPv. Consequently, through the prefrontal cortex, ENTl, and CLA, information has the potential to be represented and communicated throughout the limbic loop surrounding the entire neocortex (Figure 7C).

CONCLUSIONS AND PERSPECTIVE

In conclusion, we and other groups have demonstrated the feasibility of producing and collecting large-scale connectivity data (Osten and Margrie, 2013; Pollock et al., 2014); however, interpretation of this wealth of anatomical data presents an ongoing challenge. This resource provides a reference for determining the complete set of inputs and outputs for a given cortical region and for implicating it in a broader network context. Any of these long-range interactions may be validated at the synaptic level using transsynaptic viral tracing and may be further investigated to determine cell-type-specific connections using methods such as channelrhodopsin-assisted circuit mapping (Luo et al., 2008; Osakada et al., 2011; Petreanu et al., 2009). Moreover, these projections may be assessed functionally using available optogenetic techniques that allow one to measure the circuit level or behavioral consequences of manipulating a given pathway within a neural network (Yizhar et al., 2011).

EXPERIMENTAL PROCEDURES

Data Generation, Collection, and Online Presentation

All experimental procedures have been described previously (Hintiryan et al., 2012). In brief, double coinjections of tracers were made into different areas of the entire neocortex, hippocampus, olfactory cortical areas, and amygdala of 8-week-old male C57Bl/6J mice. PHAL (2.5%; Vector Laboratories) and CTb (647 conjugate, 0.25%; Invitrogen) were coinjected, while BDA (FluoroRuby, 5%; Invitrogen) was injected in combination with FG (1%; Fluorochrome, LLC). One week was allowed for tracer transport after which animals were perfused and their brains extracted. All brains were sliced at 50 μm thickness using a Compresstome (VF-700, Precisionary Instruments, Greenville, NC). One series of sections was stained for PHAL using Alexa Fluor 488 (Invitrogen). All sections were counterstained with a fluorescent Nissl stain, NeuroTrace 435/455 (NT; 1:1000; Invitrogen). The sections were then mounted, coverslipped, and scanned as high-resolution virtual slide image (VSI) files using an Olympus VS110 high-throughput microscope. The VSI files were converted to tiff format prior to being registered. Following registration and registration refinement pipelines, the NeuroTrace fluorescent Nissl was converted to bright-field. Next, each of the five channels for every image was adjusted for brightness and contrast to maximize labeling visibility and quality in iConnectome. Following final modifications (i.e., skewness, angles) and JPEG2000 file format conversions, images were published to iConnectome. For more details on experimental procedures, see Supplemental Information.

Data Annotation and Construction of Cortical Connectivity Matrices and Connectivity Map

Currently, informatics tools that automatically and precisely identify fine anatomic boundaries in histological brain sections are nonexistent. Consequently, analysis of the data necessitates manual annotation to index anatomic locations and semiquantitative strengths of labeled cortico-cortical pathways. Analysis is performed in two formats. The first is for the purpose of constructing a comprehensive connectivity database and is comprised of an excel sheet that indexes anatomic locations and corresponding semiquantitative densities of labeling (PHAL-labeled axons/terminal boutons; CTb- and FG-labeled neurons). These data were used to generate connectivity matrices (see Supplemental Information). The second method consists of manually rendering the observed labeling patterns using Adobe Photoshop. Each pathway is rendered in a separate layer and all layers across all experiments are stacked to allow for a composite view of labeling trends.

SUPPLEMENTAL INFORMATION

Supplemental Information includes Extended Experimental Procedures, seven figures, and two tables and can be found with this article online at http://dx.doi.org/10.1016/j.cell.2014.02.023.

AUTHOR CONTRIBUTIONS

B.Z., H.H., L.G., M.Y.S, M.B, M.S.B., N.N.F., and H.-W.D. produced, processed, and analyzed the data and prepared the images for publication into the iConnectome. B.Z. constructed the cortico-cortical connectivity map. S.Y. developed the interactive iConnectome map viewer. S.Y. also participated in the initial design of the iConnectome visualization tool and in the development of the informatics pipeline for data processing. I.B. and M.S.B. performed network analysis, constructed the connectivity matrices, and wrote a description of corresponding employed methods in the manuscript. H.-W.D., H.H., and B.Z. wrote the manuscript. All authors made constructive comments on the manuscript. A.W.T. served as project advisor and participated in the planning and organizing of the project. H.-W.D. conceived and led the project.

ACKNOWLEDGMENTS

The authors would like to thank Drs. Larry Swanson and Harvey Karten for advising this project, Daren Lee, Anand A. Joshi, Nikhil G. Sane, and Queenie

Figure 6. The CLA and ENTl

(A) Axonal projections arising from the CLA are distributed throughout the entire neocortex and ENTl on the ipsilateral hemisphere. Note: these axons display different regional and laminar distribution specificity (on right panel) Scale bars, 1 mm (left), 500 μm (top right), 200 μm (bottom).

(B) and (C) Asymmetric connections of the CLA with other cortical areas in the two hemispheres. Cortical inputs to CLA project to both sides with equal densities (B, labels: dorsal and ventral claustrum (CLAd, CLAv), and endopiriform nucleus (EPd)), while outputs from CLA to other cortical areas indicated by retrograde tracers are almost exclusively ipsilateral (C). Moreover, the CLA has a dorsal to ventral topography in its projections to the cortex, with cells in CLAv (yellow, C, right) preferentially targeting ventral cingulate (C, left, injection site in ACAv). Very little colabeling was observed among cells labeled from a neighboring, more dorsal injection (pink). Scale bars: 1 mm (left) and 200 μm (right).

(D) Neural inputs to the CLA from almost all cortical areas in medial, somatic, and lateral subnetworks. The somatomotor inputs preferentially target the dorsalmost aspect of CLA.

(E) Representative images of PHAL-labeled axons in layer 1 of a wide range of neocortical areas arising from the rostrodorsal ENTl.

(F and G) Laminar specificity of PHAL-labeled axons and CTb-labeled neurons in the ENTl after coinjections made into the AI or ILA (F). Both cortical regions provide strong, direct input to ENTl, further supported by retrograde data in (G). These data also confirm the CLA is a specific source of input to ENTl (G, middle). Scale bars, 1 mm (F, top left and G, left), 500 μm (F, bottom and G, middle), 100 μm (F, top right).

See also Figures S1B–S1E.

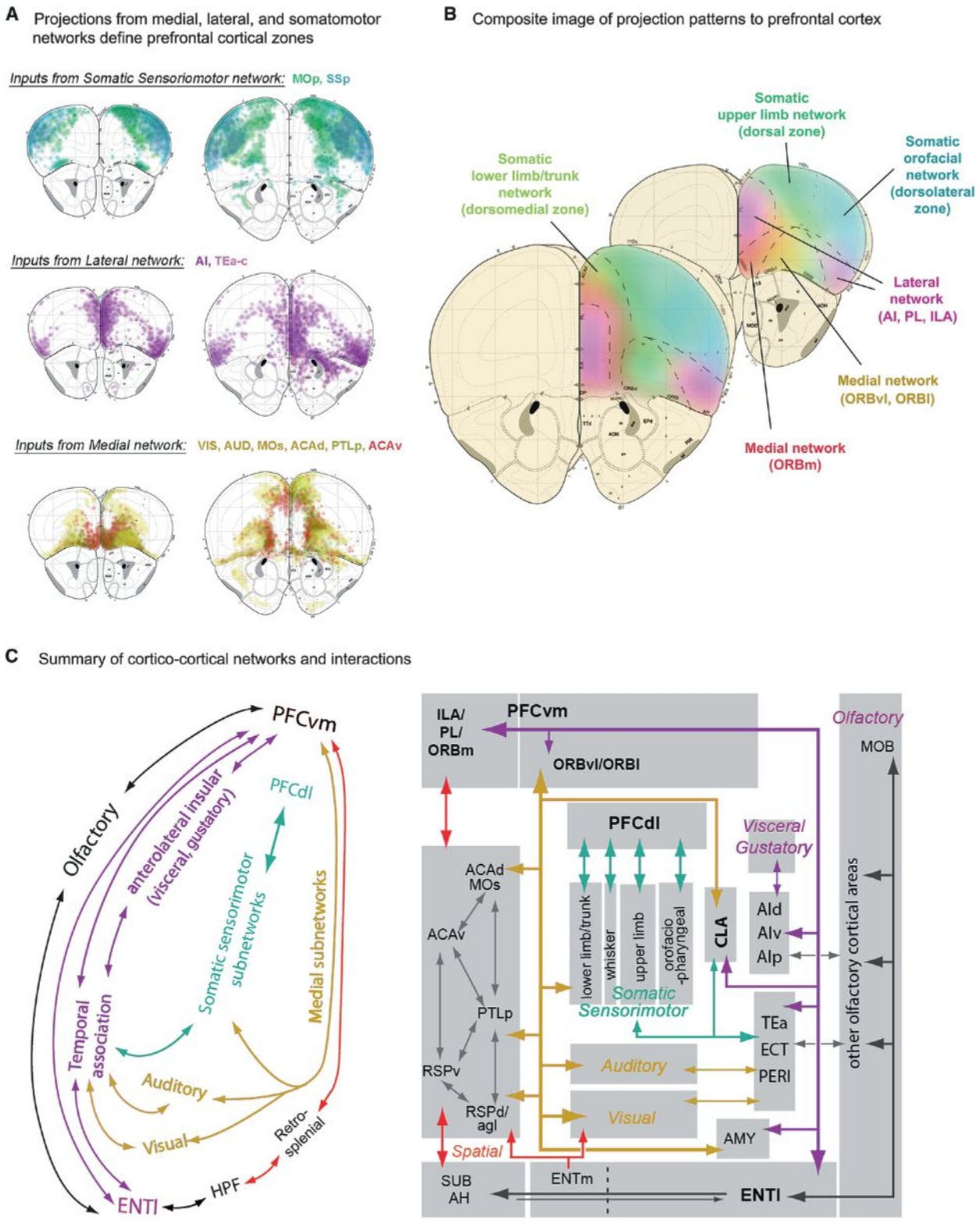

Figure 7. Interactions with Prefrontal Cortex

(A and B) Cumulative projections from components of the somatic sensorimotor, lateral, and medial networks in two representative coronal sections of the prefrontal cortex (PFC). Collectively these represent inputs from the entire neocortex to the PFC. Inputs were color coded based on the location of the injection sites in different components of the network (A). For example all primary motor projections arising from multiple injections along the length of this structure were

(legend continued on next page)

Ng for the initial development of the iConnectome visualization tool and Betty W. Lee, Carlos Mena, Vaughan Greer, and Robert De La Cruz for their contributions to the website. We acknowledge Arleen Grewal, Annie Chen, Amy Hwang, and Hyojin Ryu for their contributions in image processing. This work was supported by NIH/NIMH, MH094360-01A1 (HWD) and P41 Supplement (AWT 3P41RR013642-12S3). The Mouse Connectome Project (MCP) was initiated by the authors while still at the University of California, Los Angeles (UCLA), but the entire program and project now fully reside at the University of Southern California (USC). This manuscript is dedicated to Dr. Edward (Ted) G. Jones, a devoted scientist, colleague, and beloved friend who will be greatly missed.

Received: July 23, 2013
Revised: January 25, 2014
Accepted: February 10, 2014
Published: February 27, 2014

REFERENCES

Aggleton, J.P., Albasser, M.M., Aggleton, D.J., Poirier, G.L., and Pearce, J.M. (2010). Lesions of the rat perirhinal cortex spare the acquisition of a complex configural visual discrimination yet impair object recognition. Behav. Neurosci. *124*, 55–68.

Allen, G.V., Saper, C.B., Hurley, K.M., and Cechetto, D.F. (1991). Organization of visceral and limbic connections in the insular cortex of the rat. J. Comp. Neurol. *311*, 1–16.

Andrews-Hanna, J.R., Reidler, J.S., Sepulcre, J., Poulin, R., and Buckner, R.L. (2010). Functional-anatomic fractionation of the brain's default network. Neuron *65*, 550–562.

Behrens, T.E., and Sporns, O. (2012). Human connectomics. Curr. Opin. Neurobiol. *22*, 144–153.

Bohland, J.W., Wu, C., Barbas, H., Bokil, H., Bota, M., Breiter, H.C., Cline, H.T., Doyle, J.C., Freed, P.J., Greenspan, R.J., et al. (2009). A proposal for a coordinated effort for the determination of brainwide neuroanatomical connectivity in model organisms at a mesoscopic scale. PLoS Comput. Biol. *5*, e1000334.

Bota, M., Dong, H.-W., and Swanson, L.W. (2012). Combining collation and annotation efforts toward completion of the rat and mouse connectomes in BAMS. Front. Neuroinform. *6*, 2.

Brecht, M., Krauss, A., Muhammad, S., Sinai-Esfahani, L., Bellanca, S., and Margrie, T.W. (2004). Organization of rat vibrissa motor cortex and adjacent areas according to cytoarchitectonics, microstimulation, and intracellular stimulation of identified cells. J. Comp. Neurol. *479*, 360–373.

Bressler, S.L., and Menon, V. (2010). Large-scale brain networks in cognition: emerging methods and principles. Trends Cogn. Sci. *14*, 277–290.

Bucci, D.J. (2009). Posterior parietal cortex: an interface between attention and learning? Neurobiol. Learn. Mem. *91*, 114–120.

Carleton, A., Accolla, R., and Simon, S.A. (2010). Coding in the mammalian gustatory system. Trends Neurosci. *33*, 326–334.

Craig, A.D. (2009). How do you feel—now? The anterior insula and human awareness. Nat. Rev. Neurosci. *10*, 59–70.

de Curtis, M., and Paré, D. (2004). The rhinal cortices: a wall of inhibition between the neocortex and the hippocampus. Prog. Neurobiol. *74*, 101–110.

Dong, H.-W. (2007). The Allen Reference Atlas: A Digital Color Brain Atlas Of The C57BL/6J Male Mouse (Hoboken: John Wiley and Sons, Inc.).

Driver, J., and Noesselt, T. (2008). Multisensory interplay reveals crossmodal influences on 'sensory-specific' brain regions, neural responses, and judgments. Neuron *57*, 11–23.

Fanselow, M.S., and Dong, H.-W. (2010). Are the dorsal and ventral hippocampus functionally distinct structures? Neuron *65*, 7–19.

Feierstein, C.E., Quirk, M.C., Uchida, N., Sosulski, D.L., and Mainen, Z.F. (2006). Representation of spatial goals in rat orbitofrontal cortex. Neuron *51*, 495–507.

Felleman, D.J., and Van Essen, D.C. (1991). Distributed hierarchical processing in the primate cerebral cortex. Cereb. Cortex *1*, 1–47.

Gerdjikov, T.V., Haiss, F., Rodriguez-Sierra, O.E., and Schwarz, C. (2013). Rhythmic whisking area (RW) in rat primary motor cortex: an internal monitor of movement-related signals? J. Neurosci. *33*, 14193–14204.

Hintiryan, H., Gou, L., Zingg, B., Yamashita, S., Lyden, H.M., Song, M.Y., Grewal, A.K., Zhang, X., Toga, A.W., and Dong, H.-W. (2012). Comprehensive connectivity of the mouse main olfactory bulb: analysis and online digital atlas. Front. Neuroanat. *6*, 30.

Honey, C.J., Kötter, R., Breakspear, M., and Sporns, O. (2007). Network structure of cerebral cortex shapes functional connectivity on multiple time scales. Proc. Natl. Acad. Sci. USA *104*, 10240–10245.

Jarrell, T.A., Wang, Y., Bloniarz, A.E., Brittin, C.A., Xu, M., Thomson, J.N., Albertson, D.G., Hall, D.H., and Emmons, S.W. (2012). The connectome of a decision-making neural network. Science *337*, 437–444.

Jasmin, L., Burkey, A.R., Granato, A., and Ohara, P.T. (2004). Rostral agranular insular cortex and pain areas of the central nervous system: a tract-tracing study in the rat. J. Comp. Neurol. *468*, 425–440.

Jones, E.G. (2007). The Thalamus (2 Volume Set) (Cambridge: Cambridge University Press).

Jones, E.G., Stone, J.M., and Karten, H.J. (2011). High-resolution digital brain atlases: a Hubble telescope for the brain. Ann. N Y Acad. Sci. *1225* (*Suppl 1*), E147–E159.

Luo, L., Callaway, E.M., and Svoboda, K. (2008). Genetic dissection of neural circuits. Neuron *57*, 634–660.

Maffei, A., Haley, M., and Fontanini, A. (2012). Neural processing of gustatory information in insular circuits. Curr. Opin. Neurobiol. *22*, 709–716.

Mao, T., Kusefoglu, D., Hooks, B.M., Huber, D., Petreanu, L., and Svoboda, K. (2011). Long-range neuronal circuits underlying the interaction between sensory and motor cortex. Neuron *72*, 111–123.

Markov, N.T., Misery, P., Falchier, A., Lamy, C., Vezoli, J., Quilodran, R., Gariel, M.A., Giroud, P., Ercsey-Ravasz, M., Pilaz, L.J., et al. (2011). Weight consistency specifies regularities of macaque cortical networks. Cereb. Cortex *21*, 1254–1272.

colored green and all somatosensory projections were colored blue (A, top). ACAv was colored red to separate it as a component of the second medial subnetwork (A, bottom, see Figure S6E). Note that RSP has very little interaction with the PFC. (B) All inputs from three somatic sensorimotor subnetworks (as shown in A) converge onto three distinct zones, dorsolateral (dl), dorsal (d), and dorsal medial (dm), in the dorsolateral half of the prefrontal cortex (PFCdl, green and blue). In contrast, the medial and lateral subnetworks converge onto the ventromedial half of the prefrontal cortex with distinctive patterns. Note that caudal-most somatosensory and motor regions make some contribution to lateral-most, and caudal aspects of ORB (green and blue shading).
(C) A schematic view of cortico-cortical network information flow as seen in a top-down view of the cortex (left, lateral edge on left, PFC at the top). All subnetworks are colored according to the scheme used in (A) and (B). Right, a more detailed overview of these interactions (lateral edge of cortex on the right, PFC at the top). Somatic sensorimotor boxes are meant to include both the sensory area and its corresponding primary motor area with which it is strongly interconnected. All functionally distinctive subnetworks are organized along the longitudinal axis of the cerebrum. Information processed in the medial and lateral subnetworks is integrated within the ventromedial half of the prefrontal cortex (PFCvm) and the ENTl. The claustrum (CLA) may also provide an additional means of direct interaction between each of the subnetworks. For abbreviations, please see Figure 2 and Table S2. Additional abbreviations: AMY, amygdala; AH, Ammon's Horn; HPF, hippocampal formation.

Marx, V. (2012). High-throughput anatomy: Charting the brain's networks. Nature *490*, 293–298.

Osakada, F., Mori, T., Cetin, A.H., Marshel, J.H., Virgen, B., and Callaway, E.M. (2011). New rabies virus variants for monitoring and manipulating activity and gene expression in defined neural circuits. Neuron *71*, 617–631.

Osten, P., and Margrie, T.W. (2013). Mapping brain circuitry with a light microscope. Nat. Methods *10*, 515–523.

Petreanu, L., Mao, T., Sternson, S.M., and Svoboda, K. (2009). The subcellular organization of neocortical excitatory connections. Nature *457*, 1142–1145.

Pollock, J.D., Wu, D.Y., and Satterlee, J.S. (2014). Molecular neuroanatomy: a generation of progress. Trends Neurosci. *37*, 106–123.

Reep, R.L., Goodwin, G.S., and Corwin, J.V. (1990). Topographic organization in the corticocortical connections of medial agranular cortex in rats. J. Comp. Neurol. *294*, 262–280.

Saleem, K.S., Kondo, H., and Price, J.L. (2008). Complementary circuits connecting the orbital and medial prefrontal networks with the temporal, insular, and opercular cortex in the macaque monkey. J. Comp. Neurol. *506*, 659–693.

Saper, C.B. (1982). Convergence of autonomic and limbic connections in the insular cortex of the rat. J. Comp. Neurol. *210*, 163–173.

Sporns, O. (2010). Networks of the Brain (Cambridge: MIT Press).

Sporns, O., Tononi, G., and Kötter, R. (2005). The human connectome: A structural description of the human brain. PLoS Comput. Biol. *1*, e42.

Sporns, O., Honey, C.J., and Kötter, R. (2007). Identification and classification of hubs in brain networks. PLoS ONE *2*, e1049.

Stein, B.E., and Stanford, T.R. (2008). Multisensory integration: current issues from the perspective of the single neuron. Nat. Rev. Neurosci. *9*, 255–266.

Swanson, L.W., and Bota, M. (2010). Foundational model of structural connectivity in the nervous system with a schema for wiring diagrams, connectome, and basic plan architecture. Proc. Natl. Acad. Sci. USA *107*, 20610–20617.

Thompson, R.H., and Swanson, L.W. (2010). Hypothesis-driven structural connectivity analysis supports network over hierarchical model of brain architecture. Proc. Natl. Acad. Sci. USA *107*, 15235–15239.

Toga, A.W., Clark, K.A., Thompson, P.M., Shattuck, D.W., and Van Horn, J.D. (2012). Mapping the human connectome. Neurosurgery *71*, 1–5.

Vann, S.D., Aggleton, J.P., and Maguire, E.A. (2009). What does the retrosplenial cortex do? Nat. Rev. Neurosci. *10*, 792–802.

Weible, A.P. (2013). Remembering to attend: the anterior cingulate cortex and remote memory. Behav. Brain Res. *245*, 63–75.

White, J.G., Southgate, E., Thomson, J.N., and Brenner, S. (1986). The structure of the nervous system of the nematode *Caenorhabditis elegans*. Philos. Trans. R. Soc. Lond. B Biol. Sci. *314*, 1–340.

Winters, B.D., Saksida, L.M., and Bussey, T.J. (2008). Object recognition memory: neurobiological mechanisms of encoding, consolidation and retrieval. Neurosci. Biobehav. Rev. *32*, 1055–1070.

Witter, M.P. (2007). The perforant path: projections from the entorhinal cortex to the dentate gyrus. Prog. Brain Res. *163*, 43–61.

Yamada, Y., Yamamura, K., and Inoue, M. (2005). Coordination of cranial motoneurons during mastication. Respir. Physiol. Neurobiol. *147*, 177–189.

Yizhar, O., Fenno, L.E., Davidson, T.J., Mogri, M., and Deisseroth, K. (2011). Optogenetics in neural systems. Neuron *71*, 9–34.

Cell

Tissue-Specific Signals Control Reversible Program of Localization and Functional Polarization of Macrophages

Yasutaka Okabe[1] and Ruslan Medzhitov[1,*]
[1]Howard Hughes Medical Institute and Department of Immunobiology, Yale University School of Medicine, New Haven, CT 06520, USA
*Correspondence: ruslan.medzhitov@yale.edu
http://dx.doi.org/10.1016/j.cell.2014.04.016

SUMMARY

Tissue-resident macrophages are highly heterogeneous in terms of their functions and phenotypes as a consequence of adaptation to different tissue environments. Local tissue-derived signals are thought to control functional polarization of resident macrophages; however, the identity of these signals remains largely unknown. It is also unknown whether functional heterogeneity is a result of irreversible lineage-specific differentiation or a consequence of continuous but reversible induction of diverse functional programs. Here, we identified retinoic acid as a signal that induces tissue-specific localization and functional polarization of peritoneal macrophages through the reversible induction of transcription factor GATA6. We further found that GATA6 in macrophages regulates gut IgA production through peritoneal B-1 cells. These results provide insight into the regulation of tissue-resident macrophage functional specialization by tissue-derived signals.

INTRODUCTION

Macrophages are among the most multifunctional and heterogeneous cell types, present in virtually every mammalian tissue, where they monitor local environment and maintain homeostasis (Davies et al., 2013; Hume et al., 1983; Wynn et al., 2013). They express a broad array of sensing molecules, including scavenger receptors, pattern recognition receptors, nuclear hormone receptors, and cytokine receptors, which allows macrophages to monitor tissue microenvironments and act as sentinel cells for infection and tissue damage. In addition, macrophages perform many tissue-specific functions, which is reflected in their phenotypic diversity. Thus, alveolar macrophages, Kupffer cells, microglia, and osteoclasts all have specialized functions and phenotypes, suggesting that local tissue-derived signals may control the development of tissue-specific phenotypes (Gordon and Taylor, 2005; Murray and Wynn, 2011). However, with some exceptions (Boyle et al., 2003), these signals remain largely unknown.

It is also increasingly appreciated that distinct transcriptional master regulators control the development of tissue-specific macrophage phenotypes (Gautier et al., 2012). Several examples of transcription factors that dictate tissue-specific transcription programs in macrophages have been reported, and the deletion of these transcription factors resulted in the ablation of particular tissue macrophage subsets (Kohyama et al., 2009; A-Gonzalez et al., 2013; Takayanagi et al., 2002), suggesting their involvement in the differentiation of the corresponding macrophage populations. In addition, mature macrophages can undergo functional polarization in response to environmental signals (Stout et al., 2005). Two well-appreciated macrophage polarization programs are classically activated (M1) and alternative activated (M2) macrophages that are induced by different stimuli such as LPS+IFNγ and IL-4, respectively (Biswas and Mantovani, 2010; Gordon and Martinez, 2010). Transcription factors, including STAT1, STAT6, C/EBPβ, IRF-4, IRF5, and PPARγ, have been shown to regulate transcription programs that control M1/M2 macrophage polarizations (Lawrence and Natoli, 2011). It is also increasingly appreciated that many other functional polarization programs of macrophages likely exist, which may be expressed in either an inducible or constitutive and tissue-specific manner. However, the signals and transcription factors that control most of these programs remain to be defined.

In principle, tissue-specific phenotypes of macrophages (or any other cell type) can be generated by hard-wired, irreversible differentiation programs that are controlled by lineage-specific master regulators. Alternatively, they can be based on functional polarization programs, which are reversible and inducible on demand, analogous to M1 and M2 polarizations. In the latter scenario, one can expect that multiple transcriptional regulators may be induced to control specific functional programs at times and places specified by diverse functional requirements in different tissues.

Macrophages of the mouse peritoneal cavity are among the best-studied tissue macrophage in terms of cell biology and inflammatory responses (Cain et al., 2013). However, the tissue-specific function of macrophages in this site remains poorly defined. Peritoneal cavity is a unique body compartment for B-1 cell distribution. B-1 cells are a subtype of B cells that account for 35%–70% of B cells in peritoneal cavity, whereas they are almost absent in lymphoid tissues (0.1%–2%) (Baumgarth, 2011). Peritoneal B-1 cells generate the majority of the natural IgM antibodies, including antibody specific for phosphorylcholine (PC). B-1 cells thus constitute a key component of early

immune responses to pathogens. Additionally, B-1 cells in peritoneal cavity continuously migrate to intestinal lamina propria, where they give rise to IgA-secreting cells (Baumgarth, 2011; Fagarasan et al., 2010). The tissue-specific role of macrophages in body cavity immunity is not clear in terms of B-1 cell regulation. However, CXCL13, a chemokine that is essential for B-1 cell migration to peritoneal cavity, is abundantly expressed by peritoneal macrophages (Ansel et al., 2002), suggesting that peritoneal macrophages may have a pivotal role in B-1 cell regulation.

Here, we used peritoneal macrophage as an experimental model to investigate the tissue-specific functions and external cues that control their specific gene expression program. Based on the whole-genome gene expression analysis comparing six tissue-resident macrophages, we identified zinc finger transcription factor GATA6 as a regulator of a tissue-specific gene expression program in peritoneal macrophages. GATA6 controls anatomical localization of peritoneal macrophages, but not their development. In addition, we found that GATA6 expression and other peritoneal macrophage-specific gene expression programs are induced by local tissue-derived retinoic acid. Lastly, we show that GATA6 in peritoneal macrophages regulates gut IgA response mediated by peritoneal B-1 cells. Together, our study provides new insight into the mechanism of generation of tissue macrophage diversity.

RESULTS

Identification of GATA6 in Peritoneal Macrophages

The aim of the study was to characterize tissue-derived signals that control diversity of macrophage phenotypes. To address this, we first examined gene expression profiles of tissue-resident macrophages. We purified macrophages from peritoneal cavity, lung, liver, spleen, intestine, and adipose tissue from C57BL/6 mice (Figure S1A available online), and whole-genome gene expression was determined by DNA microarray (Figure 1A). Microarray analysis revealed diversity of tissue macrophages in terms of gene expression (Figure S1B).

Consistent with the previous study (Gautier et al., 2012), we found that zinc finger transcription factor GATA6 is uniquely expressed at a high level in peritoneal macrophages compared to tissue-derived, bone-marrow-derived (BMDM) and fetal-liver-derived macrophages (Figure 1B). Previous studies showed that transcription factors NFATc1 and Spic, which regulate tissue-specific transcription programs in osteoclast and splenic red pulp macrophages, respectively, had restricted expression among tissue macrophages (Kohyama et al., 2009; Takayanagi et al., 2002), suggesting that GATA6 may control peritoneal macrophage-specific gene expression. Mouse peritoneal macrophages are made up of two subsets (Ghosn et al., 2010): large peritoneal macrophages (LPMs) and small peritoneal macrophages (SPMs). LPMs make up the majority of peritoneal macrophages and express high levels of F4/80 but low MHC class II (MHC-II); SPMs express lower F4/80 but high levels of MHC-II (Figure 1C, left and middle). The expression of GATA6 in LPMs had bimodal distribution (Figure 1C, lower-right), but it was negligible in SPMs, thioglycollate-induced peritoneal macrophages (Thio-pMacs), and neutrophils (Figures 1C, lower-right, and 1D). In contrast, mRNA of chemokine receptor *Ccr2*, which plays a critical role in monocyte recruitment during inflammation (Kurihara et al., 1997), was highly expressed in SPMs (Figure S1C). The cell number of SPM, but not of LPM, was significantly reduced in peritoneal exudate from *Ccr2* KO mice (Figures S1D and S1E), suggesting that the majority of SPMs are originated from inflammatory monocyte population.

To examine the role of GATA6 in peritoneal macrophages, we crossed *Gata6*-floxed mice with *LysM-cre* mice (with macrophage and neutrophil specific Cre expression) to establish mice specifically deficient for *Gata6* gene in macrophage lineage (Mac-*Gata6* KO), as neutrophils do not express GATA6 (Clausen et al., 1999; Sodhi et al., 2006). Mac-*Gata6* KO mice developed LPMs in peritoneal cavity with reduced F4/80 expression (Figure 1C). Furthermore, the number of LPMs, but not SPMs, harvested from peritoneal exudate was greatly reduced in Mac-*Gata6* KO mice (Figure 1E). This was consistent with ex vivo analysis of mice genetically labeled with *Yfp* reporter for macrophage lineage (*LysM-Cre*;*R26*-stop-*Yfp*), which revealed reduction in the numbers of macrophages on parietal peritoneal membrane of Mac-*Gata6* KO mice (Figure S1F). Despite the dramatic reduction in LPM numbers, their proliferative status was not affected by GATA6 deficiency (Figure S1G). In addition, blood leukocyte counts were normal in Mac-*Gata6* KO mice (Figure S1H).

Immunofluorescence analysis of peritoneal exudate cells from control mice demonstrated restricted expression of GATA6 protein in macrophages and its absence in Mac-*Gata6* KO mice (Figure 1F). The elimination of GATA6 protein in LPMs of Mac-Gata6 KO mice was also confirmed by flow cytometry (Figures 1C, lower-right), whereas truncated *Gata6* mRNA, which lacks the targeted region, exon 2, was comparably detected in LPMs of Mac-*Gata6* KO mice (Figure 1G). These results further confirm that GATA6 is not essential for LPM development.

GATA6-Dependent Tissue-Specific Gene Expression Program

We next determined the role of GATA6 in gene regulation of peritoneal macrophages. DNA microarray identified genes suppressed in Mac-*Gata6* KO peritoneal macrophages, many of these genes being specific to peritoneal macrophages in WT mice (Figure S2A). To determine the role of GATA6 in the peritoneal macrophage-specific gene expression program, we selected 44 genes that had expression of at least 5-fold higher in peritoneal macrophages compared to all five other tissue macrophages studied here (Figure 2A). We provisionally termed these genes peritoneal macrophage-specific genes (PMSGs). Microarray analysis revealed that Mac-*Gata6* KO peritoneal macrophages strongly downregulated the expression of 39% (17 out of 44 genes) of PMSGs (Figure 2A), which was further confirmed by quantitative PCR (Figures 2B and 2C). In contrast, the rest of PMSGs had comparable expression in Mac-*Gata6* KO macrophages (Figures 2B, 2C, S2B, and S2C). Consistently, the reduction of protein expression of CD62P, CD49f, and CD73 was detected in Mac-*Gata6* KO LPMs, whereas that of CD102 was intact (Figure 2D). These findings indicate that GATA6 is essential for the induction of a subset of PMSGs. Furthermore, retroviral transduction of *Gata6* into fetal-liver-derived macrophages induced the expression of GATA6-dependent PMSGs such as *Serpinb2*, *Cd62p*, *Thbs1*, *Tgfb2*, and *Ltbp1* (Figure 2E),

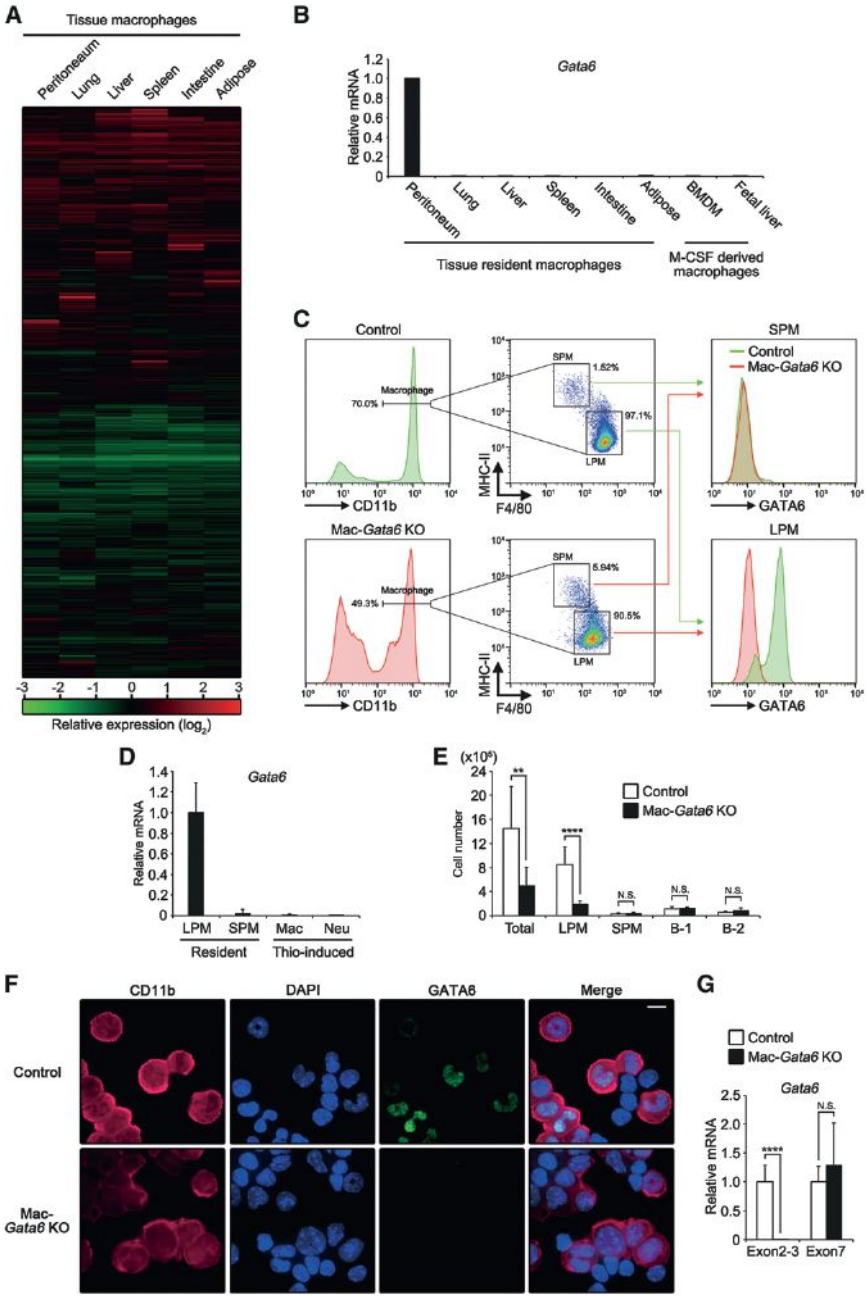

Figure 1. Identification of GATA6 in Peritoneal Macrophages

(A) Heatmap displaying hierarchical clustering results from microarray expression data derived from tissue macrophages. Expression levels were normalized by that of BMDM and expressed by relative values (log-2). Genes whose signal was under detection limit were excluded, and 17,513 genes were shown.

(B) Tissue macrophages and in-vitro-cultured macrophages were determined for *Gata6* mRNA by quantitative PCR and were expressed as relative values normalized by *Gapdh* mRNA (n = 1). Graph is representative of two independent experiments.

(C) (Left and middle) Flow cytometry analysis for macrophage subsets in peritoneal exudate cells of controls and Mac-*Gata6* KO mice. (Right) Staining of GATA6 protein in SPMs and LPMs.

(D) Quantitative PCR analysis for *Gata6* mRNA in LPMs, SPMs, Thio-pMacs, and neutrophils (n = 3–12).

(E) Numbers of total cells, LPM, SPM, B-1 cell, and B-2 cell in peritoneal exudate cells from controls and Mac-*Gata6* KO mice (n = 6–12). Data were pooled from three independent experiments with similar results.

(F) Immunofluorescence microscopy of peritoneal exudate cells from control and Mac-*Gata6* KO mice stained for CD11b, DAPI, and GATA6. Scale bar, 10 μm.

(G) Quantitative PCR analysis of LPMs for *Gata6* mRNA targeting exons 2–3 and exon 7 (n = 6–12).

Errors bars represent SD. **p < 0.01, ****p < 0.0001. N.S., not significant. See also Figure S1.

indicating that GATA6 regulates these genes in a cell-autonomous manner.

Retinoic Acid Regulates PMSG Program

We next addressed the extracellular signal(s) inducing the expression of PMSGs including GATA6. We found that peritoneal macrophages had an abundant expression of retinoic acid nuclear receptor RARβ (Figures 2A, S2B, and S2C). We also found the presence of retinoic acid response elements (RAREs) in the putative regulatory region of *Gata6* gene (within 1 kb 5′ to the transcription start site) (Figure 3A). *Rarb* and two other GATA6-independent PMSGs, *Rai14* and *Arg1*, were shown to be induced by retinoic acid in other cell types (Chang et al., 2013; de Thé et al., 1990; Kutty et al., 2001). Furthermore, the link between retinoic acid and GATA6 was previously described, though the exact molecular mechanism was unclear (Capo-Chichi et al., 2005; Mauney et al., 2010). Collectively, this suggested a possibility that retinoic acid in peritoneal macrophages may control expression of *Gata6*- and GATA6-dependent genes, as well as other PMSGs.

To test whether retinoic acid could activate the *Gata6* gene, genomic DNA covering 1 kbp upstream from *Gata6* transcription start site was cloned into luciferase reporter plasmid (Figure 3A). The reporter constructs were transfected into 3T3 cells together with RARβ expression plasmid, and the cells were stimulated with all trans-retinoic acid (ATRA), which is the most abundant form of retinoic acid in vivo. Reporter activity of WT promoter was increased about 4-fold post-ATRA stimulation, whereas mutations in either or both RAREs reduced or eliminated the

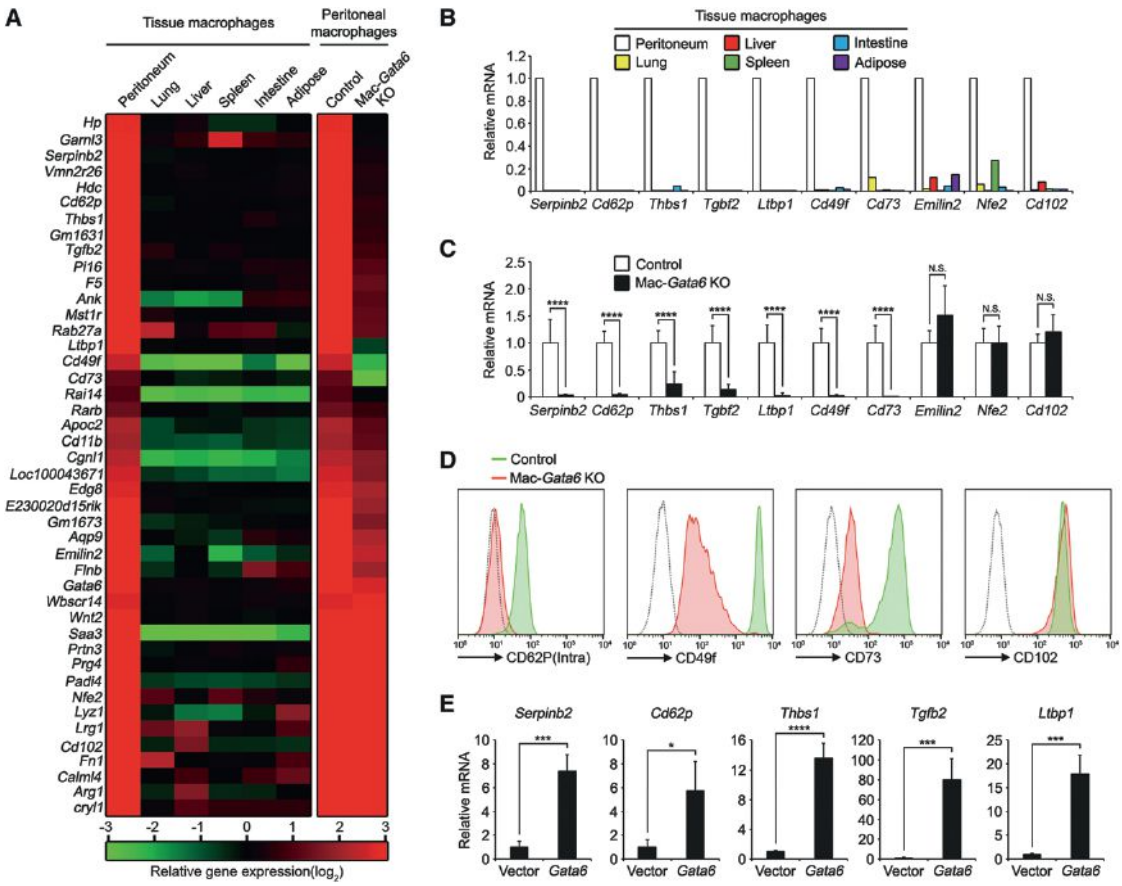

Figure 2. GATA6-Dependent PMSG Induction

(A) Heatmap of mRNA expressed at least five times over in peritoneal macrophages relative to their expression in all other tissue macrophages. Expression levels were shown as relative values normalized by that of BMDM. Note that apparent expression of *Gata6* mRNA is due to the hybridization region (exon7) of microarray probe (refer to Figure 1G).

(B and C) The mRNA expression of the indicated genes in tissue macrophages (B, representative of two independent experiments) and LPMs of littermate controls and Mac-*Gata6* KO mice (C, n = 6–12) was determined by quantitative PCR and is expressed as a relative value to *Gapdh* mRNA.

(D) Expression of indicated proteins in LPMs was analyzed by flow cytometry. Green, control; red, Mac-*Gata6* KO; dotted line, unstained control.

(E) mRNA expression of the indicated genes was determined in fetal liver-derived macrophages after retrovirus-mediated transduction of *Gata6* (n = 3).

Error bars represent SD. *p < 0.05, ***p < 0.001, ****p < 0.0001. N.S., not significant. See also Figure S2.

reporter activity, respectively (Figure 3B). We next treated freshly isolated peritoneal macrophages with pan-retinoic acid receptor inverse agonist BMS493 to determine whether blocking retinoic acid signaling affected PMSG induction. Interestingly, the expression of *Gata6* and several GATA6-independent PMSGs (*Rarb*, *Rai14*, *Arg1*, and *Fn1*) was significantly suppressed by BMS493 (Figure 3C). To further explore the role of retinoic acid signal in PMSG induction, we carried out in vivo depletion of vitamin A, which is the precursor of retinoic acid, from mice. In the previous study, mouse breeding on vitamin-A-depleted diet was shown to result in a steady decline of serum vitamin A. At 6 weeks of age, it is <50% of control value; at 8 weeks, < 20%; and at 11 weeks, < 10% (Smith et al., 1987). Six-week-old vitamin-A-depleted (VAD) mice had a comparable or slightly reduced number of peritoneal macrophages to control diet fed mice. The expression of *Gata6* mRNA was significantly downregulated in peritoneal macrophages from 6-week-old VAD mice, whereas ATRA treatment recovered the expression (Figure 3D). In addition, the mRNA expression of *Saa3*, *Lrg1*, *Arg1*, and *Fn1* was significantly suppressed in peritoneal macrophages from 6-week-old VAD mice (Figure 3E). ATRA stimulation also induced the expression of PMSGs (*Rarb*, *Rai14*, *Arg1*, and *Fn1*). These results indicate that retinoic acid inducibly and reversibly regulates gene expression of GATA6 and other PMSGs in peritoneal macrophages.

Longer periods of vitamin A deprivation (9 and 12 week old ages) showed further reduction of GATA6 expression in LPMs (Figure 4A). In a delayed fashion, downregulation of CD102 and CD11b, which are GATA6-independent PMSGs (Figures 2A–2C), was also observed (Figures 4B and 4C). In addition, peritoneal exudate cells from VAD mice revealed age-dependent reduction in the frequencies and numbers of LPMs (Figures 4C and 4D). In contrast, CD11b-F4/80 intermediate population started appearing at 9 weeks of age (Figures 4C and 4E). Flow

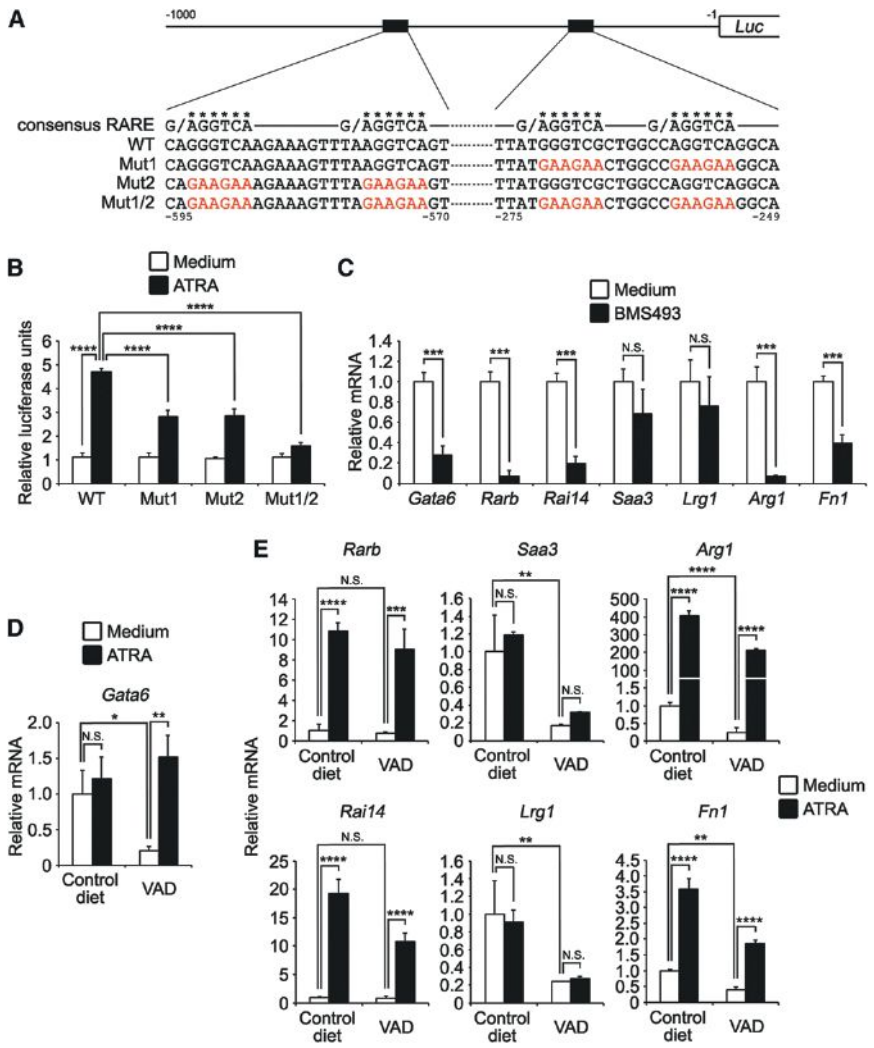

Figure 3. Activation of *Gata6* Gene and Other PMSGs by Retinoic Acid

(A) Schematic diagram of *Gata6* promoter constructs. Sequences of consensus retinoic acid response elements (RAREs) and putative RAR-binding regions in WT and mutants promoters were shown. Asterisks indicate positions of putative RAREs, and mutated nucleotides were shown by red. Numbers indicate position from *Gata6* transcription start site.

(B) 3T3 cells were transfected with GATA6 reporter plasmids and expression plasmids for RARβ and were then stimulated with 1 μM ATRA for 6 hr. The luciferase activities are shown as relative values (n = 3).

(C) Peritoneal macrophages were cultured in the presence or absence of 1 μM BMS493 for 6 hr. The expression of PMSGs was determined by quantitative PCR (n = 3).

(D and E) Peritoneal macrophages from 6-week-old mice bred with control diet or VAD were stimulated with 1 μM ATRA for 6 hr (D) or 24 hr (E), and then the expression of indicated genes was quantified (n = 3).

Error bars represent SD. *p < 0.05, **p < 0.01, ***p < 0.001, ****p < 0.0001. N.S., not significant.

cytometry and morphological analyses revealed that this population consists of at least three cell types: eosinophils (P1), macrophages (P2), and monocytes (P3) (Figure 4E). P2 macrophages displayed similar protein expression profiles with SPMs in terms of GATA6, CCR2, CD102, and MHC-II (Figure 4F), suggesting that continuous vitamin A deprivation results in recruitment of inflammatory macrophages. Indeed, further vitamin A deprivation (18 weeks old) significantly increased peripheral neutrophils (Figure S3), consistent with the previous study (Kuwata et al., 2000). Because it has been reported that peritoneal inflammation induces the disappearance of macrophages from peritoneal cavity, a phenomenon known as macrophage disappearance reaction (MDR) (Barth et al., 1995), these results suggest that long-term vitamin A deprivation, in addition to control of GATA6 expression, can lead to LPM disappearance through inflammation.

Although some tissues had severely reduced their size (e.g., lung and adipose tissue) at the late stage of vitamin A deprivation, frequency of tissue macrophages in the spleen and small intestine was comparable to that of mice bred on control diet (Figure S3), indicating that early macrophage differentiation was not affected by vitamin A deprivation.

Macrophage Accumulation in Omenta of Mac-*Gata6* and VAD Mice

Most of the vitamin A in the body is stored in liver as transcriptionally inactive metabolites (e.g., retinyl esters) and is continuously deployed into circulation (Hall et al., 2011). Vitamin-A-mediated transcriptional activation requires local conversion of these inactive vitamin A metabolites into biologically active retinoic acid (Duester, 2008; Gudas, 2012). The expression of neither *Gata6* nor retinoic-acid-inducible genes (*Rarb* and *Rai14*) was detected in circulating leukocytes, including monocytes (Figures S4A and S4B), suggesting that LPMs or their precursor cells (if they originate from circulating progenitors) receive retinoic acid signal after recruitment into peritoneal cavity or its associated tissues. Retinoic-acid-converting enzymes are abundantly expressed in peritoneum-associated adipose tissue, omentum, which is formed by a double layer of mesothelial cells that connects the stomach, pancreas, spleen, and colon (Maruya et al., 2011 and Figure 5A, left). Indeed, Raldh2, which is the rate-limiting enzyme for the last step of retinoic acid synthesis (retinaldehyde to retinoic acid) (Gudas, 2012), is highly expressed in omentum compared to other tissues (Figure 5B), suggesting a high local concentration of retinoic acid at this anatomical location.

Omentum contains at regular intervals opaque structures called milky spots, which are clusters of leukocytes such as B-1 cells (Figure 5A, right) (Rangel-Moreno et al., 2009).

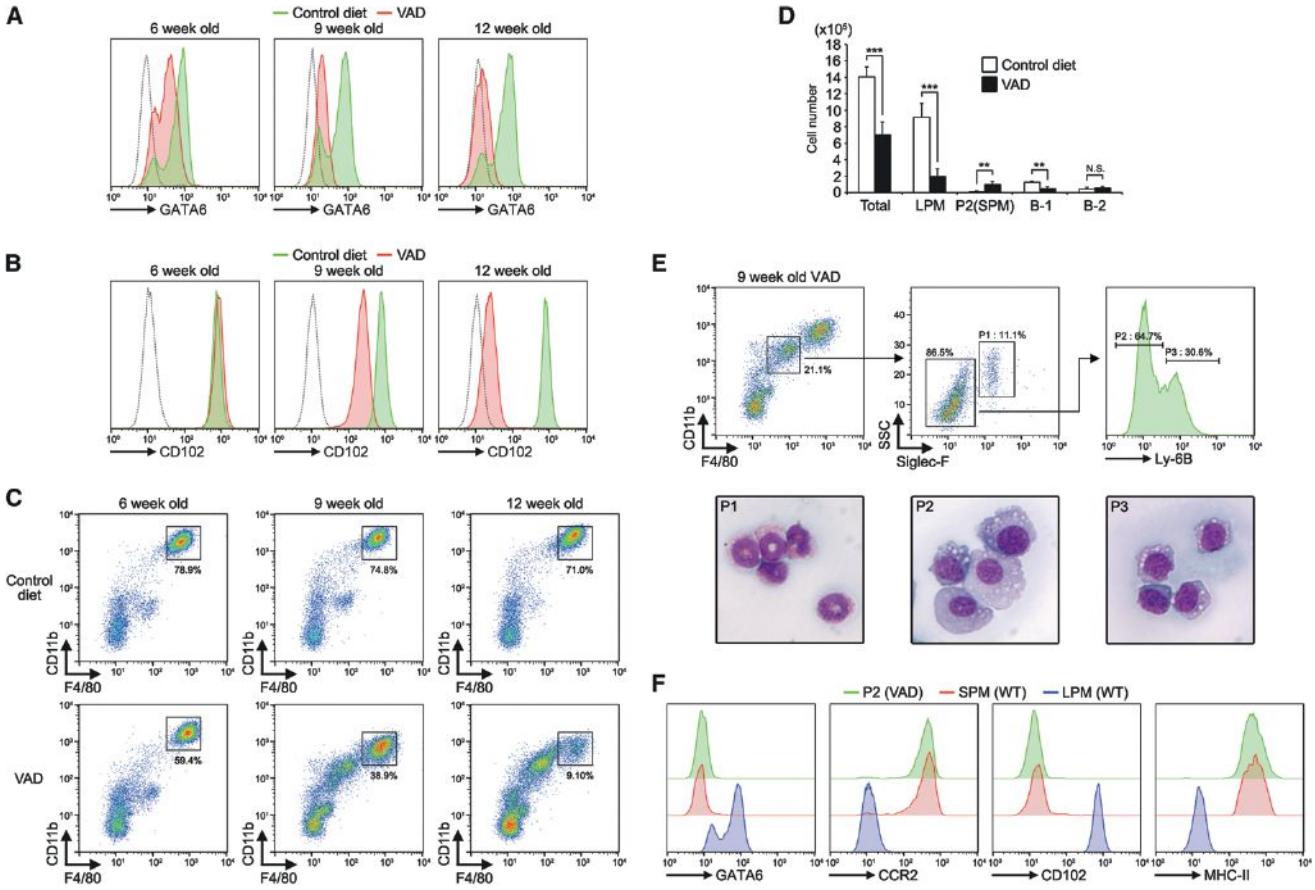

Figure 4. Essential Role of Vitamin A in PMSG Induction

(A and B) LPMs from mice fed with indicated diets were analyzed for GATA6 (A) and CD102 (B). Green, control diet; red, vitamin-A-deficient diet (VAD); dotted line, unstained control. The data are representative of at least three different mice in each group.

(C) Flow cytometry profiles of peritoneal exudate cells from 6-, 9-, and 12-week-old mice bred with control diet or VAD. The data are representative of 3–8 different mice in each group.

(D) Numbers of total cells, LPM, P2 (SPM), B-1 cells, and B-2 cells in peritoneal exudate cells from 9-week-old control diet and VAD mice (n = 5). Error bars represent SD. $^{**}p < 0.01$, $^{***}p < 0.001$. N.S., not significant.

(E) (Top) Flow cytometric gating strategy for characterization of F4/80-CD11b intermediate population. (Bottom) Wright and Giemsa staining of each of sorted subsets.

(F) P2 population in (E) and SPMs and LPMs from WT C57BL/6 mice were analyzed for GATA6, CCR2, CD102, and MHC-II by flow cytometry. The data are representative of at least two different mice in each group.

See also Figure S3.

Mac-*Gata6* KO and 9-week-old VAD mice accumulated CD11b^{+} macrophages around milky spots, as illustrated by clusters of B cells marked by B220 signal, whereas relatively few macrophages were detected in the omentum of control mice (Figure 5C). Consistent with this observation, flow cytometry analysis of omentum cells revealed increased frequency of macrophages in Mac-*Gata6* KO and VAD mice (Figure 5D, top). Omentum macrophages expressed GATA6 protein in control mice, but not in VAD or Mac-*Gata6* KO mice (Figure 5D, bottom). Together with the reduction in LPM numbers in peritoneal lavage of Mac-*Gata6* KO (Figure 1E) and VAD mice (Figure 4D), these results indicate that GATA6 and retinoic acid maintain macrophages in peritoneal cavity and that loss of these factors results in the accumulation of macrophages in the omentum. Moreover, omentum macrophages in VAD mice had reduced expression of CD102 (Figure 5D), similar to LPMs in peritoneal cavity (Figure 4B). Interestingly, administration of ATRA to VAD mice restored the expression of GATA6 in omentum (Figure 5E), confirming inducibility of GATA6 by retinoic acid in macrophages.

Intraperitoneal (IP) challenge with lipopolysaccharide (LPS) induces MDR—macrophage disappearance from peritoneal cavity (Figures 5F and S4C; Barth et al., 1995). We found that, following LPS injection, GATA6^{+} macrophages rapidly accumulated around milky spots in omentum (Figures 5C and 5D). Macrophage interaction with mesothelial cells was proposed to be a key step in MDR (Jonjić et al., 1992). Consistent with that, peritoneal macrophages from Mac-*Gata6* KO mice had enhanced interaction with mesothelial cells in vitro (Figure 5G), as well as with tissue culture plastic (Figure S4D), suggesting

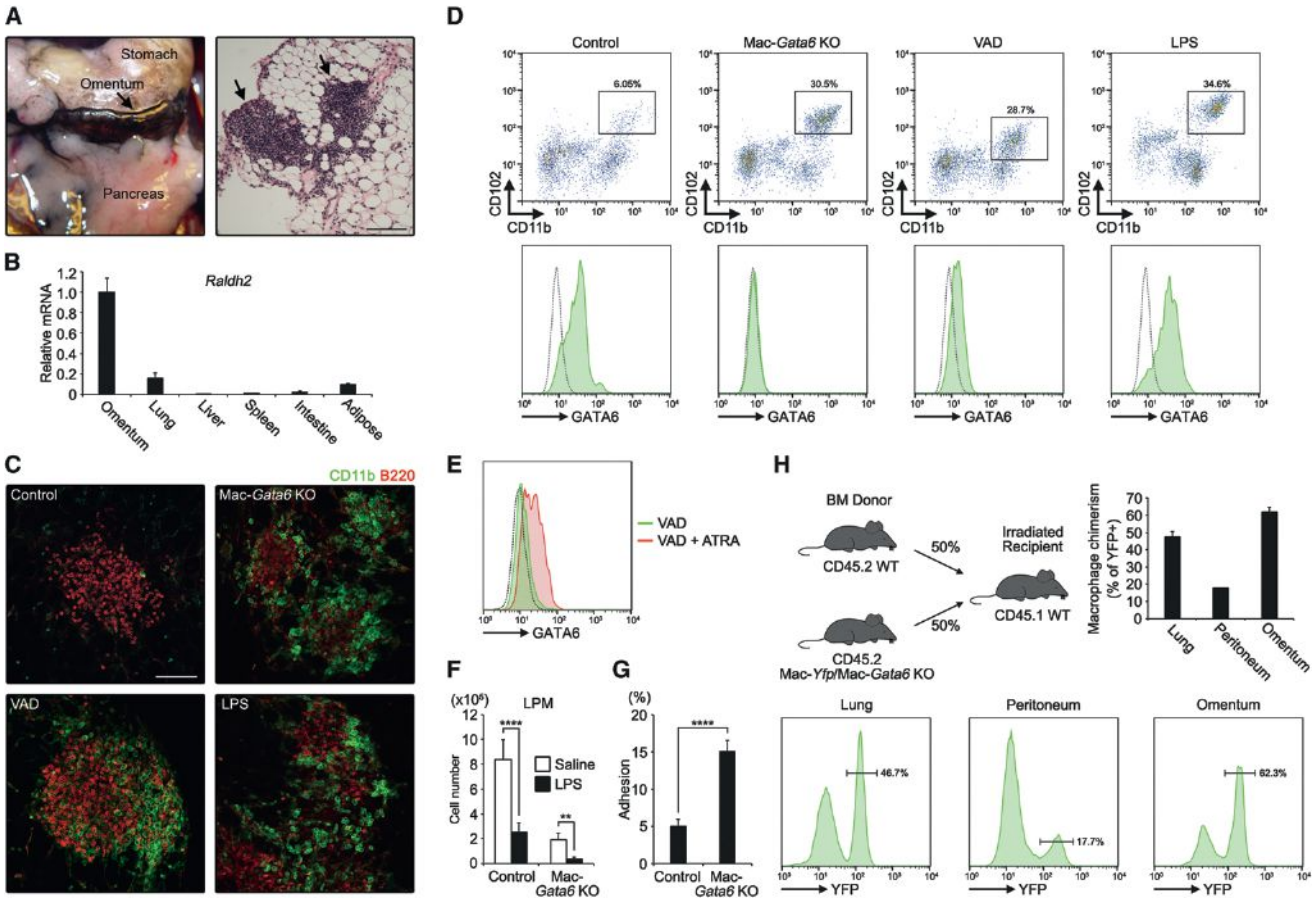

Figure 5. Accumulation of Macrophages in Omenta of Mac-*Gata6* and VAD Mice

(A) (Left) Omentum was illustrated by intraperitoneal injection of black carbon particles. (Right) Paraffin section of omentum from WT mouse was stained with hematoxylin and eosin (H&E). Clusters of leukocytes (milky spots) were indicated by arrows. Scale bar, 100 μm.

(B) Indicated tissues were determined for *Raldh2* mRNA by quantitative PCR and were expressed as relative values normalized by *Gapdh* mRNA (n = 3).

(C) Milky spots of the omenta from control, Mac-*Gata6* KO, 9-week-old VAD, and LPS-injected mice were stained as indicated color-coded lettering. Scale bars, 100 μm.

(D) (Top) Omental cells from indicated mice were analyzed by flow cytometry. (Bottom) Macrophage population in top panels (gated) was analyzed for GATA6. Dotted line showed unstained control. Plots are representative of at least five different mice in each group.

(E) Macrophages from omenta of VAD- or ATRA-treated VAD mice were analyzed for GATA6. Histogram is a representative of two different mice in each group.

(F) Absolute cell numbers of LPMs present in the peritoneal exudate cells of indicated mice (n = 3) were counted 3 hr post-IP injection of saline or 10 μg of LPS.

(G) Peritoneal macrophages from indicated mice were cultured for 2 hr on monolayers of mesothelial cells. Percentage of cells adherent to mesothelial cells was determined (n = 5).

(H) (Upper-left) Schematic of mixed bone marrow transfer. Bone marrow cells from CD45.2 WT and that from Mac-*Gata6* KO mice in macrophage-specific YFP-expressing strain (Mac-*Yfp*/Mac-*Gata6* KO) were mixed at a ratio of 1:1 and were then injected into lethally irradiated CD45.1 WT recipients. (Upper-right) Percent chimerism of YFP^+ macrophages in indicated tissues was shown (n = 4). (Bottom) Representative flow cytometry profiles for YFP were shown. YFP-positive population was gated. Error bars represent SD. $^{**}p < 0.01$, $^{****}p < 0.0001$.

See also Figure S4.

that alteration of adhesion property might be involved in macrophage redistribution in Mac-*Gata6* KO mice.

There were two possible explanations for the accumulation of macrophages in the omenta in Mac-*Gata6* KO and VAD mice. One is that cell-extrinsic signals, such as constitutive peritoneal inflammation, induce macrophage migration from peritoneal cavity to omentum in these mice. This possibility is suggested by the appearance of inflammatory macrophages (P2 or SPM) in VAD mice (Figures 4E and 4F), but not in Mac-*Gata6* KO mice (Figure 1E). Another possibility is that GATA6 controls macrophage localization in a cell-autonomous manner. As bone marrow (BM) transfer could establish $GATA6^+$ macrophage population in peritoneal cavity (Figure S4E), we examined mixed BM chimeric mice to distinguish between these possibilities. We prepared BM cells isolated from WT and Mac-*Yfp*/Mac-*Gata6* KO mice (*LysM-Cre*;*R26*-stop-*Yfp*; *Gata6*-floxed) and cotransferred into lethally irradiated mice at the 1:1 ratio (Figure 5H). Alveolar macrophages in lungs were observed to maintain initial chimerism (50%) at 5 weeks post-BM transfer (47.5% ± 3.2% for Mac-*Gata6* KO). In contrast, Mac-*Gata6*

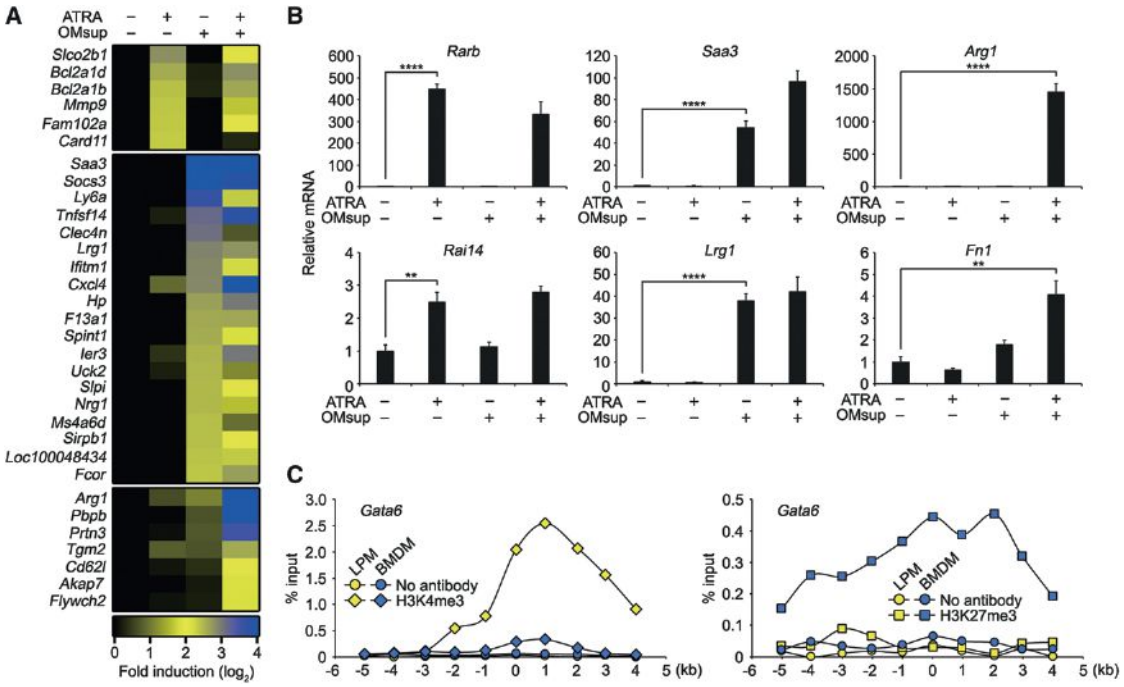

Figure 6. Induction of PMSGs by Omentum Factor

(A) Heatmap of microarray signals upregulated at least five times by 1 μM ATRA or OMsup stimulation compared to unstimulated sample and upregulated at least three times by a combination of ATRA and OMsup compared to individual stimulations after 24 hr. Expression levels were shown as fold induction to unstimulated BMDMs and were expressed by relative values (log-2).

(B) BMDMs were cultured with 1 μM ATRA and/or OMsup for 24 hr. The expression of indicated genes was analyzed by quantitative PCR and expressed as relative values normalized by *Gapdh* mRNA (n = 3).

(C) LPMs (yellow) and BMDM (blue) were analyzed by ChIP for *Gata6* loci without antibody (circle) or with antibodies against H3K4me3 (diamond) or H3K27me3 (square). The data are represented as %input. The x axis depicts probe location on each loci relative to the transcription start site.

Error bars represent SD. **p < 0.01, ****p < 0.0001. See also Figure S5.

KO macrophages greatly reduced frequency in peritoneal cavity (17.6% ± 0.2%) but increased in omentum (62.0% ± 2.7%). This indicates that the accumulation of macrophages in omentum of Mac-*Gata6* KO mice is caused by cell-autonomous defect of macrophage phenotype. In addition, these results suggest that macrophages receive retinoic acid provided by omentum and migrate to peritoneal cavity in a GATA6-dependent manner.

Coordinated Induction of PMSGs by Retinoic Acid and Omentum-Derived Factor(s)

We next examined whether ATRA alone or together with other local tissue-derived signals controls functional polarization of peritoneal macrophages. We treated BMDMs with ATRA and/or omentum culture supernatant (OMsup) as a source of additional tissue-derived signals. OMsup was prepared with serum-free medium, which did not contain any vitamin A metabolites. Genes induced by these stimuli were analyzed by microarray (Figure 6A). Interestingly, several GATA6-independent PMSGs (*Saa3*, *Lrg1*, *Arg1*, and *Prtn3*) were strongly induced in BMDMs stimulated with OMsup in the presence or absence of ATRA. Quantitative PCR analysis revealed that some PMSGs (*Rarb*, *Rai14*, and *Apoc2*) were induced by ATRA, whereas other PMSGs (*Saa3*, *Lrg1*, and *Hp*) were induced by OMsup in a retinoic-acid-independent manner (Figures 6B, S5A, and S5B). Furthermore, the induction of *Arg1*, *Fn1*, and *Prtn3* genes was only detected in the presence of both ATRA and OMsup. This result suggests that the retinoic acid and omentum-derived factor(s) play a role, alone and in combination, to control distinct subsets of PMSGs. In contrast to these GATA6-independent PMSGs, *Gata6* was not induced in BMDMs by either or both ATRA and OMsup. In addition, it was also unclear why GATA6 was only expressed in LPMs, but not in SPMs and Thio-pMacs that were present in peritoneal cavity, even though RAR mRNA was expressed in these cells (Figure S5C). Histone 3 lysine 4 trimethylation (H3K4me3) is associated with transcriptionally active or poised loci, whereas H3K27me3 is associated with gene silencing (Kouzarides, 2007). The presence of H3K4me3 modification was detected in *Gata6* locus of LPMs, whereas BMDMs and Thio-pMacs had H3K27me3 modification (Figures 6C and S5D). This indicates that *Gata6* locus of BMDMs and Thio-pMacs is epigenetically silenced, which presumably explains why *Gata6* and its target genes were not expressed in these cell types.

The expression of *Arg1* was remarkably induced by the combination of retinoic acid and omentum factor(s). Although Arg1 is one of the signature genes for IL-4/IL-13-induced M2 macrophage polarization, which is mediated by IL-4 receptor

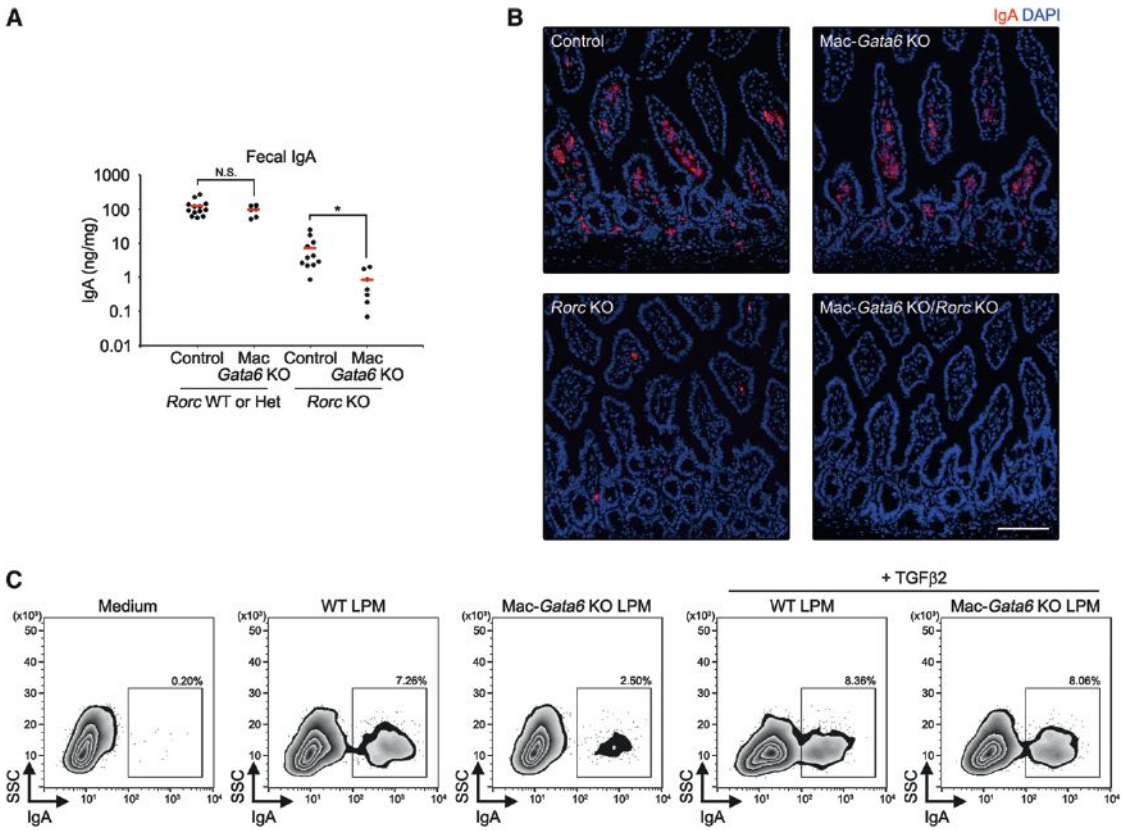

Figure 7. GATA6 in Macrophage-Dependent Regulation of Gut IgA

(A) Fecal supernatant from unimmunized indicated mice (8 weeks old) were analyzed for IgA. Each point represents one mouse. Error bars represent mean values. *$p < 0.05$. N.S., not significant.

(B) Immunohistochemistry analysis for small intestines of indicated mice. Red, IgA; blue, DAPI. Scale bars, 100 μm.

(C) Flow cytometry analysis of IgA-positive peritoneal B-1 cells cultured with or without LPMs from WT or Mac-*Gata6* KO mice and recombinant TGF-β2 in the presence of BAFF/LPS/ATRA for 4 days.

See also Figure S6.

α subunit (IL4Rα) and STAT6 (Chawla et al., 2011), the expression of *Arg1* in peritoneal macrophages was intact in *Il4ra* KO and *Stat6* KO mice (Figure S5E). Consistent with this, the M1 (*Nos2*) and M2 (*Cd206*, *Retnla*, *Chi3l3*, and *Chi3l4*) marker genes were differently expressed across different tissue macrophages (Figure S5F).

GATA6 in Macrophages Controls Gut IgA Response

We next asked whether the retinoic acid-GATA6 pathway controls peritoneal macrophage-specific functions and what these functions are. Among the genes that are highly and specifically expressed in peritoneal macrophages in a GATA6-dependent manner are *Tgfb2*; *Ltbp1*, which regulates extracellular matrix deposition of TGF-β; and *Thbs1*, which promotes activation of latent form of TGF-β (Fortunel et al., 2000) (Figures 2A–2C and 2E). TGF-β and retinoic acid are the most prominent factors inducing IgA class switching as well as gut-homing receptor expression on the B cell (Hall et al., 2011; Roy et al., 2013). In addition, peritoneal B-1 cells can give rise to IgA-secreting plasma cells in the gut (Baumgarth, 2011; Mora and von Andrian, 2009). Therefore, we asked whether GATA6 in peritoneal macrophages plays a role in gut IgA production through peritoneal B-1 cell regulation. B-1 cells of peritoneal cavity are thought to directly migrate into intestinal lamina propria and give rise to IgA-secreting cells in a manner that is independent of gut-associate lymphoid tissue (GALT) (Fagarasan et al., 2010; Uematsu et al., 2008). Because B-2 cell IgA production can mask the contribution of B-1 cells, we crossed Mac-*Gata6* KO mice to *Rorc*-deficient ($Rorc^{gfp/gfp}$) mice, which lack secondary lymphoid organs (Eberl et al., 2004). Deficiency of the *Rorc* gene resulted in a reduced but detectable amount of fecal IgA (Figure 7A). Mac-*Gata6* KO/*Rorc* KO mice had significantly reduced fecal IgA compared to *Rorc* KO mice (Figure 7A), whereas serum natural IgM-, IgA-, and PC-specific IgM were comparably detected (Figure S6A). Consistent with this, the number of IgA^+ cells in the lamina propria was much fewer in Mac-*Gata6* KO/*Rorc* KO mice (Figures 7B and S6B). GATA6 deficiency did not affect peritoneal B-1 cell population (Figure S6C), and the expression of *LysM* and *Gata6* was not detected in peritoneal B-1 cells (Figures S6D and S6E), indicating that a reduction in IgA production was not due to B-1 cell-intrinsic alteration. Additionally, GATA6 protein in small intestine was only detected in intestinal epithelial

cells, but not in lamina propria cells, and the epithelial expression was not affected in Mac-*Gata6* KO mice (Figure S6F). This excludes the possibility of the contribution of lamina propria cells (e.g., macrophages and dendritic cells) to the IgA phenotype.

Lastly, to determine the role of GATA6-dependent expression of TGF-β in the generation of IgA, we examined coculture of peritoneal B-1 cells with LPMs. Peritoneal B-1 cells underwent IgA class switching by coculture with WT LPMs in the presence of ATRA (Figure 7C). Mac-*Gata6* KO LPMs were deficient in the generation of IgA^+ B-1 cells, and this defect was restored by the addition of recombinant TGF-β2. In contrast, GATA6 deficiency in LPMs did not affect the expression of gut-homing receptors (CCR9 and integrin-α4β7) on B-1 cells (Figure S6G). These results indicate that GATA6 in peritoneal macrophages is critical for GALT-independent IgA production by peritoneal B-1 cells.

DISCUSSION

Although accumulating evidence highlights the diversity of tissue-specific macrophage phenotypes, the extracellular signals that regulate specialized macrophage functions are largely unknown. Here, we show how local tissue-derived signals, including retinoic acid, control peritoneal macrophage-specific transcriptional program. A transcription factor GATA6, which is uniquely expressed in peritoneal, but not other macrophage subsets, is induced by retinoic acid and controls a subset of peritoneal macrophage functions, including their compartmentalization and control of IgA production by B-1 cells.

Previous studies showed the presence of macrophage precursor cells in omentum (Daems and de Bakker, 1982), local proliferation of omentum macrophages (Wijffels et al., 1992), and the production of macrophage colony-stimulating factor (M-CSF) in milky spot stromal cells (Ratajczak et al., 1987), suggesting that omentum may serve as a site for peritoneal macrophage development. Together with these earlier observations, a high level of *Raldh2* expression in omentum (Figure 5B) suggests that, during macrophage development, omentum provides retinoic acid, which is required for the efficient migration of macrophages to peritoneal cavity through the induction of GATA6. In addition, our data suggest that omentum provides not only retinoic acid, but also additional factor(s) for the induction of a subset of PMSGs (Figure 6B). Thus, multiple signals that are present in the local tissue environment may control different gene expression programs in macrophages.

Although the expression of several PMSGs was induced by ATRA, OMsup, or a combination of both factors in BMDMs (Figures 6B and S5A), the induction of the *Gata6* gene by any of these signals was not detected in BMDMs, even though hematopoietic progenitors that give rise to BMDMs can generate GATA6-positive LPMs in vivo, as demonstrated by BM chimera experiments (Figure S4E). Interestingly, we found the *Gata6* locus to have silencing chromatin modifications (H3K27me3) in BMDMs and inflammatory macrophages, whereas *Gata6* locus in LPMs has an H3K4me3 mark associated with active chromatin (Figures 6C and S5D). In multipotent progenitor stage, developmental genes are bivalently marked by H3K4me3 and H3K27me3 and are thus primed for activation prior to differentiation (Kraushaar and Zhao, 2013). As cells differentiate into different lineages, these bivalent modifications resolve into monovalent H3K27me3 or H3K4me3 modifications. Thus, our findings suggest that induction of *Gata6* gene in peritoneal macrophages requires at least two steps. First, *Gata6* locus is epigenetically modified to remove the silencing histone modification H3K27me3, making it competent for induction at the second step, when omentum-derived ATRA induces *Gata6* expression through RAR. The signal involved in epigenetic modification of *Gata6* locus and the anatomical location where this signal is provided will need to be determined in future studies because this mechanism may be applicable to other compartment-specific cell differentiation pathways.

GATA6 has a bimodal expression in LPMs (Figure 1C). Interestingly, the GATA6-high LPM population but not GATA6-low population is positive for proliferation marker Ki67 (Figure S1G), suggesting that GATA6-high LPMs might reflect newly migrated population from omentum after proliferation. GATA6 target gene(s) responsible for macrophage localization in peritoneal cavity and chemoattractive signal that might regulate macrophage egress from omentum (if such signals exist) remain to be identified.

Previous studies identified transcription factors that control tissue specific transcription programs in macrophages. However, as the deficiency of these transcription factors resulted in the disappearance of corresponding macrophage subsets from tissues, it was not possible to determine the role of these transcription factors in the tissue-specific gene regulation. In this study, we found that PMSGs fall into GATA6-dependent and GATA6-independent subsets. Thus, tissue-specific macrophage phenotypes can be defined by a combination of multiple transcription factors, each controlling different functional programs. For example, high expression of transcription factors RARβ and NFE2 was detected in peritoneal macrophages (Figures 2B and S2B), suggesting that these transcription factors may have a role in GATA6-independent gene regulation. Importantly, we found that GATA6 is not essential for the development of peritoneal macrophages but is required for their maintenance in the proper tissue compartment. Thus, some macrophage subset-specific transcription factors and associated gene expression programs can control macrophage localization and maintenance in a particular tissue compartment, rather than macrophage development.

Tissue macrophages are derived from two sources. Traditionally, all tissue macrophages have been considered to derive from circulating monocytes originated from hematopoietic stem cells (Gordon and Taylor, 2005). Recent studies uncovered that a substantial portion of tissue macrophages arises from yolk sac during embryogenesis, and these cells are maintained by local proliferation (Ginhoux et al., 2010; Schulz et al., 2012). Together with the previous report (Schulz et al., 2012), our data would suggest that LPMs are most likely yolk sac derived. However, our BM transfer experiment showed that hematopoietic-stem-cell-derived macrophages are also able to express GATA6 in peritoneal cavity. Although the details of the origin of LPMs will need to be established further, the data so far suggests that a GATA6-driven program can generate LPMs from either yolk sac or hematopoietic progenitors.

Vitamin A deficiency is an important public health problem in humans, particularly in developing countries, where it is associated with increased susceptibility to gastrointestinal and lung infections, poor response to vaccination, increased HIV pathogenesis, and overall increased mortality, especially in children (Cassani et al., 2012). Vitamin A can modulate the function and development of many immune cell types, including T cells (Iwata et al., 2004; Mucida et al., 2007), B cells (Mora et al., 2006), dendritic cells (Coombes et al., 2007), innate lymphoid cells (Spencer et al., 2014), and B-1 cells (Maruya et al., 2011). Our study provides additional insights into retinoic acid function in the immune system. Specifically, retinoic-acid-dependent GATA6-TGF-β induction in peritoneal macrophages regulates B-1 cell-mediated gut IgA production. Previous studies showed that TGF-β can be provided by dendritic cells and stromal cells in intestinal lamina propria for IgA class switching in peritoneal B-1 cells (Fagarasan et al., 2010). It will be interesting to determine the contribution or distinct roles of LPM-derived and lamina propria cell-derived TGF-β in the generation of intestinal IgA. It is possible that the preferential IgA class-switching property of peritoneal B-1 cells (Kaminski and Stavnezer, 2006; Roy et al., 2013) is mediated by the priming effect of TGF-β2 provided from LPMs. B-1 cell-derived IgA plays a dominant role in the recognition of commensal bacteria compared to B-2 cell-derived gut IgA (Macpherson et al., 2000). It will be interesting to determine the role of GATA6-dependent gut IgA production in the maintenance of intestinal microbial homeostasis.

The expression level of PMSGs, including GATA6, was gradually affected by the dietary vitamin A depletion (Figures 4A-4C) and was restored by exogenous ATRA (Figures 3D and 3E) and suppressed by RAR inhibition (Figure 3C), suggesting that the availability of the instructive signals can affect the degree of tissue-specific gene expression in macrophages. Macrophages may thus constantly survey local tissue status and dynamically change their phenotype to deal with continuously changing tissue environment. Thus, the diversity of tissue macrophage phenotypes may, at least in part, be due to a reversible transcriptional program activated on demand by tissue-derived signals.

EXPERIMENTAL PROCEDURES

Extended Experimental Procedures are included in the Supplemental Information.

Mice

All mice were bred in the Yale University School of Medicine animal facility in specific pathogen-free conditions, and experiments were performed in accordance with the institutional animal care and use guidelines. Unless specifically indicated, 8- to 16-week-old same-gender littermates were used and data were pooled where indicated. *Ccr2*$^{-/-}$, *Gata6*-floxed, *LysM-cre*, Rosa26-floxed-*Yfp*, *Rorc*$^{gfp/gfp}$, *Il4ra*$^{-/-}$, and *Stat6*$^{-/-}$ mice were obtained from Jackson Laboratories. *Gata6*-floxed mice were backcrossed to C57BL/6 for 6–11 generations in our facility. Hematology analysis was performed by the animal healthcare service Antech.

Statistical Analysis

All experiments were performed at least twice. Results were statistically analyzed using an analysis of variance (ANOVA) test or Student's *t* test. A p value of < 0.05 was considered to be statistically significant.

ACCESSION NUMBERS

The GEO accession number for the microarray data reported in this paper is GSE56711.

SUPPLEMENTAL INFORMATION

Supplemental Information includes Extended Experimental Procedures and six figures and can be found with this article online at http://dx.doi.org/10.1016/j.cell.2014.04.016.

ACKNOWLEDGMENTS

We thank members of the Medzhitov laboratory and the W.M. Keck facility for microarray analysis. Y.O. was supported by the Japan Society for the Promotion of Science (JSPS), Uehara Memorial Foundation, and Kanae Foundation for the Promotion of Medical Science. R.M. lab is supported by The Blavatnik Family Foundation, grants from NIH (AI046688, AI089771, CA157461) and the Howard Hughes Medical Institute.

Received: January 16, 2014
Revised: March 22, 2014
Accepted: April 15, 2014
Published: May 1, 2014

REFERENCES

A-Gonzalez, N., Guillen, J.A., Gallardo, G., Diaz, M., de la Rosa, J.V., Hernandez, I.H., Casanova-Acebes, M., Lopez, F., Tabraue, C., Beceiro, S., et al. (2013). The nuclear receptor LXRα controls the functional specialization of splenic macrophages. Nat. Immunol. *14*, 831–839.

Ansel, K.M., Harris, R.B., and Cyster, J.G. (2002). CXCL13 is required for B1 cell homing, natural antibody production, and body cavity immunity. Immunity *16*, 67–76.

Barth, M.W., Hendrzak, J.A., Melnicoff, M.J., and Morahan, P.S. (1995). Review of the macrophage disappearance reaction. J. Leukoc. Biol. *57*, 361–367.

Baumgarth, N. (2011). The double life of a B-1 cell: self-reactivity selects for protective effector functions. Nat. Rev. Immunol. *11*, 34–46.

Biswas, S.K., and Mantovani, A. (2010). Macrophage plasticity and interaction with lymphocyte subsets: cancer as a paradigm. Nat. Immunol. *11*, 889–896.

Boyle, W.J., Simonet, W.S., and Lacey, D.L. (2003). Osteoclast differentiation and activation. Nature *423*, 337–342.

Cain, D.W., O'Koren, E.G., Kan, M.J., Womble, M., Sempowski, G.D., Hopper, K., Gunn, M.D., and Kelsoe, G. (2013). Identification of a tissue-specific, C/EBPβ-dependent pathway of differentiation for murine peritoneal macrophages. J. Immunol. *191*, 4665–4675.

Capo-Chichi, C.D., Rula, M.E., Smedberg, J.L., Vanderveer, L., Parmacek, M.S., Morrisey, E.E., Godwin, A.K., and Xu, X.X. (2005). Perception of differentiation cues by GATA factors in primitive endoderm lineage determination of mouse embryonic stem cells. Dev. Biol. *286*, 574–586.

Cassani, B., Villablanca, E.J., De Calisto, J., Wang, S., and Mora, J.R. (2012). Vitamin A and immune regulation: role of retinoic acid in gut-associated dendritic cell education, immune protection and tolerance. Mol. Aspects Med. *33*, 63–76.

Chang, J., Thangamani, S., Kim, M.H., Ulrich, B., Morris, S.M., Jr., and Kim, C.H. (2013). Retinoic acid promotes the development of Arg1-expressing dendritic cells for the regulation of T-cell differentiation. Eur. J. Immunol. *43*, 967–978.

Chawla, A., Nguyen, K.D., and Goh, Y.P. (2011). Macrophage-mediated inflammation in metabolic disease. Nat. Rev. Immunol. *11*, 738–749.

Clausen, B.E., Burkhardt, C., Reith, W., Renkawitz, R., and Förster, I. (1999). Conditional gene targeting in macrophages and granulocytes using LysMcre mice. Transgenic Res. *8*, 265–277.

Coombes, J.L., Siddiqui, K.R., Arancibia-Cárcamo, C.V., Hall, J., Sun, C.M., Belkaid, Y., and Powrie, F. (2007). A functionally specialized population of

mucosal CD103+ DCs induces Foxp3+ regulatory T cells via a TGF-beta and retinoic acid-dependent mechanism. J. Exp. Med. *204*, 1757–1764.

Daems, W.T., and de Bakker, J.M. (1982). Do resident macrophages proliferate? Immunobiology *161*, 204–211.

Davies, L.C., Jenkins, S.J., Allen, J.E., and Taylor, P.R. (2013). Tissue-resident macrophages. Nat. Immunol. *14*, 986–995.

de Thé, H., Vivanco-Ruiz, M.M., Tiollais, P., Stunnenberg, H., and Dejean, A. (1990). Identification of a retinoic acid responsive element in the retinoic acid receptor beta gene. Nature *343*, 177–180.

Duester, G. (2008). Retinoic acid synthesis and signaling during early organogenesis. Cell *134*, 921–931.

Eberl, G., Marmon, S., Sunshine, M.J., Rennert, P.D., Choi, Y., and Littman, D.R. (2004). An essential function for the nuclear receptor RORgamma(t) in the generation of fetal lymphoid tissue inducer cells. Nat. Immunol. *5*, 64–73.

Fagarasan, S., Kawamoto, S., Kanagawa, O., and Suzuki, K. (2010). Adaptive immune regulation in the gut: T cell-dependent and T cell-independent IgA synthesis. Annu. Rev. Immunol. *28*, 243–273.

Fortunel, N.O., Hatzfeld, A., and Hatzfeld, J.A. (2000). Transforming growth factor-beta: pleiotropic role in the regulation of hematopoiesis. Blood *96*, 2022–2036.

Gautier, E.L., Shay, T., Miller, J., Greter, M., Jakubzick, C., Ivanov, S., Helft, J., Chow, A., Elpek, K.G., Gordonov, S., et al.; Immunological Genome Consortium (2012). Gene-expression profiles and transcriptional regulatory pathways that underlie the identity and diversity of mouse tissue macrophages. Nat. Immunol. *13*, 1118–1128.

Ghosn, E.E., Cassado, A.A., Govoni, G.R., Fukuhara, T., Yang, Y., Monack, D.M., Bortoluci, K.R., Almeida, S.R., Herzenberg, L.A., and Herzenberg, L.A. (2010). Two physically, functionally, and developmentally distinct peritoneal macrophage subsets. Proc. Natl. Acad. Sci. USA *107*, 2568–2573.

Ginhoux, F., Greter, M., Leboeuf, M., Nandi, S., See, P., Gokhan, S., Mehler, M.F., Conway, S.J., Ng, L.G., Stanley, E.R., et al. (2010). Fate mapping analysis reveals that adult microglia derive from primitive macrophages. Science *330*, 841–845.

Gordon, S., and Martinez, F.O. (2010). Alternative activation of macrophages: mechanism and functions. Immunity *32*, 593–604.

Gordon, S., and Taylor, P.R. (2005). Monocyte and macrophage heterogeneity. Nat. Rev. Immunol. *5*, 953–964.

Gudas, L.J. (2012). Emerging roles for retinoids in regeneration and differentiation in normal and disease states. Biochim. Biophys. Acta *1821*, 213–221.

Hall, J.A., Grainger, J.R., Spencer, S.P., and Belkaid, Y. (2011). The role of retinoic acid in tolerance and immunity. Immunity *35*, 13–22.

Hume, D.A., Robinson, A.P., MacPherson, G.G., and Gordon, S. (1983). The mononuclear phagocyte system of the mouse defined by immunohistochemical localization of antigen F4/80. Relationship between macrophages, Langerhans cells, reticular cells, and dendritic cells in lymphoid and hematopoietic organs. J. Exp. Med. *158*, 1522–1536.

Iwata, M., Hirakiyama, A., Eshima, Y., Kagechika, H., Kato, C., and Song, S.Y. (2004). Retinoic acid imprints gut-homing specificity on T cells. Immunity *21*, 527–538.

Jonjić, N., Peri, G., Bernasconi, S., Sciacca, F.L., Colotta, F., Pelicci, P., Lanfrancone, L., and Mantovani, A. (1992). Expression of adhesion molecules and chemotactic cytokines in cultured human mesothelial cells. J. Exp. Med. *176*, 1165–1174.

Kaminski, D.A., and Stavnezer, J. (2006). Enhanced IgA class switching in marginal zone and B1 B cells relative to follicular/B2 B cells. J. Immunol. *177*, 6025–6029.

Kohyama, M., Ise, W., Edelson, B.T., Wilker, P.R., Hildner, K., Mejia, C., Frazier, W.A., Murphy, T.L., and Murphy, K.M. (2009). Role for Spi-C in the development of red pulp macrophages and splenic iron homeostasis. Nature *457*, 318–321.

Kouzarides, T. (2007). Chromatin modifications and their function. Cell *128*, 693–705.

Kraushaar, D.C., and Zhao, K. (2013). The epigenomics of embryonic stem cell differentiation. Int. J. Biol. Sci. *9*, 1134–1144.

Kurihara, T., Warr, G., Loy, J., and Bravo, R. (1997). Defects in macrophage recruitment and host defense in mice lacking the CCR2 chemokine receptor. J. Exp. Med. *186*, 1757–1762.

Kutty, R.K., Kutty, G., Samuel, W., Duncan, T., Bridges, C.C., El-Sherbeeny, A., Nagineni, C.N., Smith, S.B., and Wiggert, B. (2001). Molecular characterization and developmental expression of NORPEG, a novel gene induced by retinoic acid. J. Biol. Chem. *276*, 2831–2840.

Kuwata, T., Wang, I.M., Tamura, T., Ponnamperuma, R.M., Levine, R., Holmes, K.L., Morse, H.C., De Luca, L.M., and Ozato, K. (2000). Vitamin A deficiency in mice causes a systemic expansion of myeloid cells. Blood *95*, 3349–3356.

Lawrence, T., and Natoli, G. (2011). Transcriptional regulation of macrophage polarization: enabling diversity with identity. Nat. Rev. Immunol. *11*, 750–761.

Macpherson, A.J., Gatto, D., Sainsbury, E., Harriman, G.R., Hengartner, H., and Zinkernagel, R.M. (2000). A primitive T cell-independent mechanism of intestinal mucosal IgA responses to commensal bacteria. Science *288*, 2222–2226.

Maruya, M., Suzuki, K., Fujimoto, H., Miyajima, M., Kanagawa, O., Wakayama, T., and Fagarasan, S. (2011). Vitamin A-dependent transcriptional activation of the nuclear factor of activated T cells c1 (NFATc1) is critical for the development and survival of B1 cells. Proc. Natl. Acad. Sci. USA *108*, 722–727.

Mauney, J.R., Ramachandran, A., Yu, R.N., Daley, G.Q., Adam, R.M., and Estrada, C.R. (2010). All-trans retinoic acid directs urothelial specification of murine embryonic stem cells via GATA4/6 signaling mechanisms. PLoS ONE *5*, e11513.

Mora, J.R., and von Andrian, U.H. (2009). Role of retinoic acid in the imprinting of gut-homing IgA-secreting cells. Semin. Immunol. *21*, 28–35.

Mora, J.R., Iwata, M., Eksteen, B., Song, S.Y., Junt, T., Senman, B., Otipoby, K.L., Yokota, A., Takeuchi, H., Ricciardi-Castagnoli, P., et al. (2006). Generation of gut-homing IgA-secreting B cells by intestinal dendritic cells. Science *314*, 1157–1160.

Mucida, D., Park, Y., Kim, G., Turovskaya, O., Scott, I., Kronenberg, M., and Cheroutre, H. (2007). Reciprocal TH17 and regulatory T cell differentiation mediated by retinoic acid. Science *317*, 256–260.

Murray, P.J., and Wynn, T.A. (2011). Protective and pathogenic functions of macrophage subsets. Nat. Rev. Immunol. *11*, 723–737.

Rangel-Moreno, J., Moyron-Quiroz, J.E., Carragher, D.M., Kusser, K., Hartson, L., Moquin, A., and Randall, T.D. (2009). Omental milky spots develop in the absence of lymphoid tissue-inducer cells and support B and T cell responses to peritoneal antigens. Immunity *30*, 731–743.

Ratajczak, M.Z., Jaskulski, D., Pojda, Z., and Wiktor-Jedrzejczak, W. (1987). Omental lymphoid organ as a source of macrophage colony stimulating activity in peritoneal cavity. Clin. Exp. Immunol. *69*, 198–203.

Roy, B., Brennecke, A.M., Agarwal, S., Krey, M., Düber, S., and Weiss, S. (2013). An intrinsic propensity of murine peritoneal B1b cells to switch to IgA in presence of TGF-β and retinoic acid. PLoS ONE *8*, e82121.

Schulz, C., Gomez Perdiguero, E., Chorro, L., Szabo-Rogers, H., Cagnard, N., Kierdorf, K., Prinz, M., Wu, B., Jacobsen, S.E., Pollard, J.W., et al. (2012). A lineage of myeloid cells independent of Myb and hematopoietic stem cells. Science *336*, 86–90.

Smith, S.M., Levy, N.S., and Hayes, C.E. (1987). Impaired immunity in vitamin A-deficient mice. J. Nutr. *117*, 857–865.

Sodhi, C.P., Li, J., and Duncan, S.A. (2006). Generation of mice harbouring a conditional loss-of-function allele of Gata6. BMC Dev. Biol. *6*, 19.

Spencer, S.P., Wilhelm, C., Yang, Q., Hall, J.A., Bouladoux, N., Boyd, A., Nutman, T.B., Urban, J.F., Jr., Wang, J., Ramalingam, T.R., et al. (2014). Adaptation of innate lymphoid cells to a micronutrient deficiency promotes type 2 barrier immunity. Science *343*, 432–437.

Stout, R.D., Jiang, C., Matta, B., Tietzel, I., Watkins, S.K., and Suttles, J. (2005). Macrophages sequentially change their functional phenotype in

response to changes in microenvironmental influences. J. Immunol. *175*, 342–349.

Takayanagi, H., Kim, S., Koga, T., Nishina, H., Isshiki, M., Yoshida, H., Saiura, A., Isobe, M., Yokochi, T., Inoue, J., et al. (2002). Induction and activation of the transcription factor NFATc1 (NFAT2) integrate RANKL signaling in terminal differentiation of osteoclasts. Dev. Cell *3*, 889–901.

Uematsu, S., Fujimoto, K., Jang, M.H., Yang, B.G., Jung, Y.J., Nishiyama, M., Sato, S., Tsujimura, T., Yamamoto, M., Yokota, Y., et al. (2008). Regulation of humoral and cellular gut immunity by lamina propria dendritic cells expressing Toll-like receptor 5. Nat. Immunol. *9*, 769–776.

Wijffels, J.F., Hendrickx, R.J., Steenbergen, J.J., Eestermans, I.L., and Beelen, R.H. (1992). Milky spots in the mouse omentum may play an important role in the origin of peritoneal macrophages. Res. Immunol. *143*, 401–409.

Wynn, T.A., Chawla, A., and Pollard, J.W. (2013). Macrophage biology in development, homeostasis and disease. Nature *496*, 445–455.

Cell

Skin β-Endorphin Mediates Addiction to UV Light

Gillian L. Fell,[1,5,6] Kathleen C. Robinson,[1,5] Jianren Mao,[2] Clifford J. Woolf,[3,4] and David E. Fisher[1,*]
[1]Cutaneous Biology Research Center, Department of Dermatology and MGH Cancer Center, Massachusetts General Hospital, Harvard Medical School, Boston, MA 02114, USA
[2]MGH Center for Translational Pain Research, Department of Anesthesia, Critical Care and Pain Medicine, Massachusetts General Hospital, Harvard Medical School, Boston, MA 02114, USA
[3]FM Kirby Neurobiology Center, Children's Hospital Boston, Boston, MA 02114, USA
[4]Department of Neurobiology, Harvard Medical School, Boston, MA 02114, USA
[5]Co-first author
[6]Present address: Department of Surgery, Brigham and Women's Hospital, 75 Francis Street, Boston, MA 02115, USA
*Correspondence: dfisher3@partners.org
http://dx.doi.org/10.1016/j.cell.2014.04.032

SUMMARY

UV light is an established carcinogen, yet evidence suggests that UV-seeking behavior has addictive features. Following UV exposure, epidermal keratinocytes synthesize proopiomelanocortin (POMC) that is processed to melanocyte-stimulating hormone, inducing tanning. We show that, in rodents, another POMC-derived peptide, β-endorphin, is coordinately synthesized in skin, elevating plasma levels after low-dose UV. Increases in pain-related thresholds are observed and reversed by pharmacologic opioid antagonism. Opioid blockade also elicits withdrawal signs after chronic UV exposure. This effect was sufficient to guide operant behavioral choices to avoidance of opioid withdrawal (conditioned place aversion). These UV-induced nociceptive and behavioral effects were absent in β-endorphin knockout mice and in mice lacking p53-mediated POMC induction in epidermal keratinocytes. Although primordial UV addiction, mediated by the hedonic action of β-endorphin and anhedonic effects of withdrawal, may theoretically have enhanced evolutionary vitamin D biosynthesis, it now may contribute to the relentless rise in skin cancer incidence in humans.

INTRODUCTION

Despite widespread awareness that UV exposure is a major risk factor for all common cutaneous malignancies, skin cancer incidence relentlessly increases by ~3% per year (de Gruijl, 1999; Gandini et al., 2011; Robinson et al., 1997). UV-seeking behavior is a recognized risk factor, but it is incompletely understood whether the popularity of sunbathing represents a biological addiction or an aesthetic preference for tanned skin. Studies have reported that many UV seekers meet CAGE and DSM-IV criteria for a substance-related disorder with respect to UV (Harrington et al., 2011; Kourosh et al., 2010; Lazovich et al., 2010; Mosher and Danoff-Burg, 2010; Warthan et al., 2005) and that UV seekers were capable of distinguishing between true UV and mock treatment in blind tanning bed experiments (Feldman et al., 2004), and two studies of small cohorts of frequent tanners revealed that acute administration of the opioid antagonist naltrexone can induce withdrawal-like symptoms (Kaur et al., 2005, 2006b). Although a mechanism for such addiction has been lacking, these studies are consistent with the possibility of endogenous opioid-mediated addictive behavioral effects.

In the cutaneous response to UV exposure, epidermal keratinocytes respond to DNA damage via p53-mediated transcriptional induction of the *proopiomelanocortin* (*POMC*) gene (Cui et al., 2007). POMC is posttranslationally cleaved into biologically active peptides, one of which is α-melanocyte-stimulating hormone (α-MSH), which mediates the tanning process by stimulating adjacent melanocytes to produce the brown/black pigment eumelanin (D'Orazio et al., 2006). The endogenous opioid β-endorphin is also posttranslationally generated in skin by cleavage of the POMC propeptide in response to UV radiation (Cui et al., 2007; Skobowiat et al., 2011; Slominski and Wortsman, 2000). β-endorphin is the most abundant endogenous opioid, with basal plasma levels of 1–12 pM (Bender et al., 2007; Fassoulaki et al., 2007; Leppäluoto et al., 2008), and intravenous administration of β-endorphin has been shown to cause analgesia (Tseng et al., 1976). It binds with high affinity to the μ-opioid receptor (Schoffelmeer et al., 1991), although some evidence suggests that it may also act through other mechanisms that are, at present, incompletely characterized (Nguyen et al., 2012). Exogenous opioids with similar mechanisms are analgesic and have reinforcing properties that make them addictive when administered systemically. Chronic opioid exposure results in tolerance (increasing dose requirement to achieve comparable efficacy) and physical dependence (opioid antagonism produces withdrawal). β-endorphin plays a role in analgesia (Ibrahim et al., 2005; Kastin et al., 1979), as well as in the reinforcement and reward that underlie addiction (Gianoulakis, 2009; Olive et al., 2001; Racz et al., 2008; Roth-Deri et al., 2003; Trigo et al., 2009). Here, we asked whether UV exposure may

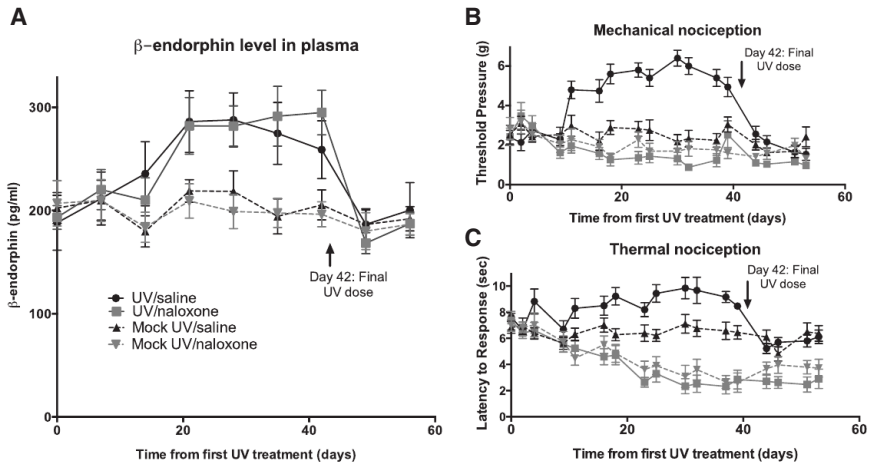

Figure 1. Plasma β-Endorphin Increases with Chronic UV Exposure and Parallels Naloxone-Reversible Changes in Pain Tolerance

(A) Plasma β-endorphin in C57Bl6 mice receiving daily UV or mock irradiation ($n > 9$ for all groups). Mice were treated twice a week with either naloxone or saline as indicated. Data are presented as the mean ± SEM, and a two-way ANOVA analysis with Bonferroni multiple comparisons test gives $p < 0.05$ for both UV-treated groups compared to both mock-treated groups (during UV treatment, days 14–42) and no significant effect of naloxone treatment within either group.

(B and C) Von Frey thresholds (B) and hot-plate thresholds (C) in chronically UV-irradiated and mock-irradiated C57Bl6 mice (mean ± SEM). Half of each group was pretreated with naloxone (10 mg/kg) 15 min prior to nociceptive testing, while the remainder received saline ($n = 10$ per group). Analgesic thresholds were further monitored for 2 additional weeks after cessation of UV/mock treatment. Two-way ANOVA with Bonferroni multiple comparisons test reveals $p < 0.0001$ for the UV/saline-treated group compared to all other groups during UV treatment, days 9–39).

stimulate changes in systemic β-endorphin levels that result in opioid-related behaviors, including alterations in nociceptive thresholds, tolerance to exogenous opioids, and dependence, as measured by withdrawal signs and conditioned place preference.

RESULTS

Systemic β-Endorphin Elevations following Chronic UV Exposure

We developed a UV-exposure mouse model in which dorsally shaved mice received a dose of 50 mJ/cm^2 of UVB 5 days per week for 6 weeks, an empirically derived suberythemic dose that is approximately equal to 20–30 min of ambient midday sun exposure in Florida during the summer for a fair-skinned person of average tanning ability (Fitzpatrick skin phototypes 2–3) (D'Orazio et al., 2006; Technology Planning and Management Corporation, 2000; US-EPA, 1994). After 1 week, significant elevations in circulating plasma β-endorphin were observed (Figure 1A). Circulating β-endorphin levels remained elevated for the duration of the 6-week exposure regimen and returned within 7 days to near-baseline levels after cessation of UV exposure. No significant changes in plasma β-endorphin were observed in mock-UV-treated mice (Figure 1A). Analgesic thresholds can be increased by peripheral administration of exogenous opioids or β-endorphin (Kastin et al., 1979). We quantified mechanical and thermal nociceptive thresholds over 6 weeks of daily UV exposure. Mechanical nociception was measured by the von Frey test (Kwan et al., 2006), which exposes fibers of increasing tensile strength to the plantar paw surface to elicit a paw-withdrawal response. Thermal nociception was tested using the hot-plate (52°C) test (Mogil et al., 1999), in which time to response (paw licking, paw flutter, or jumping) was measured. UV-irradiated mice exhibited significant increases both in mechanical (Figure 1B) and thermal (Figure 1C) nociceptive thresholds. These elevated analgesic thresholds paralleled the UV-induced elevations in plasma β-endorphin (Figure 1A). Mock-treated control mice displayed no significant elevations in pain thresholds (Figures 1B and 1C). Treatment with naloxone, an opioid antagonist, 15 min prior to analgesic testing suppressed the UV-induced increases in mechanical and thermal nociceptive thresholds (Figures 1B and 1C) despite maintained elevations in plasma β-endorphin (Figure 1A). These data demonstrate opioid receptor-mediated analgesia as a consequence of UV that parallels the elevation of circulating blood β-endorphin.

Quantifiable Opioid-Mediated Behaviors Occur with Chronic UV Exposure

Exogenous opioids produce a dose-dependent, μ-opioid receptor-mediated contraction of the sacrococcygeus dorsalis muscle at the tail base in rodents, resulting in rigidity and elevation of the tail, a phenomenon called "Straub tail" (Bilbey et al., 1960). Straub tail was evident in UV-irradiated mice by the second week of daily UV exposure, persisted for the 6 week exposure regimen, and diminished over 2 weeks after cessation of UV (Figure 2A). Treatment with the opioid antagonist naloxone (day 23 of the UV-exposure regimen) reversed the Straub tail phenotype (Figures 2B and 2C).

Opioid Tolerance and Physical Dependence after Chronic UV Exposure

We next asked whether chronic UV exposure may be accompanied by detectable opioid dependence, in which opioid cessation or antagonism produces withdrawal symptoms, and tolerance in which increasing doses are required to achieve comparable analgesia (Drdla et al., 2009). Following chronic daily UV exposure, administration of naloxone elicited many of the classic murine signs of opioid withdrawal (wet dog shake, paw tremor, teeth chatter, and rearing) (Olson et al., 2006) (Figure 3A).

Because the magnitude of the measured withdrawal symptoms, while significant, was smaller than that commonly observed with exogenously administered opioids (Broseta et al.,

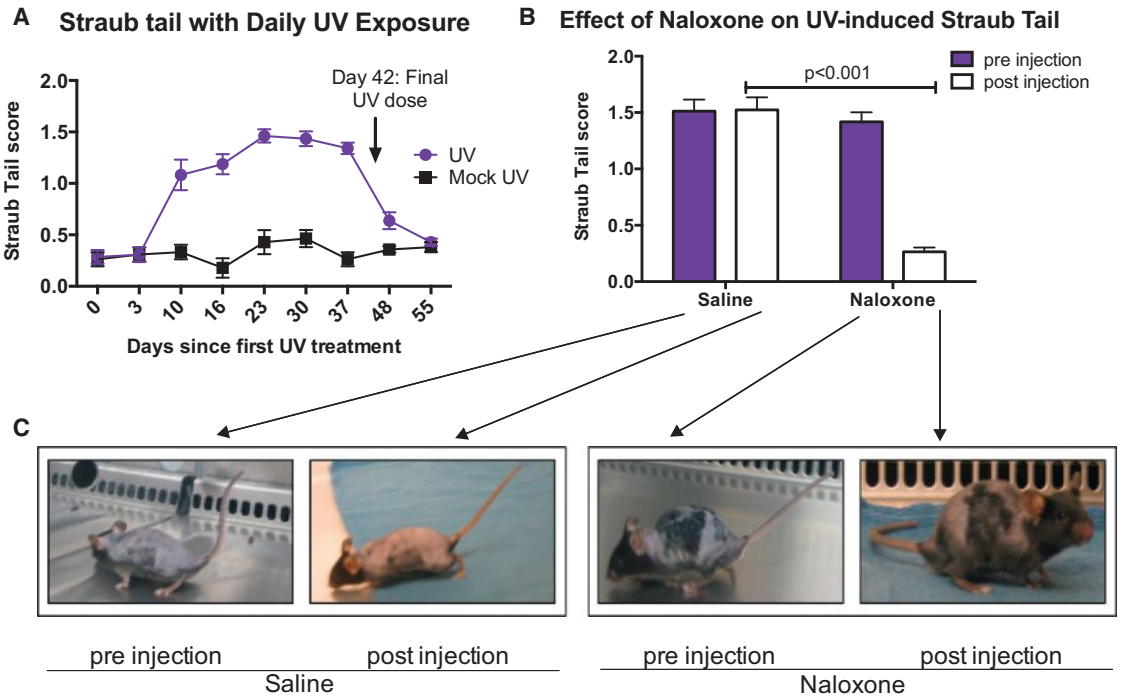

Figure 2. Straub Tail in UV-Irradiated Mice Is Reversed by Naloxone

(A) Straub tail in C57Bl6 mice over the course of 42 days of UV irradiation (n = 13) or mock irradiation (n = 6). Data are presented as the mean ± SEM for days 10–37; $p < 0.0001$ by two-way ANOVA analysis.

(B) Straub tail in at day 17 before (Pre) and 15 min after (Post) injection of naloxone (n = 7) or saline (n = 6). Data are presented as the mean ± SEM; $p < 0.001$ by Student's t test.

(C) Representative animals from each group in part (B). The beginning of black fur regrowth produces a patchy appearance.

2002), we wished to determine whether these withdrawal signs would be sufficient to elicit alterations in proactive/operant behavioral choices. We utilized a conditioned place preference/aversion assay (CPP; Skoubis et al., 2001; Weitemier and Murphy, 2009) to test whether a specific environment, paired with naloxone administration during conditioning, would be avoided in favor of a different environment paired with a neutral stimulus (saline) during conditioning in chronically UV-irradiated animals. Due to the kinetics of the UV response, we chose to use naloxone as it allowed an acute effect of limited duration. Naloxone induces conditioned place aversion in exogenous opioid-dependent mice (Glass et al., 2008; Kenny et al., 2006). Following conditioning, mice are permitted to move freely between the two environments, and changes in place preference are measured in the absence of additional naloxone or saline administration. Our conditioning environments were black and white boxes with dim and bright lighting, respectively, and to minimize apparatus bias, we assigned the black box as the naloxone (withdrawal stimulus)-paired box and the white box as the saline (neutral stimulus)-paired box, as rodents prefer dark environments to light environments in the absence of conditioning (Roma and Riley, 2005).

We observed that chronically UV-irradiated mice conditioned with naloxone in the black box avoided the black box in postconditioning preference testing. Naloxone conditioning had no effect on mock-treated (non-UV-irradiated) control mice, and saline conditioning in the black box had no effect on UV-irradiated or mock-treated mice (Figure 3B). Here, naloxone was sufficient to induce conditioned place aversion in UV-irradiated mice, suggesting that chronic UV exposure imparts an opioid-like physical dependence of sufficient magnitude to guide proactive behavior choices.

To test for the other principal feature of chronic opioid exposure, tolerance, after chronic UV treatment, we asked whether there is cross-tolerance between chronic UV exposure and morphine, altering the dose required to produce analgesia (Mao et al., 2000). After chronic UV exposure, mice required significantly higher doses of morphine than mock-treated controls to achieve comparable thermal analgesia in the hot-plate test, as reflected by a rightward shift in the dose-response curve and an increase in half-maximal effective concentration from 57 μg/kg in the mock-treated group to 270 μg/kg in the UV-exposed group (Figure 3C). The analgesic effect of UV exposure that we detected could be a result of systemic β-endorphin acting both through the peripheral nervous system and CNS, but the withdrawal effects and conditioned place aversion point to a CNS effect. It has been reported that radiolabeled β-endorphin peptides cross the blood-brain barrier (Banks and Kastin, 1990). To test whether it is plausible that skin-derived β-endorphin may cause central effects, we decided to assess whether peripherally administered

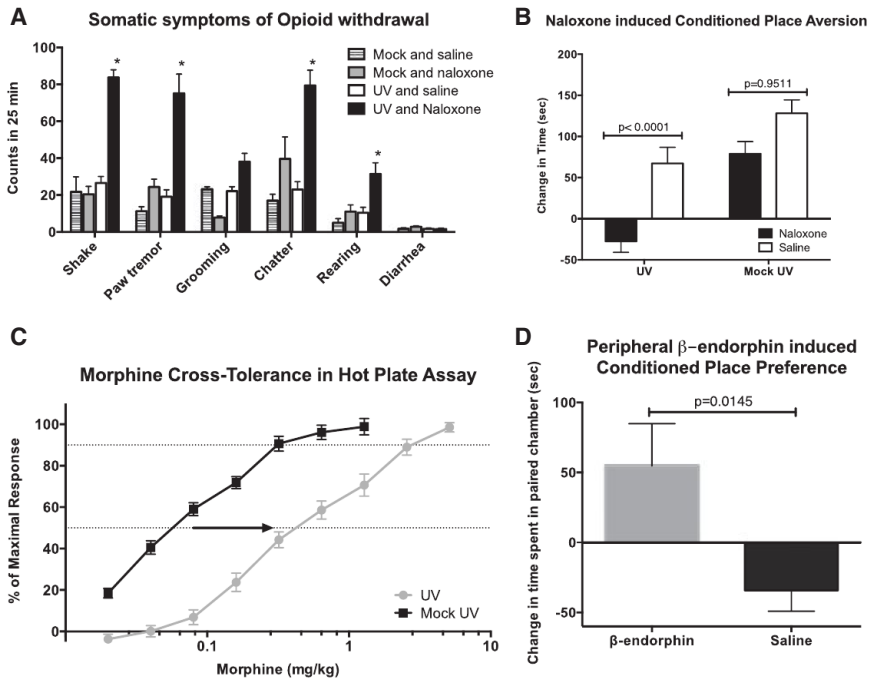

Figure 3. Chronically UV-Exposed Mice Show Symptoms of Opioid Dependence

(A) Signs of opioid withdrawal in mice under experimental conditions described in the figure: UV/saline (n = 9), mock/saline (n = 7), UV/naloxone (n = 15), and mock/naloxone (n = 7). Data are presented as the mean ± SEM; *p < 0.05 compared to UV/saline group by two-way ANOVA with Bonferroni multiple comparisons test.

(B) Conditioned place aversion testing in UV-treated mice conditioned to the naloxone-paired box (black box) with an injection of naloxone or saline (white box) following 42 days of UV or mock treatment. Mice were permitted to freely move between naloxone-paired and saline-paired boxes prior to (pretest, n = 8) and after 4 days of conditioning (test), and place preferences were assessed as change in time spent in the naloxone-paired box (postconditioning − preconditioning). Data are presented as the mean ± SEM, and p values were generated by two-way ANOVA with Bonferroni multiple comparisons test.

(C) Morphine dose-response curves in mice following 42 days of UV irradiation (n = 31) or mock exposure (n = 29). Data are presented as the mean ± SEM; p < 0.0001 by two-way ANOVA.

(D) Conditioned place-preference testing in mice administered intravenous β-endorphin or saline through the tail vein. Mice were conditioned to β-endorphin (n = 6) or saline (n = 8) in the white box and saline in the black box. Place preferences were assessed as change in time spent in the white (β-endorphin)-paired box, postconditioning − preconditioning. Data are presented as the mean ± SEM; p = 0.0145 by Student's t test.

β-endorphin injected intravenously into the tail vein could cause conditioned place preference. To attempt to match an acute intravenously administered drug dose with a chronic elevation, we chose a β⁻endorphin concentration reported to cause a similar analgesic response to that we observed in our UV-exposure experiments, (Tseng et al., 1976). β-endorphin or saline was injected into the tail vein of mice that were then conditioned to the white side of the CPP apparatus. The mice that had been conditioned with saline spent less time in the white box on the final day than on the initial day (Figure 3D); this was expected, as mice naturally prefer a dark environment. However, the mice that had received β-endorphin in the white box spent more time in the white box after conditioning (Figure 3D), indicating a conditioned place preference for the environment where they experienced β-endorphin. This shows that peripherally administered β-endorphin can cause conditioned place preference, presumably through the CNS.

These findings show that chronic UV exposure stimulates and sustains sufficient endogenous opioid release and opioid receptor activity to develop both opioid tolerance and physical dependence.

β-Endorphin Knockout Abolishes UV-Induced Behavioral Changes

To specifically examine the functional requirement for β-endorphin in these UV-associated behavioral changes, we employed β-endorphin knockout mice (lacking the C terminus of the *POMC* gene) (Rubinstein et al., 1996) and found that they exhibited no significant changes in thermal or mechanical nociceptive thresholds with chronic UV exposure (Figures 4A and 4B). The β-endorphin null mice also failed to develop signs of opioid withdrawal (Figure 4C) and, when subjected to the conditioned-place aversion test, exhibited no measurable change in place preference (Figure 4D).

Keratinocyte Expression of p53 Is Required for Elevated β-Endorphin Levels and Pain Thresholds

The UV-induced cutaneous upregulation of POMC, the precursor to both α-MSH and β-endorphin, is mediated by the tumor suppressor p53, which directly activates POMC gene transcription in keratinocytes (Cui et al., 2007). To test whether keratinocyte expression of p53 is required for UV-mediated increases in circulating β-endorphin, we crossed a mouse strain with a floxed allele of *p53* with a strain containing cre under the control of the keratin 14 promoter, which is selective to keratinocytes. We subjected the p53fl/fl K14cre and control $p53^{+/+}$ K14cre mice to the UV-irradiation regimen and assayed plasma β-endorphin levels, mechanical nociception, and naloxone-induced conditioned place aversion. Consistent with the known role of p53 in the tanning response, there was an absence of any tanning on the ears of the p53fl/fl K14cre animals (Figure 5A). Further, we observed no increase in circulating β-endorphin (Figure 5B) or in mechanical nociception threshold (Figure 5C). Moreover, the K14cre control mice showed significant naloxone-conditioned place aversion compared to the p53fl/fl K14cre animals (Figure 5D). These data indicate that keratinocyte-derived β-endorphin is a key factor in mediating UV-induced addiction.

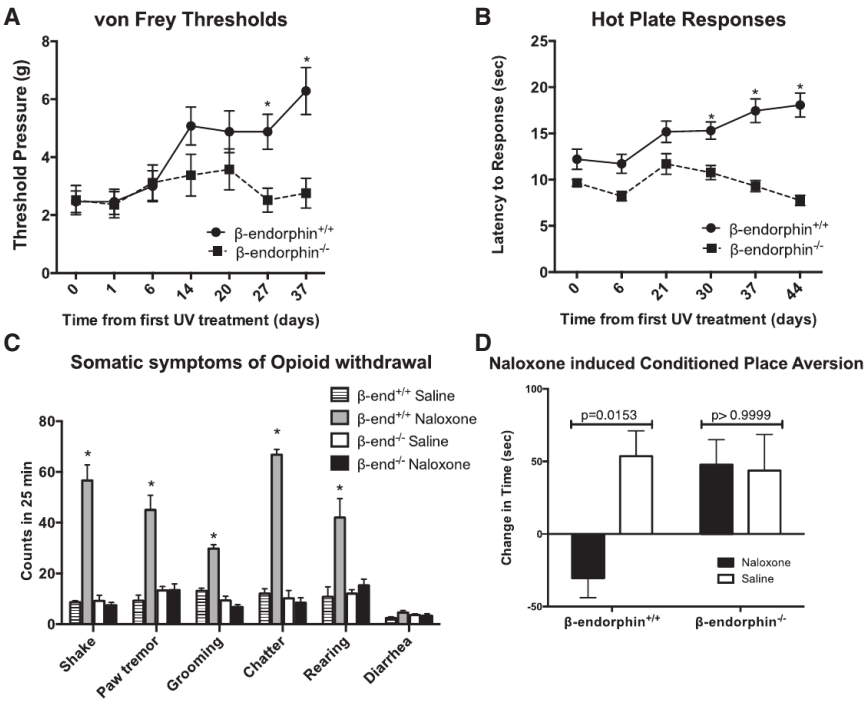

Figure 4. Genetic Lack of β-Endorphin Abolishes Changes in Pain Tolerance and Opioid Dependence with Chronic UV Exposure

(A and B) Von Frey test (A) and thermal analgesic thresholds (B) in wild-type (n = 11) and β-endorphin$^{-/-}$ (n = 13) mice over 35-day UV exposure. Data are presented as the mean ± SEM; *p < 0.05 by two-way ANOVA with Bonferroni multiple comparisons test.

(C) Signs of naloxone-precipitated opioid withdrawal in control and β-endorphin null mice after 6 weeks of UV exposure. Data are presented as the mean ± SEM; *p < 0.0001 compared to the β-endorphin$^{-/-}$/naloxone group by two-way ANOVA with Bonferroni multiple comparisons test; n > 7 for all groups.

(D) Conditioned place aversion testing in UV-treated control and β-endorphin null mice conditioned to the naloxone-paired box (black box) with an injection of naloxone or saline. All mice were conditioned to saline in the white box; n > 10 for all groups. Mice were permitted to freely move between naloxone-paired and saline-paired boxes prior to and after 4 days of conditioning, and place preferences were assessed as change in time spent in the naloxone-paired box (postconditioning − preconditioning). Data are presented as the mean ± SEM; p values were generated by two-way ANOVA with Bonferroni multiple comparisons test.

DISCUSSION

Our findings suggest that repeated UV exposure produces an opioid receptor-mediated addiction due to elevations in circulating β-endorphin, leading to increased nociceptive thresholds that are reversed by naloxone or ablated in β-endorphin null mice. Measurable withdrawal symptoms are elicited by naloxone, and proactive place-preference behaviors were strongly induced, based on prior conditioning between opioid receptor antagonism and cage color. Further, a skin-specific knockout of p53, a critical step in the UV-response pathway, prevented both the β-endorphin elevation and the behavioral responses. There remains a formal possibility that skin-specific p53 knockout could affect β-endorphin expression outside of the skin.

While these studies were performed in a nocturnal and furred animal model, significant evidence supports a strong relationship between UV exposure and addictive behaviors in humans (Feldman et al., 2004; Harrington et al., 2011; Kaur et al., 2005, 2006b; Kourosh et al., 2010; Mosher and Danoff-Burg, 2010; Warthan et al., 2005; Zeller et al., 2006). Several small studies have attempted to measure β-endorphin changes with UV exposure in humans (Gambichler et al., 2002; Kaur et al., 2006a; Levins et al., 1983; Wintzen et al., 2001), with some showing UV-induced elevations and others not, although significant confounding variables complicate such measurements, such as diurnal variations in β-endorphin (McMurray et al., 1990) and stressors that also influence β-endorphin levels (Aravich et al., 1993; Gianoulakis et al., 1996; Petraglia et al., 1990; Welch et al., 1996). While the effects of sunscreen have not been reported in this context, it does appear likely that sunscreen use would protect against UV-induced addictive behaviors.

Despite the carcinogenicity of UV and hence the serious maladaptive consequences of addiction to UV exposure, our results may also imply a potential evolutionary benefit of an endogenous mechanism that reinforces UV-seeking behavior, one that may operate by creating an opioid-mediated hedonic experience followed by dependence on the behavior to avoid the anhedonic consequences of withdrawal. Further studies may shed light on the site/sites of β-endorphin action within the brain and whether the brain regions and neuronal subpopulations involved in sun-seeking behavior are the same as those involved the analgesic response or in exogenous opioid addiction. A recent study has shown activation of known reward centers in the brains of volunteers during UV exposure (Harrington et al., 2012).

The current studies suggest that UV exposure is biologically addictive but dangerous due to UV's mutagenic activities toward formation of all common forms of skin cancer. This calls into question the perceived safety of tanning beds and current benign views of indoor tanning, reflected in the United States' current Food and Drug Administration classification of UV-emitting devices as class I and therefore minimally regulated. It may be necessary, therefore, to more proactively protect individuals, including teens, from the risks of an avoidable, potentially life-threatening exposure and to view recreational tanning and opioid drug abuse as engaging in the same biological pathway.

EXPERIMENTAL PROCEDURES

Mice

All mice used were on a C57Bl/6 background. For select experiments, mice with homozygous deletion of the C terminus of the *POMC* gene, resulting in lack of β-endorphin (β-endorphin$^{-/-}$) (Rubinstein et al., 1996), and mice with

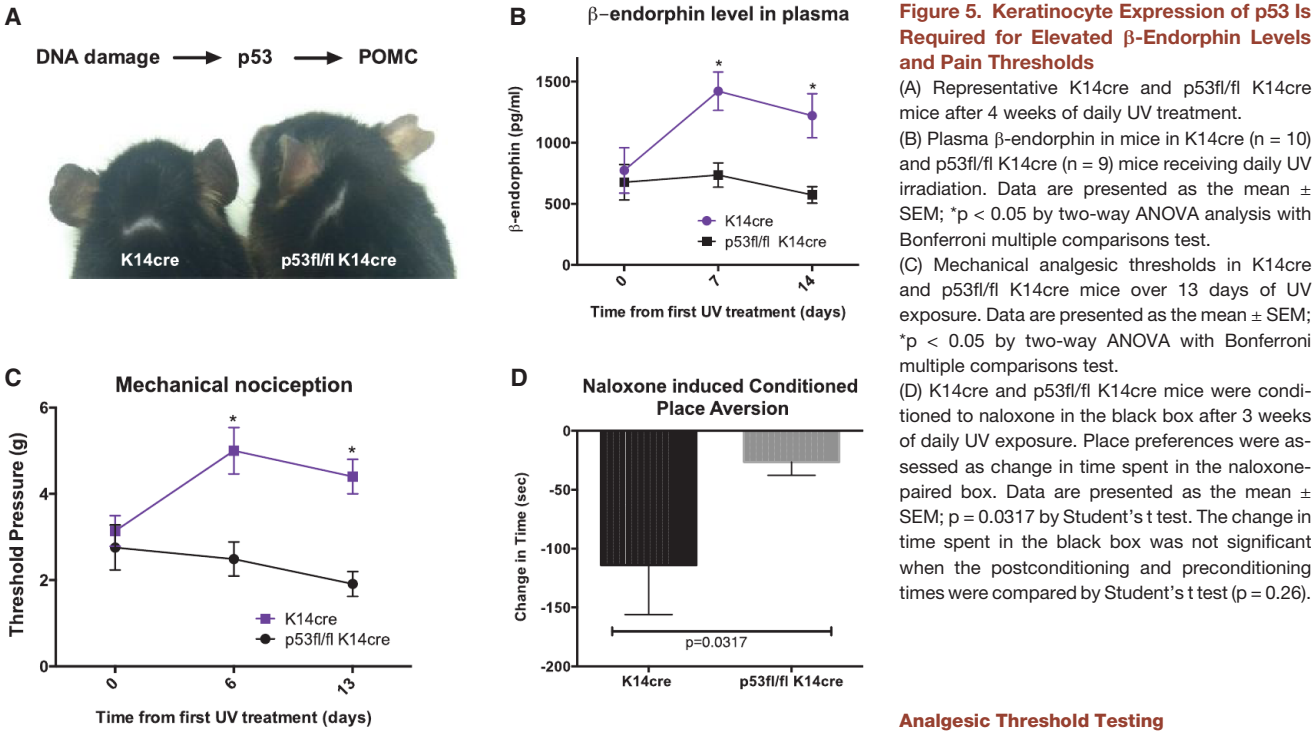

Figure 5. Keratinocyte Expression of p53 Is Required for Elevated β-Endorphin Levels and Pain Thresholds

(A) Representative K14cre and p53fl/fl K14cre mice after 4 weeks of daily UV treatment.

(B) Plasma β-endorphin in mice in K14cre (n = 10) and p53fl/fl K14cre (n = 9) mice receiving daily UV irradiation. Data are presented as the mean ± SEM; *p < 0.05 by two-way ANOVA analysis with Bonferroni multiple comparisons test.

(C) Mechanical analgesic thresholds in K14cre and p53fl/fl K14cre mice over 13 days of UV exposure. Data are presented as the mean ± SEM; *p < 0.05 by two-way ANOVA with Bonferroni multiple comparisons test.

(D) K14cre and p53fl/fl K14cre mice were conditioned to naloxone in the black box after 3 weeks of daily UV exposure. Place preferences were assessed as change in time spent in the naloxone-paired box. Data are presented as the mean ± SEM; p = 0.0317 by Student's t test. The change in time spent in the black box was not significant when the postconditioning and preconditioning times were compared by Student's t test (p = 0.26).

a floxed allele of p53 (Marino et al., 2000) and a keratin 14 promoter-driven Cre recombinase strain (Dassule et al., 2000) were used. All animal experiments were performed in accordance with institutional policies and Institutional Animal Care and Use Committee-approved protocols.

UV Irradiation and Blood Draws

Mice were dorsally shaved 2 days prior to the start of radiation exposure, then exposed to 50 mJ/cm^2/day of UVB, an empirically determined suberythematic dose, 5 days per week (Monday–Friday) for 6 weeks. Mice were reshaved once every 2 weeks if there were patches of fur regrowth.

For blood draws, mice were placed in a standard restrainer and tail vein blood was collected in EDTA microvette tubes containing 0.6 TIU aprotinin. Mice underwent blood draws prior to the stat of radiation exposure, once per week during the radiation exposure regimen, and once per week for 2 weeks following cessation of the UV regimen. Blood was drawn in the mornings prior to radiation exposure on Fridays.

Tubes of collected blood were maintained on ice until centrifugation at 3,500 rpm for 20 min at 4°C. Plasma was isolated, and samples were stored at −80°C until β-endorphin measurement. β-endorphin was quantified by radioimmunoassay (Phoenix Pharmaceuticals).

Straub Tail Measurement

Straub tail measurement was performed as described previously (Bilbey et al., 1960). Scoring was on a scale of 0–2 according to the angle of elevation of the tail from the horizontal plane (0 = tail relaxed and no elevation; 1 = tail is rigid and elevated 1°–10° from horizontal; 1.5 = 11°–45° elevation and rigidity at the base of the tail; 2 = 46°–90° elevation with rigidity at the base of the tail). For each time point, each mouse was scored every 10 s for 1 min, and the final score was the average of these six values. Mice undergoing the 6-week UV-exposure regimen or mock treatment were scored prior to the start of the regimen, once per week during the regimen, and once per week for 2 weeks following cessation of UV/mock treatment. On day 23 of the regimen after weekly Straub tail scoring, mice were injected intraperitoneally (i.p.) with either 10 mg/kg naloxone hydrochloride (Sigma) or saline. Mice underwent Straub tail scoring again 15 min following injection.

Analgesic Threshold Testing

Mice underwent mechanical and thermal analgesic testing during UV/mock treatment regimens using the von Frey test (Kwan et al., 2006) and the hot-plate test, respectively (Mogil et al., 1999). In the von Frey test, mice were placed in individual enclosures on an elevated wire mesh rack and the plantar surface of the left hind paw was serially poked with fibers of increasing tensile strength (ten times per fiber at a rate of 1/second) until a paw withdrawal response was elicited on two out of ten pokes. In the hot-plate test, mice were placed on a 52°C hot plate and time to response (paw flutter, paw licking, or jumping) was measured.

Mice were habituated to the wire mesh rack for 30 min per day and to the hot plate at room temperature for 2 min per day for 3 days prior to measuring baseline nociceptive thresholds. Mice underwent nociceptive testing twice per week on nonconsecutive days during and for 2 weeks following cessation of UV/mock treatment. Mice received an intraperitoneal injection of 10 mg/kg naloxone or saline 15 min prior to nociceptive testing.

Somatic Symptoms of Opiate Withdrawal

Mice that had undergone 6 weeks of daily UV exposure or mock exposure were injected i.p. with either 2 mg/kg naloxone or saline, and signs of opioid withdrawal were tabulated as described elsewhere (Olson et al., 2006). Mice were observed in an open-topped Plexiglas 30 cm × 15 cm × 15 cm rectangular container for 25 min each following injection, and signs of opioid withdrawal were tabulated. Wet dog shake, teeth chatter, and bouts of grooming were measured as occurrence in each 15 s interval. Individual rearing events were counted. Number of fecal pellets at the end of the 25 min interval was used to quantify diarrhea.

Conditioned Place Aversion Testing

The apparatus used consisted of a box with black interior and dim lighting and a box with white interior and bright lighting connected by a smaller gray "neutral" box, and procedures were followed as described previously (Skoubis et al., 2001; Weitemier and Murphy, 2009). Mice that had undergone 6 weeks of daily UV exposure or mock exposure were tested for baseline place preferences prior to conditioning (10 min testing time per mouse). Over the following 4 days, conditioning took place in which mice were either conditioned with naloxone (10 mg/kg injection i.p.) or saline (injection i.p.) in the black box, and all animals were conditioned with saline (injection i.p.) in the

white box. Conditioning time in each box was 30 min following injection. For each animal, there were 4 hr between conditioning in one box and condition in the other box each day. On the day following the final day of conditioning, place preferences were again tested (postconditioning, 10 min testing time per mouse).

Morphine Cross-Tolerance Testing

Morphine dose-response curves in the hot-plate test were measured as described elsewhere (Mao et al., 2000) in mice that had undergone 6 weeks of UV exposure or mock treatment. Morphine was injected at a starting dose of 0.02 mg/kg i.p. and was increased logarithmically in cumulative dose increments of 0.3 log units. Thermal analgesic thresholds were tested 15 min after each morphine injection until there was failure to respond in the hot-plate test (cutoff time was 20 s) or until there was no change in response time from one dose to the next. There were 30 min between injections and 30 min between hot-plate testings for each mouse. Percent of maximal effect was calculated based on the equation: (test latency − baseline latency) / (maximal latency − baseline latency) × 100% (Mao et al., 2000).

AUTHOR CONTRIBUTIONS

G.L.F. designed, performed, and interpreted experiments and wrote the paper. K.C.R. designed, performed, and interpreted experiments, made the figures, and wrote the paper. J.M. assisted in design and interpretation of behavioral experiments. C.J.W. assisted in design and interpretation of behavioral experiments. D.E.F. designed and interpreted experiments and wrote the paper.

ACKNOWLEDGMENTS

The authors gratefully acknowledge Dr. Charles Berde, Dr. Jeff Mogil, Ms. Vivien Igras, Mr. John Dellorusso, Ms. Teri Herbert, Ms. Leeza Hargreaves, Dr. Roydon Price, and Dr. Grewo Lim for productive discussions during the early phases of this project and for technical assistance with the experiments and manuscript. The authors thank Dr. Mary Jeanne Kreek for useful discussions. The authors also acknowledge Douglas Hayden from the MGH Biostatistics Center for consultation regarding the statistical analysis. This work was supported by NIH under award numbers R01 AR043369-16, P01CA163222, and R01 CA150226-03 and by grants from the Melanoma Research Alliance, the US-Israel Binational Science Foundation, and the Dr. Miriam and Sheldon G. Adelson Medical Research Foundation (D.E.F.).

Received: September 20, 2012
Revised: February 12, 2014
Accepted: April 3, 2014
Published: June 19, 2014

REFERENCES

Aravich, P.F., Rieg, T.S., Lauterio, T.J., and Doerries, L.E. (1993). Beta-endorphin and dynorphin abnormalities in rats subjected to exercise and restricted feeding: relationship to anorexia nervosa? Brain Res. *622*, 1–8.

Banks, W.A., and Kastin, A.J. (1990). Peptide transport systems for opiates across the blood-brain barrier. Am. J. Physiol. *259*, E1–E10.

Bender, T., Nagy, G., Barna, I., Tefner, I., Kádas, E., and Géher, P. (2007). The effect of physical therapy on beta-endorphin levels. Eur. J. Appl. Physiol. *100*, 371–382.

Bilbey, D.L., Salem, H., and Grossman, M.H. (1960). The anatomical basis of the straub phenomenon. Br. Pharmacol. Chemother. *15*, 540–543.

Broseta, I., Rodríguez-Arias, M., Stinus, L., and Miñarro, J. (2002). Ethological analysis of morphine withdrawal with different dependence programs in male mice. Prog. Neuropsychopharmacol. Biol. Psychiatry *26*, 335–347.

Cui, R., Widlund, H.R., Feige, E., Lin, J.Y., Wilensky, D.L., Igras, V.E., D'Orazio, J., Fung, C.Y., Schanbacher, C.F., Granter, S.R., and Fisher, D.E. (2007). Central role of p53 in the suntan response and pathologic hyperpigmentation. Cell *128*, 853–864.

D'Orazio, J.A., Nobuhisa, T., Cui, R., Arya, M., Spry, M., Wakamatsu, K., Igras, V., Kunisada, T., Granter, S.R., Nishimura, E.K., et al. (2006). Topical drug rescue strategy and skin protection based on the role of Mc1r in UV-induced tanning. Nature *443*, 340–344.

Dassule, H.R., Lewis, P., Bei, M., Maas, R., and McMahon, A.P. (2000). Sonic hedgehog regulates growth and morphogenesis of the tooth. Development *127*, 4775–4785.

de Gruijl, F.R. (1999). Skin cancer and solar UV radiation. Eur. J. Cancer *35*, 2003–2009.

Drdla, R., Gassner, M., Gingl, E., and Sandkühler, J. (2009). Induction of synaptic long-term potentiation after opioid withdrawal. Science *325*, 207–210.

Fassoulaki, A., Paraskeva, A., Kostopanagiotou, G., Tsakalozou, E., and Markantonis, S. (2007). Acupressure on the extra 1 acupoint: the effect on bispectral index, serum melatonin, plasma beta-endorphin, and stress. Anesth. Analg. *104*, 312–317.

Feldman, S.R., Liguori, A., Kucenic, M., Rapp, S.R., Fleischer, A.B., Jr., Lang, W., and Kaur, M. (2004). Ultraviolet exposure is a reinforcing stimulus in frequent indoor tanners. J. Am. Acad. Dermatol. *51*, 45–51.

Gambichler, T., Bader, A., Vojvodic, M., Avermaete, A., Schenk, M., Altmeyer, P., and Hoffmann, K. (2002). Plasma levels of opioid peptides after sunbed exposures. Br. J. Dermatol. *147*, 1207–1211.

Gandini, S., Autier, P., and Boniol, M. (2011). Reviews on sun exposure and artificial light and melanoma. Prog. Biophys. Mol. Biol. *107*, 362–366.

Gianoulakis, C. (2009). Endogenous opioids and addiction to alcohol and other drugs of abuse. Curr. Top. Med. Chem. *9*, 999–1015.

Gianoulakis, C., de Waele, J.P., and Thavundayil, J. (1996). Implication of the endogenous opioid system in excessive ethanol consumption. Alcohol *13*, 19–23.

Glass, M.J., Hegarty, D.M., Oselkin, M., Quimson, L., South, S.M., Xu, Q., Pickel, V.M., and Inturrisi, C.E. (2008). Conditional deletion of the NMDA-NR1 receptor subunit gene in the central nucleus of the amygdala inhibits naloxone-induced conditioned place aversion in morphine-dependent mice. Exp. Neurol. *213*, 57–70.

Harrington, C.R., Beswick, T.C., Leitenberger, J., Minhajuddin, A., Jacobe, H.T., and Adinoff, B. (2011). Addictive-like behaviours to ultraviolet light among frequent indoor tanners. Clin. Exp. Dermatol. *36*, 33–38.

Harrington, C.R., Beswick, T.C., Graves, M., Jacobe, H.T., Harris, T.S., Kourosh, S., Devous, M.D., Sr., and Adinoff, B. (2012). Activation of the mesostriatal reward pathway with exposure to ultraviolet radiation (UVR) vs. sham UVR in frequent tanners: a pilot study. Addict. Biol. *17*, 680–686.

Ibrahim, M.M., Porreca, F., Lai, J., Albrecht, P.J., Rice, F.L., Khodorova, A., Davar, G., Makriyannis, A., Vanderah, T.W., Mata, H.P., and Malan, T.P., Jr. (2005). CB2 cannabinoid receptor activation produces antinociception by stimulating peripheral release of endogenous opioids. Proc. Natl. Acad. Sci. USA *102*, 3093–3098.

Kastin, A.J., Jemison, M.T., and Coy, D.H. (1979). Analgesia after peripheral administration of enkephalin and endorphin analogues. Pharmacol. Biochem. Behav. *11*, 713–716.

Kaur, M., Liguori, A., Fleischer, A.B., Jr., and Feldman, S.R. (2005). Side effects of naltrexone observed in frequent tanners: could frequent tanners have ultraviolet-induced high opioid levels? J. Am. Acad. Dermatol. *52*, 916.

Kaur, M., Liguori, A., Fleischer, A.B., Jr., and Feldman, S.R. (2006a). Plasma beta-endorphin levels in frequent and infrequent tanners before and after ultraviolet and non-ultraviolet stimuli. J. Am. Acad. Dermatol. *54*, 919–920.

Kaur, M., Liguori, A., Lang, W., Rapp, S.R., Fleischer, A.B., Jr., and Feldman, S.R. (2006b). Induction of withdrawal-like symptoms in a small randomized, controlled trial of opioid blockade in frequent tanners. J. Am. Acad. Dermatol. *54*, 709–711.

Kenny, P.J., Chen, S.A., Kitamura, O., Markou, A., and Koob, G.F. (2006). Conditioned withdrawal drives heroin consumption and decreases reward sensitivity. J. Neurosci. *26*, 5894–5900.

Kourosh, A.S., Harrington, C.R., and Adinoff, B. (2010). Tanning as a behavioral addiction. Am. J. Drug Alcohol Abuse *36*, 284–290.

Kwan, K.Y., Allchorne, A.J., Vollrath, M.A., Christensen, A.P., Zhang, D.S., Woolf, C.J., and Corey, D.P. (2006). TRPA1 contributes to cold, mechanical, and chemical nociception but is not essential for hair-cell transduction. Neuron *50*, 277–289.

Lazovich, D., Vogel, R.I., Berwick, M., Weinstock, M.A., Anderson, K.E., and Warshaw, E.M. (2010). Indoor tanning and risk of melanoma: a case-control study in a highly exposed population. Cancer Epidemiol. Biomarkers Prev. *19*, 1557–1568.

Leppäluoto, J., Westerlund, T., Huttunen, P., Oksa, J., Smolander, J., Dugué, B., and Mikkelsson, M. (2008). Effects of long-term whole-body cold exposures on plasma concentrations of ACTH, beta-endorphin, cortisol, catecholamines and cytokines in healthy females. Scand. J. Clin. Lab. Invest. *68*, 145–153.

Levins, P.C., Carr, D.B., Fisher, J.E., Momtaz, K., and Parrish, J.A. (1983). Plasma beta-endorphin and beta-lipoprotein response to ultraviolet radiation. Lancet *2*, 166.

Mao, J., Price, D.D., Lu, J., Keniston, L., and Mayer, D.J. (2000). Two distinctive antinociceptive systems in rats with pathological pain. Neurosci. Lett. *280*, 13–16.

Marino, S., Vooijs, M., van Der Gulden, H., Jonkers, J., and Berns, A. (2000). Induction of medulloblastomas in p53-null mutant mice by somatic inactivation of Rb in the external granular layer cells of the cerebellum. Genes Dev. *14*, 994–1004.

McMurray, R.G., Hill, D., and Field, K.M. (1990). Diurnal variations of beta-endorphin at rest and after moderate intensity exercise. Chronobiol. Int. *7*, 135–142.

Mogil, J.S., Wilson, S.G., Bon, K., Lee, S.E., Chung, K., Raber, P., Pieper, J.O., Hain, H.S., Belknap, J.K., Hubert, L., et al. (1999). Heritability of nociception II. 'Types' of nociception revealed by genetic correlation analysis. Pain *80*, 83–93.

Mosher, C.E., and Danoff-Burg, S. (2010). Addiction to indoor tanning: relation to anxiety, depression, and substance use. Arch. Dermatol. *146*, 412–417.

Nguyen, A.T., Marquez, P., Hamid, A., Kieffer, B., Friedman, T.C., and Lutfy, K. (2012). The rewarding action of acute cocaine is reduced in β-endorphin deficient but not in μ opioid receptor knockout mice. Eur. J. Pharmacol. *686*, 50–54.

Olive, M.F., Koenig, H.N., Nannini, M.A., and Hodge, C.W. (2001). Stimulation of endorphin neurotransmission in the nucleus accumbens by ethanol, cocaine, and amphetamine. J. Neurosci. *21*, RC184.

Olson, V.G., Griner, N.B., Heusner, C.L., and Palmiter, R.D. (2006). Lack of neuropeptide Y attenuates the somatic signs of opiate withdrawal. Synapse *60*, 553–556.

Petraglia, F., Bacchi Modena, A., Comitini, G., Scazzina, D., Facchinetti, F., Fiaschetti, D., Genazzani, A.D., Barletta, C., Scavo, D., and Genazzani, A.R. (1990). Plasma beta-endorphin and beta-lipotropin levels increase in well trained athletes after competition and non competitive exercise. J. Endocrinol. Invest. *13*, 19–23.

Racz, I., Schürmann, B., Karpushova, A., Reuter, M., Cichon, S., Montag, C., Fürst, R., Schütz, C., Franke, P.E., Strohmaier, J., et al. (2008). The opioid peptides enkephalin and beta-endorphin in alcohol dependence. Biol. Psychiatry *64*, 989–997.

Robinson, J.K., Rigel, D.S., and Amonette, R.A. (1997). Trends in sun exposure knowledge, attitudes, and behaviors: 1986 to 1996. J. Am. Acad. Dermatol. *37*, 179–186.

Roma, P.G., and Riley, A.L. (2005). Apparatus bias and the use of light and texture in place conditioning. Pharmacol. Biochem. Behav. *82*, 163–169.

Roth-Deri, I., Zangen, A., Aleli, M., Goelman, R.G., Pelled, G., Nakash, R., Gispan-Herman, I., Green, T., Shaham, Y., and Yadid, G. (2003). Effect of experimenter-delivered and self-administered cocaine on extracellular beta-endorphin levels in the nucleus accumbens. J. Neurochem. *84*, 930–938.

Rubinstein, M., Mogil, J.S., Japón, M., Chan, E.C., Allen, R.G., and Low, M.J. (1996). Absence of opioid stress-induced analgesia in mice lacking beta-endorphin by site-directed mutagenesis. Proc. Natl. Acad. Sci. USA *93*, 3995–4000.

Schoffelmeer, A.N., Warden, G., Hogenboom, F., and Mulder, A.H. (1991). Beta-endorphin: a highly selective endogenous opioid agonist for presynaptic mu opioid receptors. J. Pharmacol. Exp. Ther. *258*, 237–242.

Skobowiat, C., Dowdy, J.C., Sayre, R.M., Tuckey, R.C., and Slominski, A. (2011). Cutaneous hypothalamic-pituitary-adrenal axis homolog: regulation by ultraviolet radiation. Am. J. Physiol. Endocrinol. Metab. *301*, E484–E493.

Skoubis, P.D., Matthes, H.W., Walwyn, W.M., Kieffer, B.L., and Maidment, N.T. (2001). Naloxone fails to produce conditioned place aversion in mu-opioid receptor knock-out mice. Neuroscience *106*, 757–763.

Slominski, A., and Wortsman, J. (2000). Neuroendocrinology of the skin. Endocr. Rev. *21*, 457–487.

Technology Planning and Management Corporation (2000). Report on Carcinogens Background Document for Broad-Spectrum Ultraviolet (UV) Radiation and UVA, and UVB, and UVC (Durham: Technology Planning and Management Corporation).

Trigo, J.M., Zimmer, A., and Maldonado, R. (2009). Nicotine anxiogenic and rewarding effects are decreased in mice lacking beta-endorphin. Neuropharmacology *56*, 1147–1153.

Tseng, L.F., Loh, H.H., and Li, C.H. (1976). Beta-Endorphin as a potent analgesic by intravenous injection. Nature *263*, 239–240.

US-EPA (1994). The Federal Experimental Ultraviolet Index: What You Need To Know (Washington, DC: United States Environmental Protection Agency).

Warthan, M.M., Uchida, T., and Wagner, R.F., Jr. (2005). UV light tanning as a type of substance-related disorder. Arch. Dermatol. *141*, 963–966.

Weitemier, A.Z., and Murphy, N.P. (2009). Accumbal dopamine and serotonin activity throughout acquisition and expression of place conditioning: correlative relationships with preference and aversion. Eur. J. Neurosci. *29*, 1015–1026.

Welch, C.C., Kim, E.M., Grace, M.K., Billington, C.J., and Levine, A.S. (1996). Palatability-induced hyperphagia increases hypothalamic Dynorphin peptide and mRNA levels. Brain Res. *721*, 126–131.

Wintzen, M., Ostijn, D.M., Polderman, M.C., le Cessie, S., Burbach, J.P., and Vermeer, B.J. (2001). Total body exposure to ultraviolet radiation does not influence plasma levels of immunoreactive beta-endorphin in man. Photodermatol. Photoimmunol. Photomed. *17*, 256–260.

Zeller, S., Lazovich, D., Forster, J., and Widome, R. (2006). Do adolescent indoor tanners exhibit dependency? J. Am. Acad. Dermatol. *54*, 589–596.

Cell

Vulnerability of Glioblastoma Cells to Catastrophic Vacuolization and Death Induced by a Small Molecule

Satish Srinivas Kitambi,[1] Enrique M. Toledo,[1] Dmitry Usoskin,[1] Shimei Wee,[1,4] Aditya Harisankar,[5] Richard Svensson,[3] Kristmundur Sigmundsson,[2] Christina Kalderén,[2] Mia Niklasson,[6] Soumi Kundu,[6] Sergi Aranda,[1] Bengt Westermark,[6] Lene Uhrbom,[6] Michael Andäng,[1,4] Peter Damberg,[7] Sven Nelander,[6] Ernest Arenas,[1] Per Artursson,[3] Julian Walfridsson,[5] Karin Forsberg Nilsson,[6] Lars G.J. Hammarström,[2] and Patrik Ernfors[1,*]

[1]Division of Molecular Neurobiology, Department of Medical Biochemistry and Biophysics, Karolinska Institutet, 17177 Stockholm, Sweden
[2]Chemical Biology Consortium Sweden, Science for Life Laboratory, Division of Translational Medicine & Chemical Biology, Department of Medical Biochemistry and Biophysics, Karolinska Institutet, 171 77 Stockholm, Sweden
[3]Department of Pharmacy, UDOPP, Chemical Biology Consortium Sweden, Uppsala University, 751 05 Uppsala, Sweden
[4]Department of Physiology and Pharmacology, Karolinska Institutet, 171 77 Stockholm, Sweden
[5]Department of Medicine, HERM, Karolinska Institutet, 141 86 Stockholm, Sweden
[6]Science for Life Laboratory, Department of Immunology, Genetics and Pathology, Uppsala University, 751 85 Uppsala, Sweden
[7]Department of Clinical Science, Intervention and Technology, Karolinska Institutet, 141 86 Stockholm, Sweden
*Correspondence: patrik.ernfors@ki.se
http://dx.doi.org/10.1016/j.cell.2014.02.021

SUMMARY

Glioblastoma multiforme (GBM) is the most aggressive form of brain cancer with marginal life expectancy. Based on the assumption that GBM cells gain functions not necessarily involved in the cancerous process, patient-derived glioblastoma cells (GCs) were screened to identify cellular processes amenable for development of targeted treatments. The quinine-derivative NSC13316 reliably and selectively compromised viability. Synthetic chemical expansion reveals delicate structure-activity relationship and analogs with increased potency, termed Vacquinols. Vacquinols stimulate death by membrane ruffling, cell rounding, massive macropinocytic vacuole accumulation, ATP depletion, and cytoplasmic membrane rupture of GCs. The MAP kinase MKK4, identified by a shRNA screen, represents a critical signaling node. Vacquinol-1 displays excellent in vivo pharmacokinetics and brain exposure, attenuates disease progression, and prolongs survival in a GBM animal model. These results identify a vulnerability to massive vacuolization that can be targeted by small molecules and point to the possible exploitation of this process in the design of anticancer therapies.

INTRODUCTION

Tumor development involves mutations that can be gain-of-function mutations in proto-oncogenes or loss-of-function mutations in tumor suppressor genes that lead to fundamental changes in the biology of the cell, resulting in cancer. Genomic studies of hundreds of glioblastoma multiforme (GBM) samples have led to a comprehensive insight into the genomic landscape of GBM, revealing both gain- and loss-of-function in core signaling pathways commonly activated, including the receptor tyrosine kinase (RTK/RAS) oncogenic pathway with alterations in *EGFR/PDGFRA/PI3K/PTEN/NF1/RAS*, the p53 pathway with changes in *TP53/MDM2/MDM4/p14ARF*, and finally, the cell-cycle regulatory pathway with alterations in *RB1/CDK4/p16INK4A/CDKN2B*, with most GBM tumors having genetic alteration in all three pathways (Chen et al., 2012b; Furnari et al., 2007; Parsons et al., 2008; Brennan et al., 2009, 2013; Verhaak et al., 2010; Cancer Genome Atlas Research Network, 2008). The consequence is a fueling of cell proliferation and enhanced survival and invasion properties, while preventing tumor cells from apoptosis and activation of cell-cycle checkpoints. Consistently, malignant gliomas are among the most devastating human cancers (Louis et al., 2007). GBM is essentially incurable, even when aggressive therapies based on surgical tumor resection and concomitant chemotherapy and radiotherapy are implemented (Stupp et al., 2005), and only 3%–5% of patients survive longer than 3 years due to disease recurrence (Dolecek et al., 2012).

The small population of GBM cells with stem/progenitor cell characteristics (Hemmati et al., 2003; Singh et al., 2003, 2004) seed growth of new tumors (Gallo et al., 2013; Pollard et al., 2009; Singh et al., 2003, 2004) and drive malignancy, metastasis, and tumor recurrence, promoting resistance against radiation-based therapy (Bao et al., 2006) and chemotherapy (Bleau and Holland, 2009; Chen et al., 2012b). These tumor-initiating cells are believed to be relatively quiescent (Alcantara Llaguno et al., 2009; Barami et al., 2009), which could contribute to disease recurrence following current therapeutic strategies targeting intracellular processes associated with cell division.

Unlike several other forms of cancer in which identification of participating gene products have resulted in series of drugs

neutralizing the function gained by the genetic alterations, the complexity and diversity of glioblastoma genetics have prevented a simple strategy for therapeutic targeting. New approaches focused on neutralizing abnormalities underlying tumor development have only had limited success so far (Dent et al., 2008; Polivka et al., 2012). We reasoned that gene products causing glioma are part of signaling pathways that are involved in diverse cellular functions. Therefore, gain- and loss-of-function mutations would be predicted to lead to acquired functions also in cellular properties not necessarily involved in cell transformation and proliferation. Hence, there should be unique cellular properties of glioma that are low or absent in other cell types. If identified, such features can be exploited for development of conceptually new strategies of therapy. In an unbiased phenotypic screen using a diversity set of small molecules on glioblastoma cells (GCs), a biological process resulting in a robust loss of viability and increased cytotoxicity was discovered. GCs are vulnerable to an MKK4-dependent signaling inducing catastrophic vacuolization and cell death.

RESULTS

Induction of Rapid and Specific Cell Death of Glioma Cells by a Small Molecule

In order to identify pathways vulnerable for targeted treatment of GCs, a phenotypic screen was performed to identify compounds active on GCs without affecting embryonic stem cells or human fibroblasts. GC cultures were independently generated from two cases of GBM, according to Pollard et al. (2009) which allows for adherent growth of cells with tumor-initiating and stem-like properties. These cell lines, designated U3013MG and U3047MG, were screened, rescreened, and confirmed using 1,364 compounds of the NIH diversity set II for phenotypic changes observed following phalloidin staining (Figure 1A and Figure S1A available online). 234 compounds showed effects after 2 days with principal phenotypes observed designated as tiny (T, dead or reduced cell size) or loose or fuse (LOF, senescence-like morphology), respectively (Figures 1B–1D). Filter screens against mouse embryonic stem cells (mESCs) and human fibroblasts reduced the initial 234 compounds to 63 with effects selective for GCs (Figures 1A and S1B). The compounds were confirmed active on U3013MG and U3047MG GCs, as well as on seven other patient-derived GC cultures that were established (U3024MG, U3017MG, U3031MG, U3037MG, U3086MG, U3054MG, and U3065MG; Figures 1A and S1E). The 63 compounds (Table S1) were examined in a recovery assay (Figures S1C and S1D) by quantification of cytotoxicity, apoptosis, and cell viability (Figure S2A) in U3013MG GCs and human fibroblast cells, as well as cell-cycle analysis by flow cytometry (Figure S2B). In the recovery assay, 2 days with compound were followed 2 more days without compound. Only 12 compounds had an irreversible effect at the same concentration that caused the acute effects (Figures S1C and S1D). Quantification of cell viability (ATP) and cytotoxicity (CytoTox-Glo) of the 63 compounds identified partly the same hit compounds (i.e., E5, E10, and A7) as most efficacious with limited effects on fibroblasts (Figure S2A). Based on these analyses and in silico absorption, distribution, metabolism, and excretion (ADME) prediction (Figures S3A–S3J), a refined list of 17 hits (Table S2) was pursued using several parameters, including cell-type-selective in vitro and in vivo efficacy, Ca^{2+} imaging, and toxicity tests. A hanging drop-based mixed culture procedure was developed for assaying selectivity (Figures S4A and S4B). U3013MG GCs and fibroblasts labeled with cell tracker red or green fluorescent dye, respectively, in cocultures confirmed selectivity (Figure S4B). Only one compound (D1) induced Ca^{2+} flux in GCs (Figures S4C–S4E). To measure toxicity, increasing concentrations of the 17 hits administered to the water of 10 days postfertilization (dpf) zebrafish embryos revealed that, whereas B6, B11, E5, E9, C2, C7, and D12 did not affect zebrafish development, embryos died, decayed, or displayed yolk edema in the presence of the remaining hits (Figure S5A). Cardiovascular toxicity of ex vivo adult zebrafish hearts (Kitambi et al., 2012) was observed for four hits (A2, A6, C9, and E9) whereas small or no effects were found on the remaining compounds (Figure S5B). In vivo efficacy was examined in a zebrafish GBM model that was developed where 3,000 U3013MG GCs labeled with cell tracker red were injected intracranially into the ventricle of 48–52 hpf larvae. The 17 hits administered to the egg water at the lowest effective in vitro cytotoxic concentration and monitoring tumor development 10 days later revealed that B7, C2, and E5 markedly reduced tumor size, with E5 being most potent (Figure S5C). Based on these analyses, further studies were focused on compound E5, which we name Vacquinol-1 due to its quinoline-alcohol scaffold (Figure 1E). Vacquinol-1 displayed high cytotoxicity (15 μM, 12 hr; Figure 1F), led to a complete loss of viability as measured by ATP depletion (Figure 1G), and selectively targeted GCs in mixed cocultures with human fibroblasts (Figures 1H and 1I). Vacquinol-1 did not affect mESCs, human fibroblasts, or osteosarcoma cells (Figures 1J–1O) but rapidly reduced the proportion of GCs in S and G2/M cell-cycle phases (7.5 μM, 12 hr; Figure 1P). Cell density had only minor effects on viability in dose response assays (Figure 1Q). The median inhibition concentration of 50% (IC_{50}) was 2.36 μM (3,000 cells/cm^2, 24 hr, Figure 1R) as compared to 139 μM by temozolomide (Figure 1S, 48 hr), a commonly used drug for treating glioma. The IC_{50} of Vacquinol-1 remained largely similar at 2, 3, and 4 days of incubation (Figures 1T–1V). Mouse glia and neuron cultures showed an IC_{50} of 15 and 29 μM, respectively (24 hr, Figures 1W and 1X), and fibroblasts showed an IC_{50} of 18.7 μM and 23 μM (24 and 96 hr, respectively; Figures 1Y and 1Z). The IC_{50} of fibroblasts was not affected by changing to GC culture medium during Vacquinol-1 treatment (Figures S1F and S1G). Furthermore, Vacquinol-1 was ineffective on bladder, prostate, breast, and neuroblastoma cancer cell lines (Figure S1H).

Induction of a Catastrophic Unconventional Cell Death Pathway by Vacquinol-1

Apoptosis is associated with a rapid loss of ATP. Vacquinol-1 administration (7.5 μM, 7 hr) led to a marked and significant increase of dead cells analyzed by flow cytometry, similar to staurosporin (1 μM, 7 hr; Figures 2A–2F). The apoptosis inhibitor Q-VAD only modestly rescued cells from death at 3 and 7 hr (Figure 2F). Active cleaved Caspase-3 was not increased by Vacquinol-1 as compared to vehicle-treated cultures, whereas doxorubicin (10 μM) markedly increased positive cells

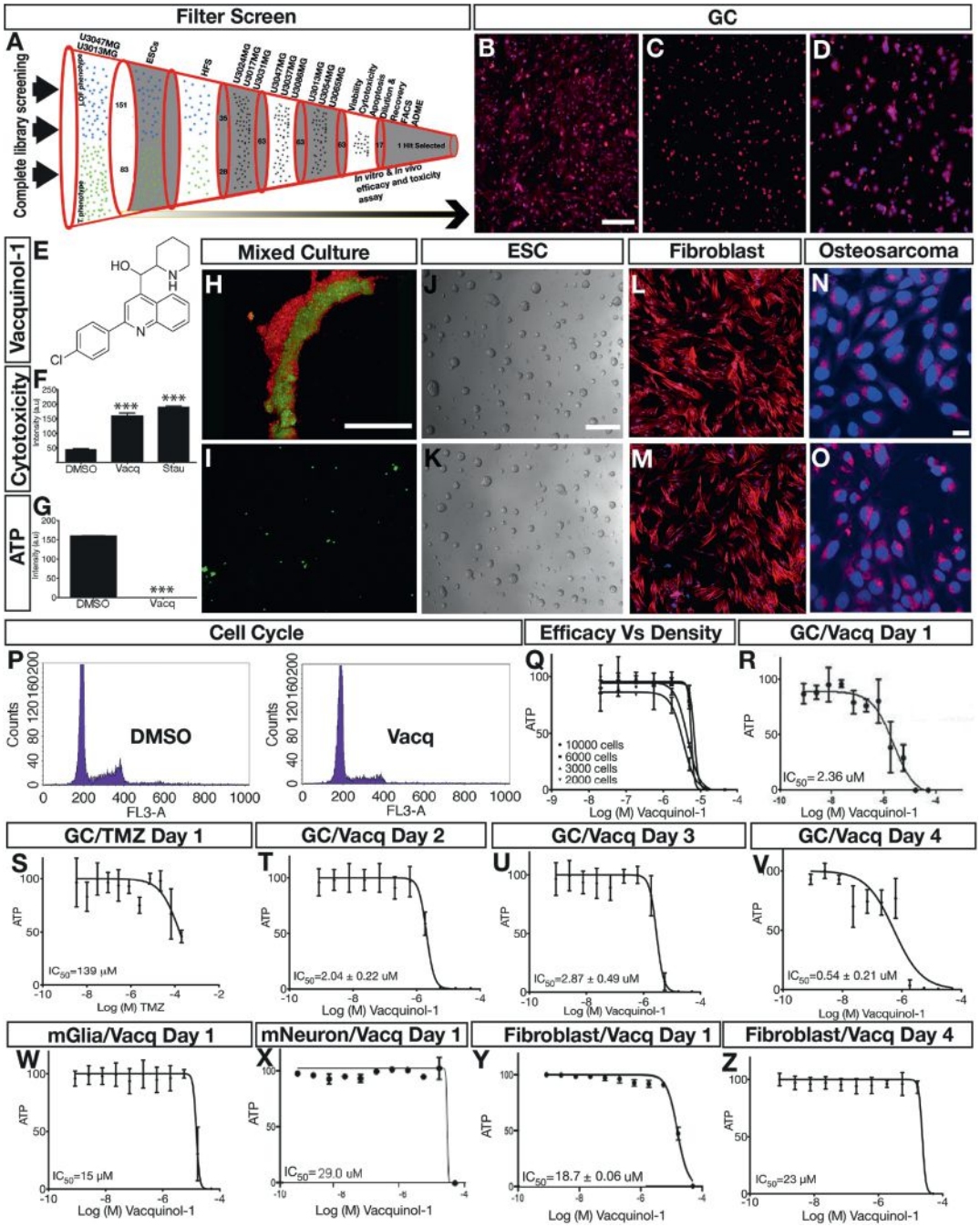

Figure 1. Identification of GC Vulnerability to Vacquinol-1

(A) Schematic representation of the screening process and hit selection.

(B–D) GC phenotypes, normal phenotype, tiny phenotype, or loose of fuse phenotype (B, C, and D, respectively).

(E) Structure of identified hit Vacquinol-1.

(F) Cytotoxicity by Vacquinol-1 (15 μM) on GCs compared to DMSO and Staurosporin (10 μM).

(G) Viability (ATP) assay of Vacquinol-1 (15 μM, 2 days).

(H and I) Selective effects of Vacquinol-1 (15 μM) (I) as compared to DMSO (H) on GCs (red) in mixed culture assay with fibroblasts (green).

(J–O) Response of mESCs (J and K), human fibroblasts (L and M), and osteosarcoma cells (N and O) (DMSO: J, L, and N; Vacquinol-1 15 μM: K, M, and O).

(P) Cell-cycle analysis.

(Q–Z) Dose response of Vacquinol-1 in viability assay (ATP). Scale bars, 50 μm (B–D), 100 μm (H and I), and 100 μm (J–O).

Abbreviations: GC, glioblastoma cells; HFS, human fibroblast, mESC; mouse embryonic stem cells; TMZ, Temozolomide; mGlia, mouse glia cells; Vacq, Vacquinol-1; Stau, staurosporin. Mean ± SD; t test, ***$p < 0.001$. See also Figures S1, S2, S3, S4, and S5.

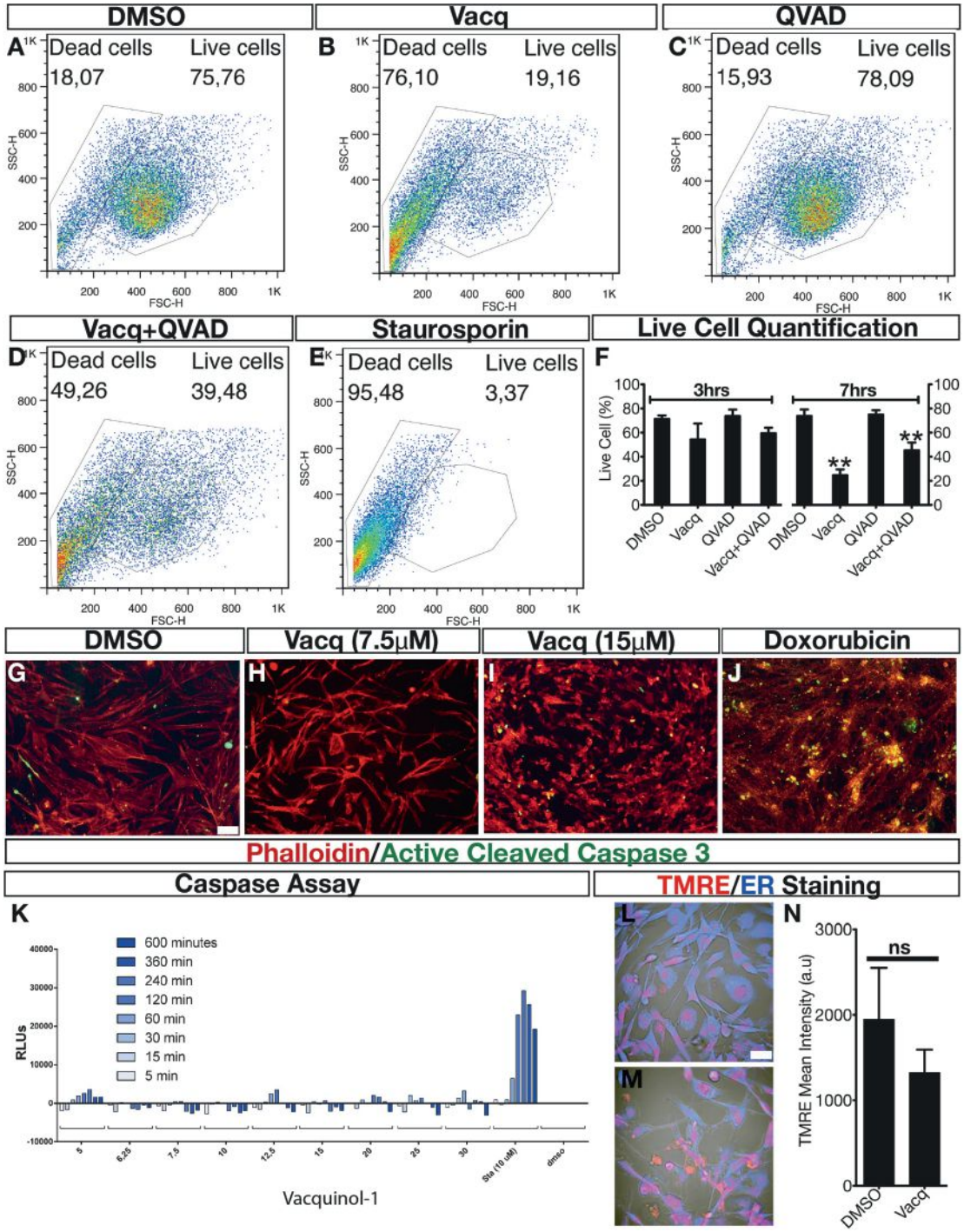

Figure 2. A Rapid Nonapoptotic Death by Vacquinol-1

(A–E) Flow-cytometry-based quantification of live and dead GC after 7 hr exposure (7.5 μM Vacquinol-1, 10 μM staurosporin).

(F) Quantification of live GCs after 3 hr or 7 hr of treatment.

(G–J) Active cleaved Caspase-3 (green) and phalloidin counterstaining (red) on GCs.

(K) Quantification of Caspase 3 and 7 activity.

(L–N) TMRE and ER tracker staining of GCs after 7 hr exposure to DMSO or 7.5 μM Vacquinol-1 followed by quantification of TMRE intensity (N). Scale bars, 50 μm (G–J, L, and M).

Abbreviations: a.u., arbitrary units; ns, not significant; RLUs, relative luminescence; Sta, Staurosporin; Vacq, Vacquinol-1. Mean ± SD; t test, **$p < 0.01$ to DMSO.

(Figures 2G–2J). Caspase-3 and Caspase-7 enzymatic activity was measured between 5 and 600 min after addition of Vacquinol-1 at increasing concentrations (5–30 μM). Unlike staurosporin, Vacquinol-1 had no effect on caspase activity at any concentration or time point (Figure 2K). The accumulation of tetramethylrhodamine ethyl ester (TMRE) in mitochondria and the endoplasmic reticulum is driven by their membrane potential. TMRE incorporation in mitochondria was largely unaffected by Vacquinol-1 (7.5 μM, 7 hr; Figures 2L–2N). In ratiometric calcium imaging with ATP as positive control, cytosolic calcium flux was not affected by Vacquinol-1 (Figures 3A, 3B, 3A′, and 3B′). These results show that Vacquinol-1-induced GC death occurs by a nonapoptotic mechanism and does not involve a disruption of active mitochondria.

Autophagy-associated cell death is the most widely studied form of nonapoptotic cell death (Gozuacik and Kimchi, 2007). LC3-II is conjugated to phosphatidylethanolamine on autophagosomic membranes. Vacquinol-1 did not increase LC3-II immunoreactivity (Figures 3C and 3D). Scanning electron microscopy on Vacquinol-1-treated GCs revealed a rapid rounding of cells and appearance of membrane invaginations curved into crater-like cups on the cell surface membrane (Figure 3F, arrowheads), indicating an endocytic-like activity. Consistently, live-cell imaging at high magnification revealed the formation of spherical protrusions, blebs, appearing within seconds of exposing the cells to Vacquinol-1 (Movie S1). With standard phase contrast optics, live imaging revealed within minutes of Vacquinol-1 exposure (15 μM) cell rounding and the formation of massive membrane ruffles and eventual death of cells by a rupture of the cytoplasmic membrane, preceded by a marked contraction of the cytoplasmic membrane followed by uncontrolled expansion resulting in its rupture (Figure 3G and Movies S2 and S3). Live imaging with Nomarski optics showed a rapid formation of intracellular vacuoles and membrane invaginations within 10 min of Vacquinol-1 (3.5 μM) with a dose-dependent increase of vacuole formation. Vacuole size and numbers increased with time (Figure 3H and Movie S3) and led to displacement of the cytoplasm with large vacuoles and eventually cell rupture. These results confirm an induction of endocytic-like activity by Vacquinol-1.

Using orthogonal (z stack projection) overlap of several bright-field focal planes in a 3D image stack taken from a single-well image field, large vacuoles of varying sizes were clearly observed as lucent, a characteristic of vacuoles resulting from macropinocytosis (Figure 4A). Another unique feature of macropinocytosis is a large nonselective internalization of fluid trapped beneath the projections of plasma membrane during membrane ruffling (Mercer and Helenius, 2012; Swanson, 2008). Hence, rapid incorporation of extracellular-phase fluid tracers is a hallmark of macropinosomes. The tracer lucifer yellow (LY) in the medium was taken up in most or all cells within 20 min (Figures 4B–4E; 7.5 μM Vacquinol-1) with an appearance within vacuoles (Figures 4F–4H). Internalization of LY was observed occasionally in nonstimulated GCs but at a very low rate compared to Vacquinol-1. Clathrin-independent endocytosis of the macropinocytosis type is sensitive to the specific inhibitor of the vacuolar-type H^+-ATPase, Bafilomycin A1 (Baf-A) (Kaul et al., 2007; Overmeyer et al., 2011). A short-term (1 hr) incubation of GCs with 100 nM Baf-A had no effect by itself on uptake of LY but completely abrogated Vacquinol-1-induced LY uptake (Figure 4I). Macropinocytosis is also sensitive to perturbation of the activity of Dynamin by dynasore (Gold et al., 2010) and actin by Cytochalasin D (Grimmer et al., 2002), which both completely prevented LY uptake, whereas inhibition of the clathrin-dependent pathway with chlorpromazine was ineffective (Figure 4I). Transmission electron microscopy (TEM) confirmed induction of a massive vacuolization in cells (7.5 μM, 6 hr; Figures 4J–4O). Clathrin-coated endosomes are regular in size and are bounded by double membrane. The numerous vacuoles observed in GCs were large and of varying size, mostly empty and bounded by a single membrane (Figures 4N and 4O), features that are consistent with macropinosomes (Overmeyer et al., 2008). The lucent vacuoles were distinct from lysosomes, autolysosomes, and late endosomes, which typically contain electron-dense organelle remnants or degraded cytoplasmic components. Swollen endoplasmic reticulum and mitochondria and distorted bilayer structures of nuclear membrane was occasionally observed (Figures 4N, 4O, and S6). In cells on the verge of lysis, the vacuoles had typically expanded to a point where much of the cytoplasmic membrane was disrupted (Figure 4M). Macropinosomes vary in size from ~0.5–5.0 μm, which is consistent with the range of Vacquinol-1-induced vacuoles quantified by TEM (7.5 μM, 6 hr; Figure 4P). Macropinocytic vacuoles recruit the late endosomal and lysosomal marker LAMP1. Consistently, a marked increase of LAMP1 immunofluorescence was observed that occasionally also was associated with membrane protrusions (7.5 μM, 6 hr; Figures 4Q–4T). These results provide evidence for initiation of massive macropinocytosis by Vacquinol-1, leading to catastrophic vacuolization and resulting in a necrotic-like cell death.

Requirement of MKK4 Activation for Vacquinol-1-Induced Macropinocytosis

An unbiased short hairpin RNA (shRNA) screen was used to identify pathways for Vacquinol-1-induced vacuolization. The approach was based on the idea that depleting a key factor in the pathway should render GCs refractive to Vacquinol-1-induced death. A DECIPHER lentiviral shRNA library consisting of 27,500 shRNAs covering 5,043 target genes (Human Module 1) were used to transduce U3013MG GCs. Surviving cells after 24 hr of Vacquinol-1 (14 μM; Figure 5A) displayed markedly different cell appearance (Figures 5B and 5C). The resulting Vacquinol-1-resistant GCs displayed an IC_{50} of 14.3 ± 1.16 μM on GC viability (Figure 5D), similar to fibroblasts (IC_{50} of 18.7 ± 0.06 μM). Sequencing of DNA prepared from the resistant GCs revealed an enrichment of *MAP2K4* shRNA viruses (Figure S7A). Fluorescence staining and western blot analyses of GCs for activating phosphorylation of MKK4 encoded by *MAP2K4* revealed a rapid and pronounced activation by Vacquinol-1 (7.5 μM) from 5 min to 26 hr of stimulation (Figures 5E–5K). No effect on histone H3K27 methylation was observed (Figure 5K). Abrogation of MKK4 activity by two independent shRNAs led to marked increase of the IC_{50} viability of Vacquinol-1-treated GCs (94% knockdown of protein level, n = 3; Figures 5L, S7B, and S7C). Phosphorylated MKK4 rapidly organized as punctate cytoplasmic staining in Vacquinol-1-treated cells (7.5 μM, 12 hr; Figures 5M and 5N). These results identify activation of MKK4 as a

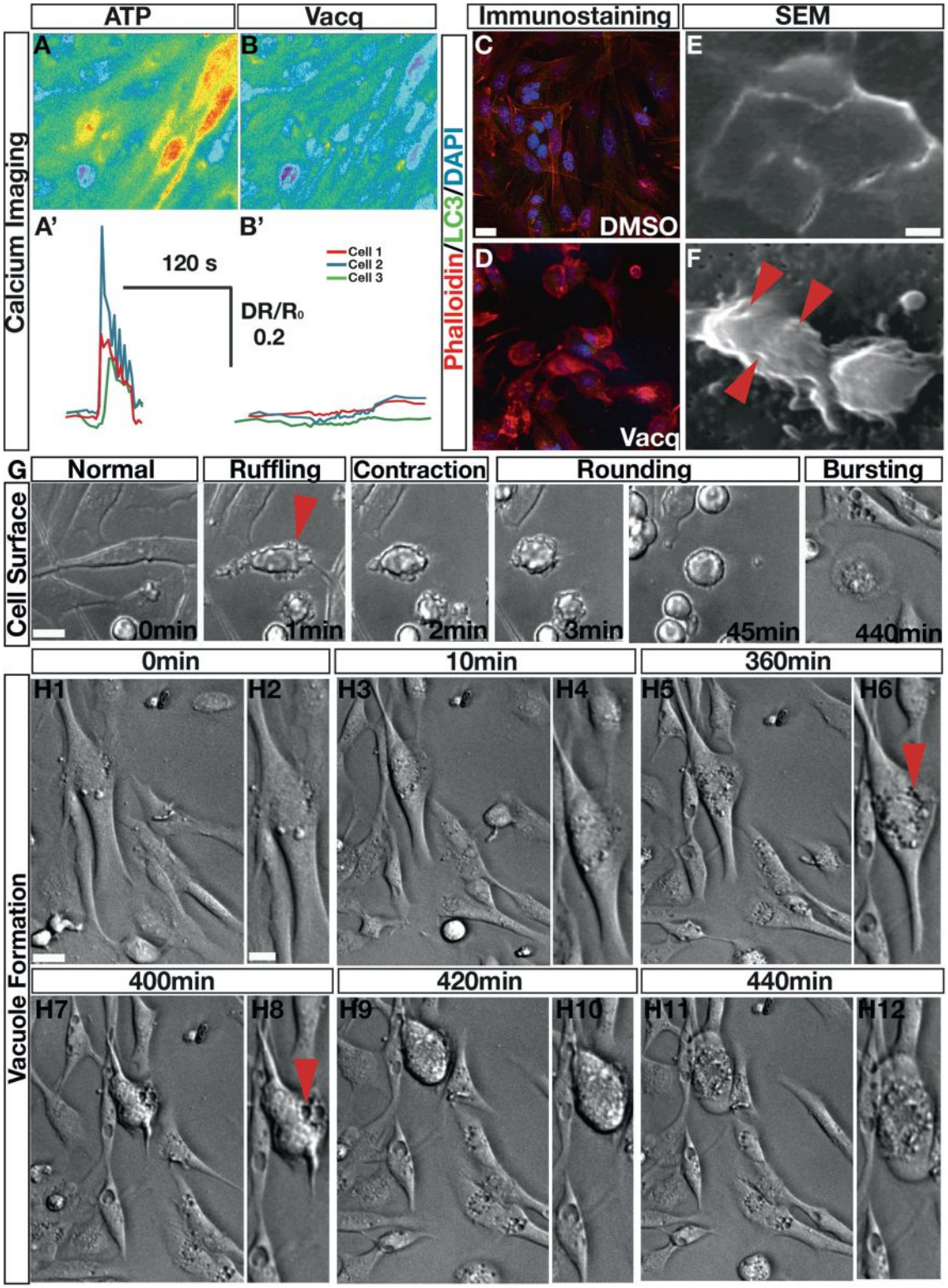

Figure 3. A Rapid Induction of Membrane Ruffling and Vacuolization by Vacquinol-1

(A and B) Ca^{2+} flux in GCs.

(C and D) LC3-II immunoreactivity (Vacquinol-1, 7.5 μM).

(E and F) SEM analyses of GCs (7.5 μM Vacquinol-1 for 7 hr, red arrowheads point at membrane indentations).

(legend continued on next page)

critical node in the signaling pathway executing Vacquinol-1-induced death of GCs.

MKK4 was confirmed required for the process of Vacquinol-1-induced macropinocytosis. Thus, following knockdown of *MAP2K4*, GCs became refractory to Vacquinol-1-induced vacuolization and LY incorporation (Figures 5O–5U), similar to osteosarcoma cells (Figures 5S and 5T), showing that resistance to death is associated with a defective formation of macropinocytic vacuoles induced by Vacquinol-1. Thus, the distinctive feature of vulnerability to macropinocytosis and death in GCs requires MKK4 activity.

Efficacy of Vacquinols Is Governed by Selective Chemical Features

Acquisition of structural analogs from NCI/DTP (http://dtp.cancer.gov), along with chemical synthesis (Extended Experimental Procedures; Data S1), was used for identification of potent derivatives, as well as insight into the SAR of Vacquinol-1 (Figure 6). Key chemical features critical for efficacy were identified by measurements of IC_{50} in viability assay. Aβ-hydroxyamino moiety in the 4 position of the quinoline core was invariably crucial. In accordance, all analogs containing either the ketone or carbamide in this position were inactive (Figure 6, compounds 2–3), as was the analog without this moiety (Figure 6, compound 5). Replacing piperidine with pyrrolidine (Figure 6, compound 6) marginally attenuated activity, whereas pyridine (Figure 6, compound 7) as an isostere of piperidine resulted in a complete loss of potency. Piperidine *N*-methylation (Figure 6, compound 8) gave a dramatic drop in effect, whereas methylation of the vicinal alcohol was tolerated (Figure 6, compound 4). Surprisingly, three of the four possible stereoisomers of Vacquinol-1 were roughly equipotent, with one isomer slightly less active (data not shown).

The quinoline core and 2-(4-chlorophenyl) moiety were more tolerant of variation, as the corresponding benzoquinoline (Figure 6, compound 15) resulted in the hitherto most potent compound identified in the Vacquinol series (IC_{50} = 0.39 μM). Additional positions of the core scaffold were amenable to functionalization with slight or no effect on activity (e.g., compound 13 and 14).

The 2-phenylquinoline core structure also appeared to be crucial for activity, as the analogous 4-pyridinyl compounds with (Figure 6, compound 20) or without (Figure 6, compound 19) the pendant 2-phenyl group were completely inactive. Similarly, removal of the 2-(4-chloro)phenyl ring resulted in complete abrogation of effect (Figure 6, compound 21). The in vitro efficacy of evaluated compounds showed a high correlation to in vivo effects in the zebrafish xenograft model (Figure 6).

In summary, these results show that modification of the β-hydroxypiperidine moiety or change of the quinoline scaffold of Vacquinol-1 lead to dramatic shifts in potency, whereas substitutions on the scaffold and pendant 2-phenyl group are tolerated. Modifications that are expected to only marginally affect physicochemical properties—e.g., pKa or logP—gave large variations in activity, supporting the hypothesis that the compounds exert their phenotypic response through binding to a specific protein target (or targets). However, as all compounds were evaluated and triaged in the primary GC viability assay, beyond binding affinity to putative pharmacological targets, pharmacokinetic properties such as membrane permeability are likely contributing factors of compound efficacy in cells.

In Vitro Preclinical Profiling of Vacquinol-1

In vitro physicochemical testing of Vacquinol-1 (i.e., solubility, pK_a, and logP/D) indicates typical characteristics of a cationic amphiphilic drug (eg., high basic pKa, high logP/D), albeit an apparent high solubility in artificial cerebrospinal fluid (ACSF). ADME profiling confirmed that Vacquinol-1 exhibits high apparent membrane permeability (Papp) in Caco-2 cell monolayers. A slight efflux was detected, which was completely inhibited by the GF120918 (Elacridar), an inhibitor of P-glycoprotein (Hyafil et al., 1993). Further, Vacquinol-1 was metabolically stable in human and mouse liver microsomes, as well as in freshly prepared human hepatocytes. Thus, Vacquinol-1 is predicted to be highly absorptive over biological membranes and resilient to metabolism, which indicates high bioavailability (Table S3).

Attenuation of Tumor Growth In Vivo and Prolonging Survival by Vacquinol-1

Based on these results, Vacquinol-1 appeared as a promising candidate molecule for the treatment of glioblastoma. The zebrafish xenograft glioblastoma model was developed for quantitative analyses of tumor development and infiltration in the host brain (Figures S7D and S7E). Within 1 week after fluorescently labeled U3013MG cells were injected, GCs rapidly expanded and formed a tumor cell mass within the ventricle and started to infiltrate the brain (Figures 7A and 7B). The developing tumors stained for human nuclear antigen (Figure S7D). Quantification of area, fluorescence level, and infiltration (distance from ventricle) revealed beneficial effects of Vacquinol-1 on all parameters (10 days, 15 μM in aquarium water; Figures 7C–7I). The ability of Vacquinol-1 to attenuate tumor progression was next examined in a mouse model for human GBM. NOD/SCID mice received intracranial injections of U3013M GCs, and the resulting tumor was allowed to develop for 7 weeks. All mice presented with large and highly vascularized tumors infiltrating the host brain and often displayed massive areas of necrosis, overtly observed during dissection of the brains (n = 5, Figure 7J1). Histopathologic analysis revealed several features of GBM, including pseudopalisading necrosis, mitotic cells, and extensive microvascular proliferation (Louis et al., 2007) (Figures 7J1–7J3 and S7F). Tumors were highly immunoreactive for human Nestin (hNestin) and human GFAP (hGFAP). Vacquinol-1 (15 μM, 0.5 μl/hr) or vehicle (DMSO) were administered intracranially into the site of original cell deposit 6 weeks after engraftment. Despite the advanced stage of cancer at the time of Vacquinol-1 administration, whole-brain morphology was

(G) Live imaging of GCs (15 μM Vacquinol-1). Images collected at times of major phenotypic changes.
(H) (H1 and H12) Live imaging with interference contrast optics of GCs (Vacquinol-1, 3.5 μM). Note increase in vacuole number and size (arrowhead points at a vacuole expanding in size). Scale bars, 50 μm (C), 5 μm (E), 20 μm (G), 20 μm (H1), and 10 μm (H2).
Abbreviations: s, seconds; min, minutes; SEM, scanning electron microscopy. See also Figure S4 and Movies S1, S2, and S3.

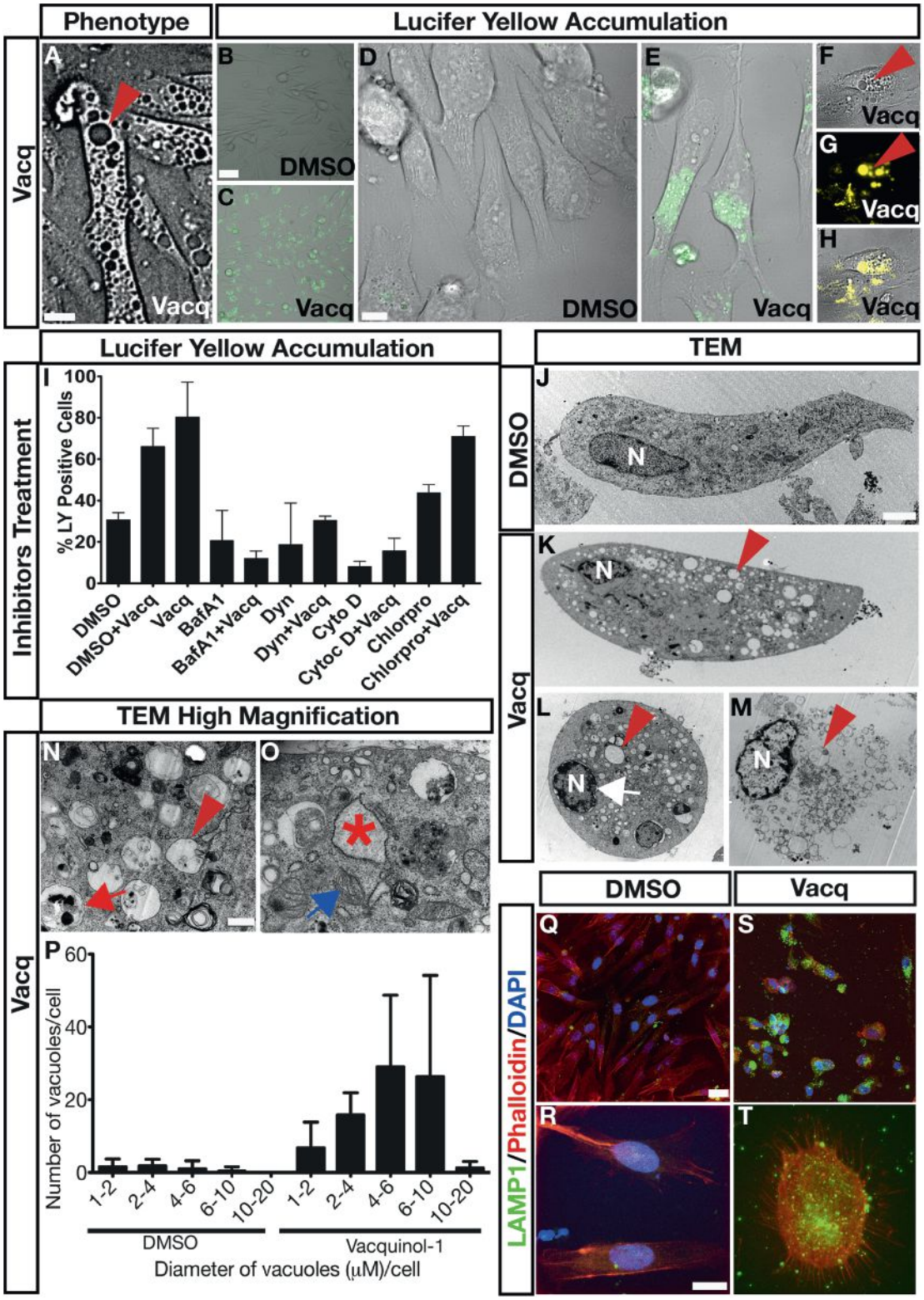

Figure 4. GC Vulnerability to Macropinocytosis and Catastrophic Vacuolization Resulting in Cell Death

(A) Merge of optical interference contrast planes (Vacquinol-1 7.5 μM, arrowhead indicates vacuole).

(B–H) LY accumulation in GCs. Arrowhead in (F)–(H) points to a LY-containing vacuole.

(legend continued on next page)

markedly normalized after 1 week treatment (Figures 7J1 and 7K). Tumors were invariantly smaller, and the area of necrosis and hGFAP and hNestin immunoreactivity was significantly reduced (Figures 7L–7O and S7G). Only tumor cells in Vacquinol-1-treated mice displayed a massive LAMP1 staining (Figures 7P and 7Q). These results show that Vacquinol-1 activates similar cellular responses in vivo as in vitro, that activation of this pathway is selective for GBM as no staining was observed in the host brain, and that it has the capacity when administered into the brain to attenuate tumor growth.

Encouraged by these results, we investigated the bioavailability of Vacquinol-1 in vivo by oral (p.o.), intravenous (i.v.), and intraperitoneal administration. The i.v. plasma kinetics lacked a clear distribution phase, which indicates a rapid tissue distribution (apparent distribution kinetic phase visible in brain i.v.) after administration and a relatively large calculated volume of distribution, as predicted by in vitro ADME data. The pharmacokinetics of Vacquinol-1 showed a maximal plasma exposure of 3,279 ng/ml and good penetrance into the brain with exposure of 1,860 ng/ml following a single oral dose of 20 mg/kg (Figures S7H, S7J, and S7K). As predicted from the in vitro evaluation of metabolic stability, Vacquinol-1 was highly stable in vivo with very low systemic plasma clearance ($t_{1/2}$ = 52 hr in plasma) (Figure S7H). Based on these results, the ability of oral Vacquinol-1 administration (20 mg/kg) once daily for 5 days to affect disease progression was examined by MRI measurements of tumor volume in the above-described xenograft GBM model. Treatment started at 6 weeks after engraftment of U3013M GCs, and animals were analyzed at week 8. During dissection, brains from vehicle treated mice displayed hemorrhage, areas of necrosis, and increased brain weight (n = 7), whereas brains from Vacquinol-1-treated mice (n = 13) showed a normal brain morphology and had a normalized brain weight (Figures 7S and S7I). Analysis by MRI revealed large tumors in all vehicle-treated mice with significantly smaller (four animals) or complete absence (nine animals) of detectable tumors in Vacquinol-1-receiving mice (Figures 7R, 7T, and S7L). These results urged us to examine whether survival can be prolonged by Vacquinol-1. Mice receiving oral administration of Vacquinol-1 2 weeks after engraftment of U3013M GCs (20 mg/kg once daily for 5 days) displayed a temporary 10.8% ± 8.1% loss of body weight but regained weight to controls 1–2 weeks after end of treatment. Vacquinol-1 significantly enhanced survival as compared to vehicle-treated mice. Vehicle-treated animals (n = 8) showed a median survival of 31.5 days, whereas only two of the eight Vacquinol-1-treated mice died during the 80 days of the experiment (Figure 7U, p = 0.0004 Mantel-Cox test). Hence, we conclude that oral administration of Vacquinol-1 substantially impairs disease progression and prolongs survival.

DISCUSSION

We have undertaken a functional screen of GCs based on the assumption that the accumulation of genetic alterations affecting intracellular signaling pathways underlying tumorigenesis also can result in gained cellular vulnerability not necessarily involved in the cancerous process. One biological process was identified in this screen that resulted in a robust loss of viability and increased display of cytotoxicity in GCs. The effect occurs independently of engaging apoptotic or autophagic pathways or overtly compromising mitochondria. Instead, cytotoxicity was found to be conferred by a mechanism involving induction of massive macropinocytosis, resulting in catastrophic vacuolization and death. This effect was found only in GCs, as mESCs, fibroblasts, mouse astrocytes, neurons, and several other types of cancer cells did not respond similarly to Vacquinol-1.

The biological process initiated by Vacquinol-1 involves massive membrane ruffling and blebbing within seconds after stimuli onset, cell rounding, followed by vacuole formation, which, in a time and concentration-dependent manner, increases in number and size and eventually leads to a disruption of cell membrane integrity and cell death. The molecular target of Vacquinol-1 and/or enrichment of downstream signaling pathways appear to confer a specificity of vacuolization to GBM cells. The massive buildup of vacuoles shows that any clearance of vacuoles by recycling or fusion with other endosomal compartments is insufficient. These characteristics are shared with macropinocytic vacuoles observed by forced expression of constitutively activated Ras (Bhanot et al., 2010; Overmeyer et al., 2008). Because TMRE staining of mitochondria was not affected, indicating that membrane potential is unperturbed, we believe that the energy-consuming processes of massive membrane ruffling, retraction of blebs, and acidification of vacuoles contributes to the cellular depletion of ATP and is part of the high cytotoxicity of Vacquinol-1. Blebs are typically associated with macropinocytosis and are caused by a loss of the tight contact between the plasma membrane and the underlying layer of actin and myosin cortex, which holds the membrane under tension. Thus, when the plasma membrane separates from the cortex, the cytoplasmic pressure leads to formation of membrane blebs, which lacks the actin cytoskeleton (Charras and Paluch, 2008). The retraction of blebs is associated with actin reassembly and reattachment of the membrane to the actin cortex. During the final stage of Vacquinol-1-induced cell toxicity, we often observed by live imaging an initial cytoplasmic membrane contraction followed by a very fast expansion of the membrane, resulting in lysis of the cytoplasmic membrane. This finding is consistent with actin reassembly followed by a complete dissolving actin cortex attachment and thereby release of the

(I) Percent of LY-positive cells in the presence or absence of indicated inhibitors.

(J–O) TEM images of GCs. Note that (K), (L), and (M) represent cells at different stages of the cell death process. Arrowheads points at vacuoles, white arrow points at nuclear membrane, blue arrow points at swollen mitochondria, asterisk indicates swollen endoplasmic reticulum, and red arrow points at relatively rare vacuoles with some electron-dense material.

(P) Quantification of number and size of vacuoles per cell.

(Q–T) Immunostaining of GC for LAMP-1. Scale bars, 20 μm (A), 50 μm (B), 10 μm (D), 1 μm (J), 200 nm (N), 50 μm (Q), and 10 μm (R).

Abbreviations: BafA1, Bafilomycin A; Chlorp, Chlorpromazine; CytoD, cytochalsin D; Dyn, Dynasore; LY, lucifer yellow; TEM, transmission electron microscopy; Vacq, Vacquinol-1. Mean ± SD. See also Figure S6.

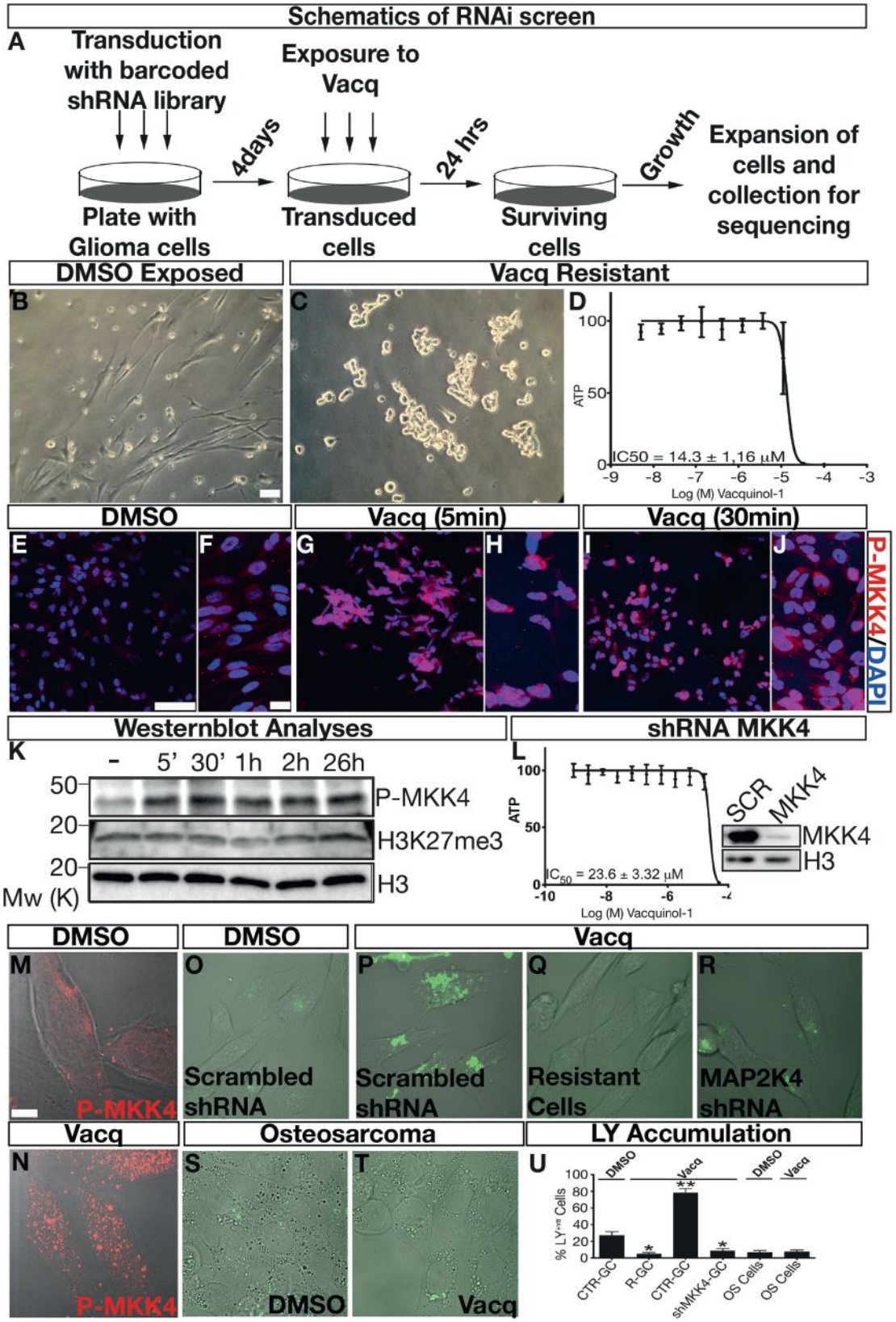

(legend on next page)

tension exerted by the hydrostatic pressure of the cytoplasmic membrane, leading to its fast expansion and lysis. This process is expected to be affected both by an increased membrane tension due to the diminishing content of cytoplasmic membrane caused by the vacuolization and by depletion of ATP that is required for actin reassembly.

Glioblastomas are highly aggressive and infiltrative and frequently recur after treatment. The main therapy involves radiation and chemotherapy with temozolomide (TMZ) (Stupp et al., 2005) that act by reducing cell viability causing apoptosis and senescence (Günther et al., 2003). Precisely how recurrence occurs is unknown but may involve clonal expansion of cells with accumulated mutations, rendering cells refractive to current treatment strategies (Zhang et al., 2010). Cellular heterogeneity of glioblastoma may also contribute to tumor recurrence, as the endogenous glioma cells with properties of cancer stem cells is a quiescent population (Alcantara Llaguno et al., 2009; Singh et al., 2004). TMZ and radiotherapy act primarily on rapidly dividing cells and may fail in due course because they cannot kill the subpopulation of relatively quiescent tumor-initiating cells (Bao et al., 2006; Chen et al., 2012a). The molecular action of Vacquinol-1 on macropinocytosis is expected to be independent of cell proliferation and therefore should target relatively quiescent stem-like tumor-initiating cells with similar efficiency as rapidly dividing cells. As it targets a new and independent pathway, Vacquinols are also expected to be efficient for drug-resistant cancer. Although Vacquinols could be efficient as monotherapy, the rapid loss of ATP would be expected also to potentiate cytotoxicity in combination therapy approaches.

The in vitro preclinical profiling and in vivo pharmacokinetics of Vacquinol-1 indicate promising CNS drug properties such that it is highly stable in vitro/in vivo with low systemic clearance and high passive permeability and that it displays good penetrance into the brain. Mice were found to be highly tolerant to Vacquinol-1, as administration with 20 mg/kg p.o. for 5 days did not result in a sustained weight loss, showing that the potential buildup of high plasma concentrations at steady state does not compromise survival. These results suggest that an adequate concentration for cytotoxicity of glioblastoma without severe unwanted effects to transpire possibly can be achieved in vivo following administration.

Macropinocytosis is induced by the activation of tyrosine kinase receptors, integrins, or other cell-surface receptors, which causes a general elevation of actin polymerization at the cell surface, resulting in membrane ruffles that close at the distal margins to engulf extracellular fluid (Haigler et al., 1979; Mercer and Helenius, 2012; Swanson, 2008). Thus, when ruffles curve into open, crater-like cups at the cell surface membrane, ruffle closure is followed by cup closure, separating the macropinosome from the plasma membrane. The massive cell ruffles observed after Vacquinol-1 addition, followed by cell membrane invaginations, could therefore be closely linked to the formation of macropinosomes.

The MAPKK, MKK4 encoded by *MAP2K4*, was found as a key signaling element for Vacquinol-1-induced macropinocytosis. MKK4 belongs to the stress/GPCR agonists/cytokine/growth factor-activated pathway, which previously is associated with inflammation, apoptosis, growth, and differentiation processes (Morrison, 2012), but we cannot find any previous knowledge on its participation in vacuolization. *MAP2K4* loss of function is observed at ~5% across a wide spectrum of cancers, including those of the breast, lung, pancreas, bile duct, prostate, and ovary, but its role appears complex, and both tumor suppressor and pro-oncogenic activities are consistent with its engagement in multiple cellular processes (Whitmarsh and Davis, 2007).

The mechanism of MKK4 activation and its requirement for macropinocytosis and vacuolization are not fully understood but could be engaged downstream of Ras-activated Rac1. *MAP2K4* has not been shown to be mutated in GBM, but nearly all tumors (88%) display alterations in receptor tyrosine kinase/Ras signaling. Constitutively active Ras, if ectopically expressed, can drive macropinocytosis in a glioblastoma cell line (Kaul et al., 2007; Overmeyer et al., 2008). It is possible that an elevated Ras signaling participates in MKK4 activation in glioblastoma and underlies the vulnerability of GCs to Vacquinol-1-induced vacuolization. However, GCs displayed a low constitutive uptake of LY in the absence of Vacquinol-1, indicating that endogenous Ras activity in these tumor cells is insufficient by itself for initiating high levels of macropinocytic activity. The critical role of MKK4 for macropinocytosis warrants studies to determine whether it is essential for induction of macropinocytosis in all its forms, including physiological processes, for instance, during uptake of bacteria, apoptotic bodies, necrotic cells, and viruses.

Vacquinol-1 (NSC13316) stems from a class of β-aminohydroxyquinolines originally developed for antimalarial application (Brown and Jacobs, 1946; Pinder and Burger, 1968; Rapport and Senear, 1946). A close analog to Vacquinol-1, NSC23925, has recently been reported to reverse P-glycoprotein-mediated efflux of several cancer drugs in multidrug-resistant cancer cell

Figure 5. Dependence on MKK4 for Macropinocytosis and Catastrophic Vacuolization in GCs

(A) Schematic illustration of the RNAi screen.

(B and C) Morphology of control and Vacquinol-1-resistant GCs.

(D) Viability (ATP) dose response of Vacquinol-1-resistant GCs.

(E–J) Immunocytochemical staining for phospho-MKK4.

(K) Western blot analysis for phospho-MKK4, H3K27me3, and H3 as loading control.

(L) Dose response of viability (ATP) of MAP2K4 shRNA-transduced GCs exposed to Vacquinol-1 and western blot analyses of the knockdown efficiency of the MKK4 shRNA-transduced cells.

(M and N) Immunocytochemical staining of GC for phospho-MKK4.

(O–T) LY accumulation in resistant cells, scrambled control, and MAP2K4 shRNA-transduced GCs and osteosarcoma cells.

(U) Quantification of percent LY-positive cells from the experiments shown in (O)–(T). Scale bars, 100 μm (B and E), 50 μm (F), and 10 μm (M).

Abbreviations: SCR or CTR, scrambled shRNA control; GC, glioblastoma cells; LY, lucifer yellow; R, resistant GCs from shRNA screen; Vacq, Vacquinol-1; OS, osteosarcoma cells. Mean ± SD; t test, *$p < 0.05$ and **$p < 0.01$. See also Figure S7.

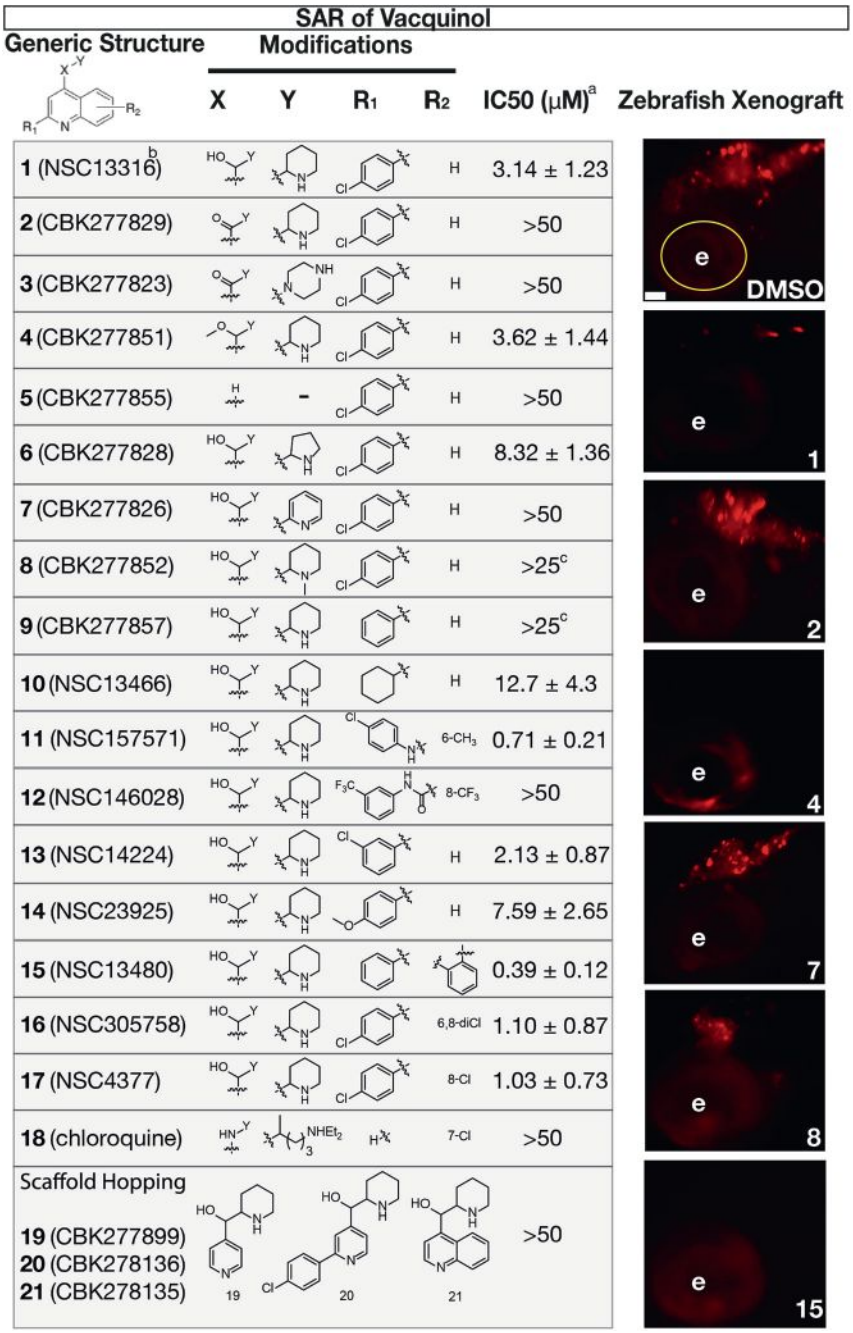

Figure 6. Structure-Activity Relationship of Vacquinols

Generic structure of Vacquinol-1 with modified positions represented by X, Y, R1, and R2. Representative compounds (compound ID) with various combinations of structural modification at site X, Y, R1, and R2 and their impact on its activity measured by dose response of viability (ATP) of GCs determined IC_{50} (24 hr) indicated, followed by some representative compound effects in the zebrafish xenograft model. Number at right bottom corner of the zebrafish xenograft panels (xenotransplanted GCs, red) indicates the compound number from the left side of the table. Scale bar, 100 μM. Abbreviations: e, eye; (a) IC_{50} values of quadruplicate data calculated from a logarithmic 11 point dose response; (b) Vacquinol-1; (c) Y_{min} not reached, indicating that the highest concentration evaluated in dose response did not reach full inhibition of viability relative to positive control, resulting in incomplete curves.

lines (Duan et al., 2009, 2012), although no direct cytotoxic effect of the compound itself was evident. In GCs, however, NSC23925 displayed an IC_{50} of 7.59 μM (Figure 6), only slightly less potent than Vacquinol-1. Compounds from the same class were recently described also as inhibitors of bacterial biofilm formation (León et al., 2013) and as inhibitors of SHIP1/2 in multiple myeloma cell lines (Fuhler et al., 2012).

Vacquinol-induced cell death does not appear to confer an unspecific cytotoxicity, as other cell types show marginal or no loss of viability in the presence of Vacquinol-1 at comparitive concentrations. Accumulation of phase-lucent vacuoles is consistently observed in all active members of the Vacquinol family of compounds (data not shown) at 10- to 100-fold lower concentrations than the corresponding IC_{50} of GC viability. No vacuoles could be observed in alternative cell lines, at any concentration, regardless of the level of cytotoxicity observed in these cells. We believe that induction of this phenotype is a critical contributor to in vivo efficacy.

The structure-activity relationship (SAR) of Vacquinols reveals an exquisite dependence on the piperidin-2-ylmethanol moiety in the 4 position of the quinoline. Few modifications were tolerated in this region, although variability could be introduced in other positions of the quinoline and/or the pendant phenyl group in the 2 position while maintaining effect. In contrast to the reported stereochemical superiority of a single isomer of NSC23925 in reversing Pgp-mediated drug resistance in SKOV-3 cell lines (Duan et al., 2012), three of the four possible isomers of Vacquinol-1 were roughly equipotent (data not shown). Thus, we did not pursue a stereospecific synthesis.

The long in vivo half-life of Vacquinol-1, in concert with its quinine-like lipophilic amine structure, suggested that the compound may be lysosomotropic in character, similar to the autophagy inhibitor chloroquine. Chloroquine has been described as toxic for glioblastoma cell lines through the induction of autophagic vacuole accumulation (Geng et al., 2010), a sensitizer of radiation-induced cell death of GCs (Firat et al., 2012) and as an adjuvant of conventional therapies of GBM (Sotelo et al.,

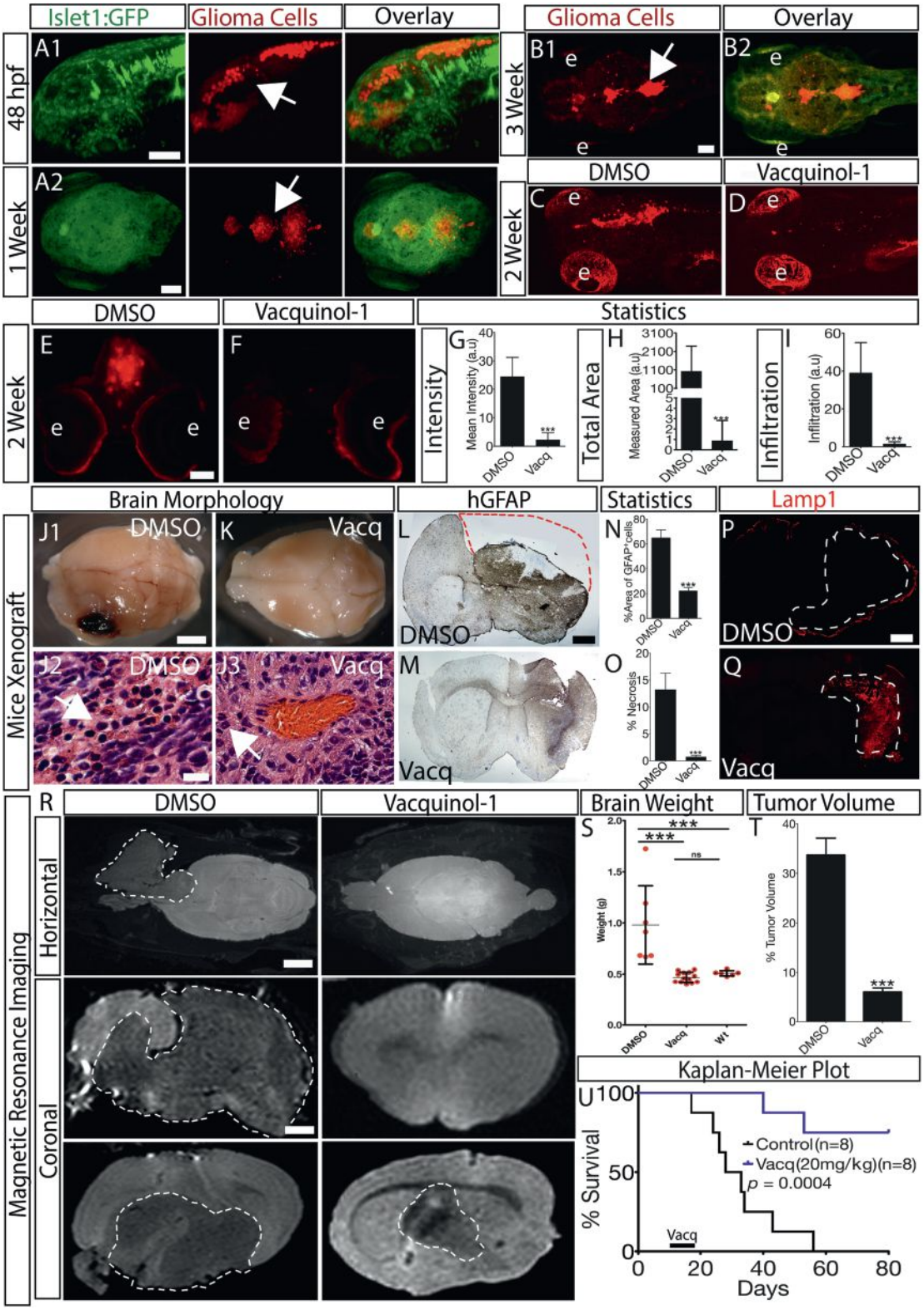

Figure 7. In Vivo Effects of Vacquinol-1 Treatment in Animal Models of GBM

(A) (A1 and A2) GCs (red) transplanted into islet1:GFP transgenic zebrafish brain imaged at 48 hours postfertilization (hpf) (A1) or after 1 week (A2). White arrows indicate transplanted cells.

(B) (B1 and B2) Three-week-old xenografted zebrafish larvae (red GCs indicated by arrow).

(legend continued on next page)

2006). However, chloroquine showed no intrinsic activity on GCs in our hands (Figure 6) and induced no vacuole accumulation. In addition, electron microscopy reveals that vacuoles induced by Vacquinol-1 are single-membrane bound, thus not autophagosomal in origin.

In addition to the long in vivo pharmacokinetic profile and oral bioavailability, Vacquinol-1 exhibits favorable overall preclinical characteristics. Although in vivo tolerance appears high and could be adequate for clinical utility, one possible obstacle for further clinical development of Vacquinol-1 is the effective therapeutic window in vitro, as unrelated toxicity appears at around 15 μM. The identification of compounds with higher selective activity toward GCs may improve this window.

By taking an unbiased strategy, we have identified a vulnerability to a macropinocytosis-associated catastrophic vacuolization as a selective feature of GBM and provide evidence for its targeted induction by a small molecule. We provide mechanistic and molecular insights for the cellular processes and signaling pathways involved and describe the structure-activity relationship of Vacquinol-1 for maintaining activity. Furthermore, our results provide evidence for an efficient in vivo induction of the same signaling pathway in animal models of GBM and show that tumor development can markedly be attenuated without apparent effects on host brain tissue. Thus, we have identified an acquired cellular property in GBM that can be readily targeted with small molecules displaying suitable properties for clinical development that rapidly and selectively depletes glioblastoma cells, attenuates disease progression, and prolongs survival in a GBM animal model.

EXPERIMENTAL PROCEDURES

GC Isolation and Screen

GBM grade IV biopsies were obtained and cultured according to Pollard et al. (2009). The NCI Diversity Set II small-molecule library was screened on GC lines U3013 and U3047 and was compared with mESCs and fibroblast cells to identify compounds affecting only GCs. The identified compounds were then exposed to a panel of other GC lines (U3013, U3047, U3024, U3031, U3037, U3086, U3054, and U3065), and the effect was documented.

Multiparametric Assays

Multiparametric assays of the 63 and 17 compounds were conducted in 384-well microtiter plates seeded with 10,000 cells. Cell viability, cytotoxicity, and apoptosis were measured using CellTiter-Glo Luminescent Cell Viability Assay, CytoTox-Glo Cytotoxicity Assay, and Caspase-Glo 9 Assay (Promega) according to the manufacturer's instructions. Mixed culture assay was performed with 1,000 labeled cells in hanging drop cultures. The dilution and recovery assay was performed by 2 day compound treatment followed by analysis after an additional 2 days without compound on GCs. Cell-cycle profiling was performed by propidium iodine flow cytometry and apoptosis by quantitative flow cytometry. Ratiometric calcium imaging and ADME analyses were performed according to previously published procedures. IC_{50} was determined using Cell Viability assay.

Live Imaging and In Vivo Tests

Live imaging was performed on an Operetta High Content imaging system (PerkinElmer). Toxicity on embryos and cardiac toxicity was assessed in Zebrafish. For tumor development, zebrafish or NOD-SCID mice were injected with ~3,000 or 100, 000 cells, respectively.

RNAi Screen

We used a DECIPHER lentiviral shRNA library consisting of Human Module 1, which includes a targeting of signaling pathways. In total 27,500 shRNAs targeting 5,043 genes were used. Viruses enriched in surviving cells after Vacquinol exposure (14 mM) were identified by deep sequencing.

Chemical Synthesis

Chemical syntheses were performed at CBCS, Karolinska Institutet, Stockholm, Sweden and SAI Life Sciences, Hyderabad, India. All final compounds were purified to ≥95% purity according to UV detection (305 ± 90 nm) and identity verified by mass spectrometry (MS) and NMR spectra before evaluated in biological assays. A full description of chemistry and associated analyses can be found in the Supplemental Information.

SUPPLEMENTAL INFORMATION

Supplemental Information includes seven figures, one data file, three tables, and three movies and can be found with this article online at http://dx.doi.org/10.1016/j.cell.2014.02.021.

ACKNOWLEDGMENTS

The authors thank Helena Samuelsson for technical help and Robert Harmel for help with the synthesis of compounds. We also thank Susan Warner and the team at Mice and Zebrafish Core facility for wonderful support during the course of experiments, the CLICK Imaging Facility supported by the Wallenberg Foundation, Erik Nilsson for setting up the spectral analysis, and the Core Facility AKM/Karolinska Experimental Research and Imaging Centre at Karolinska University Hospital for MRI. This work was supported by the Swedish Research Council for Medicine and Health, the Swedish Cancer Society,

(C–F) Whole-mount images (C and D) and sections (E and F) of GC (red) transplanted into the zebrafish brain, followed by 2 week treatment (DMSO or Vacquinol-1).
(G–I) Quantification of (C)–(F).
(J) (J1–J3) GC xenotransplanted mouse brain treated with DMSO. Hematoxylin- and eosin-stained sections of U3013MG-derived tumor in NOD-SCID brain (J2 and J3); note apopototic figures (white arrow in J2) and mitoses (white arrow in J3).
(K) GC xenotransplanted brain treated intracranially with Vacquinol-1.
(L–O) Immunohistochemical staining with anti-human GFAP antibody on GC xenotransplanted brains (DMSO, L and Vacquinol-1, M). Quantification of GFAP-positive (N) and necrotic area (O).
(P and Q) Immunohistochemical detection of LAMP1-1 (red) in GC xenotransplanted brains (DMSO, P and Vacquinol-1, Q). Tumor indicated with hatched line.
(R) MRI of GC transplanted mouse brains following treatment either with DMSO or Vacquinol-1. Both horizontal and coronal sections are shown. Each panel is from a different mouse.
(S) Measurement of total brain weight of wild-type animal or GC transplanted mice brain following treatment with DMSO or Vacquinol-1.
(T) Measurement of tumor volume in brains imaged by MRI following treatment with DMSO or Vacquinol-1.
(U) Kaplan-Meier survival curve of mice transplanted with GCs. A 5 day oral treatment with vehicle or Vacquinol-1 was started 2 weeks after the transplantation and is indicated by a black horizontal bar on the x axis. A significance or $p = 0.0004$ is shown by using log rank (Mantel-Cox) test.
Scale bars: zebrafish panels, 100 μm, 2.5 mm (L1), 5 mm (L2), 0.1 mm (L3), 2 mm (N), and 1 mm (V). Abbreviations: a.u., arbitrary units; e, eye. Mean ± SD; t test, ***$p < 0.001$. See also Figure S7.

the Swedish strategic funds (DBRM, StratNeuro), the Swedish Brain Foundation, Hållsten Foundation, Torsten Söderberg Professorship, Wallenberg Foundation (Wallenberg Scholar grant), and ERC advanced grant (232675) to P.E. (who is a Wallenberg Scholar).The contributions of K.S., C.K., R.S., P.A., and L.G.J.H. to the project were supported by Chemical Biology Consortium Sweden (CBCS) and funded by the Swedish Research Council. K.F.N., L.U., and B.W. were supported by grants from the Swedish Research Council for Medicine and Health and the Swedish Cancer Society. S.S.K., L.G.J.H., and P.E. have applied for protection of intellectual property related to the results in the manuscript.

Received: September 25, 2013
Revised: December 18, 2013
Accepted: February 6, 2014
Published: March 20, 2014

REFERENCES

Alcantara Llaguno, S., Chen, J., Kwon, C.H., Jackson, E.L., Li, Y., Burns, D.K., Alvarez-Buylla, A., and Parada, L.F. (2009). Malignant astrocytomas originate from neural stem/progenitor cells in a somatic tumor suppressor mouse model. Cancer Cell *15*, 45–56.

Bao, S., Wu, Q., McLendon, R.E., Hao, Y., Shi, Q., Hjelmeland, A.B., Dewhirst, M.W., Bigner, D.D., and Rich, J.N. (2006). Glioma stem cells promote radioresistance by preferential activation of the DNA damage response. Nature *444*, 756–760.

Barami, K., Sloan, A.E., Rojiani, A., Schell, M.J., Staller, A., and Brem, S. (2009). Relationship of gliomas to the ventricular walls. J. Clin. Neurosci. *16*, 195–201.

Bhanot, H., Young, A.M., Overmeyer, J.H., and Maltese, W.A. (2010). Induction of nonapoptotic cell death by activated Ras requires inverse regulation of Rac1 and Arf6. Mol. Cancer Res. *8*, 1358–1374.

Bleau, A.M., and Holland, E.C. (2009). [Chemotherapeutic treatment of gliomas increases the amount of cancer stem-like cells]. Med. Sci. (Paris) *25*, 775–777.

Brennan, C., Momota, H., Hambardzumyan, D., Ozawa, T., Tandon, A., Pedraza, A., and Holland, E. (2009). Glioblastoma subclasses can be defined by activity among signal transduction pathways and associated genomic alterations. PLoS One *4*, e7752.

Brennan, C.W., Verhaak, R.G., McKenna, A., Campos, B., Noushmehr, H., Salama, S.R., Zheng, S., Chakravarty, D., Sanborn, J.Z., Berman, S.H., et al. (2013). The somatic genomic landscape of glioblastoma. Cell *155*, 462–477.

Brown, R.F., and Jacobs, T.L. (1946). alpha-(2-Piperidyl)-2-aryl-4-quinolinemethanols. J. Am. Chem. Soc. *68*, 2705–2708.

Cancer Genome Atlas Research Network (2008). Comprehensive genomic characterization defines human glioblastoma genes and core pathways. Nature *455*, 1061–1068.

Charras, G., and Paluch, E. (2008). Blebs lead the way: how to migrate without lamellipodia. Nat. Rev. Mol. Cell Biol. *9*, 730–736.

Chen, J., Li, Y., Yu, T.S., McKay, R.M., Burns, D.K., Kernie, S.G., and Parada, L.F. (2012a). A restricted cell population propagates glioblastoma growth after chemotherapy. Nature *488*, 522–526.

Chen, J., McKay, R.M., and Parada, L.F. (2012b). Malignant glioma: lessons from genomics, mouse models, and stem cells. Cell *149*, 36–47.

Dent, P., Yacoub, A., Park, M., Sarkar, D., Shah, K., Curiel, D.T., Grant, S., and Fisher, P.B. (2008). Searching for a cure: gene therapy for glioblastoma. Cancer Biol. Ther. *7*, 1335–1340.

Dolecek, T.A., Propp, J.M., Stroup, N.E., and Kruchko, C. (2012). CBTRUS statistical report: primary brain and central nervous system tumors diagnosed in the United States in 2005-2009. Neuro-oncol. *14* (*Suppl 5*), v1–v49.

Duan, Z., Choy, E., and Hornicek, F.J. (2009). NSC23925, identified in a high-throughput cell-based screen, reverses multidrug resistance. PLoS ONE *4*, e7415.

Duan, Z., Li, X., Huang, H., Yuan, W., Zheng, S.L., Liu, X., Zhang, Z., Choy, E., Harmon, D., Mankin, H., and Hornicek, F. (2012). Synthesis and evaluation of (2-(4-methoxyphenyl)-4-quinolinyl)(2-piperidinyl)methanol (NSC23925) isomers to reverse multidrug resistance in cancer. J. Med. Chem. *55*, 3113–3121.

Firat, E., Weyerbrock, A., Gaedicke, S., Grosu, A.L., and Niedermann, G. (2012). Chloroquine or chloroquine-PI3K/Akt pathway inhibitor combinations strongly promote γ-irradiation-induced cell death in primary stem-like glioma cells. PLoS ONE *7*, e47357.

Fuhler, G.M., Brooks, R., Toms, B., Iyer, S., Gengo, E.A., Park, M.Y., Gumbleton, M., Viernes, D.R., Chisholm, J.D., and Kerr, W.G. (2012). Therapeutic potential of SH2 domain-containing inositol-5′-phosphatase 1 (SHIP1) and SHIP2 inhibition in cancer. Mol. Med. *18*, 65–75.

Furnari, F.B., Fenton, T., Bachoo, R.M., Mukasa, A., Stommel, J.M., Stegh, A., Hahn, W.C., Ligon, K.L., Louis, D.N., Brennan, C., et al. (2007). Malignant astrocytic glioma: genetics, biology, and paths to treatment. Genes Dev. *21*, 2683–2710.

Gallo, M., Ho, J., Coutinho, F.J., Vanner, R., Lee, L., Head, R., Ling, E.K., Clarke, I.D., and Dirks, P.B. (2013). A tumorigenic MLL-homeobox network in human glioblastoma stem cells. Cancer Res. *73*, 417–427.

Geng, Y., Kohli, L., Klocke, B.J., and Roth, K.A. (2010). Chloroquine-induced autophagic vacuole accumulation and cell death in glioma cells is p53 independent. Neuro-oncol. *12*, 473–481.

Gold, S., Monaghan, P., Mertens, P., and Jackson, T. (2010). A clathrin independent macropinocytosis-like entry mechanism used by bluetongue virus-1 during infection of BHK cells. PLoS ONE *5*, e11360.

Gozuacik, D., and Kimchi, A. (2007). Autophagy and cell death. Curr. Top. Dev. Biol. *78*, 217–245.

Grimmer, S., van Deurs, B., and Sandvig, K. (2002). Membrane ruffling and macropinocytosis in A431 cells require cholesterol. J. Cell Sci. *115*, 2953–2962.

Günther, W., Pawlak, E., Damasceno, R., Arnold, H., and Terzis, A.J. (2003). Temozolomide induces apoptosis and senescence in glioma cells cultured as multicellular spheroids. Br. J. Cancer *88*, 463–469.

Haigler, H.T., McKanna, J.A., and Cohen, S. (1979). Rapid stimulation of pinocytosis in human carcinoma cells A-431 by epidermal growth factor. J. Cell Biol. *83*, 82–90.

Hemmati, H.D., Nakano, I., Lazareff, J.A., Masterman-Smith, M., Geschwind, D.H., Bronner-Fraser, M., and Kornblum, H.I. (2003). Cancerous stem cells can arise from pediatric brain tumors. Proc. Natl. Acad. Sci. USA *100*, 15178–15183.

Hyafil, F., Vergely, C., Du Vignaud, P., and Grand-Perret, T. (1993). In vitro and in vivo reversal of multidrug resistance by GF120918, an acridonecarboxamide derivative. Cancer Res. *53*, 4595–4602.

Kaul, A., Overmeyer, J.H., and Maltese, W.A. (2007). Activated Ras induces cytoplasmic vacuolation and non-apoptotic death in glioblastoma cells via novel effector pathways. Cell. Signal. *19*, 1034–1043.

Kitambi, S.S., Nilsson, E.S., Sekyrova, P., Ibarra, C., Tekeoh, G.N., Andäng, M., Ernfors, P., and Uhlén, P. (2012). Small molecule screening platform for assessment of cardiovascular toxicity on adult zebrafish heart. BMC Physiol. *12*, 3.

León, B., Fong, J.C., Peach, K.C., Wong, W.R., Yildiz, F.H., and Linington, R.G. (2013). Development of quinoline-based disruptors of biofilm formation against Vibrio cholerae. Org. Lett. *15*, 1234–1237.

Louis, D.N., Ohgaki, H., Wiestler, O.D., Cavenee, W.K., Burger, P.C., Jouvet, A., Scheithauer, B.W., and Kleihues, P. (2007). The 2007 WHO classification of tumours of the central nervous system. Acta Neuropathol. *114*, 97–109.

Mercer, J., and Helenius, A. (2012). Gulping rather than sipping: macropinocytosis as a way of virus entry. Curr. Opin. Microbiol. *15*, 490–499.

Morrison, D.K. (2012). MAP kinase pathways. Cold Spring Harb. Perspect. Biol. *4*, a011254.

Overmeyer, J.H., Kaul, A., Johnson, E.E., and Maltese, W.A. (2008). Active ras triggers death in glioblastoma cells through hyperstimulation of macropinocytosis. Mol. Cancer Res. *6*, 965–977.

Overmeyer, J.H., Young, A.M., Bhanot, H., and Maltese, W.A. (2011). A chalcone-related small molecule that induces methuosis, a novel form of non-apoptotic cell death, in glioblastoma cells. Mol. Cancer *10*, 69.

Parsons, D.W., Jones, S., Zhang, X., Lin, J.C., Leary, R.J., Angenendt, P., Mankoo, P., Carter, H., Siu, I.M., Gallia, G.L., et al. (2008). An integrated genomic analysis of human glioblastoma multiforme. Science *321*, 1807–1812.

Pinder, R.M., and Burger, A. (1968). Antimalarials. II. Alpha-(2-piperidyl)-and alpha-(2-pyridyl)-2-trifluoromethyl-4-quinolinemethanols. J. Med. Chem. *11*, 267–269.

Polivka, J., Jr., Polivka, J., Rohan, V., Topolcan, O., and Ferda, J. (2012). New molecularly targeted therapies for glioblastoma multiforme. Anticancer Res. *32*, 2935–2946.

Pollard, S.M., Yoshikawa, K., Clarke, I.D., Danovi, D., Stricker, S., Russell, R., Bayani, J., Head, R., Lee, M., Bernstein, M., et al. (2009). Glioma stem cell lines expanded in adherent culture have tumor-specific phenotypes and are suitable for chemical and genetic screens. Cell Stem Cell *4*, 568–580.

Rapport, M.M., and Senear, A.E. (1946). The synthesis of potential antimalarials; 2-phenyl-alpha-(2-piperidyl)-4-quinolinemethanols. J. Am. Chem. Soc. *68*, 2697–2703.

Singh, S.K., Clarke, I.D., Terasaki, M., Bonn, V.E., Hawkins, C., Squire, J., and Dirks, P.B. (2003). Identification of a cancer stem cell in human brain tumors. Cancer Res. *63*, 5821–5828.

Singh, S.K., Hawkins, C., Clarke, I.D., Squire, J.A., Bayani, J., Hide, T., Henkelman, R.M., Cusimano, M.D., and Dirks, P.B. (2004). Identification of human brain tumour initiating cells. Nature *432*, 396–401.

Sotelo, J., Briceño, E., and López-González, M.A. (2006). Adding chloroquine to conventional treatment for glioblastoma multiforme: a randomized, double-blind, placebo-controlled trial. Ann. Intern. Med. *144*, 337–343.

Stupp, R., Mason, W.P., van den Bent, M.J., Weller, M., Fisher, B., Taphoorn, M.J., Belanger, K., Brandes, A.A., Marosi, C., Bogdahn, U., et al.; European Organisation for Research and Treatment of Cancer Brain Tumor and Radiotherapy Groups; National Cancer Institute of Canada Clinical Trials Group (2005). Radiotherapy plus concomitant and adjuvant temozolomide for glioblastoma. N. Engl. J. Med. *352*, 987–996.

Swanson, J.A. (2008). Shaping cups into phagosomes and macropinosomes. Nat. Rev. Mol. Cell Biol. *9*, 639–649.

Verhaak, R.G., Hoadley, K.A., Purdom, E., Wang, V., Qi, Y., Wilkerson, M.D., Miller, C.R., Ding, L., Golub, T., Mesirov, J.P., et al. (2010). Integrated genomic analysis identifies clinically relevant subtypes of glioblastoma characterized by abnormalities in PDGFRA, IDH1, EGFR, and NF1. Cancer Cell *17*, 98–110.

Whitmarsh, A.J., and Davis, R.J. (2007). Role of mitogen-activated protein kinase kinase 4 in cancer. Oncogene *26*, 3172–3184.

Zhang, J., Stevens, M.F., Laughton, C.A., Madhusudan, S., and Bradshaw, T.D. (2010). Acquired resistance to temozolomide in glioma cell lines: molecular mechanisms and potential translational applications. Oncology *78*, 103–114.

Resource

Cell

Whole-Body Imaging with Single-Cell Resolution by Tissue Decolorization

Kazuki Tainaka,[1,2,3,4] Shimpei I. Kubota,[1,4] Takeru Q. Suyama,[1] Etsuo A. Susaki,[1,2,3] Dimitri Perrin,[2] Maki Ukai-Tadenuma,[2] Hideki Ukai,[2] and Hiroki R. Ueda[1,2,3,*]

[1]Department of Systems Pharmacology, Graduate School of Medicine, The University of Tokyo, 7-3-1 Hongo, Bunkyo-ku, Tokyo 113-0033, Japan

[2]Laboratory for Synthetic Biology, RIKEN Quantitative Biology Center, 2-2-3 Minatojima-minamimachi, Chuo-ku, Kobe, Hyogo 650-0047, Japan

[3]CREST, Japan Science and Technology Agency, 4-1-8 Honcho, Kawaguchi, Saitama 332-0012, Japan

[4]Co-first author

*Correspondence: uedah-tky@umin.ac.jp

http://dx.doi.org/10.1016/j.cell.2014.10.034

SUMMARY

The development of whole-body imaging at single-cell resolution enables system-level approaches to studying cellular circuits in organisms. Previous clearing methods focused on homogenizing mismatched refractive indices of individual tissues, enabling reductions in opacity but falling short of achieving transparency. Here, we show that an aminoalcohol decolorizes blood by efficiently eluting the heme chromophore from hemoglobin. Direct transcardial perfusion of an aminoalcohol-containing cocktail that we previously termed CUBIC coupled with a 10 day to 2 week clearing protocol decolorized and rendered nearly transparent almost all organs of adult mice as well as the entire body of infant and adult mice. This CUBIC-perfusion protocol enables rapid whole-body and whole-organ imaging at single-cell resolution by using light-sheet fluorescent microscopy. The CUBIC protocol is also applicable to 3D pathology, anatomy, and immunohistochemistry of various organs. These results suggest that whole-body imaging of colorless tissues at high resolution will contribute to organism-level systems biology.

INTRODUCTION

Since the discovery of cells in the organism about 350 years ago, whole-body imaging of single cells in opaque organisms like mammals has been a fundamental challenge in biology and medicine. Imaging intact structures at single-cell resolution will enable a systems-level elucidation of cellular connectivity and dynamics. This will improve our understanding of the generation and progression of diseases with stochastic and proliferative processes such as autoimmune and malignant neoplastic diseases, because single-cell events in these diseases eventually affect the health status of the entire organism. However, even the ~30 g body of an adult mouse comprises more than 30 billion cells, which makes it difficult to comprehensively identify cellular circuits and quantitatively analyze dynamics. Conventional histology techniques are laborious and require tissue sectioning, which are challenging barriers toward rapid three-dimensional (3D) visualization of organ structures.

By contrast, optical sectioning with light-sheet microscopy in combination with recent advances in tissue-clearing techniques is a promising route toward visualizing single cells within a whole-organ or whole-body context (Dodt et al., 2007; Ertürk et al., 2012; Keller and Dodt, 2012; Susaki et al., 2014; Tomer et al., 2014). The pioneering work by Werner Spalteholz first introduced the principle of transparent 3D specimens a century ago (Spalteholz, 1914). Up until now, a number of tissue-clearing reagents (BABB, THF-DBE, Sca*l*e, SeeDB, *Clear*^{T}) and protocols (3DISCO, CLARITY, PACT-PARS) have been developed (Becker et al., 2012; Chung et al., 2013; Dodt et al., 2007; Ertürk et al., 2012; Hama et al., 2011; Ke et al., 2013; Kuwajima et al., 2013; Tomer et al., 2011; Yang et al., 2014). However, they cleared tissues to different degrees of transparency. In order to observe deep tissue structures, we aimed for a level of transparency of internal organs (such as heart, lung, kidney, liver, pancreas, spleen, stomach, and small and large intestines) and soft tissues (such as muscles) to the extent that: (1) chest and abdominal backbones and the bones of limbs through internal organs and soft tissues from both ventral and dorsal sides of the body are visible, and (2) individual cells within intact organs and tissues are resolved by whole-body or whole-organ imaging. We previously demonstrated that aminoalcohol-based chemical cocktails, termed CUBIC (*c*lear, *u*nobstructed *b*rain *i*maging *c*ocktails and *c*omputational analysis), efficiently cleared whole brains of adult mice by removing lipids to homogenizing refractive indices (RIs) without signal loss from fluorescence proteins (Susaki et al., 2014). All previous tissue-clearing methods, including ours, have mainly focused on homogenizing RIs, and some of them based on the lipid removal (BABB, 3DISCO, CLARITY, CUBIC, PACT-PARS) succeeded in the clearing and imaging of adult whole brain (Becker et al., 2012; Chung et al., 2013; Dodt et al.,

2007; Ertürk et al., 2012; Susaki et al., 2014; Yang et al., 2014), which is a relatively lipid-rich tissue. However, when applied to the whole body, thick tissues block photons in the visible region (400–600 nm) not only because of light scattering by endogenous materials with mismatched RIs, but also because of the light absorbance by endogenous chromophores—mainly hemoglobin and myoglobin (Faber et al., 2003; Weissleder, 2001). Thus, efficient decolorization of endogenous chromophores inside tissues (particularly heme, which is one of the most abundant endogenous chromophores) is needed to clear whole-body tissues. Classical treatment by the peroxide decolorizes tissues. However, this peroxide treatment causes not only serious damage to outer tissues (Steinke and Wolff, 2001), but also a significant loss of GFP signal (Alnuami et al., 2008). Heme tightly binds to hemoglobin and can be released only in highly acidic ($\leq$pH 2) or basic ($\geq$pH 11) conditions (Kristinsson and Hultin, 2004; Teale, 1959). This highly acidic or basic treatment also results in significant loss of signals from GFP-related fluorescence proteins (Haupts et al., 1998). Thus, a clearing method is needed to efficiently elute heme in moderately basic conditions to enable GFP-related fluorescence proteins to retain their fluorescence properties.

In this study, we demonstrate that aminoalcohols within CUBIC cocktails decolorized the blood by efficiently eluting the heme chromophore from hemoglobin in moderately basic conditions. An accelerated clearing protocol with CUBIC perfusion rendered nearly transparent almost all organs of adult mice, as well as the entire bodies of infant and adult mice, and enabled rapid whole-body and whole-organ imaging with single-cell resolution. We used CUBIC to diagnose the pathology of Langerhans islets in the diabetic pancreas, as well as to anatomically annotate various organ structures in 3D. We also applied CUBIC to 3D immunohistochemistry of various organs. These results suggest that whole-body imaging with single-cell resolution achieved by tissue decolorization can contribute to the foundation of the organism-level systems biology.

RESULTS

Aminoalcohols in CUBIC Cocktails Decolorized the Blood by Efficiently Eluting Heme Chromophore

To achieve whole-body imaging with single-cell resolution, it is important to decolorize endogenous chromophores such as heme. When we immersed various organs directly (i.e., without perfusion) to paraformaldehyde (PFA) and subjected them to Sca*l*eCUBIC-1 (Susaki et al., 2014; in this study, we term it "CUBIC-1" for simplicity), we found that the color of the solvent immediately turned a dark green. This observation led us to hypothesize that CUBIC-1 could solubilize and elute endogenous heme from blood-infused tissues. To test this hypothesis, we first investigated whether CUBIC reagents can directly decolorize blood. The PFA-fixed blood suspension was washed three times with CUBIC-1, resulting in transparent pellet and olive-green supernatant (Figure 1A). On the other hand, the pellet and the supernatant from PBS-treated blood suspension remained dark red and colorless, respectively. Among CUBIC-1 constituents, *N,N,N′,N′*-tetrakis(2-hydroxypropyl)ethylenediamine (termed here as "aminoalcohol #10") (Susaki et al., 2014) alone, but not other reagents, is sufficient to decolorize the blood (Figures 1A and 1B). The visible spectra of chemically treated erythrocytes were recorded to investigate what kind of olive-green molecule was eluted from the blood into the supernatant. The visible spectrum from the PBS-treated erythrocyte suspension is quite different from that of erythrocyte suspension treated by 0.1 M NaOH (initial pH = 13), aminoalcohol #10 and CUBIC-1 reagent (Figure 1C). We also recorded the visible spectra from purified hemin (free heme chromophore released from hemoglobin), purified biliverdin (which is a product of heme catabolism), iron(II) chloride, erythrocytes, and supernatant of PFA-fixed blood treated by aminoalcohol #10 (Figure 1D) or CUBIC-1 reagent (Figure S1A available online). The normalized spectra of the erythrocyte and supernatant overlapped almost completely with hemin solutions in aminoalcohol #10 or CUBIC-1, which suggests that heme is released from hemoglobin in erythrocytes when treated by aminoalcohol #10 or the CUBIC-1 reagent.

We noted that aminoalcohol #10 and CUBIC-1 reagent have buffering capacity in pH 9–11 whereas other reagents did not (Figure S1B). If buffering capacity in basic pH is critical for the decolorizing capability, we predicted that a basic solution containing 0.01 M NaOH, which usually elutes heme from hemoglobin, will lose its decolorizing capability at a higher concentration of erythrocytes because the higher concentration of cells will shift the pH from basic to neutral. To test this prediction, we prepared a mixture of erythrocytes and these chemicals at different ratios (Figure 1E). Although urea and Triton X-100 in basic solution moderately promoted heme release at high chemical ratios, these were less effective at lower concentrations. On the other hand, aminoalcohol #10 and CUBIC-1 reagent promoted heme release even at high erythrocyte ratios. As shown in Figure 1C, the absorbance ratio between 600 nm and 575 nm can be used as a quantitative index for the efficiency of heme release. OD600/OD575 values of samples from Figure 1E were therefore plotted against erythrocyte/chemical ratio (Figure S1C). These results quantitatively confirmed that aminoalcohol #10 in the CUBIC-1 reagent can efficiently promote heme release regardless of the erythrocyte/chemical ratio and can work as a decolorizing buffer at moderate basic pH. We evaluated the pH dependence on the efficiency of heme release for aminoalcohol #10, CUBIC-1 reagent, and non-buffered basic solution, respectively (Figure 1F). In non-buffered basic solution, heme was efficiently released from hemoglobin, but only at pH >11, as previously reported (Kristinsson and Hultin, 2004). On the other hand, aminoalcohol #10 efficiently eluted heme even in moderately basic conditions around pH 10, which is within the optimal pH range for fluorescence signal intensity of GFP-related fluorescence proteins (Haupts et al., 1998). CUBIC-1 reagent further promoted heme release even around pH 9, which might be attributed to a combinatorial effect with urea and/or Triton X-100. These results suggested that aminoalcohol #10 in CUBIC-1 reagent expanded the pH window for efficient heme release. To clarify the chemical properties of aminoalcohol #10 associated with its decolorizing capability, we investigated erythrocyte with a series of aminoalcohol derivatives (Figures S1D and S1E). These results revealed the chemical properties (i.e., higher amines without carboxylic groups)

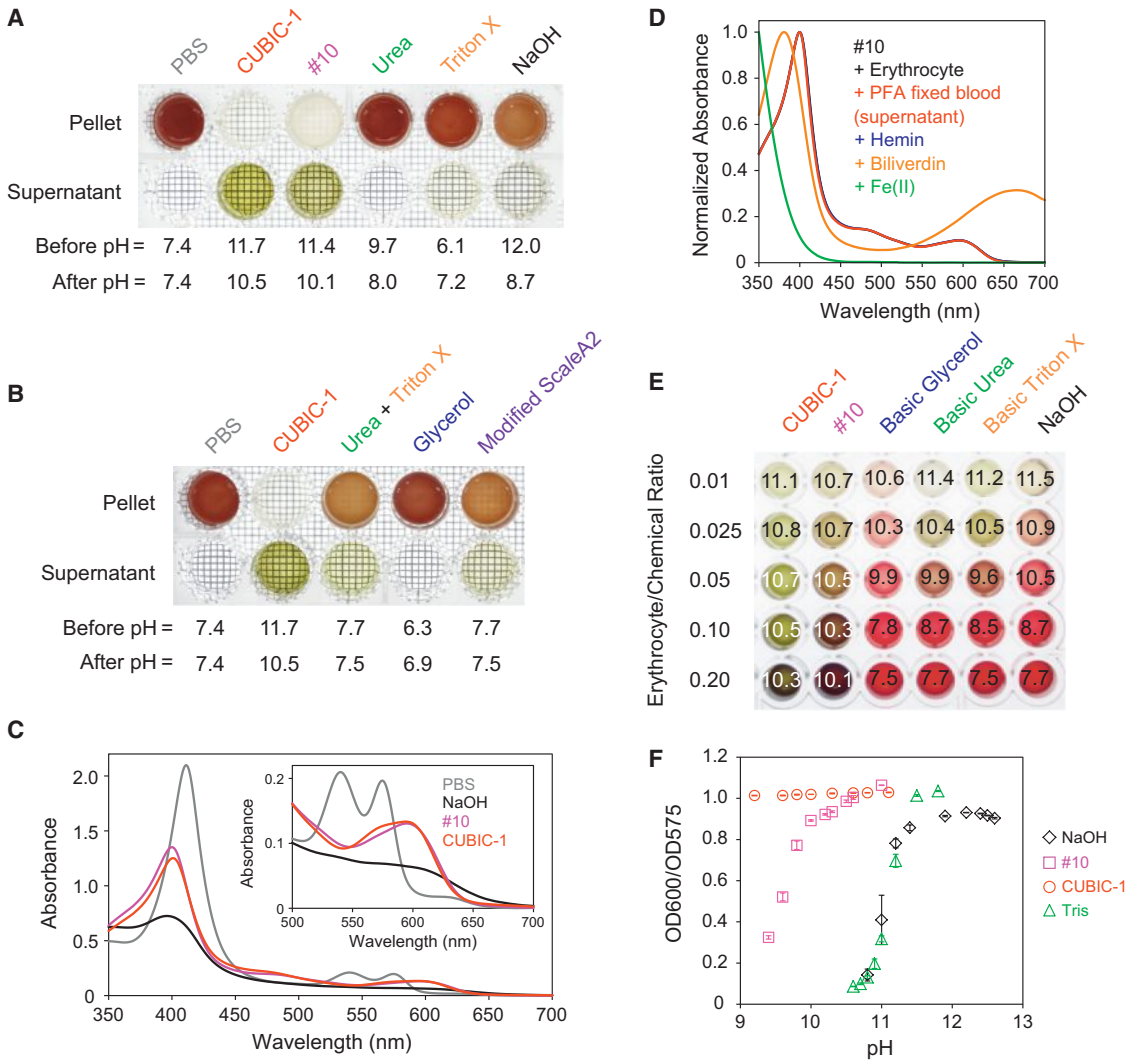

Figure 1. Aminoalcohols in CUBIC Cocktails Decolorized the Blood by Efficiently Eluting Heme Chromophore

(A) Decolorizing of the PFA-fixed blood by the previously published CUBIC-1 cocktail ("CUBIC-1") and its constituents. Numbering of aminoalcohol #10 was derived from the previous chemical screening. Bright-field images of pellet and supernatant from fixed blood samples washed with PBS, CUBIC-1 reagent, 25 wt % aminoalcohol #10, 25 wt% urea, 15 wt% Triton X-100, or 0.01 M NaOH, respectively. pH of the original liquid and supernatant is shown at the bottom.

(B) Decolorizing PFA-fixed blood by CUBIC-related chemicals. Bright-field images of pellet and supernatant from PFA-fixed blood samples washed with PBS, CUBIC-1 reagent ("CUBIC-1"), a mixture of 25 wt% urea and 15 wt% Triton X-100 ("Urea + Triton X"), 25 wt% glycerol ("Glycerol"), or a mixture of 25 wt% urea, 25 wt% glycerol and 15 wt% Triton X-100 ("Modified ScaleA2"), respectively. pH of the original liquid and supernatant is shown at the bottom.

(C) Visible spectra of a chemically treated 0.1% mouse erythrocyte suspension. Erythrocytes were mixed with PBS (gray), 0.1 M NaOH (black), aminoalcohol #10 (magenta), or CUBIC-1 reagent (red), and were incubated at 37°C overnight. Inset: magnification of the Q-band region.

(D) Normalized visible spectra of 0.1% mouse erythrocyte (black), 1/10 diluted supernatant from (A) (red), 10 μM hemin (blue), 10 μM biliverdin (orange), and 100 μM iron(II) chloride (green), in 25 wt% aminoalcohol #10.

(E) Aminoalcohol #10 in CUBIC reagents facilitates the release of heme independent of the mixing ratio with erythrocytes. Bright-field images of the 1% to 20% erythrocyte suspension mixed with CUBIC-1 reagent, 25 wt% aminoalcohol #10, 25 wt% basic glycerol, 25 wt% basic urea, 15 wt% basic Triton X-100, and 0.01 M NaOH. Indicated value in each well corresponds to pH.

(F) Aminoalcohol #10 in CUBIC reagents significantly expands the pH range of heme release. 1% erythrocyte suspension including 1-100 mM NaOH (black diamond, n = 3), aminoalcohol #10 (pH = 9.4-11.0, magenta square, n = 3), CUBIC-1 (pH = 9.2-11.1, red circle, n = 3), and 25 wt% tris(hydroxymethyl)aminomethane (pH = 10.6-11.8, green triangle, n = 3) incubated at 37°C overnight. Visible spectra of these samples were recorded. Because OD600/575 correlates with the efficiency of heme release, OD600/575 of these samples is plotted against pH.

Data represent the average ± SD. See also Figure S1.

associated with efficient decolorizing and might reflect the affinity of these chemicals to the heme chromophore. Overall, aminoalcohol in CUBIC reagents critically contributed to blood decolorization, which is assisted by its chemical capacities to buffer pH in moderately basic conditions and to expand the pH window for efficient heme release.

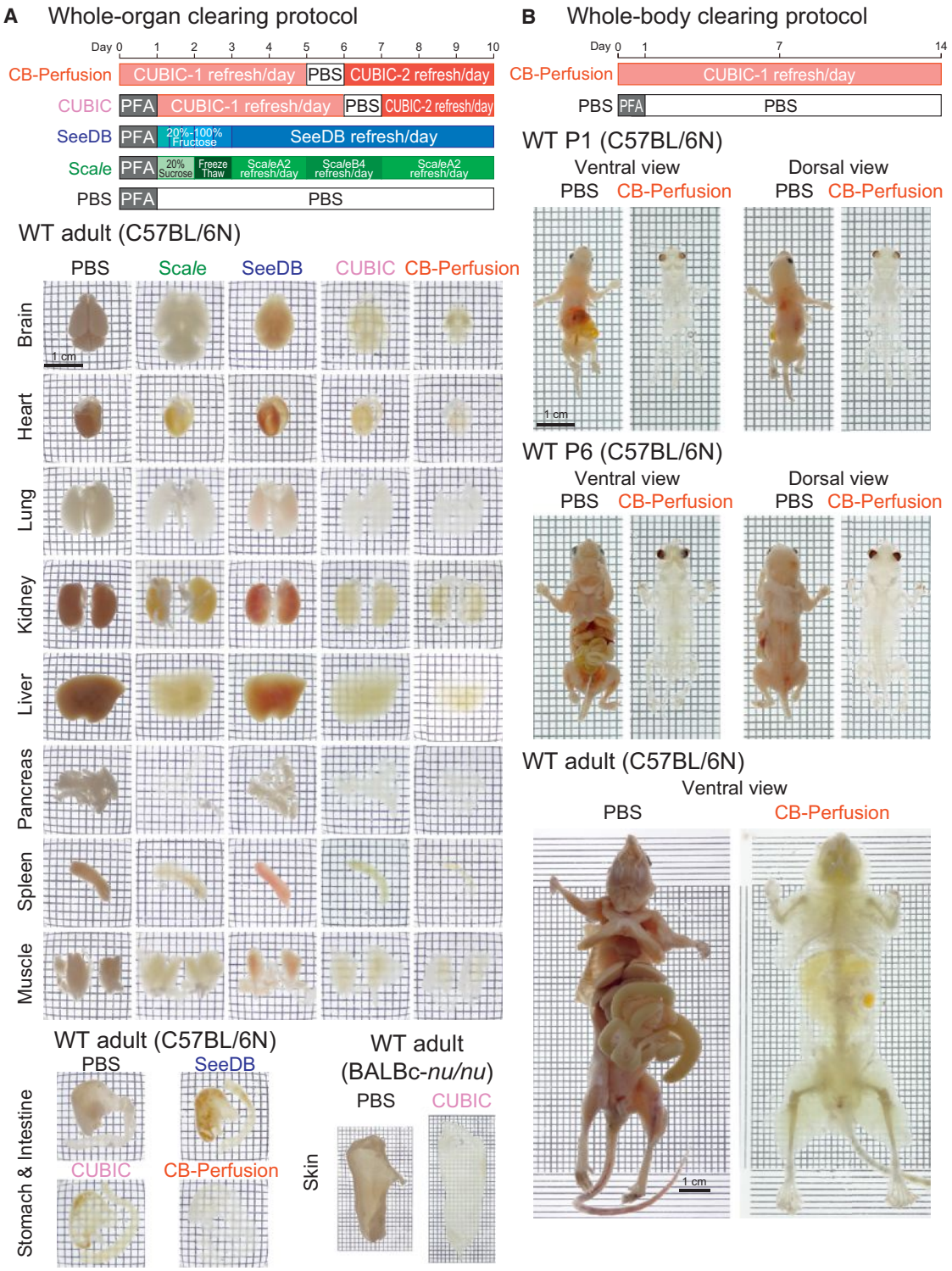

Figure 2. CUBIC Provides a Simple and Efficient Whole-Organ and Whole-Body Clearing Protocol

(A) (Top) Whole-organ clearing protocol in 10 days. (Middle) Transmission images of whole organs (brain, heart, lung, kidney, liver, pancreas, spleen, and muscle) from adult C57BL/6N. In the CB-Perfusion protocol, deeply anesthetized mice were sacrificed and transcardially perfused with PBS, 4% PFA/PBS (w/v), and 1/2 diluted CUBIC-1 reagent. The excised organs were further cleared by CUBIC-1 reagent without postfixation in 4% PFA/PBS. (Lower-left) Bright-field images of whole stomach and intestine from C57BL/6N treated with the CUBIC, CB-Perfusion protocol, SeeDB, or PBS using 10-day clearing protocol (Scale-treated

(legend continued on next page)

CUBIC Is a Simple and Efficient Whole-Organ and Whole-Body Clearing Protocol

In this study, we focused on the development of an immersion-only tissue-clearing protocol based on hydrophilic clearing reagents (Extended Experimental Procedures). We evaluated the clearing performance of Sca*l*e, SeeDB, and CUBIC protocols in various organs (Hama et al., 2011; Ke et al., 2013; Susaki et al., 2014). Each protocol was based on the experimental conditions of the original papers, as shown in Figure 2A, except for a daily exchange of the clearing medium. We measured the temporal development of average transmittance of different organs (brain, heart, lung, kidney, and liver) with each protocol (Figure S2A) and obtained transmittance curves of these organs around the visible region after 10 days (Figure S2B). The CUBIC protocol was superior to other methods in both clearing kinetics and plateau performance in transmittance for all organs studied. We confirmed that the CUBIC protocol enhanced the transmittance of organs in the 480–680 nm range, as expected from the decolorizing capability of CUBIC reagents. Bright-field images of different organs (brain, heart, lung, kidney, liver, pancreas, spleen, muscle, stomach and intestine, and skin) after 10 days also demonstrated that all organs treated with CUBIC reagents resulted in the most transparent and decolorized images (Figure 2A).

Based on the blood decolorizing capability of the CUBIC-1 reagent, transcardial perfusion of this reagent (and hence the blood decolorizaion through blood vessels) will enhance whole-organ and whole-body clearing. We thus developed a CUBIC perfusion (CB-Perfusion) protocol to achieve whole-organ and whole-body clearing. In the original CUBIC protocol, tissues were conventionally fixed by transcardial perfusion of 4% PFA (25–50 ml) and were immersed in 4% PFA at 4°C overnight as a postfixation. In the advanced CB-Perfusion protocol, tissues in the entire body were fixed by prolonged transcardial perfusion of 4% PFA (150 ml) and were then cleared by subsequent transcardial perfusion of 1/2 diluted CUBIC-1 reagents (20 ml). Each organ was then extracted and further cleared by CUBIC reagents. The CB-Perfusion protocol accelerated the clearing kinetics and further enhanced the plateau performance in transmittance when compared with the original CUBIC protocol (Figures S2A and S2B). In a bright-field imaging comparison of all organs, the CB-perfused organs were the clearest (Figure 2A). These results indicate successful development of the whole-organ clearing protocol, which finishes within 10 days.

We next attempted whole-body clearing of infant (postnatal day 1 [P1] and P6) and adult mice (19-week-old) by using this CB-Perfusion protocol. After transcardial perfusion of 4% PFA and 1/2 diluted CUBIC-1 reagent and subsequent detachment of skin, the entire body was cleared by the CUBIC-1 reagent. We noticed that the clearing medium (CUBIC-1 reagent) immediately turned a dark green color probably due to decolorization of endogenous chromophores (mainly heme). To facilitate the whole-body clearing, clearing medium were refreshed daily for 2 weeks. The clearing medium gradually became less colored, and after 2 weeks, the apparent transparency of the whole body became saturated. Whole-body samples can be then stored in CUBIC-1 reagent and even shaken at 37°C over months because the high pH of CUBIC-1 reagents prevents proliferation of microorganisms. Bright-field images of infant mice (P1 and P6) demonstrated that CB-Perfusion protocol transparentized and decolorized P1 and P6 infant mice (Figure 2B). We confirmed the visualization of chest and abdominal backbones as well as bones of limbs through internal organs and soft tissues from both ventral and dorsal sides of the body. Bright-field images of adult mice (19-week-old) demonstrated that CB-Perfusion protocol also markedly transparentized and decolorized adult mice (Figures 2B and S2C). The bones of forelimbs (including scapula, humerus, radius, and ulna) and hindlimbs (including femur, tibia, and fibula) and caudal vertebrae were clearly visualized in either V-D or the dorsal-to-ventral (D-V) images of adult mice.

CUBIC Is Applicable to Whole-Body Imaging of Infant and Adult Mice with Single-Cell Resolution

The high transparency of CB-perfused samples prompted us to perform light-sheet fluorescence microscopy (LSFM). As previously described, the CUBIC protocol is compatible with whole-brain nuclear counterstaining (Susaki et al., 2014). We thus applied nuclear counterstaining by propidium iodide (PI) to whole-body samples and imaged PI-stained CAG-EGFP transgenic (Tg) (Okabe et al., 1997) P1 mouse transparentized and decolorized by the CB-Perfusion protocol. Whole-body images were obtained from two opposite directions (D-V and V-D) (Figure 3A). Both images were sufficiently clear even at 4–5 mm depth. Nuclear staining with PI tends to highlight non-muscular organs and solid tissues, whereas CAG-EGFP signals were more intense in the muscular organs such as heart and subcutaneous tissue. Magnified images from the same sample were also obtained to visualize internal structures of head, chest, abdominal, and pelvic organs as well as limbs (Figures 3B, S3A, and S4). These images were then deconvolved by AutoQuant X3 software (we denoted the deconvolved images as prefix ''DCV-'' in the figures). For example, the granule duct in the submaxillary gland, coronary vessels in the heart, bronchiole in the lung, gastric walls in the stomach, vascular structures in the liver, renal cortex and medulla in the kidney, villus in the intestine, and penis and testis in the scrotum were clearly identified in each z stack image (Figure S4). Surprisingly, detailed structures in hippocampus and cerebellum were visible through the skull, central canal inside the spinal cords were seen through vertebrae, and internal structures of tibia in the leg were also visualized (Figures 3B and S4). We note that the magnified images of these organs resolved to single-cell levels (Figure 3C, top). We also performed whole-body imaging of PI-stained CAG-EGFP Tg P6 mouse transparentized and decolorized by the

stomach and intestine were usually fragile and torn during the procedure due to proliferation of microorganisms; thus it was impossible to take comparison data). (Lower-right) Bright-field images of skin from BALB/c-*nu/nu* treated with CUBIC reagents and PBS using the 10-day clearing protocol.

(B) Whole-body clearing protocol in 2 weeks. Bright-field images (ventral and dorsal view) of whole body (C57BL/6N P1, P6, and adult mice) stocked in PBS after fixation or subjected to the CB-Perfusion protocol. 8-week-old mouse for the PBS sample and 19-week-old mouse for the cleared sample are shown.

See also Figure S2.

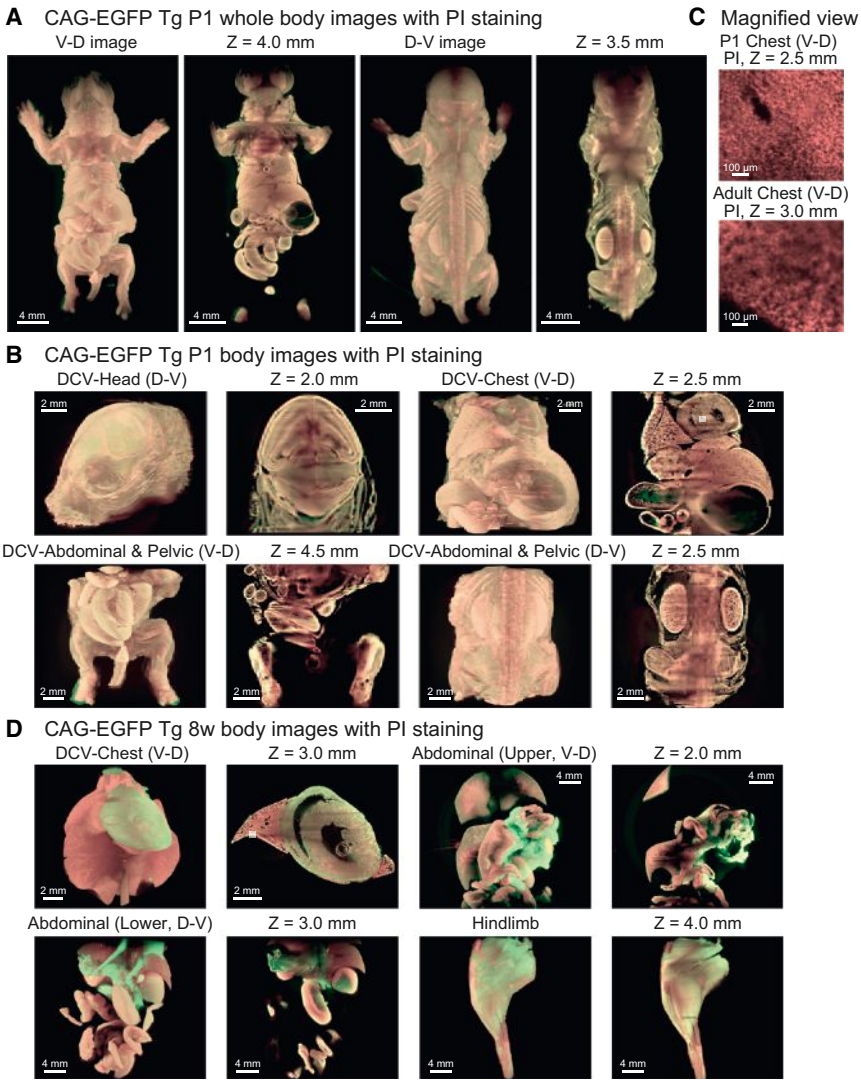

Figure 3. CUBIC Is Applicable to Whole-Body Imaging of Infant and Adult Mice with Single-Cell Resolution

(A) 3D-reconstituted and X-Y plane (indicated with Z position), lower-resolution whole-body images of PI-stained CAG-EGFP Tg P1 mouse. Images were acquired with light-sheet fluorescence microscopy (LSFM) from the ventral-to-dorsal (V-D) and dorsal-to-ventral (D-V) directions, respectively.

(B) 3D-reconstituted and X-Y plane body images of PI-stained CAG-EGFP Tg P1 mouse. Head (D-V), chest organs (V-D), abdominal, and pelvic organs (V-D and D-V) are shown. All images were deconvolved with AutoQuant X3 software. Prefix "DCV-" indicates the deconvolved image.

(C) Magnified images in (B) (Chest, Z = 2500) and (D) (Chest, Z = 3000) indicating these images taken with single-cell resolution. Each dot is PI signals of single cell nucleus.

(D) 3D-reconstituted and X-Y plane body images of the PI-stained CAG-EGFP Tg adult mouse (8-week-old). Chest organs (V-D), upper abdominal organs (V-D), lower abdominal organs (D-V), and hindlimb are shown. Enlarged parts in (C) are indicated as a white box in (B) and (D). Prefix "DCV-" indicates the deconvolved image.

See also Figures S3 and S4.

CB-Perfusion protocol. Because the P6 mouse was too large to be captured in a single view, we obtained whole-body images from three views (head, chest, and abdomen, Figure S3C). The quality of whole-body images of P6 mice was almost comparable to that of P1 mice and visualized the internal structures of head, chest, abdominal, and pelvic organs as well as limbs.

We next performed whole-body imaging of PI-stained CAG-EGFP Tg adult mice (8-week-old) transparentized and decolorized by the CB-Perfusion protocol. Adult mice bodies could not fit into existing LSFMs, so we dissected the adult body into four parts (chest organs, abdominal organs, forelimbs, and hindlimbs) and then obtained their images (Figures 3D and S3B). Adult mouse tissues exhibited much higher contrast between PI and EGFP signals than those of infant mice. For example, EGFP signals were much higher in heart, pancreas, stomach, and muscles probably because EGFP expression from CAG promoter in these organs was elevated. In z stack images of chest organs, ventricle structures in the heart and bronchiole in the lung can be clearly visualized (Figure 3D). In z stack images of abdominal organs, vascular structure in the liver, cortex, and medulla in the kidney, muscularis externa in the stomach, and villus in the intestine were also visualized (Figure 3D). Tibia and fibula as well as fiber orientation of gastrocnemius and muscles in the hindlimb were also clearly visualized (Figure 3D). We note that the images of these adult organs also achieved single-cell resolution (Figure 3C, bottom). These results demonstrated that CUBIC is applicable to the imaging of the internal structures of entire body regions (chest and abdominal organs, forelimb, and hindlimb) with single-cell resolution.

CUBIC Is Applicable to Whole-Organ Imaging with Single-Cell Resolution

For rapid whole-organ imaging, we used a knockin (KI) mouse strain expressing three tandem repeats of *mKate2* with a nuclear localization signal, under control of the CAG promoter (Niwa et al., 1991) from the 3′-UTR of *β-actin* gene locus (Tanaka et al., 2012). We used mKate2 because of its signal intensity, photostability, and rapid protein maturation (Chudakov et al., 2010; Shcherbo et al., 2009), as well as its resistance to fluorescence quenching by CUBIC reagents, as previously described (Susaki et al., 2014). We then performed whole-organ imaging of various CB-perfused organs, including heart, lung, kidney, liver, pancreas, spleen, muscle, stomach, and intestine from this β-actin-nuc-3 × mKate2 KI mouse (8-week-old) and counterstained with SYTO 16, a cell-permeable green-fluorescent nucleic acid stain. The resulting 3D-reconstituted image of each organ in this *mKate2* KI

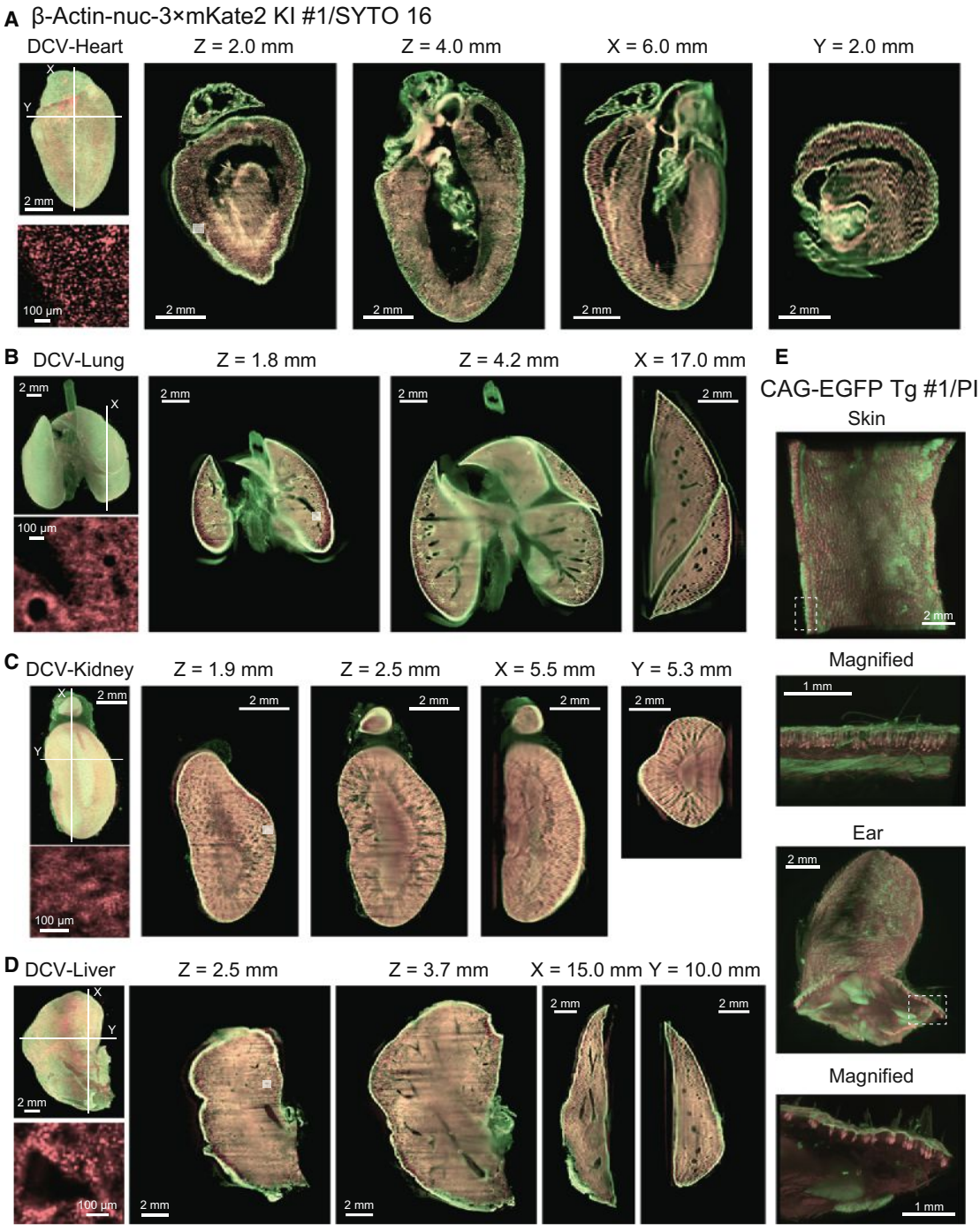

Figure 4. CUBIC Is Applicable to Whole-Organ Imaging with Single-Cell Resolution

The reconstituted 3D and section images of a heart (A), lung (B), kidney (C), and liver (D) from nuclear-stained β-actin-nuc-3 × mKate2 KI mouse (8-week-old) and skin and ear (E) from CAG-EGFP Tg mouse (10-week-old) were acquired with LSFM. Raw X-Y section images and reconstituted Y-Z and X-Z section images are at the indicated positions. Prefix "DCV-" indicates the deconvolved image. In (A–D), enlarged images indicated by a white box on z plane images are shown, indicating that these images are taken at single-cell resolution. Each dot is nuclear-localized mKate2 signals from single cell nuclei.
See also Figures S5 and S6.

mouse, as well as its horizontal, coronal, and sagittal sections, enabled the visualization of spatial gene expression patterns (from the CAG promoter at *β-actin* 3′-UTR) and examination of detailed internal structures (Figures 4A–4D and S5A–S5F). For example, 3D reconstitution images of the heart successfully visualized not only lumens of atria and ventricle, but also internal

papillary muscle, coronary vascular structures, and even valve structures (Figure 4A). In lungs, the networks of trachea, bronchi, and bronchiole in both lobes were clearly identified (Figure 4B). In the kidney, 3D reconstitution images easily distinguished between renal cortex, medulla, and pelvis (Figure 4C). In the liver, two kinds of vascular structures were identified as thicker vessels, which would indicate the hepatic artery, and thinner vessels, which would indicate the portal vein (Figure 4D). Langerhans islets and pancreatic ducts were identified in the pancreas (Figure S5A). Splenic white pulp and red pulp were identified in the spleen (Figure S5B). Orientations of muscle fibers and blood vessels were observed in the muscle (Figure S5C). Corpus glands were significantly highlighted, and pylorus and cardia were clearly observed in the stomach (Figure S5D). Mesentery and villi were seen in the intestine (Figure S5E). We also obtained 3D reconstitution images of brain as well as kidney and muscle, which are contralateral to those in Figures 4C and S5C from the identical mouse body (Figure S5F). In addition to imaging internal organs and muscles, we collected skin and ears from pelage-removed CAG-EGFP Tg mouse and subjected them to CUBIC reagents with nuclear-counterstain PI. We then performed whole-organ imaging of these tissues (Figure 4E). EGFP signals highlighted epidermis, muscle layer under hypodermis, and residual pelage, whereas PI signal intensity was relatively higher in hair matrix cells. Taken together, these results demonstrate that CUBIC enables whole-organ imaging with single-cell resolution of almost all organs by using various fluorescence proteins.

The successful whole-organ imaging using mKate2 led us to test other fluorescence proteins, including EGFP and YFP. We performed similar whole-organ imaging of each organ from three strains of CB-perfused adult mice: CAG-EGFP Tg (Figure S6A), an EGFP-fused histone-2B-expressing strain (R26-H2B-EGFP [CDB0239K]; Figure S6B) (Abe et al., 2011), and a Thy1-YFP-H Tg strain (Figure S6C) (Feng et al., 2000), respectively. PI was used as nuclear staining for whole-organ imaging of these strains. When we captured the section images of each organ from CAG-EGFP Tg (Figure S6A) and β-actin-nuc-3 × mKate2 KI mice (Figures 4 and S5), the spatial distribution of fluorescence proteins (EGFP and nuc-3 × mKate2) was markedly different. This is because EGFP was localized in the nucleus and cytosol, whereas mKate2 was localized only in the nucleus. Similarly, we could obtain 3D reconstitution images of whole organs from R26-H2B-EGFP and the neuronal marker Thy1-YFP-H (Figures S6B and S6C). These results demonstrate that CUBIC protocol enables whole-organ imaging with various fluorescence proteins (mKate2, EGFP, and YFP) and that whole-organ imaging with single-cell resolution can extract 3D single-cell information of internal anatomical structures in different organs.

CUBIC Is Applicable to 3D Pathology of Langerhans Islets in the Diabetic Pancreas

One attractive application of whole-body and whole-organ imaging with single-cell resolution is 3D pathology of organs. To test this potential, we investigated the spatial distribution of Langerhans islets (LIs) in diabetic and normal pancreases by using the CB-Perfusion protocol. As a model, we first focused on diabetic pancreases because BABB-based analysis combined with optical projection tomography (OPT) has already been applied (Alanentalo et al., 2007). Streptozotocin (STZ) is a well-known cytotoxic agent for pancreatic β cells, which disrupts the ability of β cells to secrete insulin and stabilize blood sugar levels (King, 2012). High-dose STZ injection destroys β cells, which are major constituents of LIs and induce type I diabetes mellitus. LIs contract because of β cell destruction after the onset of diabetes. We therefore performed comprehensive and statistical analysis of diabetic LIs in the whole pancreas of adult mice. We dissected and transparentized pancreases from saline-treated control mice (n = 3) and acute type I diabetic mice (n = 3, whose blood sugar levels were over 400 mg/dl as shown in Table S1) by the CB-Perfusion protocol with PI staining. Acquired images enabled us to morphologically distinguish the characteristic clusters (LIs) from the characteristic tracts (pancreatic ducts) (Figure 5A). We identified and 3D reconstituted all LIs according to Figure 5A and Extended Experimental Procedures. The image analysis also provided a spatial distribution of LIs in the pancreas. For example, larger LIs tend to be localized along pancreatic ducts. By using the extracted LI data, we can compare the total number of LIs between diabetic and healthy mice. As expected, the average number of LIs was significantly reduced by the onset of diabetes (Figure 5B, left, $p = 0.005$). The differences of average LI volume between diabetic and healthy mice were also marginally significant (Figure 5B, center, $p = 0.09$), which is consistent with the observed reduction in the existence probability of larger LIs in diabetic mice ($>1.0 \times 10^7$ μm^3, Figure 5B, right). These data indicate that larger LIs are more susceptible to β cell impairment induced by STZ administration. Overall, these results indicate that CUBIC enables 3D pathology of a diabetic pancreas.

CUBIC Is Applicable to 3D Anatomy of Various Organs

The successful 3D pathology of diabetic pancreases prompted us to generalize this to 3D anatomy of various organs, which may provide a versatile platform for elucidation of cellular mechanisms underlying the physiology and pathology of observed anatomical structures. As a test case, we analyzed whole-heart images from *mKate2* KI mouse. We noted that mKate2 signals are more intense in the surface of the tracts, which can be morphologically annotated as coronary vessels (Figure 6A). We extracted, by using the surface analysis in the Imaris software, high-intensity signals in the heart and excluded the surfaces of smaller volume size, resulting in 3D images of coronary vessels covering the entire heart (Figure 6A and Movie S1). Internal structures such as tendinous cords and valves could be also visualized (Figure S7A). We also analyzed whole-lung images from the same *mKate2* KI mouse. We noted that mKate2 signals in respiratory tract fall to undetectable levels, and thus we can extract low-intensity signals in the lungs, resulting in a bronchial tree covering the entire lung (Figure 6B and Movies S2 and S3). Interestingly, the 3D-reconstituted image of the tree includes main stem bronchus, bronchi, bronchioles, and even alveoli structures. We next analyzed whole-kidney images from the same *mKate2* KI mouse. Renal cortex, medulla, and pelvis were clearly distinguished and annotated with characteristic signal patterns of SYTO16 and mKate2 (Figure 6C and Movie S4). We further analyzed whole-liver images from the same *mKate2* KI mouse (Figure 6D and Movie S5). We extracted two vessel structures inside of the image, which were characterized

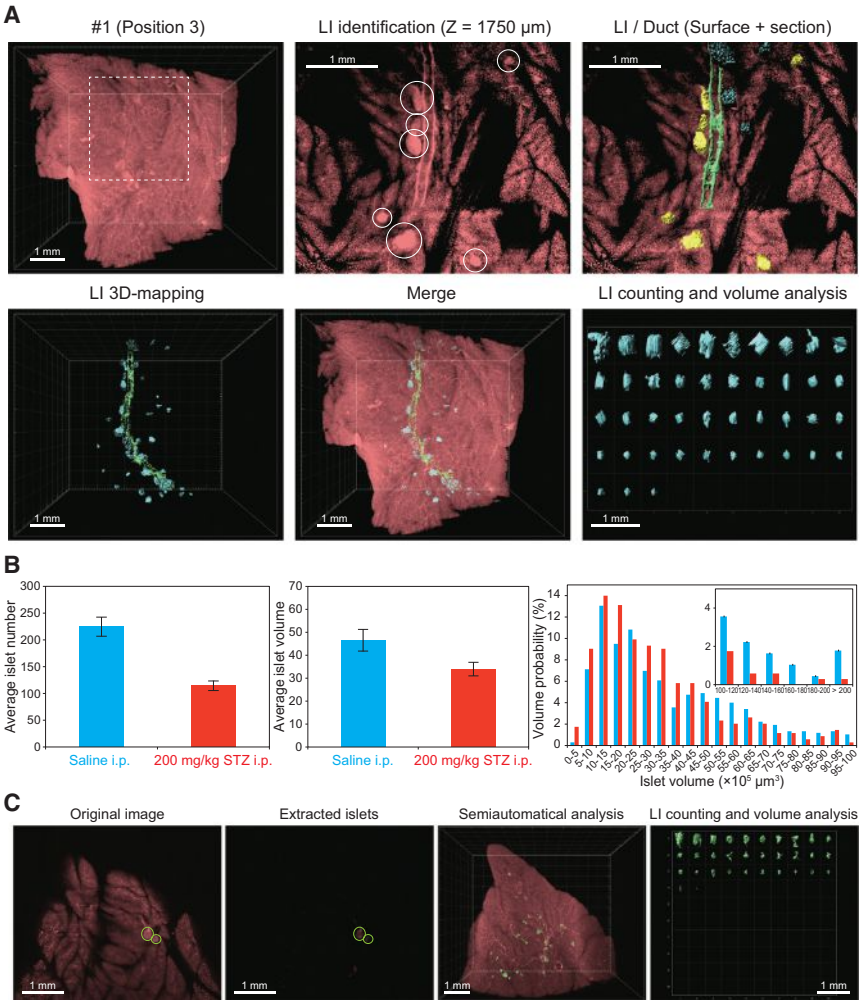

Figure 5. CUBIC Is Applicable to the 3D Pathology of Langerhans Islets in the Diabetic Pancreas

(A) The procedures for image analysis of LIs in pancreases. First, LIs in each X-Y plane image were manually identified. Seven LIs (white circles) were identified in the center-top panel. Then, these LIs were visualized in a 3D image with surface analysis on the Imaris software. In the upper-right panel, the seven LIs (yellow) are in the plane. Four other LIs (blue) are not in the same plane. The pancreatic duct (green) is also indicated. The spatial distribution of LIs (blue) as well as a pancreatic duct (green) is displayed in the lower-left and lower-center panels. Finally, LI counting and volume analysis were conducted on the Imaris software, shown in the lower-right panel.

(B) Statistical analysis of LIs in the whole pancreas from control mice (n = 3) and diabetes mice (n = 3). Data represent the average ± SE. The average number of LIs was significantly reduced by the onset of diabetes (left, p = 0.005). The differences of average LI volume between diabetic and healthy mice were also marginally significant (center, p = 0.09), which is consistent with the observed reduction in the existence probability of larger LIs in diabetic mice (right, > 1.0 × 10^7 μm^3).

(C) Computational, semi-automated identification of LIs. Position 1 image of #1 mouse was used. (Left and center) Raw and processed image with extracted islets (green circles) at plane 80. (Right) Reconstituted 3D image with all identified islets. See also Table S1.

by high and low SYTO 16 signals, and were thus identified as hepatic arteries and portal veins, respectively. Finally, we extended similar anatomical analysis to whole-body images of PI-stained CAG-EGFP Tg P1 mouse (Figure 3). Each organ inside of the chest and upper abdomen were clearly visualized (Figure S8A and Movie S6) with their inside structures, such as a bronchial tree in the lung (Figure S8B), vascular structures in the liver (Figure S8C), villi in the intestine (Figure S8D), and spatial relations of esophagus and esophageal gland (Figure S8E). These results suggest that CUBIC enables 3D anatomy of various organs even in whole-body images, which will provide a versatile platform for systems-level elucidation of cellular circuits underlying the physiology and pathology of various organs of interest.

CUBIC Is Applicable to 3D Immunohistochemistry of Various Organs

Another challenge for establishing whole-organ imaging is the development of 3D immunohistochemistry (3D-IHC). In our previous work, we have demonstrated that CUBIC was applicable to the 3D-IHC using large blocks of brain tissue (Susaki et al., 2014). According to the protocol, we performed 3D-IHC of nuclear-stained whole-organ samples (Figure 7A). Organ samples with CB-Perfusion were subjected to CUBIC-1 treatment, followed by 3D-IHC with antibodies to two proteins expressed in the organs. We used α-smooth muscle actin (α-SMA) antibody to label the heart, stomach, and intestine and pan-cytokeratin antibody to the lung. After immunostaining, organ samples were treated with CUBIC-2 for several hours to 1 day, and the resulting samples were observed with LSFM. The immunostained signals were detected over 1 mm depth and were visualized as 3D-reconstituted images (Figure 7). In the heart, the immunofluorescence signal for α-SMA antibody clearly highlighted vascular structures (Figure 7B). Epithelial cells in the lung were visualized by immunostaining with the antibody to pan-cytokeratin (Figure 7C). Previously reported staining pattern of pan-cytokeratin was recapitulated by CUBIC-based 3D-IHC (Xiang et al., 2007). α-SMA antibody also visualized smooth muscular cells in the stomach and intestine (Figures 7D and 7E). The CUBIC protocol is thus applicable to the 3D-IHC of various organs.

DISCUSSION

Aminoalcohols in CUBIC Enable Decolorization of Blood

Almost all animals are not transparent because their body is composed of RI-mismatched materials as well as light-absorbing

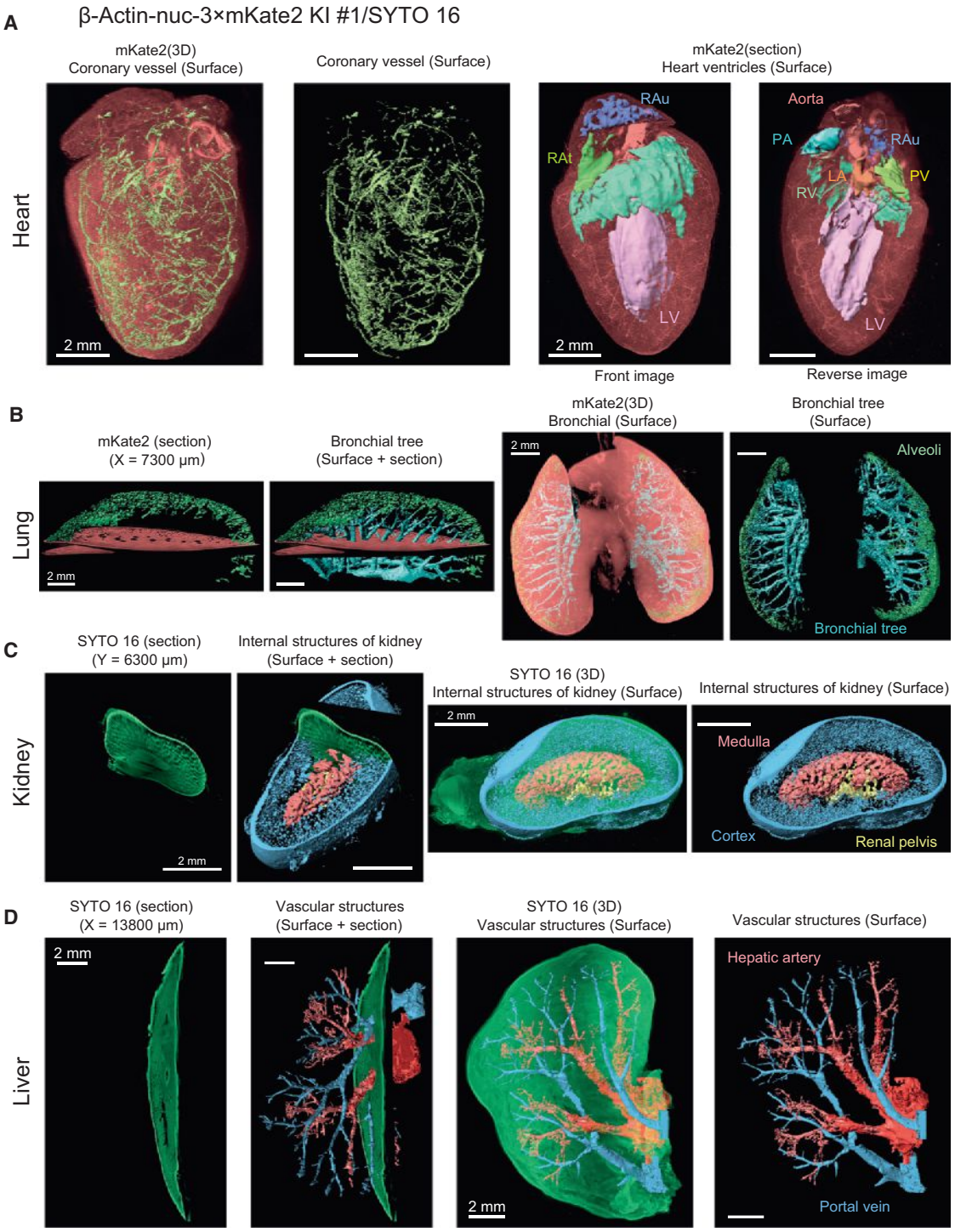

Figure 6. CUBIC Is Applicable to the 3D Anatomy of Various Organs

Extraction of internal structures was performed with surface analysis of Imaris software. The reconstituted 3D images of the heart (A), lung (B), kidney (C), and liver (D) from the SYTO 16-stained β-actin-nuc-3 × mKate2 KI mouse (8-week-old) in Figure 4 were used. After surface extraction by the software, each structure was manually curated and extra surface signals were eliminated.

(A) Structural identification of coronary vessels and ventricles in the heart. Contiguous mKate2 signals with high or low intensity within the heart were extracted as coronary vessels (left two panels) or ventricles (right two panels). RAu, right auricle; RAt, right atrium; RV, right ventricle; LA, left atrium; LV, left ventricle; PA, pulmonary artery; PV, left ventricle.

(legend continued on next page)

pigments. Although a number of tissue-clearing methods (BABB, THF-DBE, Sca*l*e, SeeDB, *Clear*^{T}) and protocols (3DISCO, CLARITY, PACT-PARS) have been developed, the importance of tissue decolorization may have been overlooked because these methods were mainly optimized for pigment-less brains and hence focused on the adjustment of mismatched RIs (Becker et al., 2012; Chung et al., 2013; Dodt et al., 2007; Ertürk et al., 2012; Hama et al., 2011; Ke et al., 2013; Kuwajima et al., 2013; Yang et al., 2014). However, when applied to whole body, thick tissues may block photons in the visible region due to the absorbance by endogenous pigments. Animals genetically lacking endogenous pigments have see-through bodies such as the medaka, in which superficial organs can be visualized across body surfaces (Ohshima et al., 2013; Wakamatsu et al., 2001). Therefore, to visualize detailed structures in deeper organs by single-photon excitation microscopy, we must overcome the light absorbance by heme, which is one of the most abundant chromophores in the body (Faber et al., 2003; Weissleder, 2001), in addition to light scattering by mismatched RIs. In the previous study, we demonstrated that aminoalcohols in CUBIC cocktails significantly enhanced whole-brain clearing via homogenizing mismatched RIs (Susaki et al., 2014). In this study, we discovered another unexpected chemical nature of aminoalcohols: tissue decolorization. Q bands (~500–700 nm) of heme in erythrocytes treated with aminoalcohol #10 or CUBIC-1 reagent were considerably changed from those of hemoglobin-bound form (Figure 1C). These results imply that the aminoalcohols could be tightly bound to heme porphyrin instead of oxygen and histidine in hemoglobin, which may facilitate heme release and explain the unexpected expansion of the effective pH window for heme release. Additionally, the buffering capability of aminoalcohol #10 in moderately basic conditions should also contribute to the decolorizing performance (Figures 1E and 1F). Importantly, the buffering capability of aminoalcohol #10 is exerted in moderately basic conditions, which is the optimal pH range for the fluorescence signal from GFP-related fluorescence proteins (Haupts et al., 1998). In fact, treatment of individual organs by CUBIC reagents led to much higher transmittance in the visible region than that of organs treated by other reagents (Figure S2B), whereas CUBIC reagents could preserve the fluorescence signal from various kinds of GFP-related fluorescence proteins (Figure S6).

CUBIC Enables Whole-Body Clearing and Whole-Body Imaging with Single-Cell Resolution

In this study, we demonstrated that the CB-Perfusion protocol, which enabled both tissue decolorization and adjustment of mismatched RIs, achieved the visualization of chest and abdominal backbones through internal organs as well as bones of limbs through soft tissues from both ventral and dorsal sides of the adult and infant mice (Figure 2B). We also demonstrated that the CB-Perfusion protocol achieved whole-body (Figure 3) and whole-organ (Figure 4) imaging with single-cell resolution. We note that CUBIC is also compatible with other protocols. For example, we previously demonstrated that CUBIC reagents are applicable to clear acrylamide-gel-embedded samples prepared according to the CLARITY protocol (Susaki et al., 2014). Therefore, we expect that another CLARITY-inspired protocol, PARS, can be a useful fixation method for the endogenous molecules before CUBIC treatment. Because the PARS method is based on the intracardiac circulation of detergents (Yang et al., 2014), similar to the CB-Perfusion protocol, additional circulation of decolorizing medium (CUBIC cocktails) might increase transparency in the PARS method.

There are still some fundamental technical challenges remaining in both whole-body clearing and whole-body imaging. Although in this study CUBIC cocktails facilitated the transparency of internal organs and soft tissues for the infant and adult mice body by tissue decolorization, these clearing reagents are not effective for bones. Conventionally, decalcification is rendered by the continuous immersion of acids (such as formic acids) or chelating agents (such as EDTA) (Mack et al., 2014). Therefore, the combination of effective chelating solution with CUBIC cocktails might provide further decalcification properties for the current chemical cocktail. Alternatively, larger chemical screening for tissue-clearing reagents (Susaki et al., 2014) could afford a series of alternative candidates for tissue- and/or bone-clearing reagents that may provide more clearing potency with fewer drawbacks. In whole-body imaging, further optimization of LSFM setup is also required to seamlessly capture whole-body images of adult mice. Because the movable range of the stage was limited in the currently existing LSFM setup, the largest field of view corresponded to a P1 mouse. An entire adult mouse is much thicker, wider, and longer than the body of an infant mouse. Thus, extension of focus depth in the illuminated light-sheet, expansion of the movable range of the stage, and seamless tiling of the reconstituted images should be improved in future LSFM setups.

CUBIC Is Applicable to 3D Pathology, Anatomy, and Immunohistochemistry

Whole-body and whole-organ imaging with single-cell resolution will play a fundamental role in achieving 3D studies of pathology and anatomy, which will aid in systems-level elucidation of cellular mechanisms underlying abnormal and normal body states. In this study, we applied CUBIC-based whole-body clearing and LSFM-based whole-organ/whole-body imaging to achieve 3D pathology, anatomy, and immunohistochemistry.

(B) Structural identification of the bronchial tree (light blue) and peripheral alveoli (green) in the lung. Contiguous mKate2 signals with moderate intensity within or on the edge of the lung were extracted as the bronchial tree or alveoli, distinguished by their values of surface area.
(C) Structural identification of renal cortex, medulla, and pelvis in the kidney. High-intensity signals in SYTO 16 channel and high- or low-intensity signals of mKate2 channel were extracted as the cortex, medulla, or pelvis, respectively.
(D) Structural identification of vessels in the liver. Two types of vascular structures (with or without high-concentrated nuclei signals around the vessel) were distinguished. Contiguous SYTO 16 signals with low or moderate intensity were extracted as the portal vein (blue) or wall of the hepatic artery (red), respectively. In mKate2 channel, similar contiguous signals with low intensity were also extracted and merged with the hepatic artery structure (red).
See also Figures S7 and S8.

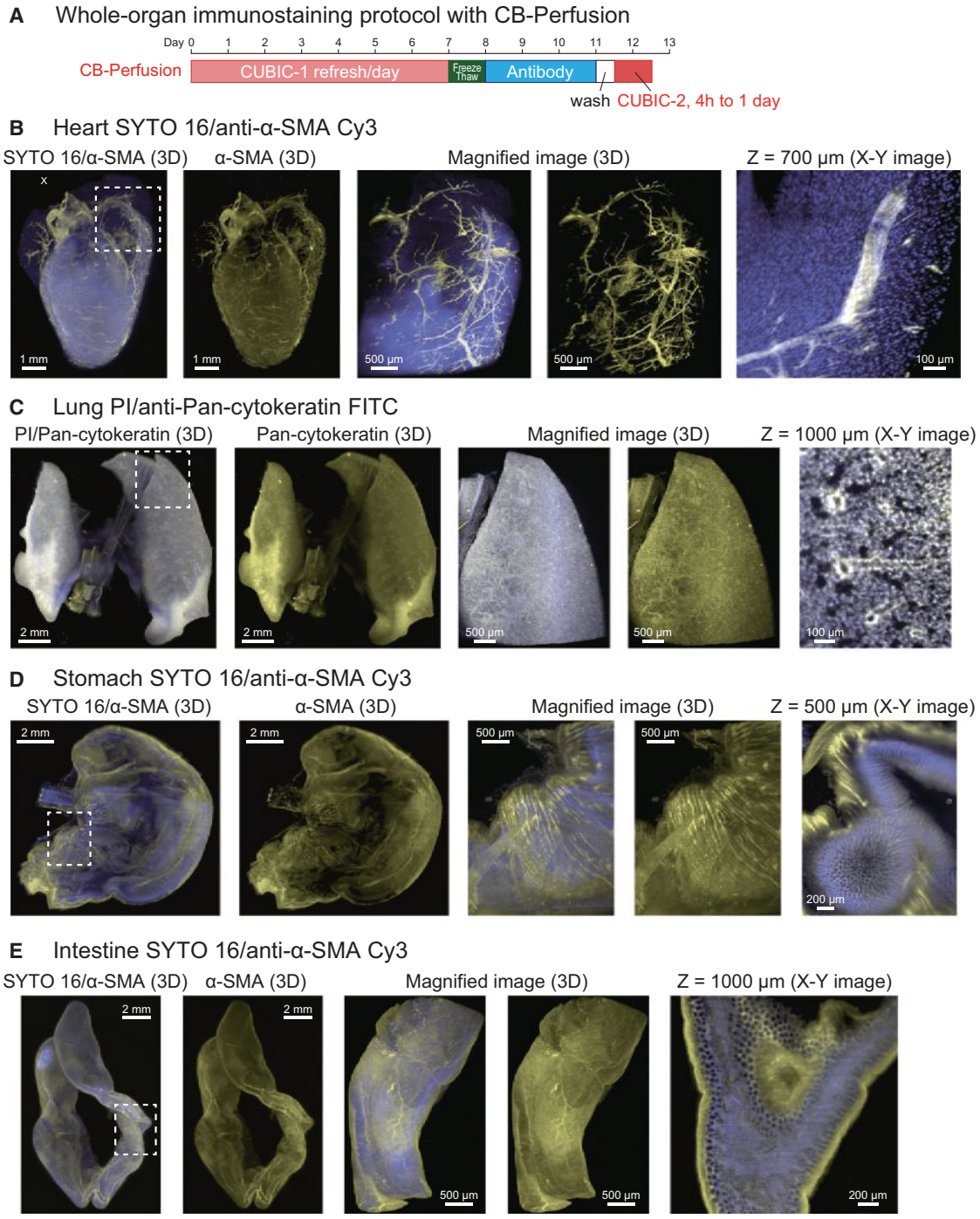

Figure 7. CUBIC Is Applicable to the 3D Immunohistochemistry of Various Organs

(A) CUBIC protocol for 3D immunohistochemistry (3D-IHC) of CB-perfused various organs. The reconstituted 3D and section images of a SYTO 16- or PI-stained heart (B), lung (C), stomach (D), and intestine (E) from C57BL/6N mouse (11-week-old) immunostained with Cy3-conjugated anti-α-SMA for heart, stomach, and intestine or FITC-conjugated anti-pan cytokeratin for lung were acquired with LSFM. Magnified 3D images and raw X-Y section images are at the indicated positions.

As a model case study, we analyzed entire pancreases in diabetic and normal mice to reveal the volume distribution of LIs between diabetic and healthy mice. As expected, the total number and volume distribution of LIs were significantly different between normal and diabetic mice (Figure 5). We also note that larger LIs tend to be localized along pancreatic ducts and

are more susceptible to β cell impairment induced by STZ administration.

The application of whole-body and whole-organ imaging techniques is not limited to the pancreas but can be extended to other organs. In this study, we demonstrated that 3D anatomy is feasible for other medically important structures from whole-organ (Figure 6) or whole-body images (Figure S8) such as coronary vessels in the heart; the bronchial tree in the lungs; glomeruli distributed through the cortex and the medullary rays in the kidney, artery, and vein networks of the liver; and villi in the intestine. Although such medically important structures are annotated manually in this study, automated or semi-automated extraction of medically important anatomical structures will facilitate 3D pathology and anatomy in future. As a pilot study, we attempted and succeeded in semi-automated extraction of medically important anatomical structures in abdominal and chest organs such as LIs in the pancreas (Figure 5C) and the coronary vessels in the heart (Figure S7B). We also note that CUBIC application is not limited to transgenic mice with fluorescence reporter (Figure 7). Because 3D-IHC is compatible with CUBIC, this whole-organ and whole-body clearing technique can be widely applied to various mice without fluorescence reporter. When combined with informatics as well as immunohistochemistry, CUBIC will thus contribute to the systems-level elucidation of cellular mechanisms underlying the generation and progression of diseases especially with stochastic and proliferative processes such as autoimmune diseases. New research fields such as organism-level systems biology based on whole-body imaging with single-cell resolution lie ahead.

EXPERIMENTAL PROCEDURES

Additional details are available in the Extended Experimental Procedures.

Decolorization of the Blood by Aminoalcohols in CUBIC Cocktails

PFA-fixed blood was thoroughly mixed with each chemical, and resultant pellet and supernatant were imaged by bright-field microscopy. For taking visible spectra data, erythrocytes were mixed with each chemical and incubated at 37°C overnight. The mixtures and supernatant were diluted 10-fold with each chemical. The visible spectra of samples was recorded by UV/Vis spectrometer (JASCO, V-550, Japan). In the decoloring capacity test, the mixtures of erythrocytes and each chemical with different mixing ratios (erythrocyte/chemical = 0.01 to 0.20) were incubated at 37°C overnight. Bright-field images of these samples were captured. In the pH dependency of heme release, erythrocytes were mixed with each chemical and incubated at 37°C for 1 hr. The OD575 and OD600 values of the mixtures were measured with the PowerWave XS and the attached operation software (Bio-Tek).

Mice

The *β-actin-mKate2* knockin mouse (β-actin-CAG-nuc-3 × mKate2) strain was established in our laboratory. We also used the R26-H2B-EGFP KI (CDB0238K) (Abe et al., 2011), Thy1-YFP-H Tg (Feng et al., 2000), C57BL/6-Tg (CAG-EGFP) (Okabe et al., 1997), BALB/cAJcl-*nu/nu*, and wild-type C57BL/6N mouse strains. We fed DietGel Recovery (LSG Corporation, 72-06-5022, Japan) to mice for imaging the intestine. Diabetes was induced in male C57BL/6N mice at 8 weeks by a single intraperitoneal administration of saline or 10 mg/ml streptozotocin (total 200 mg/kg, Wako Pure Chemical Industries, 197-15153) at day 0. Blood glucose values were measured by a blood glucose monitor (GLUCOCARD G Black; ARKRAY) after fasting for 6 hr at day 0 and 4. Mice with blood glucose levels over 300 mg/dl (n = 5) at day 4 and saline-administered mice (n = 4) were used for clearing with CUBIC perfusion and PI staining. All experimental procedures and housing conditions were approved by the Animal Care and Use Committee of Graduate School of Medicine, the University of Tokyo or by the Animal Care and Use Committee of the RIKEN Kobe Institute, and all of the animals were cared for and treated humanely in accordance with the Institutional Guidelines for Experiments Using Animals.

The CUBIC Protocol and Other Clearing Methods

Two CUBIC reagents were prepared as previously reported (Susaki et al., 2014). For preparation of CUBIC-treated (non-perfused) samples, the fixed organs were immersed in CUBIC-1 reagent for 5 days and were further immersed in CUBIC-2 reagent. To make CUBIC-1 reagent penetrate throughout the whole body, we also performed the CB-Perfusion protocol. The anesthetized adult mouse was perfused with 10 ml of 10 U/ml of heparin in PBS, 150 ml of 4% (w/v) PFA in PBS, 20 ml of PBS (to wash out PFA), and 20 ml of 50% (v/v) CUBIC-1 reagent (1: 1 mixture of water: CUBIC-1) in this order via left ventricle of the heart. (The protocol was slightly modified for infant mice.) The resulted whole animal or excised organs were continuously immersed in CUBIC-1 reagent for 5 days to several weeks. Organs were further immersed in CUBIC-2 reagent. These samples were stained with nucleic acid stains PI (Life Technologies, P21493) or SYTO 16 (Life Technologies, S7578), when indicated. We also performed SeeDB standard protocol (Ke et al., 2013) and Sca*l*eA2 and Sca*l*eB4 protocol (Hama et al., 2011). Light transmittance was measured with an integrating sphere (Spectral Haze Meter SH 7000, Nippon Denshoku Industries).

Microscopy and Image Analysis

Whole-body and organ fluorescence images were acquired with light-sheet fluorescence microscopy (LSFM) (Ultramicroscope, LaVision BioTec, Germany) as reported previously (Dodt et al., 2007; Susaki et al., 2014). All raw image data were collected in a lossless 16-bit TIFF format. 3D-rendered images were visualized, captured, and analyzed with Imaris software (version 7.6.4 and 7.7.1, Bitplane). Blind 3D deconvolution for a set of our LSFM z stack images was performed with software AutoQuant X3 (Media Cybernetics). Anatomical structures and LI quantification were performed with surface analysis of Imaris software. Automated detections of anatomical structure were performed with Fiji (Schindelin et al., 2012) and using a filtering method implemented in C++.

SUPPLEMENTAL INFORMATION

Supplemental Information includes Extended Experimental Procedures, eight figures, one table, and six movies and can be found with this article online at http://dx.doi.org/10.1016/j.cell.2014.10.034.

AUTHOR CONTRIBUTIONS

H.R.U., K.T., and S.I.K. designed the study. K.T., S.I.K., and T.Q.S. performed most of the experiments. E.A.S. developed CB-Perfusion protocol. D.P. contributed to the image informatics. M.U.-T. and H.U. produced β-actin-nuc-3 × mKate2 KI mice. All authors discussed the results and commented on the manuscript text.

ACKNOWLEDGMENTS

We thank the lab members at RIKEN CDB, QBiC, and The University of Tokyo, in particular, H. Yukinaga, J. Hara, J. Yoshida, C. Imai, and Y. Niwa for their kind help in preparing the materials; A. Millius for reviewing and editing the manuscript; K. Matsumoto for helpful suggestions in developing the CB-Perfusion protocol; Y. Abe, T. Sengoku, and S. Kondo for their kind help in developing the CB-Perfusion protocol and transmittance evaluation; and S. Shoi for his kind help in statistical analysis. We also thank T. Abe and H. Kiyonari for providing materials for targeting vectors and R26-H2B EGFP mice; LARGE, RIKEN CDB for housing the mice; D. Asanuma and K. Hirose for their kind help in measuring visible spectra; H. Sekiya, K. Kanemaru, D. Ino, J. Suzuki, K. Miyazono, S. Ehata, K. Takahashi, H. Takayanagi, S. Sawa, G. Matteo, Y. Mori, and Y. Yoshioka for their kind comments and suggestions; and Media

Cybernetics for supporting the usage of AutoQuant X3. This work was supported by the Program for Innovative Cell Biology by Innovative Technology and the Brain Mapping by Integrated Neurotechnologies for Disease Studies (Brain/MINDS) from the Ministry of Education, Culture, Sports, Science and Technology (MEXT) of Japan, a Grant-in-Aid for Scientific Research (S) (grant no. 25221004), a Grant-in-Aid for Scientific Research on Innovative Areas (grant no. 23115006), and a Grant-in-Aid JSPS Fellows (grant no. 26-1180) from MEXT/Japan Society for the Promotion of Science (JSPS), the strategic programs for R&D (President's discretionary fund) of RIKEN, an intramural Grant-in-Aid from the RIKEN Center for Developmental Biology and RIKEN Quantitative Biology Center, a grant from Core Research for Evolutional Science and Technology (CREST), Japan Science and Technology Agency (JST), a Grant-in-Aid from Japan Foundation for Applied Enzymology, a Grant-in-Aid from the Shimabara Science Promotion Foundation, and by the RIKEN Foreign Postdoctoral Researcher Program.

Received: August 18, 2014
Revised: September 30, 2014
Accepted: October 11, 2014
Published: November 6, 2014

REFERENCES

Abe, T., Kiyonari, H., Shioi, G., Inoue, K.I., Nakao, K., Aizawa, S., and Fujimori, T. (2011). Establishment of conditional reporter mouse lines at ROSA26 locus for live cell imaging. Genesis *49*, 579–590.

Alanentalo, T., Asayesh, A., Morrison, H., Lorén, C.E., Holmberg, D., Sharpe, J., and Ahlgren, U. (2007). Tomographic molecular imaging and 3D quantification within adult mouse organs. Nat. Methods *4*, 31–33.

Alnuami, A.A., Zeedi, B., Qadri, S.M., and Ashraf, S.S. (2008). Oxyradical-induced GFP damage and loss of fluorescence. Int. J. Biol. Macromol. *43*, 182–186.

Becker, K., Jährling, N., Saghafi, S., Weiler, R., and Dodt, H.U. (2012). Chemical clearing and dehydration of GFP expressing mouse brains. PLoS ONE *7*, e33916.

Chudakov, D.M., Matz, M.V., Lukyanov, S., and Lukyanov, K.A. (2010). Fluorescent proteins and their applications in imaging living cells and tissues. Physiol. Rev. *90*, 1103–1163.

Chung, K., Wallace, J., Kim, S.Y., Kalyanasundaram, S., Andalman, A.S., Davidson, T.J., Mirzabekov, J.J., Zalocusky, K.A., Mattis, J., Denisin, A.K., et al. (2013). Structural and molecular interrogation of intact biological systems. Nature *497*, 332–337.

Dodt, H.U., Leischner, U., Schierloh, A., Jährling, N., Mauch, C.P., Deininger, K., Deussing, J.M., Eder, M., Zieglgänsberger, W., and Becker, K. (2007). Ultramicroscopy: three-dimensional visualization of neuronal networks in the whole mouse brain. Nat. Methods *4*, 331–336.

Ertürk, A., Becker, K., Jährling, N., Mauch, C.P., Hojer, C.D., Egen, J.G., Hellal, F., Bradke, F., Sheng, M., and Dodt, H.U. (2012). Three-dimensional imaging of solvent-cleared organs using 3DISCO. Nat. Protoc. *7*, 1983–1995.

Faber, D.J., Mik, E.G., Aalders, M.C., and van Leeuwen, T.G. (2003). Light absorption of (oxy-)hemoglobin assessed by spectroscopic optical coherence tomography. Opt. Lett. *28*, 1436–1438.

Feng, G.P., Mellor, R.H., Bernstein, M., Keller-Peck, C., Nguyen, Q.T., Wallace, M., Nerbonne, J.M., Lichtman, J.W., and Sanes, J.R. (2000). Imaging neuronal subsets in transgenic mice expressing multiple spectral variants of GFP. Neuron *28*, 41–51.

Hama, H., Kurokawa, H., Kawano, H., Ando, R., Shimogori, T., Noda, H., Fukami, K., Sakaue-Sawano, A., and Miyawaki, A. (2011). Sca*l*e: a chemical approach for fluorescence imaging and reconstruction of transparent mouse brain. Nat. Neurosci. *14*, 1481–1488.

Haupts, U., Maiti, S., Schwille, P., and Webb, W.W. (1998). Dynamics of fluorescence fluctuations in green fluorescent protein observed by fluorescence correlation spectroscopy. Proc. Natl. Acad. Sci. USA *95*, 13573–13578.

Ke, M.T., Fujimoto, S., and Imai, T. (2013). SeeDB: a simple and morphology-preserving optical clearing agent for neuronal circuit reconstruction. Nat. Neurosci. *16*, 1154–1161.

Keller, P.J., and Dodt, H.U. (2012). Light sheet microscopy of living or cleared specimens. Curr. Opin. Neurobiol. *22*, 138–143.

King, A.J.F. (2012). The use of animal models in diabetes research. Br. J. Pharmacol. *166*, 877–894.

Kristinsson, H.G., and Hultin, H.O. (2004). Changes in trout hemoglobin conformations and solubility after exposure to acid and alkali pH. J. Agric. Food Chem. *52*, 3633–3643.

Kuwajima, T., Sitko, A.A., Bhansali, P., Jurgens, C., Guido, W., and Mason, C. (2013). *Clear^T*: a detergent- and solvent-free clearing method for neuronal and non-neuronal tissue. Development *140*, 1364–1368.

Mack, S.A., Maltby, K.M., and Hilton, M.J. (2014). Demineralized murine skeletal histology. Methods Mol. Biol. *1130*, 165–183.

Niwa, H., Yamamura, K., and Miyazaki, J. (1991). Efficient selection for high-expression transfectants with a novel eukaryotic vector. Gene *108*, 193–199.

Ohshima, A., Morimura, N., Matsumoto, C., Hiraga, A., Komine, R., Kimura, T., Naruse, K., and Fukamachi, S. (2013). Effects of body-color mutations on vitality: an attempt to establish easy-to-breed see-through medaka strains by outcrossing. G3 *3*, 1577–1585.

Okabe, M., Ikawa, M., Kominami, K., Nakanishi, T., and Nishimune, Y. (1997). 'Green mice' as a source of ubiquitous green cells. FEBS Lett. *407*, 313–319.

Schindelin, J., Arganda-Carreras, I., Frise, E., Kaynig, V., Longair, M., Pietzsch, T., Preibisch, S., Rueden, C., Saalfeld, S., Schmid, B., et al. (2012). Fiji: an open-source platform for biological-image analysis. Nat. Methods *9*, 676–682.

Shcherbo, D., Murphy, C.S., Ermakova, G.V., Solovieva, E.A., Chepurnykh, T.V., Shcheglov, A.S., Verkhusha, V.V., Pletnev, V.Z., Hazelwood, K.L., Roche, P.M., et al. (2009). Far-red fluorescent tags for protein imaging in living tissues. Biochem. J. *418*, 567–574.

Spalteholz, W. (1914). Über das Durchsichtigmachen von menschlichen und tierischen Präparaten (Leipzig: S. Hierzel).

Steinke, H., and Wolff, W. (2001). A modified Spalteholz technique with preservation of the histology. Ann. Anat. *183*, 91–95.

Susaki, E.A., Tainaka, K., Perrin, D., Kishino, F., Tawara, T., Watanabe, T.M., Yokoyama, C., Onoe, H., Eguchi, M., Yamaguchi, S., et al. (2014). Whole-brain imaging with single-cell resolution using chemical cocktails and computational analysis. Cell *157*, 726–739.

Tanaka, K.F., Matsui, K., Sasaki, T., Sano, H., Sugio, S., Fan, K., Hen, R., Nakai, J., Yanagawa, Y., Hasuwa, H., et al. (2012). Expanding the repertoire of optogenetically targeted cells with an enhanced gene expression system. Cell Rep. *2*, 397–406.

Teale, F.W. (1959). Cleavage of the haem-protein link by acid methylethylketone. Biochim. Biophys. Acta *35*, 543.

Tomer, R., Khairy, K., and Keller, P.J. (2011). Shedding light on the system: studying embryonic development with light sheet microscopy. Curr. Opin. Genet. Dev. *21*, 558–565.

Tomer, R., Ye, L., Hsueh, B., and Deisseroth, K. (2014). Advanced CLARITY for rapid and high-resolution imaging of intact tissues. Nat. Protoc. *9*, 1682–1697.

Wakamatsu, Y., Pristyazhnyuk, S., Kinoshita, M., Tanaka, M., and Ozato, K. (2001). The see-through medaka: a fish model that is transparent throughout life. Proc. Natl. Acad. Sci. USA *98*, 10046–10050.

Weissleder, R. (2001). A clearer vision for *in vivo* imaging. Nat. Biotechnol. *19*, 316–317.

Xiang, Y.Y., Wang, S., Liu, M., Hirota, J.A., Li, J., Ju, W., Fan, Y., Kelly, M.M., Ye, B., Orser, B., et al. (2007). A GABAergic system in airway epithelium is essential for mucus overproduction in asthma. Nat. Med. *13*, 862–867.

Yang, B., Treweek, J.B., Kulkarni, R.P., Deverman, B.E., Chen, C.K., Lubeck, E., Shah, S., Cai, L., and Gradinaru, V. (2014). Single-cell phenotyping within transparent intact tissue through whole-body clearing. Cell *158*, 945–958.

A smarter approach to FLUORESCENCE IMAGING

Introducing the ZOE™ Fluorescent Cell Imager.
No darkroom, no training, no overwhelming user interface.

Combining brightfield capabilities with multichannel fluorescence, this cell imager is both affordable and easy to use — your perfect solution for routine cell culture and imaging applications.

Learn more at **bio-rad.com/info/newzoe**

BIO-RAD

Introducing

bio-techne®

HIGHEST QUALITY PRODUCT PORTFOLIO

TRUSTED GLOBAL BRANDS

R&D systems

NOVUS BIOLOGICALS™

TOCRIS

bio-techne®

LEARN MORE bio-techne.com/launch

Building Innovation Opportunities

bio-techne.com	North America	Europe • Middle East • Africa	China	Rest of World
info@bio-techne.com techsupport@bio-techne.com	TEL 800 343 7475	TEL +44 (0)1235 529449	info.cn@bio-techne.com TEL +86 (21) 52380373	bio-techne.com/find-us/distributors TEL +1 612 379 2956

Bio-Techne is a trading name for R&D Systems